UNIVERSITY OF BIRMINGHAM

RELATIONS BETWEEN FAULT SURFACE MORPHOLOGY AND VOLUME STRUCTURE: 3-D SEISMIC ATTRIBUTE ANALYSIS DEEPWATER NIGER DELTA FOLD AND THRUST BELT

By

Babangida Wushishi Jibrin

A thesis submitted to the University of Birmingham for the degree of

DOCTOR OF PHILOSOPHY

School of Geography, Earth and Environmental Sciences, University of Birmingham, Edgbaston, Birmingham, B15 2TT

June, 2011

Abstract

Thrust faults in deepwater Niger Delta are well imaged in the PGS Joint Development Zone (JDZ) three-dimensional seismic data and the cross sectional geometries of these structures have previously been described. However studies have shown that faults exhibit complex geometries that are often highly simplified and these techniques may not be sufficient to highlight the spatial variation of fault surface topography and the complex relationship with the volume surrounding the faults. *The main contribution of this thesis to structural geology are novel methods that uses structural attribute plots of thrust faults and slices of seismic attribute data sampled parallel to the faults to investigate links between fault surface topography and the structure of the volumes adjacent to the faults*.

Firstly, a seismic attribute extraction and image enhancement technique was applied to the seismic amplitude data to guide the detailed interpretation of the cross sectional geometry of the faults. Traces of the faults were then used to calculate surface and structural attribute models of the faults. Curvature plots of sixteen faults show that thrust faults in deepwater Niger Delta exhibit corrugations on a range of wavelength and amplitude. The corrugations are characterized by large-scale anticlastic and synclastic geometries parallel to fault transport direction suggesting that most of the faults possess non-developable geometries.

Secondly, the structure of the volumes in the immediate vicinity of the faults was investigated using slices of seismic attribute data sampled parallel and adjacent to the thirteen faults. Analysis of slices sampled close to the faults show a highly variable pattern of disruption across the faults. In half of the faults the hanging wall is more disrupted than the footwall, while in the other half the footwall is more disrupted than the hanging wall, implying that

thrust zones exhibit complex geometries that may have a significant impact on thrust zone architecture that existing models of thrust zone geometry have yet to address.

Finally, potential links between fault surface morphology and the structure of the volumes adjacent to the faults was investigated. Results suggest that disruptions near fault surfaces may be related to discrete zones of intense fault surface maximum curvature, anomalous surface gradient and change in pattern of anticlastic and synclastic fault Gaussian surface curvature in the fault transport direction. No significant wall rock disruption was observed where fault surface curvature is planar.

Dedication

This thesis is dedicated to my late father, Alhaji Mohammad Inuwa Jibrin who regretfully passed away a week before the commencement of the PhD. The work is also dedicated to my late brother; Abdul-Rashid Jibrin and his late wives, my mother; Hajiya Maimuna Jibrin, my step-mother; Hajiya Hussaina Jibrin, my mother-in-law; Mrs. Ladi Shambo, my wife; Hassana Jibrin, my children; Umar-Farooq, Hamza and Ali and finally my brothers and sisters.

Acknowledgements

I thank the Petroleum Technology Development Fund (PTDF) for providing funding for the PhD under the flagship of the Overseas Scholarship Scheme (OSS). I am particularly grateful to the staff of training department at PTDF especially Mallam Aminu Galadima and Mr. Garba Bako. My profound gratitude goes to Professor Tim Reston – my supervisor, for his guidance, insight and support throughout the project. His knowledge of the research theme and guidance are truly invaluable.

I am grateful to Dr. Jonathan P. Turner - my first supervisor for setting up the project and ensuring that the thesis was on the right track despite leaving the University mid-way into the research. His wealth of knowledge in structural geology has helped a lot in the successful completion of the thesis. I wish to thank Professor Graham K. Westbrook who took over supervision from Jonathan for ensuring that the methods used in testing the hypothesis were thoroughly explored. His sound knowledge of seismology and seismic attribute analysis was invaluable to this thesis. I thank Dr. Jason Hilton for his words of encouragement and opinions on what is expected in a PhD thesis.

I wish to thank Petroleum Geo-Services (PGS) for providing the seismic data for this thesis. I thank Mr David Pratt for facilitating the release of the data and giving me the opportunity to present early results of my research at PGS office in London and the permission to use the data for presentation at the 29th International annual conference of the Nigerian Association of Petroleum Explorationists (NAPE) in December 2009, and the annual meeting of the Tectonic Studies Group (TSG) in January 2010.

I thank IHS Inc/Seismic Micro Technology (SMT) for providing *Kingdom* 8.4 used for the stratigraphic and structural interpretation of the seismic data in Chapter Four, dGB Earth

Sciences for donating *OpendTect* software used in volumetric seismic attribute extraction and image enhancement described in Chapter Three and Badleys Geoscience for donating their *TrapTester* software used for fault statistical analysis in Chapter Four, three-dimensional fault surface attribute modelling in Chapter Five and fault slicing in Chapter Six. The software programs were provided free to the University of Birmingham for academic use. I thank Dr. Peter Bretan of Badleys Geoscience for guiding me through *TrapTester* by electronic mail, telephone and during visits to Badley's office in Lincolnshire. I particular wish to thank Dr. Brett Freeman for reviewing early drafts of Chapters Five and Six and for making useful suggestions that improved the quality of the thesis. I thank Mr. Arnaud Huck of dGB Earth Sciences and Dr. Saleh Al-Dossary (Saudi-Aramco) for reviewing early drafts of Chapter Three.

I want to thank my colleagues and friends at the University especially Dr. Chinnan Dikwal, Giuma Reeh, Saleem Mohammed, Sarah King, Waqas Malik, Fred Sam, Ken McDermott, Craig Magee, Paul Anderson, Phil Jardine, Plamen Andreev, Andy Rees, Dr. Leyla Seyfula, Dr. Kate Thatcher and Dr. Nick Schofield for their words of support. I am also grateful to Aruna Mistry, Gretchel Coldicott and Dr. Stephanie Handley-Sidhu for supporting me during the most trying moments of my stay in Birmingham. I am grateful to Dr. Babatunde Anifowose and his family for generously accommodating me during the period of the viva. Finally I wish to thank my wife and children for their understanding, perseverance and support during the period of my long stay away from home.

Table of Contents

List of figures

Chapter One

Chapter Two

Chapter Three

Chapter Four

Chapter Five

Chapter Six

List of Tables

Chapter Two

Chapter Three

Chapter Five

Chapter Six

CHAPTER ONE-INTRODUCTION

1.1 Background

This thesis uses a three-dimensional seismic data of parts of deepwater Niger Delta in the Gulf of Guinea referred to as the Joint Development Zone (JDZ) (Figure 1.1) to describe volume seismic attribute extraction and image enhancement techniques applied to the seismic data. The data was used to investigate the structural and stratigraphic framework of the study area, the three-dimensional structural attribute plots of thrust faults mapped from the data and finally investigate potential implications of fault surface morphology on the structure of the volumes adjacent to the faults.

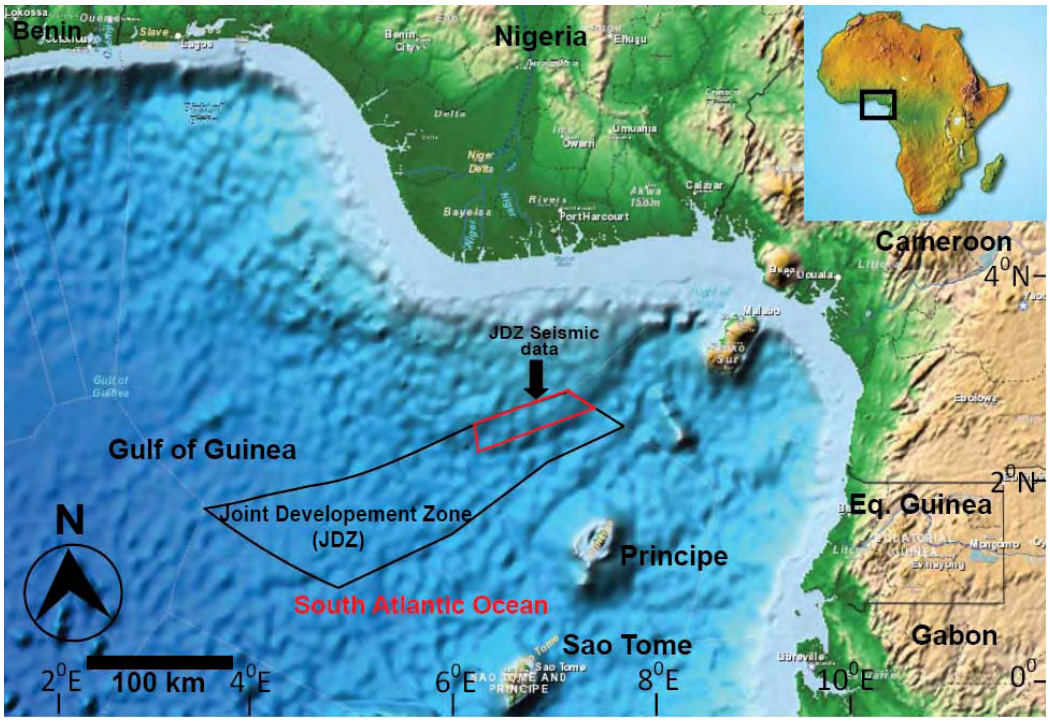

Figure 1.1: Topographic map of the Gulf of Guinea showing the location of the Joint Development Zone (JDZ) and the three-dimensional seismic survey. Image courtesy of National Oceanic and Atmospheric Administration Centre (NOAAC).

1.1.1 Fault geometry

Studies have shown than most faults are corrugated on a spectrum of wavelength, amplitude and scale of observation and examples of corrugations have been described in various tectonic settings (e.g. Jones *et al*. 2009; Resor & Meer, 2009; Jackson & McKenzie, 1999; Wright, 2008; Neetham *et al*. 1996; Abe *et al*. 2010; Carena & Suppe, 2002; van Gent *et al*. 2010; Dunham *et al*. 2011; Kaven & Pollard, 2010; Lohr *et al*. 2008; Prapasanabon & Pigott, 2008; Power *et al*. 1987; Scholz, 1990). Unlike fault roughness, curvature is an inherent three-dimensional property of most faults and a useful attribute in describing fault surface topography (e.g. Caladine, 1983; Wright, 2008; Jones *et al*. 2009).

Data used for analyzing fault geometry are often two-dimensional (e.g. laser-scans and seismic data) and where three-dimensional seismic data are available, the geometry of faults is in most cases investigated in two-dimensional cross sections. To date, most of the knowledge regarding fault surface geometry is predominantly from field outcrop (e.g. Wright, 2008; Jones *et al*. 2009; Resor & Meer, 2009; Jackson & McKenzie, 1999; Candela *et al*. 2009). However, two-dimensional analogue models of listric normal faults (e.g. McClay & Ellis, 1987; Yamada & McClay, 2003a; Yamada & McClay, 2003b), few models of normal faults mapped from seismic data (e.g. Wright, 2008; Lohr *et al*. 2009; Neetham *et al*. 1996; Marchal *et al*. 2003) and a thrust fault modelled using earthquake aftershock data (Carena & Suppe, 2002) have also been used to investigate the geometry of faults.

1.1.2 Structure of fault zones and links with fault surface geometry

In the past, analogue models have been used to describe the internal structure across listric normal faults with emphasis on investigating hanging wall deformation. Most of the models assume that the footwall is passive while the hanging wall is deformed (e.g. Yamada & McClay, 2003a; Yamada & McClay, 2003b). On the other hand, the pattern of deformation across natural thrust faults in deepwater Niger Delta is still poorly understood. Although the structure of outcrop fault zones has been investigated in the past (e.g. Kim & Sanderson, 2005; Gudmundsson & Geyer, 2006; Shipton & Cowie, 2001; Hausegger *et al*. 2009; Childs *et al*. 2009; Kim *et al*. 2004; Berg *et al*. 2005; Resor & Meer, 2009), mapping fault zones using seismic data is difficult and hardly attempted. This may be largely due to poor seismic imaging especially in the footwall regions of most faults and resolution limits of seismic data (e.g. Ajakaiye & Bally, 2002; Morley, 2003). A good understanding of the internal structure of subsurface fault zones can help in assessing the variability of deformational styles across faults, predicting the structural properties in the immediate vicinity of faults and the pattern of hydrocarbon migration (e.g., Faulkner *et al.* 2003; Woodcock *et al*. 2007; Iacopini & Butler, 2011; Kim *et al.* 2004; Basford & Paton, 2011).

The influence of surface curvature on the deformation of geological surfaces has been a topical issue for many years. Since Lisle's classical analysis of links between the curvature of buckle-folds and intensity of fractures (Lisle, 1994), several authors have used surface curvature to predict strain in outcrop and horizon surfaces mapped from seismic data (e.g. Roberts, 2001; Jones *et al*. 2009; Masafero *et al*. 2007; Wright, 2008; Sigismondi & Soldo, 2003; Samson & Mallet, 1997; Mynatt *et al.* 2006; Bergbauer & Pollard, 2003; Chopra & Marfurt, 2009;). However, instances where

curvature – strain relationships are inconsistent have also been reported (e.g. Keating & Fischer, 2008; Pearce *et al.* 2011).

1.2 Motivation

1.2.1 Structural and stratigraphic framework of deepwater Niger Delta

The Niger Delta is one of the most prolific hydrocarbon basins in the world and consists of a major fold and thrust belt that is presently an exploration hotspot (e.g. Morgan, 2003; Billotti, 2005). Until recently, few good quality three-dimensional seismic data of compression deepwater Niger Delta structural domain are available and little is known about the geologic framework of the distal limits of the southern Niger Delta sedimentary lobe. Earlier investigations of the structural framework of distal Niger Delta were based on reconnaissance seismic lines and the focus was mapping fracture zones, basement and diapiric structures (e.g. Burke, 1972; Mascle, 1976; Emery *et al*. 1975; Damuth, 1994; Merki, 1972).

In recent years, the availability of high resolution seismic data acquired during speculative surveys driven by oil and gas exploration activities is beginning to provide more insight into the structural framework of deepwater Niger Delta especially in the western and central parts (e.g. Corredor *et al*. 2005; 2005 Briggs *et al*. 2006, 2008; Cobbold *et al*. 2009; Bilotti *et al*. 2005; Morgan, 2003; Ajakaiye & Bally, 2002a; Ajakaiye & Bally, 2002b; Maloney *et al*. 2010). In 2002 Petroleum Geo-Services (PGS) acquired a seismic data that images parts of deepwater Niger Delta contractional domain. These data are in addition to seismic attribute volumes calculated on the data in this thesis are for the first time used to investigate the structural and stratigraphic framework of the distal limits of deepwater Niger Delta north of the southern Niger Delta sedimentary lobe (Figure 1).

1.2.2 Fault geometry, structure of fault zones and links between thrust zone structure and fault surface morphology

In the last decade digitally acquired laser-scan data (e.g. Light Detection and Ranging, LiDAR) have been used to describe the surface morphology of exhumed fault surfaces. (e.g. Jones *et al*. 2009; Wright, 2008; Resor & Meer, 2009). Furthermore, qualitative observation of curvature plots of exhumed fault surfaces in Central Greece and Northern Spain and normal faults mapped from Niger Delta seismic data by the Birmingham research group has demonstrated the usefulness of curvature for analyzing the three-dimensional geometry of faults and highlighted close correlation between discrete zones of intense fault surface curvature and fracturing in field outcrops, and correspondence between the pattern of fault surface curvature and areas of intense horizon folding in seismic data. (Wright, 2008).

In deepwater Niger Delta, thrust faults are typical structural features of thin-skinned gravity-driven deformation of thick piles of Tertiary deltaic sediments and several models have been used to explain the cross sectional geometry of the faults (e.g. Corredor *et al*. 2005; Bilotti *et al*. 2005; Rowan *et al*. 2004). However, despite the availability of good quality seismic data ideally suited for analyzing fault geometry and the importance of faults in hydrocarbon exploration, the three-dimensional surface morphology of deepwater Niger Delta thrust faults has yet to be systematically investigated implying that the knowledge of thrust fault geometries in three-dimension is limited. Therefore, in this thesis the surface morphology of thrust faults mapped from deepwater Niger Delta contractional domain is investigated for the first time using structural attributes of the faults (e.g. curvature and gradient).

In the past, potential links between the curvature of geological surfaces and deformation has been limited to the analysis of seismically mapped horizons and field outcrops of buckle-folds (e.g. Lisle, 1994; Roberts, 2001; Chopra *et al*. 2006; Murray, 1968; Thomas *et al*. 1974; Fischer & Wilkerson, 2000; Hennings *et al*. 2000; Masafero *et al*. 2003; Jones *et al*. 2009; Mynatt *et al*. 2007; Rijks & Jauffred, 1991; Schultz-Ela & Yeh, 1992; Thomas *et al*. 1974; Pearce *et al*. 2006; Ghosh & Mitra, 2009). In hydrocarbon exploration and production, some correlation between the curvature of reservoirs, fracture intensity and increased oil productivity have been reported (e.g. Murray, 1968; Hart *et al*. 2002).

However, despite the widespread acceptability of curvature as a useful tool in predicting strain, the fundamental control of fault surface curvature on the structure of volumes in the vicinity of the faults using seismic data has yet to be properly addressed except for cross sectional analysis of analogue and natural listric normal fault geometries and hanging wall deformation (e.g. White *et al*. 1986; Williams *et al*. 1987; McClay & Ellis, 1987; Imber *et al*. 2003; Fossen, 2010).

Recently laser-scan technology has been used to analyse the geometry of outcrop fault surfaces and several workers have used the Arkitsa fault surface in Greece as an example of the usefulness of the tool in investigating outcrop fault surface geometry and related wall rock deformation (e.g. Jones *et al*. 2005; Wright *et al*. 2008; Resor & Meer, 2008; Resor, 2008). However, the extension of these insights to thrust faults mapped from seismic data is still at its infancy. Although attempts have been made in the past to investigate links between fault surface curvature and the curvature of horizons mapped adjacent to the faults, investigating the structure of faults zones using three-dimensional seismic data is difficult and may be due to poor seismic

imaging of thrust zones, resolution limits of seismic data and the paucity of detailed three-dimensional models of natural fault surfaces. However, despite the resolution limits of seismic data, models of fault surfaces derived from noise filtered seismic attribute data can provide reliable three-dimensional representation of fault planes. In addition, volume seismic attributes can be helpful in mapping the structural pattern of the volumes surrounding the faults.

As oil and gas exploration moves to geologically complex frontier basins, the need for detailed and accurate prediction of reservoir properties ahead of drilling expensive wells becomes imperative. Since most oil and gas deposits in the Niger Delta are predominantly found in siliclastic rocks that may be fractured, investigating the relationship between fault shape and wall rock structure is an important step in estimating the structural permeability and effective drainage of hydrocarbon-bearing reservoirs (e.g. Bretan, personal communications; Kim *et al*. 2004). Whilst fault curvature can be constrained at the scale of seismic resolution, it may not be possible to predict the structure of fault zones ahead of drilling oil and gas wells. Therefore, any method that uses the shape of faults to predict the structure of the volumes adjacent to the faults could optimise the cost effectiveness of hydrocarbon exploration and development programs (Turner, personal communications).

1.3 Objectives

The objectives of this thesis are as follows:

- Apply volumetric seismic attribute extraction techniques to the seismic amplitude data to enhance the imaging of discontinuities in the data.

- Describe the stratigraphic and structural framework of the study area using the data.

- Investigate the three-dimensional surface morphology of naturally occurring thrust faults mapped from the data and compare with the geometry of faults mapped in outcrop and seismic data from different tectonic settings.
- Develop new methods of using seismic attribute data to investigate the structure of the volumes in the vicinity of thrust faults.
- Develop new methods of comparing fault surface geometry with the structure of the volumes adjacent to the faults.

1.4 Methodology

Fault slicing, three-dimensional volumetric seismic attribute analysis and visualization are the three key methods used in this thesis to achieve the set out objectives. Fault slicing is a method of resampling three-dimensional seismic data parallel to the interpreted position of a fault plane (Figure 1.2). In fault slicing, a fault surface is first interpreted and used as the reference surface parallel to which seismic data are sampled in the volume and projected as fault surface attributes in depth/two way travel time (Brown *et al*. 1987).

In this thesis, amplitude data that have been processed to highlight structures (similarity and maximum curvature) are used to map fault surfaces in exquisite detail and to investigate the structure of the volumes adjacent to the faults. The fundamental assumption is that the two attributes can be used as reliable measures of small-scale deformation in fault zones (Figure 1.3). Similarity (Tingdahl & de Rooij, 2005) is a form of "coherency" (Bahorich & Farmer, 1995) that expresses the similarity or

otherwise of adjacent seismic traces. A high similarity means the trace segments are similar in waveform and amplitude and a low similarity means they are not similar. The attribute is particularly effective at highlighting faults because discontinuities tend to reduce the similarity of seismic traces.

Volume curvature attributes provide supplementary information to coherency attributes and have been used in the past to predict fracture density in outcrop and horizon surfaces mapped from seismic data on the premise that extreme values of curvature may result in increased intensity of fractures (e.g. Chopra & Marfurt, 2007; Roberts, 2001; Lisle, 1994; Klein *et al*. 2008; Sigismondi & Soldo, 2003; Masafero *et al*. 2003; Blumentritt *et al*. 2006; Helmore *et al*. 2004; Hakami *et al*. 2004; Marfurt, 2006; Haberman *et al*. 2009; Fisk *et al*. 2010; Nissen, 2002).

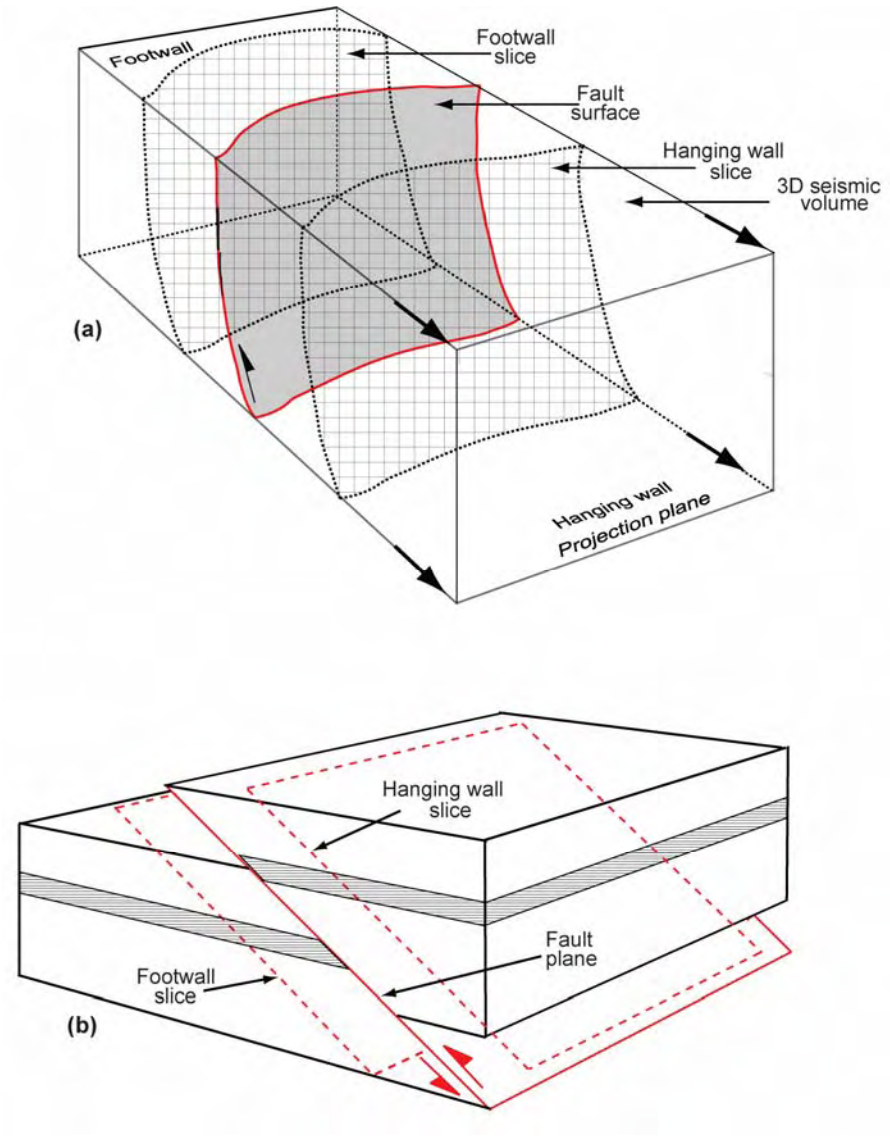

Figure 1.2: Schematic illustrations of sampling three-dimensional data parallel to a fault in the wall-rocks using the concept of fault slicing (a) (Brown *et al*. 1987). In this thesis, seismic data are sampled parallel to interpreted thrust faults (b) to investigate the structure of the volumes adjacent to the faults and analyse potential links between fault shape and wall rock structure.

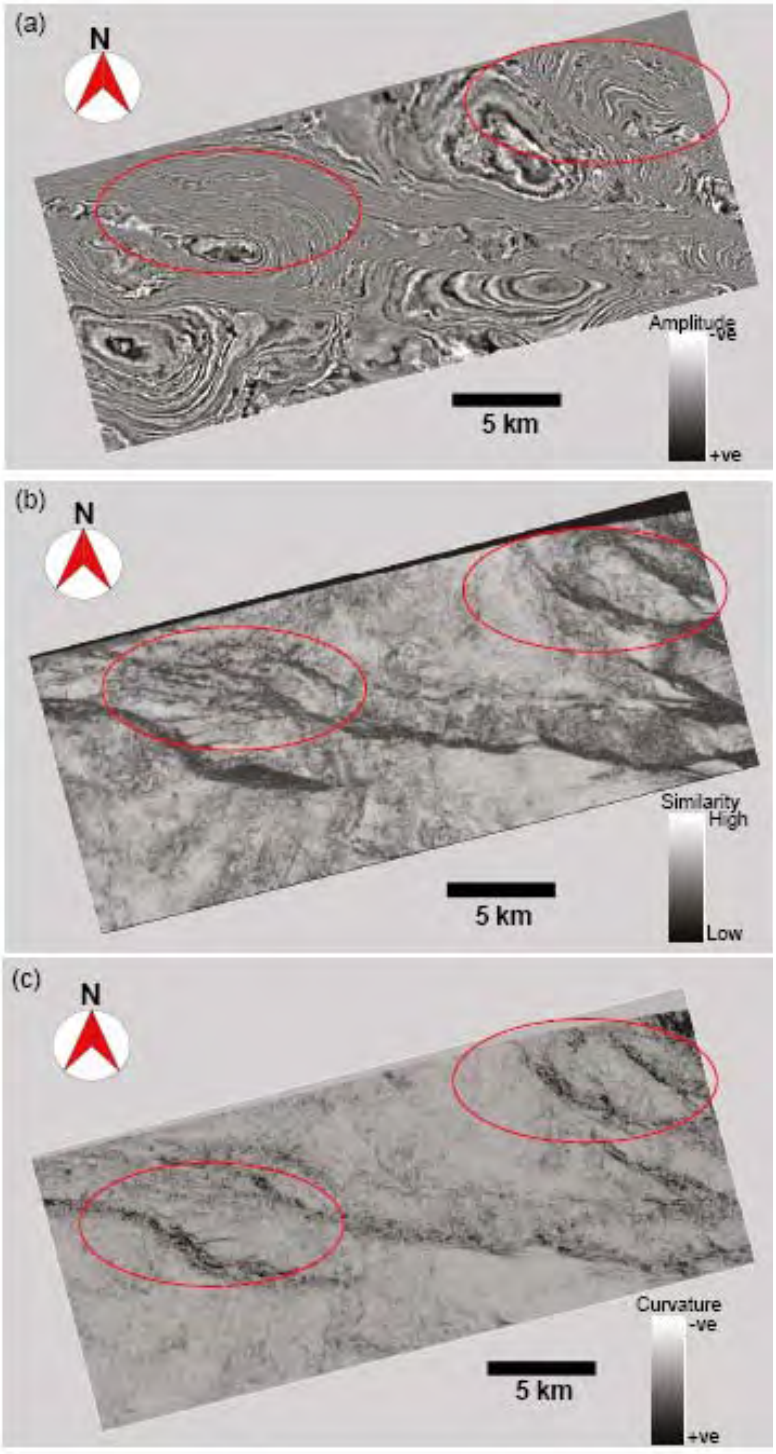

Figure 1.3: Time slices extracted from deepwater Niger Delta seismic attribute volumes illustrating the importance of seismic attributes in seismic interpretation. The areas highlighted indicate zones of low reflectivity in amplitude data (a) seen as discete regions of low similarity (b) and curvature anomalies (c). Note the enhanced resolution and sharpness of the discontinuities in the similarity and curvature data.

1.5 Research questions

The following pertinent questions are proposed to achieve the objectives of this thesis:

- Are thrust faults in deepwater Niger Delta planar or corrugated?
- Can volume seismic attributes be used to map disruptions that may be related to deformation in the volumes adjacent to thrust faults?
- Are disruptions adjacent to thrust fault planes related to fault surface morphology?

1.6 Thesis structure

This section summarises the key points of the remaining six chapters of this thesis.

Chapter Two presents a detailed description of the basic concepts of the theory and geological significance of curvature. The review of the geological significance of curvature to characterize the geometry of geological surfaces and deformation inherent on the surfaces is discussed from two perspectives.

- Review of present methods of characterizing fault surface geometry.
- Review of present methods of predicting wall rock deformation from the geometry of faults. The potential contribution of the methods proposed in this thesis to the present knowledge of fault zone architecture and fault curvature – strain relationships is highlighted.

Chapter Three focuses on seismic attribute extraction and image enhancement techniques applied to the seismic data. The primary aim of the attribute extraction is to produce structurally enhanced data that can guide accurate mapping of fault traces and in investigating the structure of the volumes surrounding the faults. Seismic attribute volumes, time and fault slices sampled from the data have been used to

demonstrate the potential usefulness of the attributes in the context of the objectives of this thesis.

Chapter Four investigates the structural and stratigraphic framework of the study area using the seismic amplitude and similarity volumes. The data was primarily used to map and describe cross sectional geometry of the main discontinuities (thrust faults), the internal seismic reflectivity pattern and the structural pattern across the study area. Regionally extensive horizons were mapped and used to describe present day seabed geomorphology, structural patterns and fault growth/interaction. In addition, horizons adjacent to several faults were tracked and used to produce fault/horizon intersection models used in fault statistical analysis.

Chapter Five presents a workflow for calculating and describing fault surface morphology using structural attributes of the fault surfaces (curvature and gradient) used in investigating the spatial variation of fault surface morphology. The scale-dependence of fault surface curvature was tested and curvature plots of the faults were compared with similar plots of outcrop and fault surfaces mapped from seismic data in different tectonic settings. Finally the potential implication of fault surface topography on the structure of the volumes adjacent to the faults was proposed.

Chapter Six focuses on using novel methods to investigate the seismic structure of the volumes adjacent to thrust faults and potential links with fault surface morphology. Firstly, slices of seismic attribute data sampled in the hanging wall and footwall of thirteen faults were used to investigate the structure of the volumes adjacent to the faults. Secondly, the investigation was constrained by analyzing the seismic structure of reflector units mapped and correlated across four thrust faults. Lastly potential links

between fault surface morphology and disruption in the volumes adjacent to the faults was investigated.

Chapter seven summarizes key findings of the thesis and contribution to structural geology. The limitations of the methods and future work that could improve the results are also highlighted.

CHAPTER TWO-BACKGROUND THEORY AND LITERATURE REVIEW

2.1 Introduction

This chapter reviews the basic theory of surface curvature and summarizes previous research on fault curvature analysis that forms the backdrop for the ideas presented in this thesis. The first part summarizes the theory of surface curvature and the application of the concept of curvature to describe the geometry of geological surfaces and deformation inherently due to the pattern of curvature. This is followed by a section outlining recent methods of using curvature to analyze the geometry of faults and links with wall rock deformation. Finally, potential contributions of the novel ideas used in this thesis to test the hypothesis that fault surface geometry may influence the structure of the volumes surrounding the faults are highlighted.

2.2 Theory and definition of curvature

In two-dimensions, a curve in the *xy*-plane can be thought of as a consecutive string of arcs of a circle characterized by variable centres and radii. The curvature, *k*, at any given point on this curve is the reciprocal of the radius, *R*, of the particular arc segment at that point (Figure 2.1). A sense for both the sign and magnitude of curvature of any curve can be obtained by replacing the radii by vectors normal to the curve. The configuration of normal vectors on the curve illustrates the pattern of curvature such that planar surfaces have zero curvature, antiforms have positive curvature and synforms display negative curvature.

$$k = 1/\mathrm{R} \qquad \text{Equation 2.1}$$

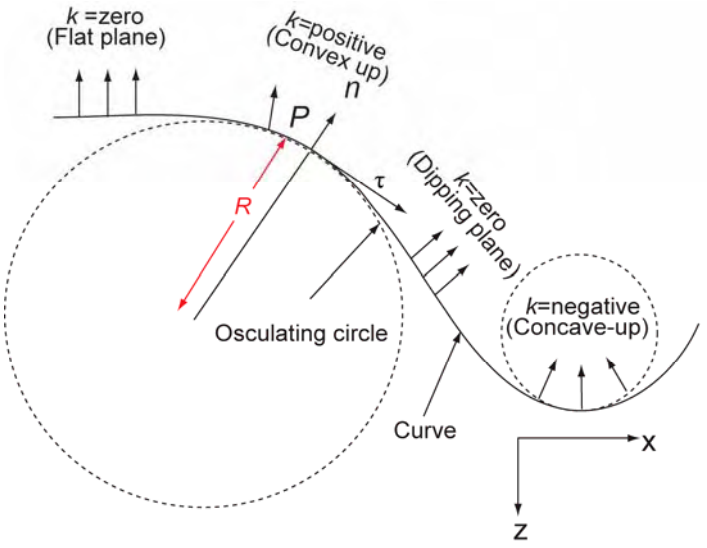

Figure 2.1: Cartoon illustrating the concept of two-dimensional curvature for a point *P* on a curve. The arrows indicate the position of normal vectors *n* to the curve and at a point *P*, the vector tangent to the curve is τ. Curvature is the reciprocal of the radius of the circle tangent to the curve at point *P* (After Roberts, 2001 & Mai, 2010).

In three-dimensions, at any point *P* on a curved surface, there exists many ways of slicing along one of many section planes with orientations such that they contain the surface normal *n* at point *P* (Figure 2.2a). The trace of the surface is usually curved and is called the normal curvature of the surface (k_n). The magnitude of the normal curvature k_n is dependent on the chosen normal section and a change in the magnitude of normal curvature is obtained if the section plane is progressively turned about the surface normal *n*. Curvature in three-dimension represents the values of the radii of the two orthogonal circles fit tangent to a surface. Since curvature is the reciprocal of the radius of these circles, maximum curvature (k_{max}) represents the circle that fits the tangent to the surface with the largest radius and minimum curvature (k_{min}) is the other circle tangent to the surface with the smallest radius (Figure 2.2b)

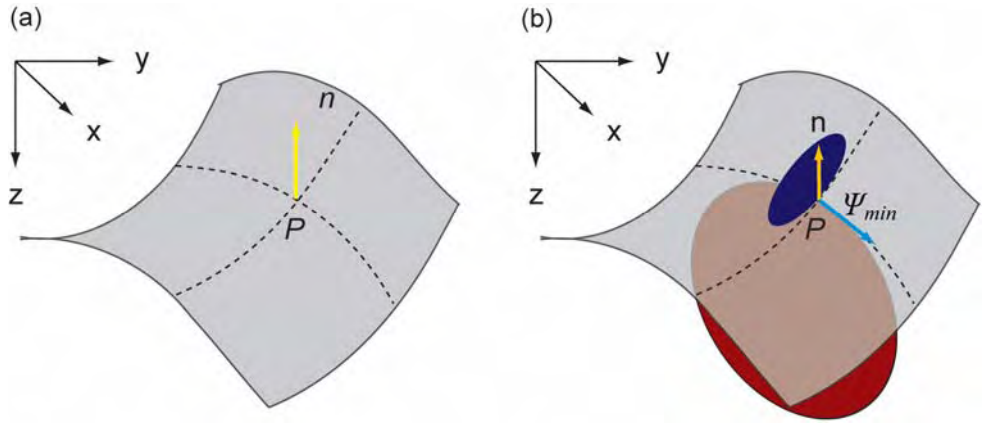

Figure 2.2: Cartoon illustrating the concept of three-dimensional curvature in a quadratic surface with a surface normal *n* at a point *P* (a). The circle (blue) tangent to the surface whose radius is minimum defines the magnitude of maximum curvature (k_{max}). The plane perpendicular (red) to that containing the maximum curvature defines the magnitude of minimum curvature (k_{min}) (After Roberts, 2001 & Mai, 2010).

The Gaussian curvature (k_{Gauss}) of a surface is the product of the principal curvatures, k_{max} and k_{min} (Gauss, 1827) with the overall shape of the Gaussian curved surface being defined by the signs of the principal curvatures (k_{max} and $k_{min.}$).

$$k_{Gauss} = k_{max} . k_{min} \qquad \text{Equation 2.2}$$

Gaussian curvature of zero occurs where one of the two principal curvatures has a value of zero and is normally exhibited by developable surfaces (Lisle, 1994). Surfaces with zero Gaussian curvature restore to a plane without deforming or changing the area of the surface (e.g. corrugations, perfectly cylindrical folds in which the corrugation and/or fold axes define the axis of least principal curvature) (Figure 2.3a). Domes, hemispheres and periclines are synclastic surfaces and have positive Gaussian curvatures because the principal curvatures have the same signs (Figure 2.3b). Saddled-shaped or anticlastic surfaces (e.g. *Pringle* crisps) have negative Gaussian curvatures because the principal curvatures have opposite signs (Figure 2.3c). Anticlastic and synclastic surfaces cannot be restored to a plane without deforming the surface and are termed non-developable surfaces (Lisle, 1994). In

Chapter Six, a hypothetical description of the consequences of fault surface curvature on the structure of the volumes adjacent to fault is presented.

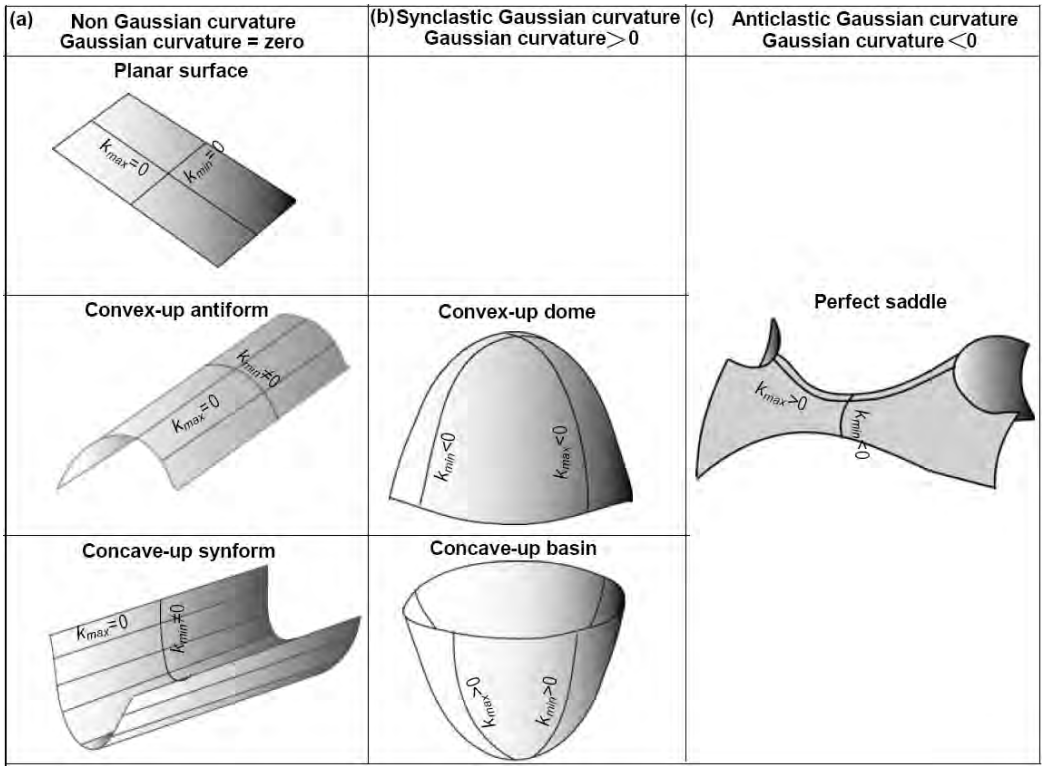

Figure 2.3: Schematic classification of end-member Gaussian curvature of surfaces. The product of the principal curvatures k_{max} and k_{min} is the Gaussian curvature k_{Gauss} of a surface. If one of the principal curvatures is zero, the surface has a zero Gaussian curvature (a). Where the principal curvatures have the same sign and greater or less than zero in each case (i.e. +ve and +ve, -ve and -ve), the surface has a positive Gaussian curvature (b) and if one of the principal curvatures is negative, the surface has a negative Gaussian curvature (c). Surfaces with positive (synclastic) and negative (anticlastic) Gaussian curvatures are non-developable while zero Gaussian curvature is developable (Lisle, 1994).

2.3 Previous methods of investigating fault surface geometry

2.3.1 Fault surfaces modelled from laser scan data (e.g. LiDAR)

In the last few years, terrestrial laser scanning techniques (LiDAR, i.e. Light Detection and Ranging) have been used to acquire geometric measurements of exhumed fault surfaces. For example, Jones *et al.* (2009) used the technique to acquire laser-scan data used in analyzing the surface geometry of a fault in Arkitsa, Greece (Figure 2.4). The maximum curvature plots of the fault was used to identify

corrugations and a suggestion that field-based investigation of fault curvature can be extended to faults mapped from seismic data. Kokkalas *et al*. (2007) used a similar tool to suggest that the Arkitsa fault is corrugated based on analysis of digital terrain models.

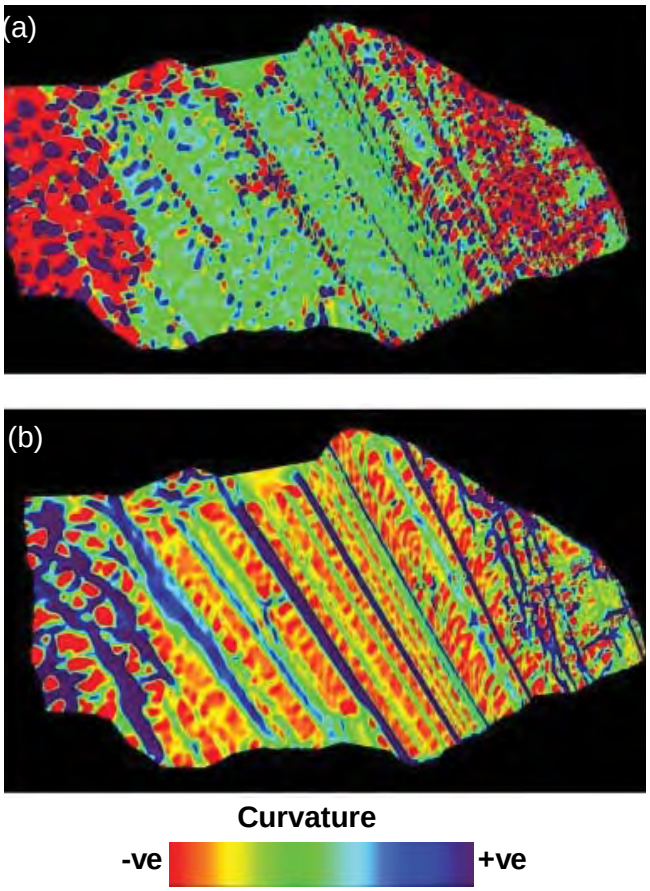

Figure 2.4: Plots of Gaussian (a) and maximum curvature (b) of part of Arkitsa fault panel in Greece. The maximum curvature plot highlights the main corrugations of the fault plane (Jones *et al*. 2008).

Wright (2008) used LiDAR acquired geometrical data to describe the surface morphology of outcrop fault surfaces in the Aegean, Northern Spain and SW England and proposed that corrugations are widespread manifestations of fault surface curvature. Sagy & Brodsky (2008) analysed a fault scarp in Oregon, USA and described the widespread occurrence of medium to short-wavelength undulations and slip-parallel elliptical bumps along the corrugation axes. Resor & Meer (2009)

described slip-parallel corrugations on a range of wavelengths on a fault scarp in Arkitsa in Greece and suggested that millimetre-scale striations along the corrugations are evidence of slip directions. Furthermore, they proposed that slip heterogeneity due to bumps and depressions on the surface may play an important role in the evolution of fault surface morphology.

2.3.2 Fault surfaces modelled from seismic data

To date, few three-dimensional models of faults mapped from seismic data have been analyzed using structural attributes of fault surfaces. Wright (2008) analyzed the detailed curvature plots of normal faults mapped from Niger Delta seismic data and described the widespread occurrence of corrugations. Lohr *et al.* (2008) mapped undulations on a synsedimentary normal fault and described corrugations elongated sub-parallel to fault dip. Van Gent *et al*. (2010) identified corrugations with orientation parallel to slip direction on fault surfaces mapped from NW Groningen Block seismic data from Netherlands. Slip indicators were identified based on paleostress analysis of the fault surface. Prior to that, Neetham *et al*. (1996) suggested that most faults are not planar and that corrugations when mapped on fault surfaces may relate to and help constrain slip vectors on the fault surfaces. They futher speculated that slip oblique to the corrugations could lead to considerable wall rock strain.

Prapasanobon & Pigott (2008) analyzed the geometry of faults mapped from seismic data offshore Myanar, Gulf of Thailand and in the Maracaibo Basin, Venezuela and described grooves, ridges and steps as common features of the faults in the three tectonic settings. Marchal *et al*. (2003) investigated the three-dimensional geometry of a normal growth fault mapped from onshore Niger Delta seismic data and identified

vertical and horizontal undulations interpreted to be related to fault propagation. These observations imply that fault surfaces modelled from seismic data across a wide range of tectonic settings exhibit surface topography similar to outcrop fault surfaces and the methods used in analyzing fault geometry in the field can be extended to faults mapped from seismic data.

2.3.3 Fault surfaces modelled from earthquake aftershock data

Carena & Suppe (2002) described the three-dimensional geometry of Northridge thrust fault, California, modelled using earthquake aftershocks data in *Gocad* 3-D earth-modelling software environment. A model of the fault surface shows corrugation with a pronounced lateral ramp and secondary corrugations parallel to the ramp and proposed a correlation between the trend and plunge of mean slip direction with that of the corrugations. Similarly, Resor (2003) described the three-dimensional surface model of the Aliakmon fault zone, NW Greece using earthquake aftershock data and highlighted the usefulness of three-dimensional surface models of the fault in comparison to two-dimensional model.

2.4 Previous research linking fault geometry with wall rock deformation

2.4.1 Field outcrop data

Several workers have in the past investigated potential links between outcrop fault surface geometry and wall rock structure. Jones *et al.* (2008) described the three-dimensional geometry of panels of an exposed fault surface in Arkitsa, Greece, and suggested a correlation between high surface curvature and fault plane rupture. They opined that a similar relationship may exist using seismic data. Kokkalas *et al*. (2007) applied terrestrial laser scanning to investigate the surface morphology of the Arkitsa

fault zone in Central Greece and suggested a correlation between high surface curvature and fracture density. Wright (2008) demonstrated some qualitative relationship between the curvature of outcrop fault surfaces in the Aegean, Northern Spain and Central Greece and the pattern of surface fractures and highlighted the scale dependence of the analysis. The correlation was based on superimposing fracture maps interpreted from field observations and digital photographs on curvature plots of the faults (Figure 2.5).

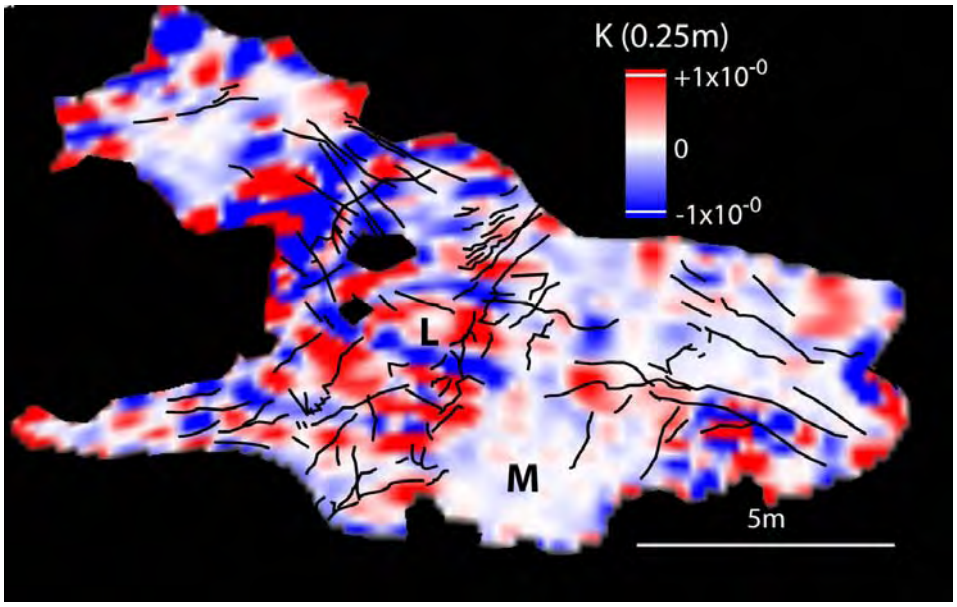

Figure 2.5: Surface fractures (solid lines) superimposed on the Gaussian curvature of a fault scarp in Greece. Curvature has been computed using a grid size of 0.25 m. Note the confinement of most of most fractures to a zone where the Gaussian curvature is changing abruptly from positive (red) to negative (blue) in the fault transport direction (Wright, 2008).

2.4.2 Seismic data

Wright (2008) demonstrated close correlation between the curvature of faults and horizons mapped from the Forcados seismic data in the Niger Delta. On the basis that intense horizon curvature may be due to deformation, he proposed a link between fault surface curvature and wall rock deformation (Figure 2.6). Lohr *et al.* (2008) showed how strain in the hanging wall of an inverted fault can be predicted using

seismic and well data. The results suggest considerable strain along the fault trace that may be related to the geometry of the fault. They proposed that this pattern of fault geometry-strain relationship probably accounts for the heterogeneous distribution of fractures observed in well data.

Prapasanobon & Pigott (2008) described grooves and ridges observed on fault planes mapped from seismic data offshore Myanar, Gulf of Thailand and Maracaibo Basin, Venezuela. They suggested that the structures are similar to undulations seen in outcrop fault surfaces, and proposed a link between the pattern of seismic reflection anomalies and fault surface geometry. Wagner *et al*. (2006) used fault displacement analysis to suggest a correlation between fault surface geometry and strain distribution in the hanging wall of a fault mapped from Lower Saxony seismic data in Germany. The study speculated that the pattern and intensity of strain distribution may depend on the angular differences between the orientation of corrugation axes and fault transport direction. This interpretation corroborates previous observations by Neetham *et al*. (1996).

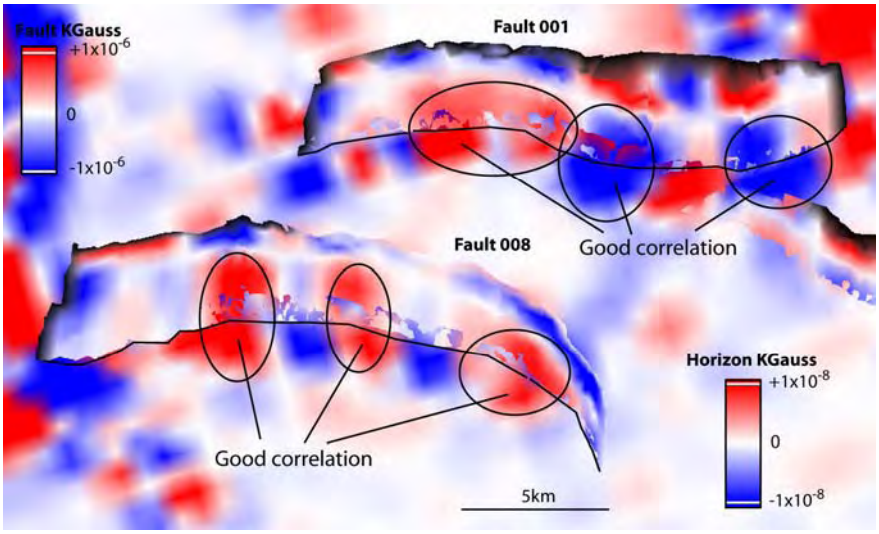

Figure 2.6: Perspective view comparing Gaussian curvature of two fault planes cutting an horizon (solid lines are lines of intersection) interpreted from Niger Delta three-dimensional seismic data. Regions where fault and horizon curvature appears to correlate are highlighted (Wright, 2008).

2.5 Discussion and conclusion

A summary of previous analysis of fault geometry and deformation in the wall rocks due to fault surface geometry is presented in Table 2.1. It is apparent that our present understanding of fault surface topography is largely from laser-scan analysis of exhumed fault surfaces in comparison to fault surfaces mapped from seismic data. In addition most of the faults mapped from seismic data that have been analyzed are extensional and hardly investigated using fault surface structural attributes (e.g. curvature).

In the last few years, seismic technology has improved tremendously and high resolution seismic data that can permit the detailed mapping and reconstruction of fault surfaces with some good degree of accuracy and resolution as good as or better than 10 m are now available. To date few three-dimensional models of thrust faults mapped from seismic data have been analyzed despite evidences suggesting that the spatial variation of fault surface morphology is better investigated in three-dimensions (e.g. Neetham *et al*. 1996).

The surface models and curvature plots of the faults presented in this thesis are the first for thrust fault planes mapped from deepwater Niger Delta seismic data. In addition to the useful geometrical information two-dimensional cross sectional models of faults may provide, the surface and curvature models of the faults can improve our understanding of the three-dimensional variation of fault surface morphology and the complex relationships with the structure of contiguous volumes adjacent to the faults especially where well data is not available.

The potential usefulness of fault curvature – wall rock structure analysis in hydrocarbon exploration has been highlighted in Chapter One. However, in addition the three-dimensional fault surface geometrical data generated in this thesis can provide the database needed to analyze the pattern of slip across corrugated faults, origin of fault corrugations, bumps and depressions observed in previous analysis of fault surface geometry, links between corrugation and the mechanical stratigraphy of wall rock volumes, relationships between corrugation axes and fault surface orientation and implication of fault surface topography on wall rock structure. Some of these observations are hypothetically testable by analyzing surface and attributes plots of fault surfaces in relation to the structure of the volumes surrounding the faults and is the focus of this thesis.

Although attempts have been made in the past to investigate the structure of outcrop fault surfaces and damage zones in general, characterizing the structure of fault zones and potential links with fault surface morphology using seismic data can be difficult and has yet to be properly investigated. This may be due to uncertainty in distinguishing disruptions related to deformation from distortion of seismic reflectivity in the vicinity of fault planes due to poor seismic imaging and resolution limits of seismic data (e.g. Dutzer *et al*. 2009). However, where the quality of the data is exceptionally good, seismic attribute extraction techniques may significantly enhance the quality of the data for structural interpretation. The potential usefulness of seismic attributes is the reason for dedicating a good part of this thesis to calculating several measures of volume reflector attributes. Furthermore software programs for rendering, visualizing and analyzing seismic attribute volumes and anomalies in the vicinity of fault surfaces can help in analyzing the pattern of seismic reflectivity in the vicinity of the faults.

Previous analysis of links between fault surface geometry and wall rock deformation using seismic data were based on the visual correlation between fault surface curvature and the curvature of horizons mapped adjacent to the faults. The assumption is that intense curvature of horizons may be due to wall rock deformation and hence linked to the pattern of fault surface curvature. In outcrop the analysis may be limited by the quality of exhumed fault surfaces and where the quality is good mapping wall rock structure beyond the exposed surfaces may be very difficult. Therefore, this thesis builds on previous observations by using novel methods to:

- Investigate the seismic properties of the volume adjacent to several thrust faults using fault slicing and seismic attribute analysis. The interactive sampling and extraction of seismic attribute data within depths of interest in the volume adjacent to several faults using fault slicing technique can help in describing the structure of the volumes in the immediate vicinity of the faults and how the structure changes away from the fault.
- Investigate the pattern of seismic attribute anomalies sampled adjacent and parallel to the faults to map indirect seismic indicators of fault transport direction.
- Investigate how the knowledge of the curvature of fault surfaces mapped from seismic data can be used to predict disruptions and hence deformation that may be related to the shape of the faults. The main advantage of visually comparing curvature plots of the faults and volume structure sampled parallel to the faults in the wall rocks is that it permits a direct visual comparison of fault geometry with volume structure adjacent to the faults with little interpretation bias since the seismic attribute data can be used to directly infer fault zone structure based on seismic attribute anomalies across the faults.

Year	Researchers	Data type and structural setting	Focus of study
2010	Van Gent *et al.*	Seismic (Extensional)	Analysis of slip and paleostress using undulations mapped from fault surfaces, NW Groningen Block, Netherlands.
2009	Jones *et al*.	Laser scan (LiDAR) (Extensional)	Analysis and visualization of outcrop fault surface, Arkitsa fault panels, Greece.
2009	Resor & Meer	Laser scan (LiDAR) (Extensional)	Relationship between outcrop fault geometry and slip heterogeneity, Arkitsa, Greece.
2009	Brodsky *et al*.	Laser scan (LiDAR) (Extensional)	Evolution of outcrop fault surface morphology, Oregon, USA.
2008	Propasanobon & Pigott	Seismic (Extensional and transpressional)	Analysis of fault surface geometry and seismic reflection anomalies, offshore Myanmar, Venezuela, and Gulf of Thailand.
2008	Tim Wright	Laser scan (LiDAR) and seismic (Extensional)	Characterization of fault curvature and implications for wall rock deformation, Aegean, N. Spain, SW England.
2008	Lohr *et al*.	Seismic (Extensional)	Evolution of a fault surface from 3-D attributes analysis and displacement measurements, NW German Basin.
2008	Wagner *et al*.	Seismic (Strike-slip)	Relationship between fault geometry and horizon strain, Lower Saxony, Germany.
2007	Kokkalas *et al.*	Laser scan (LiDAR) (Extensional)	Application of laser-scan data to analyze the geometry of an exposed fault surface, Arkitsa, Central Greece.
2003	Marchal *et al.*	Seismic (Extensional)	3-D analysis of normal growth fault surface, Niger Delta.
2003	Philip Resor	Earthquake aftershock (Extensional)	3-D fault geometry and slip distribution
2002	Carena & Suppe	Earthquake aftershock (Compressional)	Analysis of Northridge thrust fault surface, California, USA.
1996	Neetham *et al.*	Seismic (Extensional)	Analysis of 3-D fault geometry and displacement patterns, North Sea.
1994	R. Lisle	Seismic and outcrop	Surface curvature-strain relationship. Concept of surface developability.

Table 2.1: Summary of previous research on modelling and analyzing fault surface morphology.

CHAPTER THREE- VOLUME SEISMIC ATTRIBUTE EXTRACTION AND IMAGE ENHANCEMENT TECHNIQUES

3.1 Introduction

The focus of this chapter is to propose a workflow and present results of three-dimensional volume seismic attributes extraction and image enhancement techniques applied to a deepwater Niger Delta seismic data. The seismic attribute data constitute the database for investigating the stratigraphic and structural framework of the area in Chapter Four. Whilst no detailed interpretation is presented in this chapter, a demonstration of the usefulness and graphical relationships between the attributes in assessing the structural framework of the study area and the structure of the volumes adjacent to faults mapped in Chapter Four and modelled into surface and attribute plots in Chapter Five is highlighted. The data is central to investigating potential links between thrust zone structure and fault surface morphology.

3.2 Methodology

3.2.1 Seismic data

The principal data is a 3000 km^2 post-stack time migrated three-dimensional seismic data acquired and processed by Petroleum Geo-Services (PGS) in 2002 (Figure 3.1). The data images a zone of gravity-driven compressional deformation on the lower slope of the Niger Delta at the outer fringes of the southern Niger Delta sedimentary lobe in water depths ranging from ~1300 m to 2700 m and is part of a larger 10000 km^2 West Africa Mega-Survey regional seismic project. Geographically, the area is a zone of overlapping maritime boundary between Nigeria and São Tomé and Princípe and referred to as “The Joint Development Zone” (JDZ) (Figure 1.1).

The data has a line and trace spacing of 25 m x 12.5 m respectively (1126 lines and 10741 traces). Detailed description of the seismic resolution, phase and polarity of the data is presented in Chapter Four. Although seismic attribute extraction and image enhancement techniques were applied to the full seismic volume, the results presented in this chapter are examples from the central parts of the study area.

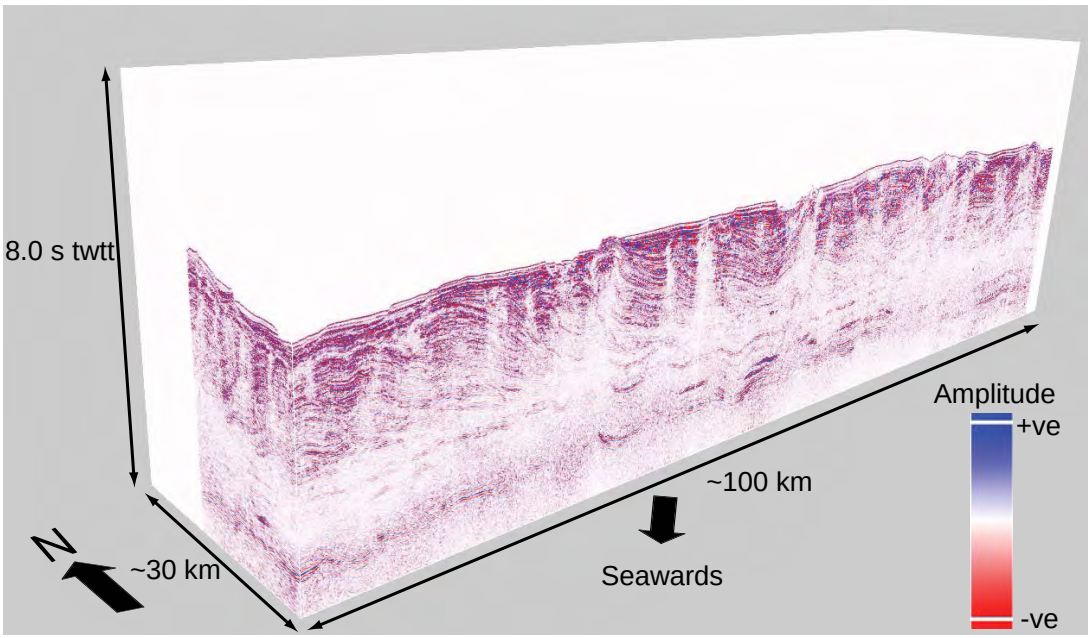

Figure 3.1: Perspective view of the 3000 km^2 JDZ seismic amplitude volume spanning 0 s to 8 s two way travel time. Vertical exaggeration is ~ 4.

3.2.2 Workflow

The workflow is summarized in Figure 3.2 and primarily includes estimating reflector dips in a three-dimensional grid and applying structurally-oriented filtering along reflector dip and azimuth to calculate three generations of structurally-enhanced dip-steering data from which the seismic attributes volumes were calculated.

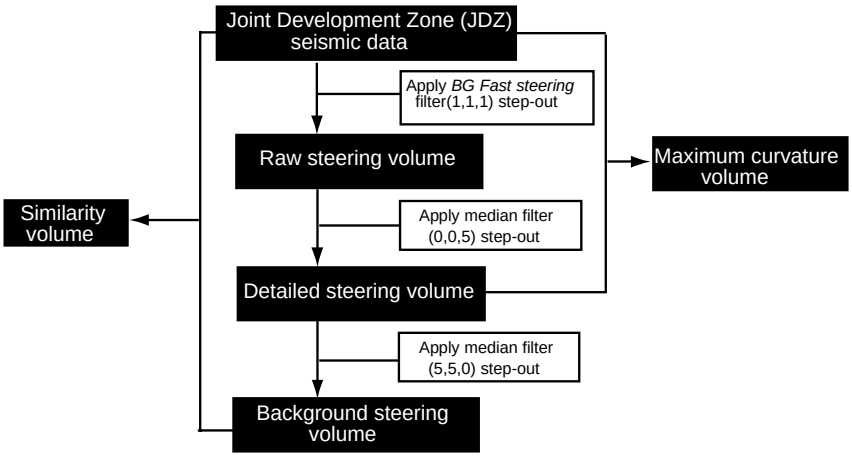

Figure 3.2: Workflow for three-dimensional volumetric seismic attributes extraction and image enhancement techniques applied to the JDZ seismic data.

In the first stage of the workflow, seismic attribute extraction and image enhancement project was created in *Opendtect* software and the seismic data loaded into the project. In *OpendTect*, seismic attributes are calculated using user-defined parameters that are based on factors such as the quality of the seismic data, frequency, sampling rate, bin size, desired wavelength of structures (short or long-wavelength), size of the dataset and computing hardware capabilities. Once the parameters are selected, the seismic attributes are evaluated on-the-fly prior to multi-trace volume batch processing and storage. The data can then be exported for interpretation in SEG-Y compatible formats.

Table 3.1 is a summary of the attribute parameters used for the calculation of the seismic attributes presented in this chapter. The time gate operator is a measure of the desired wavelength of structures mapped in the data and is usually normalized to seismic frequency and wavelength. A smaller time gate will image short-wavelength structures and a larger time gate will image broader structures. The step-out defines the radius of investigation (in the inline, crossline, sample) format. The steering determines the directivity of the attribute extraction and the application of full steering ensure that attributes are calculated from one trace to another driven by the dips of the seismic traces. The concept of steering the

calculation of seismic attribute data presented in this thesis is described and illustrated in section 3.3.1 of this chapter.

Attribute	**Time gate (ms)**	**Lateral position**	**Other settings**
Raw steering	-	Step-out (1,1,1)	-
Detailed steering	-	Step-out (0,0,5)	-
Background steering	-	Step-out (5,5,0)	-
Similarity	(-24, 24)	-	No steering
Dip-steered similarity	(-24, 24)	Step-out (1,1,1)	Full steering
Maximum curvature	-	Step-out (1,1,1)	Full steering

Table 3.1: List of parameters used in the calculation of seismic attribute volumes. The time gate is the time window sample, the step out is the radius of investigation in inline, crossline and sample format. The steering data is a filter that provides directivity for the calculation of volume seismic attributes and is itself an attribute. These parameters can be selected to suit the quality of the input data and the desired end results.

3.3 Results

3.3.1 Dip-steering

The computation of dip-steering volumes forms the foundation for structural filtering and calculating seismic attributes along structural dips (e.g. Chopra & Marfurt, 2007; 2011) using steering methods developed by Tingdahl (2003) and described by Brouwer (2007). The steering cube is a volumetric grid of inline and crossline data representing the dip of the seismic reflectors (Figure 3.3). The steering data has a physical unit of μs/m, and is a measure (in microseconds) of the amount of movement up and down one meter in the inline and crossline direction on the same reflector.

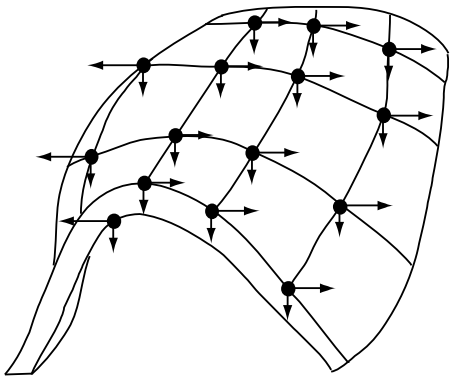

Figure 3.3: Three-dimensional Schematic illustration of dip-steering calculations in *Opendtect*. The steering cube is a volumetric grid of inline and crossline dip representing the dip of the seismic reflectors. The arrows indicate the steering directions (Tingdahl & de Rooij, 2003).

In the dip-steering calculation, attributes are conceptually guided along a three-dimensional surface on which the seismic phase is approximately the same. This process creates a virtual horizon at each position by following the dip/azimuth information in the steering cube from trace to trace. The application of full steering mode to the process ensures that the location and azimuth of the seismic traces is updated at every trace location. The full steering mode enhances the sharpness of discontinuities in dipping and non-dipping seismic traces since the dip and azimuth of the traces are updated at every trace position. The data was then used as input to subsequent filtering and extraction of volume seismic attributes (e.g. similarity and curvature). The difference between *'no steering'*, and *'full steering'* is shown in Figures 3.4a and b.

First, a "raw steering" volume was calculated using *BG* Fast Steering filter. The filter is based on the analysis of the vertical and horizontal gradient of amplitude data to calculate estimates of reflector dips. From the raw steering data, two structurally filtered and enhanced volumes were calculated by the application of dip-steered median filters. The filters primarily remove noise and enhance laterally continuous seismic events by filtering along structural dips thereby improving the interpretability of the data (Tingdahl & de Rooij, 2005). The detailed

steering volume is a second generation data that contains localized dip information of seismic traces derived by filtering the raw steering data and was used with the seismic reflection data as input to calculate seismic curvature. The data is used because of the detailed dip information needed to identify subtle flexures that may be related to reflector curvature (e.g. Chopra & Marfurt, 2007; Klein *et al*. 2008; Brouwer, 2007).

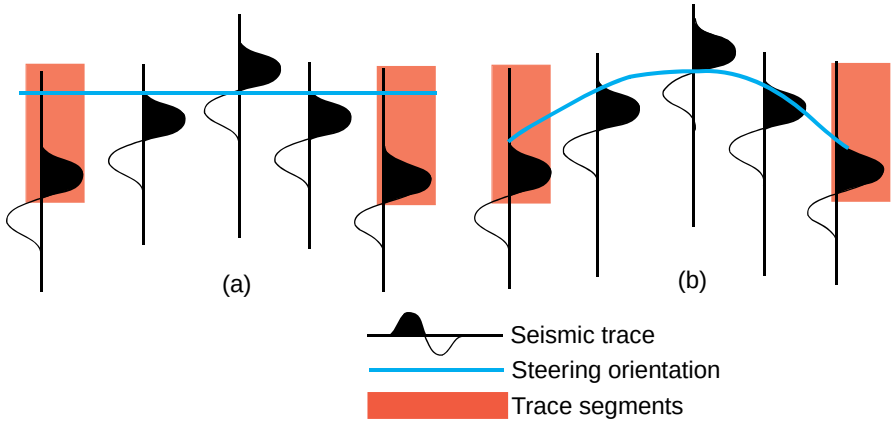

Figure 3.4:Two-dimensional Schematic illustration of dip-steering calculations in *Opendtect*. A seismic event is followed from the central position by tracking the position of the local dip and azimuth in the data. In (a) no steering is applied and the trace segments are aligned horizontally. However, in (b) the application of full steering ensures the location and azimuth of the traces is updated at every trace location (Tingdahl & de Rooij, 2003).

The background dip-steering volume is a third generation dip-steering volume calculated from the detailed steering volume by applying a lateral filter in the inline and crossline directions (i.e. dip is averaged) and with the seismic data as input was used to calculate volume similarity. Previous work has shown that similarity calculated with steering data representative of a sub-regional dip (background steering data) provides the best similarity of seismic traces (Brouwer, 2007). Detailed description of the concept of dip-steering in volume seismic attribute extraction is described in Tingdahl & de Groot (2003), Tingdahl (2003), Tingdahl & de Rooij (2005) and Brouwer (2007).

Figure 3.5 shows the input seismic volume and the three generations of steering volumes calculated from the seismic reflectivity data spanning 3.0 s to 6.0 s two way time. The

enhanced resolution of the structures becomes apparent as the filters are applied to the seismic data. Figure 3.6 shows time slices extracted at 4.0 s from seismic amplitude data and the steering volumes. Extreme values of dip (dark and light shades) represent zones of high dipping events. Discontinuities (red block arrows) are located at the location of high negative dips while the light shades represent zones of high positive structural dips adjacent to the large discontinuities that may be related to folding in deepwater Niger Delta compressional domain. Note the clear pattern of WNW-ESE zones of trending discontinuities highlighted by the detailed and background dip-steering data.

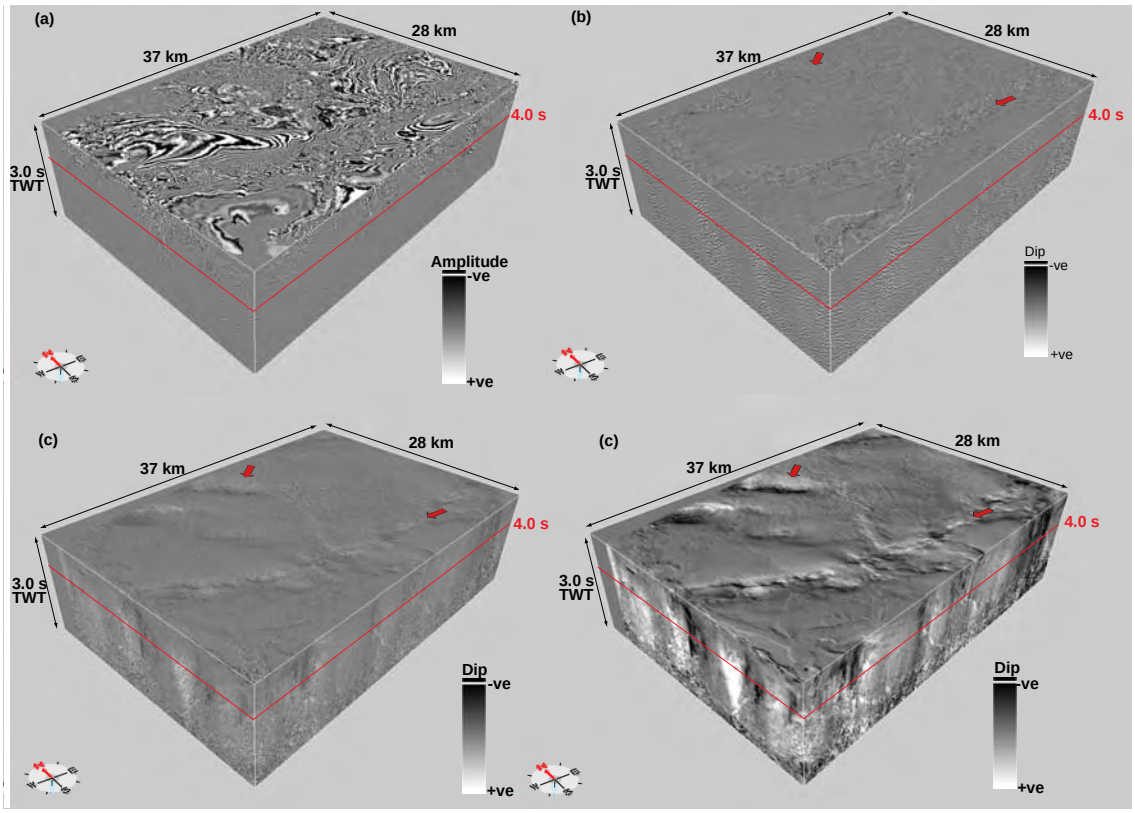

Figure 3.5: Perspective views of seismic amplitude volume (a) raw steering volume (b), detailed steering volume (c) and background steering volume (d) spanning 3.0 s to 6.0 s two way travel time. Note the progressively enhanced resolution of structures in the dip-steering data (block red arrows) as a result of the application of structurally-oriented filters. The red outline indicates the location of time slices extracted at 4.0 s from the volumes and shown in Figure 3.6. Vertical exaggeration is ~ 3.0.

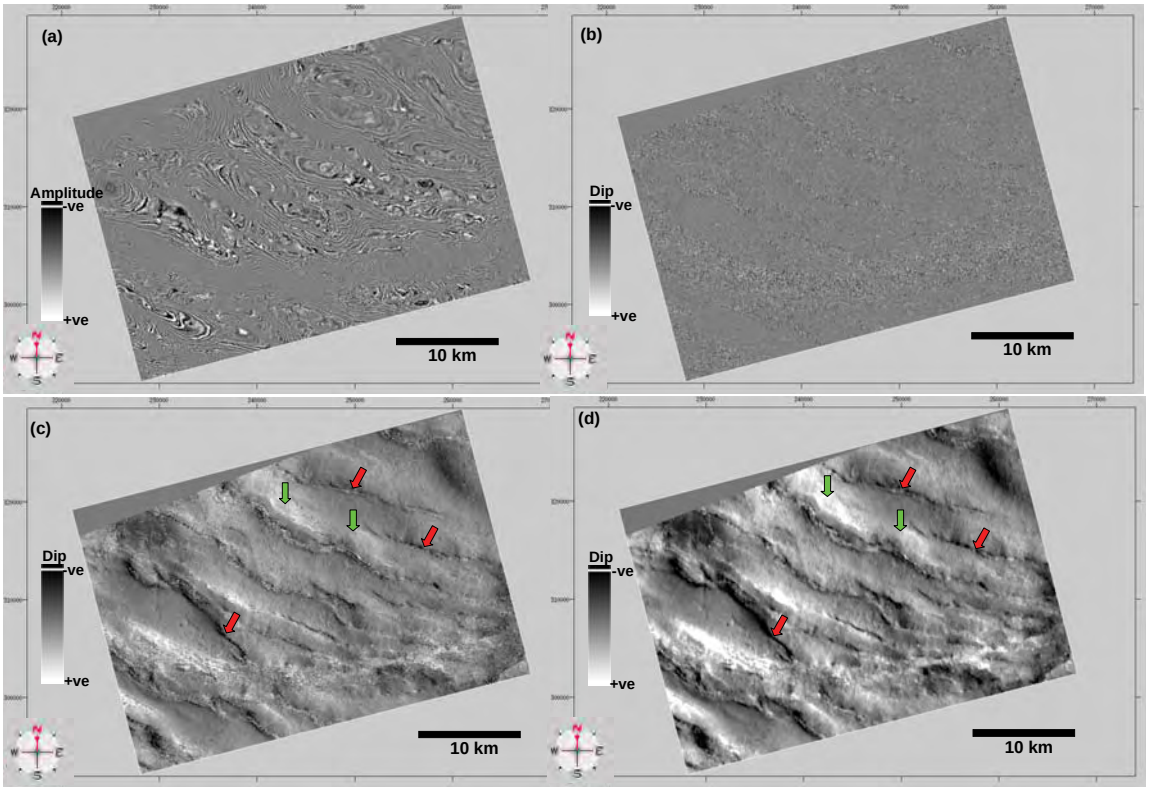

Figure 3.6: Time slices sampled through seismic amplitude volume (a) raw steering volume (b) detailed steering volume (c) and background steering volume (d). All slices were extracted at 4.0 s from the seismic attribute volumes in Figure 3.5. The block red arrows represent zones with high negative dip in a predominantly WNW-ESE orientation highlighted in the filtered steering data and interpreted to represent the location of major discontinuities. High positive dip values (block green arrows) represent structural highs that may be regions of folding related to thrusting in deepwater Niger Delta.

3.3.2 Seismic curvature

The basic theory of surface curvature in two and three-dimensions has been described in Chapter Two. In seismic data, curvature attributes are based on the morphology of seismic reflectors and provide supplementary information to the traditional coherency attributes (Roberts, 2001; Chopra, 2009; Mai, 2010). In curvature analysis, it is assumed that the curvature of a horizon can be used to indirectly predict the state of deformation of the surface on the premise that deformation will be intense where the magnitude of curvature is highest (e.g. Lisle, 1994: Roberts, 2001). Detailed description of previous use of surface curvature as proxy for deformation is discussed in Chapter One.

A recent significant development in curvature attribute calculation is the concept of three-dimensional estimates of the attribute using the dip and azimuth of seismic traces. Volume curvature calculated with dip-steering reduces noise in the data and ensures that meaningful values of curvature are eventually calculated (e.g. Bergbauer *et al.* 2003). In addition, noise filtered volume curvature is useful in volume visualization of the data and in mapping subtle flexures, folds and subsurface distribution of strain based on the pattern of curvature. The attribute may also help in distinguishing reflector anomaly related to disruption from undisturbed geometry when used in combination with discontinuity attributes (e.g. Chopra & Marfurt, 2007; 2009; Blumentritt *et al*. 2005; Wynn & Stewart, 2003).

A measure of volume curvature that defines the largest absolute curvature is used in this thesis (maximum curvature). This attribute has been described as effective at delimiting faults and fault geometries (e.g. Roberts, 2001; Keating & Fischer, 2008). The mathematical aspects of estimating volumetric dip and curvature are described in several publications (e.g. Tingdahl & de Rooij, 2005; Al-Dossary & Marfurt, 2006; Klein *et al.* 2008). The application of this concept and the importance of dip-steering in extracting volume seismic attributes are described in sub-section 3.3.1

Figure 3.7 shows the primary seismic amplitude data and the calculated maximum curvature volume spanning 3.0 s and 6.0 s two way travel time. A fairly quick assessment of the two volumes shows a close correlation between the pattern of reflectivity and curvature. The black arrows show a correlation between strong and horizontal pattern of reflectivity with low volume curvature. The green arrows indicate regions in the data where weak pattern of reflectivity closely matches an arcuate zone of high maximum curvature. Figure 3.8 shows an amplitude timeslice and equivalent maximum curvature timeslice extracted from the data at 4.0 s. In the curvature time slice, a clearly defined pattern of WNW-ESE trending zones of

disruptions by the juxtaposition of positive and negative maximum curvature hardly discernible in the amplitude time slice (black block arrows) was detected. The spacing (separation) between the two anomalies (+ve and –ve curvature) has in the past been used to identify dip-slip faults with the separation providing a qualitative measure of displacement (Roberts, 2001; Klein *et al*.2008). A similar cross sectional relationship between the two attributes is observed using a fault slice sampled at 800 m away from a thrust fault plane in the hanging wall (Figure 3.9).

Discontinuities in amplitude and maximum curvature slices are identified by the break in continuity of seismic reflection and high negative curvature/change in polarity of volume maximum curvature (positive to negative or vice versa) respectively. Reflectors at the top halves of the section (block green arrow) are continuous with high positive maximum curvature, implying that the pattern of curvature may primarily be related to the geometry of the reflectors and perhaps not due to disruption as shown by the strong continuity of the reflectors (White block arrows). In the deeper parts of the slices, the complex pattern of reflectivity and similarity makes any meaningful inference impossible.

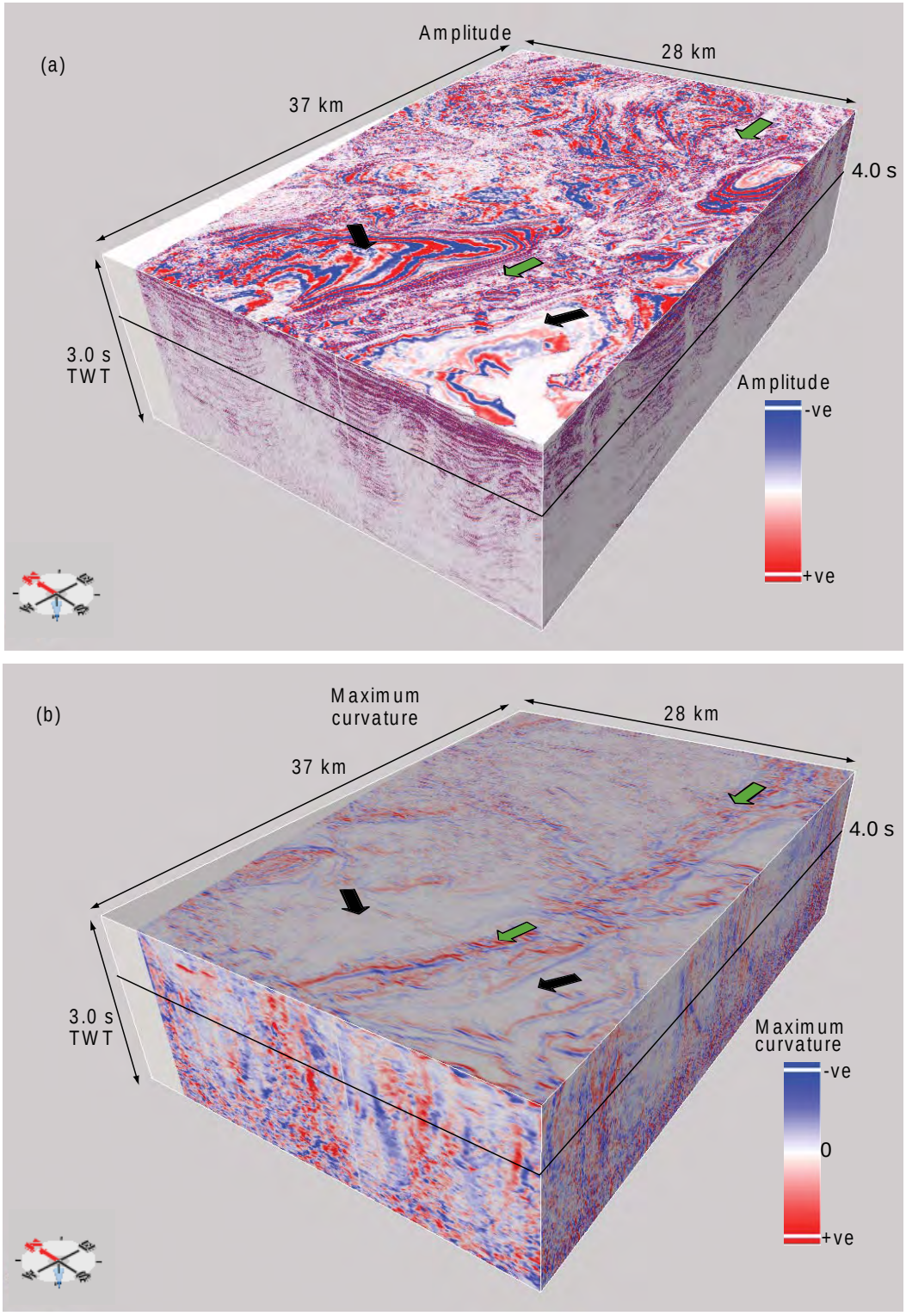

Figure 3.7: Perspective views of seismic amplitude volume (a) and maximum curvature volume (b) calculated on the seismic data spanning 3.0 s to 6.0 s two way time. The black arrows show a correlation between strong and horizontal pattern of reflectivity with low/zero volume curvature. The green arrows indicate regions in the data where weak pattern of reflectivity closely matches an arcuate zone of high maximum curvature. The black outline shows the location of time slices extracted at 4.0 s from the two volumes and shown in Figure 3.8. Vertical exaggeration is ~ 3.0.

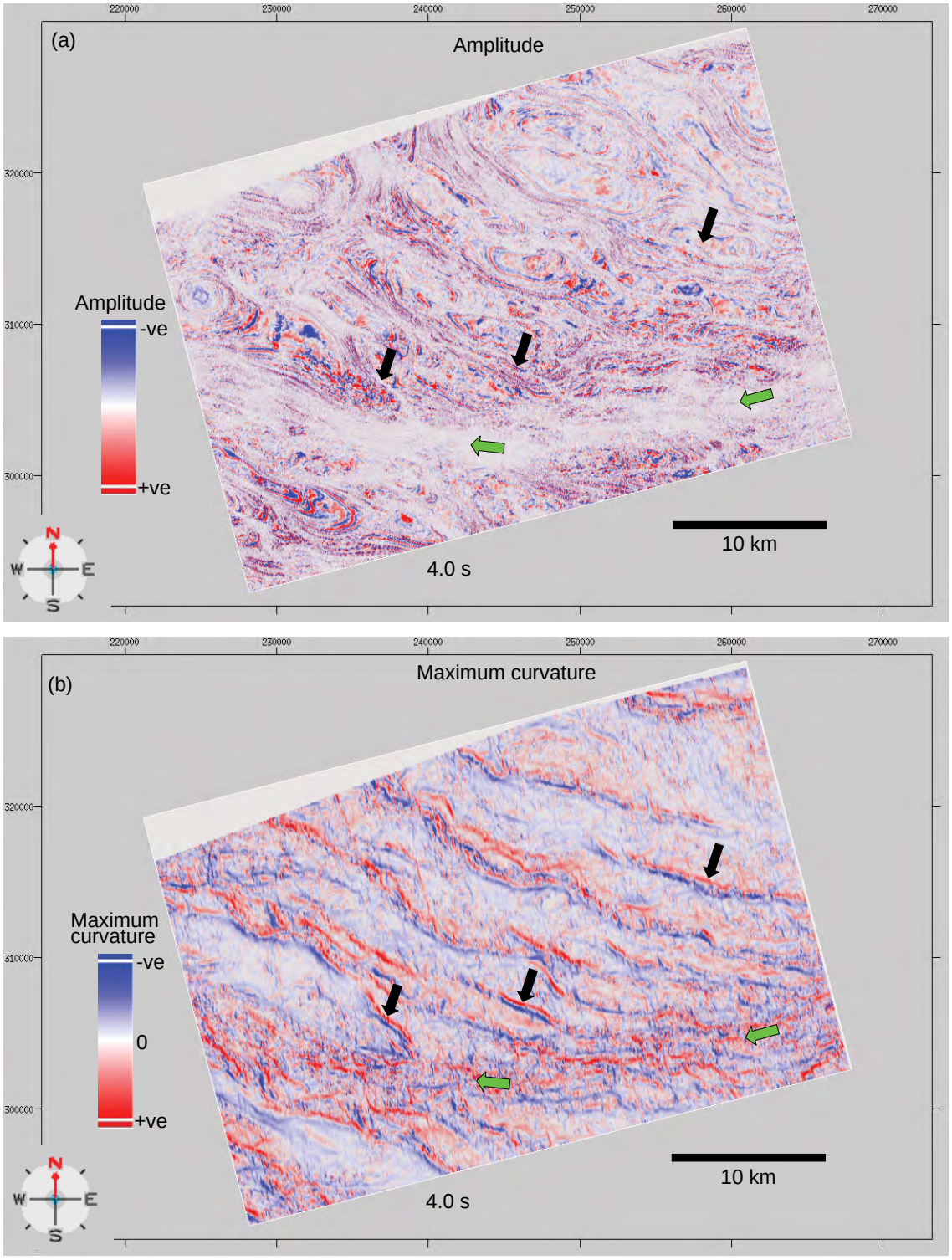

Figure 3.8: Time slice of seismic amplitude (a) and maximum curvature (b) extracted at 4.0 s from the seismic attribute volumes in Figure 3.7. Note the WNW-ESE trending zones of reflection and curvature anomalies (block arrows) seen as a zone of low reflectivity in the amplitude data but appears as zones of juxtaposed positive and negative curvature polarity interpreted to represent the location of large the discontinuities.

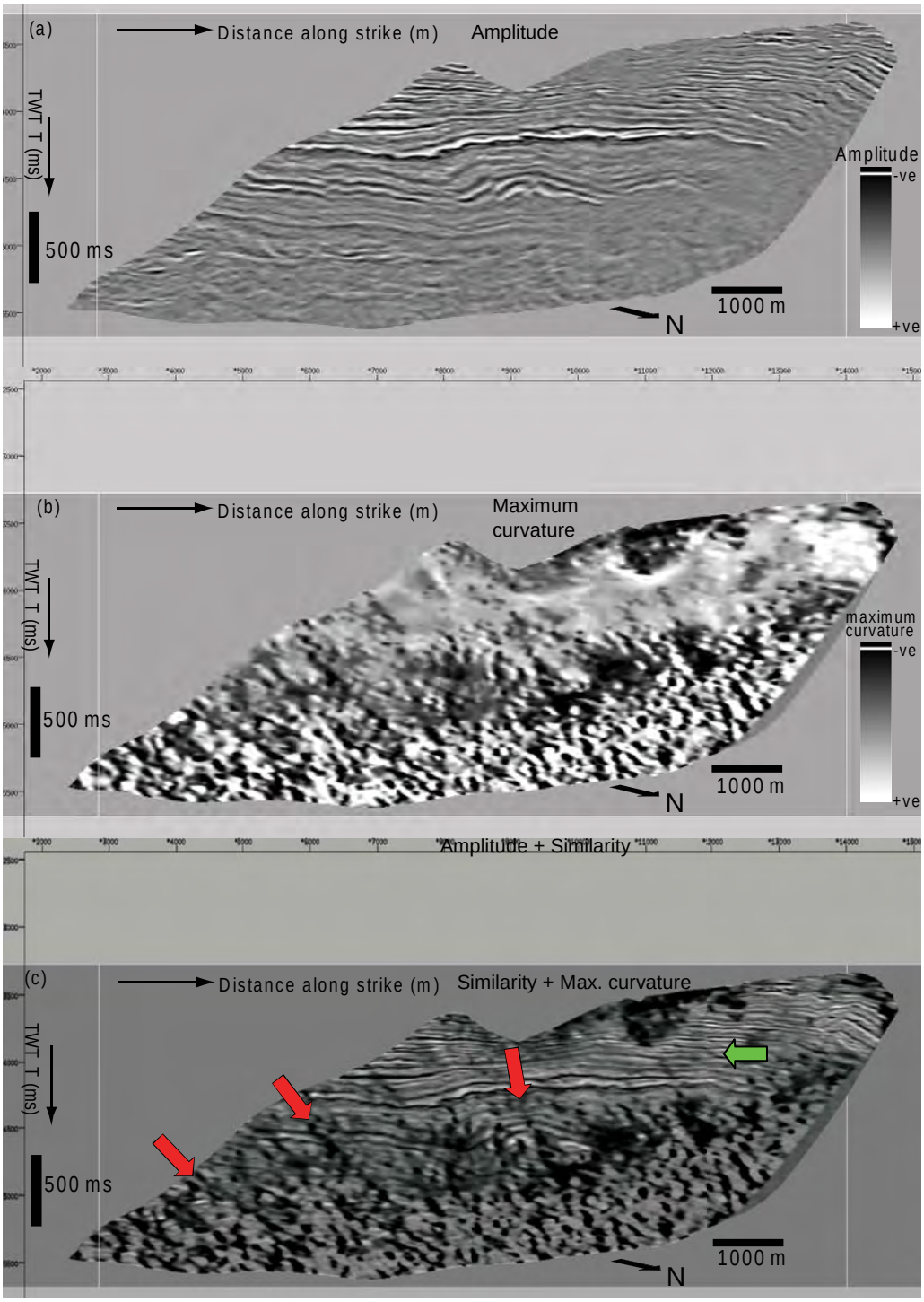

Figure 3.9: Strike views of fault slices sampled through volume seismic amplitude (a) maximum curvature (b) and the integration of the two attributes (c). The slices were sampled at 800 m parallel to and away from an interpreted thrust fault and projected as fault surface attributes in the hanging wall. The upper parts of the section (green block arrow) shows where pronounced pattern of curvature correlates with strong continuity of reflectors. Note the close correlation between reflector disruptions with change in polarity of curvature (red arrows). The effect of noisy amplitudes in the deeper parts of the section makes any meaningful inference impossible. Vertical scale is milliseconds two way travel time and horizontal scale is in meters. Vertical exaggeration is ~ 1.6.

3.3.3 Seismic similarity

Similarity is expresses how two or more neighbouring seismic trace segments look alike in waveform and amplitude and is primarily a discontinuity attribute. The concept of similarity applied to fault detection was introduced by Tingdahl & de Rooij (2005). In *OpendTect*, similarity is calculated by measuring waveform similarity of adjacent trace pairs and the time difference between the traces interpreted as vectors (Figure 3.10). Mathematically, similarity (*S*) is the Euclidean distance in hyperspace between vectors of the segments, normalized between 0 and 1 to the sum of the lengths of the vectors (Equation 3.1). A high similarity (maximum of 1) means the trace segments are similar in waveform and amplitude. If the two traces show a lot of dissimilarity (minimum of 0), the similarity is interpreted to be low and may be due to locally displaced/disrupted strata usually at the location of faults. Comprehensive description of the mathematical aspects of similarity calculation is discussed in Tingdahl & de Rooij (2005).

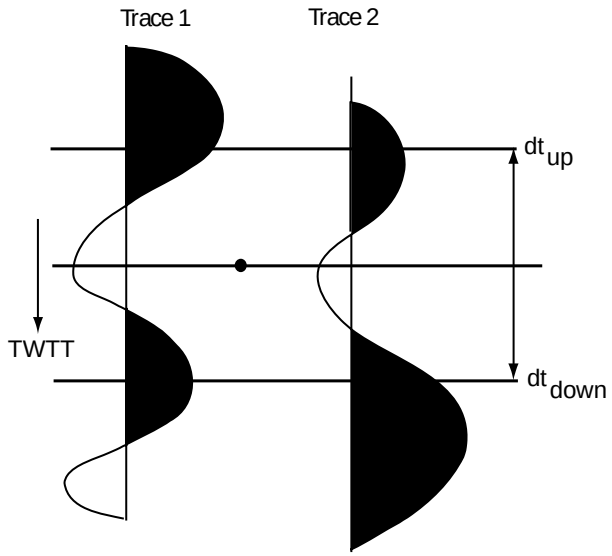

Figure 3.10: Schematic illustration of the concept of calculating the similarity between two trace segments in *OpendTect*. The similarity between the two trace pairs is mathematically the Euclidean distance between vectors of the segments normalized to the sum of the lengths of the vectors.

$$S = 1 - \frac{|v-u|}{|v|+|u|} \quad \text{i.e.} \quad \frac{\left|\text{trace segment 1 - trace segment 2}\right|}{\left|\text{trace segment 1}\right|+\left|\text{trace segment 2}\right|} \qquad \text{Equation 3.1}$$

where

$$v = \begin{bmatrix} f(t_1, x_v, y_v) \\ f(t_1 + d_t, x_v, y_v) \\ . \\ . \\ f(t_2 - d_t, x_v, y_v) \\ f(t_2, x_v, y_v) \end{bmatrix}, \quad u = \begin{bmatrix} f(t_1, x_u, y_u) \\ f(t_1 + d_t, x_u, y_u) \\ . \\ . \\ f(t_2 - d_t, x_u, y_u) \\ f(t_2, x_u, y_u) \end{bmatrix}$$

where,

t is the time-depth of investigation, dt is the sampling interval, t_1 and t_2 are the limits of the time gate, (x_v, y_v) and (x_u, y_u) are the two trace positions that are compared and f is the amplitude value in the cube. The time window is usually best normalized to seismic wavelength or frequency. However, it may be useful to test several parameters with the view to using the best values that reduces smearing while at the same time enhancing the resolution and sharpness of the discontinuities. A time window of + and -24 ms, equivalent to an average seismic wavelength of the seismic data within the window of investigation was used to calculate volume similarity attributes presented in this thesis.

Unlike coherency (Bahorich & Farmer, 1995) that is not sensitive to amplitude scaling, similarity takes into account the amplitude differences between two trace segments in addition to wave shape (Tingdahl & de Rooij, 2005). The differences in the response of attributes at fault locations depend on the dip of the traces, as such the background similarity will be low while the contrast between discontinuities and the background will be high. The application of full steering ensures that the local dip and azimuth of the traces are followed

from the position of investigation to the trace segments. The trace segments used are shifted upwards or downwards so that they have the same phase as the central position of investigation. For fault detection, the application of dip-steering reduces the sensitivity of similarity to dipping reflectors (that may not be due to disruptions) by aligning adjacent trace segments with a lag time. This results in the attenuation of background noise while enhancing discontinuities due to the dissimilarity of the trace segments (Figure 3.11) (Tingdahl & de Rooij, 2005).

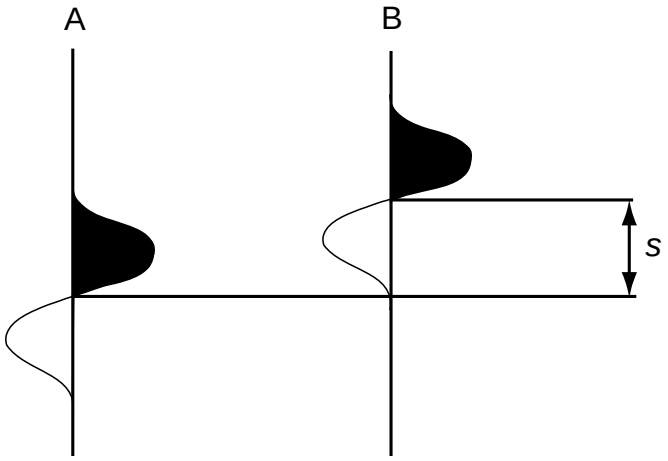

Figure 3.11: Schematic illustration of the effect of dip on trace similarity. The two trace segments A and B are different when compared horizontally. A has high values when B has low, however, if the dip is considered trace B is shifted downwards *s* milliseconds before the comparison and the two segments will be similar. This ensures that the effects of dipping reflectors in similarity calculations are minimized (Tingdahl, 2003).

Figures 3.12 is a volumetric comparison between seismic amplitude and similarity volumes spanning 3.0 s to 6.0 s two way time. A fairly quick assessment of the two volumes shows a correlation between the pattern of reflectivity and similarity. The red block arrows show a region of high similarity that matches a strong pattern of reflectivity. The green arrow shows an arcuate zone of low similarity that corresponds with low reflectivity pattern in the seismic amplitude data. Figure 3.13 is a time slice comparison between seismic amplitude and similarity extracted from the data at 4.0s. Compared to the reflectivity data, similarity attribute not only enhances the imaging of the large discontinuities but also highlights important structures that may be due to fault growth and interaction (block red arrows). The

resolution of the arcuate zone of complex disruption characterized by very low similarity (green block arrows) has also been enhanced. Figure 3.14 demonstrates the relationship between seismic amplitude and similarity using sliced sections of the two attributes sampled at 500 m parallel to a thrust fault plane in the hanging wall. The integration of seismic amplitude and similarity attributes shows a good correlation between disruption of seismic reflectors and low similarity at the location of the block arrows.

Figure 3.15 is a volumetric demonstration of the importance of dip-steering and structural filtering for similarity computation. In Figure 3.15a similarity was calculated without applying dip-steering, while dip-steering was applied in Figure 3.15b. Although the two volumes appear to be identical, time slices extracted at 4.0 s from the data shows that discontinuities in the dip-steered data have higher contrast with an improved resolution of the complex zone of disruption indicated by the block green arrows (Figure 3.16). The sharpness of the edges of the discontinuities has also been improved significantly (block arrows). In contrast, the non-steered similarity attribute has a noisier background with low contrast at the location of the WNW-ESE trending zone of disruptions. A similar observation is made when a fault slice sampled parallel to a thrust fault 800 m in the hanging wall through dip-steered and non-steered similarity volumes (Figure 3.17). The significant improvement in the sharpness of discontinuities is particularly important in this thesis because slices of seismic attribute data sampled adjacent to several faults are used to investigate the seismic structure of thrust zones.

Figure 3.18 is a demonstration of the qualitative relationship between volume similarity and maximum curvature attributes. In the two volumes, disruptions appear as zones of low similarity and juxtaposed/anomalous pattern of maximum curvature. The block green arrows indicate regions in the two volumes where correlation between high similarity and low

maximum curvature is strong. Figure 3.19 are time slices extracted at 4.0 s to demonstrate the relationship between the pattern of similarity and maximum curvature for detecting discontinuities in plan view. The block black arrows show a good correlation between low similarity and anomalies in the pattern of maximum curvature. The block green arrows indicate regions in the two volumes where similarity is low with a complex pattern of maximum curvature.

A similar cross sectional relationship between the two attributes is observed using a fault slice sampled at 800 m away from a thrust fault plane in the hanging wall (Figure 3.20). In the two slices, disruptions are located where similarity is low with curvature anomalies, i.e. low similarity closely matches change in polarity of maximum curvature (block red arrows). In the upper parts of the slice similarity is high with an intense pattern of positive maximum curvature (block green arrow), while in the deeper parts noisy/complex pattern of curvature makes any meaningful inference difficult.

Figure 3.21 is a graphical demonstration of the relationship between volume discontinuities highlighted by the similarity attribute and maximum curvature. The data used for the plots were sampled from the seismic attribute volumes in Figure 3.18. In Figure 3.21a, a correlation between low volume curvature and high similarity is observed, implying that although the reflectors are slightly folded they are not significantly disrupted. However, in Figure 3.21b, a progressively increasing pattern of volume curvature closely matches a corresponding decrease in similarity, implying that reflectors in the sampled volume are significantly folded and disrupted.

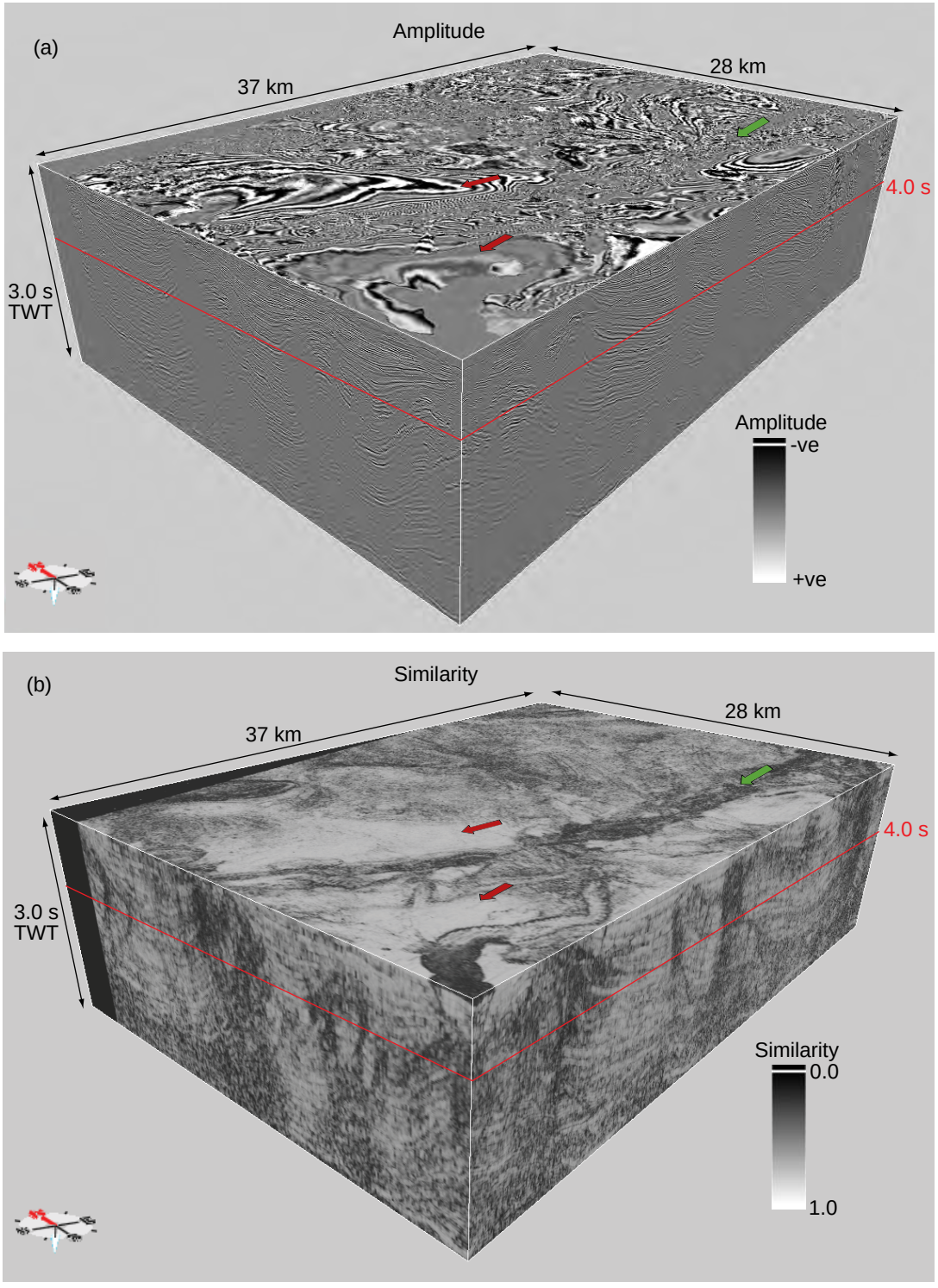

Figure 3.12: Perspective views of seismic amplitude volume (a) and similarity volume (b) spanning 3.0 s to 6.0 s two way time. The block red and green arrows highlight correlation between high similarity and strong reflectivity and low similarity and weak pattern of reflectivity respectively. The red outline indicates the location of time slices extracted at 4.0 s and shown in Figure 3.13. Vertical exaggeration is ~ 3.0.

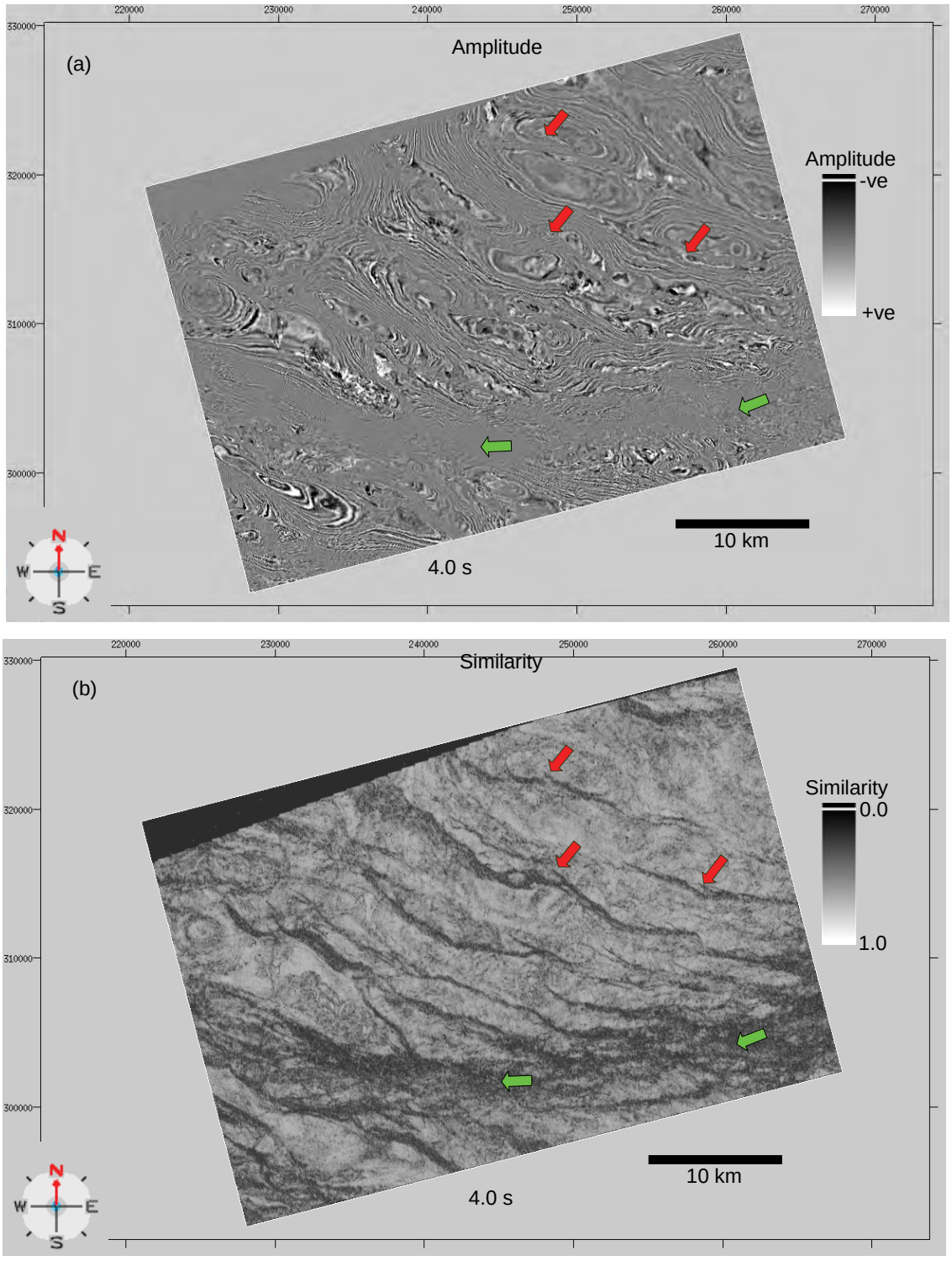

Figure 3.13: Time slices of seismic amplitude volume (a) and similarity volume (b) extracted at 4.0 s from the seismic attribute volumes in Figure 3.12. Compared to the seismic amplitude data, the similarity time slice clearly shows a well defined WNW-ESE trending pattern of discontinuities (block red arrows) and the E-W trending zone of intense disruption indicated by the green block arrows.

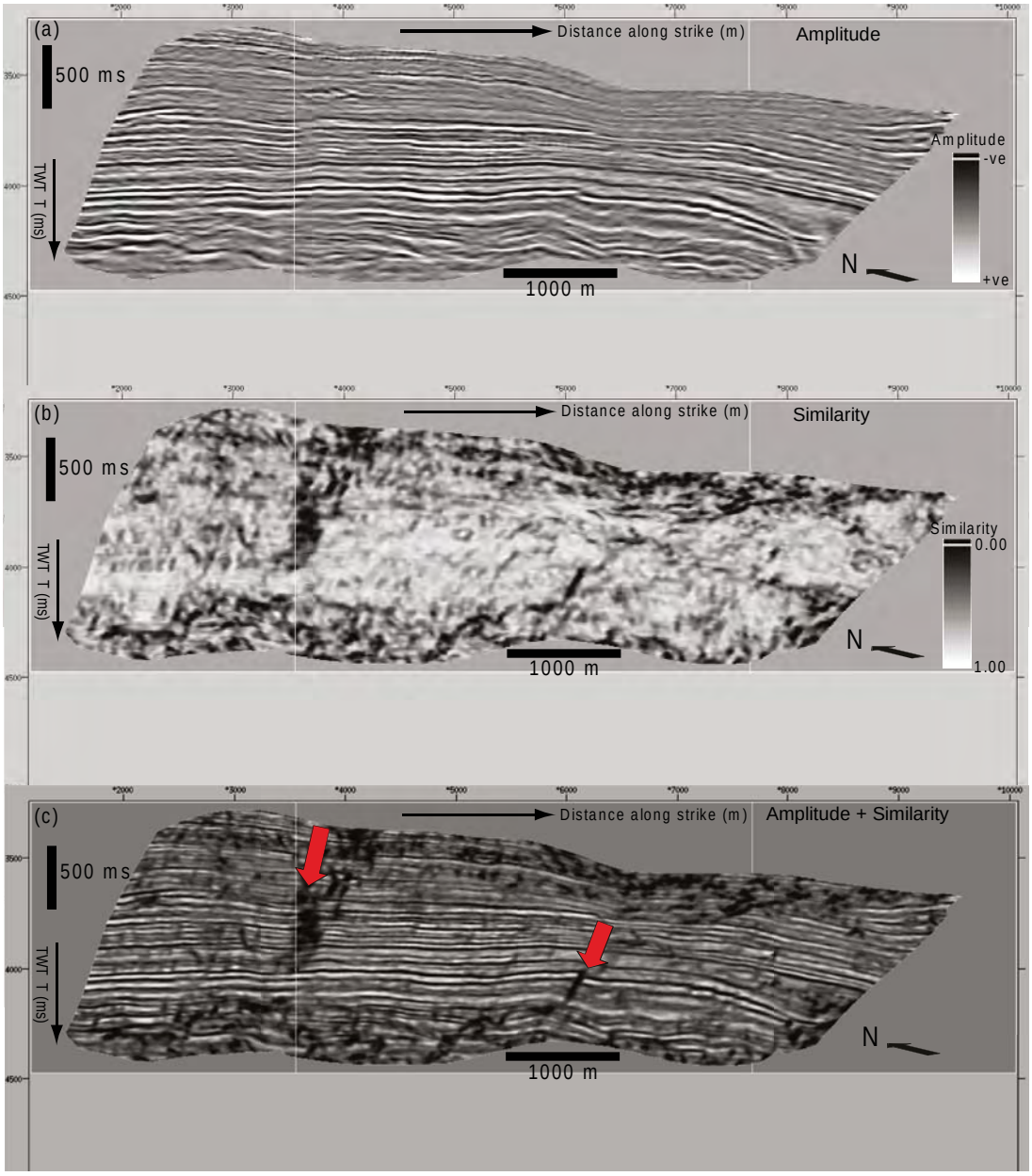

Figure 3.14: Strike views of fault slices sampled through volume seismic amplitude (a) similarity (b) and the integration of the two attributes (c). The slices were sampled 500 m parallel to and away from an interpreted thrust fault in the hanging wall and projected as fault surface attributes. The block red arrows show good correlation between reflector discontinuity and low similarity. Vertical scale is milliseconds two way travel time and horizontal scale is in meters. Vertical exaggeration is ~ 1.6.

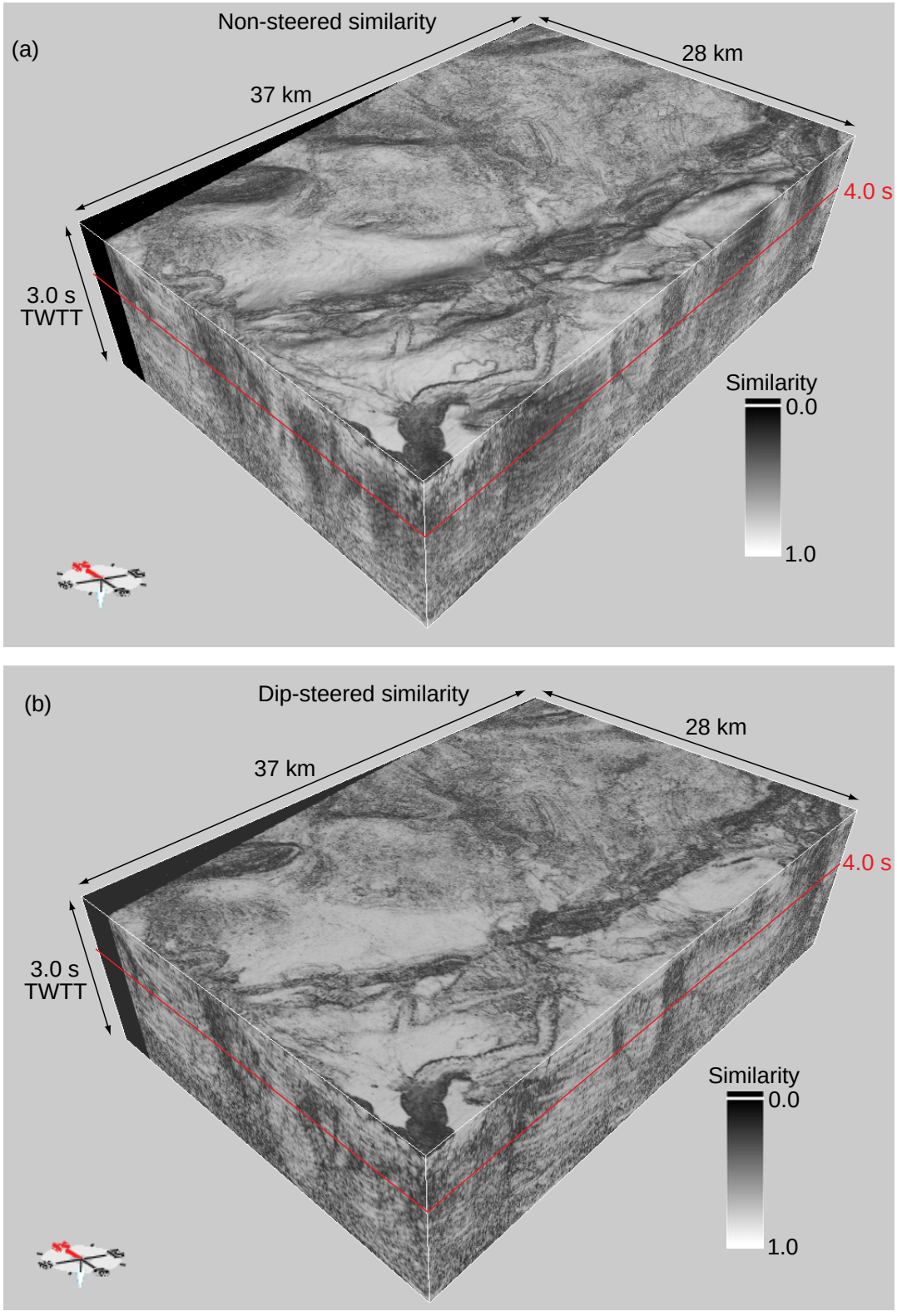

Figure 3.15: Perspective views of similarity volume calculated without dip-steering and (a) and with dip-steering (b). Both volumes span 3.0 s to 6.0 s two way time. The red outline indicates the location of time slices extracted at 4.0 s from the volumes and shown in Figure 3.13. Vertical exaggeration is ~ 3.0.

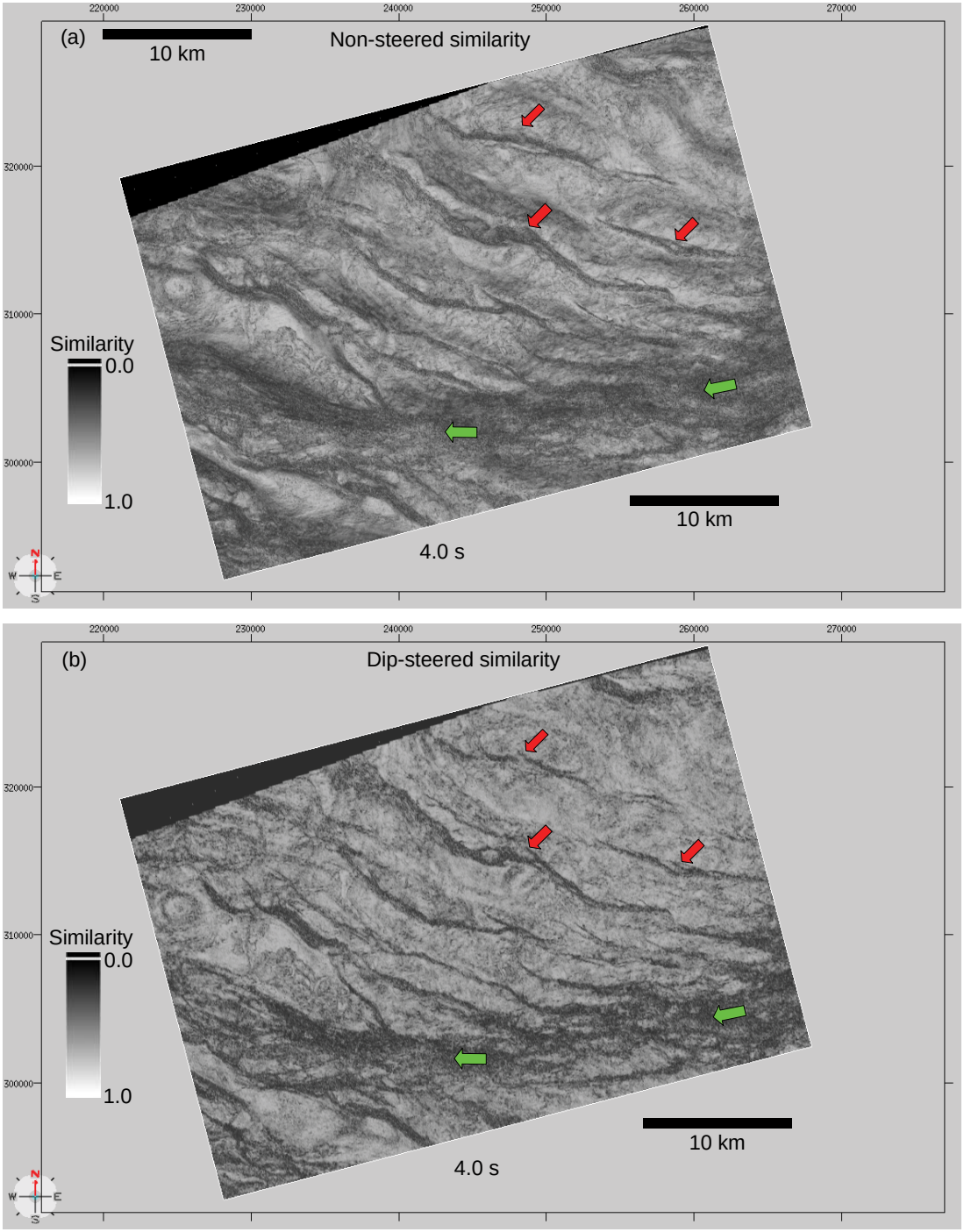

Figure 3.16: Time slices of non-steered similarity (a) and dip-steered similarity (b) extracted at 4.0 s from the similarity attribute volumes in Figure 3.15. Compared to non-steered similarity data, dip-steered similarity attribute has enhanced the sharpness of the WNW-ESE trending zones of low similarity, important structures that may be related to fault propagation/interaction (block red arrows) and the arcuate zone of intense disruption (green block arrows).

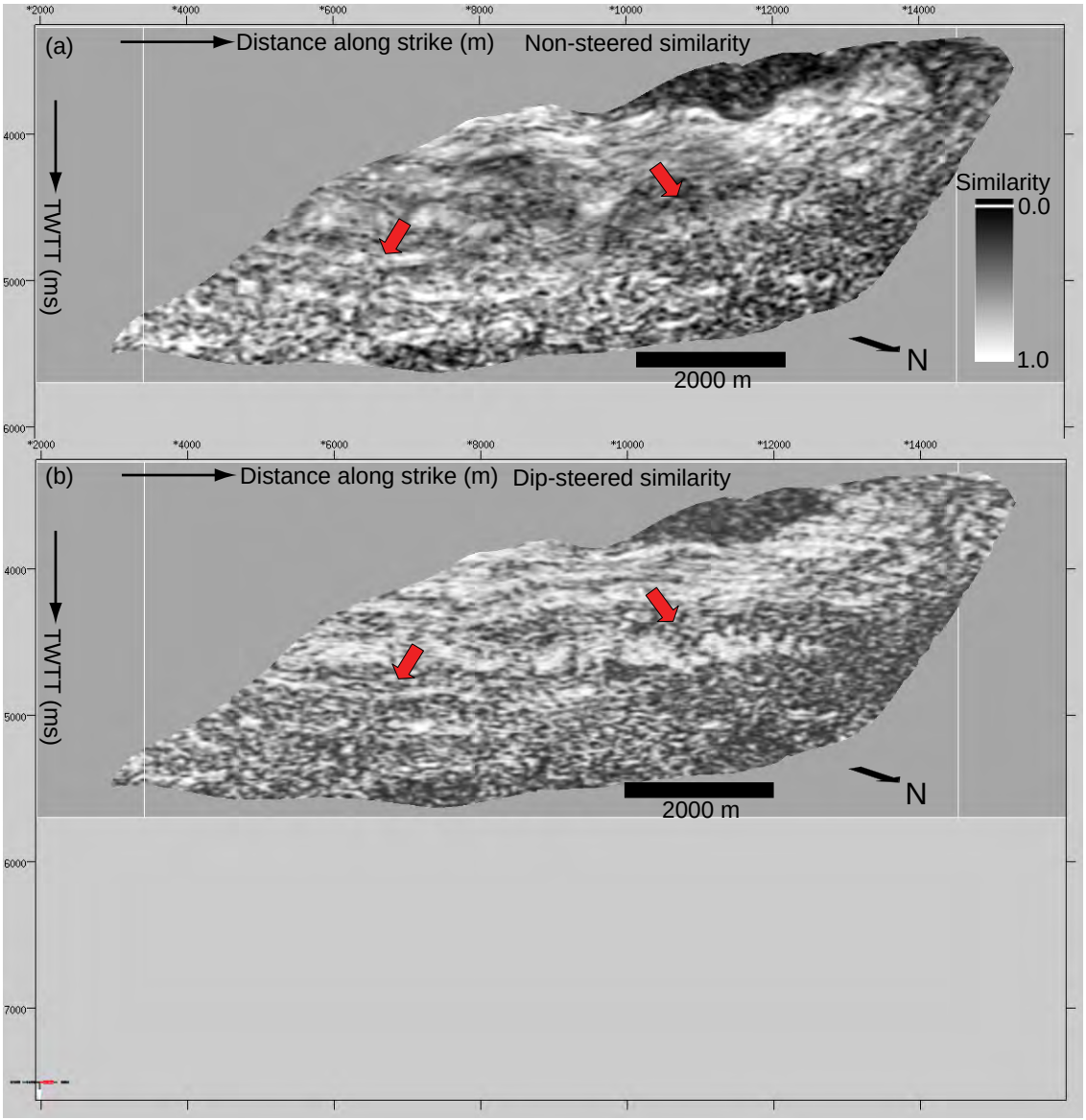

Figure 3.17: Strike views of fault slices sampled through non-steered similarity (a) and dip-steered similarity volumes. The slices were sampled at 500 m parallel to and away from an interpreted thrust fault in the hanging wall and projected as fault surface attributes. The block red arrows show how the sharpness of discontinuities was improved by the application of dip-steering to similarity calculation. Vertical scale is milliseconds two way travel time and horizontal scale is in meters. Vertical exaggeration is ~ 1.6

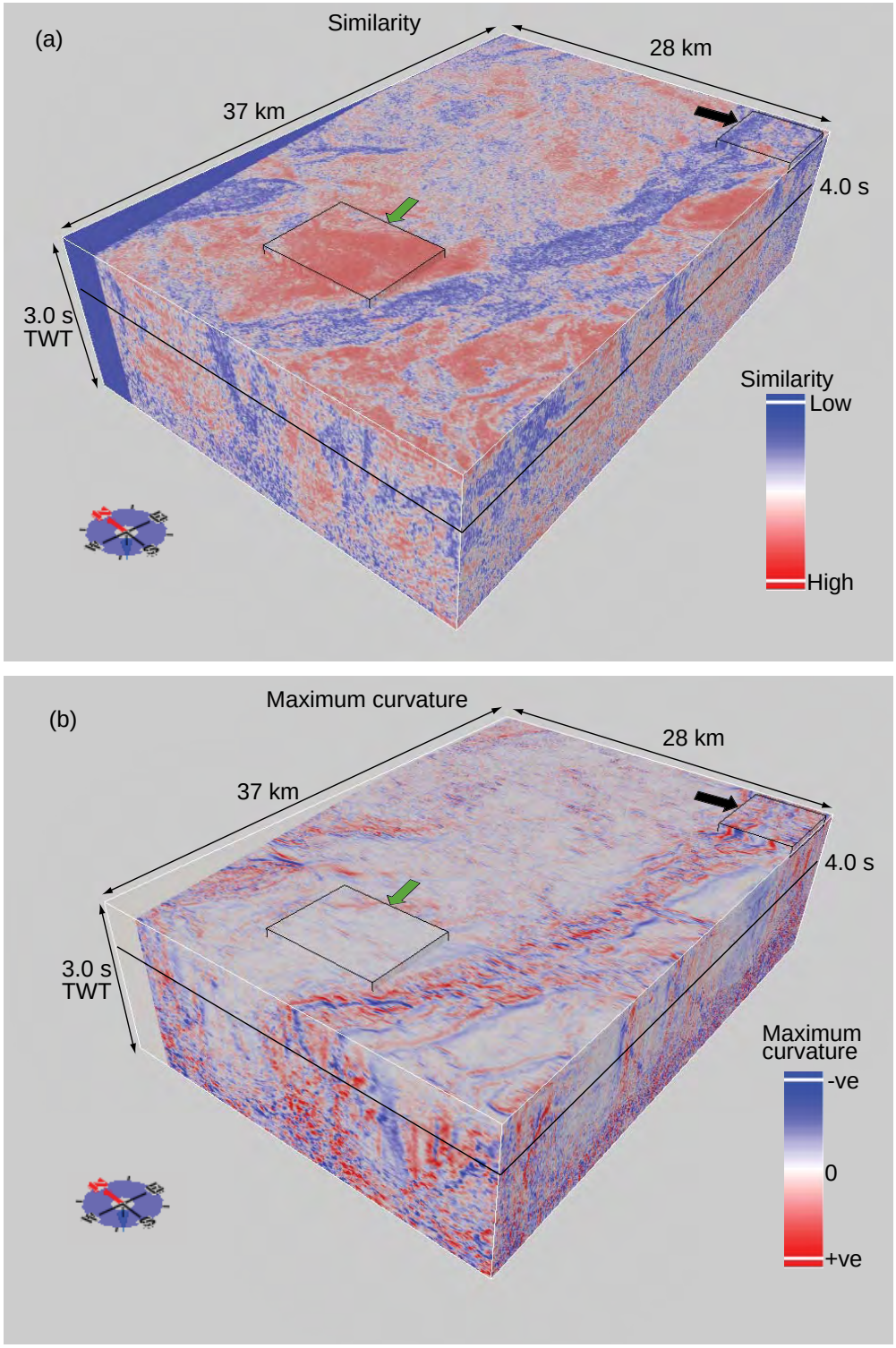

Figure 3.18: Perspective views of similarity volume (a) and maximum curvature volume (b) spanning 3.144 s to 6.0 s two way time. The block black arrow show a correlation between low similarity and intense pattern of maximum curvature, while the block green arrows shows region in the data where high similarity corresponds with low volume curvature. The black outline indicates the location of time slices extracted at 4.0 s and shown in Figure 3.19. Cross plots of the attributes in the boxed areas are shown in Figure 3.22. Vertical exaggeration is ~ 3.0.

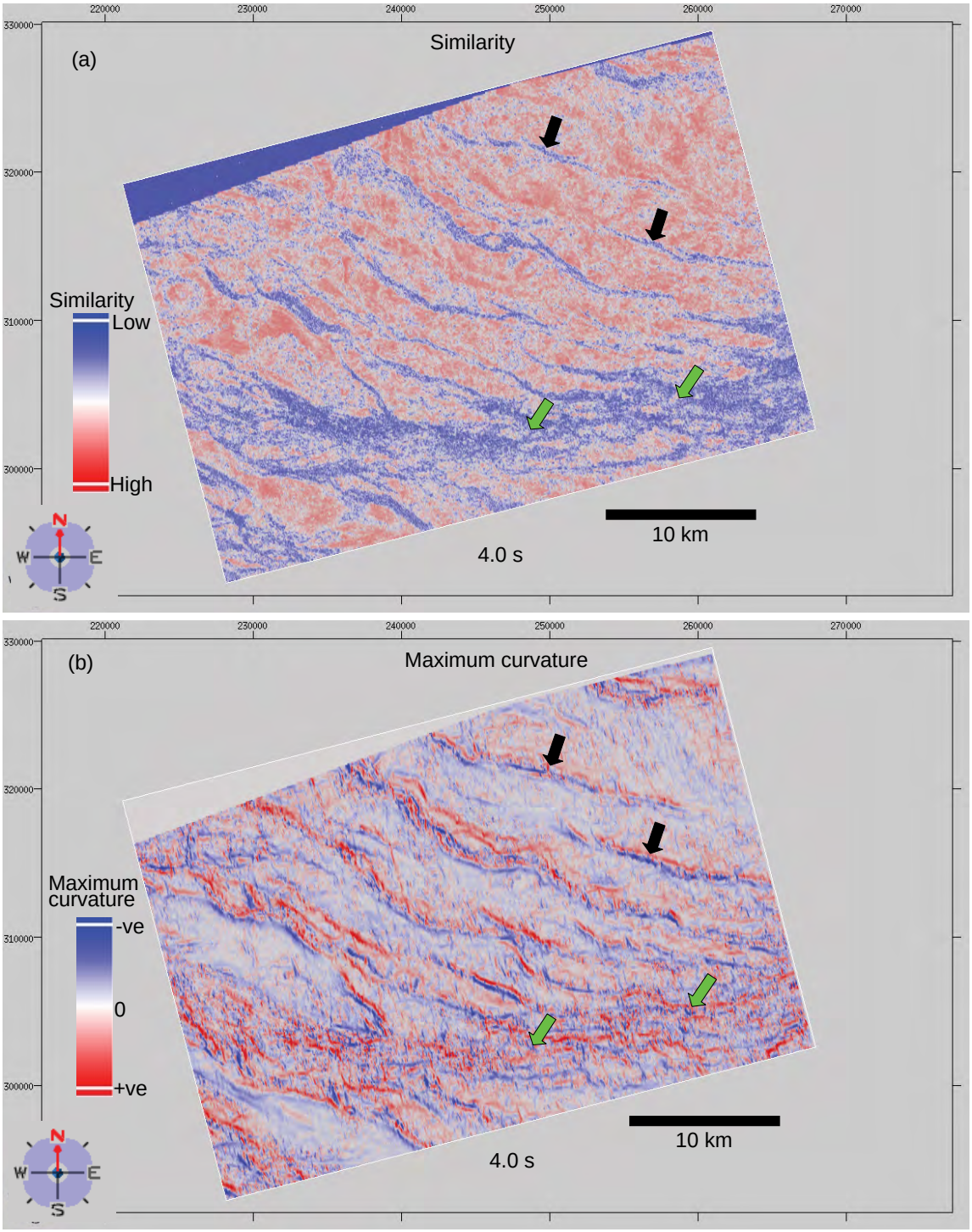

Figure 3.19: Time slice of dip-steered similarity (a) and maximum curvature (b) extracted at 4.0 s from the seismic attribute volumes in Figure 3.18. Note the WNW-ESE trending zones of disruption (block black arrows) seen as a zone of low similarity in the similarity data that appears as zones of juxtaposed positive and negative curvature polarity that may be due to faulting. The green arrows show an arcuate zone of low similarity and complex pattern of curvature.

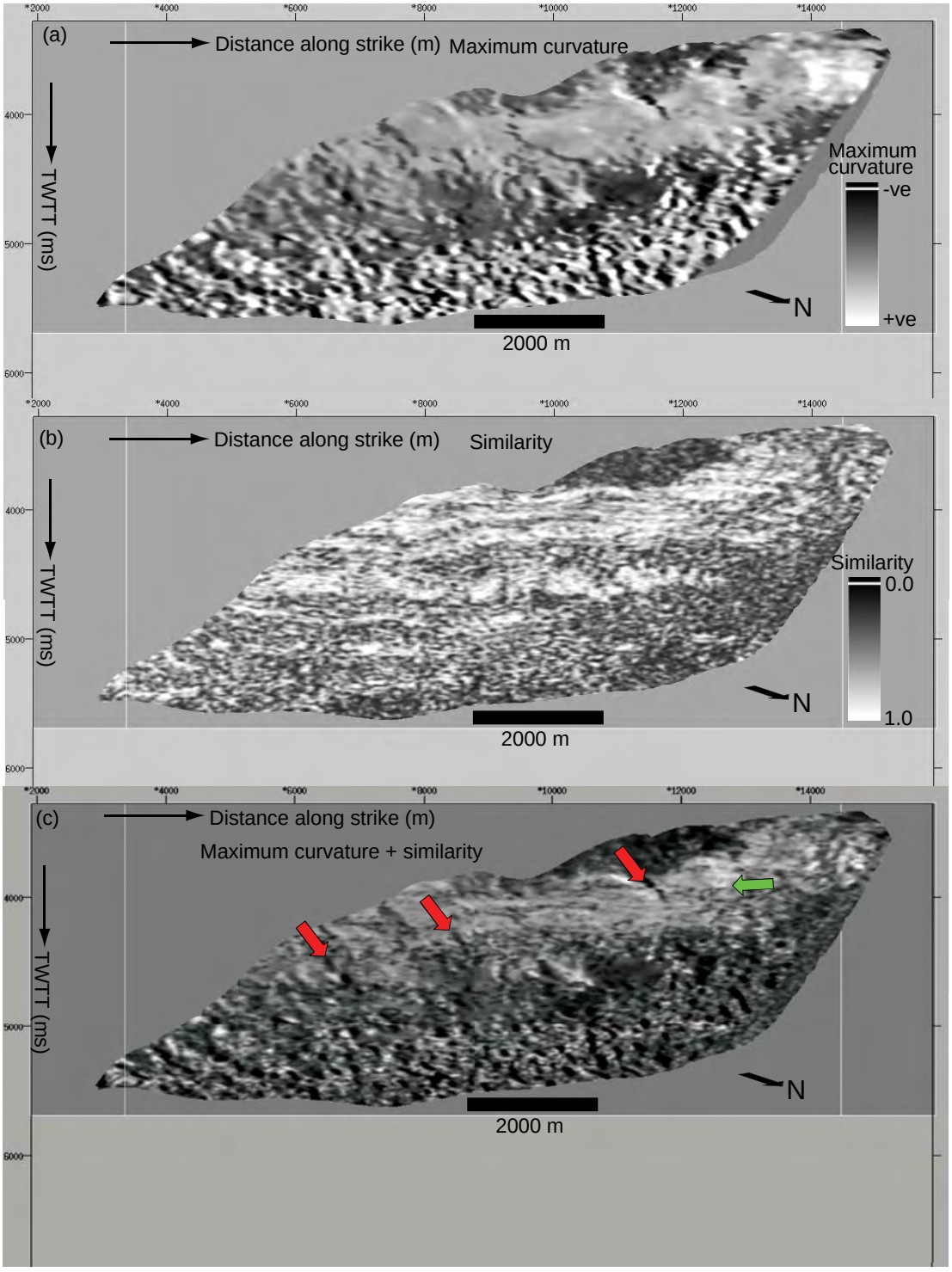

Figure 3.20: Strike views of fault slices sampled through volume maximum curvature (a) similarity (b) and the integration of the two attributes (c).The slices were sampled 800 m parallel to and away from an interpreted thrust fault in the hanging wall and projected as fault surface attributes. The block red arrows show good correlation between low similarity and change in curvature polarity probably representing the location of discontinuities. The green arrow shows a region of intense positive maximum curvature at the top half of the section that appears as a zone of high similarity. Vertical scale is milliseconds two way travel time and horizontal scale is in meters. Vertical exaggeration is ~ 1.6.

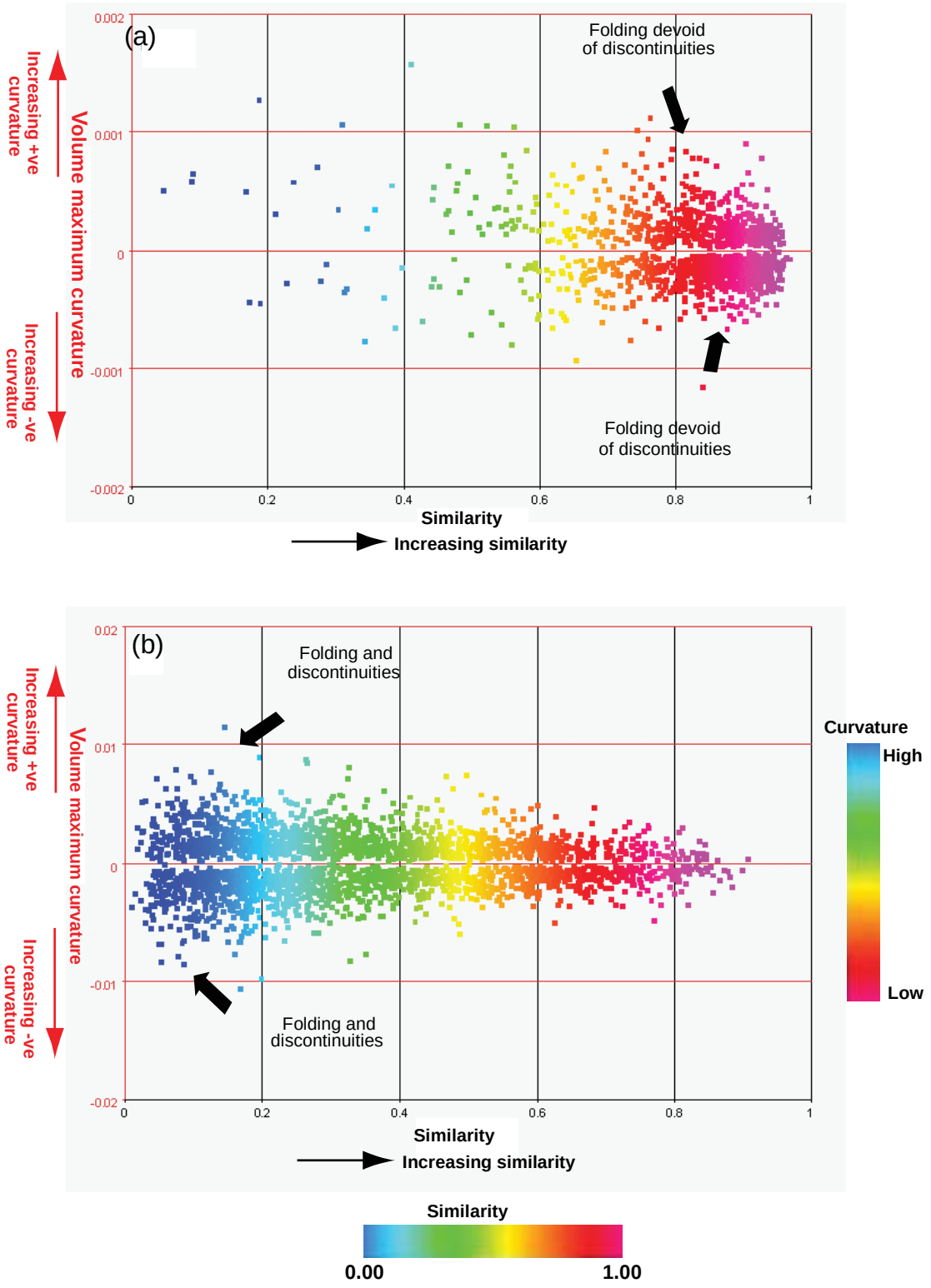

Figure 3.21: Colour-coded cross plot of volume similarity verses maximum curvature for the boxed region indicated by the block green and black arrows in Figure 3.18. In (a) high volume similarity correlates with decreasing volume maximum curvature, while in (b) progressively increasing volume curvature closely matches low volume similarity as indicated by the arrows.

3.4 Discussion and conclusion

Seismic attributes have been used for many years to delineate faults and stratigraphic features that are difficult to map using standard amplitude seismic data (e.g. Lisle, 1994; Bahorich & Farmer, 1995; Roberts, 2001; Hart *et al*. 2002; Masafero *et al*. 2003; Chopra & Marfurt, 2006; Chopra, 2009; Luo *et al*. 1996; Rijks *et al*. 1991; Taner *et al*. 1994). However, one of the challenges of seismic interpretation is the ability to distinguish between seismic anomalies related to real geological features and those related to noise, both of which may occur in the same data.

The coherence cube (Bahorich & Farmer, 1995) has traditionally been used to highlight reflector edges and faults that the seismic amplitude data may not show. The coherence cube is calculated from seismic data using a measure of coherency that quantifies the seismic discontinuity of each trace segment using cross correlation. Discontinuities attributable to faults include dip, azimuth, seismic reflector offset, seismic amplitude and waveform variation (Chopra & Marfurt, 2005). In coherence data, such discontinuities appear as incoherent linear or curved features with low coherence (e.g. Marfurt *et al*. 1999).

However, in the last few years, curvature attributes have been used as complementary means of structural interpretation in addition to seismic discontinuity attributes such as coherency, semblance and variance. The combination of curvature and coherence add value to seismic interpretation by revealing subtle structural and stratigraphic information that might otherwise have been missed if one is used in isolation (e.g. Chopra, 2009).

Three-dimensional volume attribute extraction techniques have been applied to deepwater Niger Delta seismic data with the primary aim of extracting reflector volume morphology/shape and continuity that may be associated with deformation and relevant to the

structural and stratigraphic interpretation of the data and in investigating the structural pattern of the volumes adjacent to faults. The workflow is primarily centred on calculating volume measures of dip in the inline and crossline directions and the application of structurally-oriented filters to enhance the contrast and resolution of multi-trace seismic attributes, from which seismic similarity and maximum curvature volumes are extracted.

The dip-steering and filtering sequences are important preconditioning procedures prior to using the data as input to calculating seismic attributes. Filtering the data can significantly impact on the reliability of detecting discontinuities and minimise the impact of noise in interpreting crossplots of the seismic attributes (Chopra & Marfurt, 2010). This assertion is particularly important in this thesis since crossplots of curvature and similarity extracted across thrust fault surfaces are used for investigating the seismic structure of the volumes surrounding the faults.

A demonstration of the importance of similarity attribute as a useful attribute in highlighting discontinuities has been presented. However, while both similarity and coherency measures how similar or different two trace segments are, coherency is a simple cross-correlation of the trace-segments while similarity measures how far apart the vectors are in hyperspace and normalizes that to the vector's length. Coherency is not sensitive to amplitude scaling, while Similarity is. Hence comparing traces with identical waveform, apart from a scale-factor will give 1 with coherency (as the shape of the wave is identical) while similarity will be less than 1 (as it is sensitive to the scale difference). Furthermore, the quality of the similarity attribute has been improved by the application of dip-steering. Similarity calculated on normal seismic data provide poor resolution of the discontinuities, while the application of dip-steering has improved the resolution significantly by correcting for the dip of the seismic reflectors (Figures 3.16 & 3.17). Therefore, the discontinuities highlighted by the seismic attributes data

presented in this chapter are presumed to be disruptions related to the underlying geology and not due to noise, acquisition footprints, processing artefacts and dipping events.

In this thesis, a measure of normal curvature that defines the largest absolute curvature of a reflector was calculated. The attribute highlights reflector geometry and highlights can detect regions of folding and flexure usually related to faulting (Klein *et al* 2007). However, while the similarity attribute detects a fault as a point of discontinuity, curvature attribute measures lateral changes in dip magnitude and has two opposite anomalies on either side of a fault (Figures 3.8, 3.19 and 3.20). This phenomenon is also demonstrated graphically in Figure 3.21. For this reason, curvature anomalies often do not align with discontinuities detected by similarity attribute. This observation is particularly important when using the two attributes to detect anomalies related to disruption at the same location in the volumes adjacent to faults. It may be useful to use both attributes for detailed structural analysis of the structure of fault zones since the curvature and discontinuity of reflectors may be due to deformation in the volumes adjacent to the faults.

Preliminary interpretation of the seismic attributes has revealed a well defined pattern of WNW-ESE trending zones of disruption and folding in the study area. The structures are interpreted to represent the location of thrust faults and folds formed as a result of the gravity-induced compressional deformation above detachment surfaces in deepwater Niger Delta (e.g. Damuth, 1994; Corredor, *et al*. 2005; Bilotti, *et al.* 2005; Briggs, *et al*. 2009).

In conclusion, the improved contrast and sharpness of discontinuities as a result of the volume seismic attribute extraction and image enhancement techniques applied to the seismic data and the confidence that the seismic attribute anomalies are most likely related to the underlying geology is the motivation for using the data to investigate the structural and stratigraphic framework of the study area in Chapter Four and using traces of faults mapped

from the data to calculate and analyze surface and structural attribute plots of the faults in Chapter Five. In Chapter Six, the data is primarily used to investigate the internal seismic structure of the volumes adjacent to the faults.

CHAPTER FOUR-STRATIGRAPHIC AND STRUCTURAL FRAMEWORK OF THE JDZ SEISMIC DATA

4.1 Introduction

This chapter describes the structural and stratigraphic setting of distal parts of southern Niger Delta sedimentary lobe in deepwater Niger Delta fold and thrust best imaged in the JDZ seismic data (Figure 1.1). The chapter is divided into three sections. An outline of the geological setting of the Niger Delta is first presented. The seismic data and workflow for interpreting the data is then described. Finally seismic observations of the stratigraphic and structural framework of the study area are presented.

4.2 Geological setting

4.2.1 Introduction

The Niger Delta is one of the largest Cenozoic delta systems and classical shale tectonics provinces located in the West African continental margin covering an area of ~140,000 km^2 (Doust & Omatsola, 1990; Hooper *et al*. 2002; Wu & Bally, 2000). The delta was formed in the Cretaceous by rifting and shearing between Africa and South America as manifested by several fracture zones expressed as trenches and ridges including the Fernando Po Fracture Zone located ~30 km east of the study area (Figure 4.1). Geometrically the Niger Delta has an arcuate shape split into two lobes by the Charcot Fracture Zone (western and southern lobes). The lobes are the products of interacting sedimentation and deformation (Doust & Omatsola, 1990; Morgan, 2003).

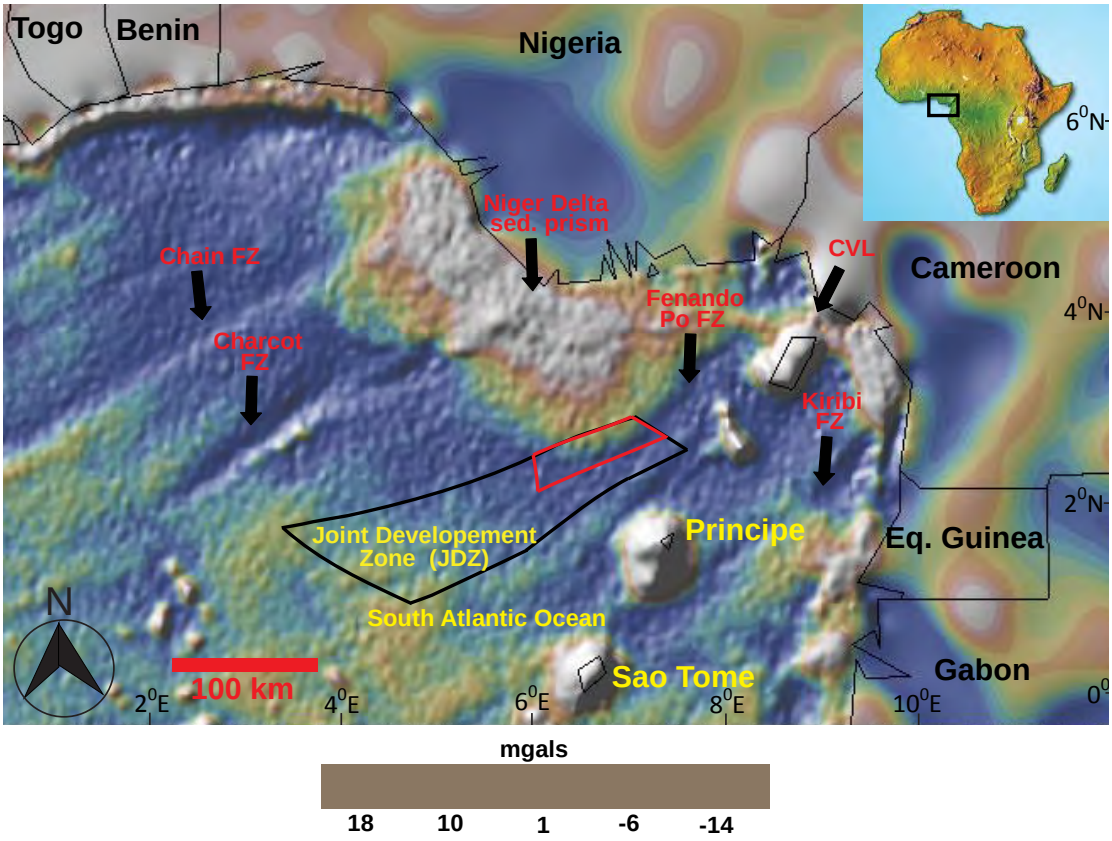

Figure 4.1: Free-air gravity map of the Gulf of Guinea showing the location of the Niger Delta, the Joint Development Zone (JDZ) and key structural features of the region. The thick sediments of the Niger Delta and Cameroon Volcanic Line (CVL) have positive gravity anomalies surrounded by negative gravity lows of the fracture zones indicated by the block arrows. The red outline represents the location of the JDZ seismic data (Gravity map from Sandwell & Smith, 1997).

4.2.2 Stratigraphic setting

The Cenozoic stratigraphy of the Niger Delta is divided into three diachronous Formations that form a major regressive upward coarsening cycle broken up into a series of offlap cycles named the Akata, Agbada and Benin Formations of Eocene to Recent age reflecting a regressive mega-sequence with a thickness of ~12 km (Short & Staeuble, 1967; Avbovbo, 1978; Evamy *et al*. 1978; Whiteman, 1982; Knox & Omatsola, 1989; Doust & Omatsola, 1990; Weber & Doukoru, 1975).

The base of the deltaic succession consists of pro-delta marine shale of the Akata Formation thought to be of Late Cretaceous to Palaeocene age. Directly above the

Akata Formation is a paralic sequence of predominantly sands and minor clay and silt intercalations representing the Miocene to Pliocene sediments of the Agbada Formation. (Doust & Omatsola, 1990: Avbovbo, 1978). The uppermost Benin Formation consists of continental sands but is absent in deepwater settings (Morgan, 2003). Detailed description of the formations is discussed in the references listed above. Figure 4.2 is a summary of the generalized regional stratigraphy depicting the units and a seismic cross sectional display of the reflectivity patterns of the equivalent sedimentary units in the study area.

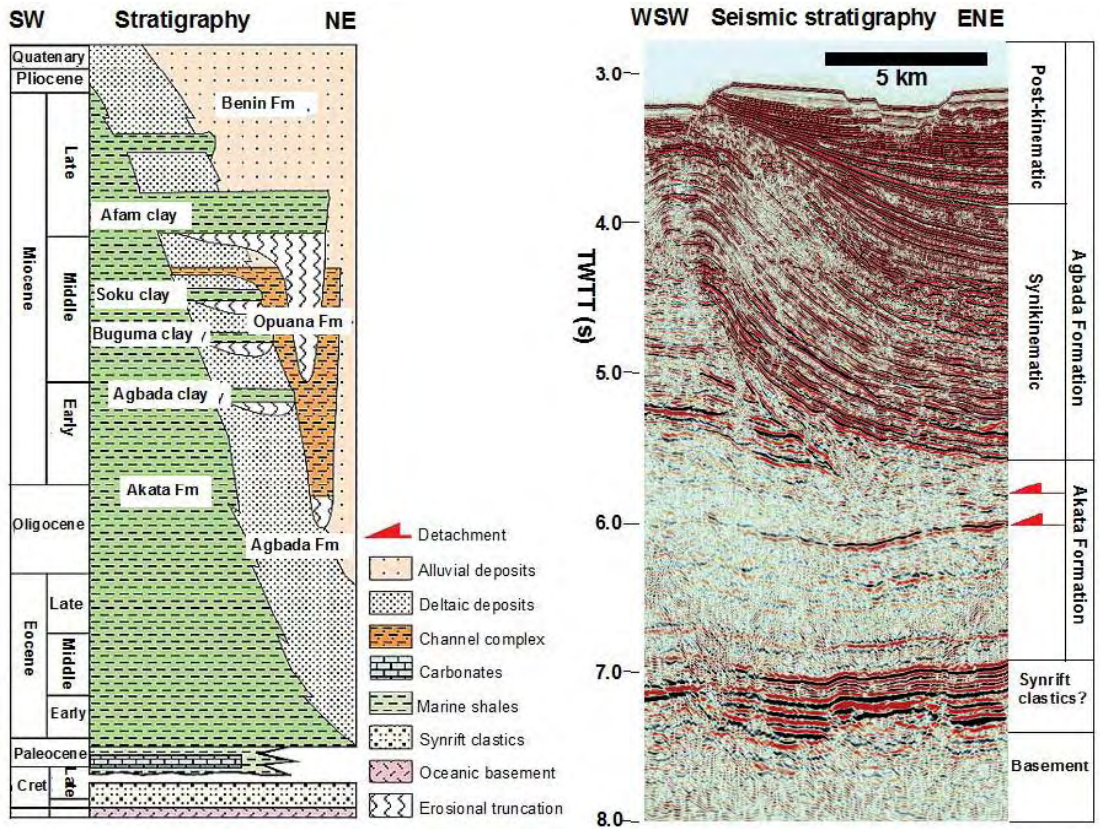

Figure 4.2: Schematic diagram of the regional stratigraphy of the Niger Delta and cross sectional seismic display from the JDZ data showing seismic facies representing key Niger Delta stratigraphic units. The red arrows show the location of two regionally extensive reflections that may be related to detachment surfaces in the study area (Stratigraphic column from Corredor *et al*. 2005).

4.2.3 Structural setting

A variety of structural styles is exhibited in the Niger Delta encompassing the distal limits imaged in the JDZ seismic data (e.g. Rowan *et al*. 2004; Corredor *et al*. 2005; Bilotti *et al*. 2005; Damuth, 1994; Briggs *et al*. 2009). Corredor *et al*. (2005) identified five structural domains based on the interpretation of regional two-dimensional seismic lines and bathymetric data and organised into a series of belts each characterised by a specific structural style (Figure 4.3).

The structural framework is conceptually made of a gravity slide/glide complex divided into a landward zone of extension, mid-slope zone of translation and a toe-thrust zone of folding and thrusting. The later is divided into an inner (proximal) and outer (distal) thrust domains partitioned by a detachment (inter thrust) zone (Figure 4.4). Most of the faults in the two domains verge oceanwards and sole into the detachment surfaces (e.g. Corredor *et al*. 2005; Briggs *et al*. 2009; Steele *et al*. 2009). The distal part of the deepwater Niger Delta is speculated to be underlain by oceanic basement (Briggs *et al*. 2009). Linked together on a regional scale, the bathymetric slope and structural pattern indicates that large portions of thick sedimentary prism are gravitationally moving downslope (basinward) under the weight of the sedimentary overburden via detachment surfaces located within the overpressured clays of the Akata Formation (e.g. Damuth, 1994).

Compressional deformation in the distal parts of deepwater Niger Delta is probably still active and is expected to be manifested in the form of thrust faults and folds, gravity flow structures and bathymetric ridges representing the hanging wall of thrust faults on the seabed. This chapter focuses on the distal parts of the outer fold and

thrust belt south east of the southern Niger Delta sedimentary lobe (dashed box in Figure 4.4).

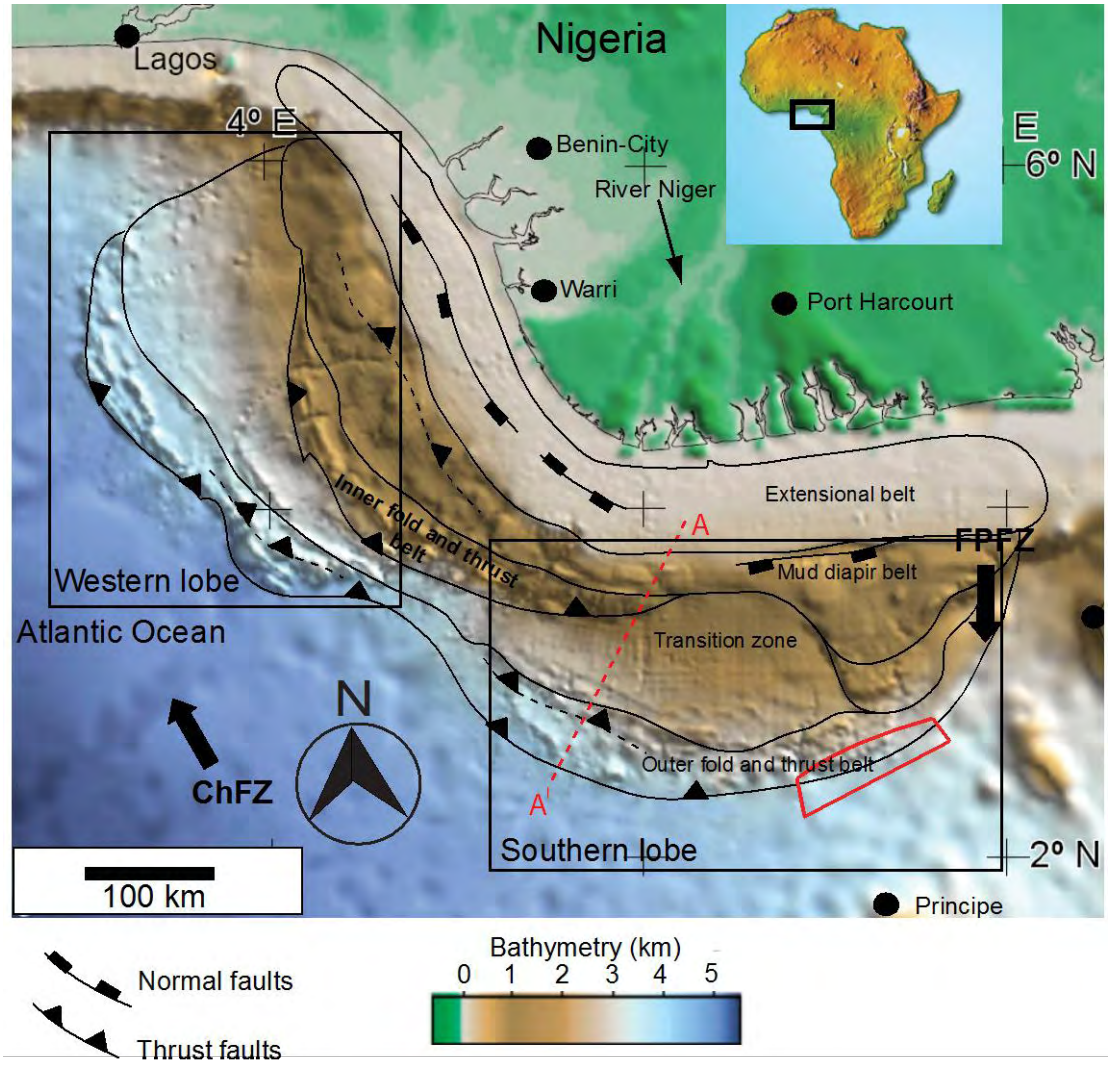

Figure 4.3: High resolution bathymetric image showing the main structural domains in the Niger Delta that includes: (1) Extensional province, (2) Mud-diapir belt, (3) Inner fold and thrust belt, (4) Transition zone, and (5) Outer fold and thrust belt. The block black arrows represent major fracture zones in the Gulf of Guinea (Charcot [ChFZ] and Fernando Po [FPFZ] fracture zones respectively). The red outline is the approximate location of the study area. The interpreted NE-SW cross section is shown in Figure 4.3 (Bathymetry from Corredor *et al*. 2005).

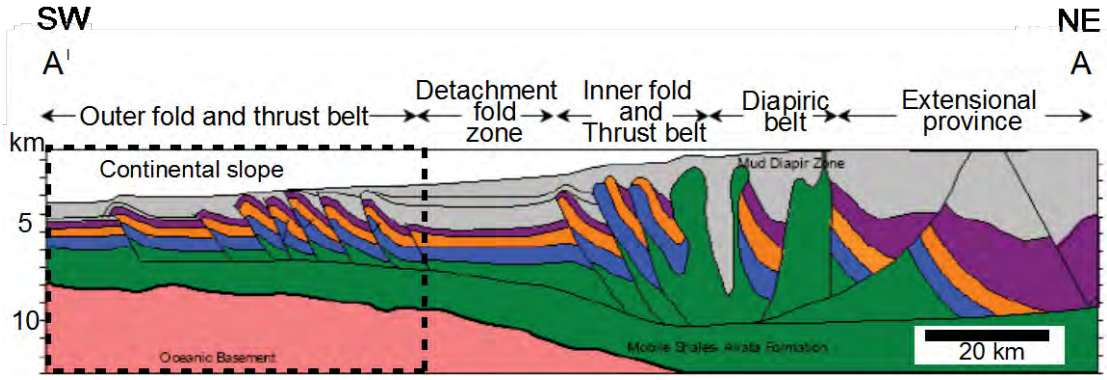

Figure 4.4: Interpreted regional seismic profile across the Niger Delta showing the key structural elements and links between extension on the shelf and contraction in deepwater settings via detachment surfaces (Bilotti *et al.* 2005). The dashed black box shows the approximate location of the JDZ. Vertical scale is in kilometers and exaggeration is 3. The location of the profile is shown in Figure 4.3.

4.3 Methodology

4.3.1 Seismic data

The seismic data is a NE – SW rectangular oriented volume covering an area of ~3000 km^2 with a line and trace spacing of 25 m x 12.5 m respectively (1126 lines and 10741 traces) acquired with 6 km offset length, streamer spacing of 100 metres with a fold of 60, 8 s recording interval and a sampling rate of 4 ms (Figure 3.1). The data are displayed with a reverse polarity (European convention) and have been zero phase migrated (i.e. the wavelet is symmetrical with the maximum amplitude situated on the geological interface that caused the reflection) so that an increase in acoustic impedance causes a negative amplitude response (trough) and is red, while a decrease in acoustic impedance causes a positive amplitude response (peak) and is black in vertical seismic sections in seconds two way travel time (Figure 4.5).

The quality of the seismic data is generally good but deteriorates beneath faults and in the forelimb regions of faults (Figure 4.6). The low resolution in the footwall is probably a result of rocks with contrasting velocities across faults that commonly

occur in young Tertiary sedimentary sequence and trishear folding in the forelimb of the faults. In addition, there is the tendency for a rapid decrease in vertical resolution especially within the basal detachment units interpreted to be due to homogenous nature of the unit, fluid overpressures and the attenuation of propagating seismic waves with increasing depth. Similar observations have been made in seismic data that images parts of deepwater Niger Delta Central (e.g. Ajakaiye & Bally, 2002; Briggs *et al.* 2006; Morley, 2003; Maloney, 2010).

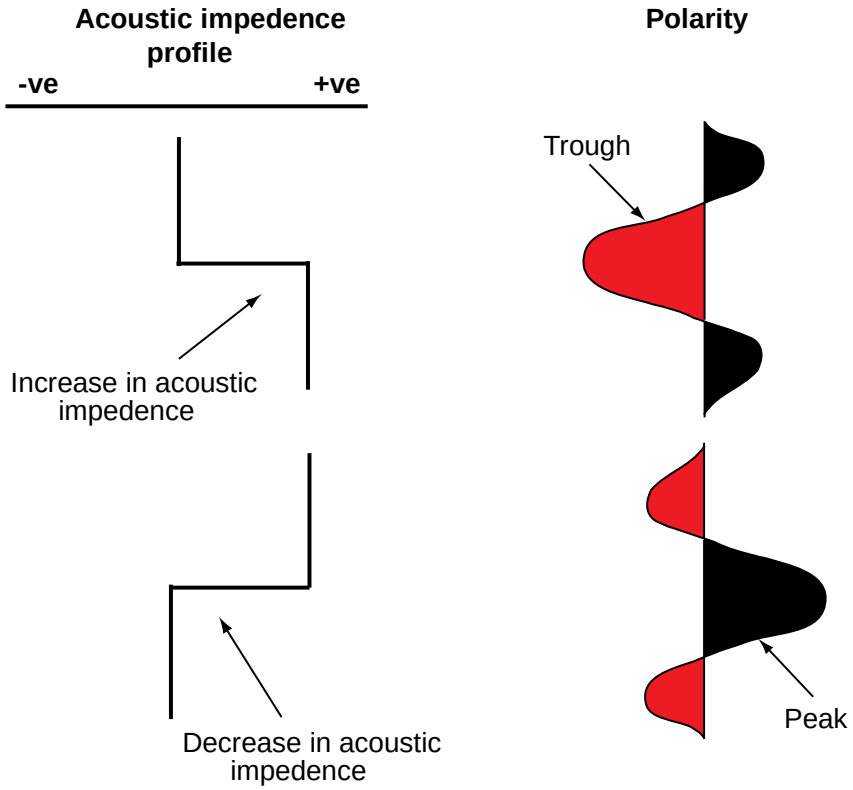

Figure 4.5: Schematic illustration of the polarity of the JDZ seismic data. An increase in acoustic impedance is a trough and displayed in red, while a decrease is a peak and displayed in black.

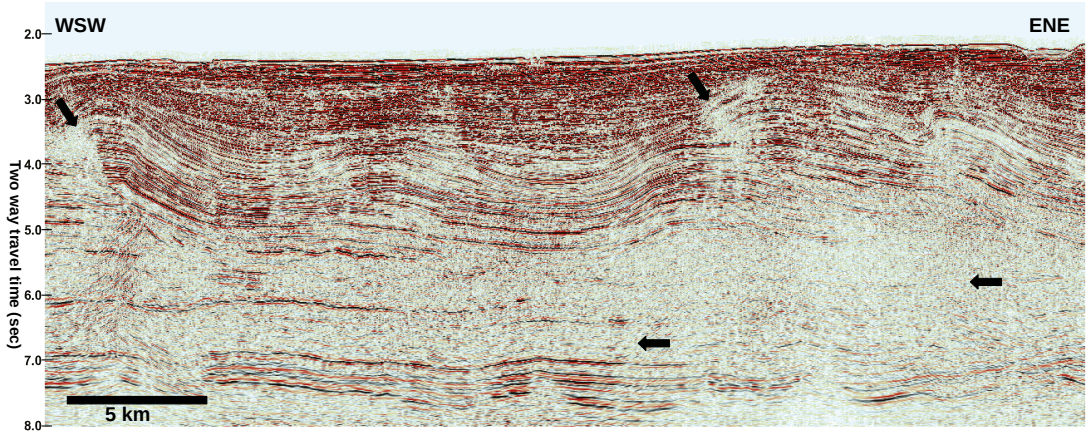

Figure 4.6: Seismic cross section showing the typical pattern of reflectivity in the study area. The block arrows highlight regions exhibiting poor reflectivity related to imaging beneath faults, trishear folding in the forelimbs of the faults and the reduction in seismic resolution with increasing depth. Note also that most of the faults are best imaged between 3.0 s and 6.0 s two way travel time. (See location in Figure 4.11). Vertical scale is in seconds two way travel time and horizontal scale is in kilometres.

The dominant frequency in the data varies with depth and is between 40 Hz and 60 Hz at the interval of interest where most of the discontinuities are well imaged (3.0 s to 6.0 s two way time). A frequency of 46 Hz is used to calculate the vertical resolution of the data. This frequency appears to be the strongest in the amplitude spectrum plot (Figure 4.7). The vertical resolution is equal to one-quarter of the seismic wavelength $\lambda/4$, (Brown, 2004) and varies from ~10 m at shallower sections of the seismic data but decreases to ~18 m at deeper sections of the seismic volume based on the downward increase in interval velocity. The horizontal resolution is ~100 m based on the width of the Fresnel zone (Sheriff & Geldert, 1995). Velocity data used in calculating seismic resolution was obtained from a two-dimensional interval velocity profile of the deepwater Niger Delta outer fold and thrust belt in Cobbold *et al.* (2009).

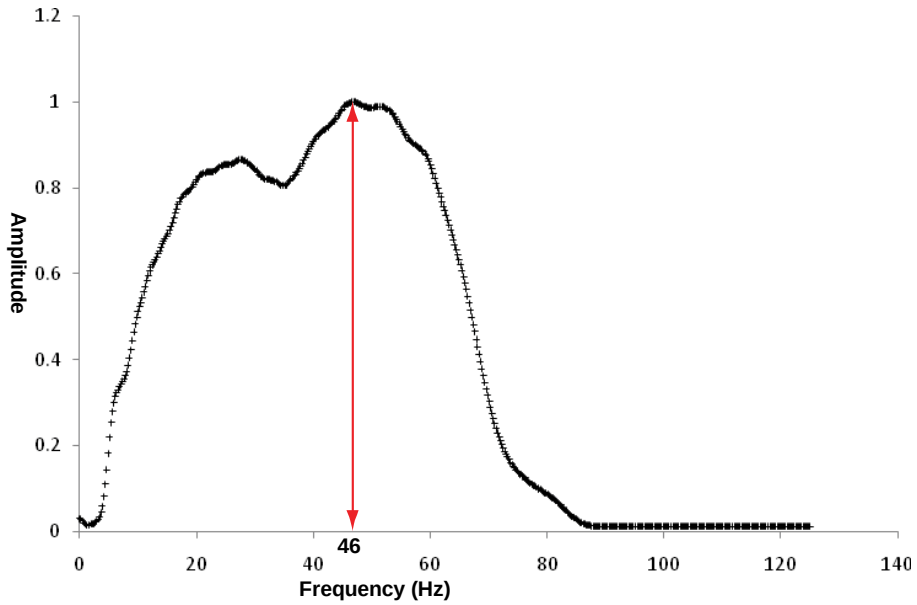

Figure 4.7: Plot of amplitude spectrum in Central JDZ sampled between 3.0 and 6.0 seconds two way travel time. This interval represents the part of the data containing most of the faulted volumes. The strongest frequency is 46 Hz and was used in estimating the resolution of the data

4.3.2 Workflow

Figure 4.8 is a summary of the workflow for describing the stratigraphic and structural setting of the seismic data.

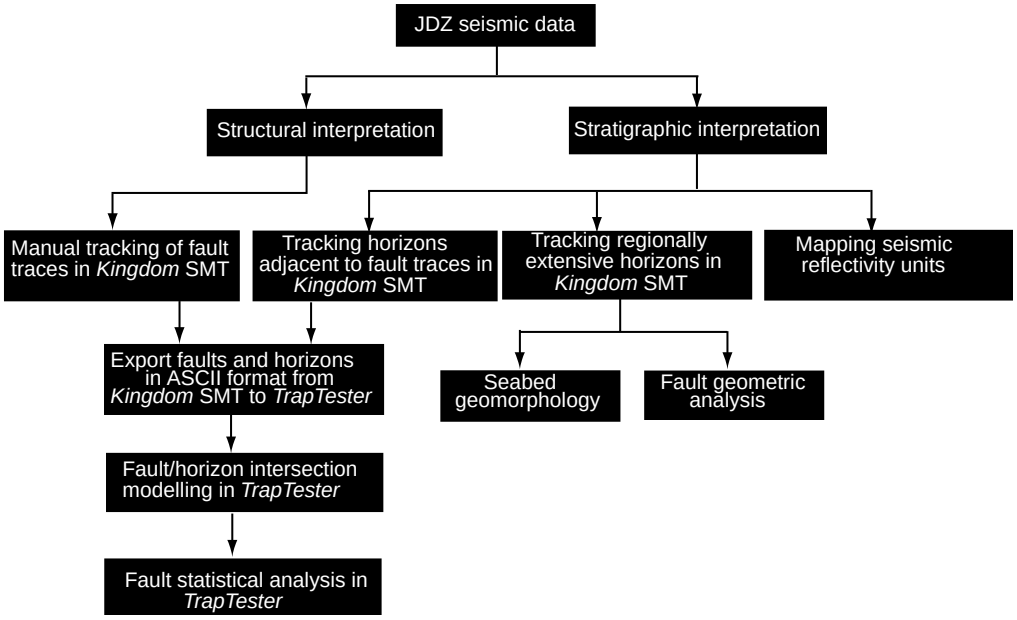

Figure 4.8: Workflow for investigating the structural and stratigraphic framework of the JDZ seismic data

4.3.2.1 Structural interpretation

The first working step was to load the data into *Kingdom* (Seismic Micro-Technology) JDZ seismic interpretation project. A rapid assessment of the seismic data shows that the major discontinuities are orthogonal to the survey grid. The faults were thus mapped on at least every inline in the direction orthogonal to the faults (e.g. Brown *et al.* 1993). The fault traces were tracked in vertical amplitude cross sections in two way travel time based on reflection terminations and offsets. Reflector offset is best seen between 3.0 s and 6.0 s two way travel time where most of the discontinuities are well imaged. In places, the imaging of reflector termination is poor and similarity attribute cross sections (In vertical and horizontal profiles) were used to guide the interpretation. The similarity volume highlights discontinuities based on low similarity at the location of the discontinuities. Detailed description of how the attribute was extracted and its importance in mapping discontinuities in seismic data is described in Chapter Three.

4.3.2.2 Stratigraphic interpretation

4.3.2.2.1 Seismic stratigraphy

The stratigraphic framework of the study area was interpreted based on the seismic reflectivity patterns using several seismic cross sections across the study area. Additional cross sections on a smaller scale are used to investigate detailed pattern of reflectivity especially in the deeper parts of the seismic data where the resolution is poor. No well data is available for this thesis, therefore, the interpretation was based on the pattern of amplitude continuity, strength and internal geometry of the units.

4.3.2.2.2 Horizon interpretation

Horizon interpretation was carried out for two reasons. Firstly, horizons in the hanging wall and footwall of faults were mapped and used to produce models of fault/horizon intersections. Unlike normal faults, thrust faults have reverse displacement and a single horizon in *Kingdom* SMT software cannot be carried over across the faults. To overcome this problem, a horizon is mapped in the hanging wall and correlated across the fault by mapping another but equivalent horizon in the footwall. This means that a single offset horizon in *Kingdom* is represented by two horizons across a fault (Figure 4.9). The horizons were mapped on every line manually and in places using two-dimensional auto-hunt tool based on visual amplitude character recognition to correlate the horizons across the faults. The interpreted horizons were then imported into Badleys's *TrapTester* in ASCII file format and models of the fault/horizon intersection are produced.

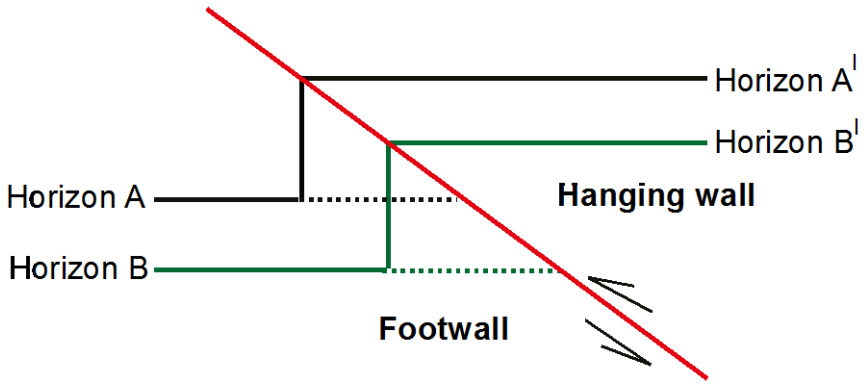

Figure 4.9: Schematic illustration of tracking horizons across reverse/thrust faults in *Kingdom* SMT. A single horizon across thrust faults is made up two horizons mapped and correlated across the fault. However, in an attempt to "force" a single horizon across a thrust fault, an impression of a vertical fault plane at the location of the hanging wall cut is created.

Secondly, a key horizon offset by most of the major discontinuities was mapped and used to describe aspects of fault interaction. In mapping the horizon, interpretation was carried to the fault cut in the hanging wall and stopped below that point in the footwall. An impression of a vertical fault plane at the location of the hanging wall

fault cut is created (Figure 4.9). The seabed reflection was mapped as across the whole of the study area and depth converted using a velocity of 1500 m/s^{-1} and used to describe present day seabed seismic geomorphology. It is not possible to assign definitive ages to the horizons in the absence of well data other than to infer the ages relative to their location within the Agbada-Akata Formation sedimentary sequences. Interpretation of faults and horizons was done using *Kingdom* interpretation software provided by Seismic Micro-Technology (SMT).

4.3.2.3 Fault statistical analysis

Models of fault/horizon intersections for eleven faults mapped in the central parts of the study area are analysed using the fault statistical tool in *TrapTester* software. To calculate reliable plots of fault/horizon intersection models, the trim distance and patch width were selected. The trim distance determines how much horizon data is excluded from the modelling, while the patch width determines the amount of horizon data included in the modelling (Figure 4.10a). Horizon raw data outside the patch width are not used for the modelling. Increasing the patch width will increase more horizon raw data in the modelling. In creating fault polygons, horizon patches must be incorporated into an extension surface that encompasses the entire fault (Figure 4.10b). Data points in the fault polygon are created where the horizon extension surfaces intersects the edge of the fault.

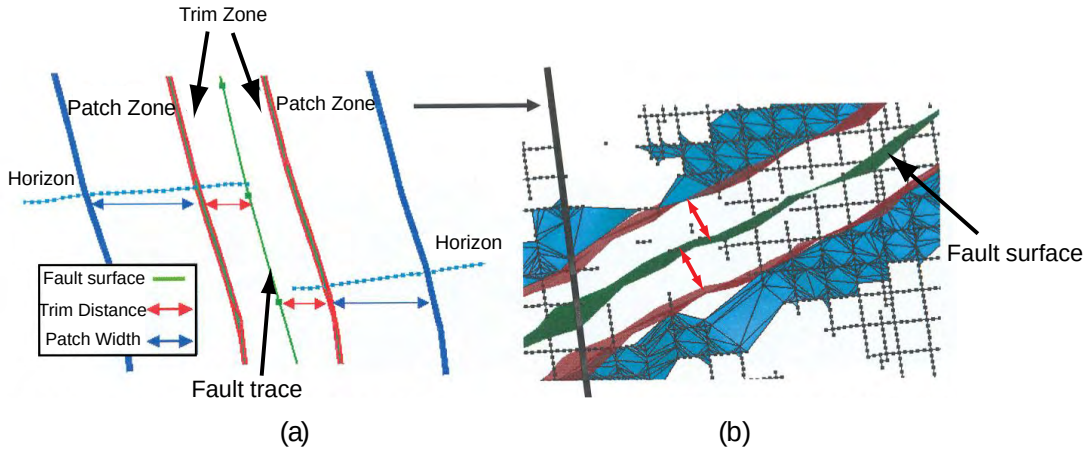

Figure 4.10: Schematic illustration of fault/horizon intersection modelling parametization. The fault trim distance defines the amount of horizon data not included in the modelling, while the patch width describes the amount of horizon data included in the modelling (a). Figure (b) is a map view illustration of the triangulation of horizon raw data within the patch zone (*TrapTester* manual, 2010).

In *TrapTester* the default measure of displacement is throw. However, a better measure of displacement for faults with highly variable dips is the integrated line between horizon terminations and can be estimated by the dip separation. For a purely dip-slip fault, the dip separation is similar to the displacement of the fault (Peacock *et al*. 2000) and was used as proxy for displacement for all the faults analyzed. Dip plots of the faults were made using a velocity model of deepwater Niger Delta (Morgan, 2003). In addition a strain summation plot of the faults was made to estimate the amount of shortening due to compression in the central parts of the study area. Finally the strike and dip orientation of the faults and fault length versus maximum displacement (dip separation) scaling relationships are calculated and compared to global thrust databases in the literature. Plots of fault/horizon intersection models and statistical analysis were done using *TrapTester* structural modelling software provided by Badleys Geoscience.

4.4 Seismic observation

4.4.1 Introduction

Twelve seismic lines have been selected across the JDZ and used to illustrate the internal seismic reflectivity patterns, cross sectional geometries of the faults and in general the structural framework of the study area (Figure 4.11).

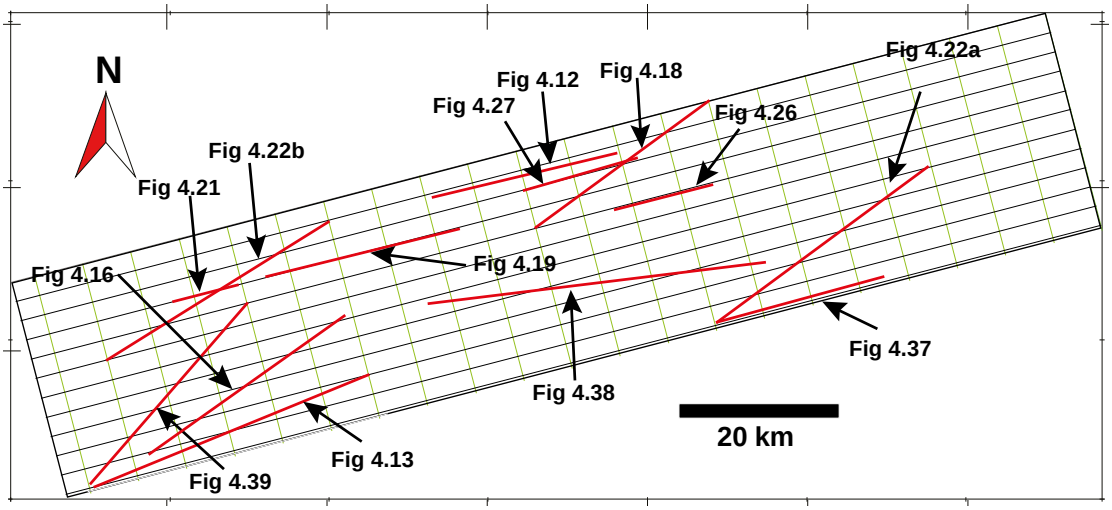

Figure 4.11: JDZ survey grid showing the location of seismic cross sections used to describe the stratigraphic and structural setting of the study area.

4.4.2 Stratigraphic interpretation

Based on the seismic reflection patterns, I have identified five seismic stratigraphic units in the study area:

[1] The deepest unit consists of a thin succession of seismically transparent reflections (Unit V).

[2] A succession of strong and stratified reflections above Unit V (Unit IV).

[3] A thick and generally poorly reflective unit with at least two regionally extensive bedding parallel reflections above Unit IV (Unit III).

[4] A conformably bedded succession of seismic reflectors exhibiting a variable pattern of amplitude and offset by most of the discontinuities above Unit III (Unit II).

[5] The shallowest unit is made up of a succession of seismic reflectors with variable thickness above Unit II (Unit I).

4.4.2.1 Unit V

The top of this unit is a fairly laterally continuous reflection typically located between 7.2 s and 7.5 s two way travel time with amplitude that fluctuates from weak to strong. The underlying interval is predominantly seismically transparent with very low amplitude and hardly any reflector continuity (Figure 4.12 & 4.13). This pattern of reflectivity has previously been observed in deepwater Niger Delta West and interpreted to resemble the reflectivity of normal oceanic crust (Briggs *et al*. 2009). The thickness of this unit varies across the seismic data but is generally thicker in the distal parts of the study area. No structures are resolvable 200 ms two way time below the top of the unit. This reflection is interpreted as the top of the basement in the study area.

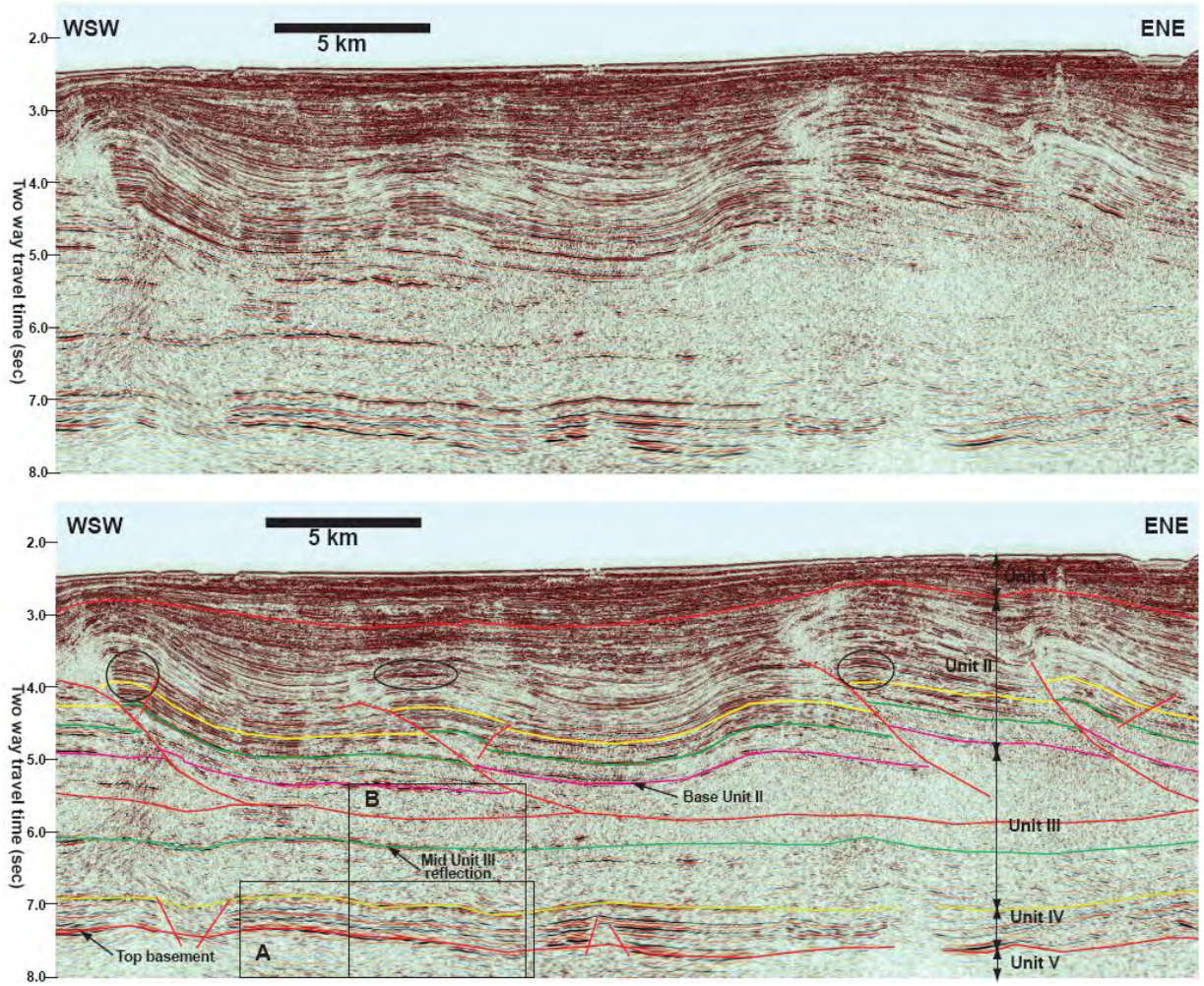

Figure 4.12: Uninterpreted and interpreted seismic cross section illustrating the seismic reflectivity patterns in the proximal parts of the study area. The black circle highlights amplitude anomalies at the crests of hanging wall folds (See the location in Figure 4.11). Vertical scale is in seconds two way time and horizontal scale is in kilometres.

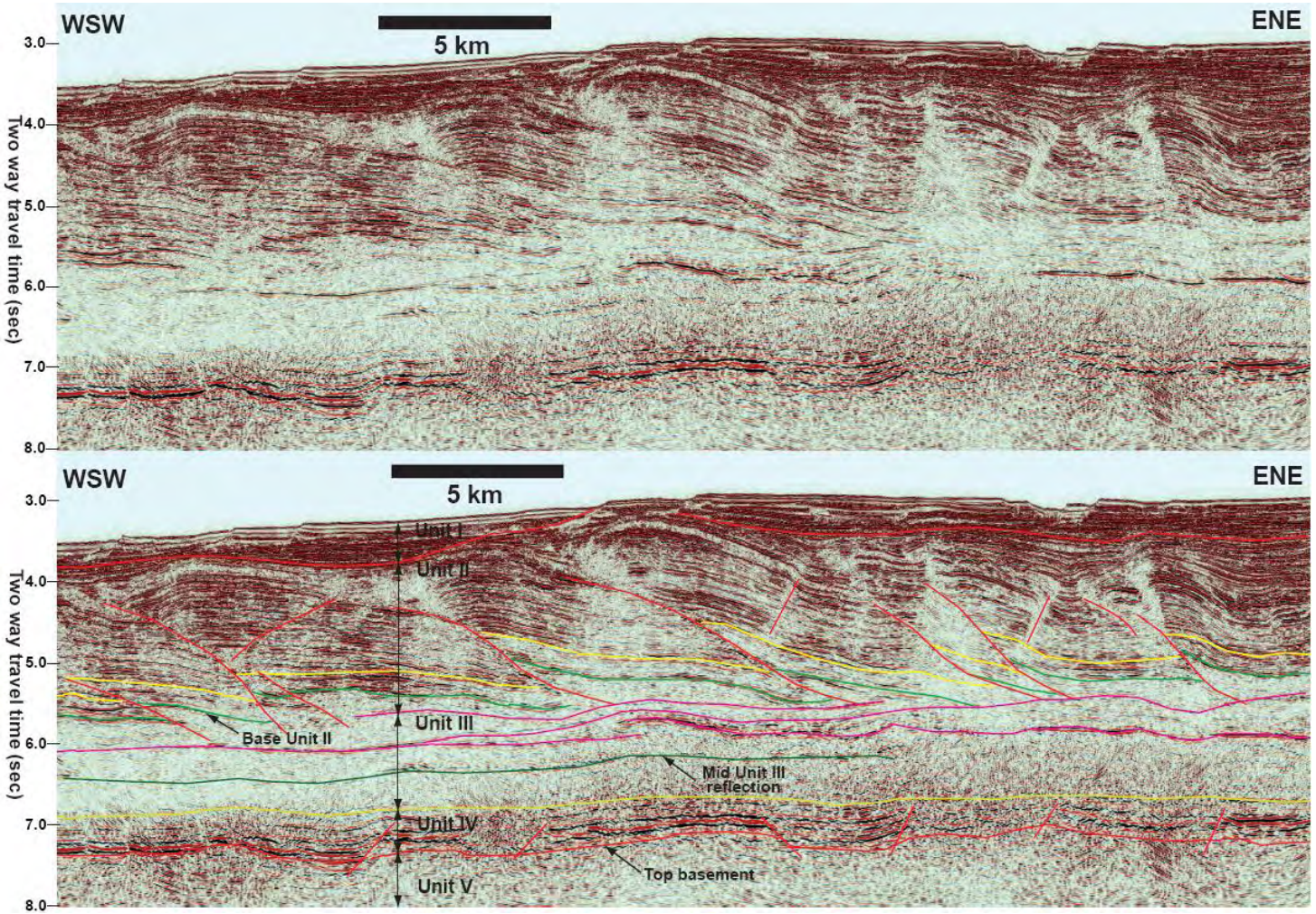

Figure 4.13: Uninterpreted and interpreted seismic cross section illustrating the seismic reflectivity patterns in the distal parts of the study area (See the location in Figure 4.11). Vertical scale is in seconds two way time and horizontal scale is in kilometres.

4.4.2.2 Unit IV

The top of this unit is a strong reflection with a high acoustic impedance contrast implying a change in density and velocity from the overlying unit. (Figures 4.12 & 4.13). The unit is well stratified with strong reflector continuity (Figure 4.14) occasionally offset by disruptions that appear to extend to the top half of Unit V. The top of the unit is typically located between 6.5 s and 7.0 s two way travel time in the proximal and distal parts of the JDZ. However, two way time structure map of the reflection shows that in the central parts of the study area, the top of the unit is between 6.0 s and 7.3 s, with a topography characterized by prominent NW – SE trending highs and lows intersected by a major NNE – SSW trending ridge. The later is probably due to faulting with geometries similar to graben and horst (Figure 4.15). The thickness of the unit varies across the seismic data and is generally thinner in the distal part of the data and thicker eastwards (proximal JDZ). The continuity of the reflectors in the unit is best in the central parts of the study area. A similar reflectivity package was observed in parts of western deepwater Niger Delta and speculated to represent synrift/post-rift succession of Upper Cretaceous age (Morgan, 2003).

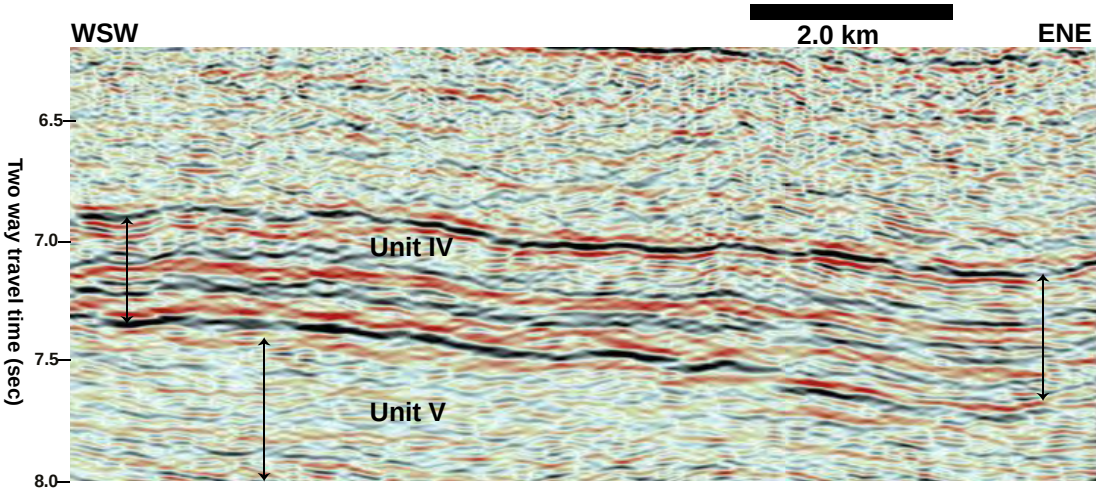

Figure 4.14: Seismic cross section illustrating the reflectivity pattern in Unit IV. This line is a close-up view of Unit IV in Figure 4.12 (labelled A).Vertical scale is in seconds two way time and horizontal scale is in kilometres.

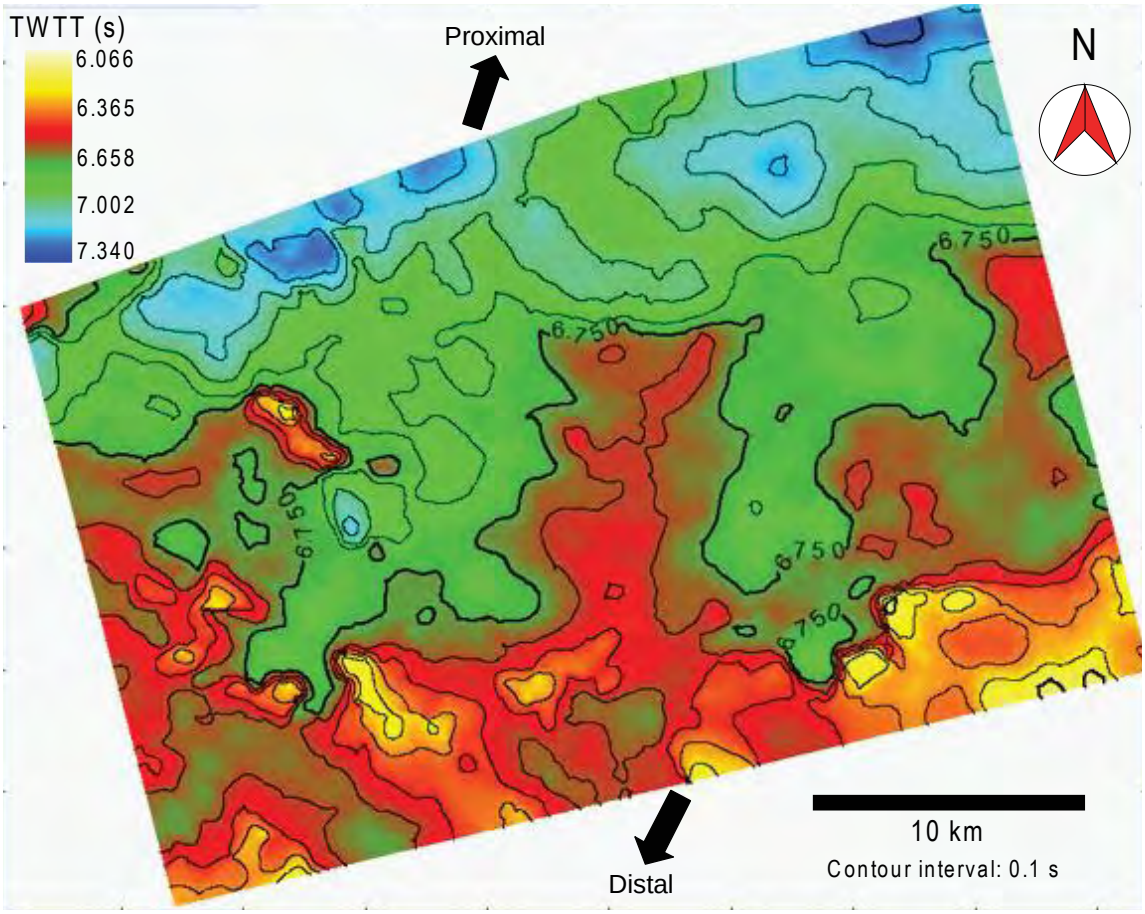

Figure 4.15: Two way travel time contoured structural map of top of Unit IV in Central JDZ. Note the NNW – SSE trending topographic highs and lows and the NW – SW trending ridge. The top of the unit lies between 6.6 s and 7.1 s two way travel and generally shallower basinwards.

4.4.2.3 Unit III

This unit is a thick zone of discontinuous and poor reflectivity with low amplitude if any (Figures 4.12 & 4.13). The main feature of the unit is the existence of multiple regionally extensive reflections in at least two stratigraphic levels with minor occurrences of localized high amplitude reflections in places. The top of the unit varies across the study area but is typically located beneath a faulted reflection below which the seismic pattern becomes mainly transparent. This pattern of reflectivity has also been observed in the central and western parts of deepwater Niger Delta (Maloney *et al*. 2010; Cobbold *et al*. 2009: Corredor *et al*. 2005). However, in distal JDZ, the unit is characterized by isolated saucer-shaped reflections located near the top of Unit IV (Figure 4.16).

Unit III is interpreted to represent the deepwater equivalent of the pro-delta marine clays of the Akata Formation described by Avbovbo (1978) and Knox & Omatsola (1990). The localized discontinuous high amplitude reflections within the succession are interpreted to represent minor sand and silt intervals, while the saucer-shaped reflections observed in the distal parts of the study exhibit geometries similar to sills (Schofield, personal communications). The Akata Formation is thought to be made up of marine shales described as the major source rocks for hydrocarbon generation in the Niger Delta (e.g. Avbovbo, 1978; Doust & Omatsola, 1990; Ekwezor & Daukoru, 1994; Kulke, 1995; Reijers *et al*. 1997). In the Niger Delta, the lack of acoustic impedance contrast within the unit in the Niger Delta was interpreted to be due to high pore pressure probably (caused by rapid sedimentation and under-compaction of sediments) hydrocarbon generation and maturation (Cobbold *et al*. 2009; Osborne & Swarbrick, 1998).

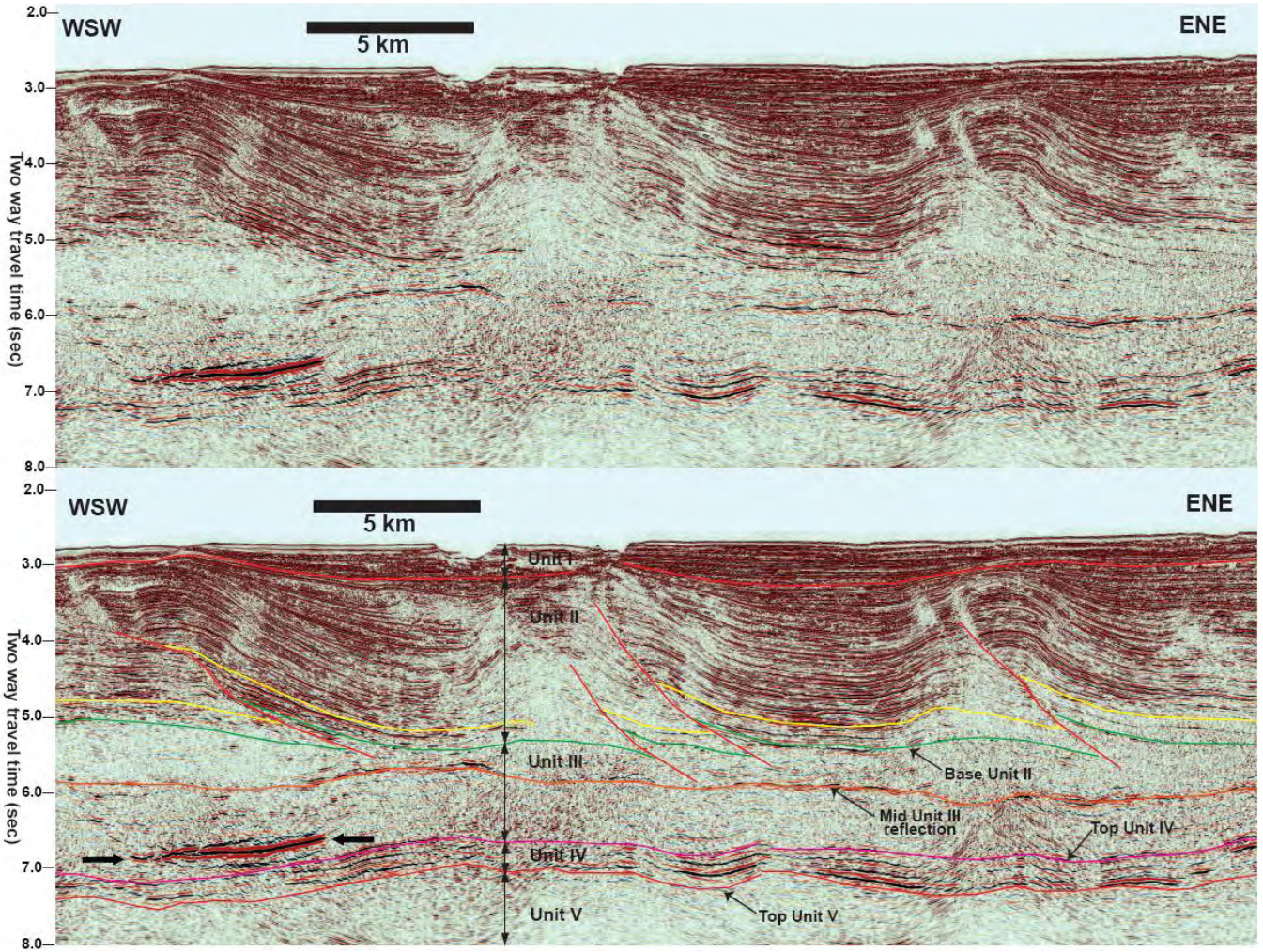

Figure 4.16: Uninterpreted and interpreted seismic cross section illustrating the reflectivity pattern of a sill within Unit III (block arrows). (See the location in Figure 4.11). Vertical scale is in two-way-time and horizontal scale is in kilometres.

4.4.2.3.1 Strong reflections within Unit III

There are at least two strong and extensive bedding-parallel reflections within Unit III that some of the faults appear to sole into. The first reflection lies between 5.5 s to 6.0 s two way travel time and most of the faults in the central parts of the study area appear to sole into this reflection. The continuity of this reflection fluctuates, typified by changes in stratigraphic level and hard to track but is in most places located near the top of Unit III (Figures 4.12, 4.13).

The second reflection is the most regionally extensive and located in the middle of Unit III and referred to as Mid Unit III reflection in this thesis. The top of this reflection varies but is located between 5.4 s and 6.5 s two way travel time, well imaged in the central parts of the study area (Figure 4.16), with topography similar to that observed in top Unit IV reflection (Figure 4.17). The reflection is generally laterally continuous with amplitude that fluctuates from weak to strong. However, the continuity of this reflection is in places lost where there is abrupt thickening of Unit III in parts of the data (Figures 4.18). In places the reflection is seen to bifurcate resulting in a new shallower reflection that some faults appear to sole into (Figure 4.19). In previous work, the occurrence of similar reflections near the base of Unit II and in the middle parts of Unit III (deepwater equivalent of the Agbada and Akata Formations respectively) was interpreted to imply that maximum fluid pressures in at these depths and that the basal units of Unit II are sealing (Cobbold *et al*. 2009).

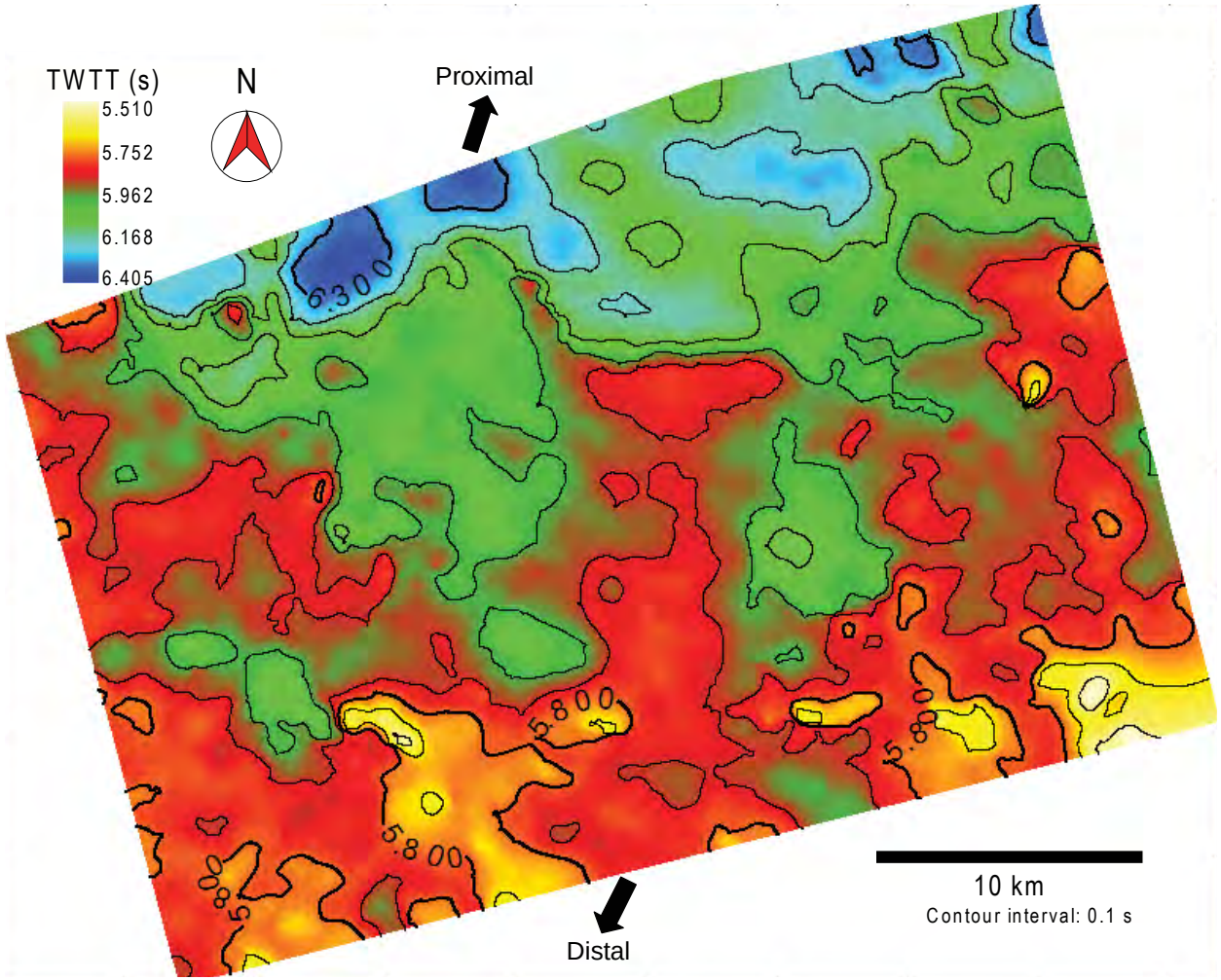

Figure 4.17: Two way time structural map of Mid Unit III reflection in the central parts of the study area. Note the seawards shallowing pattern of the topography with relief similar to top Unit IV two way time structure map.

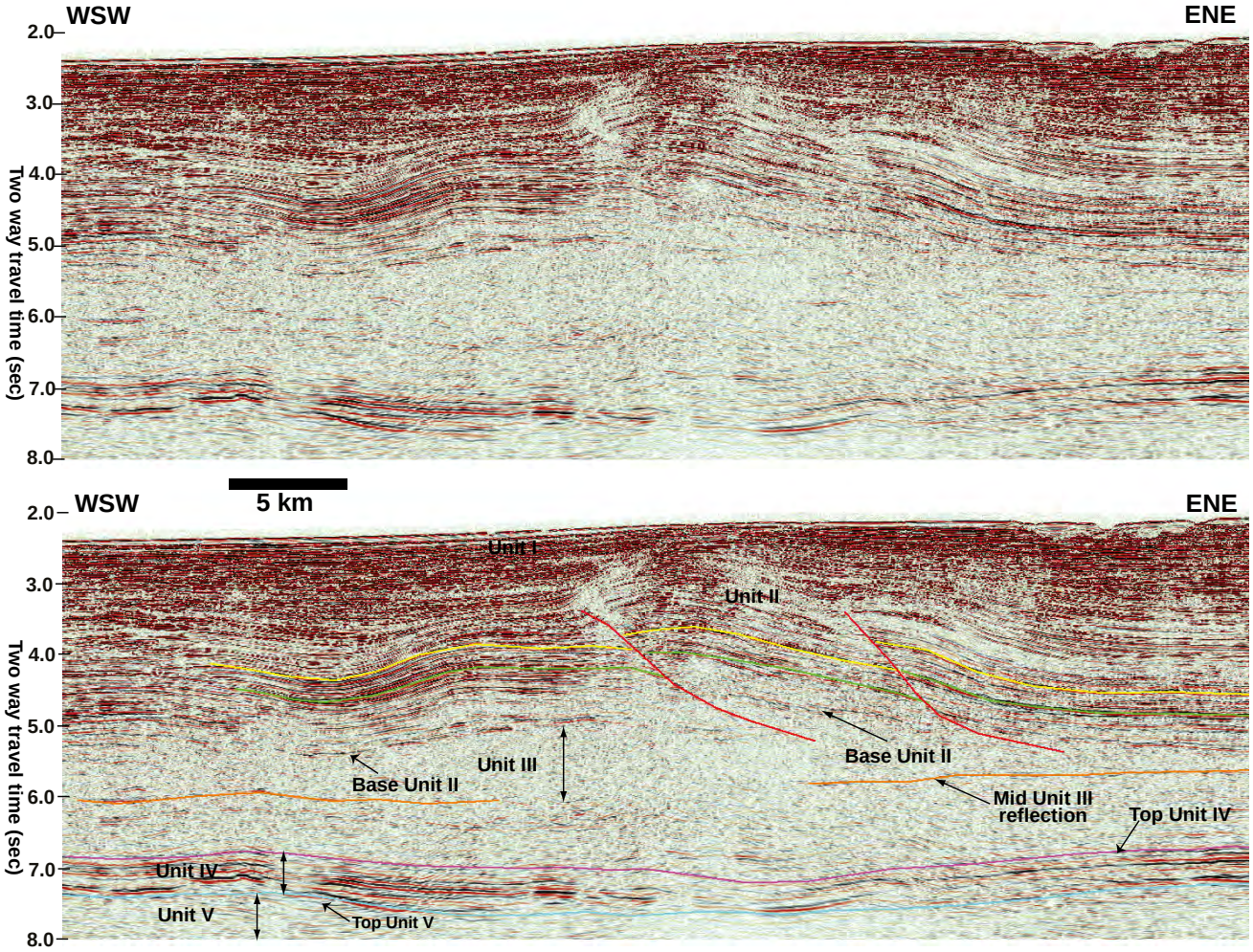

Figure 4.18: Uninterpreted and interpreted seismic cross section illustrating the loss of coherence of Mid Unit III reflection in places where there is abrupt thickening of Unit III (See the location in Figure 4.11). Vertical scale is in two-way-time and horizontal scale is in kilometres.

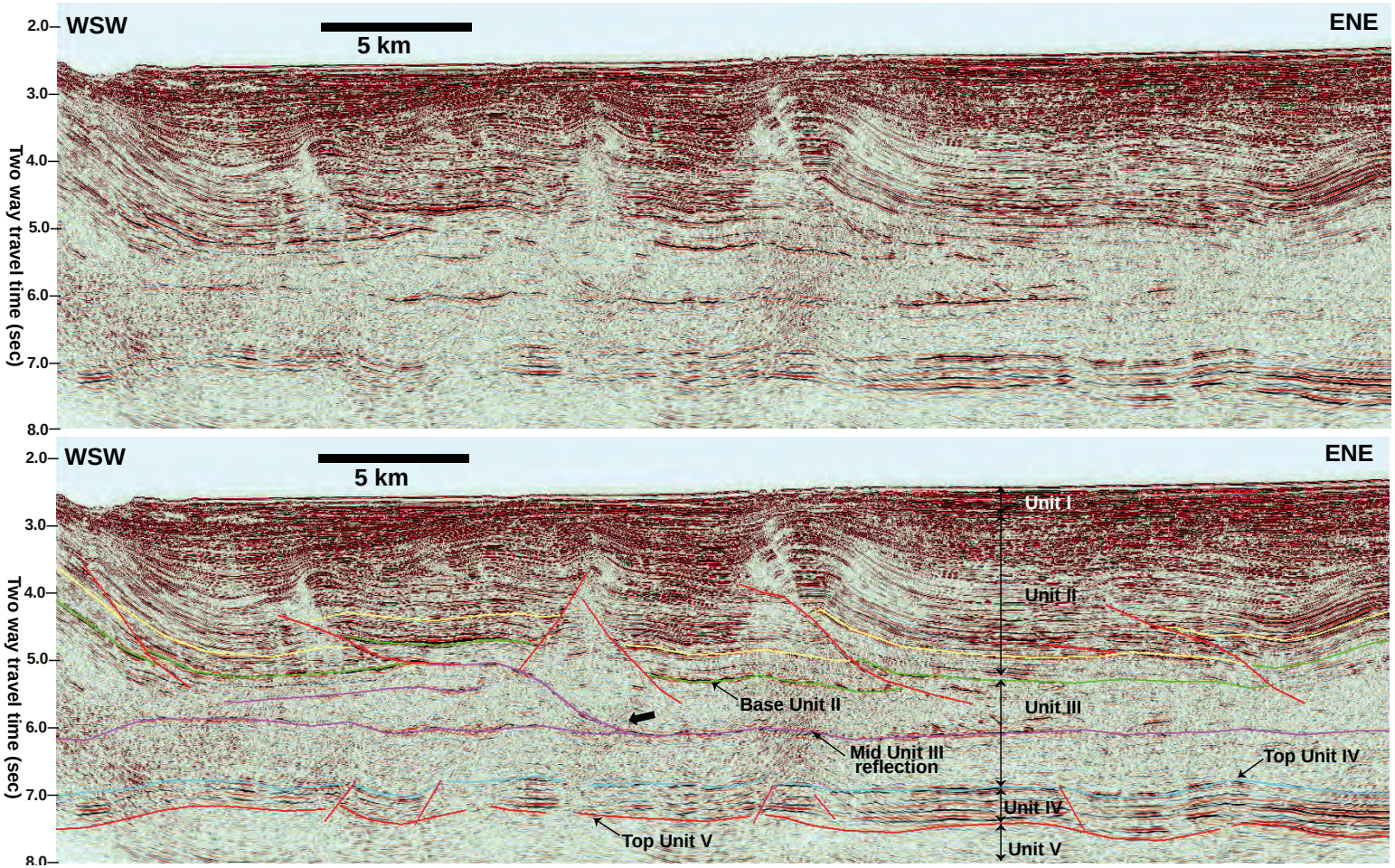

Figure 4.19: Uninterpreted and interpreted seismic cross section illustrating the bifurcation of Mid Unit III reflection (block arrow). (See the location in Figure 4.11). Vertical scale is in two-way-time and horizontal scale is in kilometres.

4.4.2.3.2 Unit III subdivision

In general, Mid Unit III reflection is observed to separate Unit III into two sub units. However, this division is only seen where the reflection is strong (Figure 4.20). The top of upper Unit III interval varies across the seismic data but is typically below a faulted reflection above, below which the seismic reflectivity pattern becomes transparent. The base is at or near the top of Mid Unit III reflection. The top of lower Unit III interval is usually the Mid Unit III reflection and the base is the top of Unit IV. Both units are characterized by discontinuous low amplitude reflectivity pattern except in the distal parts of the JDZ where high amplitude saucer-shaped reflections interpreted as sills are found in Lower Unit III. The proximity of the distal parts of the study area to the Cameroon volcanic zone suggests a possible link between Miocene volcanic activities and sedimentation in the area (Figure 4.3).

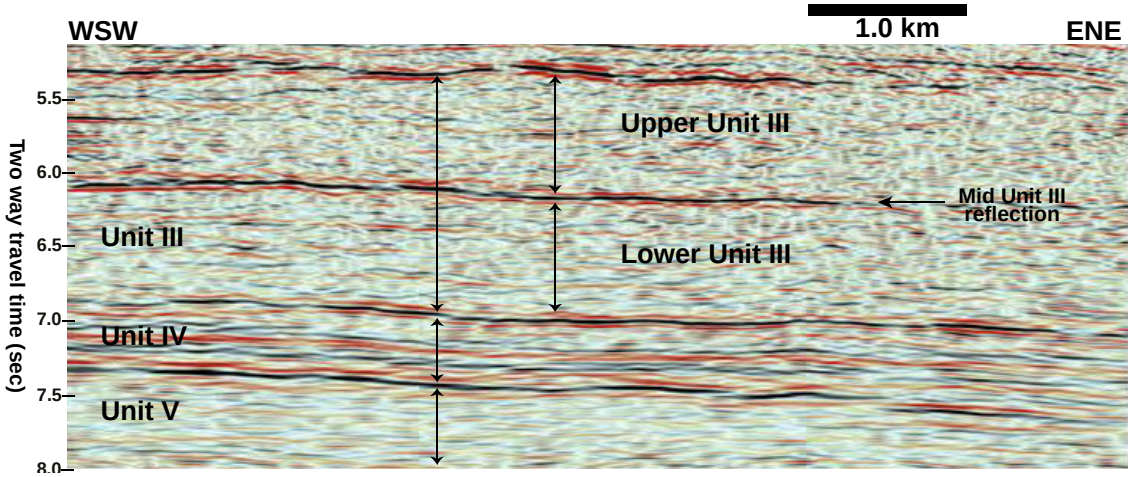

Figure 4.20: Seismic cross section illustrating the division of Unit III into an upper and lower Unit III based on the location of Mid Unit III reflection. This line is a close-up view of Unit III in Figure 4.12 (labelled B). Vertical scale is in two-way-time and horizontal scale is in kilometres.

4.4.2.4 Unit II

This unit is made up of a relatively conformable succession and offset by most of the major discontinuities. The unit exhibits a variable pattern of reflectivity probably a reflection of alternating lithologies with contrasting acoustic impedance (Figures 4.12 & 4.13). The thickness of the unit is fairly uniform across the study area and is typically 2.0 s two way travel time thick. The uppermost part of the unit consists of strong, high amplitude and continuous reflections some of which could be unconformities. The reflections are in places truncated by the edges of channel deposits located between the forelimb and backlimb of successive thrusts. The base of the unit is a strong reflection that coincides with a change in the pattern of reflectivity from Unit II to Unit III. A similar surface was mapped near the boundary between the Akata and Agbada Formations and was interpreted as a major sequence boundary (Morgan, 2003).

Unit II is interpreted to represent the deepwater equivalent of Agbada Formation of Miocene age deposited by channelized turbidites, debrites and hemipelagites (e.g. Doust & Omatsola, 1990; Morgan, 2003). The sandy parts of the unit are speculated to be the main hydrocarbon-bearing reservoirs while the shales are the main seals to the reservoirs (Doust & Omatsola, 1990). The uniform thickness of Unit II in the study area is evidence that the unit is most likely the deepwater equivalent of Agbada Formation in the study area.

4.4.2.5 Unit I

Unit I is a zone of variable thickness characterized by very strong pattern of reflectivity in places truncated by the edges of channel systems and normal faults that occasionally extend into Unit II (Figures 4.12 & 4.13). The base of the unit is a strong reflection that marks the transition from Unit I to II and based on toplap of reflectors

in Unit II is probably an unconformity. Unit I is interpreted to represent the deepwater equivalent of post-thrusting succession of Upper Miocene age and part of the Agbada Formation sequence (Morgan, 2003). The top of this unit is a strong reflection interpreted as the seabed.

4.4.2.5.1 Strong reflections within Units I and II

Unit I and the uppermost parts of Unit II are characterized by regionally strong and extensive reflections with reversed polarity to the seabed reflection. This anomaly may be due to the accumulation of free gas at the base of a gas hydrate stability zone normally related to Bottom Simulating Reflections (Westbrook, personal communications) (Figure 4.21). In the study area, BSRs are well developed along a zone of anticlinal uplift with internal geometry similar to detachment folds in the proximal and distal parts of the JDZ (Figures 4.22a & b).

The reflection typically cut across dipping strata in Unit II at the crests of structural highs but becomes parallel to Unit I at the flanks. Down dip from the BSR in Unit II, some of the dipping units show amplitude brightening probably due to the presence of gas (Figure 4.22b). A single BSR appear to be prominent in the study area, however, in places more than one exist at different stratigraphic levels. This implies that locally more than one BSR may indicate the presence of higher hydrocarbon gases (Westbrook, personal communications). Although patches of BSRs have been reported to occur within Agbada sands in the Niger Delta (e.g. Hovland *et al*. 1997; Sultan *et al*. 2010), this is the first time it is observed in parts of deepwater Niger Delta imaged in the JDZ seismic data. The large-scale occurrence of these reflections strongly supports the assumption that Units I and II represents the deepwater equivalent of Agbada Formation in the study area.

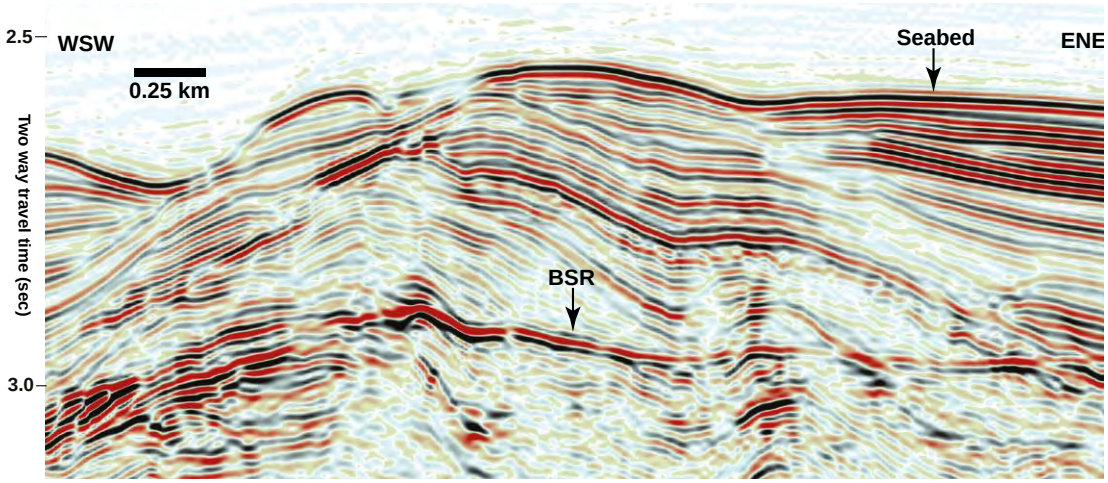

Figure 4.21: Seismic cross section illustrating the reflectivity pattern of a Bottom Simulating Reflector (BSR) in the JDZ. Note the polarity of the BSR is reverse to seafloor reflection. Vertical scale is two way travel time in milliseconds and horizontal scale is in kilometres.

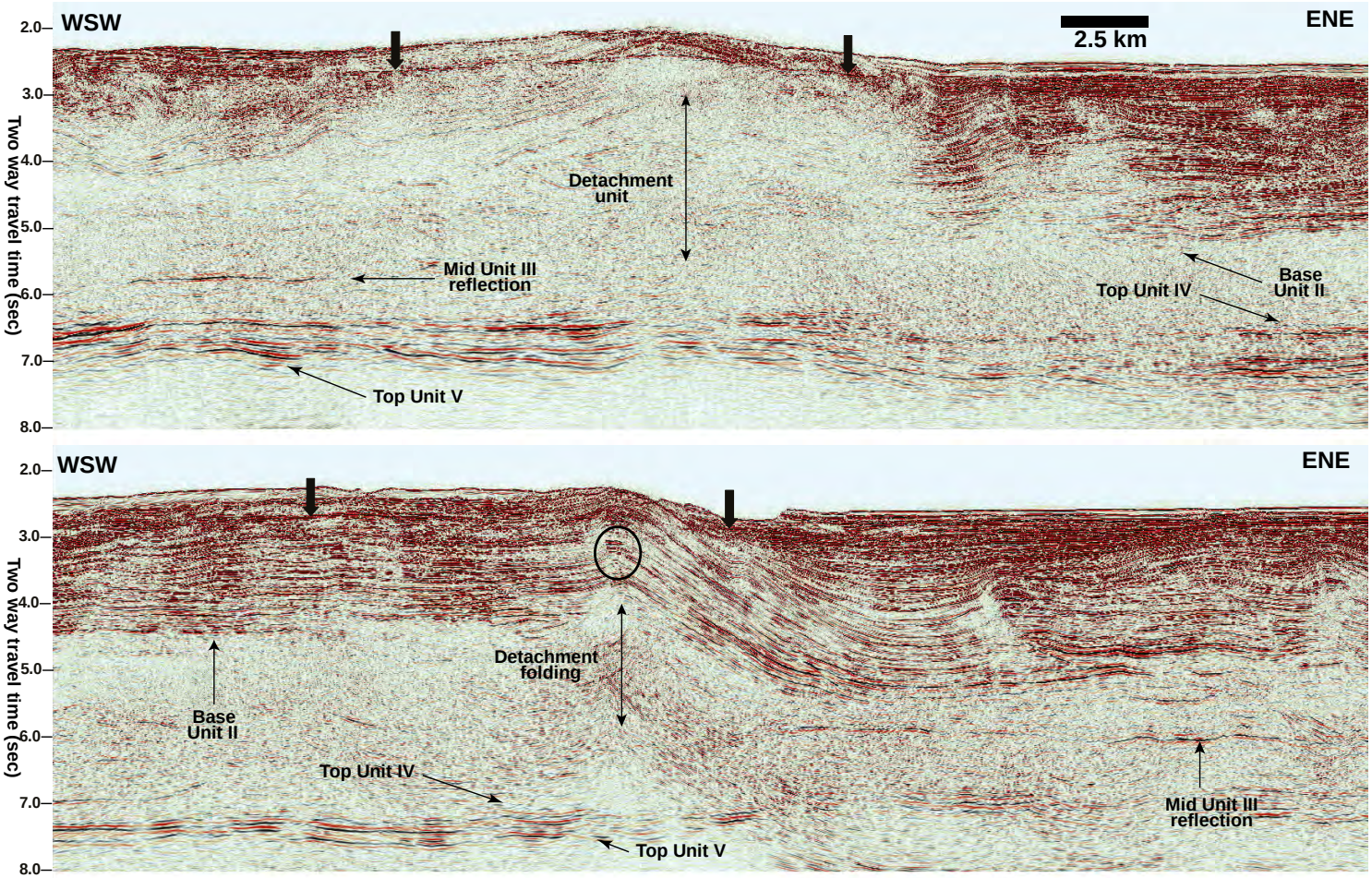

Figure 4.22: Seismic amplitude cross section showing a Bottom Simulating Reflector (BSR) in the proximal and distal parts of JDZ (block arrows) (See the location in Figure 4.11). The black circle highlights amplitude anomalies in the crestal parts of the detachment fold in Figure 4.24b. Vertical scale is two way travel time in seconds and horizontal scale is in kilometres.

4.4.3 Horizon interpretation

4.4.3.1 Seabed

The top of Unit I is a strong laterally continuous reflection (trough) interpreted as the seabed (Figure 4.23). This horizon provides high resolution imaging of seafloor manifestation of gravity collapse and contractional deformation in deepwater Niger Delta fold and thrust belt imaged in the JDZ seismic data. The seabed is incised by deepwater channel systems, bathymetric swells, surface manifestation of active thrusts and fluid escape features probably from hydrocarbon-charged sediments in Unit II. An E-W arcuate bathymetric ridge divides the seabed into two parts (upper and lower slope). The location of the ridge coincides with the distal edge of the southern Niger Delta prograding sedimentary lobe and is probably an extension of the arcuate thrust front seen in the structural province map in Figure 4.3.

The lower slope is incised by large deepwater turbidite channels that extend from the upper parts of the slope to beyond the outermost parts of distal JDZ in a N-S direction in the western half of the seabed, and NNE – SSW in the eastern parts of the seabed, cutting across bathymetric ridges that represent the crests of thrust folds. This implies that the channels post-date deformation in the study area. The deepwater channels are typically 1000 m to 3000 m in width, with steep edges of up to 3 km in length (Figure 4.24). These channels typically provide routes for sediment transportation from the shelf and mud-diapir-bounded mini-basins higher on the slope to deepwater settings (Morgan, 2003). The overall seaward sloping pattern of the seabed suggests a strong control of gravity in sedimentation in the JDZ.

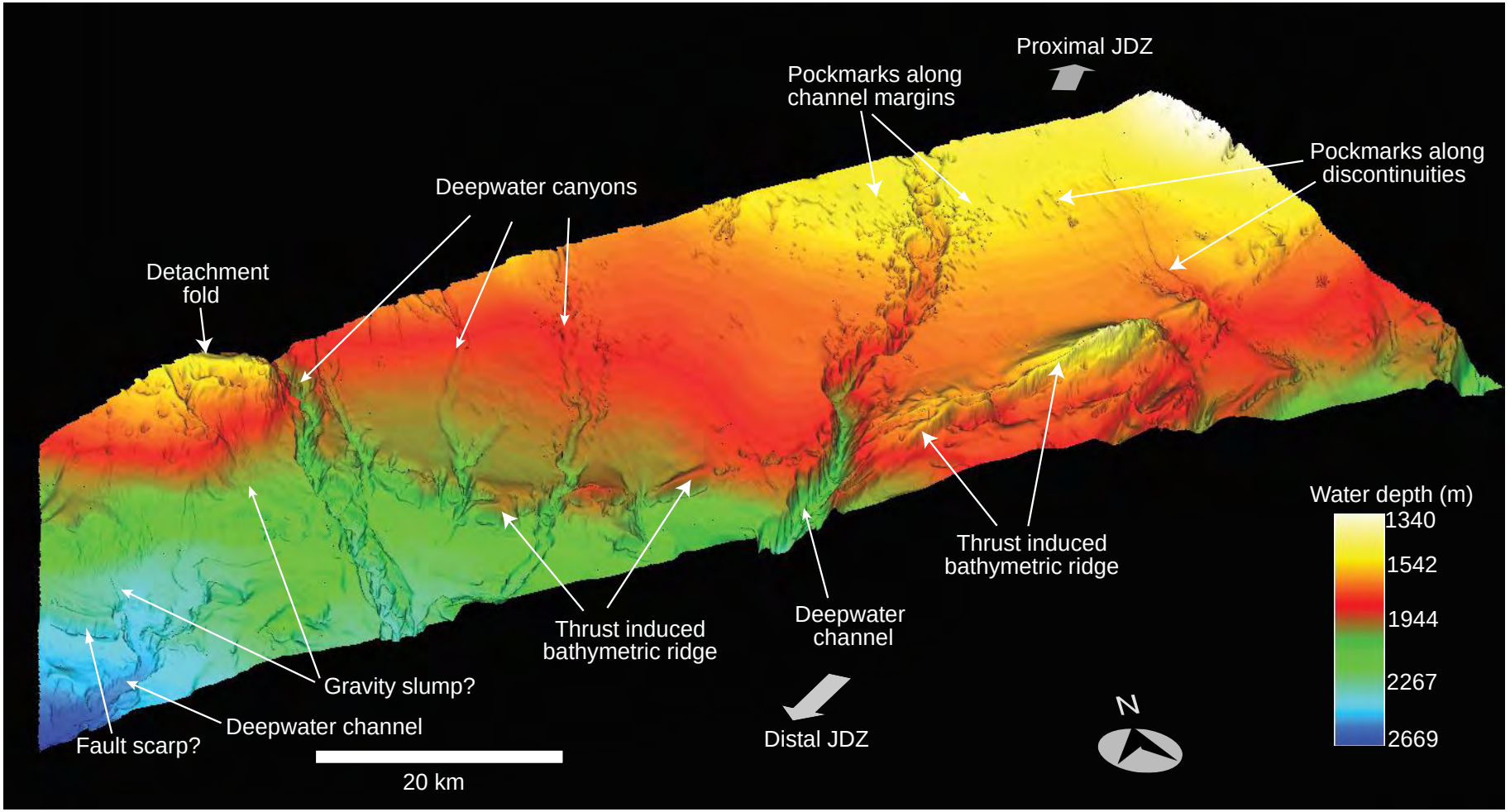

Figure 4.23: Perspective view of the JDZ 3000 km^2 depth converted seabed horizon showing present day seabed geomorphology that includes bathymetric ridges incised by deepwater canyons, gravity slump and fluid escape features. Note the large concentration of fluid escape features in the proximal parts of the study area. Image generated from dense grid of horizon tracked every line on 3D seismic data. Illumination and view is from the northeast.

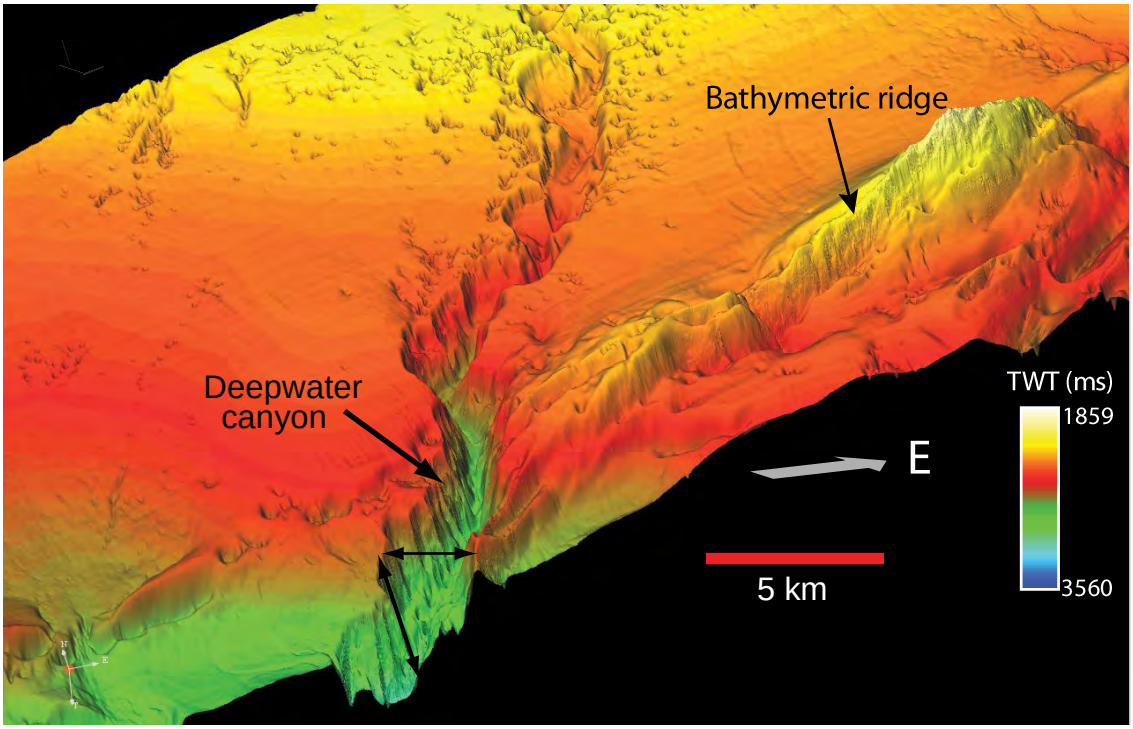

Figure 4.24: Perspective view of Central JDZ seabed horizon illustrating the geomorphology and dimensions of a deepwater canyon system.

The seabed in Eastern JDZ is characterized by an extensive field of circular craters with geometries similar to pockmarks. Pockmarks are crater-like depressions resulting from fluid flows at the seabed (Hovland, 1997). Pockmarks in the study area occur within linear zones of discontinuities in the northeastern parts of the seabed, at the edges of the proximal parts of a major deepwater channel and in places randomly distributed (Figure 4.25). The concentration of pockmarks along the channel margins probably suggests the presence of fluid migration pathways from the channel to the surface. Similar pockmark belts mapped on the lower slope of the Congo Basin are interpreted to indicate shallow buried turbiditic channel complex (Gay *et al.* 2003). Random pattern of pockmark distribution without apparent link to discontinuities or channel system may probably be due to fluid migration from shallow depths (e.g. Hovland, 1997).

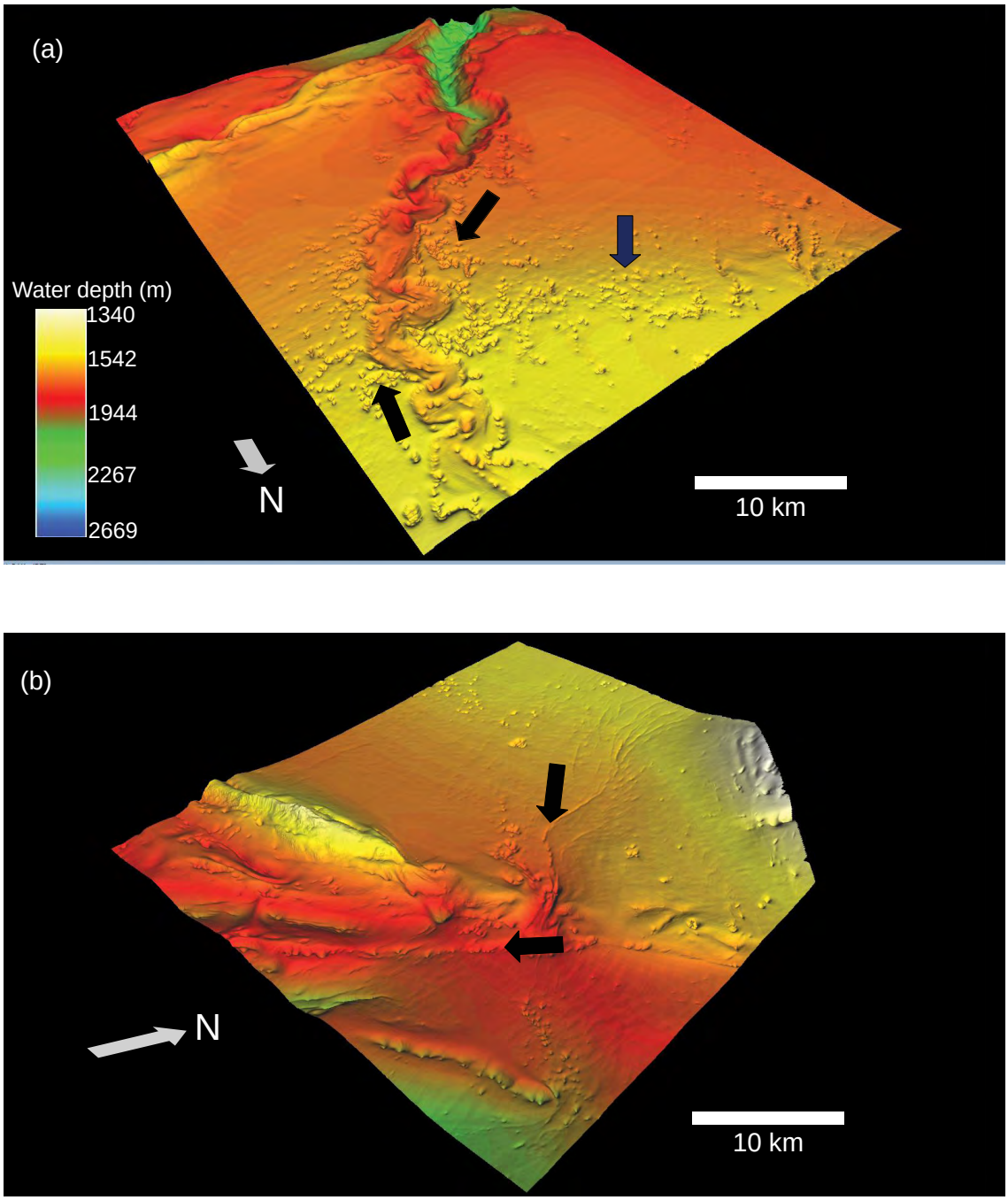

Figure 4.25: Perspective close up view of JDZ seabed showing clusters of pockmarks (block arrows) at the margin of a deepwater channel (a) and along lineaments (b) in central and southeastern parts of the study area.

Seismic evidence exists to show links between clusters of pockmarks found on the seabed and possible fluid migration pathways to the surface. Figure 4.26 shows a seismic cross section and the equivalent similarity cross sections. Note an extensive amplitude anomaly at the crestal parts of a hanging wall fold in the seismic amplitude

cross section (black circle). The equivalent similarity cross section shows pockmarks craters located directly above vertical zones of low similarity. Fluid accumulation within the permeable sedimentary units of Units I and II (the equivalent of Agbada Formation) probably resulted in the vertical migration of excess pore fluids along discontinuities resulting in the formation of pockmark craters on the seabed.

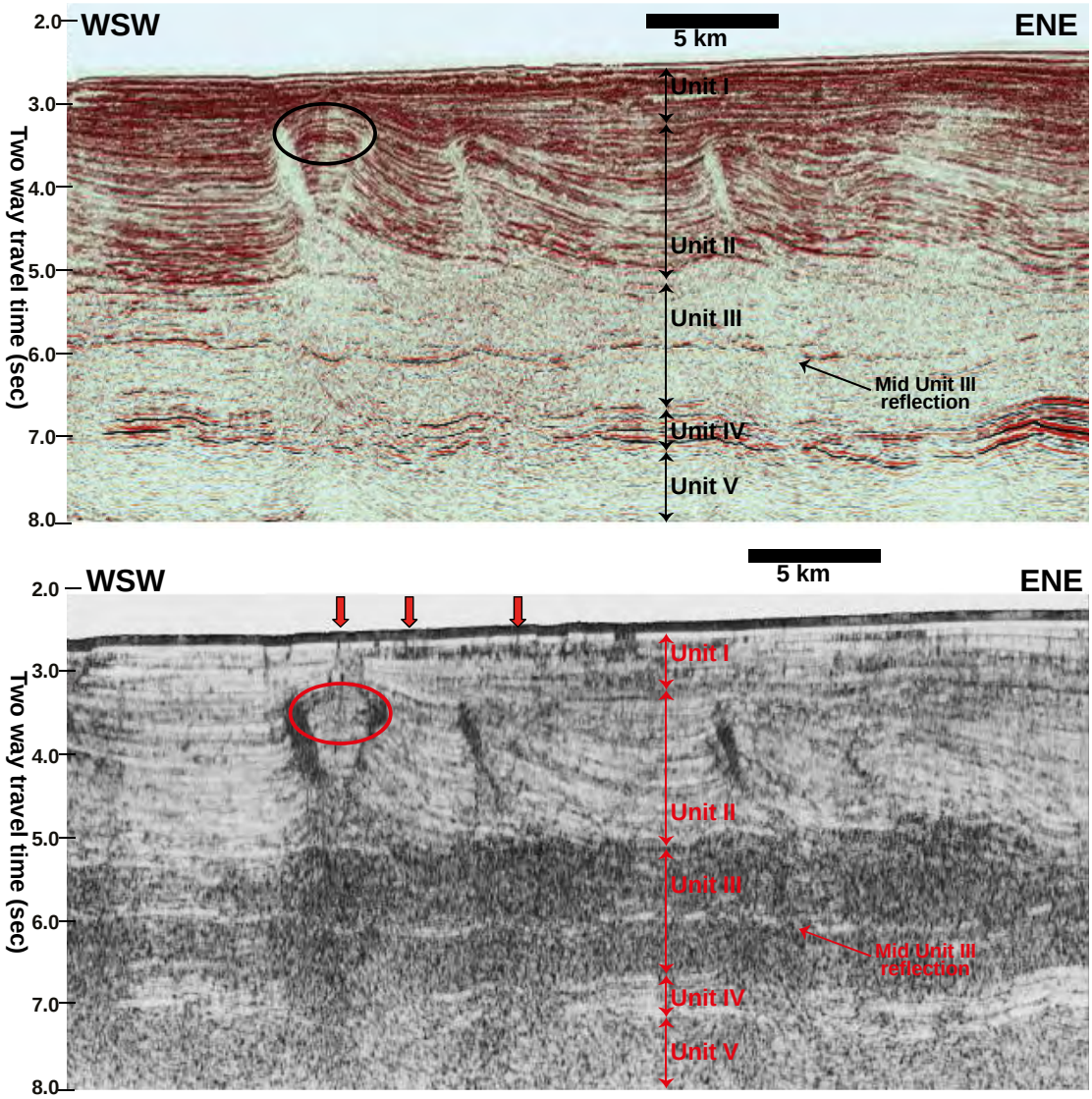

Figure 4.26: Seismic amplitude cross section (a) and similarity cross section (b) showing possible relationship between pockmarks on seabed, amplitude anomalies and fluid migration pathways. Fluid migration from a possibly gas-charged reservoir might have been through faults in the complexly deformed zone exhibiting low similarity (location in Figure 4.11). Vertical scale is two way travel time in milliseconds and horizontal scale is in kilometres.

4.4.4 Structural framework

4.4.4.1 Introduction

Faults were manually picked across the JDZ area and are presented in map view in Figure 4.27. Thrust faults in the JDZ are discrete, planar surfaces, with reverse sense of displacement and predominantly verge seawards (Figure 4.28). The faults sole into at least one or more strong layer parallel detachment levels located near the top and middle of Unit III. The faults offset the upper parts of Unit II into blocks of fairly uniform thickness. Displacement is predominantly within the unit, but in the shallower parts of the conformable succession of Unit I, well developed hanging wall folds progressively take up displacement. Most of the faults die out near the base of Unit II but in places reach the seabed. The faults have low dips with increased cross sectional curvature towards Unit III. Detailed description of the surface morphology of the faults is described in Chapter Five.

Folds related to thrusting in central JDZ typically have a long planar backlimb that dips less than the underlying thrust ramp (Figure 4.29). The forelimbs of the folds are short and dip more steeply compared to the backlimbs. These folds are geometrically similar to shear fault-bend folds described by Connors *et al.* (1998), Suppe (1984), Suppe *et al.* (2004), Krueger & Grant (2006), Suppe & Medwedeff (1990), and Corredor *et al*. (2005). Although in places, detachment folding is a major structural feature of the study area (Figure 4.22b). A comprehensive description of the mechanics of these structures can be found in the references listed above and Maloney (2011).

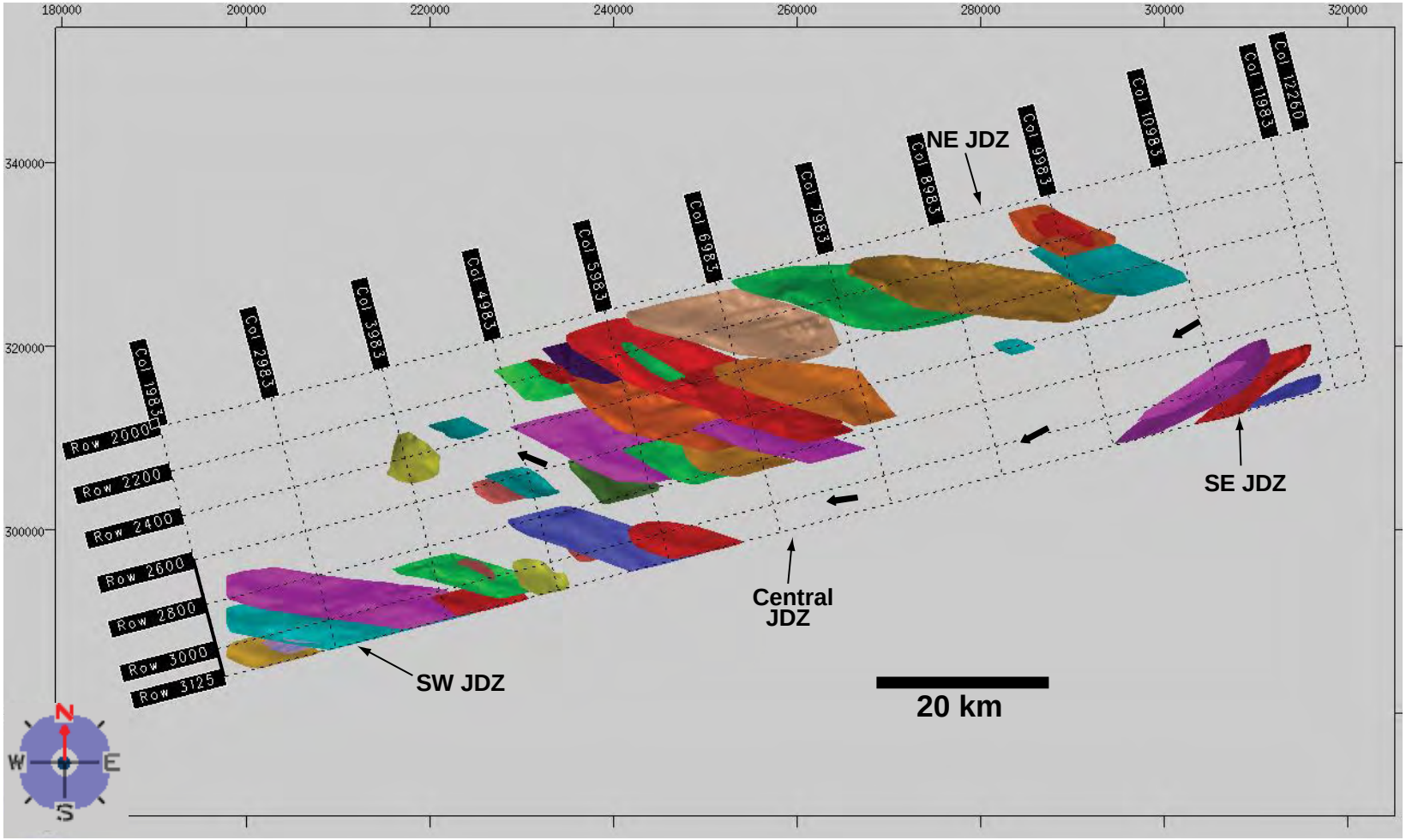

Figure 4.27**:** Map view of fault surfaces mapped in the JDZ. Figure 4.31 is a close up perspective views of the faults in the four labelled regions. The dashed red line illustrates a significant structural boundary separating two contrasting patterns of faulting in the JDZ. The orientation of the faults is predominantly WNW – ESE, but in the southeast the faults have a NE – SW orientation.

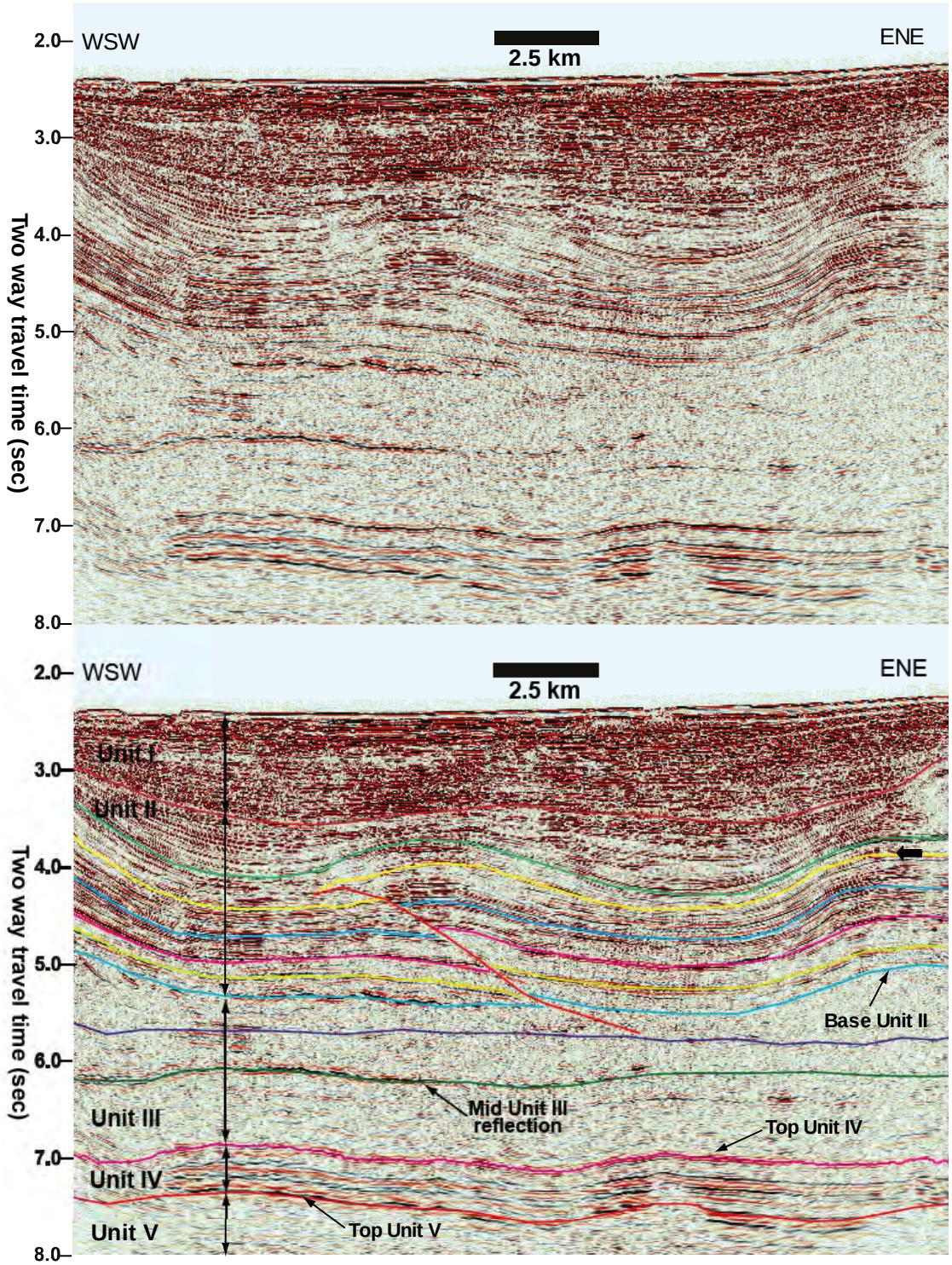

Figure 4.28**:** Uninterpreted and interpreted seismic cross section showing the geometry of a thrust fault in the JDZ (Fault L in Figure 4.32). Faults typically exhibit ramp and flat geometry, dips are slightly greater than those on the backlimb. Map view of the hanging wall horizon in yellow (block arrow) is presented in Figure 4.34. (see location in Figure 4.11). Vertical scale is two way time in seconds and horizontal scale is in kilometres.

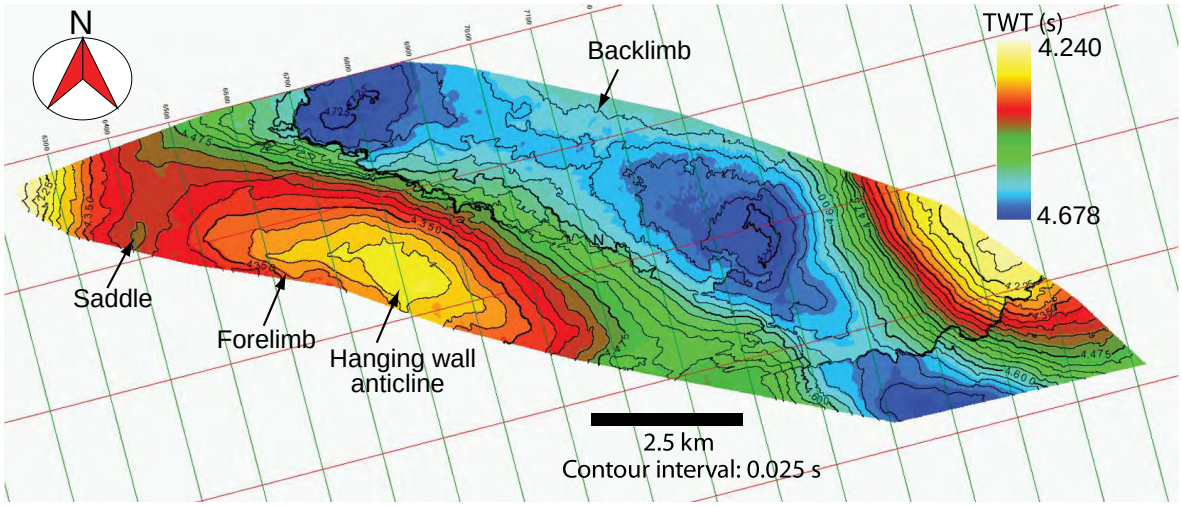

Figure 4.29**:** Two way time relief map of a typical hanging wall fold in JDZ seismic data. This horizon is the yellow reflection mapped in the hanging wall of the fault in Figure 4.28.

In plan view, two patterns of thrust geometries separated by an arcuate thrust ridge are observed in central JDZ. Faults north of the ridge are predominantly curved, segmented and trend WSW – ENE (Figure 4.30). Faults south of the ridge are relatively planar, trend E-W and occasionally appear to connect to faults north of the ridge. The NE part of the study area is relatively undeformed. Several large faults in the dataset exhibit examples of fault relay and transfer zones previously described in extensional settings (e.g. Peacock & Sanderson, 1991; Childs *et al*. 2009). Figures 4.31 & 4.32 show two way time maps of a horizon offset by most of the faults and the location of seismic lines used in describing the structural and stratigraphic framework of the study area. Gridded perspective views of selected areas are used to illustrate geometrical relationship between thrust faults highlighted in Figures 4.33 to 4.35.

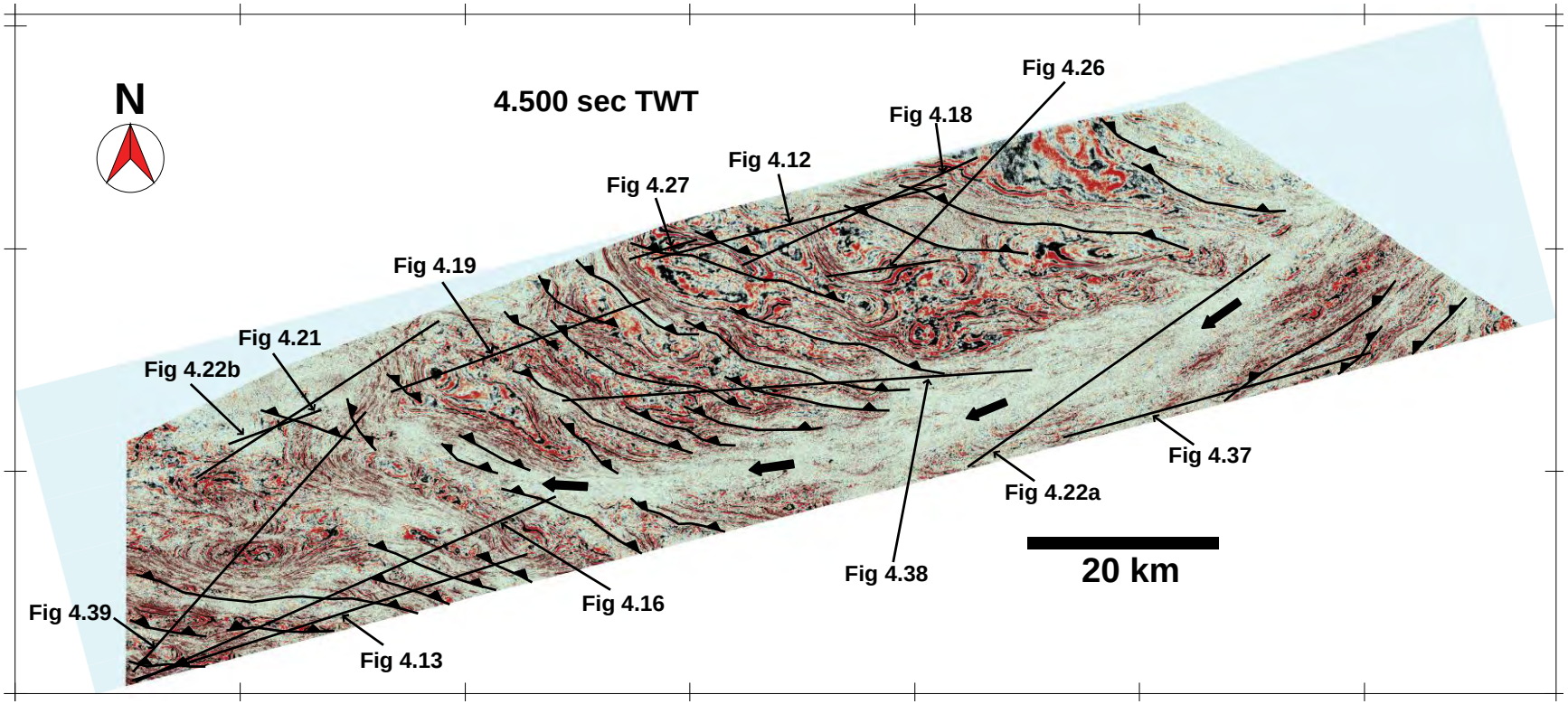

Figure 4.30: Seismic amplitude timeslice sampled at 4.5 seconds two way travel time illustrating the geometry of faults across the JDZ (black lines). The green lines represent the location of seismic cross sections used to show the cross sectional geometries of the faults and the seismic reflectivity patterns across the JDZ. Note the intense zone of deformation that separates two pattern of fault strike (block arrows). Faults north of the arcuate thrust front have NW – SE orientaion while faults south of the ridge strike WNW – ESE.

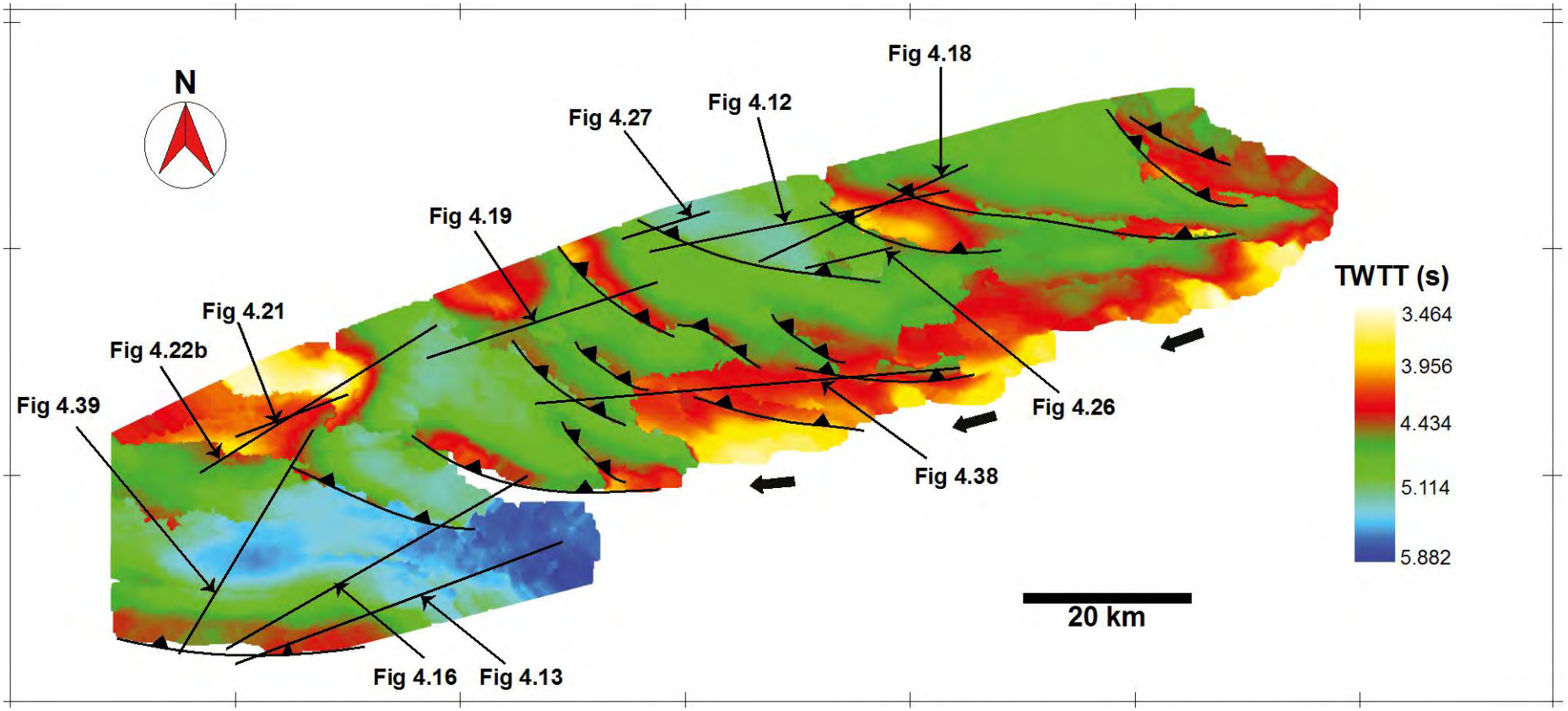

Figure 4.31**:** Two way time structure map of a regionally extensive horizon offset by most of the thrust faults within Unit II in the study area. The southern parts of the study area are complexly faulted due to an arcuate thrust front seen as a zone of intense deformation in Figure 4.30 (block arrows).

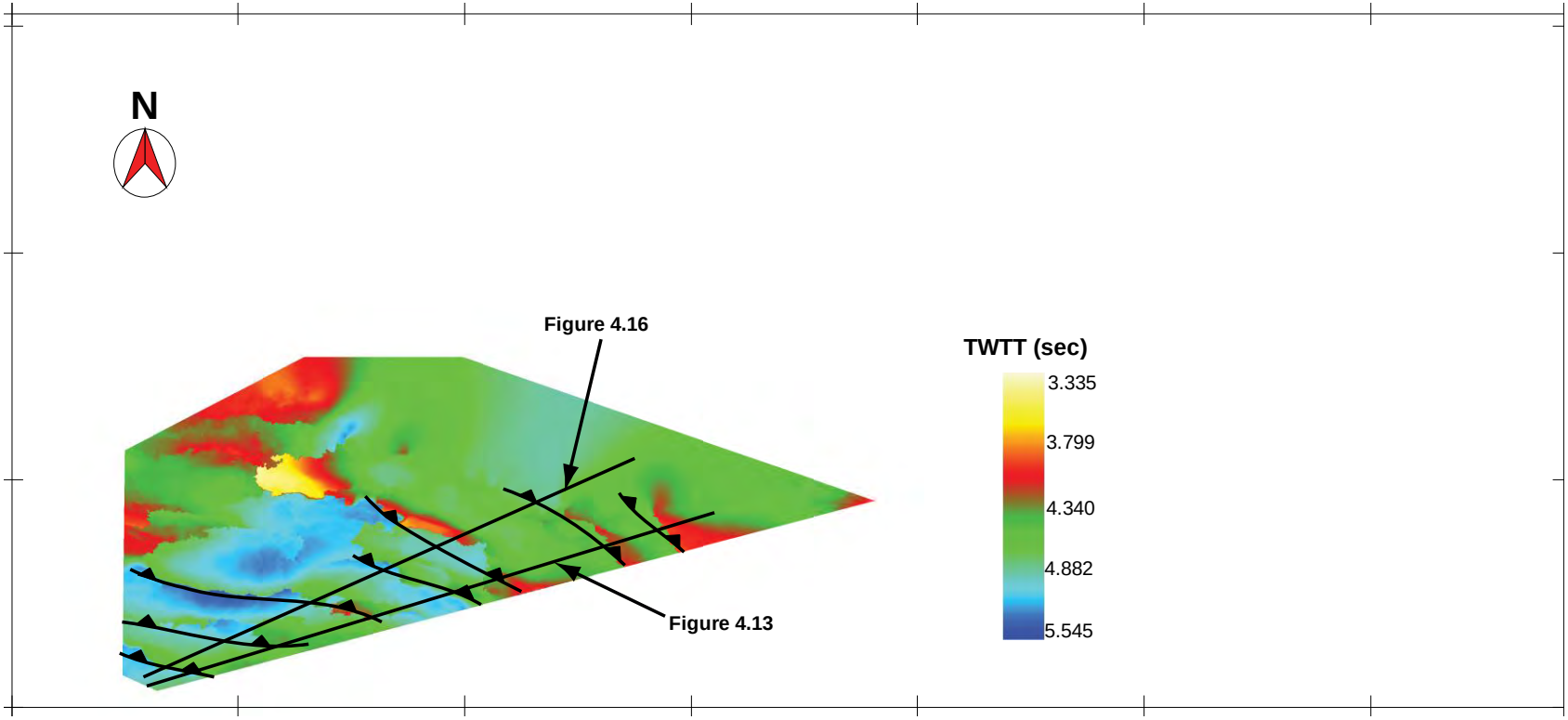

Figure 4.31**:** Two way time structure map of a regionally extensive horizon offset by most of the thrust faults within Unit II in the distal parts of the study area.

4.4.4.2 *Fault geometrical characteristics*

Most of the faults in the central parts of the study area exhibit hard linkage, implying the gradational propagation of fault segments into an overlap position eventually developing into soft-linked relay structures (Walsh & Watterson, 1991; Peacock *et al*. 2000). Soft linkage of the faults is achieved by the smooth transfer of displacement through unbreached relays (Figure 4.33), while hard-linkage is via breached relays and connecting faults (Figures 4.34 & 4.35). Evidence suggests that some of the faults connected by breached relays may be continuous; probably implying that geometric coherence is maintained by segments of the faults. These relationships are conceptualized in Figure 4.36.

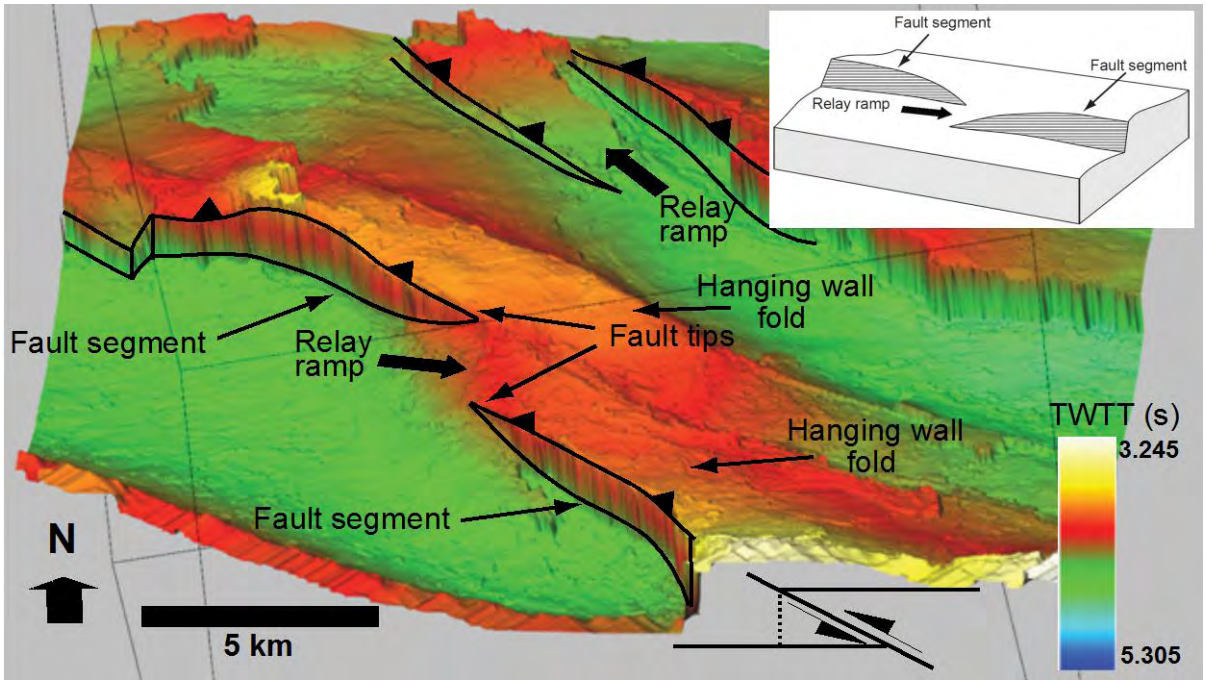

Figure 4.33**:** Perspective close up view of a gridded horizon highlighting relay structures observed in the central parts of the JDZ. The polygons are a representation of fault planes created when mapping reverse faulted horizons in Kingdom software. While it is an anomaly it may provide a rough estimate of displacement. Note that for most of the faults "displacement" is highest in the middle of the faults and lowest at the tips.

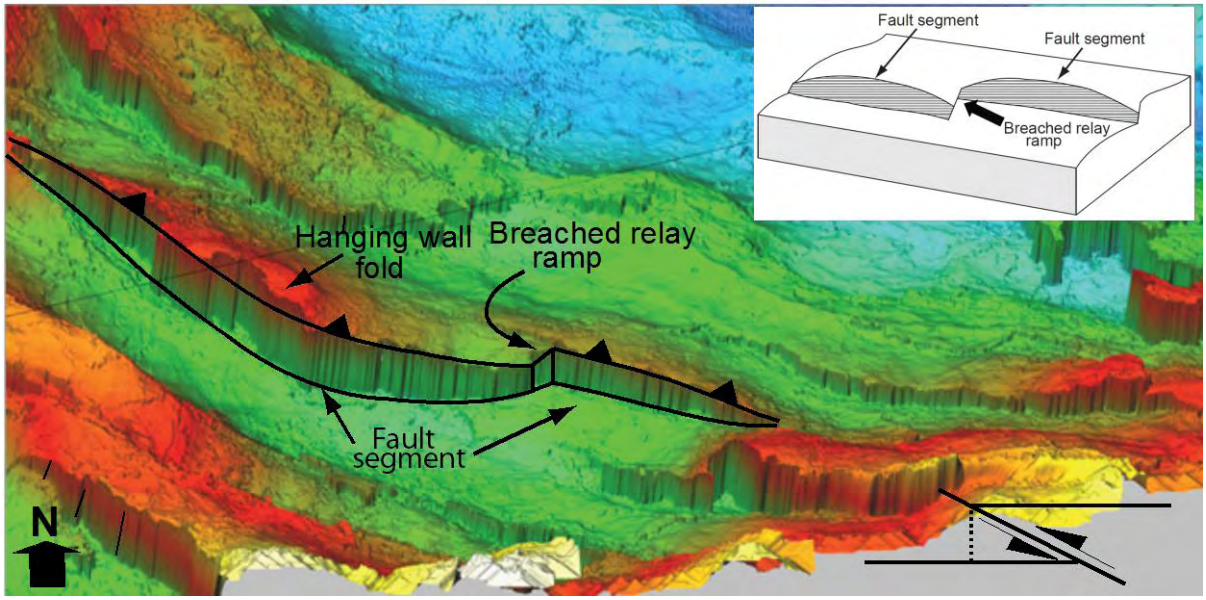

Figure 4.34**:** Perspective close up view of a gridded horizon highlighting breached relay structure observed in the central parts of the JDZ. The polygons are a representation of fault planes created when mapping reverse faulted horizons in Kingdom software. While it is an anomaly it may provide a rough estimate of displacement. Note that for most of the faults "displacement" is highest in the middle of the faults and lowest at the tips. Time bar is the same as in Figure 4.32.

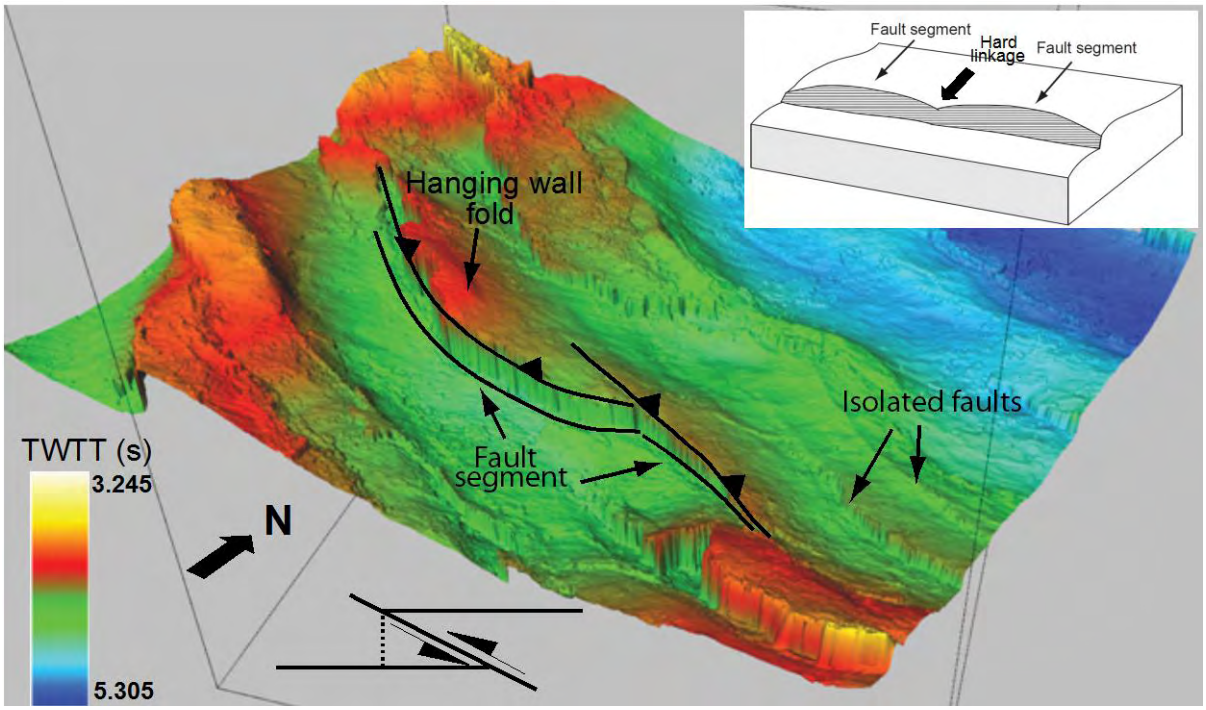

Figure 4.35**:** Perspective close up view of a gridded horizon highlighting hard-linkage of previously unconnected faults observed in the central parts of the JDZ. The polygons are a representation of fault planes created when mapping reverse faulted horizons in Kingdom software. While it is an anomaly it may provide a rough estimate of displacement. Note that for most of the faults "displacement" is highest in the middle of the faults and lowest at the tips.

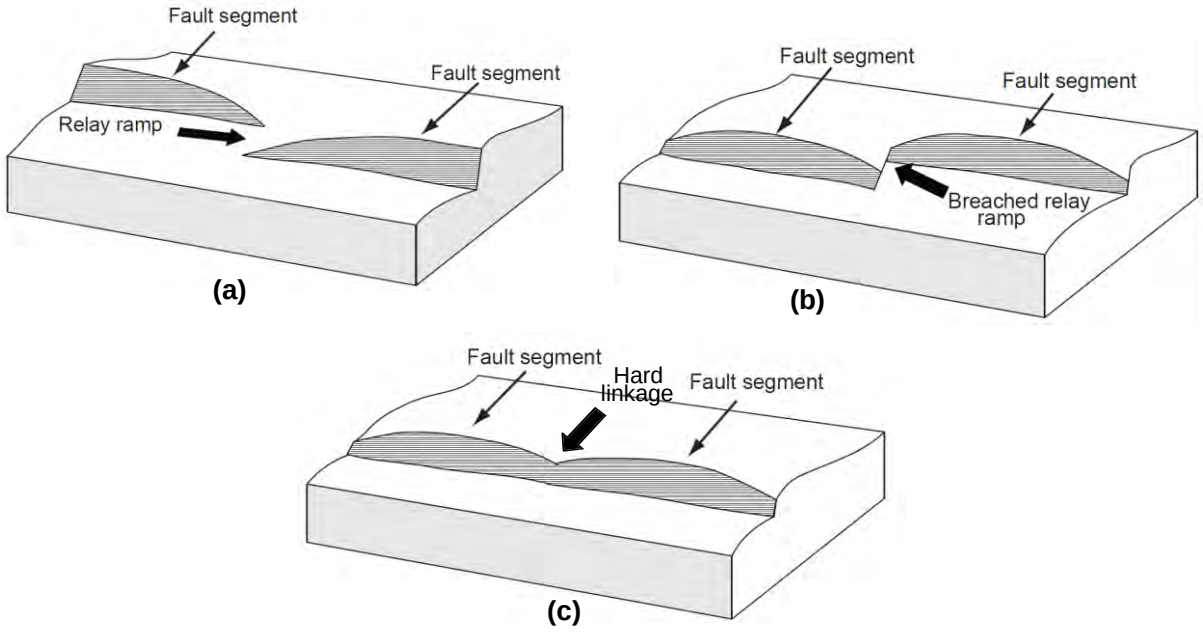

Figure 4.36**:** Conceptualized models illustrating the pattern of fault interaction in the central parts of the JDZ (modified from Walsh & Watterson, 1991).

4.4.4.3 Structural patterns

In general, two patterns of thrusting are observed in the JDZ. The reference point for this division is an arcuate thrust front that divides the area into two parts (Figure 4.30). Thrust faults north of the ridge (proximal JDZ) are widely spaced with individual thrust width of between 5 km and 10 km, but the spacing may occasionally be more than 10 km (Figure 4.12). The strike direction of the thrust faults is consistently NW-SE, however, occasional change in thrust vergence from seawards to landwards is observed. Most of the faults sole into an upper detachment surface located near the top of Unit III but in places appear to offset the reflection and sole into the Mid Unit III reflection. The folds possess large structural closure with widths of up to 5 km and characterized by stacked amplitude anomalies (Figure 4.12). The faults are blind and usually terminate at the base of Unit I. A striking feature of thrusting in eastern proximal JDZ is the change in the vergence of the faults from E-W and

then continuing SW-NE (Figures 4.37 & 4.38). The faults in these areas are stratigraphically shallower and generally complex with folds that occasionally reach the seafloor.

Faults south of the ridge (distal JDZ) are more regularly spaced, the average width of individual thrust faults is between 2 km and 5 km. The hanging wall folds in places reach the seabed creating a bathymetric expression (Figures 4.39). The faults are stratigraphically shallower than in the proximal JDZ and appear to sole into a detachment surface located at approximately 5.8 s two way travel time. The thrust faults are predominantly blind with the upper tips terminating against the base of Unit I. Thrust sequences involving the progressive down stepping of basal thrusts such that older thrust sheets are carried on the back of younger thrust sheets are observed in parts of distal JDZ. In places, the faults appear to glide oceanwards with the entire stratigraphic section along one or more detachment surfaces (Figure 4.13).

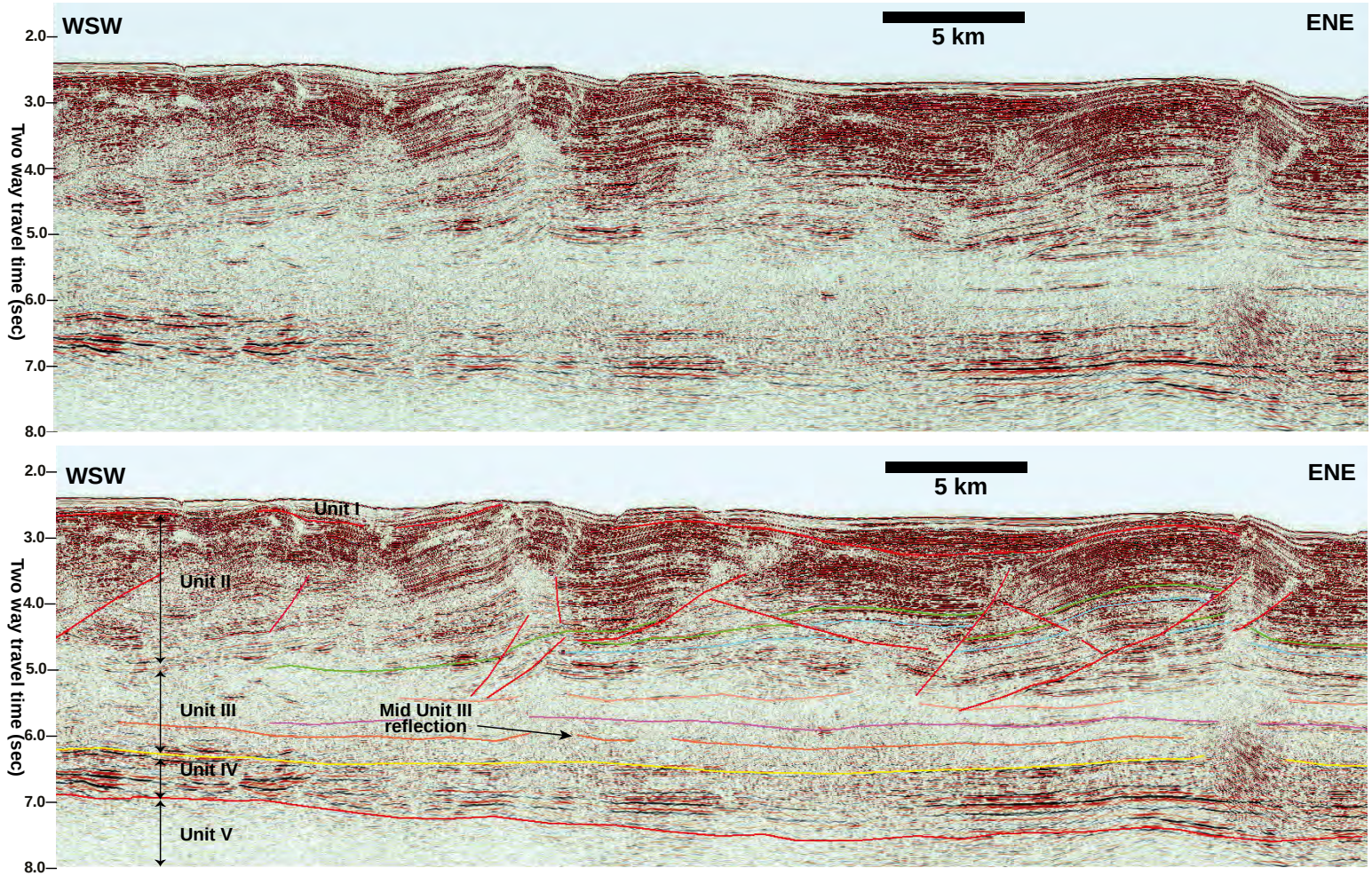

Figure 4.37: Uninterpreted and interpreted seismic cross section showing the complex pattern of thrusting in SE JDZ. (See the location in Figure 4.11). Vertical scale is two way travel time in milliseconds and horizontal scale is in kilometres.

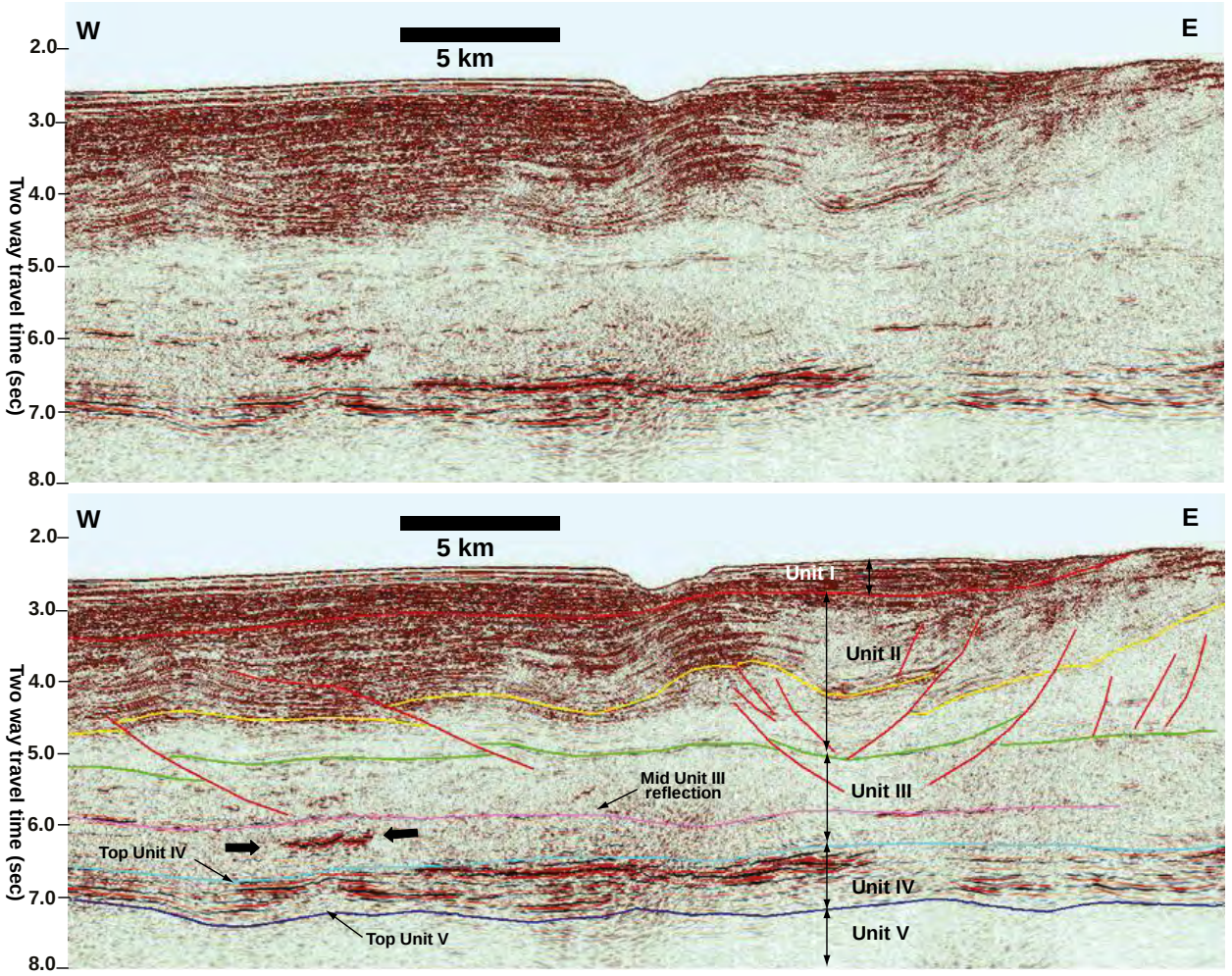

Figure 4.38: Uninterpreted and interpreted seismic cross section showing the change in vergence of thrust faults in SE JDZ. The black arrows highlight a sill, a common feature of lower Unit III in the distal parts of the JDZ (See the location in Figure 4.11). Vertical scale is two way travel time in milliseconds and horizontal scale is in kilometres.

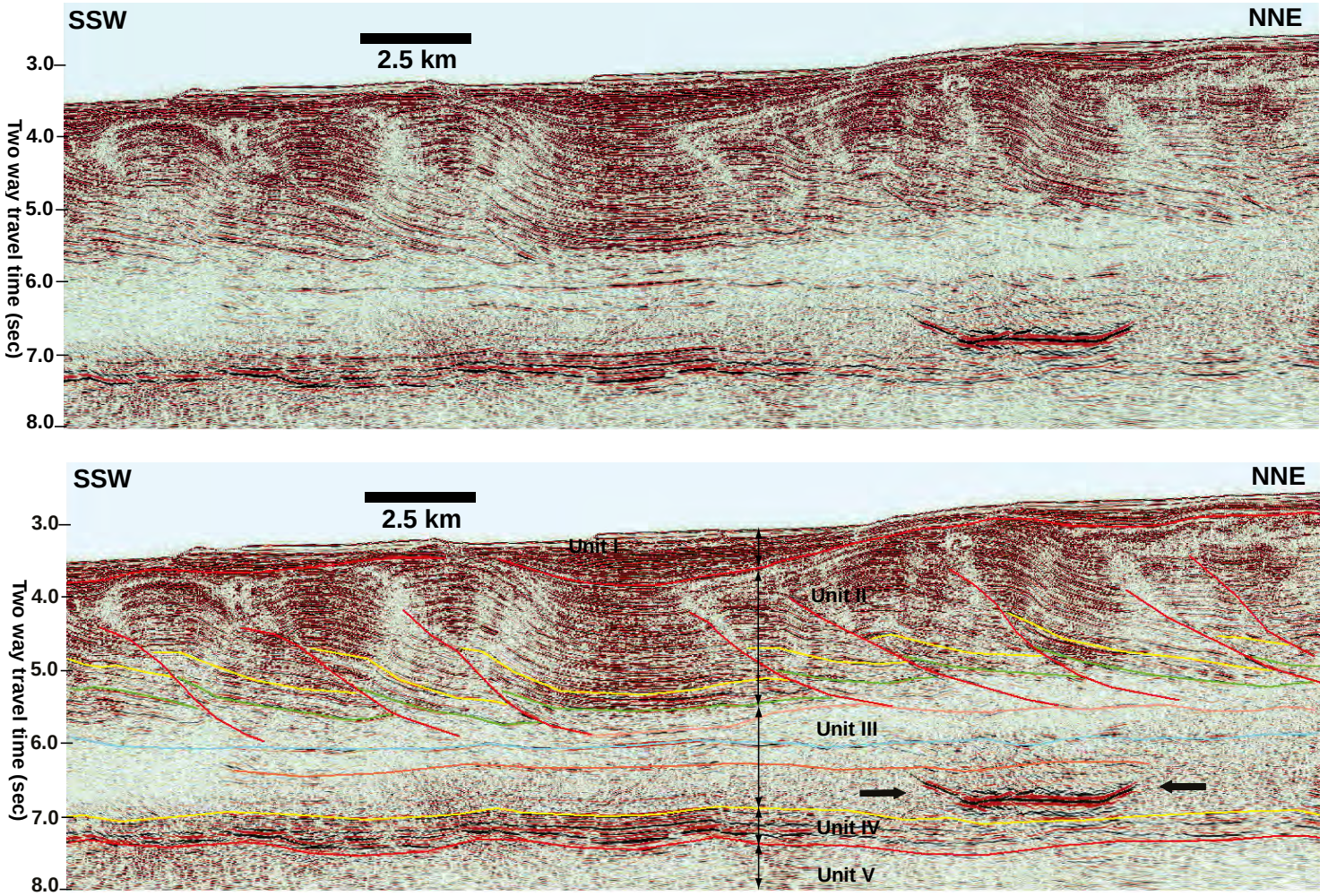

Figure 4.39: Uninterpreted and interpreted seismic cross sections in western JDZ illustrating the regularly spaced pattern of thrusting. The black arrows highlight a sill, a common feature of lower Unit III in the distal parts of the JDZ (See the location in Figure 4.11). Vertical scale is two way travel time in milliseconds and horizontal scale is in kilometres.

4.4.4.5 Fault statistical analysis

4.4.4.5.1 Strike and dip plots

The strike and dip plots of eleven faults in central JDZ are presented in Figure 4.40. Although the faults were interpreted in the time domain, the dip plots were calculated using an interval velocity profile of deepwater Niger Delta (Morgan, 2003). The faults strike in a predominantly WNW-ESE direction with a mean orientation of $110/290^0$ and dips ranging between 27^0 and 35^0 in the northeast direction. The dip values are within the range typically quoted for thrust faults (e.g. Walsh & Watterson, 2001).

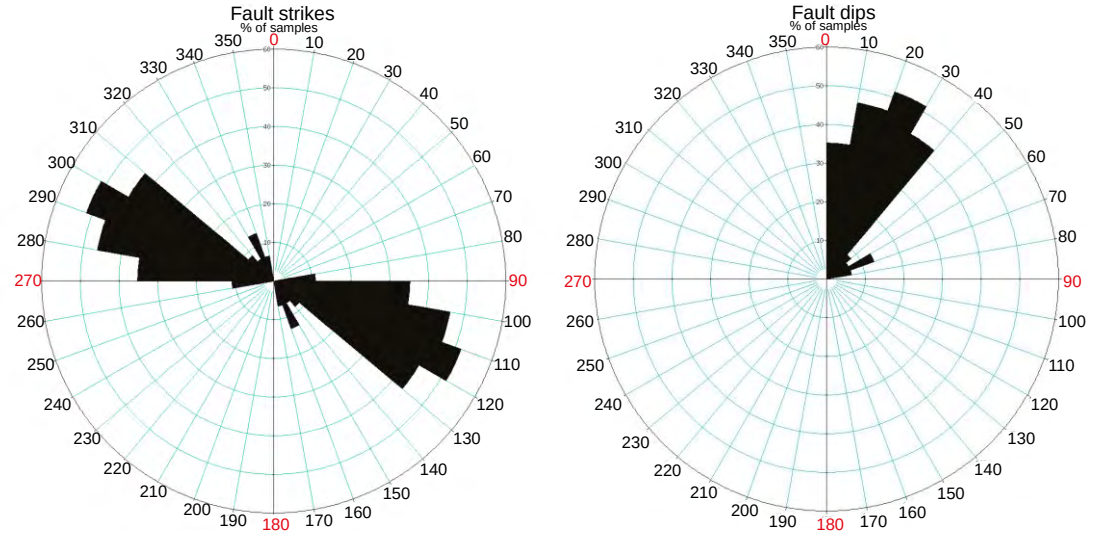

Figure 4.40: Strike and dip plots of eleven thrust faults mapped in central JDZ. Fault strike is predominantly WNW – ESE and dipping NE with low dip values typical of thrust faults.

4.4.4.5.2 Fault length versus maximum displacement (dip-separation) plots

Log-log plots of the fault length versus maximum displacement and heave are shown in Figure 4.41 & 4.42 respectively. The data have been superimposed on global thrust database in literature for comparison. The maximum displacement versus fault length regression for the thrust faults in the JDZ seismic volume yielded a best-fit exponent of n =1.04 and a correlation coefficient of 0.96. The best fitting power-law exponent of 1.04 is between the range of 1.0 and 2.0 suggested in previous studies for most

normal and thrust faults (e.g. Kim & Sanderson, 2005). The plots demonstrate that thrust faults mapped from central JDZ fall within the range of fault length – maximum displacement ratios of between 0.1 and 0.01, implying that the faults accommodate offsets of between 0.1 and 10% of their lengths. It is interpreted that the thrust faults have scaling characteristics compatible with thrust faults mapped in undifferentiated clastics (Drozdzewski *et al*. 1980, 1985; Gillespie, 1991; Gillespie *et al*. 1993; Rowan, 1997; Bergen & Shaw, 2010), basement rocks (Elliot, 1976; Fox, 1959; Jackson *et al*. 1996; Wood *et al*. 1969) and Schultz *et al.* (2006), and are not unusual structures. It is possible that conclusions drawn from these faults may have wider applicability.

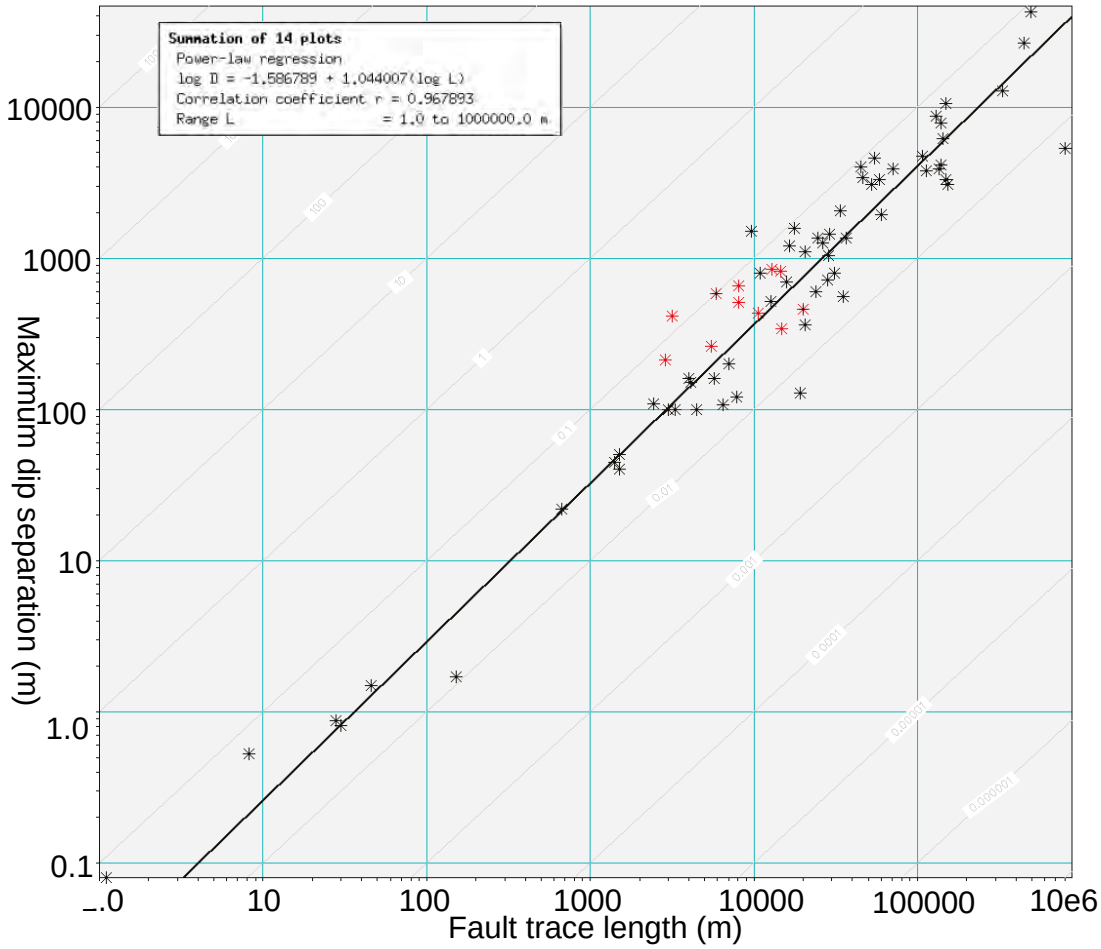

Figure 4.41: Fault length versus maximum displacement plots from eleven thrust faults (red) superimposed on global thrust dataset (black). The plots show that faults in the study area have typical D_{max} vs. Length scaling properties with global thrust faults database in literature.

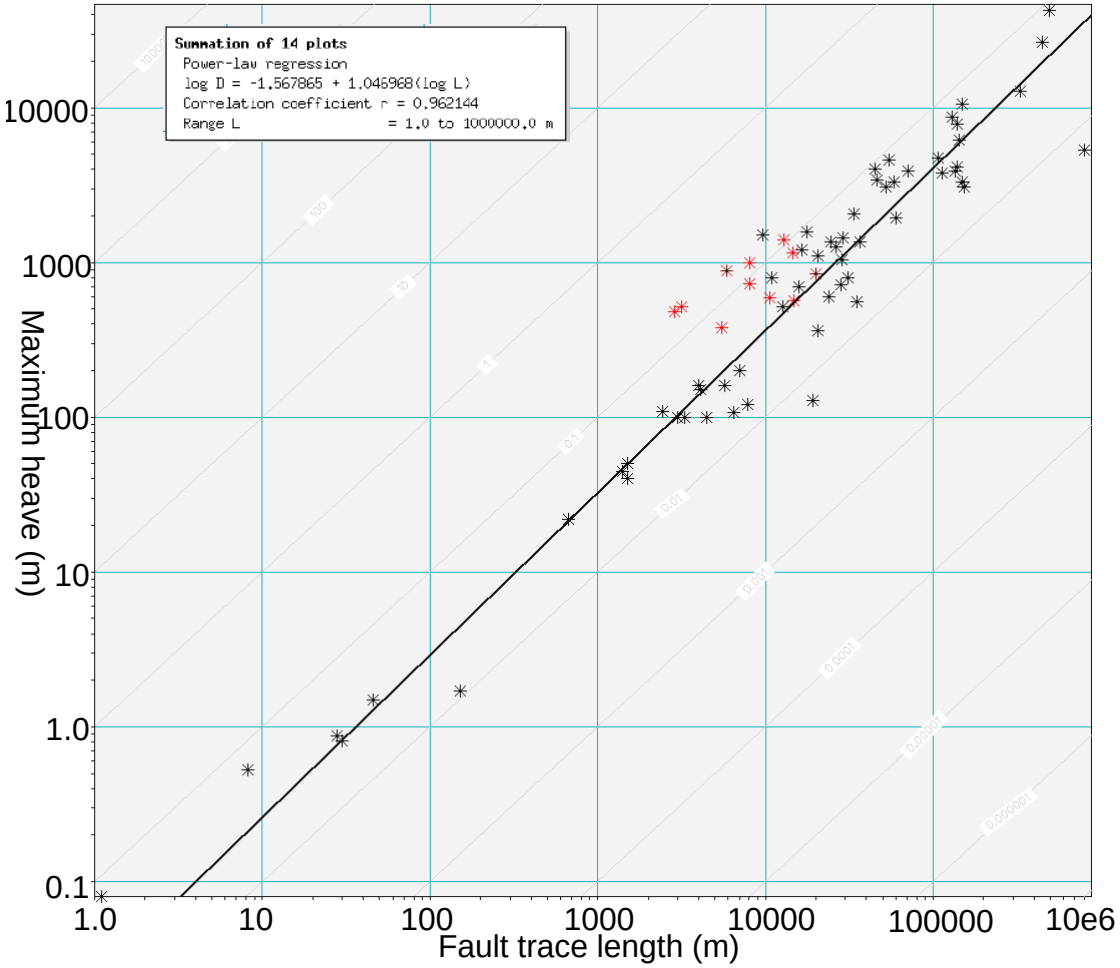

Figure 4.42: Fault length versus maximum heave plots from eleven thrust faults superimposed on global thrust dataset (black). The plots shows faults in the study area have typical Maximum heave vs. Length scaling properties with global thrust faults database in literature.

4.4.4.5.3 Strain summation plot

The strain summation plot of eleven fault arrays mapped in central JDZ (Figure 4.43) shows a maximum compression of ~0.05% and the lowest values of strain occur at fault boundaries. The plot also shows that large faults and perhaps folding initiated at the cessation of faulting account for most of the strain. The dashed area on the plot represents the location of the arcuate ridge that divides the faults into two domains in central JDZ.

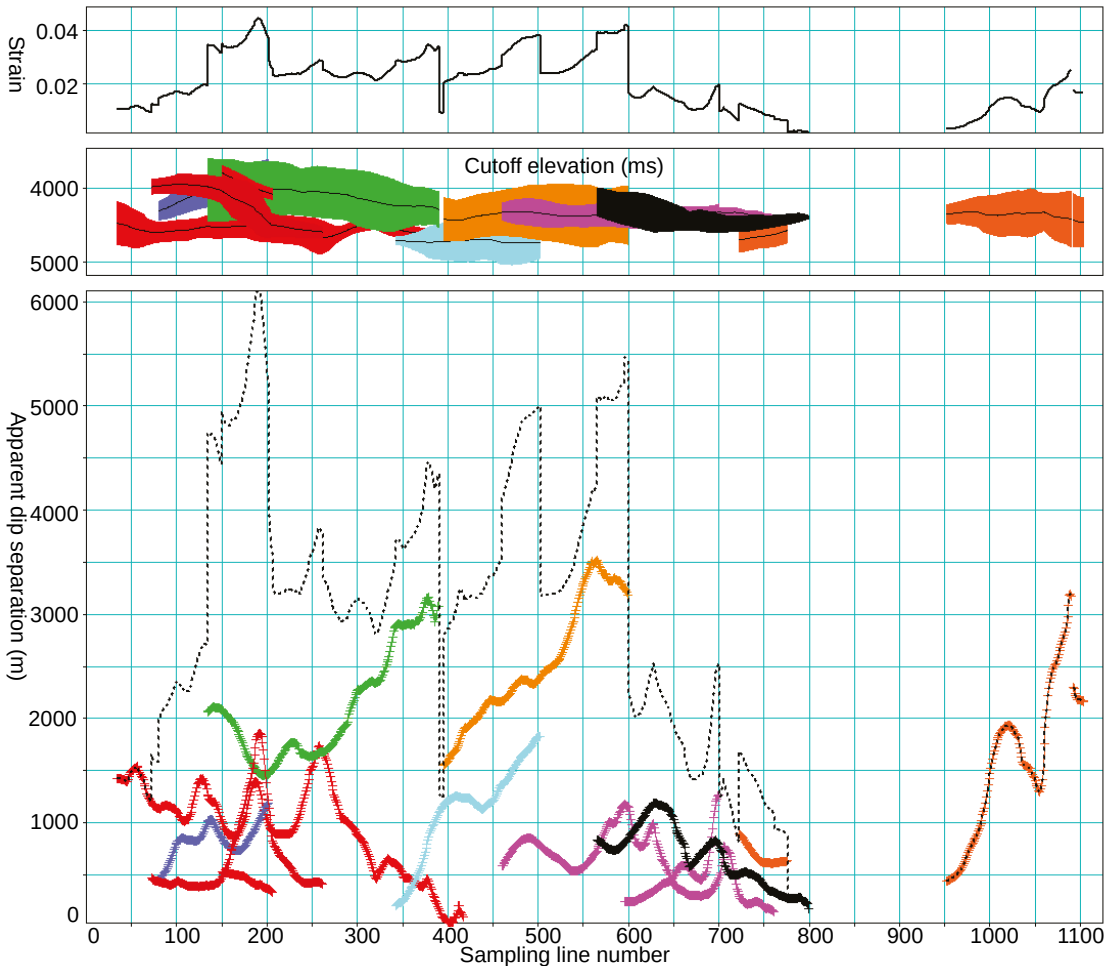

Figure 4.43: Strain summation plots of twelve thrust faults in central JDZ. Note the low magnitudes of strain at fault boundaries.

4.5 Summary and conclusion

The seismic data has provided the opportunity to investigate the structural and stratigraphic manifestation of gravity-driven compressional deformation in the outer reaches of deepwater Niger Delta toe of slope imaged in the data. The interpretation has produced data that can help provide more insight into the structural and stratigraphic framework of the study area that hitherto has not been fully investigated. In addition, a database of faults have been generated that will be used to investigate the three-dimensional surface morphologies of the faults.

- Five seismic reflectivity units have been identified and are interpreted to represent the prograding cyclic sequence of sedimentation in the JDZ that can be correlated with the principal stratigraphic subdivisions of the Niger Delta. The overall seaward thinning of the seismic packages and shallowing of the interpreted basement is in agreement with previous suggestions that the deepwater Niger Delta has a wedge taper geometry (Bilotti *et al*. 2005), with a shelfward dipping regional detachment within Unit III and a bathymetric slope dipping away from the shelf. Although no seismic evidence of fluid overpressures have been observed, the existence of at least two strong reflections within the seismically transparent reflective package of Unit III and the listric nature of most of the thrust faults at or near the top of the unit could be evidence for possible high pore pressure at these depths. The existence of these reflections is an indication of episodic intervals of gravity collapse that may have facilitated the seaward advancement of thrust faults.
- Deformation is thin-skinned as Evident by ocean-verging thrust fold and folds decoupled from the basement (Unit IV) by detachment surfaces within Unit III. Faults exhibit cross sectional geometries similar to models described in literature (e.g. Corredor *et al*. 2005; Bilotti *et al*. 2005). In the central parts of the study area, faults typically have cross sectional geometries similar to shear fault-bend folds with relatively long, gentle backlimbs that dip less than the thrust ramp angle and growth strata that indicate components of kink-band migration and limb rotation (Suppe, 1994). Most of the faults are blind i.e. die out near the base of UnitII where hanging wall folds are well developed.

- Faults in the central parts of the study area exhibit hard linkage by the gradational propagation of segments into an overlap position that develops into soft-linked

relay structures. Soft linkage of the faults is achieved by the smooth transfer of displacement through unbreached relays, while hard linkage is via breached relays and connecting faults. Evidence suggests that some of the faults connected by breached relays are continuous, implying that geometric coherence may have been maintained by segments of the faults and is described using the model of kinematic coherence (Walsh & Watterson, 1991).

- Fault length versus maximum displacement plots of faults mapped in the central part of the study area have been compared with published data from compressional geological settings encompassing a range of rock types and scales of faulting. Results show that thrust faults in the JDZ have typical scaling properties. Additional data have thus been added to global thrust scaling database previously published.

- Thrust faults in the study area can be classified into two groups based on the width of the individual thrust faults and the geometry of the hanging wall folds. In the proximal parts of the JDZ, thrust faults are widely spaced with large structural closure of the hanging wall folds. In the eastern parts of the proximal domain, faults are complex and typically verge in the opposite direction. In the distal parts of the study area, thrust faults are regularly spaced with hanging wall folds that occasionally creates bathymetric expressions on the seabed.

- The high concentration of pockmarks in proximal JDZ and the large structural closure of hanging wall folds characterized by stacked amplitude anomalies and discernable flat spots imply the possible existence of an active hydrocarbon system in proximal JDZ. In addition, several lenses of sills observed in Unit III may impact on hydrocarbon generation and expulsion in the study area. If

hydrocarbon migration into traps is occurring after the intrusion of magma, then the sills could act as barrier to fluid flow, depending on post-emplacement tectonics (Schofield, personal communications).

- Seismic cross sections show that faults in the study area have variable cross sectional geometries but possess scaling properties typical of thrust faults. This chapter sets the scene for investigating the three-dimensional surface models of the faults in Chapter Five.

CHAPTER FIVE- THREE-DIMENSIONAL ANALYSIS OF FAULT SURFACE MORPHOLOGY

5.1 Introduction

The focus of this chapter is to describe techniques for processing, visualizing and investigating the three-dimensional surface morphology of thrust faults mapped from JDZ seismic data using structural attributes of the fault surfaces. In addition to providing data that will allow the spatial variation of fault surface morphology to be investigated in three-dimensions, the attribute plots of the faults constitute an integral part of the database for investigating potential relationships between fault surface morphology and the structure of the volumes surrounding the faults described in Chapter Six.

5.2 Methodology

5.2.1 Data

The primary database consists of traces of sixteen thrust faults mapped from the central and western parts of the JDZ seismic data. The fault traces were mapped on at least every second line in vertical inline direction and in places every 100 ms in time slice orientation. In places where the discontinuities are well imaged, the traces were mapped on every line to provide sufficient data for detailed analysis of fault surface morphology. The workflow for calculating and analyzing surface and geometric plots of the faults is summarized in Figure 5.1.

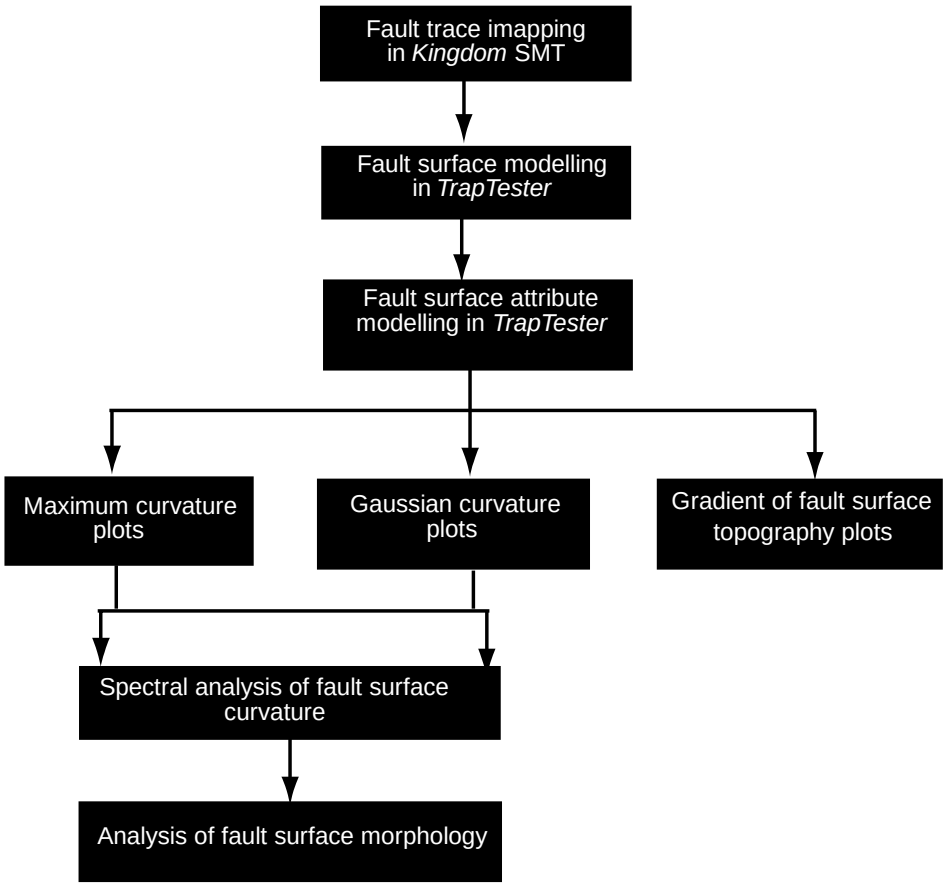

Figure 5.1: Flow diagram summarizing the workflow for investigating the three-dimensional geometric properties of thrust faults mapped from JDZ seismic data.

5.2.2 Workflow

5.2.2.1 Fault surface modelling

In the first stage of the workflow a JDZ fault surface geometry analysis project was created in *TrapTester* software. Traces of sixteen thrust faults manually picked on at least every inline from the seismic data were imported into the project in *SeisworksR2003* ASCII format. Fault surfaces are generated with reference to a coordinate system that minimises the variation of elevations of the fault surface. This plane can be thought of as the best fit plane and is computed from the eigensolutions of covariance matrix of the raw fault segments. The plane is referred to as "the natural

coordinate plane" (ncp) with axes *u*, *v* and *w* of the natural coordinate system (ncs), being *u* parallel to strike, *v* parallel to dip and *w* being perpendicular above the natural coordinate plane (Figure 5.2).

To make interpretation easier, a convention is adapted such that *u* follows the strike of the plane, *v* follows the dip direction and w is perpendicular to (*u*, *v*) above the plane. This convention means that all planes are uniquely defined and gives meaning to the signs of the gradients and curvature.

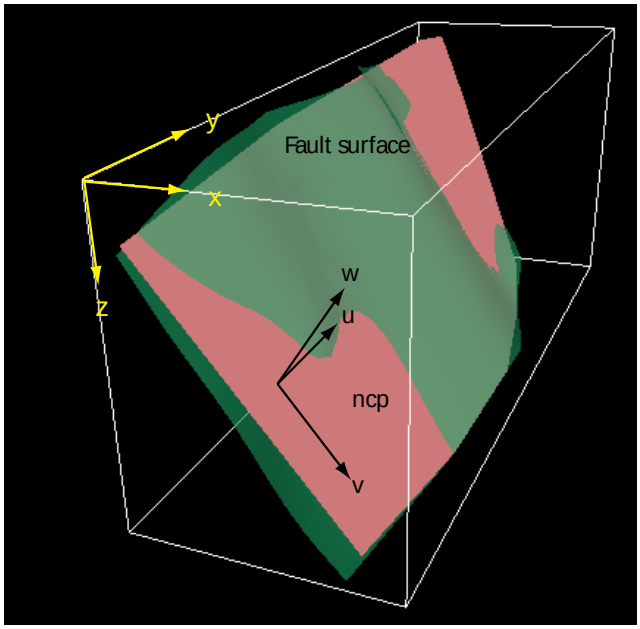

Figure 5.2: Schematic illustration of surface mesh and natural coordinate plane (ncp) and natural coordinate systems (ncs). The ncp overcomes many of the issues encountered when attempting to calculate and project grids onto reconstructed fault surfaces (*TrapTester* manual, 2010).

The natural coordinate plane (ncp) ensures better surface interpolation onto a regular grid and is a requirement for the curvature calculation method in *TrapTester*. Surface attribute operations are referred to as the texture plane (tp) and are derived from the natural coordinate plane (ncp), have the same strike, *u*, but *v* in this case is defined to be vertical and *w* is horizontal. Therefore the texture plane defines the strike projection. The resulting surface model is a regular grid of elevation, w, perpendicular

to the natural coordinate plane that is interpolated to honour the original raw data points to constrain the surface models of the faults (Figures 5.3 and 5.4) using the multilevel B-Spline algorithm of Lee *et al*. (1997).

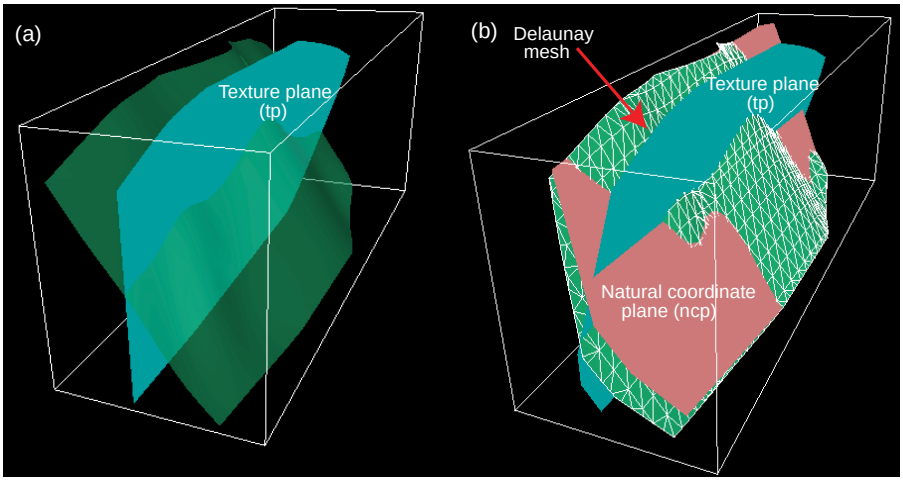

Figure 5.3: Schematic illustration of the texture plane (a) and its relationship with the fault surface and the natural coordinate plane (b). (*TrapTester* manual, 2010).

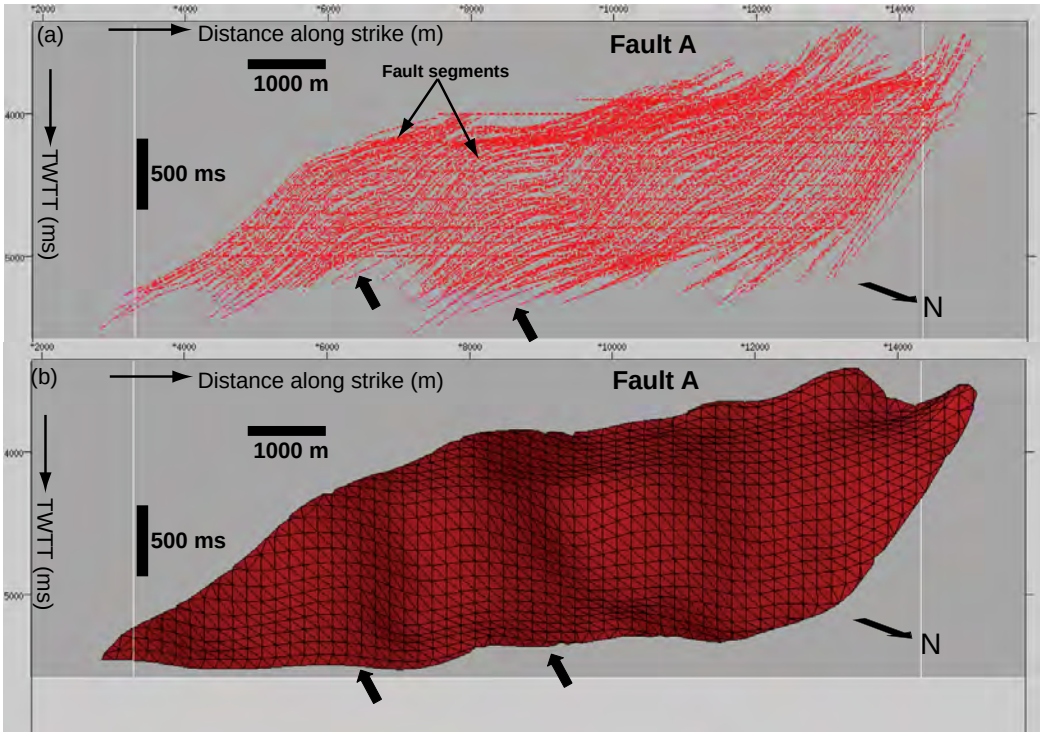

Figure 5.4: Strike view of a dense grid of fault traces mapped from the JDZ seismic data in the inline and time slice orientation (a) and meshed surface model of the faults produced from the differential geometry of the grid that is interpolated to honour the original raw data (b). The block arrows illustrate a similarity in the pattern of topography that exists in the original raw data and the modelled surface (block arrows). Vertical scale is in milliseconds two way travel time and horizontal scale is in meters. Vertical exaggeration is ~1.6.

5.2.2.2 Data processing

The objective of calculating surface models of the faults is to create a database that can be used to calculate and analyze fault geometrical properties in three-dimensions. Therefore, there is the need to process the data prior to calculating surface and attribute plots of the faults.

Fault surface attributes calculated over raw data is usually noisy and may reflect the geometry of noise (e.g. Lisle, 1994; Lisle & Robinson, 1995; Samson & Mallet, 1997; Stewart & Podolski, 1998; Roberts, 2001; Carena & Suppe, 2002). It is thus imperative that some smoothing is applied to the surface models of the faults in order to reduce the effect of elevation changes between raw data points inevitably introduced as a result of the dense grid of fault traces mapped from the seismic data. Data smoothing has been described as a necessary conditioning process prior to analyzing the geometry of gridded geological surfaces. However, the degree of smoothing required primarily depends primarily on the wavelength of structures being analyzed. (e.g. Jones *et al*. 2008; Bergbauer & Pollard, 2003; Stewart & Wynn, 2000; Carena & Suppe, 2002). Smoothened surfaces may help to isolate relevant data while retaining major geometrical features that exist in the original data prior to curvature analysis. In addition, the length scale of the curvature measurements (i.e. the size of the grid parameter) can be varied in order to determine the spectrum of curvature.

In this thesis, surface models of the faults calculated using fault traces with individual width of 25 m were smoothened by varying the grid sizes based on a detailed analysis of the impact of grid sizes on fault surface attribute modelling using a thrust fault (Fault A) with pronounced surface topography chosen from the database (Figure 5.5).

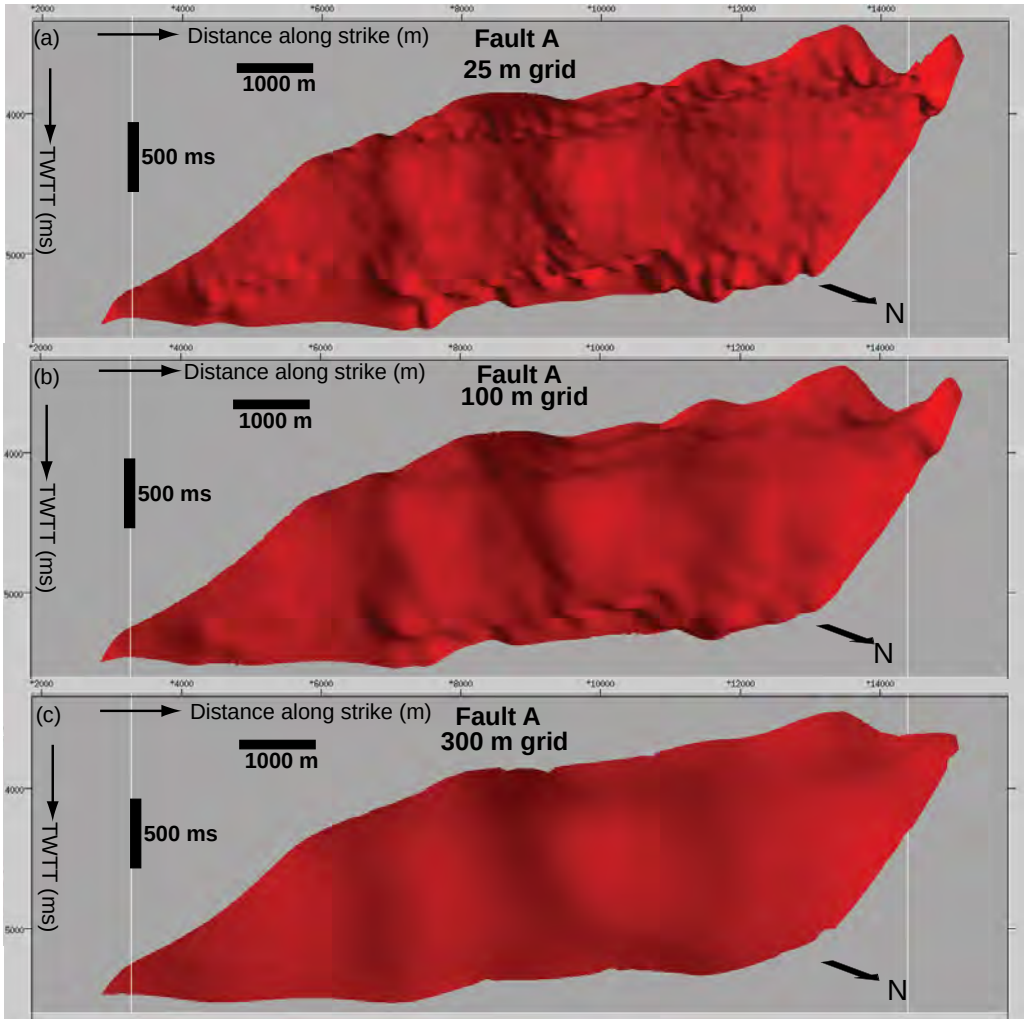

Figure 5.5: Strike view of fault surfaces modelled from raw fault segments at 25 m grid size (a) 100 m grid size (b) and 300 m grid size (c). In this thesis the surface models of the faults are smoothened by increasing the grid spacing to highlight the large-scale surface structures such as the broad undulations clearly seen in the smoothened surfaces. Vertical scale is in milliseconds two way travel time and horizontal scale is in meters. Vertical exaggeration is ~1.6.

5.2.2.3 Fault surface attribute modelling

5.2.2.3.1 Curvature

Detailed description of the definition and theory of surface curvature is presented in Chapter Two. Curvature is defined as the rate of change of orientation of the tangent vector with respect to change in arc length. It can be calculated in any direction but there are two mutually perpendicular directions where the curvature is at its maximum

and minimum (i.e. k_{max} and k_{min}). In *TrapTester*, curvature is calculated by using a method that assumes that surfaces can be described adequately using 2nd order polynomial. The differential geometry and principal curvatures can then be computed analytically from the equation of the polynomial using the methods described by Pete & Sahota (1985). However, unless the surface can be defined entirely analytically, curvature computations are always approximate and scale-dependent.

The reciprocal of a curvature value is equal to the radius of the curvature and the sign of curvature is determined by which side of the surface the centre of the curvature lies. It is possible for k_{max} and k_{min} to have their centres on opposite sides of the surface and hence have opposite signs. By convention, if a surface is convex-down in a given direction, curvature in that direction is negative. Conversely, when the surface is convex-up, curvature is positive in that direction (Figure 5.6).

Two surface curvature attributes are utilized to analyse the geometry of thrust faults presented in this thesis. The Gaussian curvature (k_G) of a surface is the product of the two mutually orthogonal principal curvatures (k_{max} and k_{min}) with the overall shape of the surface being defined by their signs (Lisle, 1994). Maximum curvature k_{max}, one of two principle curvatures, is a curvature of a normal section with the largest value and is orthogonal to minimum curvature k_{min} (Roberts, 2001). The importance of the two attributes (Gaussian and maximum curvature) in the context of the focus of this thesis is described in Chapter Two.

5.2.2.3.2 Gradient of fault surface topography

Although curvature is the main structural attribute of the faults being analyzed, plots that can highlight the gradient of fault surface topography are also used in assessing

the spatial variation of fault surface morphology. Surface gradient is a measure of the "steepness" along the strike and dip of the fault planes and is defined in the *u* and *v* directions by convolving a finite difference operator with the grid of elevations. The resultant gradient is the modulus of the two gradient vectors (Figure 5.7). The gradient in the strike direction is positive if the elevation relative to the ncp, *w*, decreases along strike. The gradient in the *v* direction is negative if the elevation relative to the ncp, w, increases down dip.

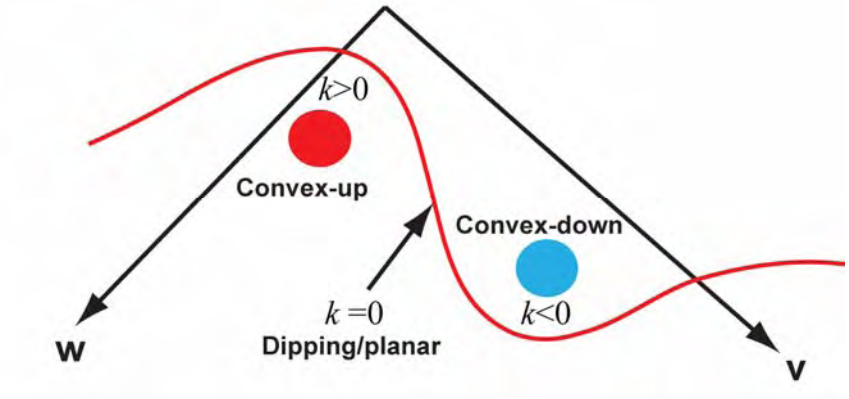

Figure 5.6: Schematic illustration of the conventions used to present curvature plots of fault surfaces (*TrapTester* manual, 2010).

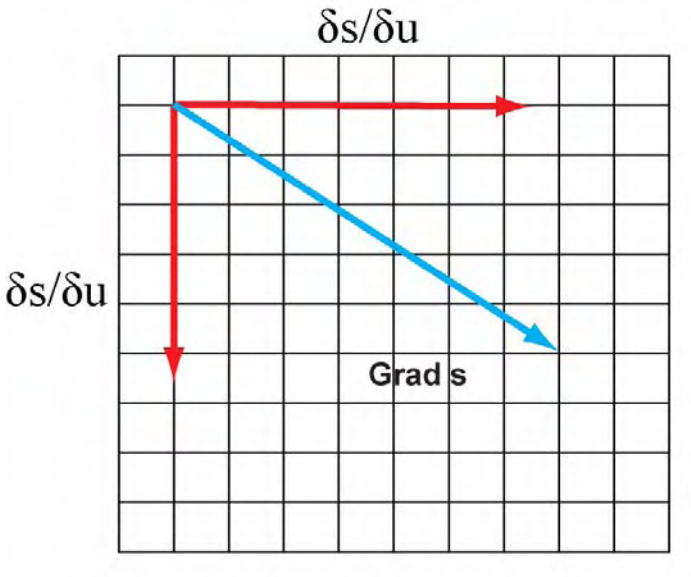

Figure 5.7: Schematic illustration of the definition of the gradient of fault surface topography (*TrapTester* manual, 2010).

5.2.2.4 Fault surface attribute presentation and sampling resolution

The curvature plots of the faults described in this thesis are presented to enable the visualization and analysis of fault curvature as the inverse of the radius of curvature (Roberts, 2001). A red-white-blue colour bar is used to denote synclastic (positive), planar (zero) and anticlastic (negative) fault surface Gaussian curvature, and convex (positive), planar (zero) and concave (negative) fault surface maximum curvatures respectively at the scale of observation. In *TrapTester*, curvature is only computed at a single scale of resolution and it is not possible at present to examine curvature spectra. In this thesis, the curvature plots of sixteen thrust fault planes are first described using a single sampling resolution. However, the surface model and curvature plots of a thrust fault plane with pronounced surface relief is used demonstrate the multi-spectral nature of curvature and the relevance of testing curvature spatial resolution in analyzing fault surface topography. A spectrum colour bar is used for the gradient plots to indicate the pattern of gradient of fault surface topography.

5.3 Fault surface attribute analysis

5.3.1 Introduction

The three-dimensional surface models of twenty five thrust faults mapped across the JDZ seismic data have been produced to permit a detailed analysis of fault surface morphology. However, sixteen of the faults mapped in the central and western parts of the study area have been selected for detailed geometrical analysis and are referred to as Faults A to O (Figure 5.8). The faults are well imaged in the two parts of the study area and offset thick succession of reflective packages of contrasting acoustic

properties that will allow a realistic investigation of potential links between fault shape and the structure of the volumes adjacent to the faults in Chapter Six.

Figure 5.9 is an amplitude time slice extracted at 4.500 s showing the geometry of the faults in plan view and the location of seismic cross sections used to illustrate vertical cross sectional geometries of the faults in Figures 5.10 and 5.11. A detailed description of the cross sectional geometries of faults in the JDZ are presented in Chapter Four.

5.3.2 Surface modelling

Figures 5.12 to 5.15 show the strike views of the sixteen faults with traces used to calculate surface models of the faults. Faults in the study area develop as a result of the gravity-induced compression of thick deltaic sediments and have thus been subjected to a relatively simple history of strain with no evidence of reactivation to suggest that a later episode of deformational processes that would have altered the original fault surface topography. The faults exhibit undulations whose dimensions vary but generally undulated with the orientation of the corrugations in the direction of fault dip. The occurrence on undulations of the fault surfaces is consistent with fault geometries previously interpreted to allow faults to slip (e.g. Neetham *et al.* 1996; Van Gent *et al.* 2010).

Figure 5.16 show surface models of four faults with fault traces (dashed red lines) and planes of interpretation. Note that in all the faults, there is a close relationship between the geometry of the fault traces and undulations. However, the plane of interpretation is independent of fault surface topography (block black arrows). Fault surface topography is controlled by the shape of the fault traces the wavelength of the

undulations is greater than the minimum distance between individual fault traces (25 m) in all the four models. Therefore, the surface features are interpreted to be real and may not be artefacts of interpretation and surface modelling. The irregularities on the surface models of the faults are also highlighted by plots of gradient of fault surface topography of the sixteen faults (Figure 5.17 to 5.20). In section 5.3.2.2, a demonstration of the consistency of fault surface topography when traces of the fault were mapped in the inline, cross line and horizontal orientation. (i.e. the persistence of undulations irrespective of plane of interpretation) is presented. Table 5.1 summarises measurements of fault topographic dimensions for the sixteen faults. In measuring the dip length of the undulations a velocity of 2000 ms was used to convert time to depth based on a velocity profile of deepwater Niger Delta in Morgan (2003).

Fault	Approximate along strike length (km)	Approximate along dip length (km)	Approximate surface area (km^2)
A	12	2.0	24
B	9.0	2.5	22.5
C	21	2.5	52.5
D	8.0	2.6	20.8
E	7.0	2.0	14
F	5.5	2.2	12.1
G	23	1.5	34.5
H	8.5	2.0	17
I	20	2.5	50
J	10	3.0	30
K	20	2.5	50
L	24	3.0	72
M	5.5	3.0	16.5
N	16	2.5	40
O	9.1	2.0	18.2
P	10.2	2.0	20.4

Table 5.1: Summary of surface measurement data for sixteen faults mapped in the central and western parts of the study area.

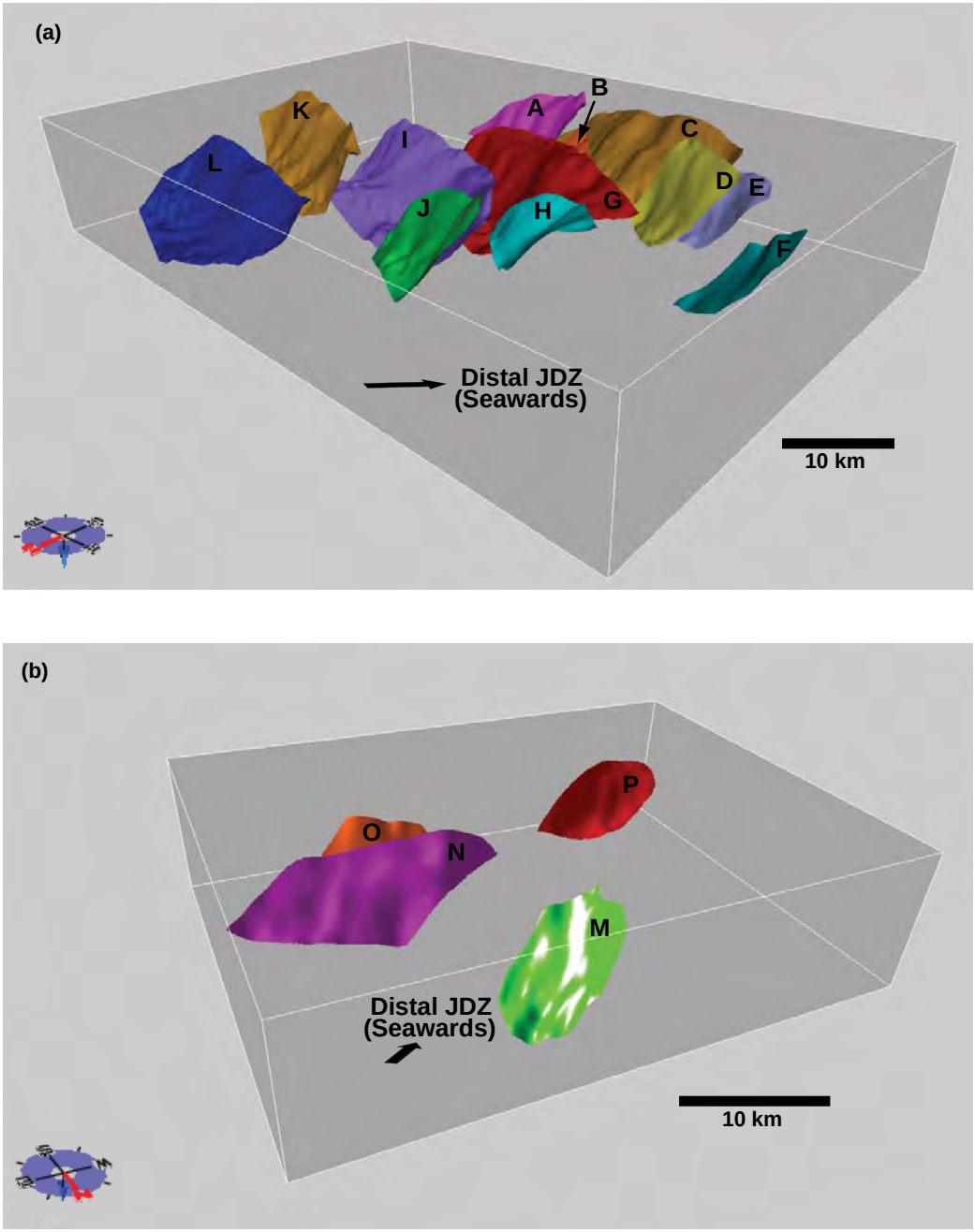

Figure 5.8: Perspective views of surface models of sixteen thrust faults mapped in central JDZ (a) and western JDZ (a). The surface models of the faults constitute the database for analyzing fault plane morphology. Cross sectional location of the faults are shown in Figures 5.9, 5.10 and 5.11. Vertical exaggeration is ~2.

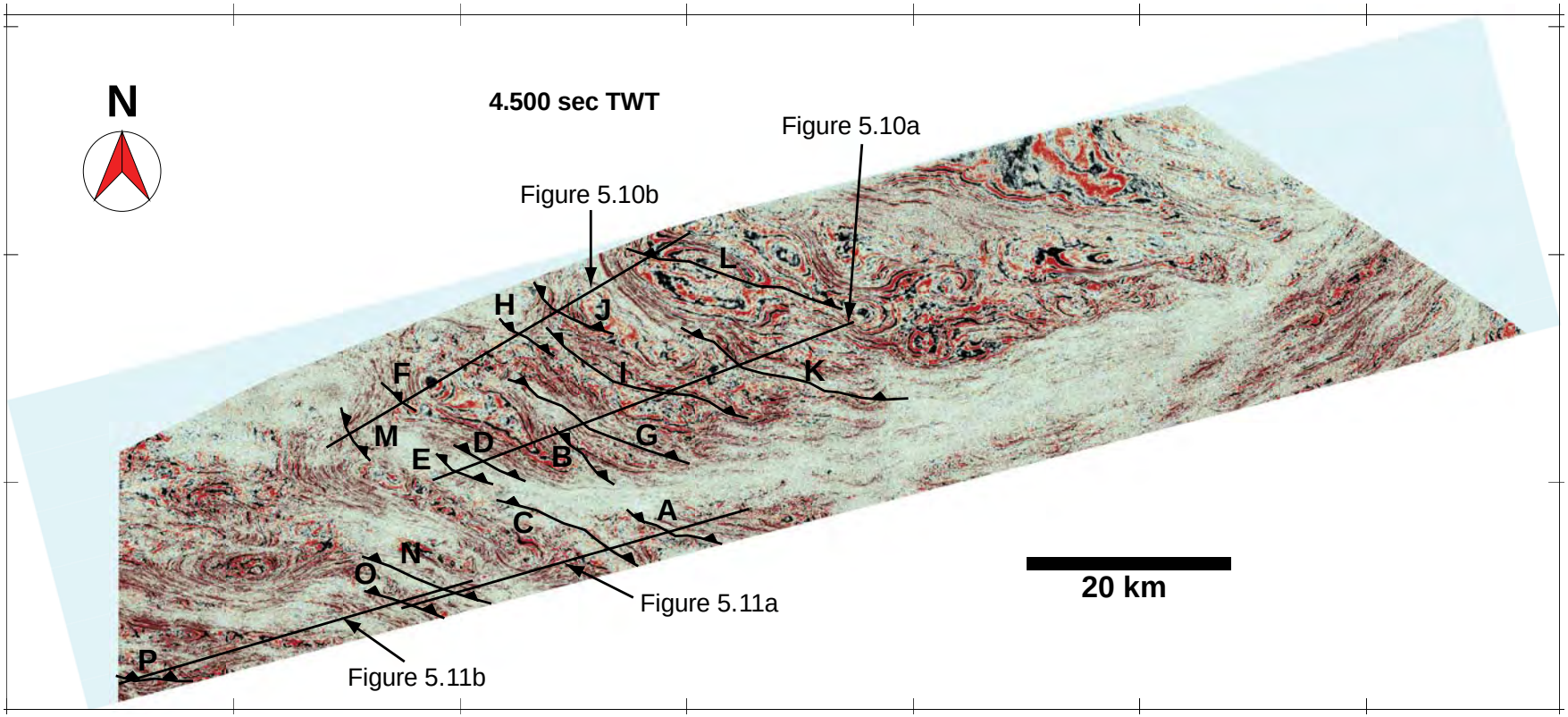

Figure 5.9: Interpreted horizontal seismic amplitude time slice extracted at 4.500 seconds two way travel time showing plan view geometries of sixteen faults and the location of seismic lines showing the cross sectional geometries of the faults.

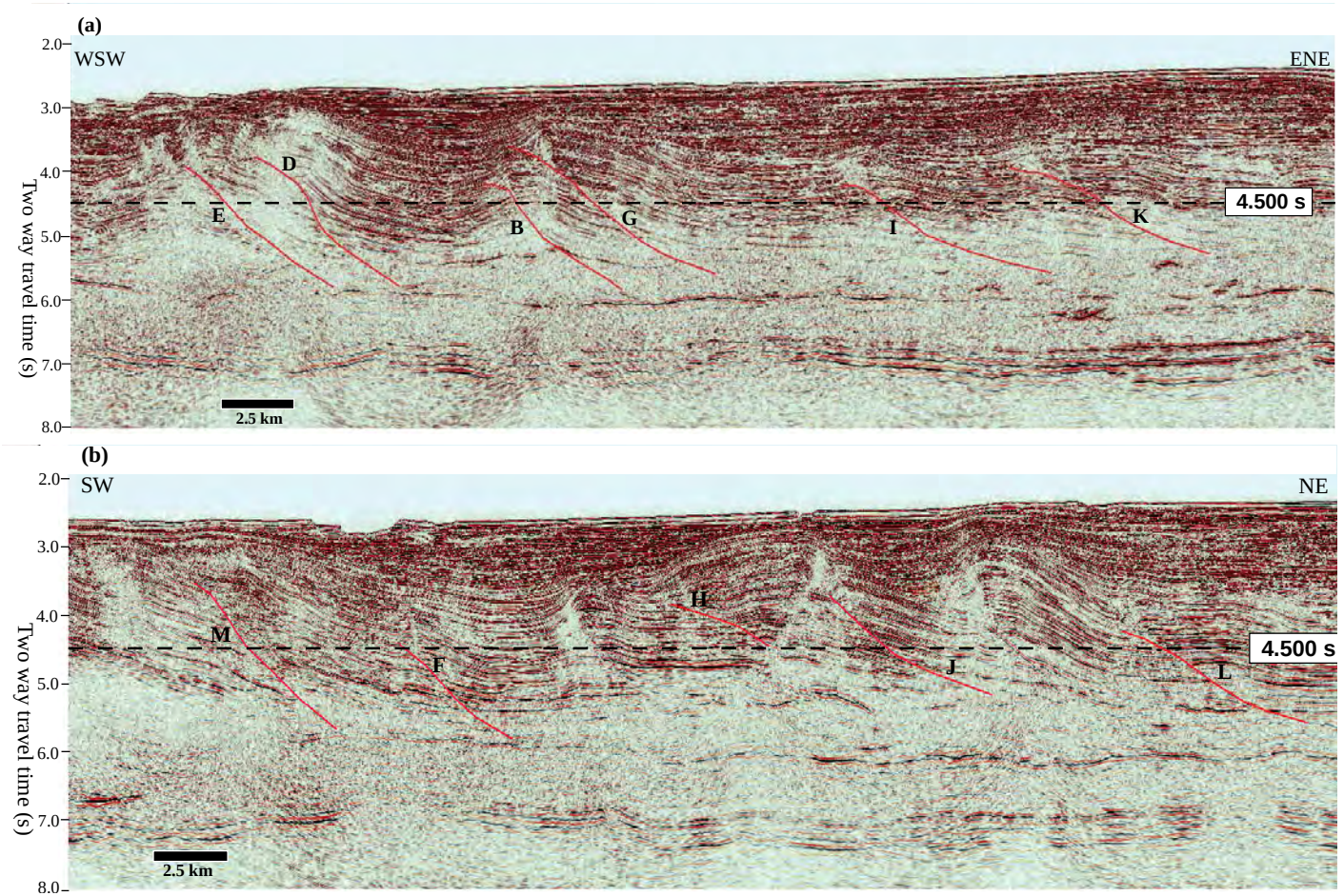

Figure 5.10: Interpreted WSW – ENE seismic line showing the cross sectional geometries of Faults B, D, E, G, I and K (a) and SW – NE line showing the cross sectional geometries of Faults F, H, J, L and M (b) . Vertical scale is in seconds two way travel time and horizontal scale is in kilometres.

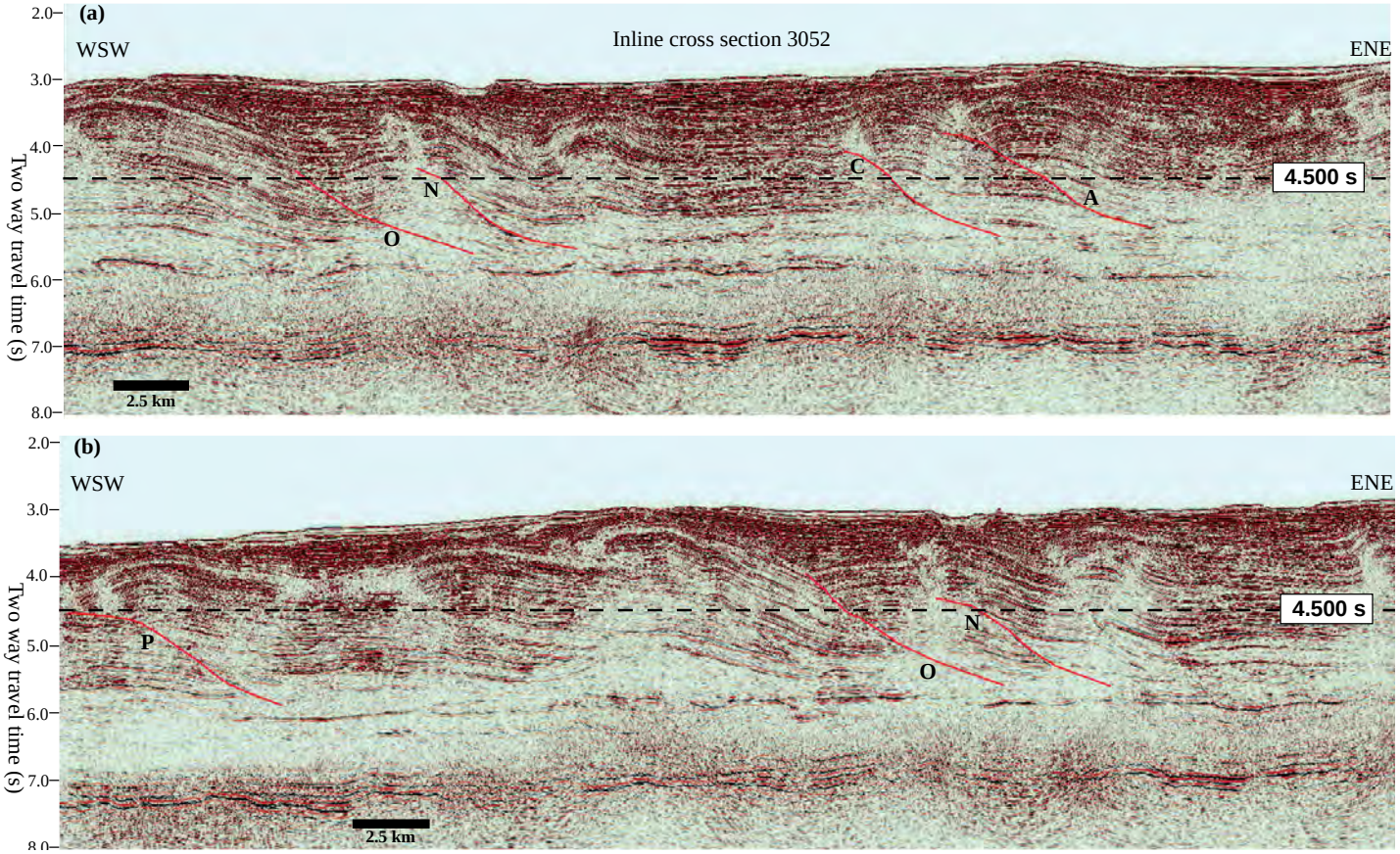

Figure 5.11: Interpreted WSW – ENE seismic lines showing lines showing the cross sectional geometries of Faults A, C, N and O (a) and Fault P (b). Vertical scale is in seconds two way travel time and horizontal scale is in kilometres.

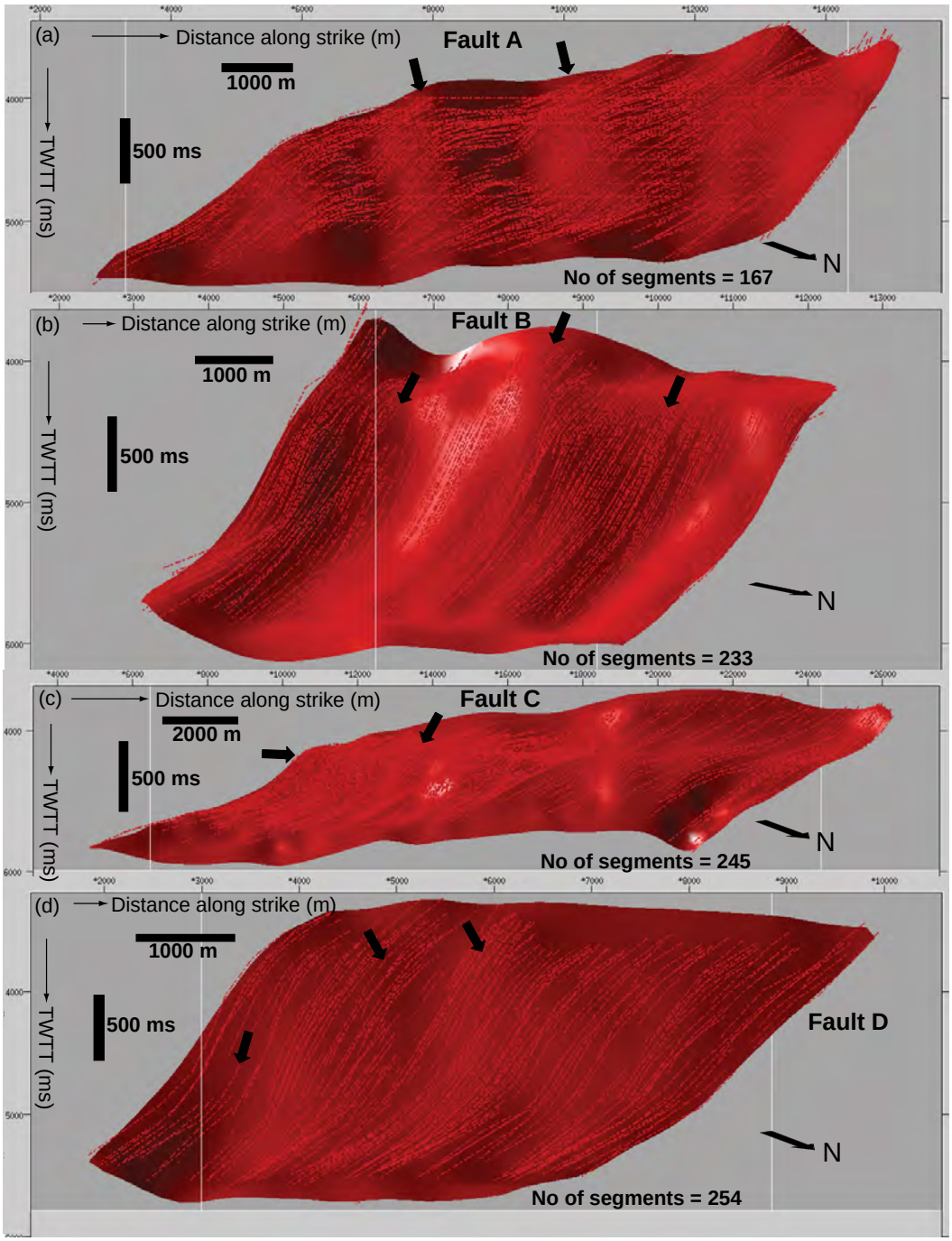

Figure 5.12: Strike views looking SW of illuminated surface models of Faults A to D with fault traces mapped from central JDZ seismic data (dashed red lines). Note the variable pattern of surface topography highlighted by the illumination in all the surface models. The block black arrows show regions of pronounced undulations on the surfaces. Vertical scale is in milliseconds two way travel time and horizontal scale is in meters. Vertical exaggeration is ~1.6.

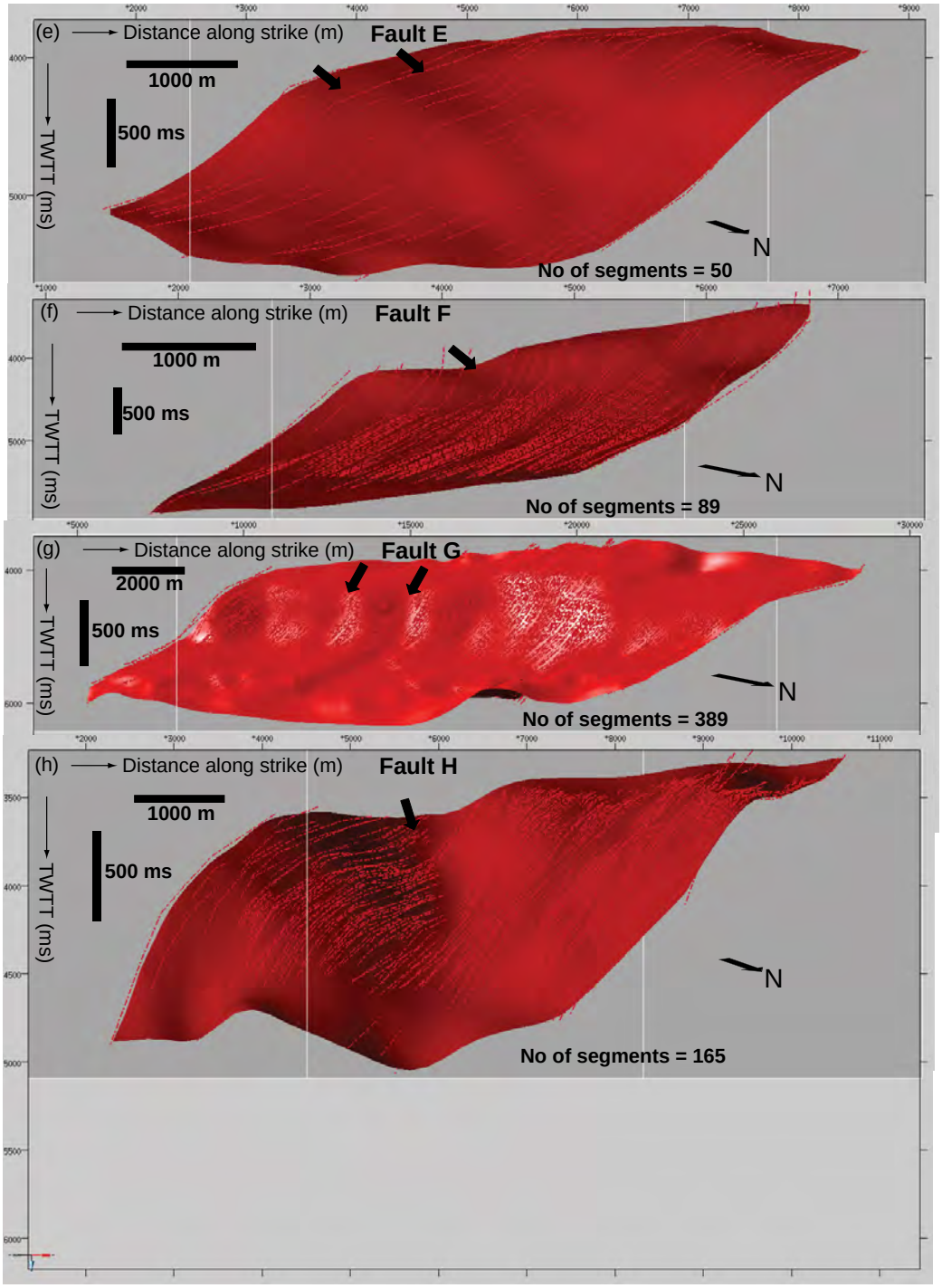

Figure 5.13: Strike view looking SW of illuminated surface models of Faults E to H with fault traces mapped from central JDZ seismic data (dashed red lines). Note the variable pattern of surface topography highlighted by the illumination in all the surface models. The block black arrows show regions of pronounced undulations on the surfaces. Vertical scale is in milliseconds two way travel time and horizontal scale is in meters. Vertical exaggeration is ~1.6.

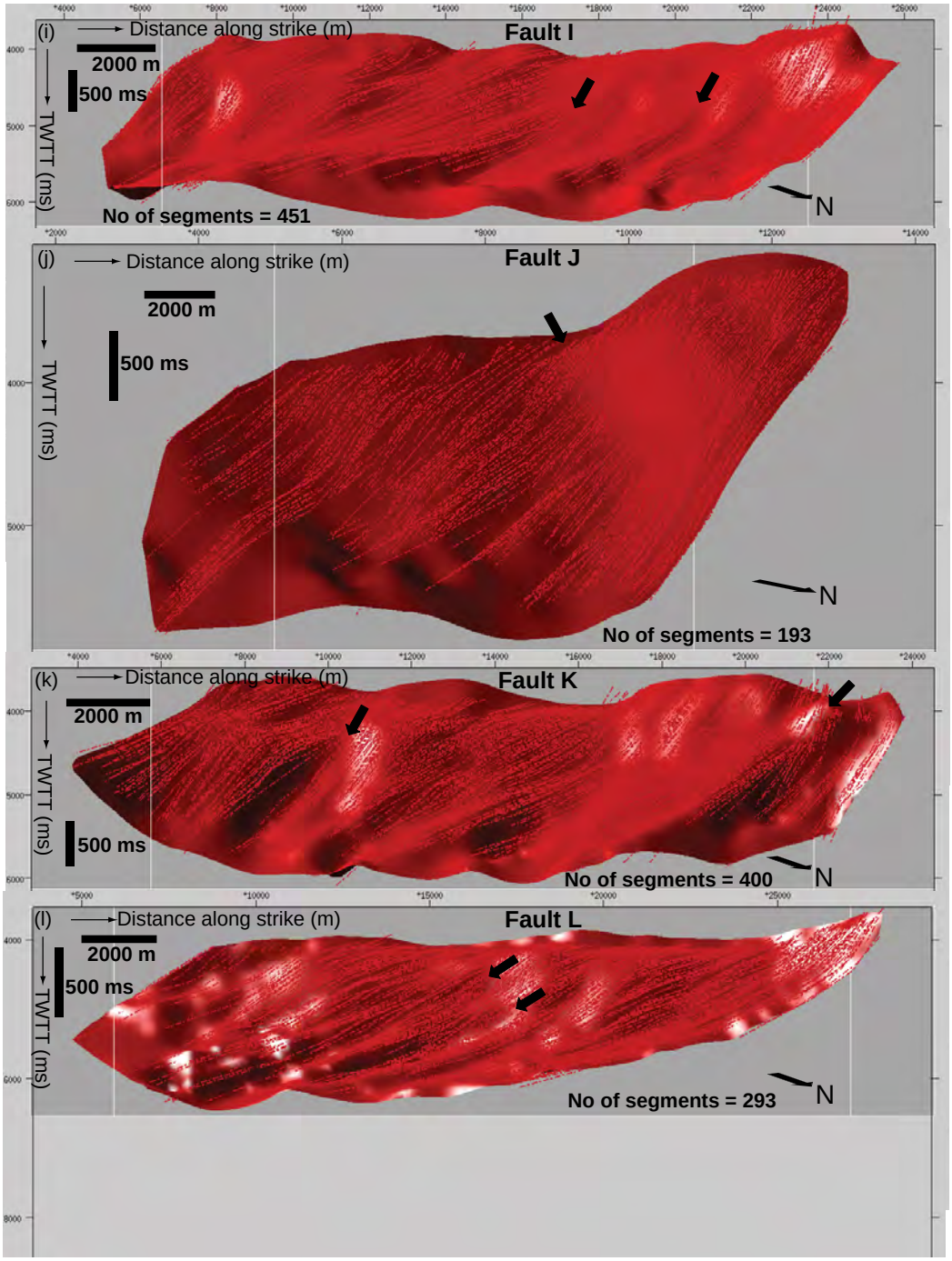

Figure 5.14: Strike view looking SW of illuminated surface models of Faults I to L with fault traces mapped from central JDZ seismic data (dashed red lines). Note the variable pattern of surface topography highlighted by the illumination in all the surface models. The block black arrows show regions of pronounced undulations on the surfaces. However, fault J appears to be fairly planar except for a region of abrupt change in surface topography indicated by the block black arrow. Vertical scale is in milliseconds two way travel time and horizontal scale is in meters. Vertical exaggeration is ~1.6.

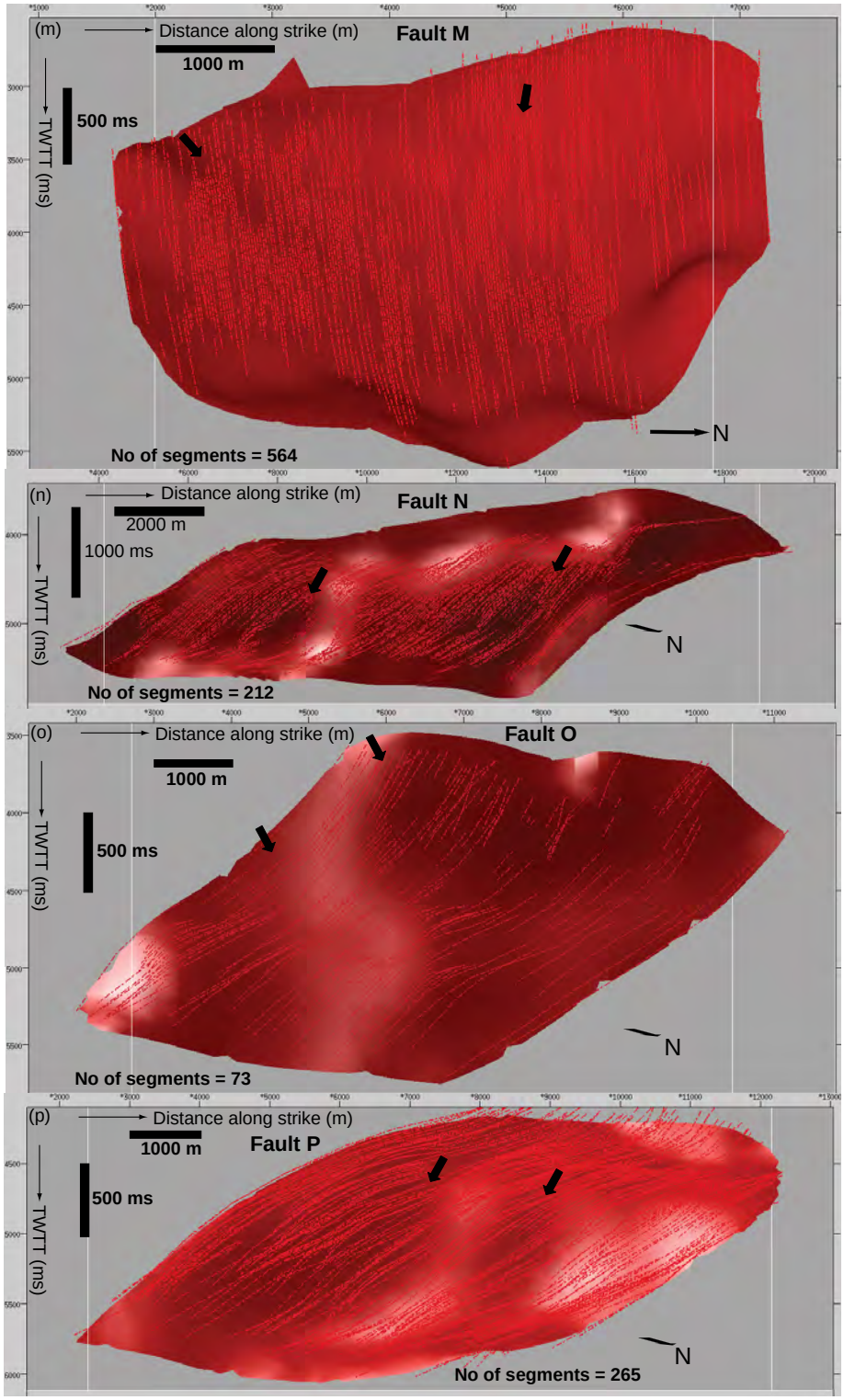

Figure 5.15: Strike view looking SW of illuminated surface models of Faults M to P with fault traces mapped from central JDZ seismic data (dashed red lines). The faults were mapped from the western parts of the study area. Note the variable pattern of surface topography highlighted by the illumination in all the surface models. The block black arrows show regions of pronounced undulations on the surfaces. Vertical scale is in milliseconds two way travel time and horizontal scale is in meters. Vertical exaggeration is ~1.6.

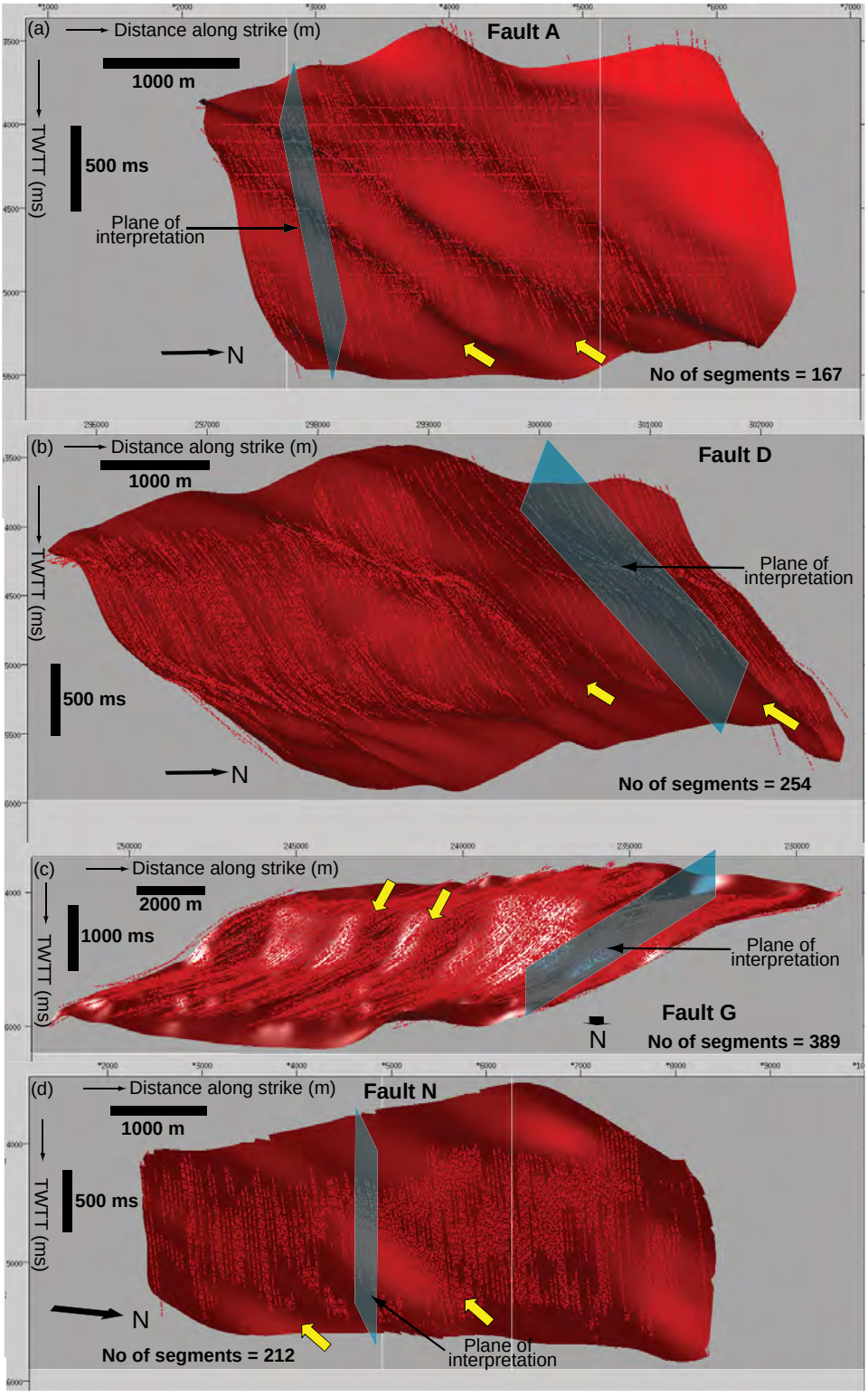

Figure 5.16: Strike view of illuminated surface models of Faults A, D, G and N respectively. The dashed red lines show the location of the interpreted fault traces while the blue rectangle represents the plane of interpretation. The block yellow arrows highlight corrugations picked by the illumination that are independent of the fault interpretation plane (illumination is from the left). Vertical scale is in milliseconds two way travel time and horizontal scale is in metres. Vertical scale is in milliseconds two way travel time and horizontal scale is in meters. Vertical exaggeration is ~1.6.

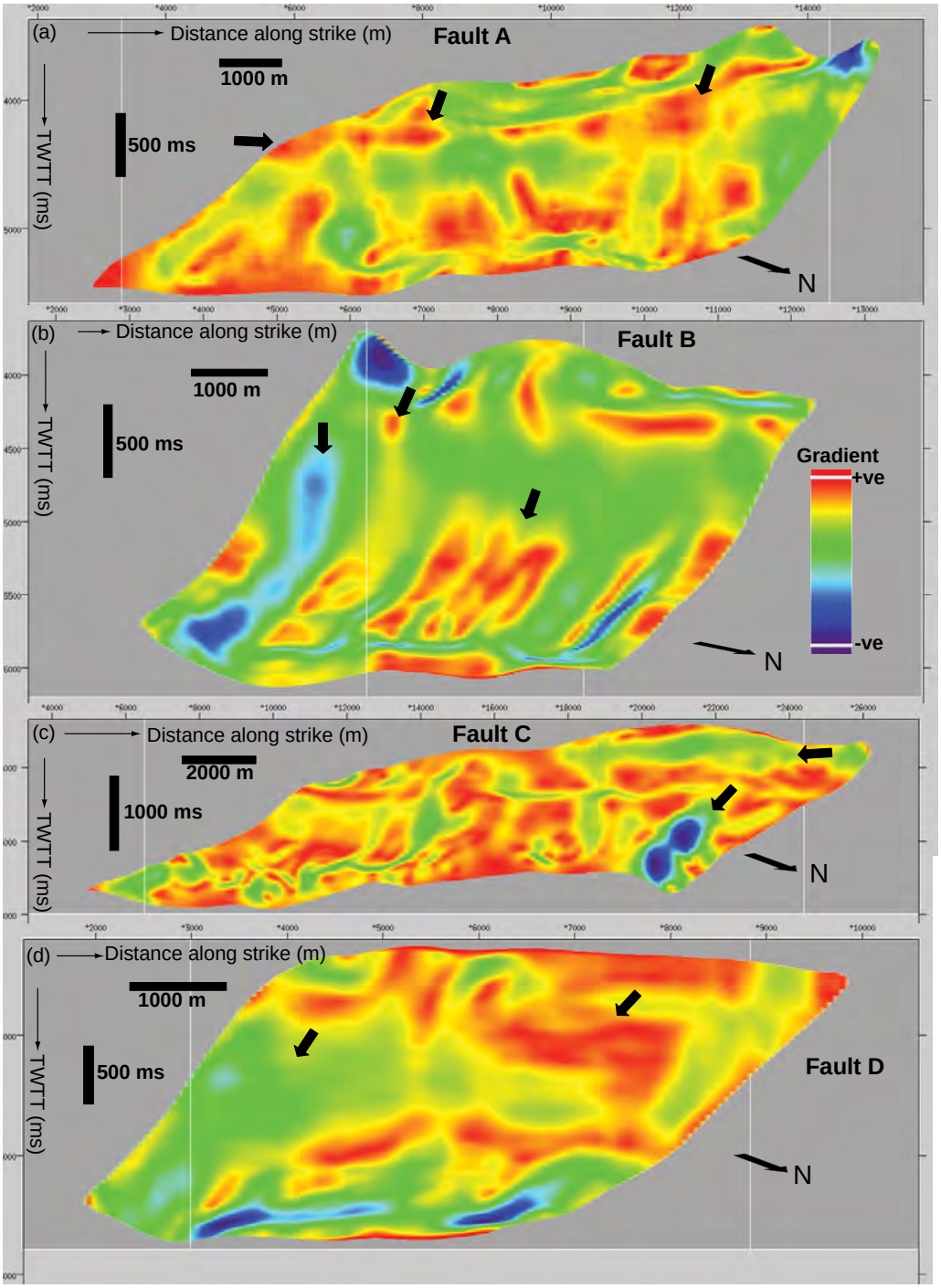

Figure 5.17: Surface gradient plots of Faults A to D. The block black arrows highlight regions of anomalous/change in pattern of surface gradient. Vertical scale is in milliseconds two way travel time and horizontal scale is in meters. Vertical exaggeration is ~1.6.

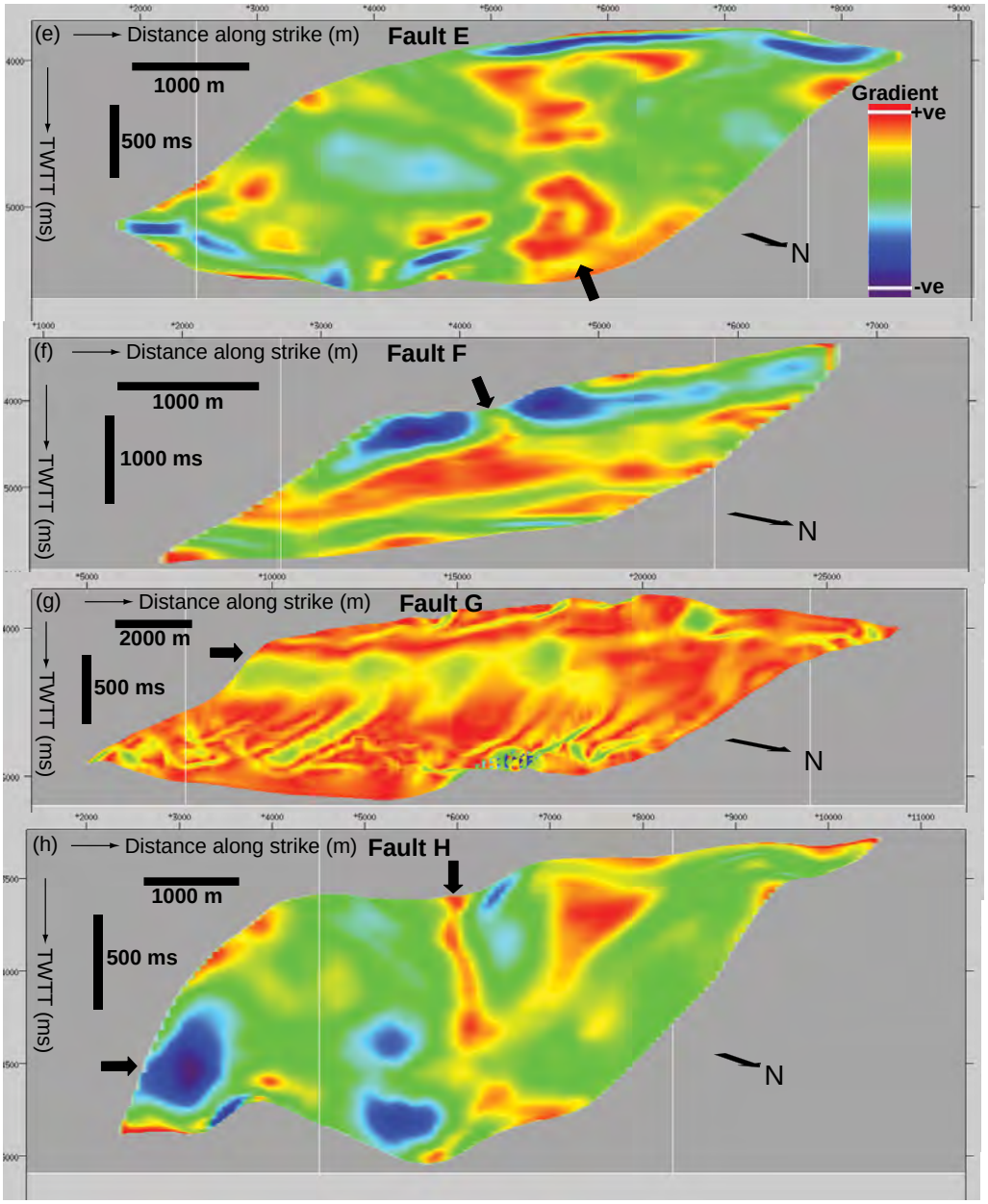

Figure 5.18: Surface gradient plots of Faults E to H. The block black arrows highlight regions of anomalous/change in pattern of surface gradient. Vertical scale is in milliseconds two way travel time and horizontal scale is in meters. Vertical exaggeration is ~1.6.

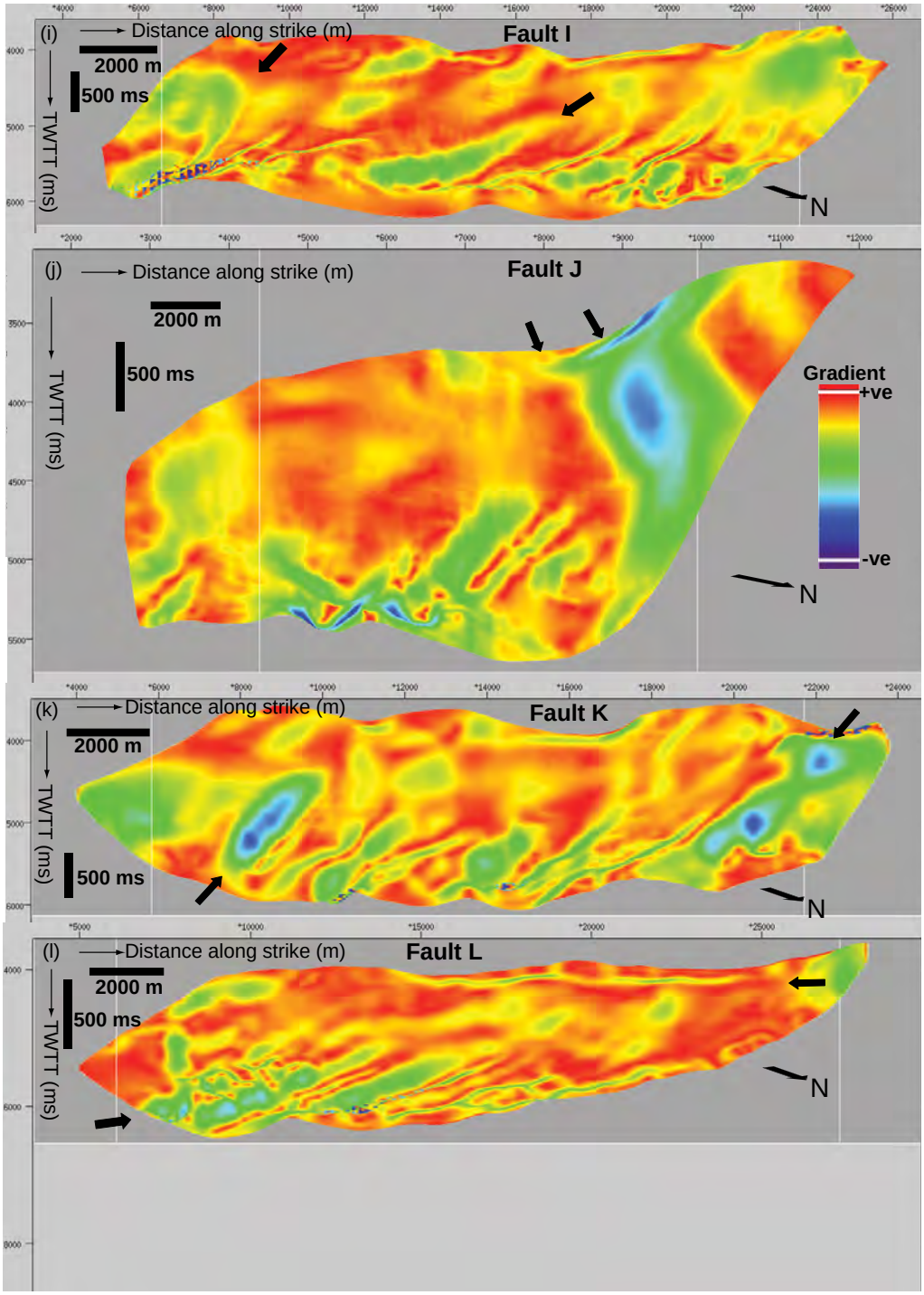

Figure 5.19: Surface gradient plots of Faults I to L. The block black arrows highlight regions of anomalous/change in pattern of surface gradient. Vertical scale is in milliseconds two way travel time and horizontal scale is in meters. Vertical exaggeration is ~1.6.

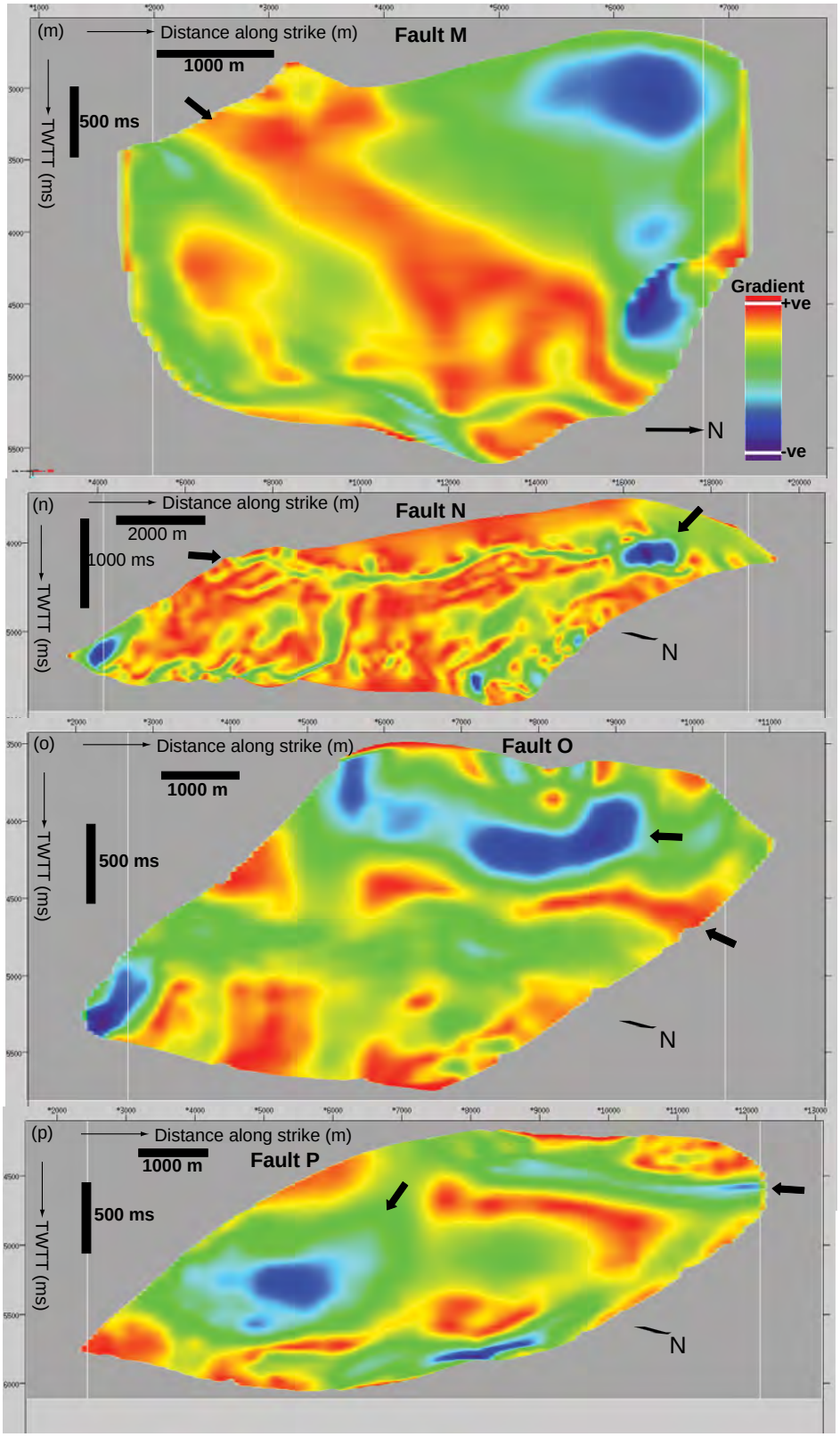

Figure 5.20: Surface gradient plots of Faults M to P. The block black arrows highlight regions of anomalous/change in pattern of surface gradient. Vertical scale is in milliseconds two way travel time and horizontal scale is in meters. Vertical exaggeration is ~1.6.

5.3.3 Maximum curvature (k_{max})

The maximum curvature plots of the sixteen thrust faults modelled at a surface grid size of 200 m and curvature sampling resolution of 100 m are presented in Figures 5.21 to 5.24. This implies that surface features with at least four times the width of the individual fault traces interpolated to produce the surface models can be visualized (Nyquist, 1828). The plots show that all the faults are corrugated, and corrugations are exhibited as semi-linear antiforms (negative maximum curvature) and synforms (positive maximum curvature) that in places bifurcate along the axes and separated by discrete zones of relatively planar geometries. Table 5.2 is a summary of measurements of fault surface topographic features. The antiforms and synforms are displayed as narrow to broad ridges and grooves with lengths of between 1 km and 2 km, widths of between 0.3 km and up to 2 km with a maximum curvature range of -0.0006 to +0.001 at the scale of the selected curvature sampling resolution. The maximum curvature plots highlight variation in the orientation of the corrugation profile plane with the overall continuity of the corrugations characterized by bumps and depressions.

Typical corrugation wavelengths range from 0.5 km and up to 2.6 km based on peak to peak measurements with amplitudes of between 0.05 km and 0.8 km (Figure 5.25) and appears to be broader in the upper parts of most of the plots but become narrower with depth. Plots of average corrugation wavelengths versus amplitude shows two contrasting pattern of relationships (Figure 5.26). Generally corrugation amplitudes increase with increasing wavelength for some of the faults. This interpretation is consistent with previous analysis of similar relationships in outcrop and normal faults mapped from seismic data (Wright, 2008; John, 1987). The corrugations observed on

the thrust faults can be described as short to long-wavelength at the scale of observation. The majority of the plots show that the faults exhibit horizontal/cross corrugations perpendicular to the main down-plunging corrugation axes. These structures are major sources of curvature in most of the faults analyzed (Figures 5.27 & 5.28). Horizontal corrugations are interpreted to be related to fault-bends and are a common feature of thrust faults in deepwater Niger Delta fold and thrust belts. The mechanics of fault bends in deepwater Niger Delta thrust faults is described in Corredor *et al*. (2005) and Bilotti *et al*. (2004).

An addition source of curvature at the toe of a few of the faults is observed and may be related to detachment surfaces that most of the faults sole into (Figure 5.29). The overall pattern and orientation of the corrugations is fairly uniform in all the thrust fault surfaces except for a few of the faults mapped from the western part of the study area that appear not to have a well defined pattern of down-plunging main corrugation axes compared with faults in the central parts of the study area. Slices of volume seismic amplitude sampled parallel to and in the vicinity of some of the faults in the hanging and footwall suggest the continuity of the corrugations in spite of the layered sedimentary succession implying that corrugations development in the study area may not be related to mechanical stratigraphy of the faulted wall rock (Figure 5.29, 5.30 and 5.31). Normalized frequency histograms show that the plots have predominantly positive curvature at the sampled curvature resolution (Figure 5.32).

Within the limits of seismic resolution and at the scale of observation, no slip indicators have been mapped on the corrugations. However, previous analysis of non reactivated fault surfaces in outcrop and seismic data suggests that corrugations are parallel to recent slip directions with a good correlation between axis of corrugation

plunge with fault dip (e.g. Kokkalas *et al*. 2003: van Gent *et al*. 2010; Lohr *et al*. 2008; Sagy *et al*. 2007; Resor & Meer, 2009; Jones *et al*. 2009; Candela *et al*. 2009; Neetham *et al*. 1996; Lohr, 2008; Sagy *et al*. 2007; Carena & Suppe, 2002).

Therefore, the corrugations observed on the thrust fault planes are presumed to be oriented sub-parallel to the southwest regional transport direction in the Niger Delta (Figures 5.33 & 5.34) and are similar to corrugations mapped in previous analysis of fault surface geometry in field outcrop and seismic data from different tectonic settings (e.g. Wright, 2008; Brown & Scholtz, 1985a; Power *et al*. 1997; Lee & Bruhn, 1996; Renard *et al*. 2006; Sagy *et al*. 2007; Lohr *et al*. 2008; Lohr, 2007; Streit & Hillis, 2004; Marchal *et al*. 2003; Needtham *et al*, 2006; Kokkalas *et al*. 2007; Candela *et al*. 2009; Jones *et al*. 2008; Carena & Suppe, 2002). However, in Chapter Six, a demonstration of how indirect evidence of slip direction can be predicted using volume seismic attribute data sampled adjacent to some of the faults is illustrated.

Fault	Corrugation length (km)	Corrugation width (km)	Corrugation wavelength (km)	Corrugation amplitude (km)	Average wavelength/ amplitude ratio
A	1	~1	1 – 2	0.2 – 0.4	5:1
B	1.8	0.5 – 2	0.7 – 2	0.3 – 0.4	4:1
C	1.5	0.5 – 2	1.2– 1.5	0.4 – 0.5	3:1
D	1	0.5 – 1	~2	0.1 – 0.2	13:1
G	1	0.3 – 2	1.5 – 2	0.2 – 0.5	5:1
H	1	0.5 – 1	~2	0.3 – 0.4	6:1
I	1 – 2	0.5 – 1.2	2 – 4	0.1 – 0.2	20:1
J	1.2	1.2 – 2	2.4 – 2.6	0.05 – 0.3	14:1
K	1.2 – 1.7	0.5 – 1.2	1.5 – 2.5	0.2 – 0.8	4:1
L	1.5 – 1.8	0.5 – 1	0.8 – 2.4	0.1 – 0.3	8:1
M	1 – 2	0.3 – 1	0.5 – 1.5	0.1 – 0.3	5:1
N	1	0.7 – 1.2	1.5 – 2.5	0.05 – 0.3	11:1

Table 5.2: Summary of corrugation dimensions measurements for twelve faults mapped in the central and western parts of the study area.

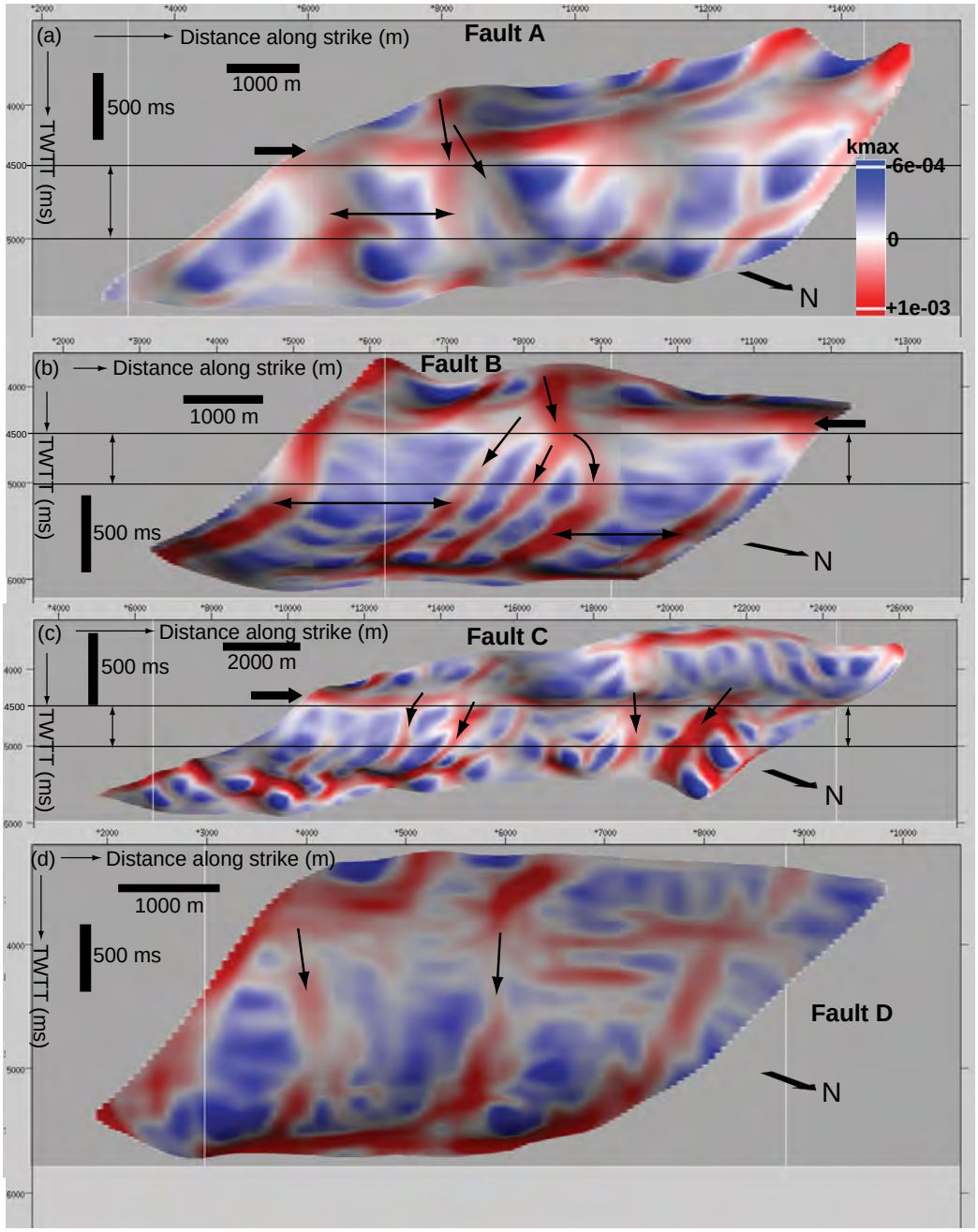

Figure 5.21: Strike views looking SW of surface maximum curvature plots of Faults A to D. Note the parallel to sub-parallel orientation of corrugations highlighted by the attribute (block black arrows). Note also the convergence and divergence of corrugations (block green arrows). The horizontal lines in Faults A to C represent the interval sampled to demonstrate the pattern of corrugation amplitudes in Figure 5.25. Vertical scale is in milliseconds two way travel time and horizontal scale is in meters. Vertical exaggeration is ~1.6.

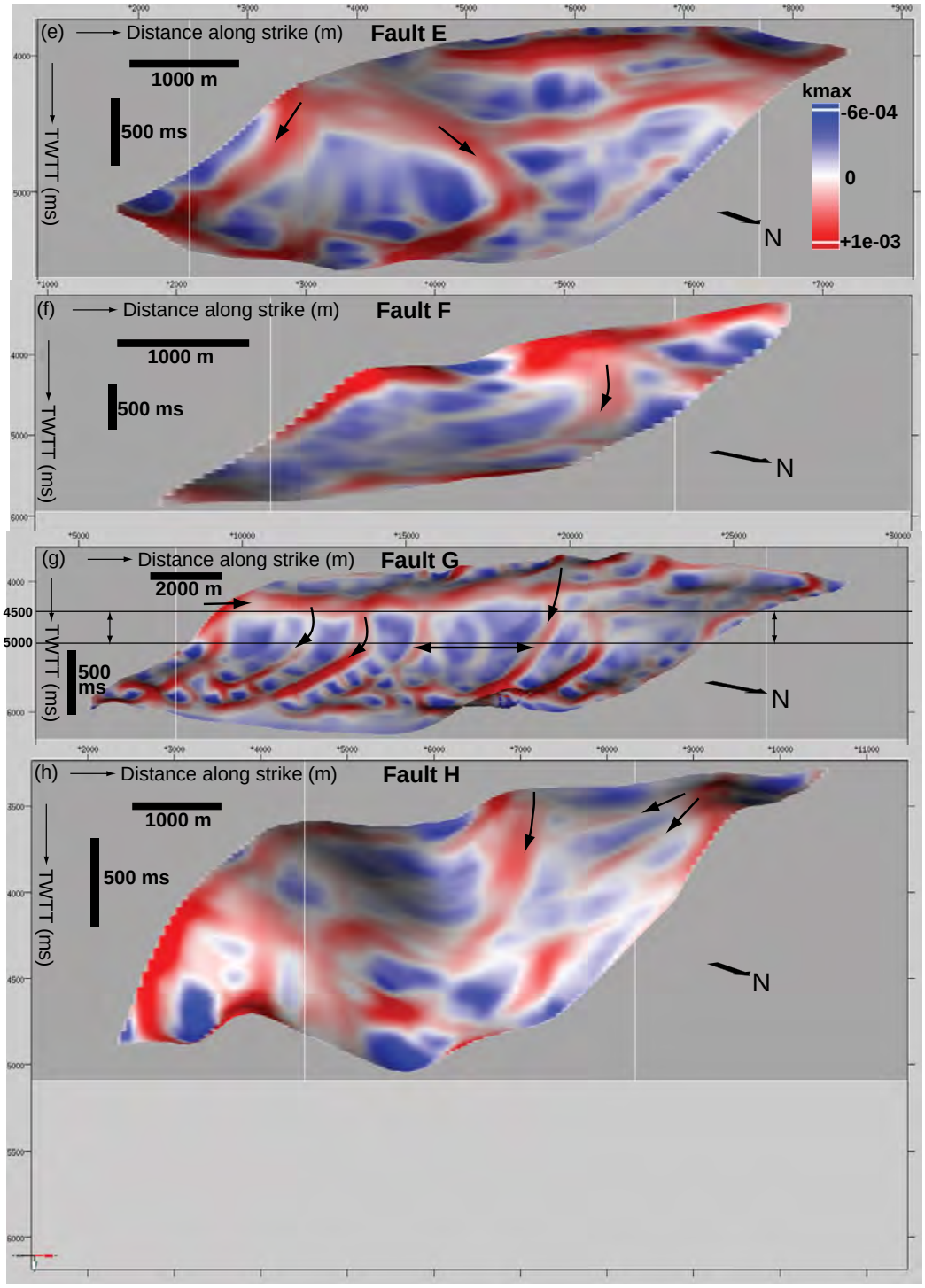

Figure 5.22: Strike views looking SW of surface maximum curvature plots of Faults E to H. Note the sub-parallel orientation of corrugations highlighted by the attribute especially in Faults E and G. Vertical scale is in milliseconds two way travel time and horizontal scale is in meters. The horizontal lines in Faults G represent the interval sampled to demonstrate the pattern and dimensions of corrugation amplitudes in Figure 5.25. Vertical exaggeration is ~1.6.

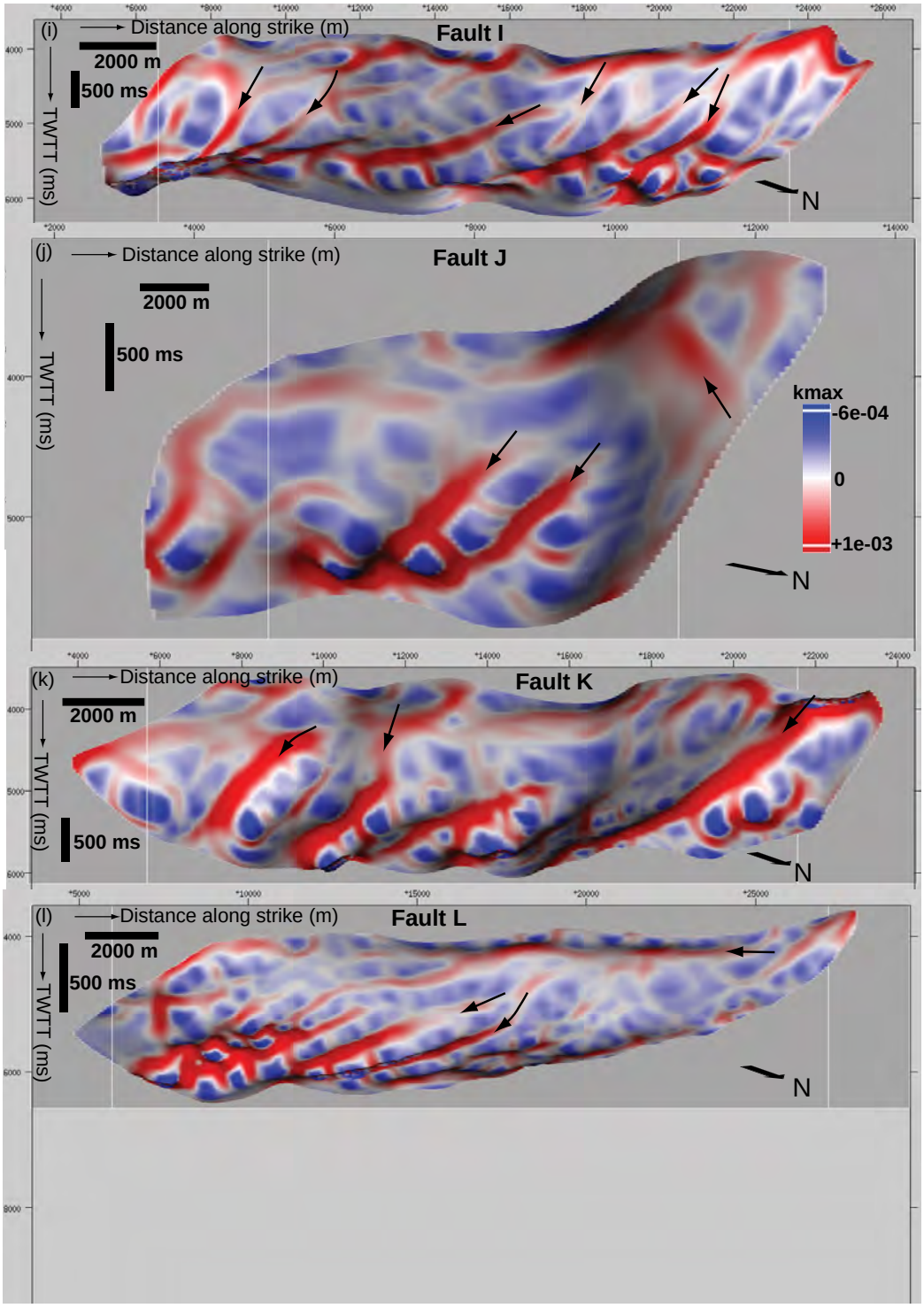

Figure 5.23: Strike views looking SW of surface maximum curvature plots of Faults I to L. Note the sub-parallel orientation of corrugations highlighted by the attribute. Note the divergence of corrugations in Faults I and L. Vertical scale is in milliseconds two way travel time and horizontal scale is in meters. Vertical exaggeration is ~1.6.

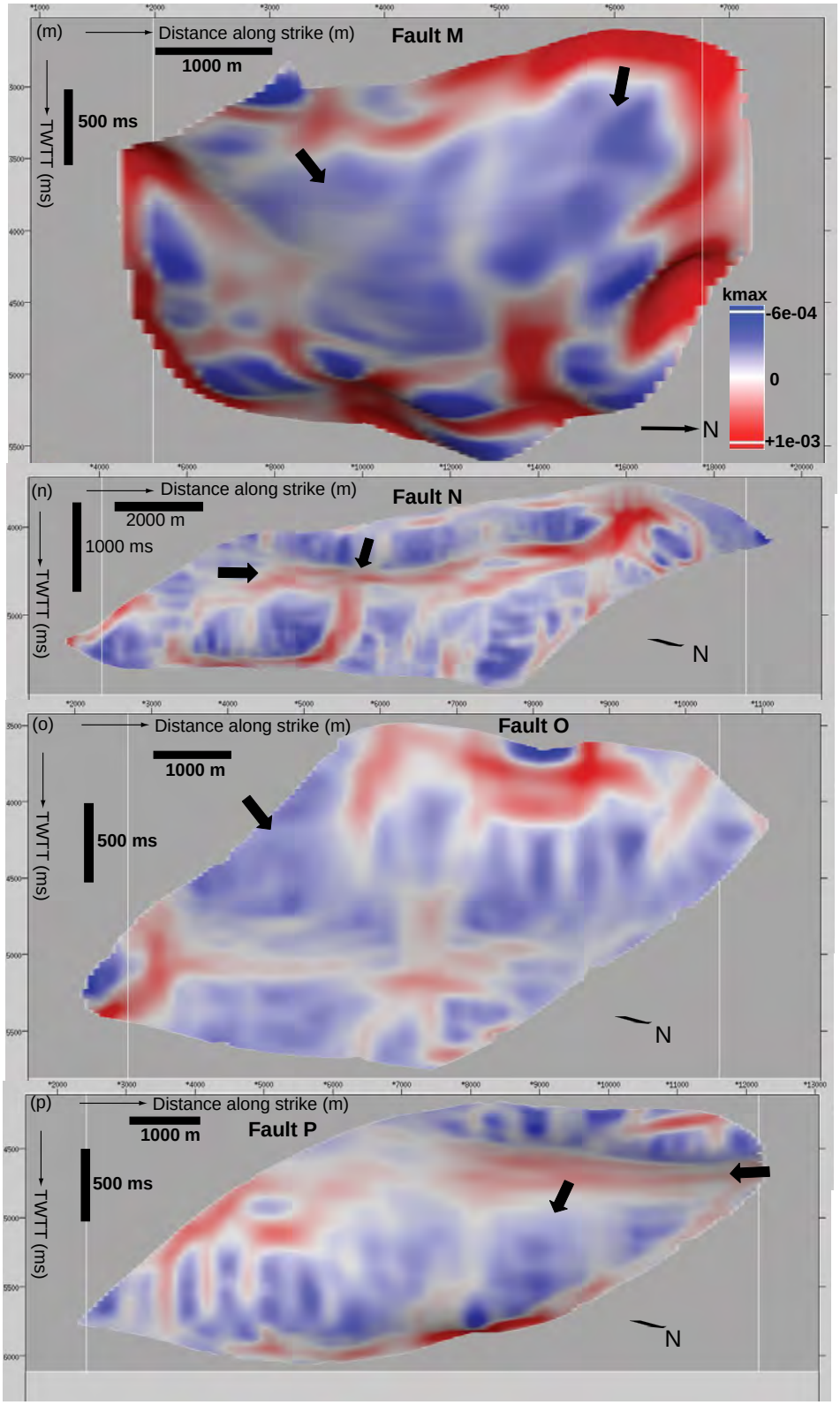

Figure 5.24: Strike views looking SW of surface maximum curvature plots of Faults I to L. With the exception of Fault N, the pattern of corrugation is not as well defined as in the curvature plots of faults mapped in central JDZ. Vertical scale is in milliseconds two way travel time and horizontal scale is in meters. Vertical exaggeration is ~1.6.

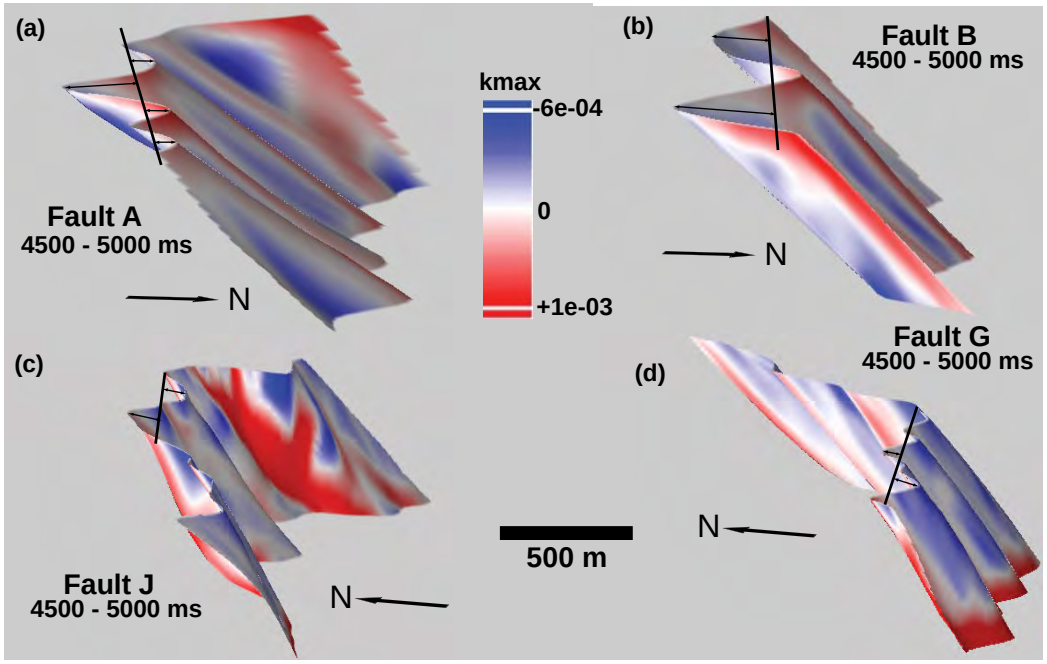

Figure 5.25: Perspective views of the surface maximum curvature plots of Faults A, C, F and G showing the pattern of corrugation and amplitude. The corrugations have amplitudes of up to 500 m. Vertical exaggeration is ~1.6.

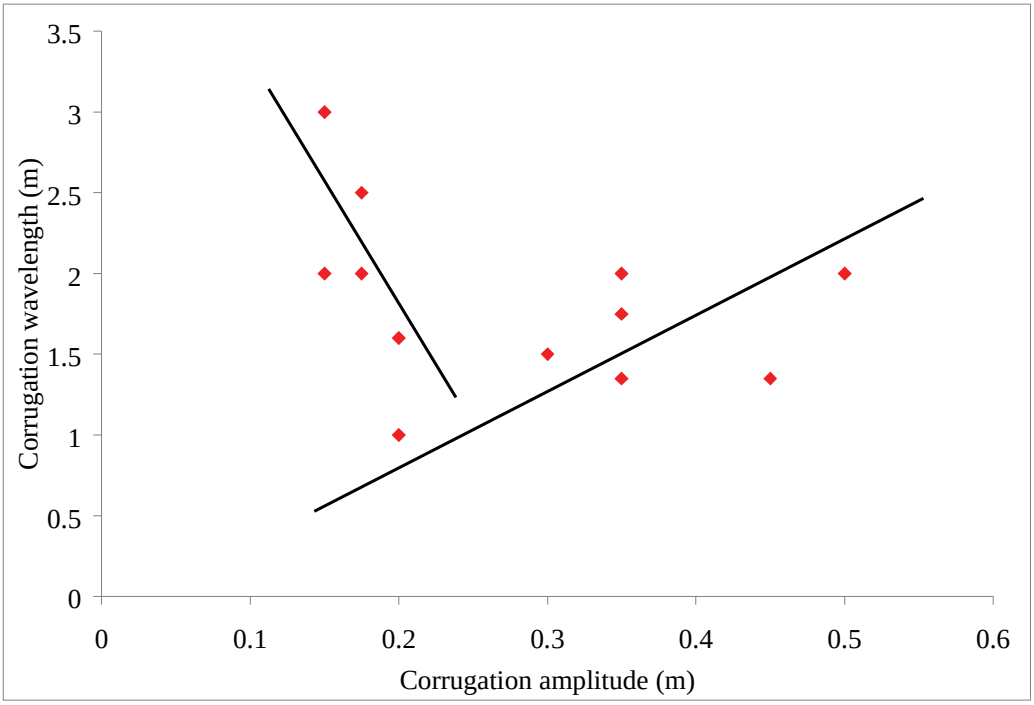

Figure 5.26: Plot of average corrugation wavelength versus amplitude of twelve faults. Note two contrasting patterns of linear relationship between wavelength and amplitude.

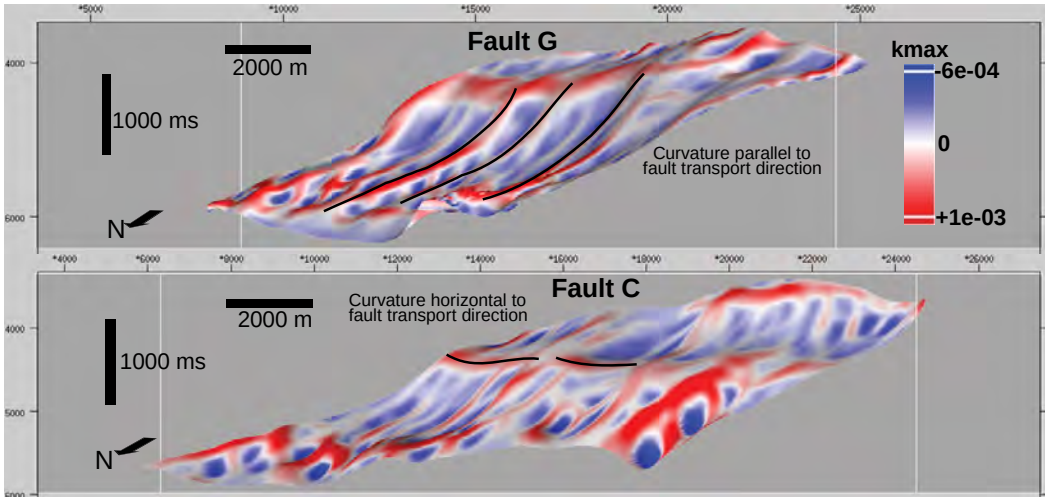

Figure 5.27: Perspective views of surface maximum curvature plots of Faults C and G illustrating vertical and horizontal patterns of corrugations. Vertical exaggeration is ~1.6.

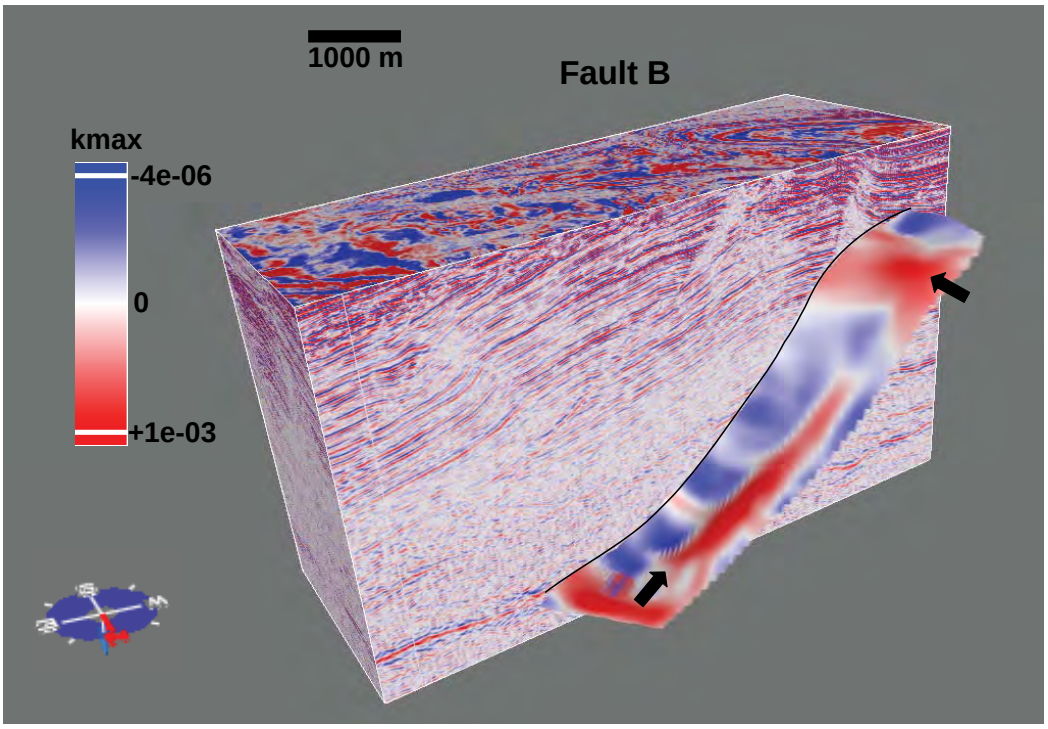

Figure 5.28: Perspective view of Fault B illustrating relationship between the pattern of corrugation and reflectivity of the hanging wall volume (block arrows).

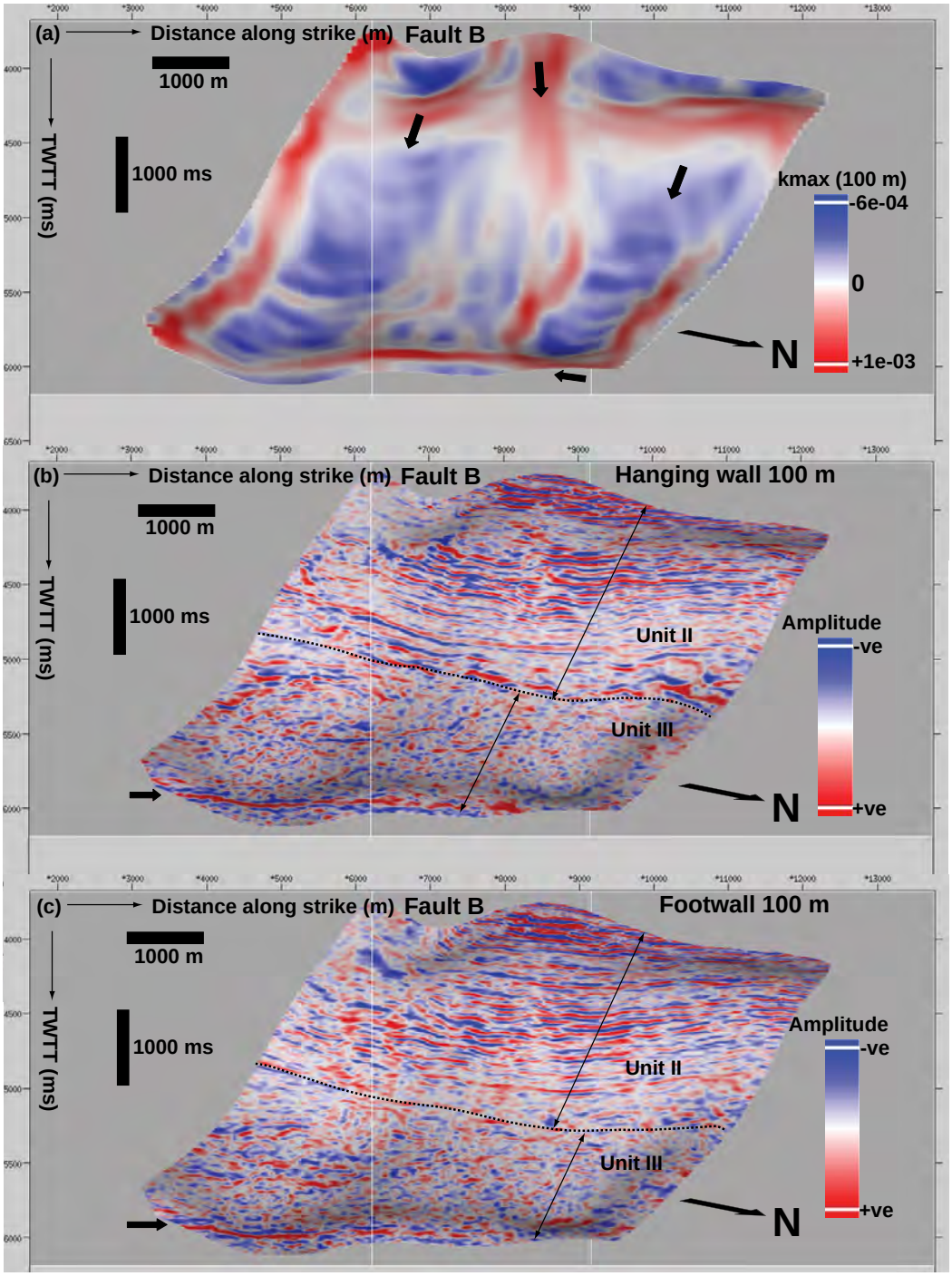

Figure 5.29: Strike view of maximum curvature plot of Fault B (a) and slices of seismic amplitude data in the hanging wall and footwall 100m parallel to the fault. Note the pattern of corrugation in the curvature plot and two contrasting patterns of reflectivity that may be related to lithology in the hanging wall and footwall of the fault. Mechanical stratigraphy does not appear to affect the down plunge continuity of the corrugations. The block arrows highlight a form of corrugation that may be related to detachment surfaces. Vertical scale is in milliseconds two way travel time and horizontal scale is in meters. Vertical exaggeration is ~1.6.

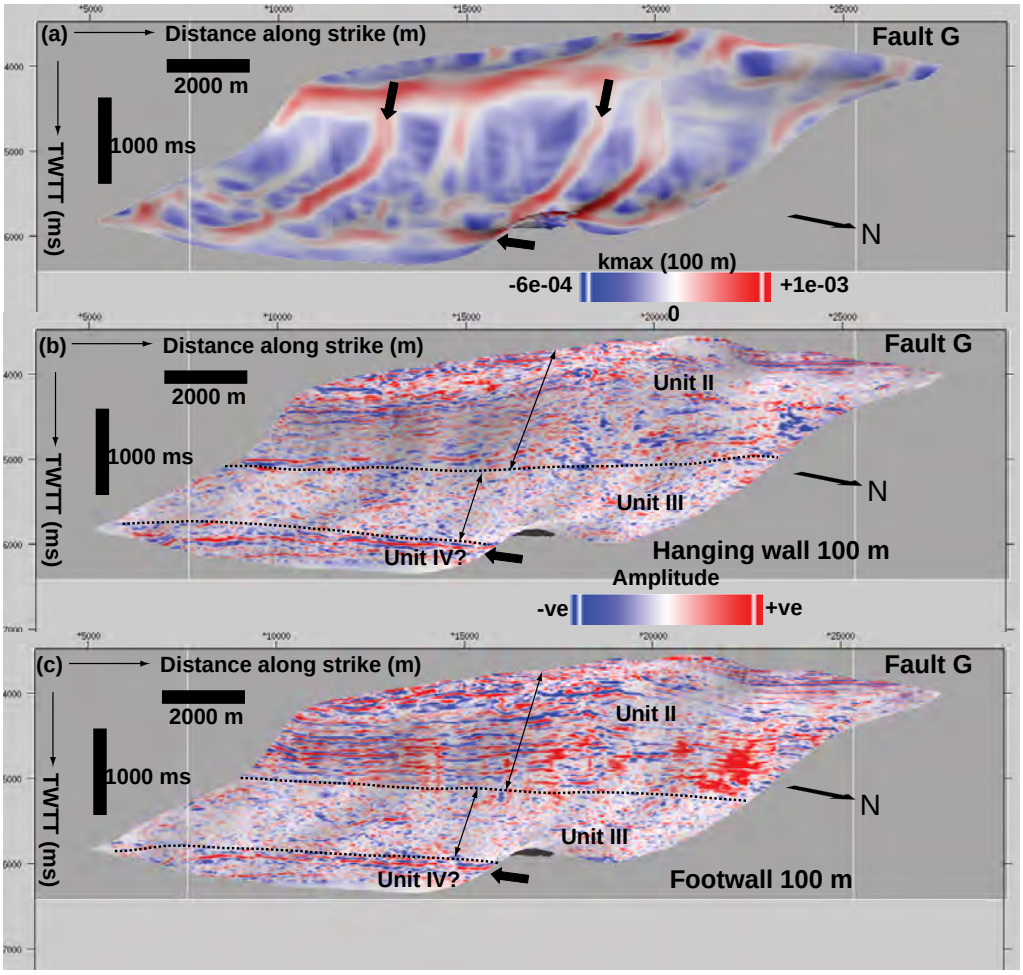

Figure 5.30: Strike view of maximum curvature plot of Fault B (a) and slices of seismic amplitude data in the hanging wall and footwall 100m parallel to the fault. Note the pattern of corrugation in the curvature plot and two contrasting patterns of reflectivity that may be related to lithology in the hanging wall and footwall of the fault. Mechanical stratigraphy does not appear to affect the down plunge continuity of the corrugations. The block arrows highlight a form of corrugation that may be related to detachment surfaces. Vertical scale is in milliseconds two way travel time and horizontal scale is in meters. Vertical exaggeration is ~1.6.

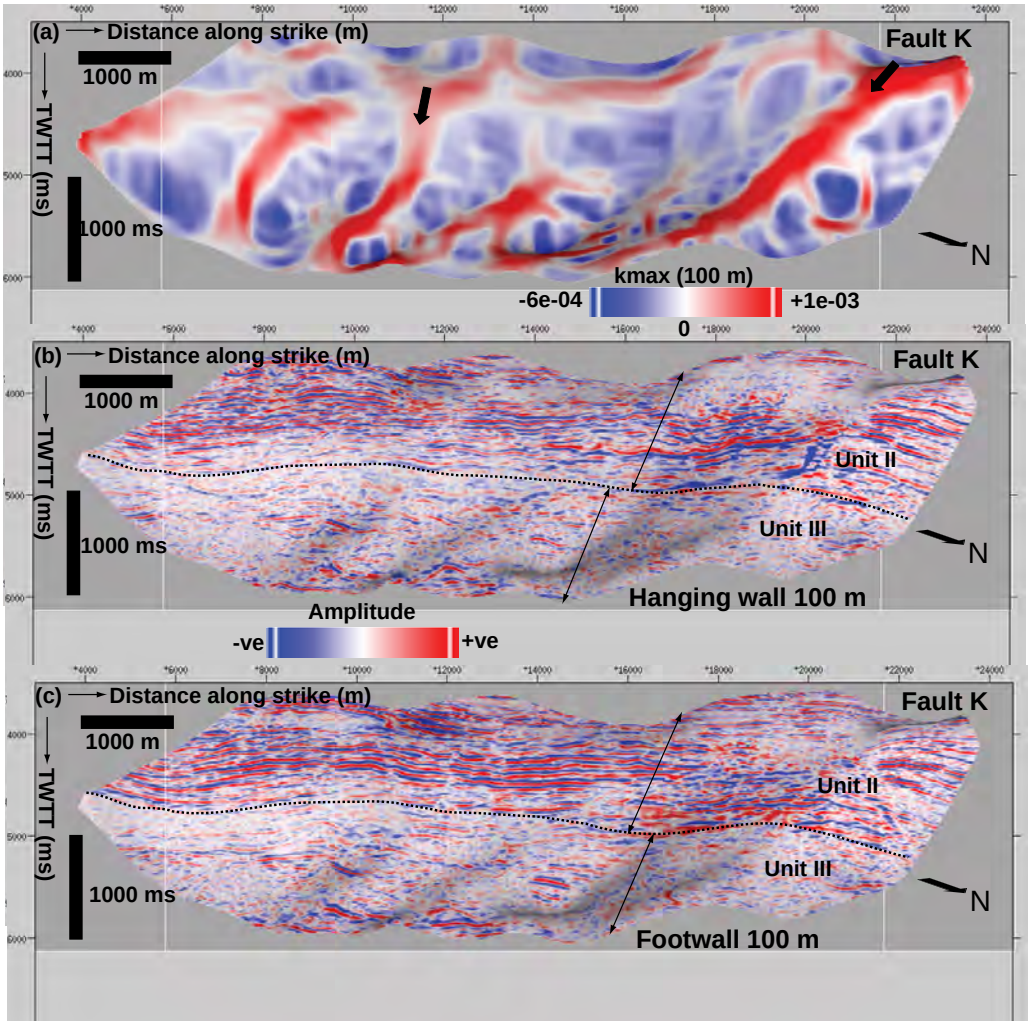

Figure 5.31: Strike view of maximum curvature plot of Fault B (a) and slices of seismic amplitude data in the hanging wall and footwall 100m parallel to the fault. Note the pattern of corrugation in the curvature plot and two contrasting patterns of reflectivity that may be related to lithology in the hanging wall and footwall of the fault. Mechanical stratigraphy does not appear to affect the down plunge continuity of the corrugations. The block arrows highlight a form of corrugation that may be related to detachment surfaces. Vertical scale is in milliseconds two way travel time and horizontal scale is in meters. Vertical exaggeration is ~1.6.

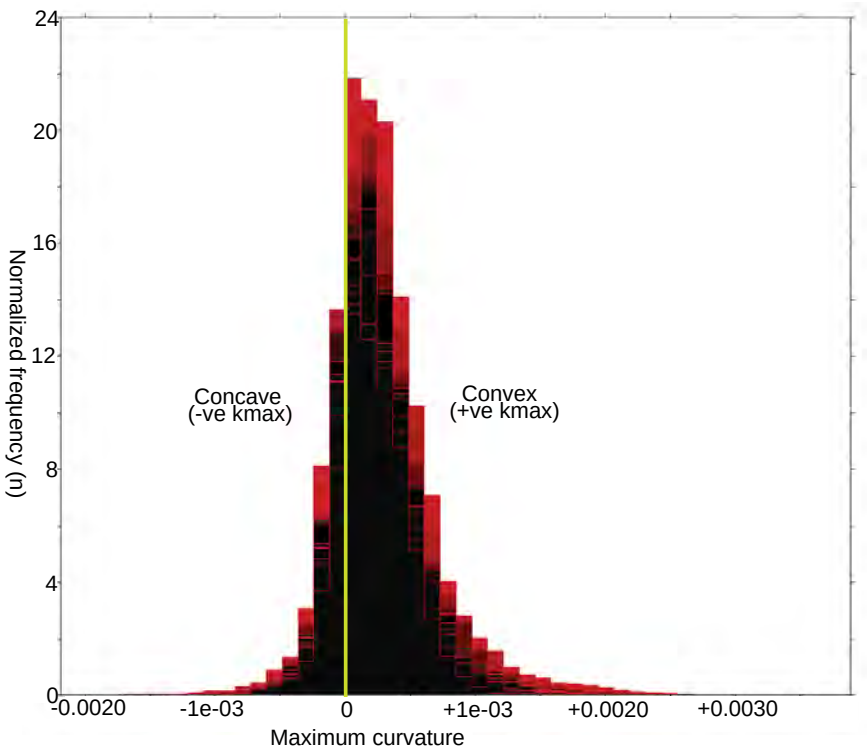

Figure 5.32: Normalized frequency histogram of the surface maximum curvature plots of Faults A to 0 illustrating the statistical distribution of maximum curvature of the faults at the scale of resolution presented in this thesis.

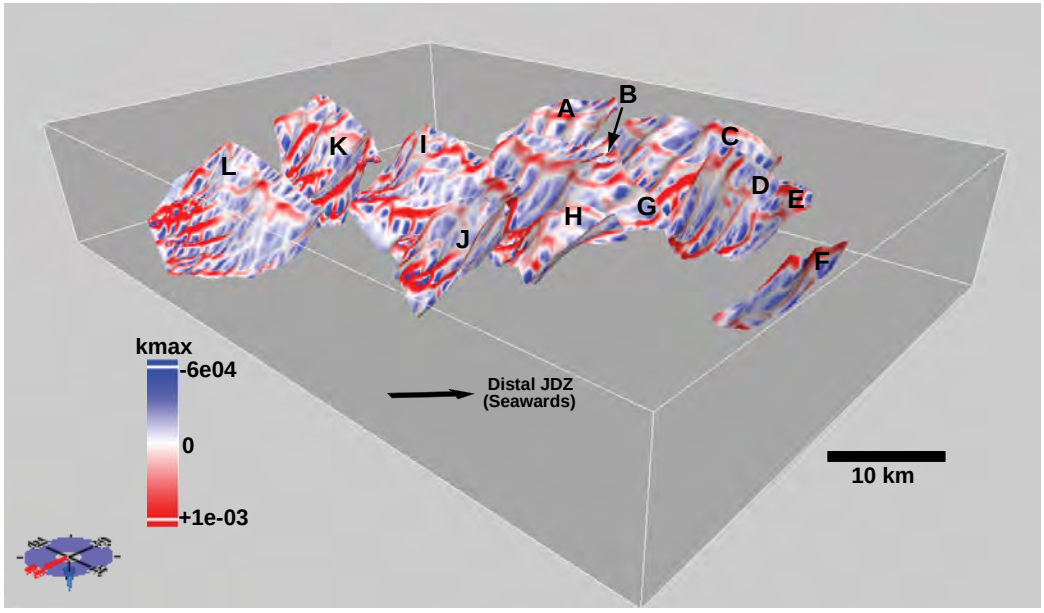

Figure 5.33: Perspective views of the surface maximum curvature plots of thrust fault planes in central JDZ illustrating the seaward orientation of corrugations. Vertical exaggeration is ~1.6.

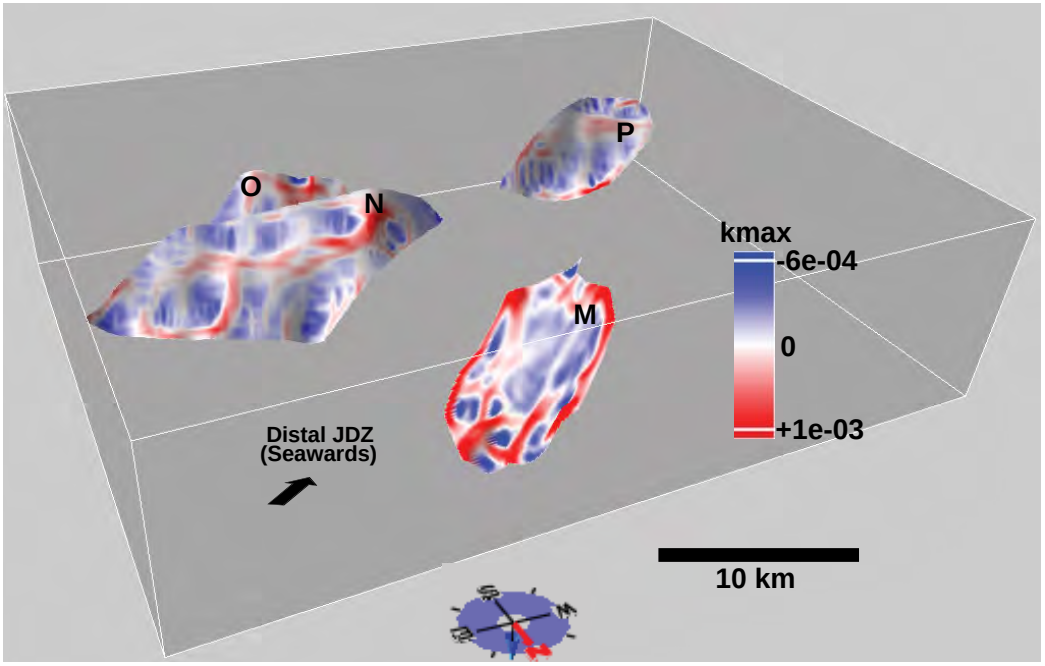

Figure 5.34: Perspective views of the surface maximum curvature plots of thrust fault planes in central JDZ illustrating the seaward orientation of corrugations. Vertical exaggeration is ~1.6.

5.3.4 Gaussian curvature (k_{Gauss})

The Gaussian curvature plots of the thrust faults modelled at a surface grid of 200 m and curvature sampling resolution of 100 m are presented in Figures 5.35 to 5.38. This implies that surface features with at least four times the width of the individual fault traces interpolated to produce the surface models can be visualized (Nyquist, 1828). The plots show that all the faults exhibit Gaussian curvature at a wide range of scales with large scale synclastic (culminations) and anticlastic (depressions) geometries typified by reversal in curvature polarity in the fault transport direction. These structures are well developed in the upper parts of the faults with fault bends in places highlighted by horizontal reversal of curvature polarity, while the bottom parts of the plots exhibit complex patterns of curvature.

Table 5.3 is a summary of dimensions of culminations and depressions mapped on the sixteen faults. Figure 5.39 is an example of the typical dimensions of culminations and depressions in four faults modelled between 4500 ms and 5000 ms where the structures are best developed. Generally, culminations have widths and lengths of 0.05 km to 2 km and 0.05 km to 0.7 km respectively. The depressions possess widths ranging from 0.05 km to 1.5 km and lengths of up to 0.6 km. Therefore it implies that the two structures have a fairly similar dimension. This is further confirmed by the combined frequency histogram of the Gaussian curvature plots of the sixteen faults in Figure 5.40 that shows a nearly identical pattern of negative and positive Gaussian curvature distribution in the sixteen faults.

In general the culminations and depressions appears to be geometrical properties of the faults (Figures 5.41 & 5.42) oriented parallel to the direction of seaward gravitational transportation and compression of deltaic sediments (Figures 5.43 & 5.44) and probably a manifestation of slip variation on the surfaces that may complicate slip along fault surfaces and potentially influence stress in the volumes adjacent to the faults (Chester & Chester, 2000; Candela *et al*. 2009). The similarity in the statistical distribution of anticlastic and synclastic curvatures implies that the faults are not perfectly cylindrical and hence fit into the class of non-developable surfaces (Lisle, 1994). Analysis of the links between the pattern of fault surface Gaussian curvature and volume structure is discussed in Chapter Six.

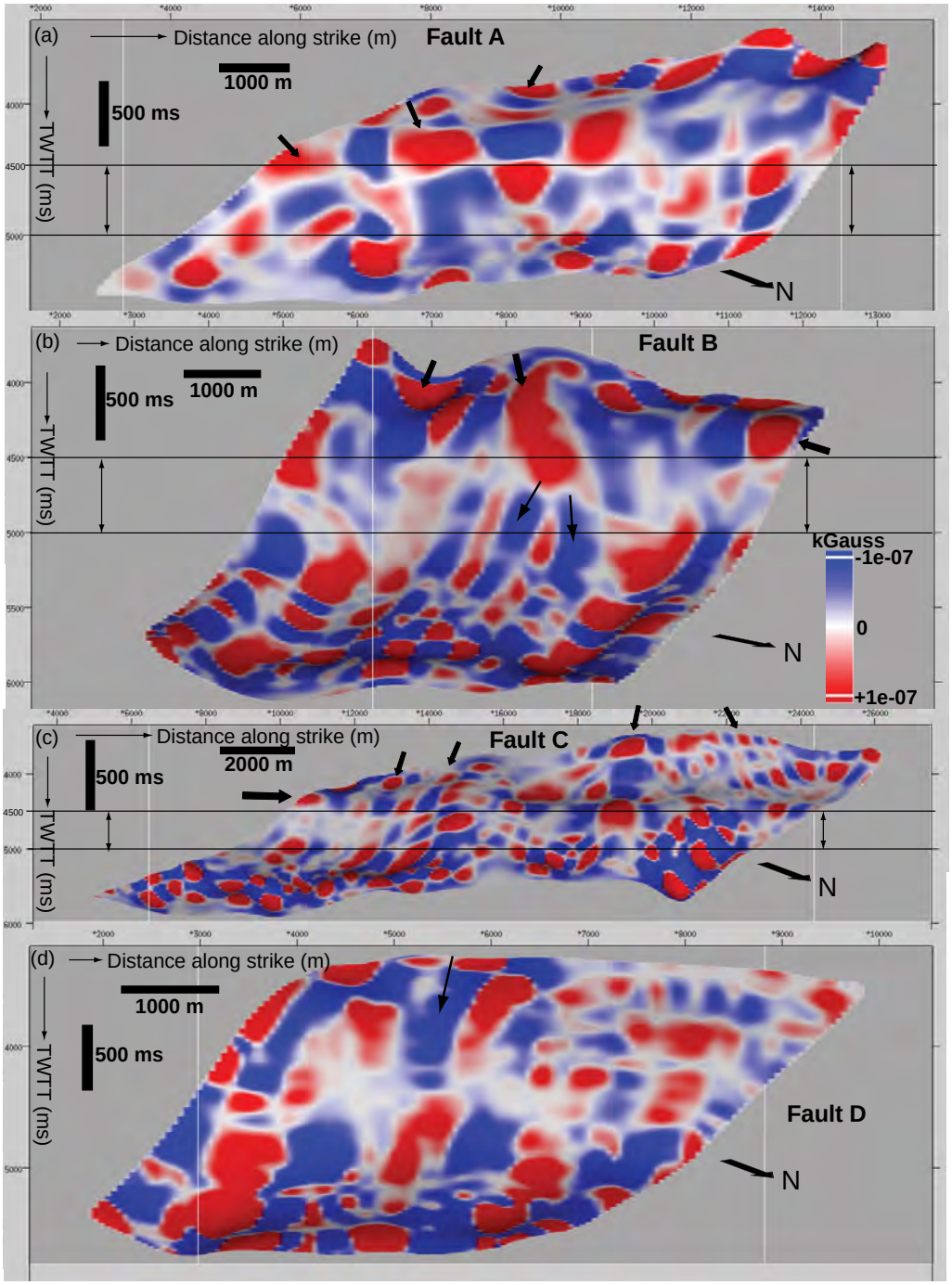

Figure 5.35: Strike views looking SW of surface Gaussian curvature plots of Faults A to D. Note the anticlastic and synclastic pattern of the corrugation axes indicated by the block black arrows. Note the random pattern of curvature in the bottom halves of the plots. The horizontal lines in Faults A to C represent the interval sampled to demonstrate the dimensions of culminations and depressions in Figure 5.39. Vertical scale is in milliseconds two way travel time and horizontal scale is in meters. Vertical exaggeration is ~1.6.

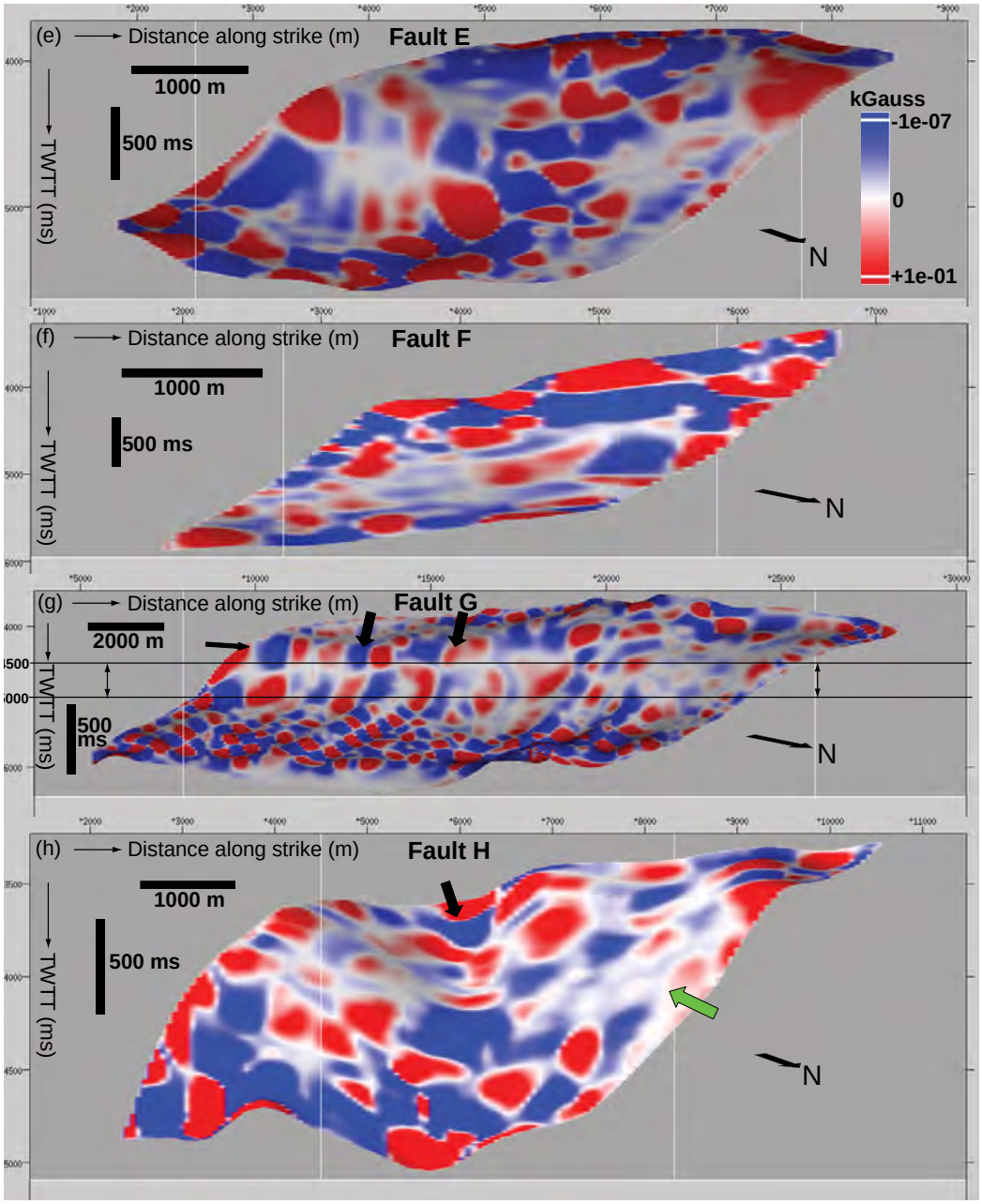

Figure 5.36: Strike views looking SW of surface Gaussian curvature plots of Faults E to H. Note the anticlastic and synclastic pattern of the corrugation indicated by the block black arrows. The green arrow indicates a prominent region of low curvature in Fault H. Note the poorly defined pattern of curvature in the bottom halves of the plots. The horizontal lines in Faults G represent the interval sampled to demonstrate the dimensions of culminations and depressions in Figure 5.39. Vertical scale is in milliseconds two way travel time and horizontal scale is in meters. Vertical exaggeration is ~1.6.

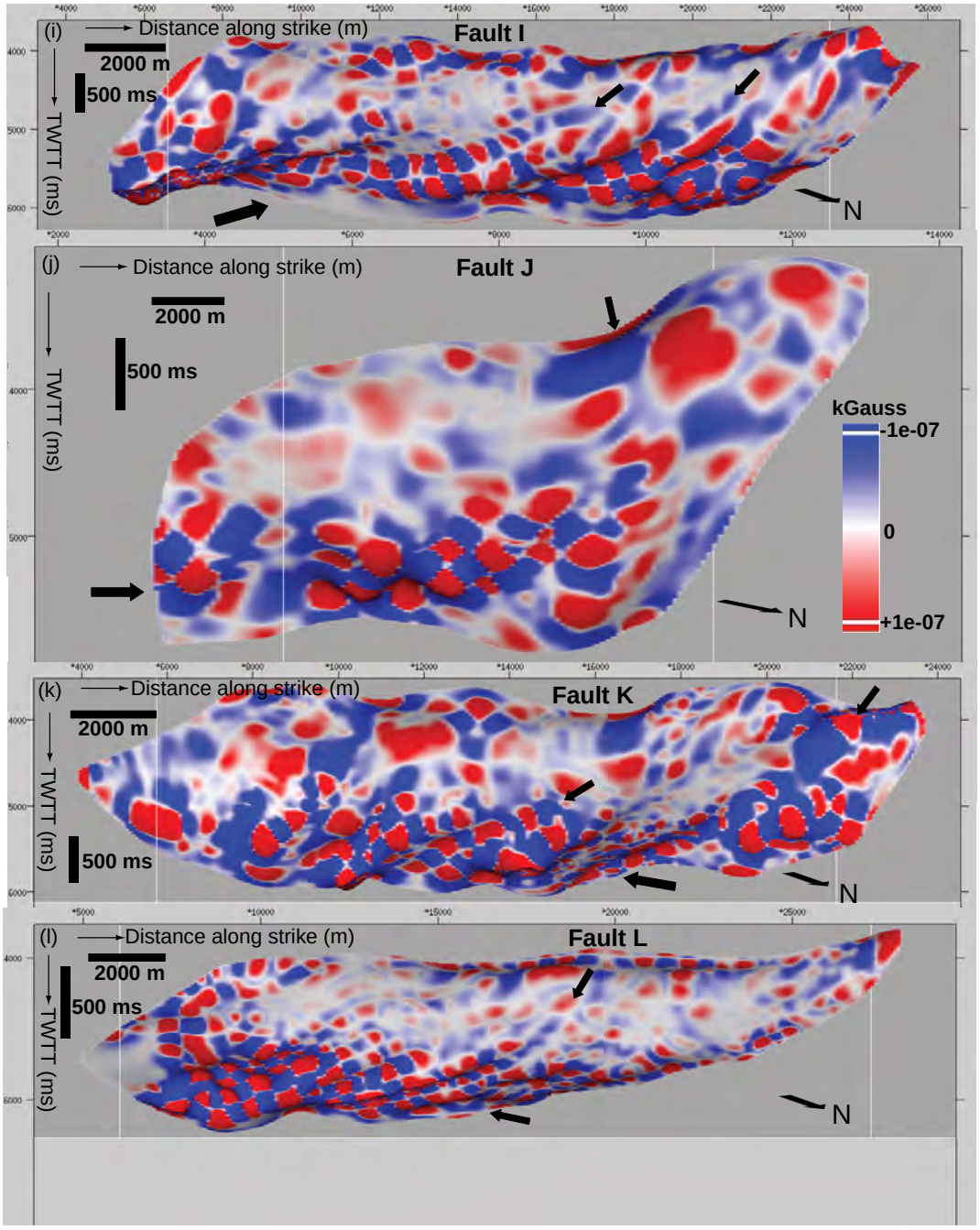

Figure 5.37: Strike views looking SW of surface Gaussian curvature plots of Faults I to L. Note the anticlastic and synclastic pattern of corrugation indicated by the block black arrows and the poorly defined pattern of curvature in the bottom halves of the plots. Vertical scale is in milliseconds two way travel time and horizontal scale is in meters. Vertical exaggeration is ~1.6.

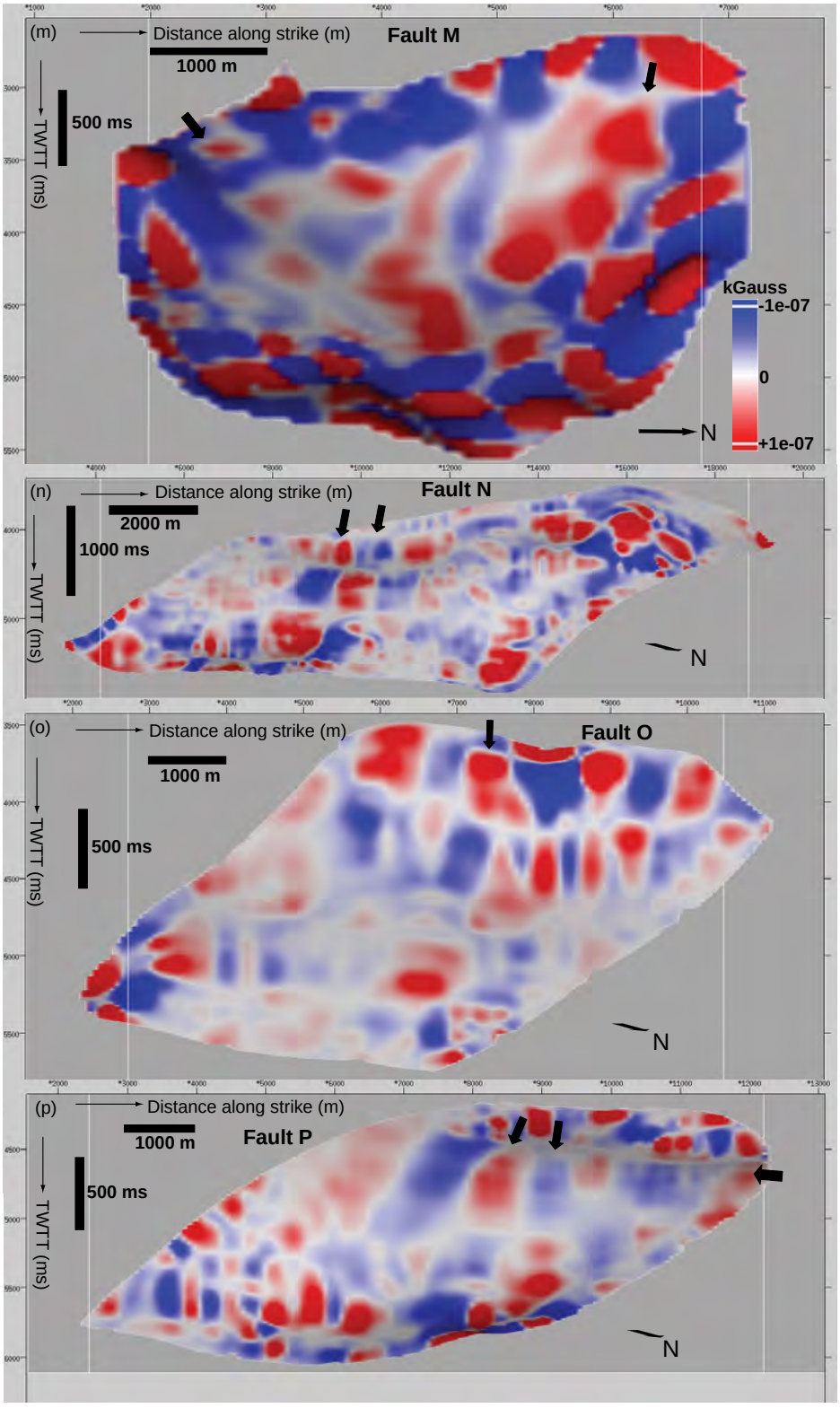

Figure 5.38: Strike views looking SW of surface Gaussian curvature plots of Faults I to L. Note the anticlastic and synclastic pattern of corrugation indicated by the block black arrows and the poorly defined pattern of curvature in the bottom halves of the plots. Vertical scale is in milliseconds two way travel time and horizontal scale is in meters. Vertical exaggeration is ~1.6.

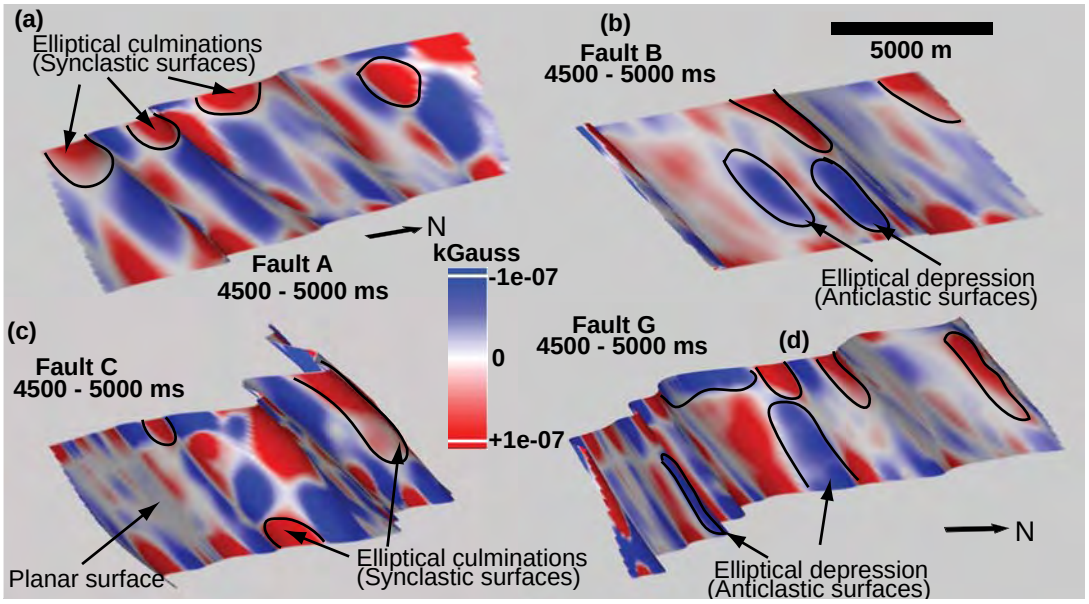

Figure 5.39: Perspective views looking west of the surface Gaussian curvature plots of Faults A (a), C (b), F (c) and G (D) illustrating the pattern and dimensions of culminations and depressions. Vertical exaggeration is ~1.6.

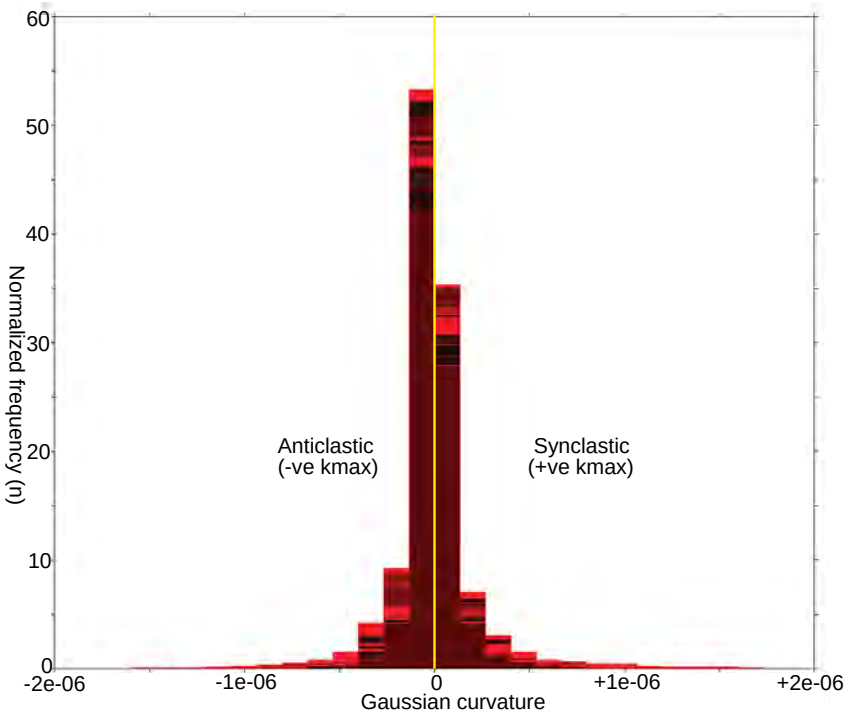

Figure 5.40: Normalized frequency histogram of the surface Gaussian curvature plots of Faults A to O showing a statistically fairly equal distribution of Gaussian curvature at the scale of sampling grid size.

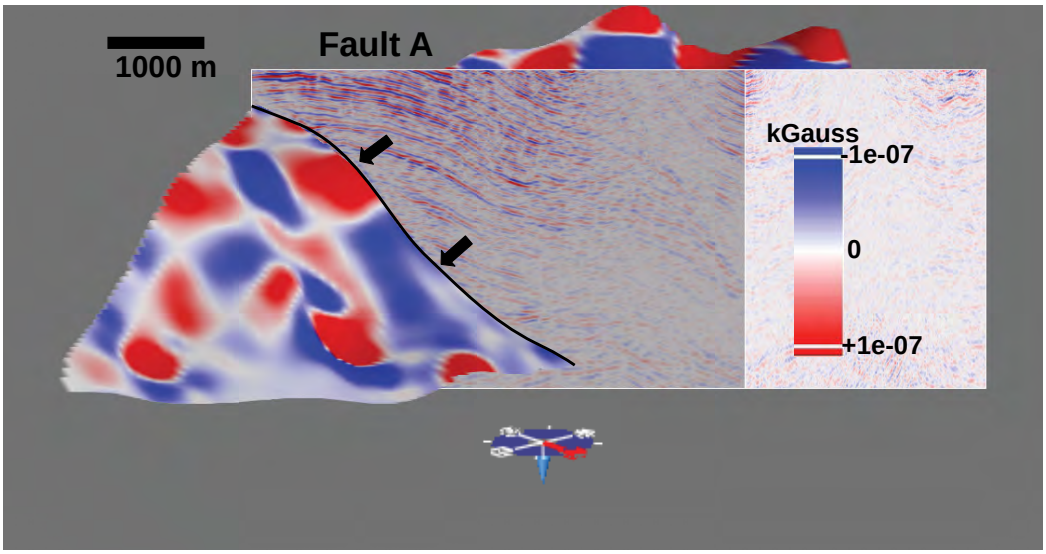

Figure 5.41: Perspective views of Gaussian curvature plot of Fault A illustrating the relationship between the pattern of curvature and reflectivity pattern in the hanging wall. The culminations (red) and depressions (blue) are geometrical properties of the fault surface (block arrows).

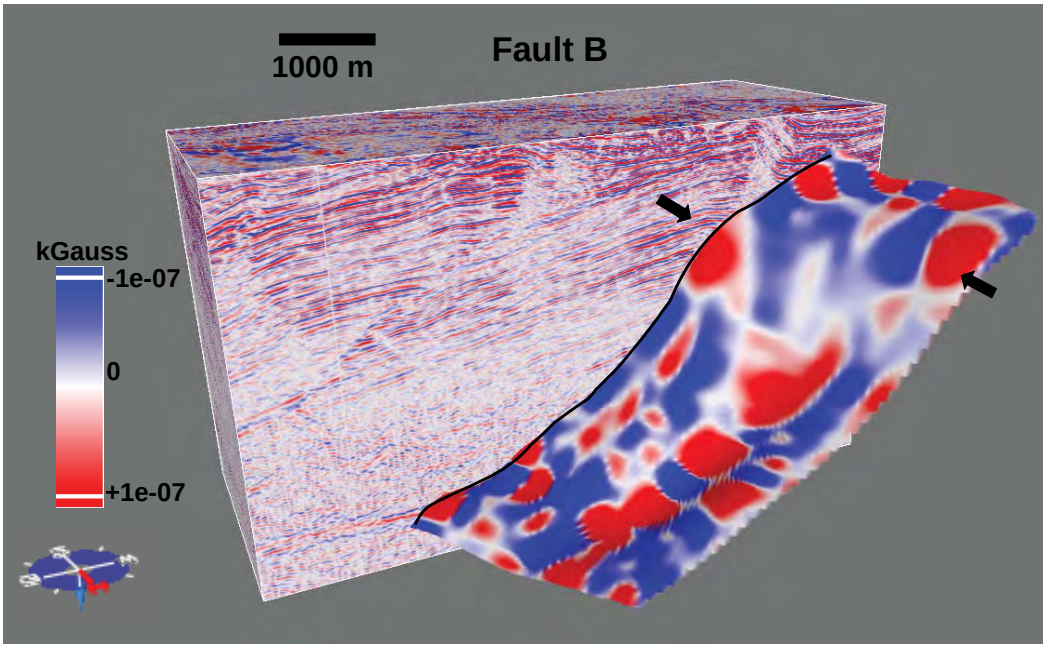

Figure 5.42: Perspective views of Gaussian curvature plot of Fault B illustrating the relationship between the pattern of curvature and reflectivity pattern in the hanging wall. The culminations (red) and depressions (blue) are geometrical properties of the fault surface (block arrows).

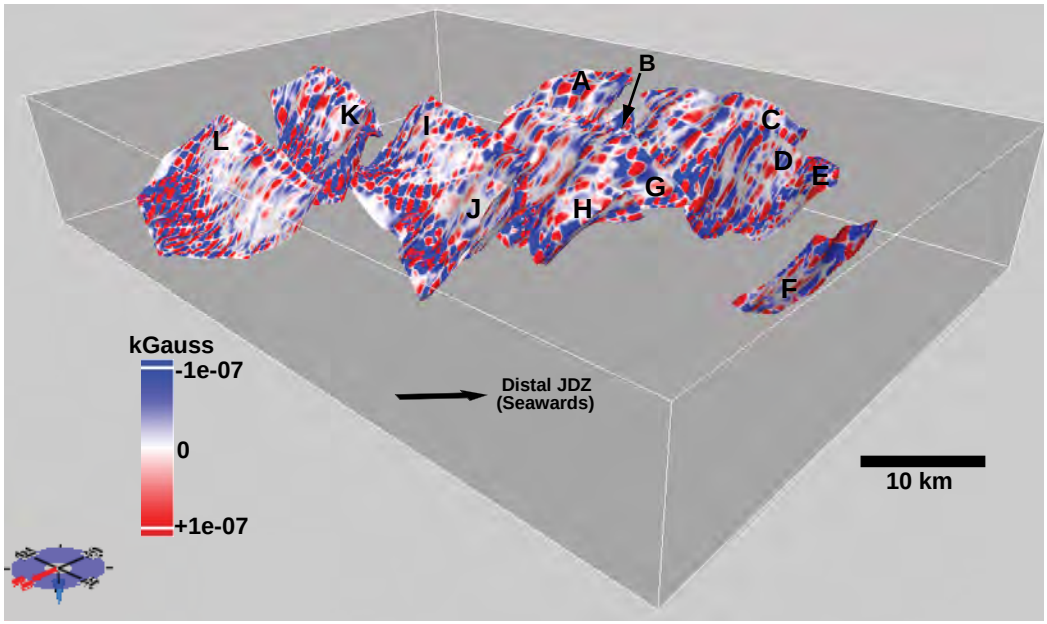

Figure 5.43: Perspective views of Gaussian curvature plots of faults in central JDZ illustrating the seaward orientation of culminations and depressions on corrugation axes. Vertical exaggeration is ~1.6.

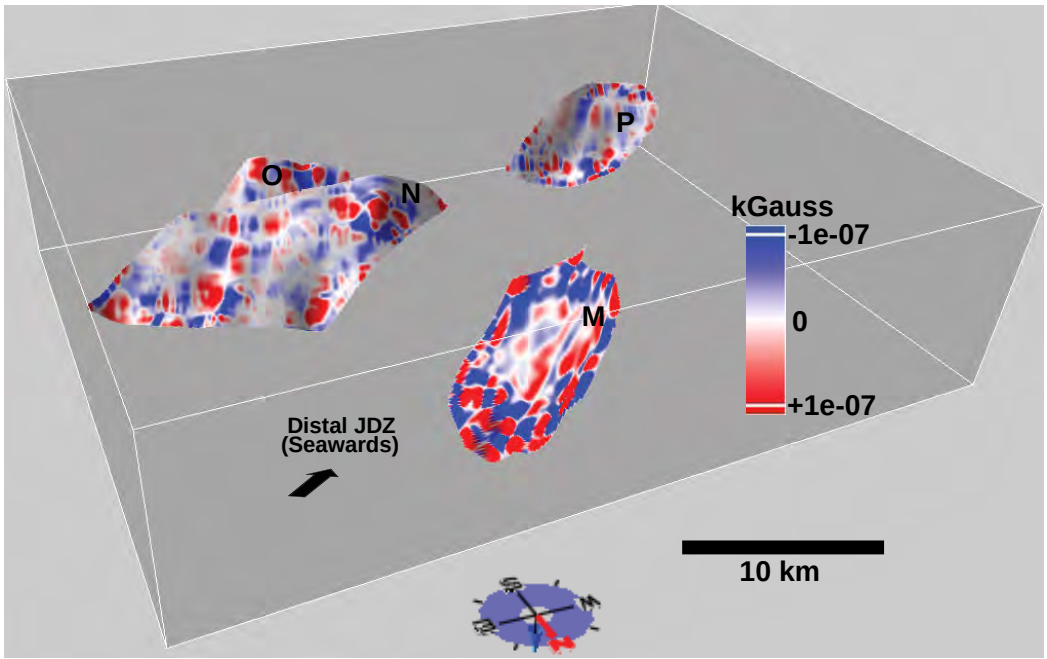

Figure 5.44: Perspective views of Gaussian curvature plots of faults in western JDZ. Except for Fault M, the culminations and depressions on the corrugation axes are oriented seawards in the direction of regional fault transport in the study area. Vertical exaggeration is ~1.6.

Fault	Culminations (+ve k_{Gauss})		Depressions (-ve k_{Gauss})	
	Width (km)	Length (km)	Width (km)	Length (km)
A	0.4 – 1	0.2 – 0.4	0.3 – 1	0.2 – 0.4
B	0.2 – 1	0.1 – 0.3	0.2 – 0.8	0.2 – 0.4
C	0.2 – 1	0.05 – 0.2	0.2 – 1.2	0.05 – 0.3
D	0.1 – 0.7	0.2 – 0.7	0.1 – 0.6	0.2 – 0.7
E	0.1 – 0.5	0.1 – 0.5	0.2 – 0.6	0.1 – 0.4
F	0.1 – 0.5	0.1 – 0.3	0.1 – 0.9	0.1 – 0.3
G	0.2 – 1	0.05 – 0.3	0.2 – 0.8	0.05 – 0.2
H	0.05 – 0.6	0.05 – 0.2	0.2 – 0.8	0.05 – 0.3
I	0.1 – 0.6	0.05 – 0.6	0.1 – 0.8	0.05 – 0.7
J	0.2 – 2	0.1 – 0.6	0.2 – 2.5	0.05 – 0.4
K	0.2 – 1.8	0.1 – 0.5	0.1 – 1.5	0.1 – 0.6
L	0.05 – 1	0.05 – 0.2	0.05 – 0.7	0.05 – 0.2
M	0.1 – 0.6	0.05 – 0.5	0.05 – 0.5	0.1 – 0.5
N	0.1 – 0.6	0.1 – 0.5	0.05 – 0.5	0.05 – 0.2
O	0.1 – 0.8	0.05 – 0.4	0.1 – 0.8	0.1 – 0.4
P	0.05 – 0.6	0.05 – 0.45	0.1 – 0.8	0.05 – 0.4

Table 5.3: Summary of dimensions of culminations and depressions mapped on the sixteen faults in the study area.

5.3.5 Spectral analysis of fault surface curvature

The impact of fault surface grid size on fault surface attribute plots becomes apparent when surface models and curvature plots of Fault A are analyzed. The fault segments were independently picked in the inline, cross line and horizontal cross sections and surface models of the fault produced (Figure 5.45). The surface models show that the fault has a consistently uniform surface morphology when mapped in the inline, cross line and horizontal orientation. (i.e. undulations persist when traces of the fault are mapped in different orientations). Figures 5.46 and 5.48 show the maximum and Gaussian curvature plots of the three models of the fault. A visual and statistical comparison of the plots reveals a very similar pattern of curvature (Figures 5.47 and

5.49) and corrugation amplitudes (Figure 5.50). This is the basis for selecting the fault for detailed investigation of the relationship between fault surface grid size and curvature sampling resolution.

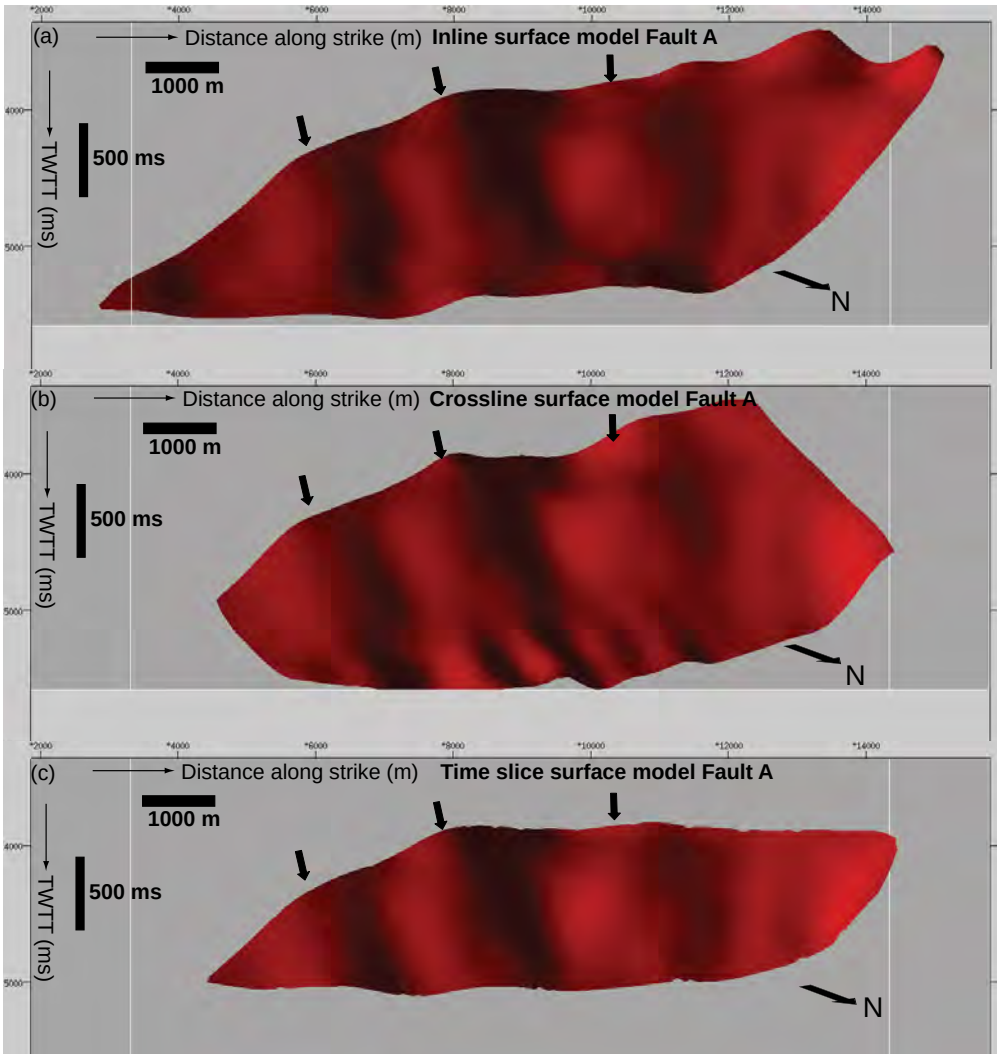

Figure 5.45: Perspective views looking SW of surface models of Fault A mapped in vertical cross section in inline (a) crossline (b) and time slice orientations (c). Note the similar pattern of undulations in the three surface models (block black arrows). Vertical scale is in milliseconds two way travel time and horizontal scale is in meters. Vertical exaggeration is ~1.6.

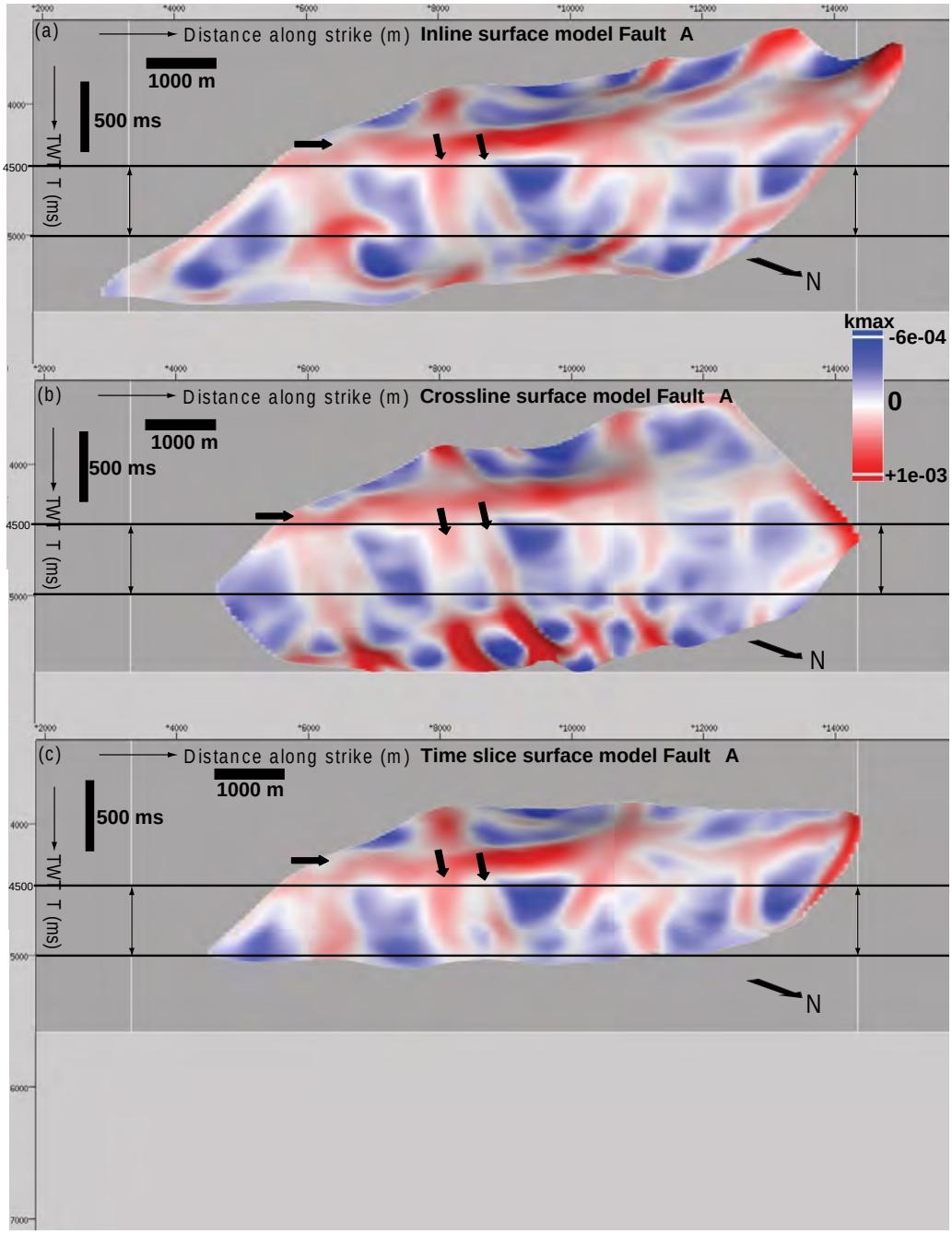

Figure 5.46: Strike views looking SW of maximum curvature plots of Fault A using fault surface modelled from fault segments mapped in inline (a) crossline (b) and time slice orientations (c). Note the similar pattern of corrugation in the three plots (block arrows). The horizontal lines indicate the interval sampled to demonstrate the pattern and dimensions of corrugation amplitudes in Figure 5.49. Vertical scale is in milliseconds two way travel time and horizontal scale is in meters. Vertical exaggeration is ~1.6.

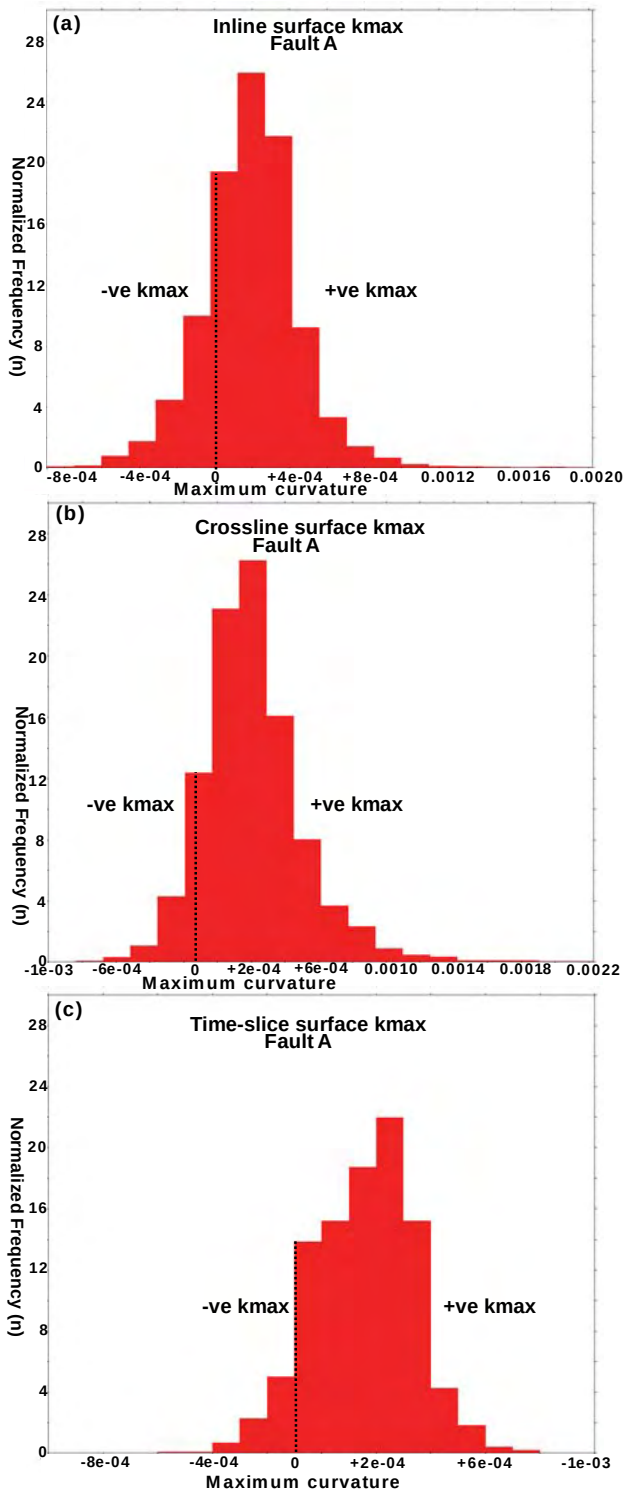

Figure 5.47: Normalized frequency histograms of the surface maximum curvature plots of Fault A using surface models mapped in inline (a), crossline (b) and time slice orientations (c). Note the similarity in the statistical distribution of maximum curvature of the three plots of the same fault.

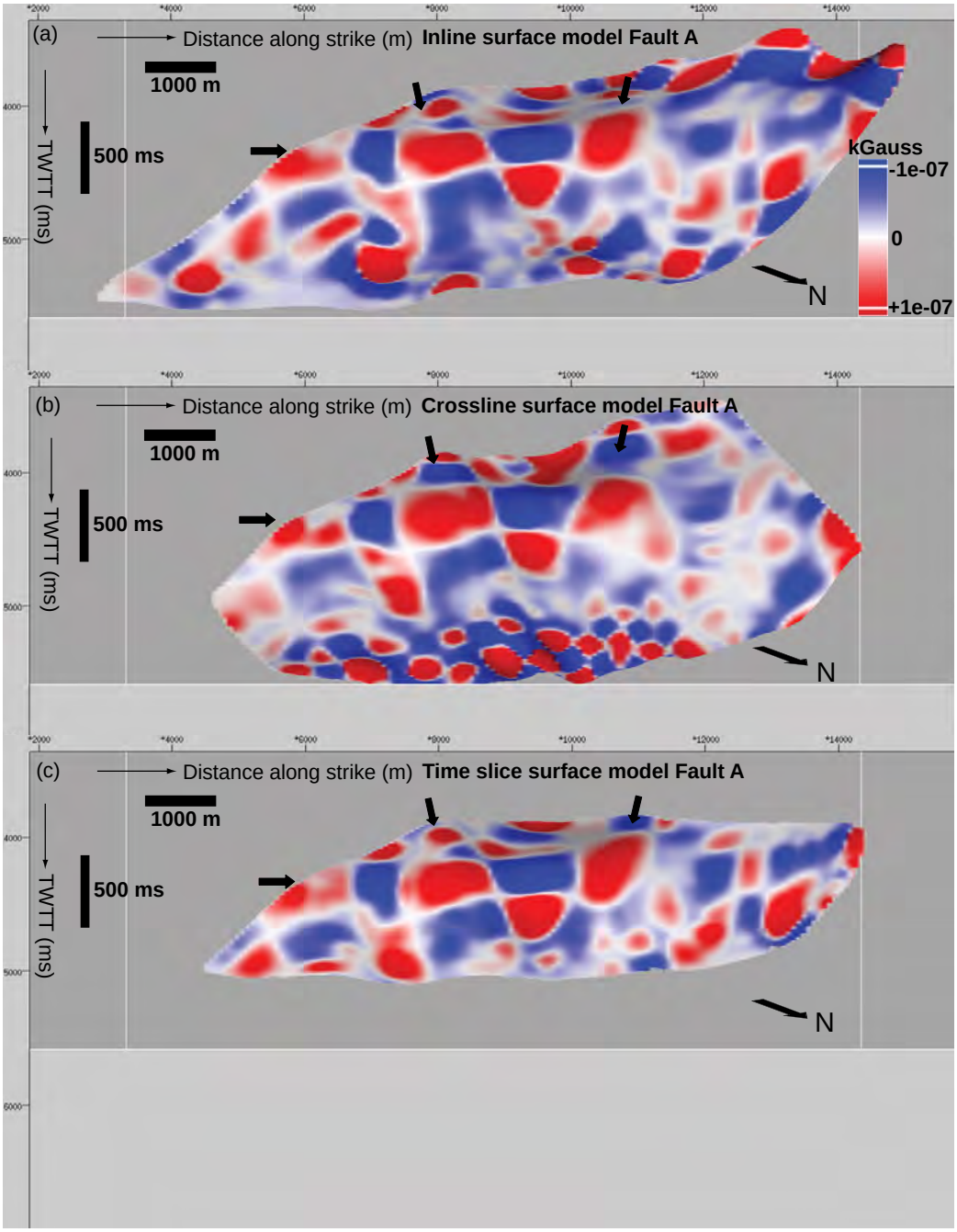

Figure 5.48: Strike views looking SW of Gaussian curvature plots of Fault A using fault surfaces modelled from fault segments mapped in inline (a) crossline (b) and time slice orientations (c). Note the similar pattern of culminations, depressions and polarity reversal along the corrugation axes (block arrows) in the three plots of the same fault. Vertical scale is in milliseconds two way travel time and horizontal scale is in meters. Vertical exaggeration is ~1.6.

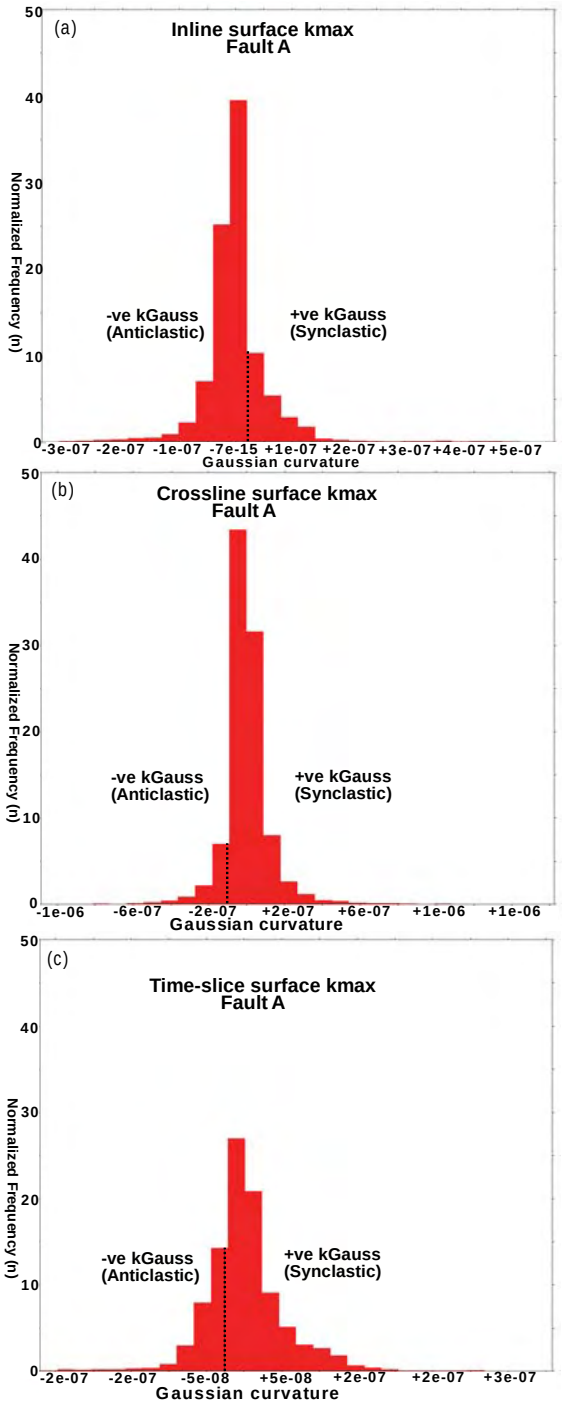

Figure 5.49: Normalized frequency histograms of the surface Gaussian curvature plots of Fault A using surface models mapped in inline (a), crossline (b) and time slice orientations (c). Note the similar statistical distribution of Gaussian curvature in the three plots of the same fault

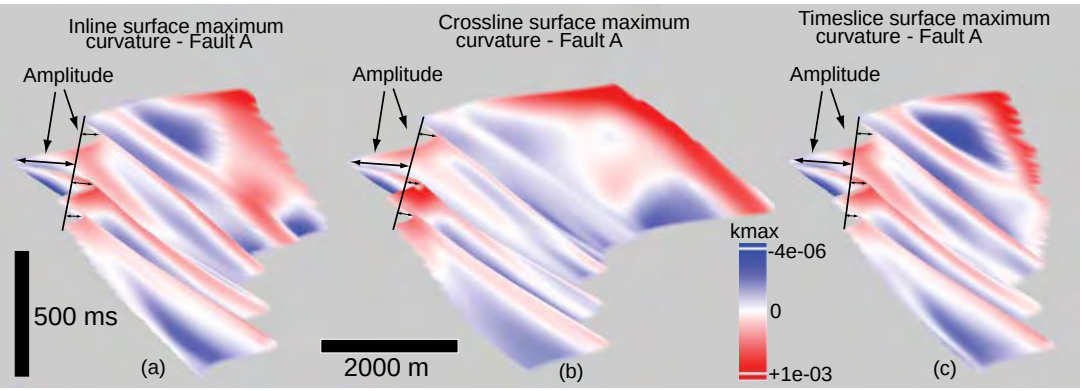

Figure 5.50: Perspective views looking SW of surface maximum curvature plots of Fault A using models sampled between 4500 ms and 5000 ms mapped in inline (a), crossline (b) and time slice orientations (c). Note the similar pattern of corrugation amplitude in the three plots of the same fault. Vertical exaggeration is ~1.6.

Figures 5.51 to 5.56 the shows maximum and Gaussian curvature plots of the fault modelled using surface grid sizes of between 25 m and 400 m and curvature sampling resolution ranging from 25 m to 300 m. The curvature plots demonstrate that the output of curvature analysis depends on fault surface grid size and curvature sampling dimensions.

Generally as the surface grid size approach curvature sampling resolution, fault surface morphology is dominated by high frequency data (e.g. Figures 5.51b, 5.54b and 5.55b). However, at low curvature sampling resolution, the plots are smoother. A noticeable change in the pattern of the curvature is observed when larger surface grids are used. Nearly all the plots are smoother irrespective of curvature sampling resolution (e.g. Figures 5.52c and d, 5.53c and 5.56c and d). At this scale of observation, large scale corrugations with wavelengths of up to 2000 m are clearly visible.

In previous work, data filtering and smoothing have been used prior to analyzing the geometry of fault surfaces using laser scan data of exhumed fault planes (e.g. Jones *et al*. 2008; Kokkalas *et al*. 2007), horizons mapped from seismic data (e.g. Lisle, 1994;

Stewart & Wynn, 2000; Wright, 2008; Ericsson *et al*. 1998; Bergbauer & Pollard, 2000) and models of fault surfaces produced from earthquake aftershock data (Carena & Suppe, 2002). This is because curvature is scale dependent and analysis will emphasize the shortest wavelength of a surface assuming the data is not up-scaled (e.g. Jones *et al*. 2008; Stewart & Wynn, 2000).

Therefore, high frequency data that may mask genuine features of surface geometry must be suppressed. Stewart & Wynn (2000) suggested mapping a wide range of curvature spectrum using different grid sizes to potentially capture a range of wavelengths. This demonstrates that unlike the curvature of bedding surfaces, a lot of effort is required to analyze fault surface curvature since is a subtle attribute of fault surfaces (e.g. Jones *et al*. 2008).

Most of the high frequency data contained in the gridded fault surfaces contributes to the small-scale undulations, while the low frequency data constitute the broader surface morphology. The highest frequency contained in a gridded data set is referred to as "Nyquist frequency". This frequency is the inverse of twice the grid spacing. For a sampled surface to be truly representative of the original surface, the sampling resolution must be at least twice the diameter of the smallest surface undulation. Sampling resolution below the diameter of the smallest surface corrugation introduces an alias (Nyquist, 1928).

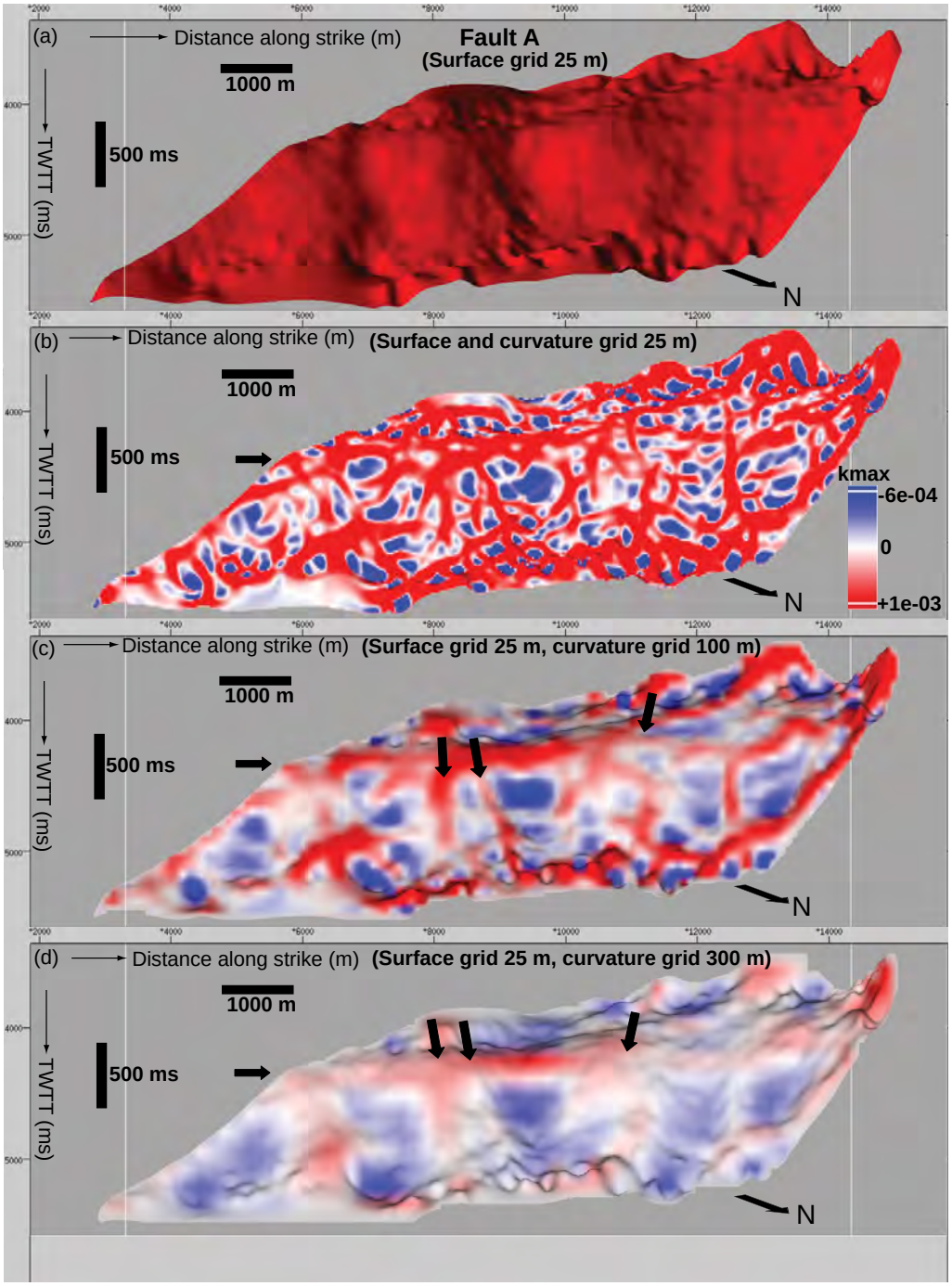

Figure 5.51: Strike view looking SW of surface model of Fault A modelled with a grid size of 25 m (a) and maximum curvature plots with sampling grid size of 25 m (b), 100 m (b), and 200 m (c). Note the high frequency of data as fault grid size equals curvature sampling resolution (25 m). The block black arrows indicate how the pattern of curvature changes with increasing curvature grid dimensions. Vertical scale is in milliseconds two way time and horizontal scale is in meters. Vertical exaggeration is ~1.6.

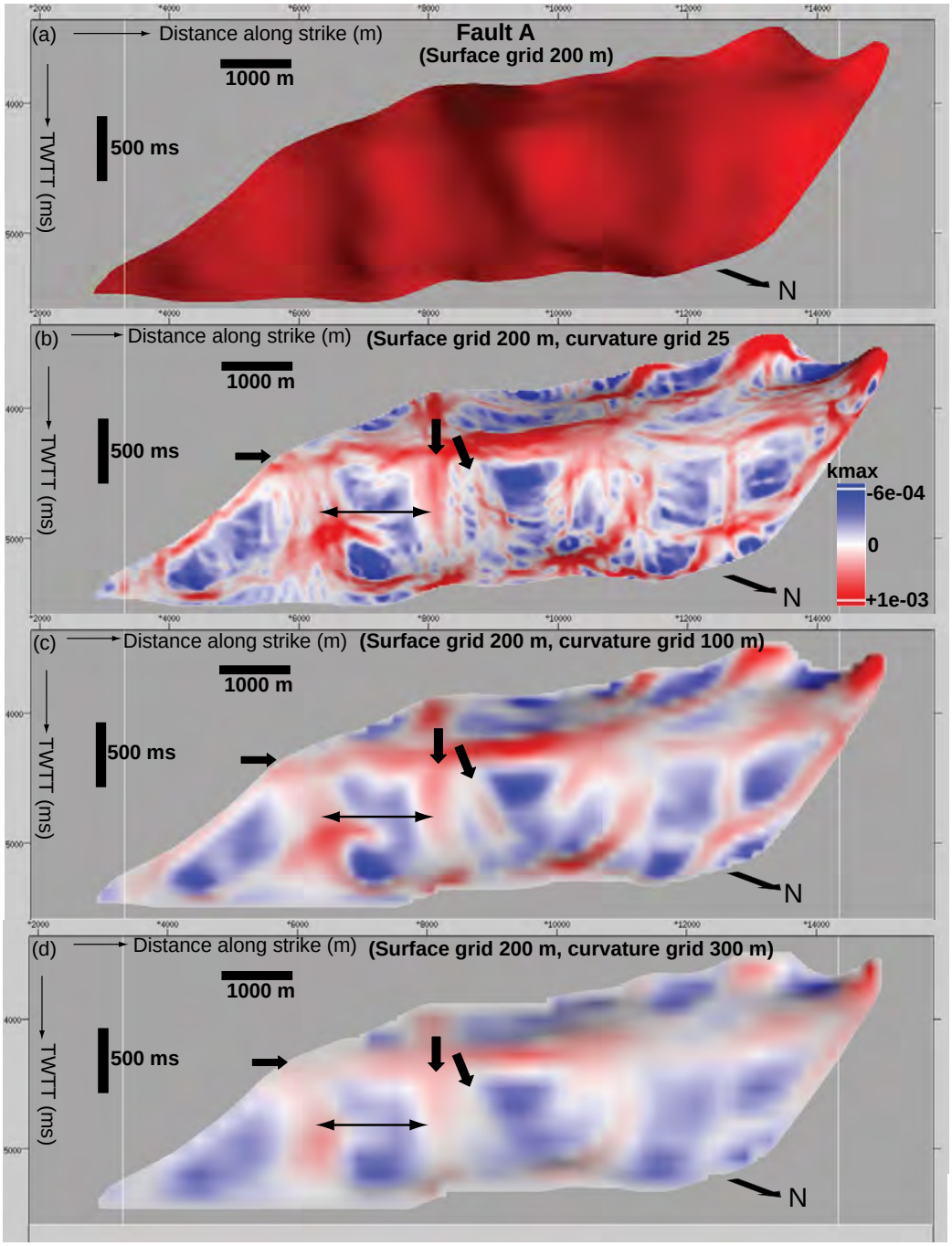

Figure 5.52: Strike view looking SW of surface model of Fault A modelled with a grid size of 200 m (a), maximum curvature plots with sampling grid size of 25 m (b), 100 m (c), and 200 m (d). Note the bifurcation of corrugation resolved at 100 m curvature sampling resolution compared to 25 m (High resolution) and 300 m (Low resolution) sampling grid dimensions. This is the basis for selecting a surface grid of 200 m and curvature sampling dimension of 100 m in the plots presented in this thesis. Vertical scale is in milliseconds two way time and horizontal scale is in meters. Vertical exaggeration is ~1.6.

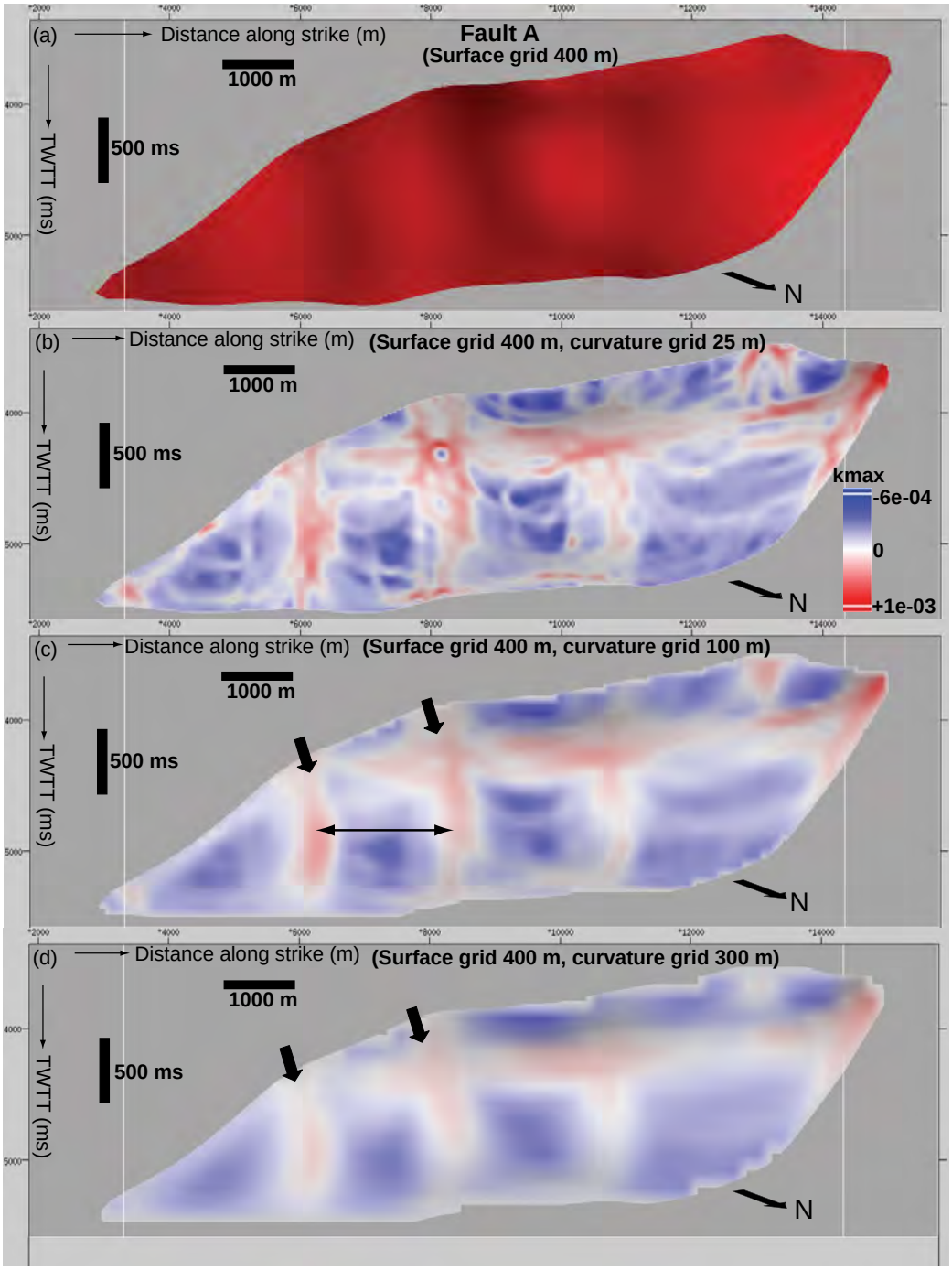

Figure 5.53: Strike view looking SW of surface model of Fault A modelled with a grid size of 400 m (a), maximum curvature plots with sampling grid size of 25 m (b), 100 m (c), and 200 m (d). Note the bifurcation of corrugation resolved at 100 m curvature sampling resolution and hardly resolved at 25 m and 300 m sampling resolution. Vertical scale is in milliseconds two way time and horizontal scale is in meters. Vertical exaggeration is ~1.6.

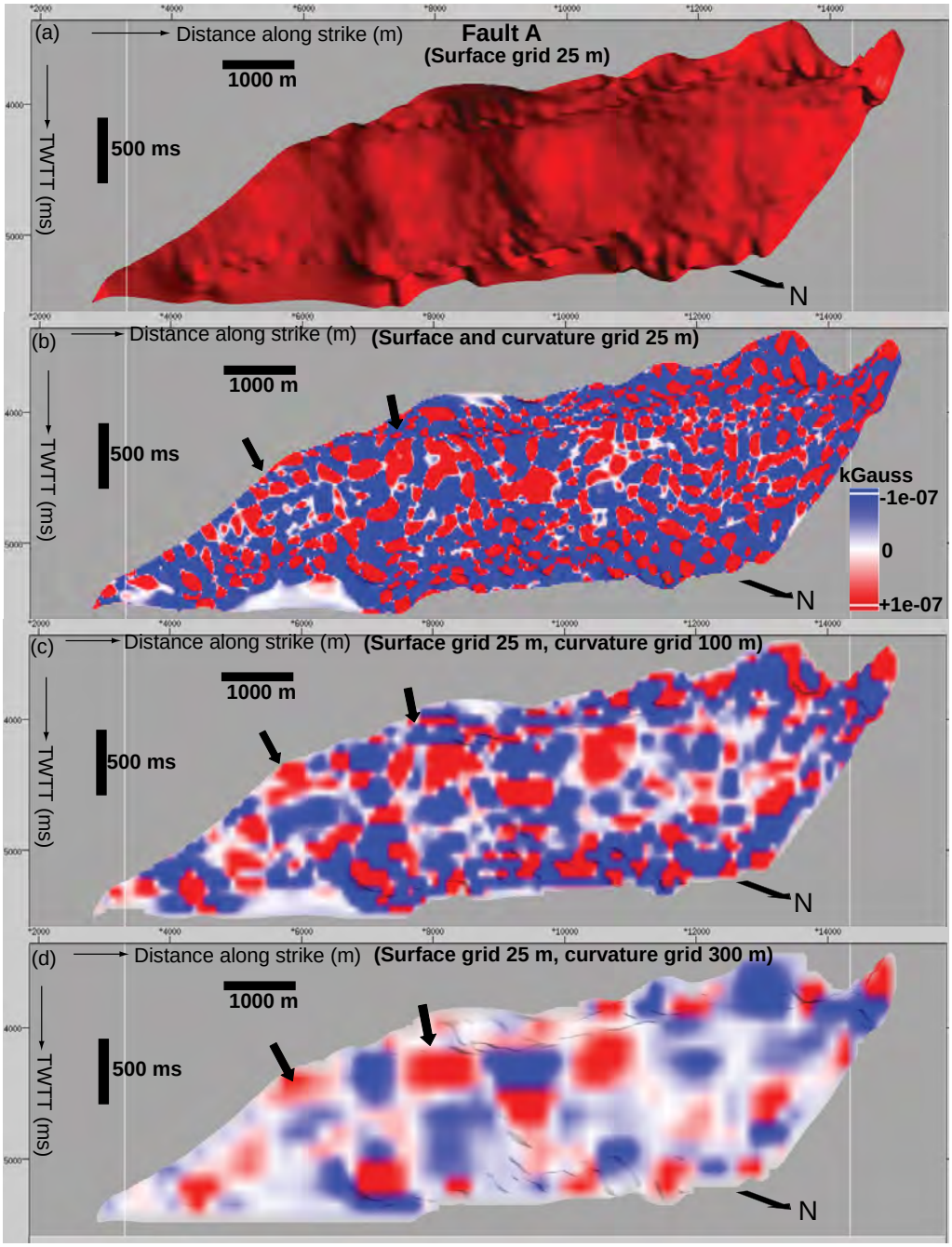

Figure 5.54: Strike view looking SW of surface model of Fault A modelled with a grid size of 25 m (a) Gaussian curvature plots with sampling grid size of 25 m (b), 100 m (c), and 200 m (d). Note the high frequency of data as fault grid size equals curvature sampling resolution (25 m). The block black arrows highlight reversal in curvature polarity along corrugation axes that appears to be better resolved when the curvature grid dimension is increased. Vertical scale is in milliseconds two way time and horizontal scale is in meters. Vertical exaggeration is ~1.6.

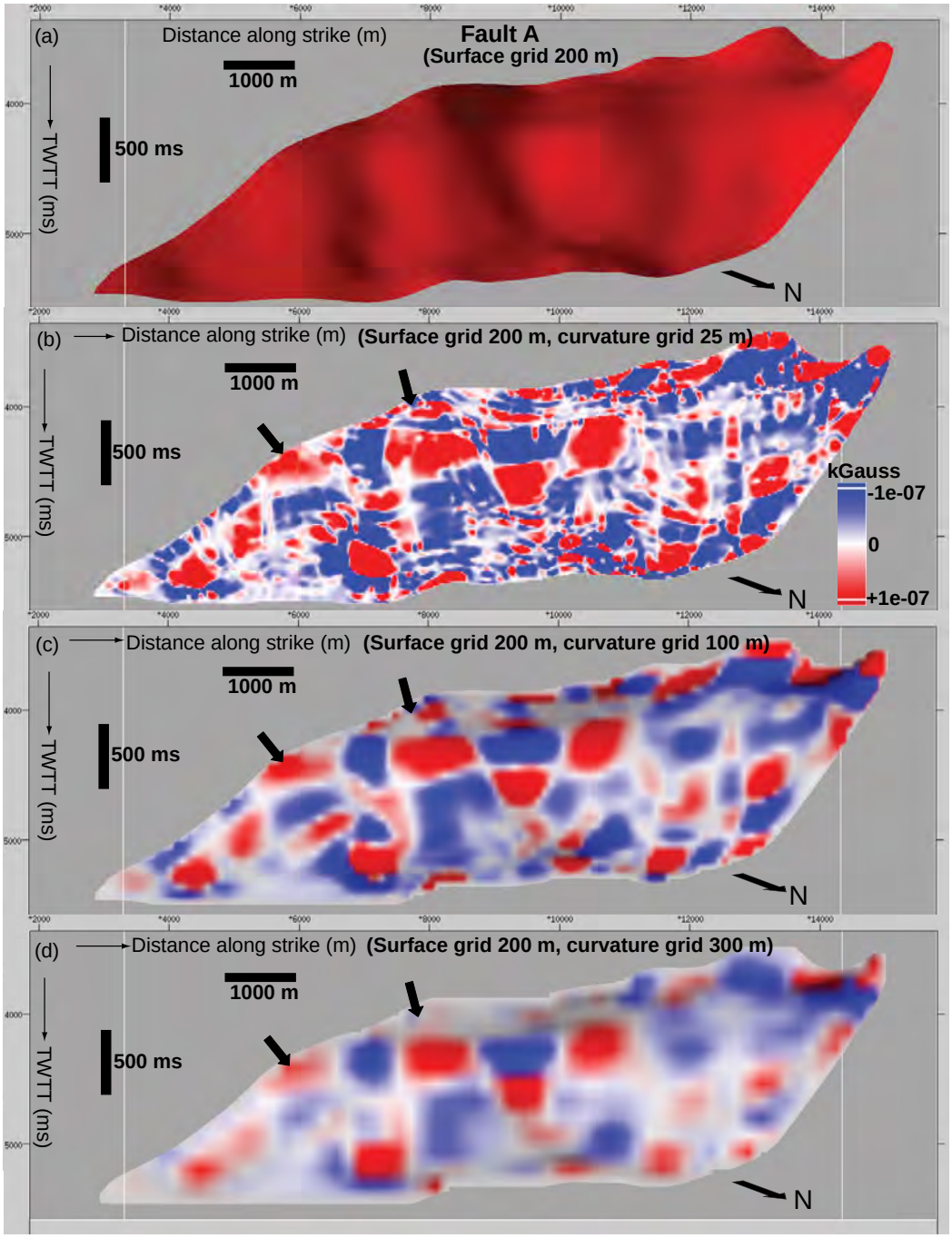

Figure 5.55: Strike view looking SW of surface model of Fault A modelled with a grid size of 200 m (a), maximum curvature plots with sampling grid size of 25 m (b), 100 m (c), and 200 m (d). Note the smoother pattern of culminations and depressions as the surface and curvature dimensions are increased (block black arrows). Vertical scale is in milliseconds two way time and horizontal scale is in meters. Vertical exaggeration is ~1.6.

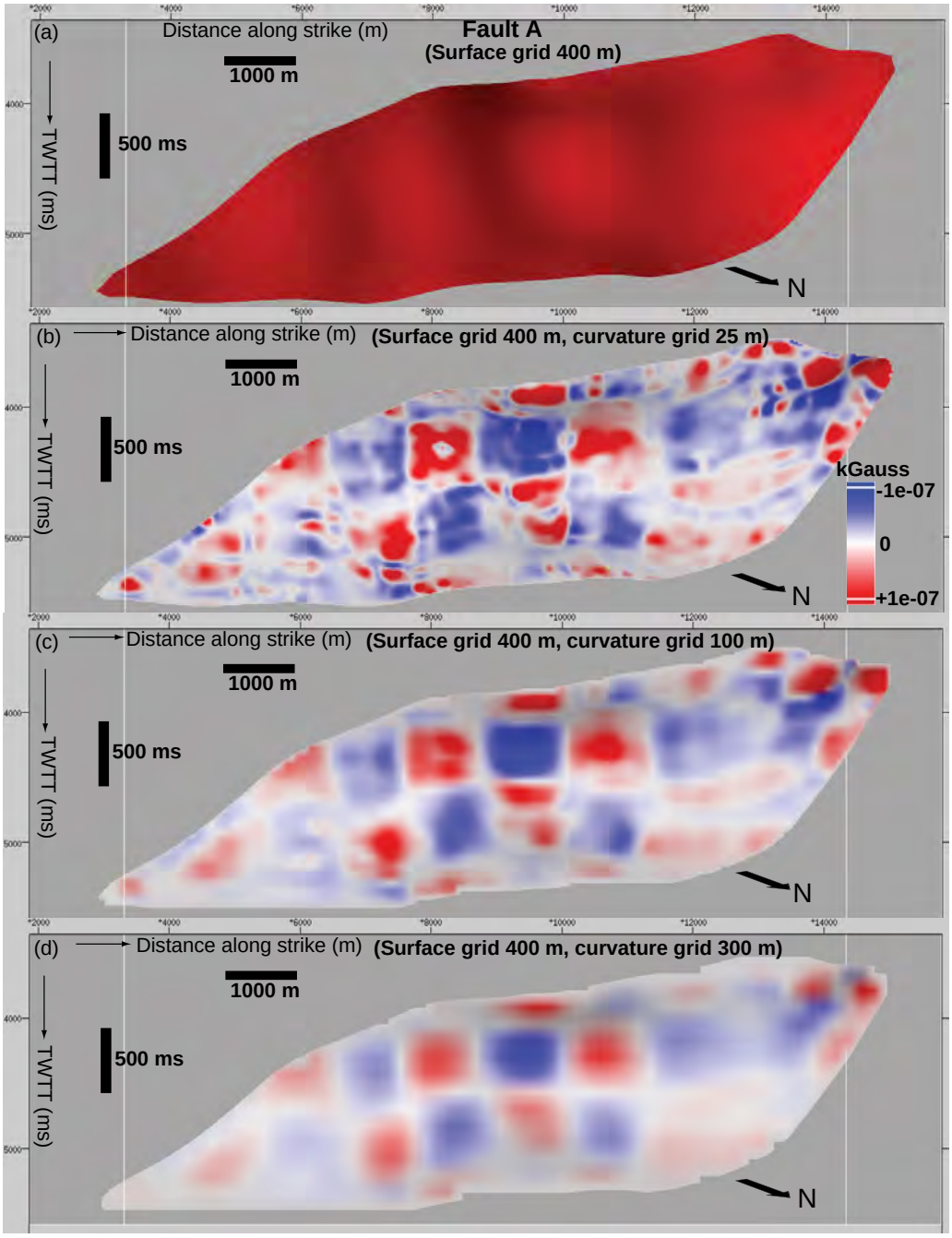

Figure 5.56: Strike view looking SW of surface model of Fault A modelled with a grid size of 400 m (a), maximum curvature plots with sampling grid size of 25 m (b), 100 m (c), and 200 m (d). Note the smoother pattern of culminations and depressions with a large surface grid. High curvature grid dimensions could result in high frequency data leaking into low frequency spectrum resulting in aliasing. Vertical scale is in milliseconds two way time and horizontal scale is in meters. Vertical exaggeration is ~1.6.

In effect, since the fault traces were mapped on at least every seismic line (line spacing is 26 m), a surface grid of 25 m is bound to be dominated by high frequency

undulations some of which could be inherent features of the fault surface, but many of which might be artefacts. Therefore, in calculating and presenting the curvature plots of the faults presented in this thesis, a sampling resolution of 100 m is used. This is less than the smallest wavelength of corrugation observed on the fault surfaces and appears to show fault surface features that may be hard to resolve at high sampling resolution (25 m) and low sampling resolution (300 m). For example the bifurcation of corrugation in the maximum curvature plot in Figure 5.52c is better resolved at a curvature sampling resolution of 100 m than 25 m and 300 m. Ericsson *et al*. (1998) suggested that a better correlation between calculated curvatures and measured wall rock strain is obtained using smoothened surface grids that highlights longer wavelength measurements and geometrical properties of folded surfaces at the scale of interest (Pearce *et al*. 2011). This may also be the case when using seismic data to investigate small-scale disruption related to deformation in the vicinity of faults.

In this study inherent noise due to picking fault traces was minimized by smoothing surface models of the faults for two purposes 1) characterize fault surface morphology and 2) investigate links between fault surface topography and the structure of the volumes adjacent to the faults. Although the larger wavelength corrugations are of primary interest in investigating the qualitative large-scale links between fault surface morphology and volume structure, fault curvature plots modelled at high resolution were used Therefore, in investigating the quantitative links between fault surface morphology and volume structure, seismic attribute volumes calculated using the default bin spacing of the seismic data are compared with curvature plots of the faults sampled at high resolution.

5.4 Discussion and conclusion

5.4.1 Modelling fault surface and attribute plots

The surface models of the faults presented in this chapter demonstrates that thrust faults in deepwater Niger Delta fold and thrust belt with surface areas ranging between 12 km^2 and up to 40 km^2 are undulated and exhibit surface morphologies across a range of scales commonly seen in normal faults in outcrop and seismic data. (e.g. Jones *et al*. 2008; Wright, 2008; Wright, 2008; Candela *et al*. 2008; Lohr *et al*. 2008; van Gent *et al*. 2010: Resor & Meer, 2008; Jackson & McKenzie, 1999; Sagy & Brodsky, 2009; Kokkalas *et al*. 2007). This observation is further confirmation that thrust faults exhibit undulations that are real features of fault surfaces that can be mapped using seismic data. These structures and other forms of irregularities have been observed in curvature and gradient plots of the faults.

Geometrical analysis of sixteen faults reveals a widespread occurrence of well developed corrugations. In addition to the more regular corrugations, nearly all the fault surfaces exhibit cross corrugation and fault bends that are major sources of intense curvature. Maximum curvature plots shows that corrugations occur as semi-linear to linear grooves and ridges with lengths and widths of up to 2 km and wavelengths ranging between 0.5 km and 2.5 km and oriented in the fault transport direction interpreted to represent the direction of seaward gravitational deformation in deepwater Niger Delta. In addition corrugation amplitudes with dimensions ranging between 0.05 km and 0.4 km have been observed. Plots of average wavelengths versus amplitudes suggest a linear relationship for some of the faults. Similar observations have been made in normal faults mapped in outcrop and seismic data from different tectonic settings, implying that curvature is a generic feature of faults

irrespective of their tectonic setting. Nearly all the faults exhibit pronounced Gaussian curvature characterized by large scale culminations and depressions with widths of 2 km and lengths ½ of the widths. The overall pattern of Gaussian curvature suggests that most of the faults posses non-developable geometries, i.e. geometries that cannot be restored to plane without deforming the surfaces (Lisle, 1994).

Analyzing fault surface topography using curvature as an attribute can provide reliable means of assessing the variability of fault surface topography in three-dimensions. However, the curvature of surfaces is highly scale dependent and requires careful data processing to separate spatial scales of structures. In this analysis, long-wavelength fault surface corrugations have been enhanced by smoothing fault surface models, although at the risk of eliminating surface roughness inherent on the fault surface. Different processes may dominate fault surface topography observed at different fault grid and curvature sampling resolutions (e.g. Lee & Bruhn, 1996). In analyzing the curvature of geological surfaces, short-wavelength features dominate the plots, but up-scaling the fault surface grid can reveal longer wavelength features (e.g. Wynn & Stewart, 2003; Bergbauer *et al*. 2003). However, care should be taken when interpreting curvature plots of highly smoothened surfaces because excessive smoothing could result in fewer high frequencies being resolved resulting in aliasing and erroneous curvature models of the fault surfaces (e.g. Bergbauer *et al*. 2003).

The effect of data smoothing in analyzing the geometry and curvature of gridded geological surfaces has been described by Bergbaeur & Pollard (2000), Carena & Suppe (2002) and Lisle (1994). The latter showed how the application of a low pass spatial filter resulted in a better definition and interpretable pattern of the curvature of Goose egg dome structure. Similarly, Carena & Suppe (2002) described how

earthquake aftershock data was conditioned prior to calculating surface model of the Northridge thrust fault resulting in a better interpretation of the three-dimensional fault plane geometry. It is interpreted that at high surface curvature sampling resolution, the roughness of the surface probably constitutes a good proportion of the overall fault surface morphology, while at low curvature sampling resolution curvature is the predominant surface feature. In any case, the primary objective of this thesis is to map large-scale geometric features that make up the fault surfaces and such analysis is probably better investigated using curvature as an attribute of fault surfaces.

Fault corrugations have been described to be self-affine i.e. exhibit similar patterns when viewed at different scales and different sampling frequencies (e.g. Sagy *et al.* 2007; Candela *et al*. 2009; Thibout *et al*. 1996). Although distinguishing "real" fault surface corrugations from artefacts of fault trace mapping and surface modelling is difficult (e.g. van Gent, *et al.* 2010), the detailed interpretation of dense grid of fault traces using seismic amplitude combined with similarity attribute data, and the consistent pattern of fault surface morphology demonstrates that the corrugations highlighted by fault surface attributes are real and can be seen at a range of fault surface grid and attribute sampling resolution. Although analyzing outcrop fault surfaces can provide additional details that can be used to constrain geometric and kinematic indicators on fault planes, fault models produced from detailed interpretation of seismic data can provide good representation of the fault surface and realistic plots of curvature irrespective of the orientation the fault traces are mapped.

Although the origin of corrugations in normal faults is currently a topic of interest to structural geologists, large-scale corrugations in normal faults (wavelengths of

hundreds of meters to kilometres) are speculated to evolve by mechanisms such as reactivation of pre-existing faults, folding of fault surfaces, coalescence of fault segments to form through-going fault planes (e.g. Ferrill *et al*. 1999; Lohr *et al*. 2008; Marchal *et al*. 2003) and the preservation and/or amplification of inherent random roughness in the direction of the most recent slip (e.g. Sagy *et al*. 2007; Kokkalas *et al*. 2007; Sagy & Brodsky, 2009). In addition, faults are speculated to exhibit surface curvature primarily due to the effects of host rock mechanical stratigraphy during slip and non-uniform tectonic deformation (e.g. Martel, 1999). John (1987) also suggested that corrugations mapped in outcrop developed along slip direction during fault movement as mullion structures and may have been syn-tectonic in origin. Bergen & Shaw (2010) demonstrated the preponderance of displacement profiles with multiple maxima implying that thrust faults in deepwater Niger Delta may have developed by segment linkage. No evidence exists to demonstrate the origin of the corrugations observed on the thrust faults presented in this thesis rather than to speculate that the structures probably evolved by interaction between fault segments.

In previous work, it has been suggested that the down plunge continuity of corrugations may be a reflection of mechanical stratigraphy of the faulted wall rocks (Resor & Meer, 2010) and that culminations and depressions along the corrugation are the result of geometrical and rheological inhomogeneities (Sagy & Brodsky, 2009). However, in the JDZ, slices of volume seismic data sampled in the vicinity of some of the faults suggest that down plunge corrugation continuity persists despite the layered sedimentary sequence in the hanging wall and footwall. However, it appears the structures are better developed with broader wavelengths in the more competent units of Unit II described as the deepwater equivalent of predominantly sandy Agbada Formation. However, the wavelengths decreases as the faults sole into detachment

surfaces in Unit III described in Chapter Four as the deepwater equivalent of marine clays of the Akata Formation.

5.4.2 Potential implications of fault surface morphology on the structure of the volumes adjacent to faults volume

The principal aim of analyzing the surface morphology of the faults presented in this thesis is to investigate how fault geometry may influence the structure of fault zones and plots of the two attributes shows that most of the faults exhibit a wide range of maximum and Gaussian curvature. Both measures of curvature (Gaussian and maximum) have been previously used to identify areas of highest strain resulting from the bending and stretching of outcrop surfaces and horizons mapped from seismic data but hardly applied to investigate the consequences of fault surface curvature on the structure of contiguous wall rock volumes using seismic data. However, previous work has shown that potential links between fracturing/faulting and surface curvature can only be investigated if reliable geometrical plots of fault planes are calculated (e.g. Pearce *et al*. 2011; Jones *et al*. 2009) and this is the reason for dedicating a whole chapter of the thesis to calculating and analyzing the surface morphology of several faults. Therefore, the plots provide the opportunity to investigate links relationship between fault surface curvature and the structure of the volumes adjacent to the faults and in particular test the developability or non-developability of the fault surfaces using Gaussian curvature plots of the faults.

The concept of developability and non-developability of surfaces has in the past been used to relate curvature to strain. For example, Lisle (1994) and Bergbauer & Pollard (2003) measured the Gaussian curvature of buckle-folds to predict areas of fracture intensity. Assuming brittle failure, fracture intensity is likely to be highest where

Gaussian curvature is not zero because it is in these areas that the bedding has had to distort the most to accommodate folding. This observation implies that anticlastic and syncalstic curvatures cannot be restored to a plane without deforming the surface. Conceptualized models of surface geometries that can be obtained by combining positive, negative and zero principal curvature axes with flow paths as translation occurs over the surfaces in relation to the concept of the developability of surfaces is presented in Figure 5.57 (Wright, 2008).

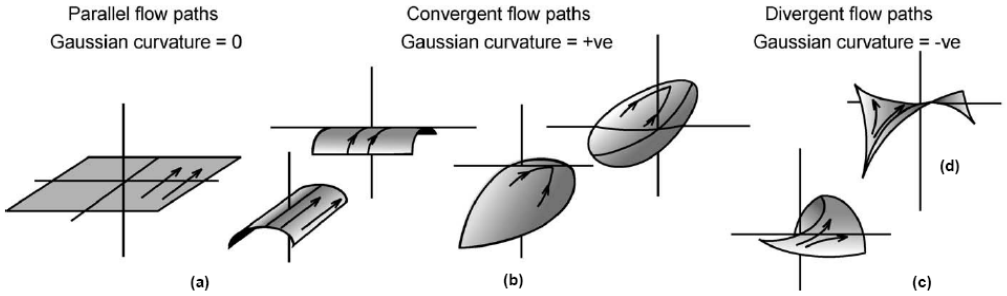

Figure 5.57: Schematic representation of the various geometries that can be obtained by combining positive, negative and zero Principal curvature axes. 5.57a is a developable flat plane, 5.57b are developable partial cylinders formed by combining one positive or negative axis with a zero axis. 5.57b and 5.57c are non-developable surfaces produced by two axes with non-zero axes of the same sign while 5.57d are saddles produced by combining two non-zero principal curvature axes with opposite signs. Arrows are shown to indicate flow paths of two points as they are translated over the surface (Wright, 2008).

In addition, Euler (1767) recognized that the normal curvature (k_n) of any section through a Gaussian curved surface is defined by the value of the two principal curvatures (k_{max} and $k_{min.}$) and the angle between the section line and the maximum principal curvature. The principal curvature orientations represent lines of zero surface torsion, τ. Surface torsion describes the rate of change of orientation of the osculating plane, the plane that passes through three points along a line that traverses a curved surface – the greater the surface torsion the more closely spaced are the three points. Thus, surface torsion is zero along lines parallel to k_{max} and k_{min} and maximal

along lines oriented 45º to them. The greater the difference between the maximum and minimum principal curvatures (k_{max} and k_{min} respectively), the higher the value of τ.

Maximum surface curvature represents surface normal with the smallest radius of curvature and hence likely to be deformed (i.e. the smaller the radius the more curved a surface is since k =1/R) (e.g. Lisle, 1994; Samson & Mallet, 1997). In previous work, the maximum curvature of horizons mapped from seismic data has been described as potentially useful in highlighting faulting (e.g. Roberts, 2001; Lisle, 1994; Samson & Mallet, 1997). The potential usefulness of the two attributes (Gaussian and maximum curvature) is the basis for dedicating a chapter to characterize the curvature of fault surfaces mapped from the seismic data. This chapter provides the database of fault surface attribute plots and with the volumetric seismic attribute data calculated in Chapter Three has set the scene for investigating potential links between fault surface morphology and the structure of the volume surrounding the faults in Chapter Six.

CHAPTER SIX: INVESTIGATING THE SEISMIC STRUCTURE OF THRUST ZONES AND LINKS WITH FAULT SURFACE MORPHOLOGY

6.1 Introduction

The focus of this chapter is to investigate the structure of the volumes surrounding thirteen thrust faults mapped in Chapter Four using seismic attribute data calculated in Chapter Three. The surface and attribute plots of the faults were calculated in Chapter Five. The ultimate objective is to investigate potential links between fault surface morphology and the structure of the volumes adjacent to the faults.

6.2 Methodology

6.2.1 Data

The database includes seismic attribute volumes (similarity and maximum curvature) calculated to enable detailed description of the seismic structure of fault zones and three-dimensional structural attribute plots of thirteen thrust faults. Detailed descriptions of the seismic attribute extraction and image enhancement workflow and analysis of the surface morphology of the faults are presented in Chapters Three and Five of this thesis respectively.

6.2.2 Workflow

The proposed workflow is summarized in Figure 6.1. The workflow primarily involves investigating the structure adjacent to several thrust faults using seismic attribute data sampled parallel and adjacent to the faults in the hanging wall and footwall based on the concept of fault slicing (Brown *et al.* 1987) modified to suit the

focus of this thesis. Finally, potential links between fault surface morphology and the structure of the volumes adjacent to the faults was investigated across thrust faults using slices of seismic attribute data sampled parallel to the faults and along reflector units in the volumes adjacent to four fault surfaces.

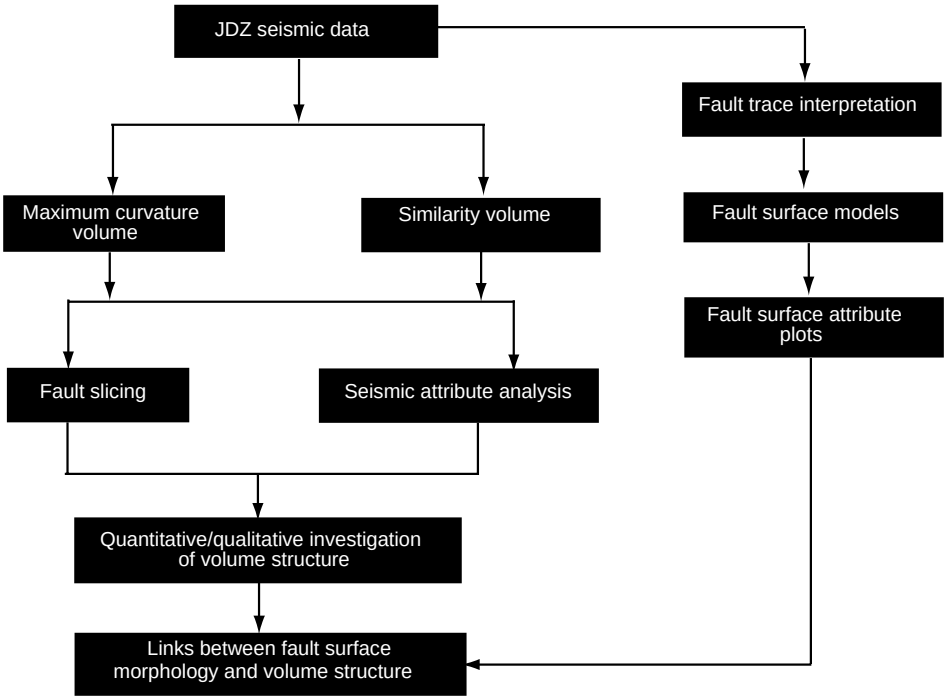

Figure 6.1: Summary of workflow for investigating the seismic structure adjacent to thrust faults and links with fault surface topography.

6.2.2.1 Structure of fault zones

Dip-steered seismic attribute volumes were calculated and imported into a *TrapTester* project. In the first stage, five slices sampled between 200 m and 1000 m through seismic attribute volumes in the hanging wall and footwall of nine faults were made and the structure adjacent to the faults analyzed based on visual seismic attribute analysis of the slices. Secondly, the structure adjacent to four faults was investigated by analyzing density plots of seismic attribute data extracted along reflector units mapped across four faults using several user-defined seismic attribute filter editors.

6.2.2.1.1 Data presentation and display

A spectrum colour bar is used to show the density of seismic attributes sampled through seismic attribute data. Density plots typically show the graphical distribution of seismic attribute data in the depth/time direction of the units. The default view is "colour- mapped" in which the data points are "binned" by the number of divisions on the plot and colour coded. High frequency colour bin is an indication of the large concentration of data points, and a low frequency is an indication of few data points or the non existance of data within the sampled interval. The colour-binned density plot is thus a three-dimensional plot of the attributes. The three axes include the x and y representing the fault attribute and the horizontal time axis, while the frequency colour bin constitutes the third axis.

6.2.2.1.2 Analysis of disruptions in thrust zones

The seismic structure adjacent to the faults was interpreted based on the fundamental assumption that plots of seismic attribute data (similarity and curvature) can provide graphical estimates of disruptions in the units adjacent to the faults. This assumption is based on the premise that anomalies in reflector curvature and similarity adjacent to faults can provide reliable estimates of disruptions that may be related to deformation in fault zones. A scale of 0 to 1 is use to analyze slices and plots of similarity data sampled adjacent to the faults. Similarity values close to 0 are interpreted as low and related to disruptions while values approaching 1 are described as high in similarity and not related to disruptions. Values between 0 and 1 are interpreted as moderate similarity. For volume maximum curvature, it is assumed that the higher the intensity of curvature (positive and negative polarity) the more the likelihood of disruptions.

Values between the extreme end members are interpreted as low curvature and not related to disruptions.

6.2.2.2 Links between fault surface morphology and volume structure

Two novel techniques are used to investigate potential links between fault surface topography and the structure of the volumes adjacent to the faults. Qualitatively, the investigation was performed by visual comparison between structural attribute models of fault surfaces (curvature and gradient of fault surface topography) and seismic attribute anomalies observed in fault slices sampled through seismic attribute data in the hanging wall and footwall 100 m parallel to nine faults (Figure 6.2a). The quantitative links between volume structure and fault surface morphology was investigated using density plots of seismic attributes extracted from reflector units sampled 50 m adjacent to four faults plotted against fault surface attribute data sampled adjacent to the units (Figure 6.2b).

6.2.2.2.1 Fault slicing

Fault slicing is an interactive method of sampling three-dimensional seismic data in the hanging wall and footwall of an interpreted fault and projected onto the fault plane in vertical depth/two way travel time (Figure 6.2). In the past, fault slicing has been used to map splinter faults adjacent to large parent faults, tracking correlative horizons across faults, in fault seal prediction and analyzing fault-fault intersections (Brown *et al*. 1987; Jev *et al*. 1993: Yielding *et al*. 1997; van der Pal, 1988; Bouvier, 1989: Dee *et al*. 2005). However, this is the first time it has been used as part of a study to investigate disruptions in thrust zones that may be related to fault surface topography.

6.2.2.2.2 Data sampling

Ideally fault slices should be extracted as close to fault surfaces as possible to obtain accurate seismic character of the volumes adjacent to faults. However, because seismic data are usually distorted near fault planes (e.g. Sheriff, 2006) and to avoid sampling potentially noisy data, the closest slice to the faults was sampled 200 m away from the faults. Three other slices were sampled at 200 m intervals (i.e. 400 m, 600 m and 800 m) in the hanging wall and footwall of four faults were used in estimating the quantitative pattern of disruption across the faults. In investigating quantitative links between fault surface morphology and the structure of the volumes adjacent to the faults, slices were sampled 50 m in the hanging wall and footwall and reflector units extracted from the slices across the faults. However, five slices sampled between 200 m and 1000 m were made adjacent to nine faults and used to describe the qualitative pattern of structure in the hanging wall and footwall of the faults.

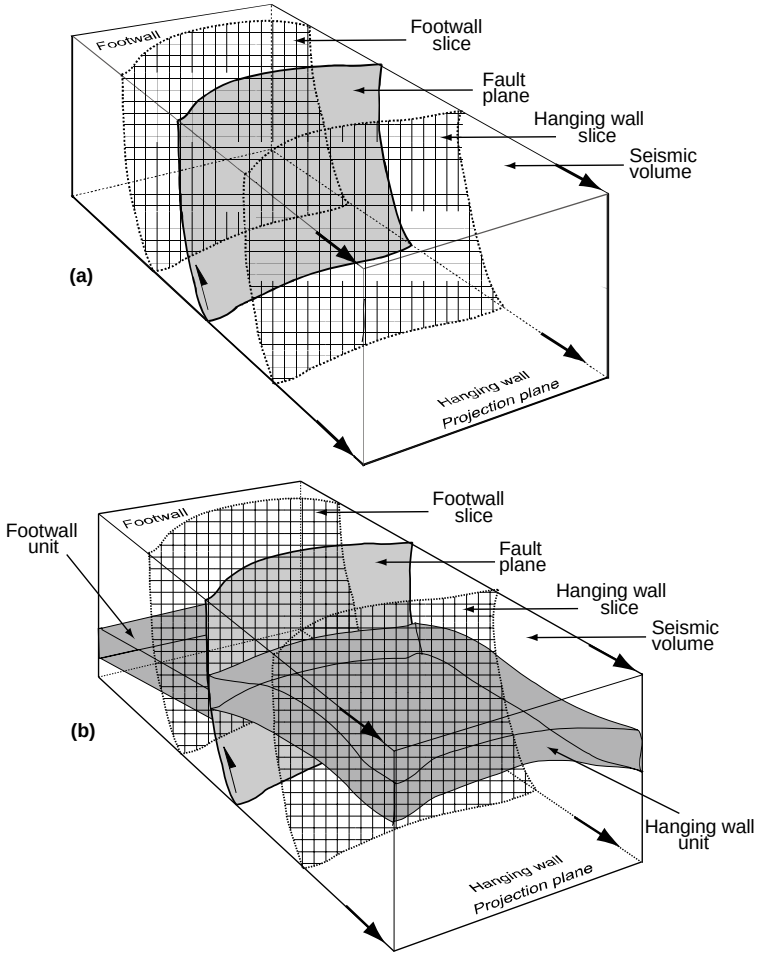

Figure 6.2: Schematic diagram illustrating the technique used to sample volume seismic data in the hanging wall and footwall of thrust fault planes based on the concept of fault slicing (Brown *et al*. 1987). In this thesis, this concept is used to qualitatively and quantitatively investigate the structure adjacent to thrust faults and potential links with fault surface morphology (Figure 6.2a and 6.2b respectively)

6.3 Description of volume structure

6.3.1 Introduction

The objective of this section is to demonstrate the basis for investigating the structure adjacent to four faults using specific reflection intervals mapped across the faults in the hanging wall and also to show how slices of the seismic attribute data can be used as proxy for small-scale disruption in fault zones. A demonstration of a typical seismic attribute response of the Niger Delta stratigraphy in the context of the

objectives of this chapter is presented in Figure 6.3 using a fault slice sampled 500 m in the hanging wall parallel to Fault A. Detailed description of the seismic stratigraphy of the study area is presented in Chapter Four.

The fault slice sampled through seismic amplitude data shows alternation of strong and continuous reflectors with transparent/weak reflections probably reflecting alternating lithologies with contrasting acoustic properties in the upper and lower parts of the slice respectively. In the same manner, two contrasting patterns of volume similarity are observed. In the predominantly strong and continuous reflection interval, similarity is high, the only exception being at the location of disruptions. The lower parts of the slices exhibits low/chaotic pattern of similarity that may reflect the response of under-compacted rocks to the attribute calculation, and not necessarily due to deformation related disruptions.

Two patterns of reflector maximum curvature are observed. In the bottom parts of the slice, a chaotic pattern of volume curvature is observed. However, curvature is coherent in the upper parts and predominantly positive in polarity. Discontinuities in the upper parts of the slices are located where similarity is low with a change in curvature polarity (Figure 6.4). The deeper parts of the slices have significant coherent and random noise and hence no meaningful interpretation of the relationship between the attributes is possible.

In the quantitative analysis of thrust zone structure, volume similarity and curvature are investigated as potential measures of deformation in only the more competent units. Discontinuous reflectors with low similarity and abrupt reversal in volume curvature polarity within the unit are assumed to be due to small-scale brittle deformation. It has been demonstrated in Chapter Four that most of the faulting is

within Unit II, interpreted as the predominantly sandy and more competent Agbada Formation equivalent in the study area (upper parts of the slices). However, where reflectors within the competent units cannot be mapped and correlated across the faults, a visual qualitative comparison between the overall pattern of fault surface topography and seismic attribute anomalies observed in the slices sampled through seismic attribute data in the hanging wall and footwall is adopted. This is the method used to analyze the internal structure across seven faults (Faults B, H, J, K, M, N & P) and in investigating links between the internal structure across the faults with fault surface morphology.

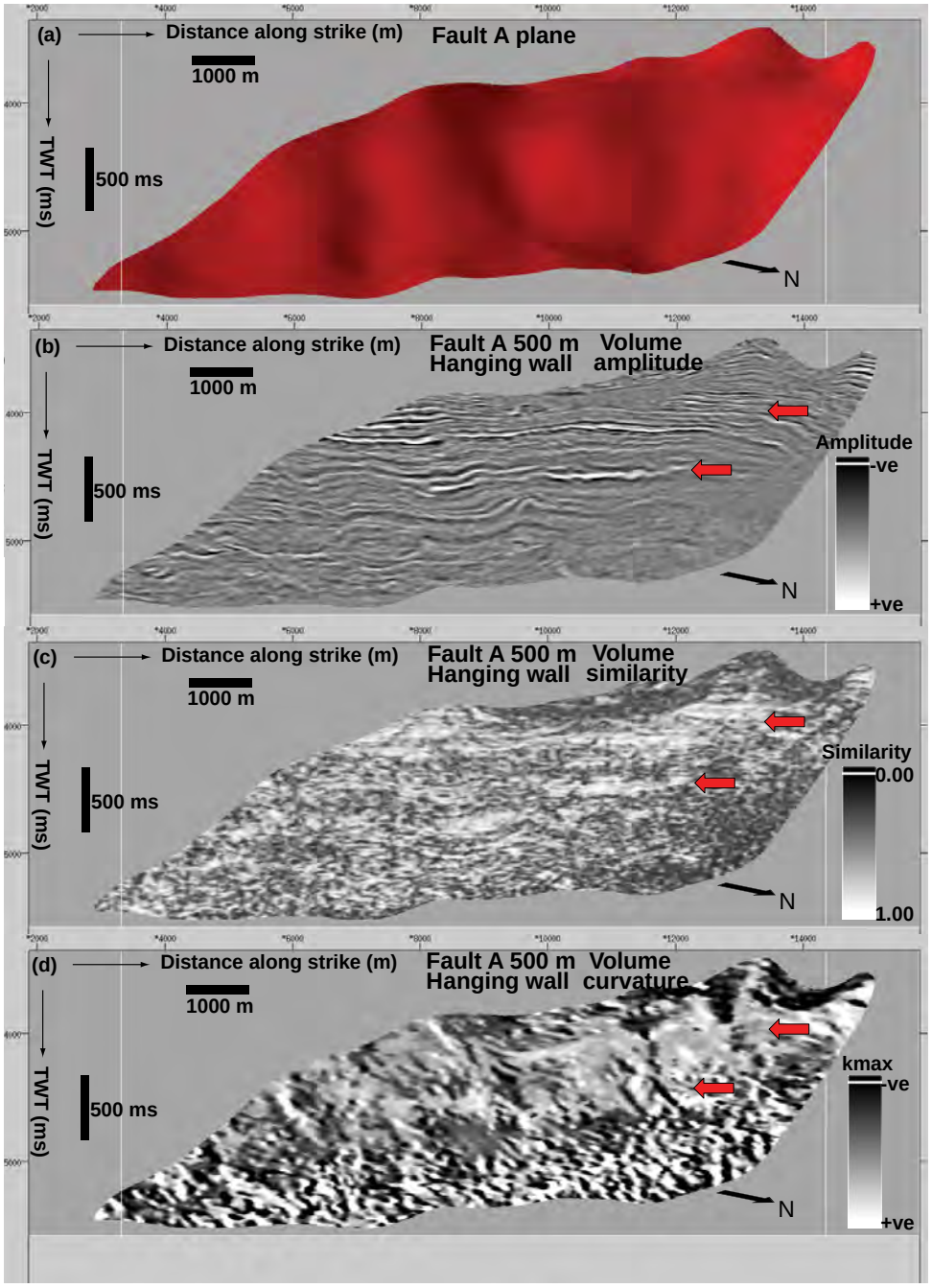

Figure 6.3: Strike views of surface model of Fault A (a), seismic amplitude slice (b), similarity slice (c) and maximum curvature slice (c). The slices were sampled through seismic attribute data 500 m parallel to a thrust fault plane in the hanging wall and projected as fault surface attributes. The block arrows show alternation of strong and weak reflections (b), high and low similarity (c) and positive and negative pattern of maximum curvature (d). The effect of noise in the deeper part of the section makes any meaningful inference impossible. Vertical scale is milliseconds two way travel time and horizontal scale is in meters. Vertical exaggeration is ~1.6.

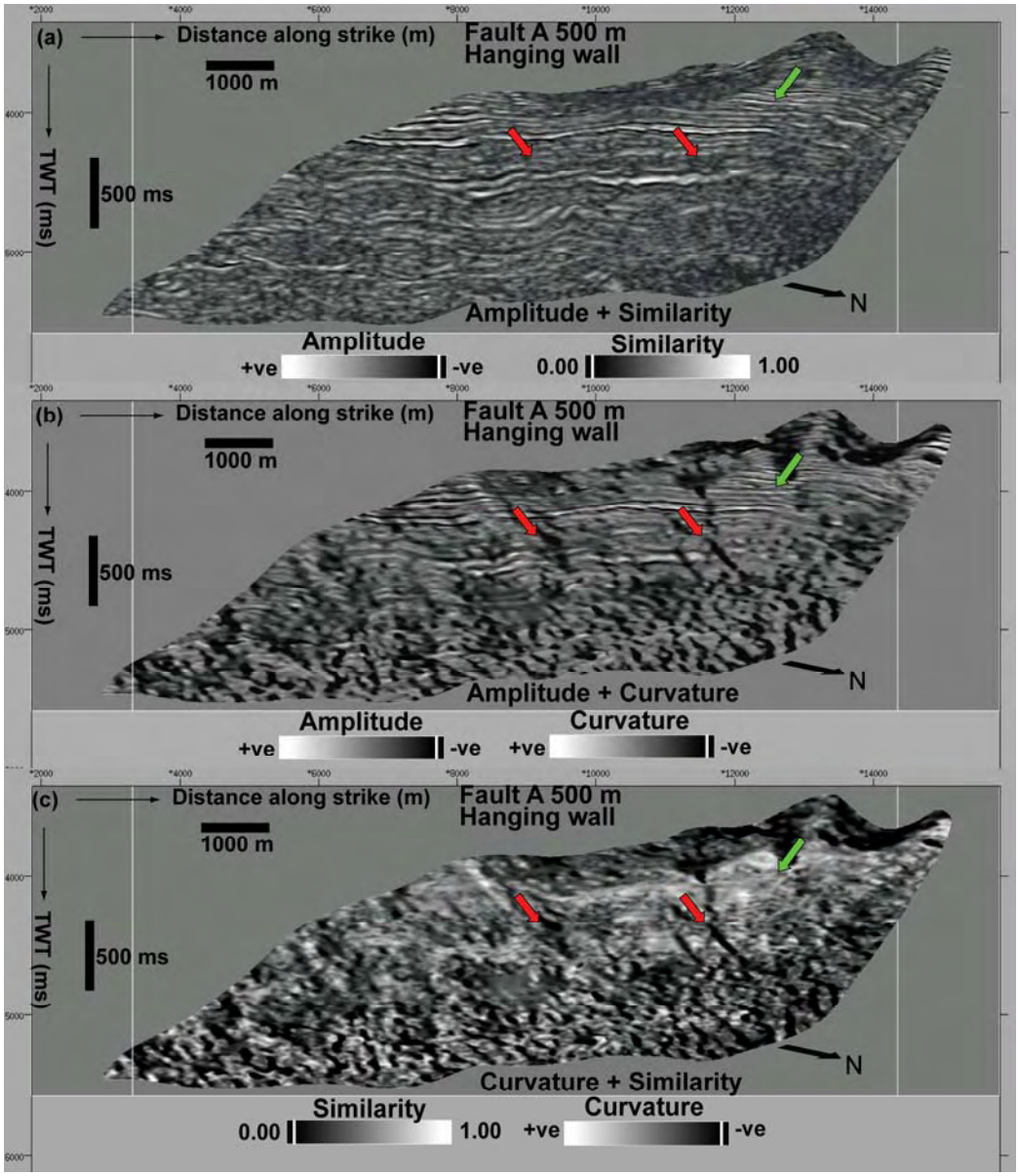

Figure 6.4: Strike views of the integration of seismic amplitude and similarity slices (a) seismic amplitude and maximum curvature slices (b) and similarity and curvature slices (c). All slices were sampled through seismic attribute volume 500 m away and parallel to Fault A in the hanging wall and projected as fault surface attributes. Note the strong correlation between discontinuous reflectors with low similarity and change in the polarity of curvature at the location of discontinuities. The pronounced positive maximum curvature at the upper parts of the slices matches strongly continuous reflections high in similarity. The effect of noise in the deeper parts of the section makes any meaningful inference impossible. Vertical scale is milliseconds two way travel time and horizontal scale is in meters. Vertical exaggeration is ~1.6.

6.3.2 Quantitative description of volume structure

6.3.2.1 Introduction

In this section, the structure adjacent to four thrust faults selected from the fault surface database are described using slices sampled through maximum curvature and similarity volumes between 200 m and 800 m in the hanging wall and footwall parallel to the faults using a sampling interval of 200 m (Faults A, G, J & L). Subsequently, slices sampled through similarity volume between 200 m and 1000 m in the hanging and footwall parallel to nine addition faults were used to describe fault zone structure (Faults B, C, H, I, K, M, M, O & P). Cross sectional geometries of these faults are presented in Figures 5.10 and 5.11 in Chapter Five. Figures 6.5, 6.7, 6.9 and 6.11 show cross sectional geometries of the four faults and the location of the hanging wall and footwall units being analyzed. Strike views of the surface models of the faults are shown in Figures 6.6, 6.8, 6.10 and 6.12.

Fault A is located in the proximal parts of the JDZ, is strongly corrugated and offset reflectors interpreted to be within Unit II equivalent of the predominantly sandy Agbada Formation (Figure 6.5). The fault has a strike length of ~12 km, a surface area of ~24 km^2 with pronounced variation in surface topography (Figure 6.6). Fault G is located in the proximal parts of the study area, has a strike length of ~9 km, a surface area of ~35 km^2 and offset reflectors in Unit II interpreted to represent the predominantly sandy Agbada Formation. In addition to corrugations parallel to fault transport direction, the fault exhibits horizontal corrugation parallel to the main corrugation axes (Figure 6.8).

Fault J was mapped from the proximal part of the study area and has fairly planar ramp geometry but strongly curved at the fault bend (Figure 6.9). The fault surface has a strike length of ~25 km, a surface area of ~30 km^2, with a highly variable pattern of topography (Figure 6.10). Fault L has a fairly planar cross sectional geometry but surface model of the fault shows a variable pattern of topography. The fault has a strike length of ~24 km and a surface area of ~72 km^2 (Figures 6.11 & 6.12).

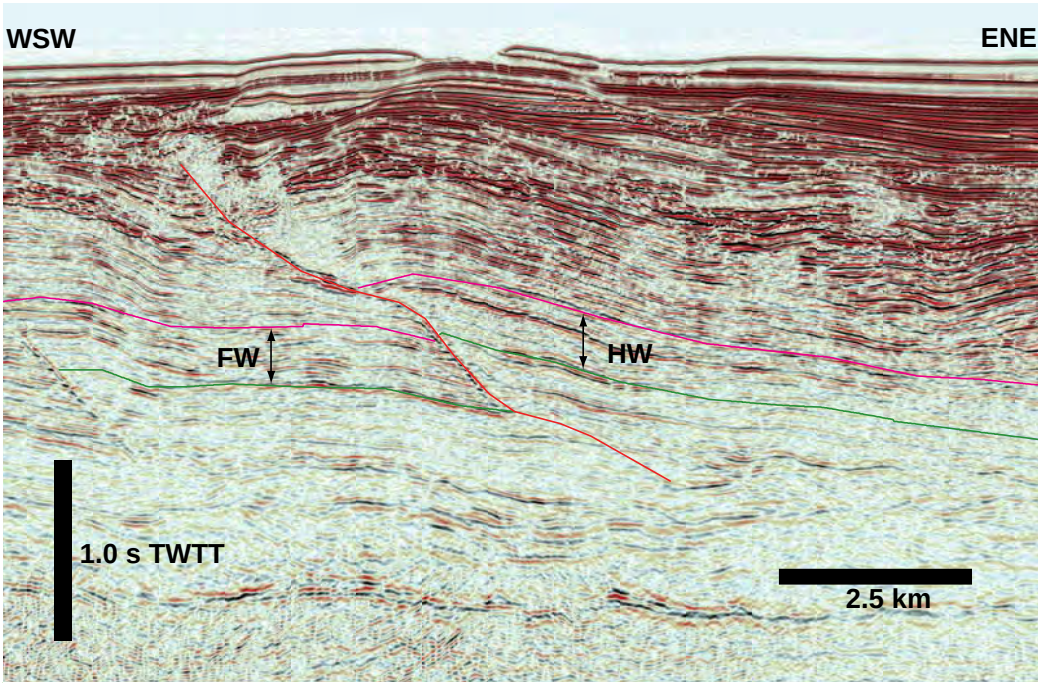

Figure 6.5: Seismic line showing the cross sectional geometry of Fault A and the hanging wall and footwall units being investigated. Vertical scale is in seconds in two way time and horizontal scale is in kilometres.

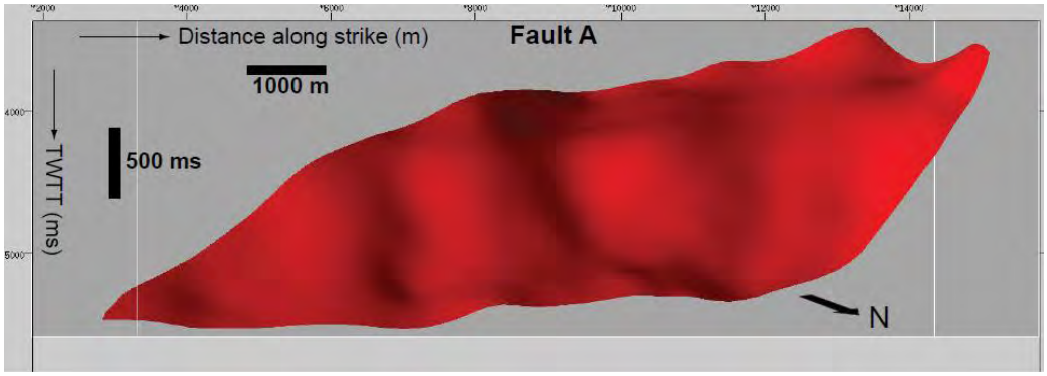

Figure 6.6: Strike view of the surface model of Fault A. Note the pronounced pattern of corrugations on the fault surface. Vertical scale is in milliseconds in two way time and horizontal scale is in meters. Vertical exaggeration is ~1.6.

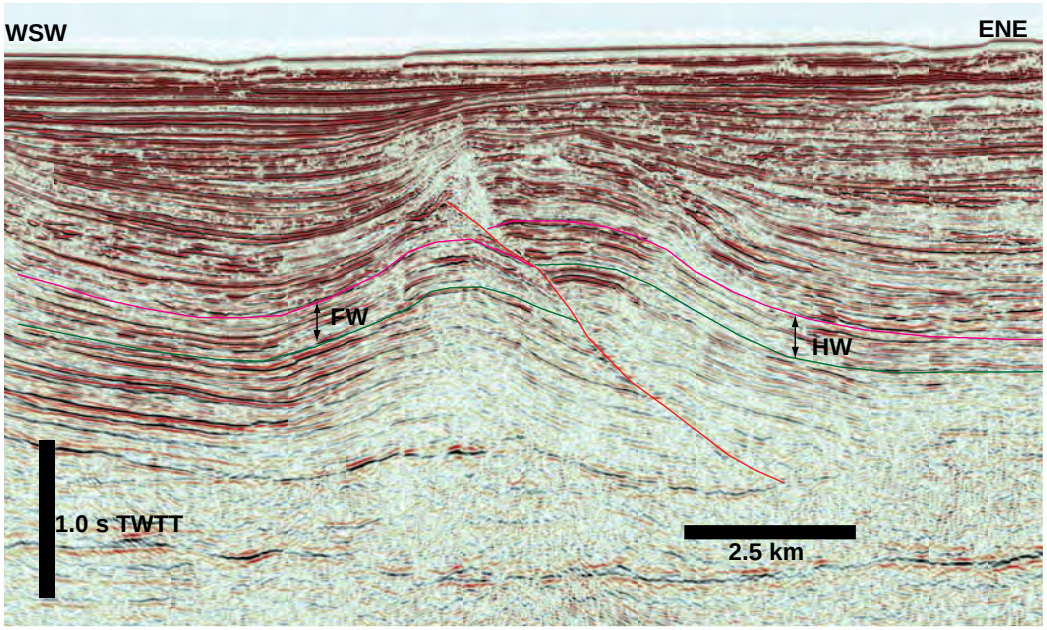

Figure 6.7: Seismic line showing the cross sectional geometry of Fault G and the hanging wall and footwall units being investigated. Vertical scale is in seconds in two way time and horizontal scale is in kilo metres.

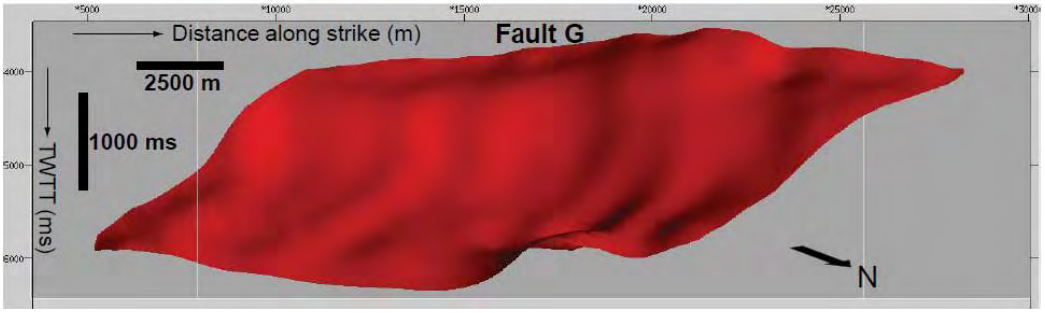

Figure 6.8: Strike view of the surface model of Fault G. Note the pronounce topography in the upper parts of the fault and the well defined groves and ridges parallel to fault dip direction. Vertical scale is in milliseconds in two way time and horizontal scale is in meters. Vertical exaggeration is ~1.6.

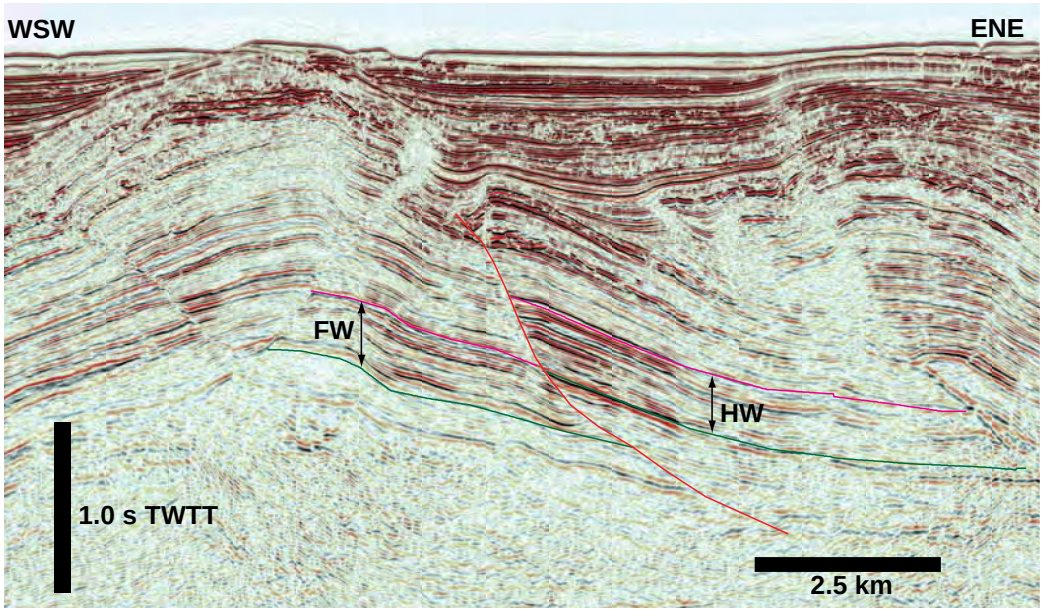

Figure 6.9: Seismic line showing the cross sectional geometry of Fault J and the hanging wall and footwall units being investigated. Vertical scale is in seconds in two way time and horizontal scale is in kilometres.

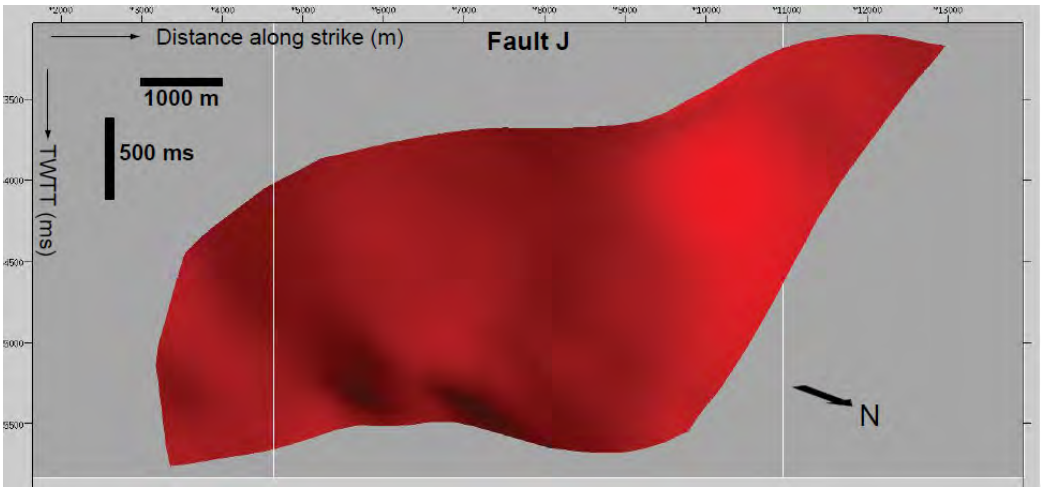

Figure 6.10: Strike view of the surface model of Fault J. Fault surface topography is fairly planar in the central parts except for localized zones of pronounced curvature in the middle parts of the surface. Vertical scale is in milliseconds in two way time and horizontal scale is in meters. Vertical exaggeration is ~1.6.

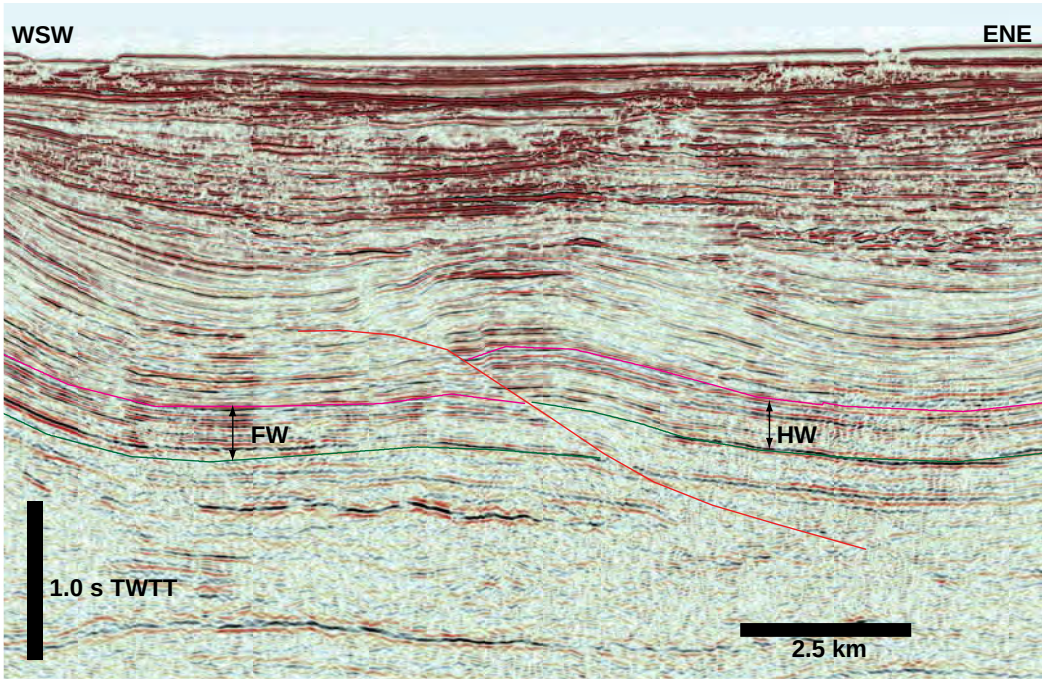

Figure 6.11: Seismic line showing the cross sectional geometry of Fault L and the hanging wall and footwall units being investigated. Vertical scale is in seconds in two way time and horizontal scale is in kilometres.

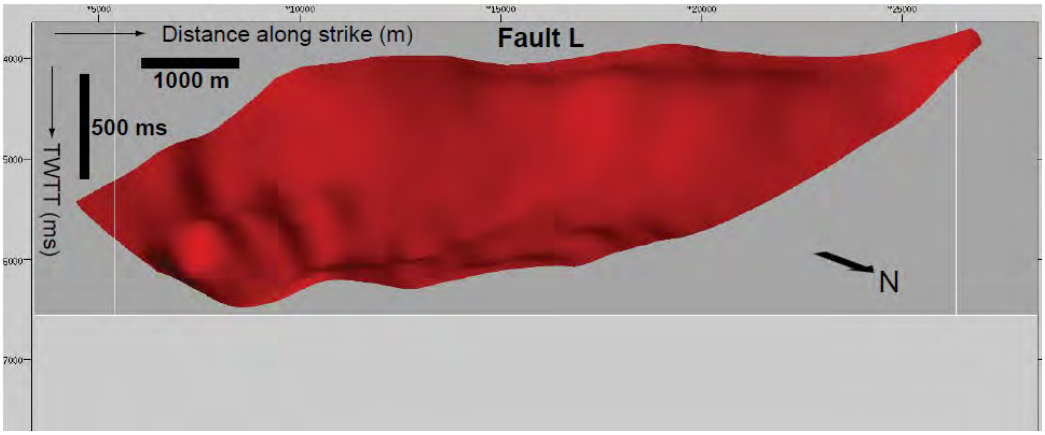

Figure 6.12: Strike view of the surface model of Fault L. Note the pronounced topography in the upper parts of the surface. Vertical scale is in milliseconds in two way time and horizontal scale is in meters. Vertical exaggeration is ~1.6.

6.3.2.2 Volume maximum curvature

Figures 6.13 and 6.14 shows volume maximum curvature slices sampled in the hanging wall and footwall parallel to Fault A. Density plots of the attribute extracted in the hanging wall and footwall units correlated across the faults are presented in Figures 6.15 and 6.16.

Qualitatively in the hanging wall near the fault plane, a high frequency change in curvature pattern is observed. But away from the fault plane, volume curvature is predominantly positive especially at the top halves of the slices, indicating convex up folding in the hanging wall. In the footwall, curvature is generally more coherent especially at the top halves of the slices when compared to the hanging wall. The variation in magnitude of positive volume maximum curvature in the footwall is probably an indication of folding of the units as the distance away from the fault increases.

In Fault G, volume curvature is high and predominantly positive in polarity especially in the top halves of the slices in the hanging wall (Figure 6.17). The coherent pattern of curvature at the top halves of the slice coincides with the location of a fault bend and a major source of horizontal corrugation seen in the curvature plot of the fault in Chapter Five. Volume curvature in the bottom halves is random and hardly interpretable. In the footwall, the curvature pattern is similar to that in the hanging wall except that it is less coherent in the upper parts of the slices. The bottom parts exhibit random pattern of curvature (Figure 6.18).

In Fault J, volume curvature is low in all the hanging wall and footwall slices except along a discrete zone exhibiting fairly coherent pattern of curvature where there is an

abrupt change in fault strike. Otherwise, the fault surface is generally planar (Figure 6.21 & 6.22). In Fault L, curvature of predominantly positive polarity is high in the upper parts of the slices as the distance away from the fault surface increases. The curvature pattern in the footwall is similar to that in the hanging wall except that it is less coherent in the upper parts and random in the lower parts of all the slices (Figures 6.25 & 6.26).

Graphically in Fault A, the unit is characterized by high absolute maximum curvature close to the fault (Figure 6.15a). Away from the fault plane towards 800 m, volume curvature is predominantly positive, implying folding of the units (Figure 6.15d). In the vicinity of the fault plane in the footwall, absolute volume maximum curvature is equally high but low in density compared to the hanging (Figure 6.16a). However, as the distance away from the fault plane increases to 800 m, the units appear to be folded as shown by the consistently high density of positive volume maximum curvature (Figure 6.16d).

In Fault G, the polarity of curvature is predominantly negative in the hanging wall close to the fault, but at 400 m curvature is both positive an negative. However as the distance away from the fault increases, curvature is largely positive in polarity (Figure 6.19). In the footwall, volume curvature is higher as shown by the high density of both positive and negative maximum curvature (Figure 6.20). In Fault J, volume maximum curvature is low in the hanging wall and footwall as shown by the fairly uniform low magnitudes of curvature (Figures 6.23 7 6.24). In Fault L, near the fault in the hanging wall curvature is both positive and negative in polarity but predominantly positive as the distance away from the fault increases (Figure 6.27). In the footwall, a similar pattern of curvature is seen near the fault, but as the distance

away from the fault increases curvature is predominantly negative in polarity with lower density compared to the hanging wall (Figure 6.28).

6.3.2.3 Interpretation

The high absolute volume maximum curvature (positive and negative in polarity) in the hanging wall and footwall of Fault A near the fault plane may be due to disruption related to small-scale deformation. This observation is further confirmed by the discontinuous pattern of seismic reflection near the fault in both the hanging wall and footwall in Figure 6.5. Away from the fault plane, the predominantly positive polarity of volume maximum curvature indicates the folding of the units. Similarly the high curvature near the fault surface in Fault G may be an indication of deformation, but as the distance away from the fault plane increases the pattern of curvature is largely a reflection of the convex-up geometry of the reflectors (i.e. folding), but in the footwall away from the fault the geometry of the reflectors is concave-up.

In Fault J, reflector curvature near the fault plane in the hanging wall and footwall is low compared to the same location in Fault A. This observation is further confirmed by the relatively strong and continuous pattern of reflectivity adjacent to the fault trace in Figure 6.7, implying insignificant disruption close to the fault and away from the fault in the hanging wall and footwall. In Fault L, volume curvature is high in both the hanging wall and footwall near the fault plane and polarity is both positive and negative, implying that reflectors close to the fault may have been disrupted. Away from the fault plane in the hanging wall volume curvature is predominantly positive but negative and positive in the footwall and reflects the geometry of the reflectors.

In general, the high frequency change in the polarity of curvature is related to disruption s while a unimodal pattern of curvature is related to reflector geometry. In Chapter three, it has been demonstrated that curvature has two anomalies at the location of discontinuities (positive and negative curvatures on either sides of a discontinuity). This analysis shows that the attribute is primarily a good proxy for reflector geometry. However, since most folded surfaces end up being faulted, it may still be useful in combination with another attribute that can detect the continuity or discontinuity of reflectors. In the next section, results from an alternative seismic attribute (similarity) applied to analyze the internal structure adjacent to the faults are shown and described.

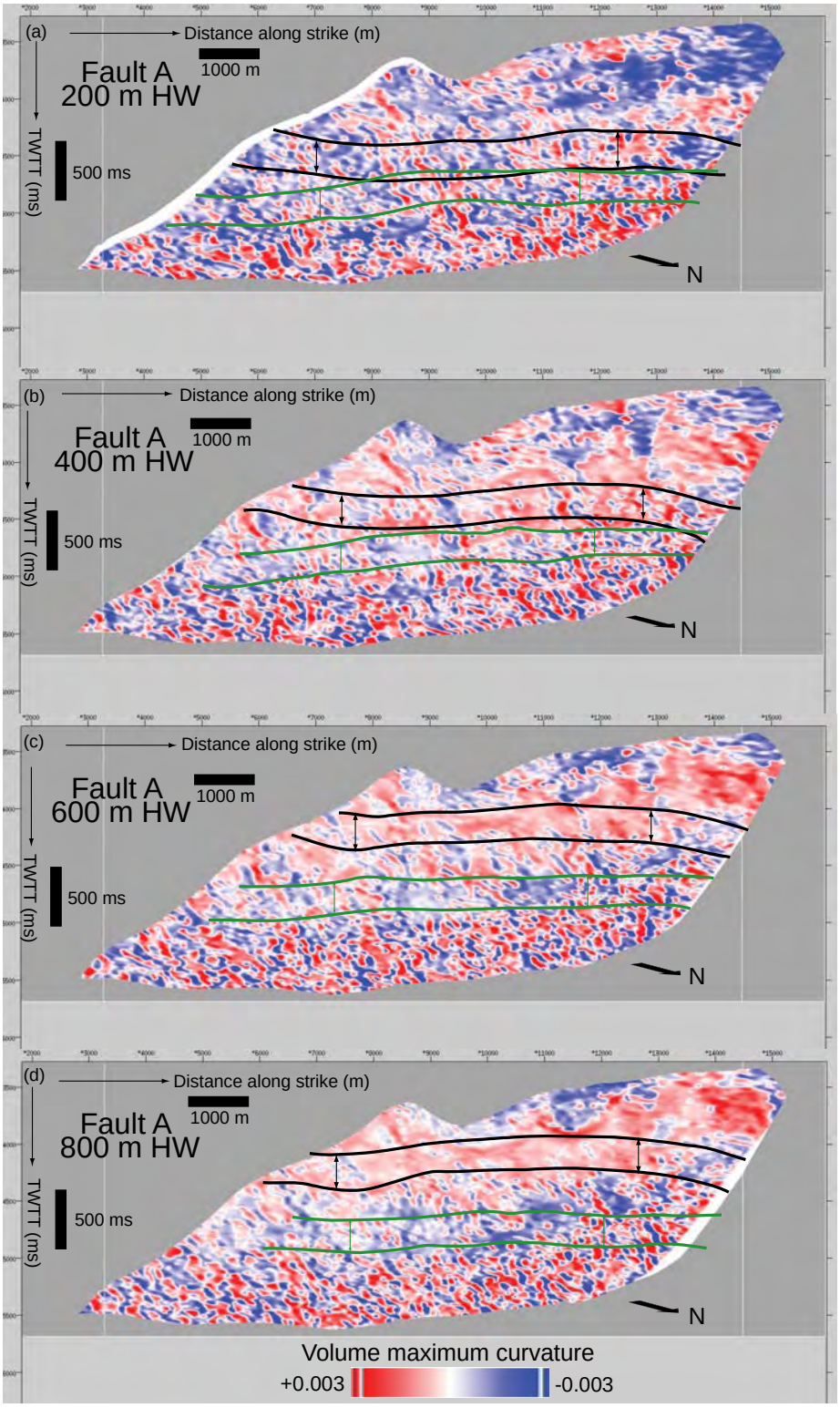

Figure 6.13: Strike views of maximum curvature slices sampled through maximum curvature volume at 200 m (a), 400 m (b), 600 m (c) and 800 m (d) in the hanging wall parallel to Fault A and projected as fault surface attribute. The black lines represent the hanging wall unit graphically analyzed in Figure 6.15, while the green lines represent projection of the footwall unit in the hanging wall. Note the gradual increase in the intensity of positive curvature away from the fault plane. Vertical scale is in milliseconds in two way travel time and horizontal scale is in meters. Vertical exaggeration is ~1.6.

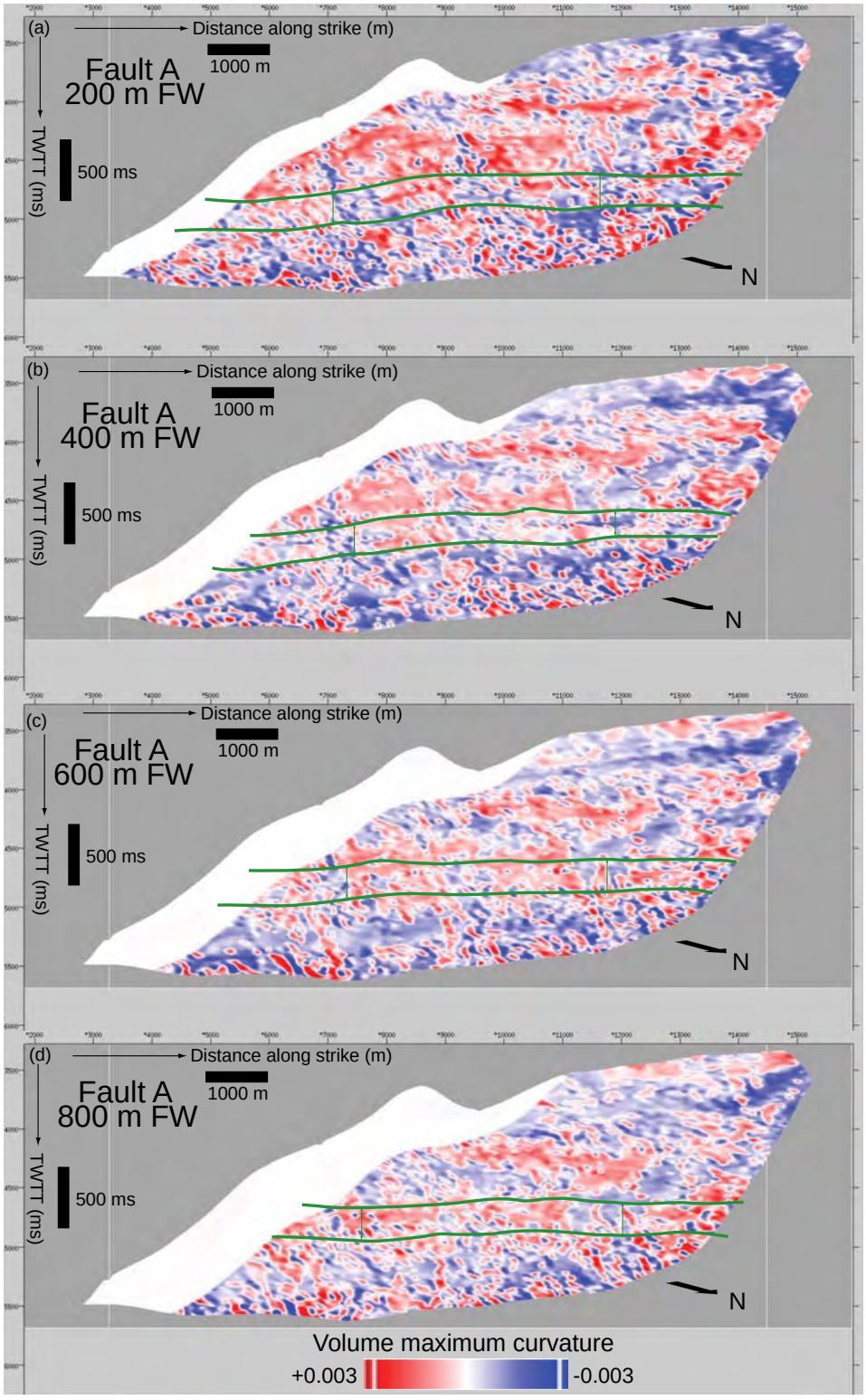

Figure 6.14: Strike views of maximum curvature slices sampled through maximum curvature volume parallel to Fault A at 200 m (a), 400 m (b), 600 m (c) and 800 m (d) in the footwall and projected as fault surface attribute. The green lines represent the footwall unit graphically analyzed in Figure 6.16. Note the high positive maximum curvature in all the slices in the footwall. Vertical scale is in milliseconds in two way travel time and horizontal scale is in meters. Vertical exaggeration is ~1.6.

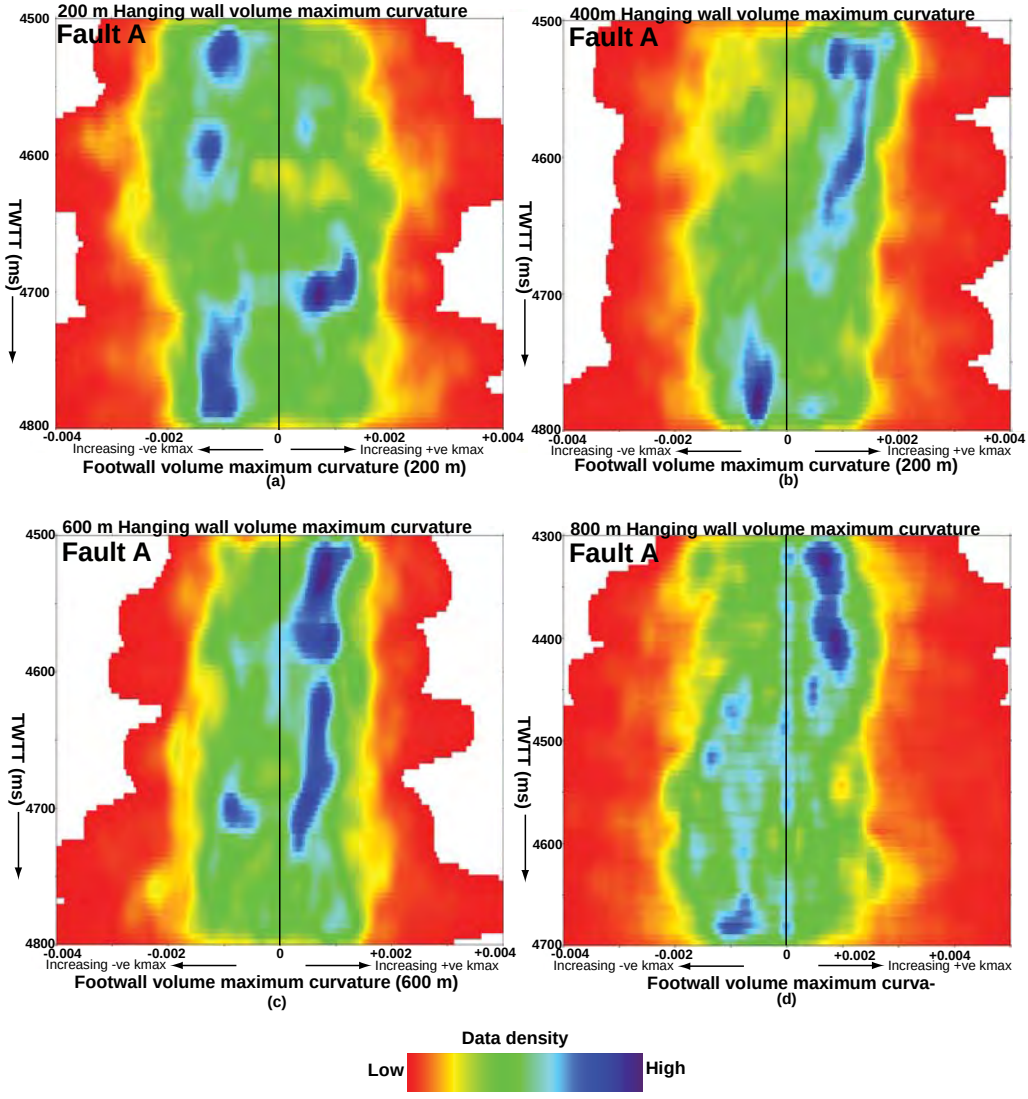

Figure 6.15: Density plots of volume maximum curvature sampled at 200 m (a), 400 m (b), 600 m (c) and 800 m (d) in the hanging wall of Fault A. The plots are quantitative estimates of volume maximum curvature extracted from the hanging wall units in Figure 6.13. The purple and red shades represent high and low density of curvature data respectively. Note the juxtaposition of high density positive and negative maximum curvature near the fault and the high density of positive maximum curvature towards 800 m. Vertical scale is in milliseconds in two-way-time.

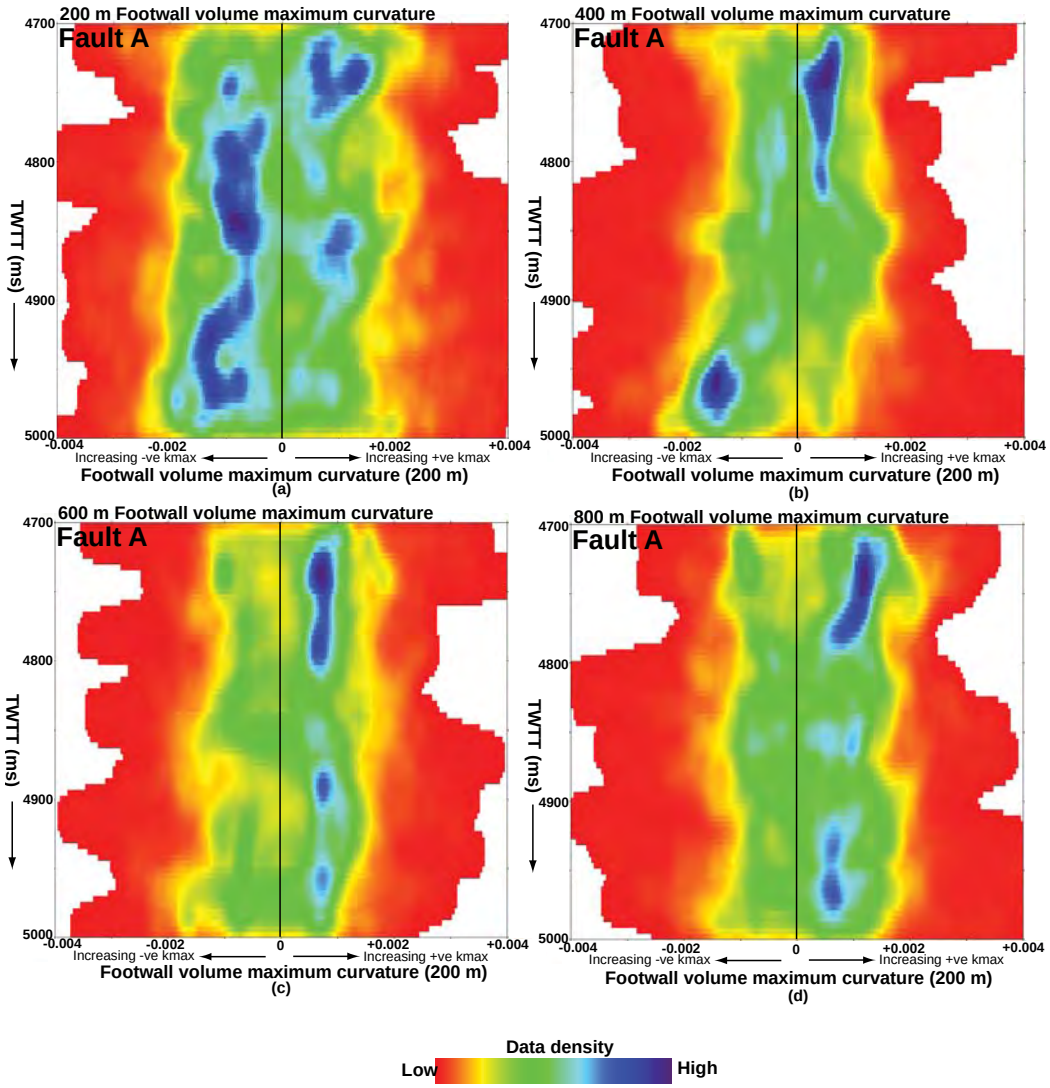

Figure 6.16: Density plots of volume maximum curvature sampled at 200 m (a), 400 m (b), 600 m (c) and 800 m (d) in the footwall of Fault A. The plots are quantitative estimates of volume maximum curvature extracted from the footwall units in Figure 6.14. The purple and red shades represent high and low density of curvature data respectively. Note the high density of positive and negative maximum curvature near the fault plane and the high density of positive maximum curvature as the distance away from the fault plane increases to 800 m. Vertical scale is in milliseconds in two-way-time.

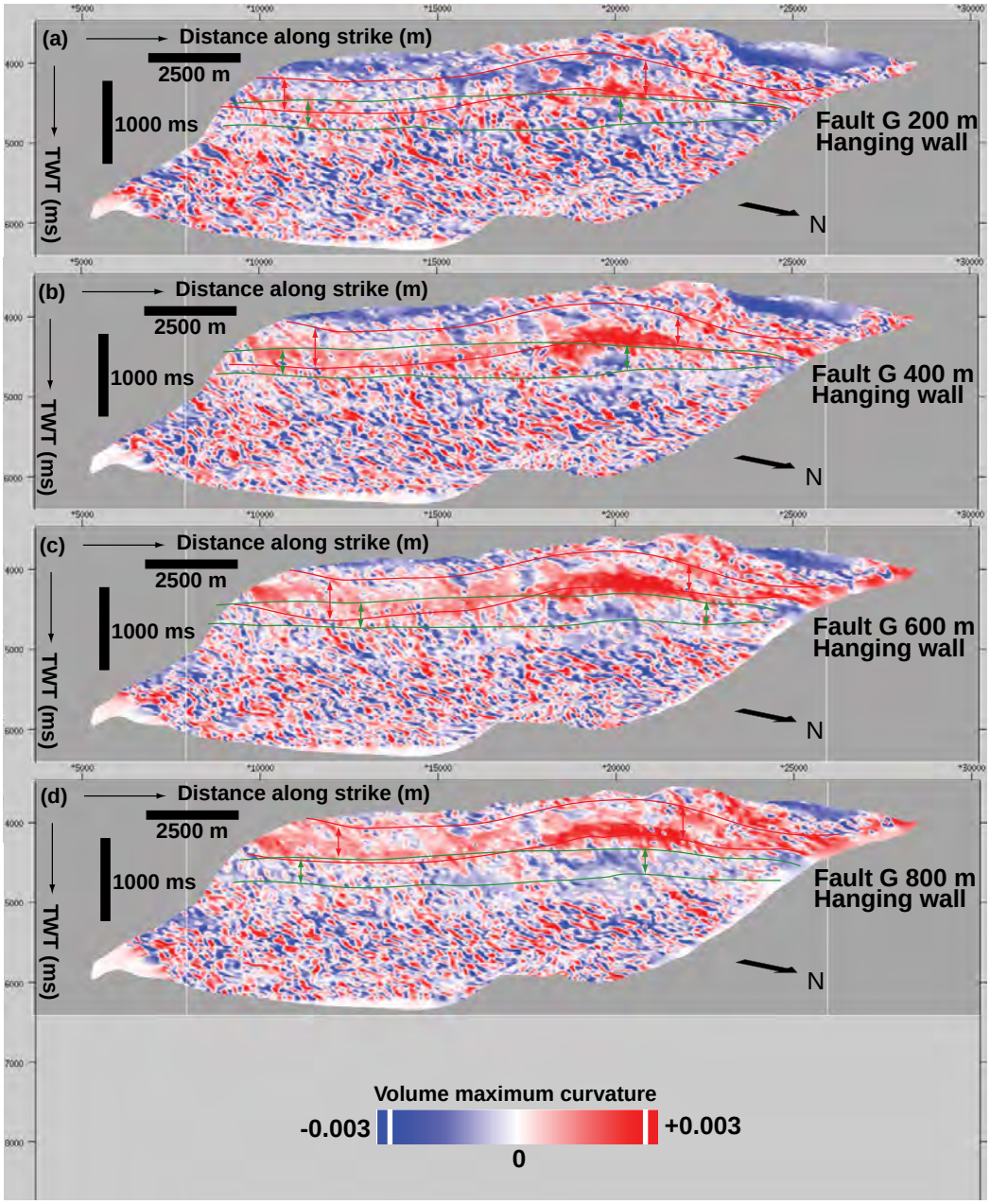

Figure 6.17: Strike views of maximum curvature slices sampled through maximum curvature volume at 200 m (a), 400 m (b), 600 m (c) and 800 m (d) in the hanging wall parallel to Fault G and projected as fault surface attribute. The red lines represent the hanging wall unit graphically analyzed in Figure 6.19, while the green lines represent projection of the footwall unit in the hanging wall. Note the gradual increase in the intensity of positive curvature away from the fault plane in the upper halves of the slices. Vertical scale is in milliseconds in two way travel time and horizontal scale is in meters. Vertical exaggeration is ~1.6.

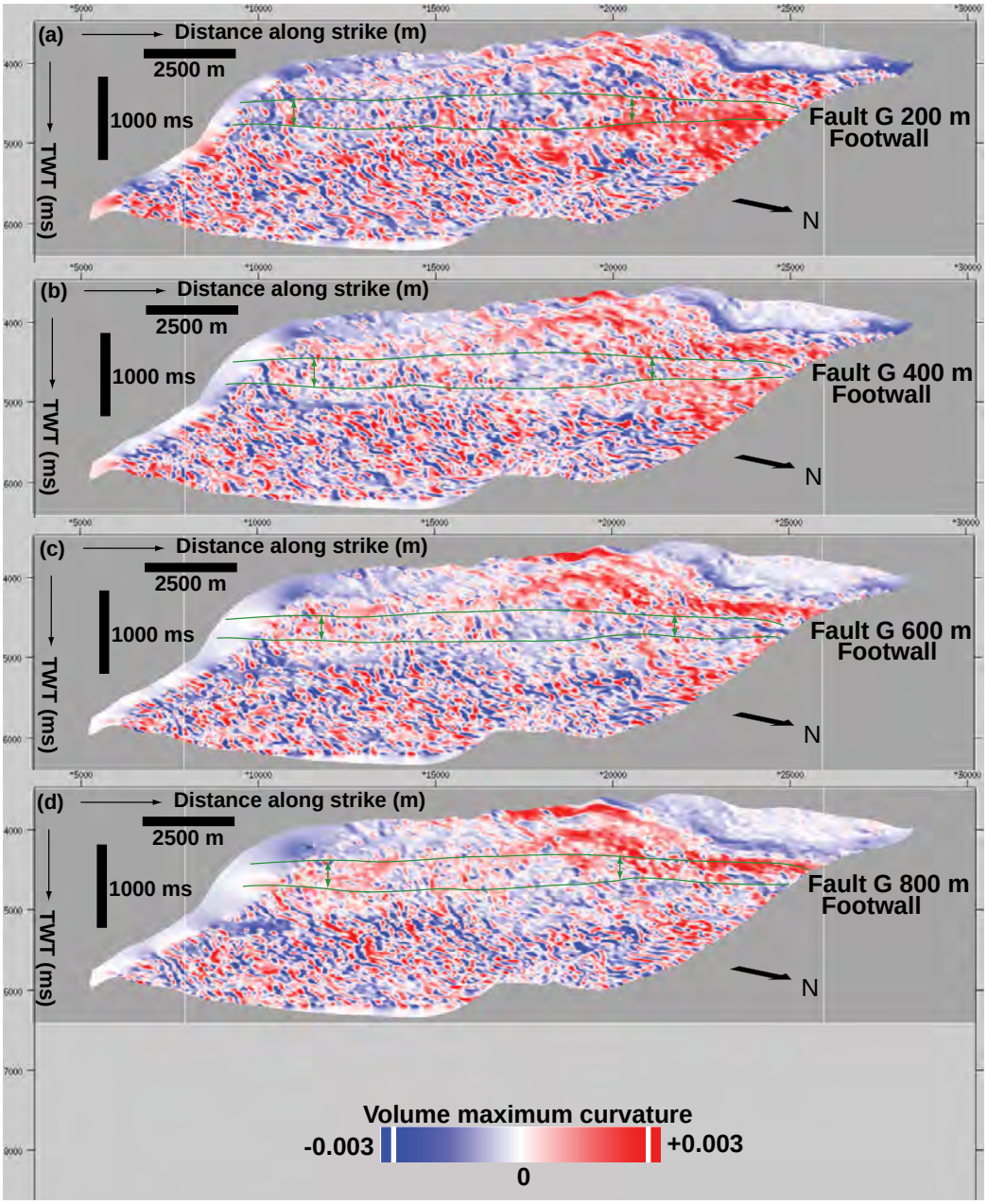

Figure 6.18: Strike views of maximum curvature slices sampled through maximum curvature volume parallel to Fault G at 200 m (a), 400 m (b), 600 m (c) and 800 m (d) in the footwall of Fault G and projected as fault surface attribute. The green lines represent the footwall unit graphically analyzed in Figure 6.20. Note the random pattern of curvature in all the slices. Vertical scale is in milliseconds in two way travel time and horizontal scale is in meters. Vertical exaggeration is ~1.6.

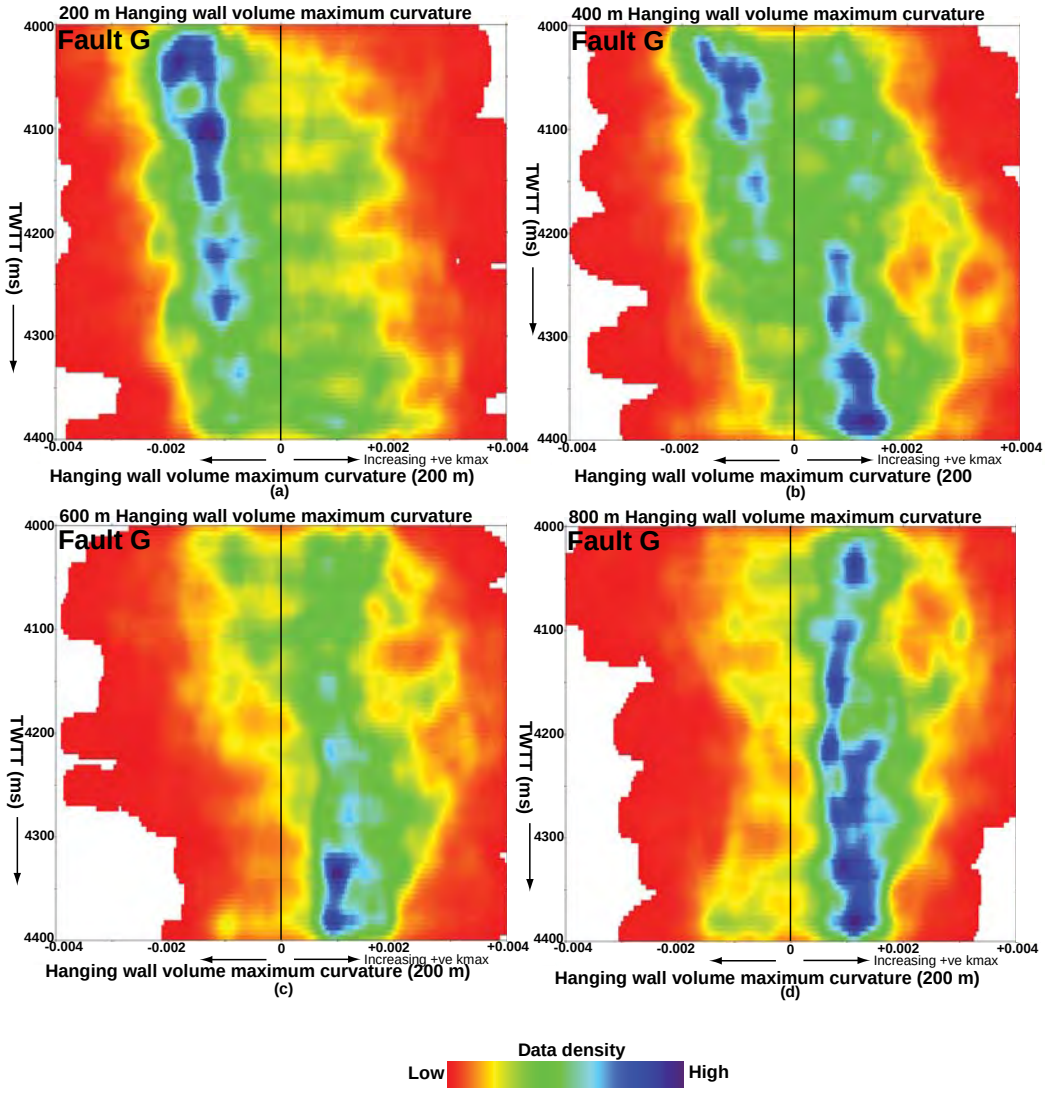

Figure 6.19: Density plots of volume maximum curvature sampled at 200 m (a), 400 m (b), 600 m (c) and 800 m (d) in the hanging wall of Fault G. The plots are quantitative estimates of volume maximum curvature extracted from the hanging wall units in Figure 6.17. The purple and red shades represent high and low density of curvature data respectively. Note the juxtaposition of high density positive and negative maximum curvature at 400 m and the high density of positive maximum curvature towards 800 m. Vertical scale is in milliseconds in two way time.

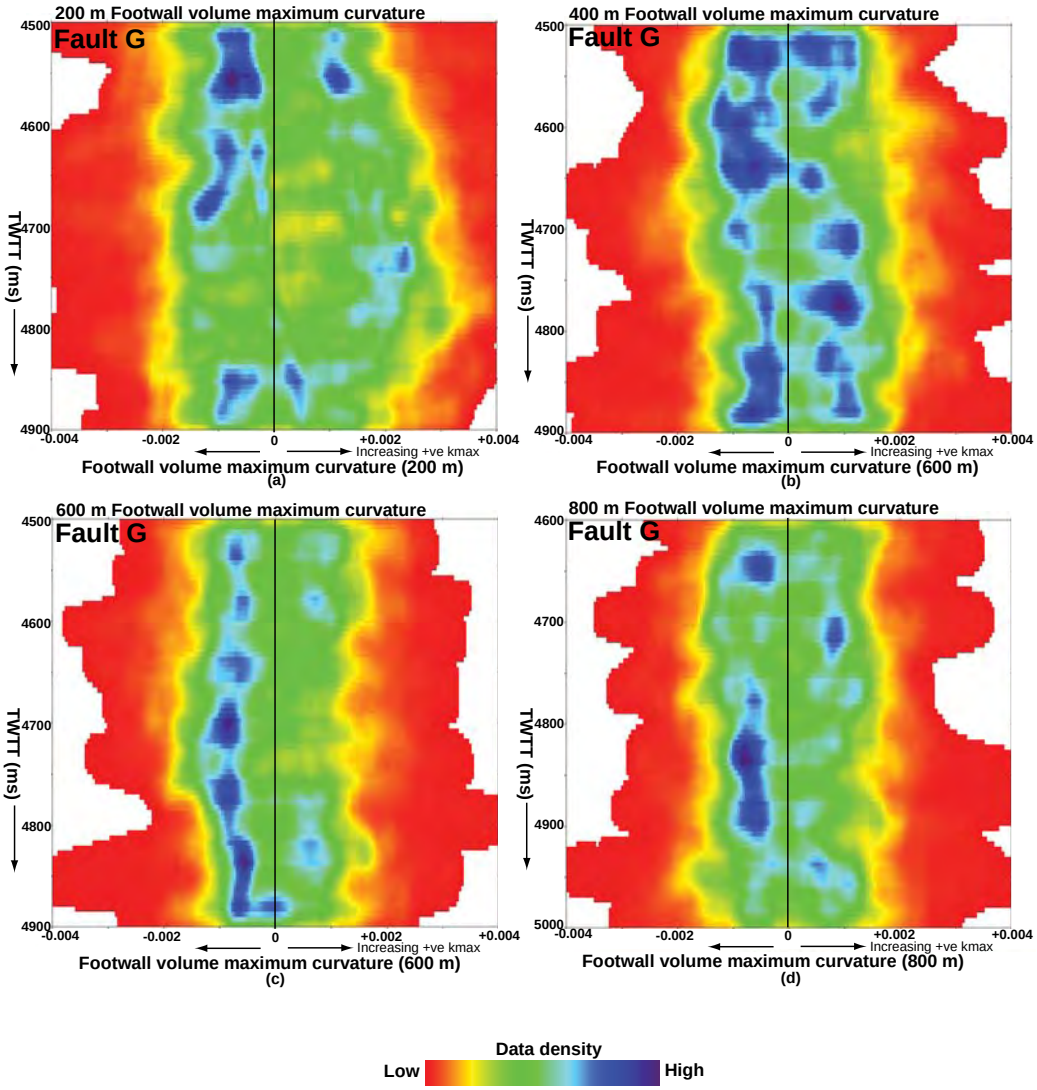

Figure 6.20: Density plots of volume maximum curvature sampled at 200 m (a), 400 m (b), 600 m (c) and 800 m (d) in the footwall of Fault G. The plots are quantitative estimates of volume maximum curvature extracted from the hanging wall units in Figure 6.18. The purple and red shades represent high and low density of curvature data respectively. Note the juxtaposition of high density positive and negative maximum curvature near the fault surface and the preponderance of negative maximum curvature away from the fault. Vertical scale is in milliseconds in two way time.

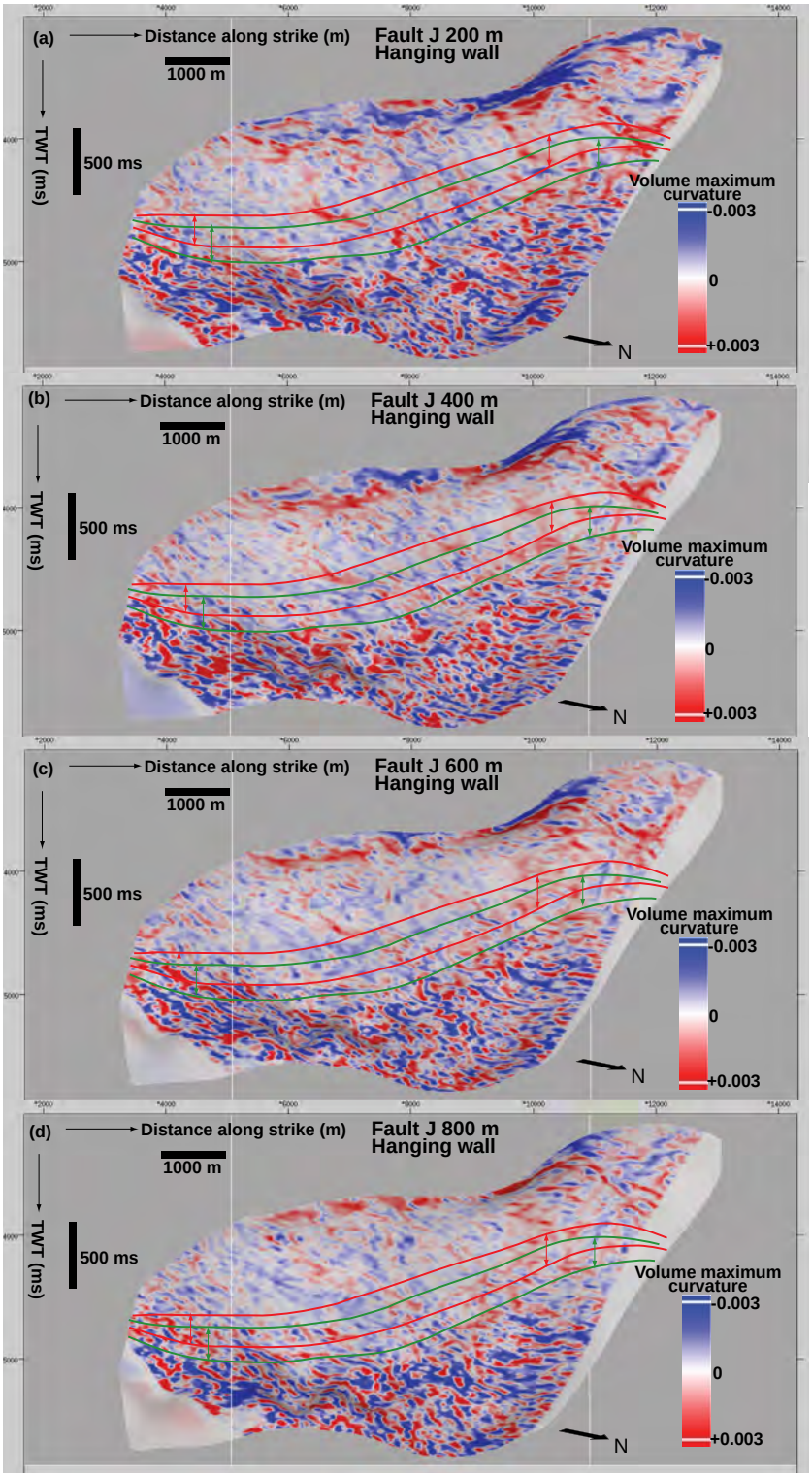

Figure 6.21: Strike views of maximum curvature slices sampled through maximum curvature volume at 200 m (a), 400 m (b), 600 m (c) and 800 m (d) in the hanging wall parallel to Fault J and projected as fault surface attribute. The red lines represent the hanging wall unit quantitatively analyzed in Figure 6.23, while the green lines represent projection of the footwall unit in the hanging wall. Note the random pattern of curvature in all the slices. Vertical scale is in milliseconds in two way travel time and horizontal scale is in meters. Vertical exaggeration is ~1.6.

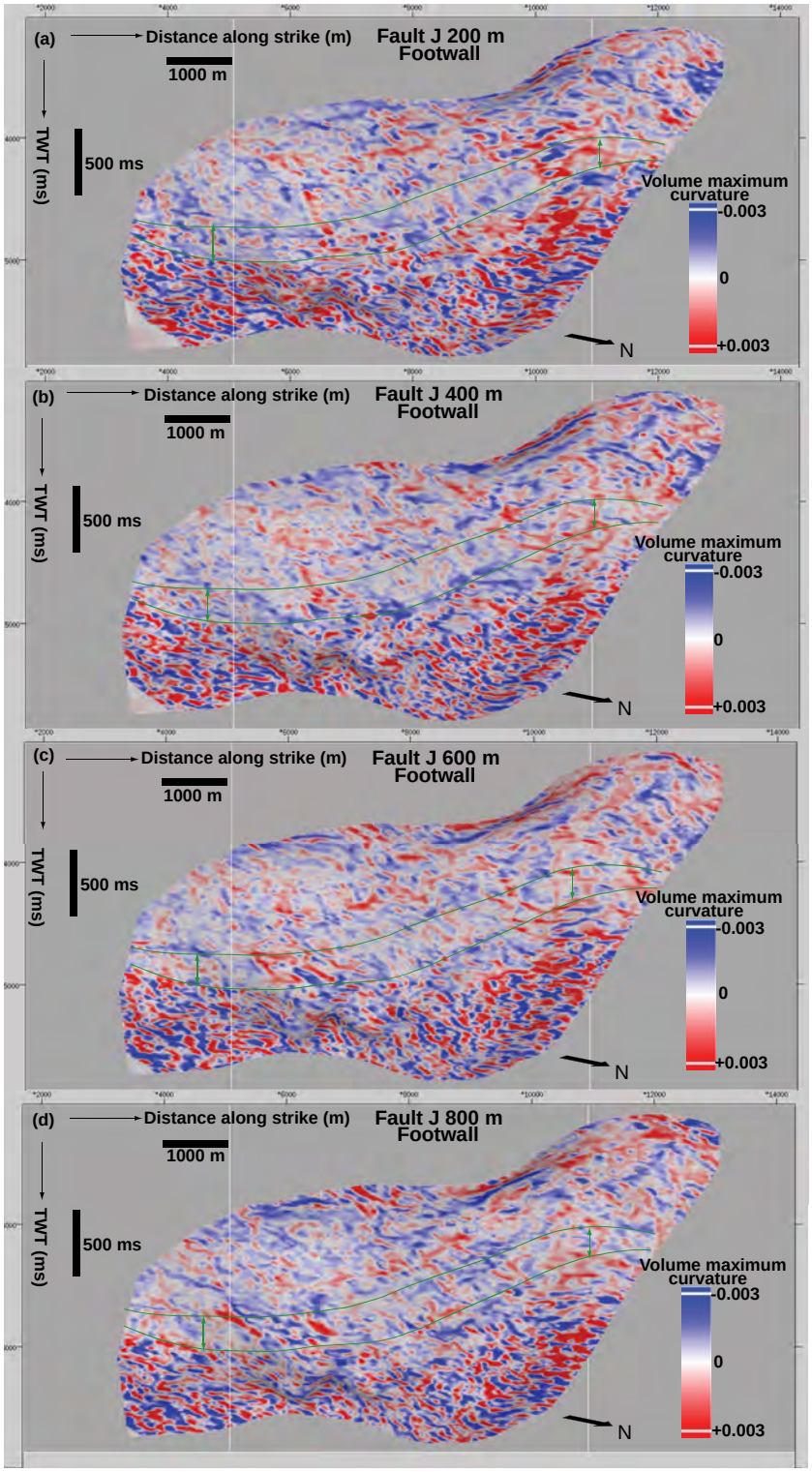

Figure 6.22: Strike views of maximum curvature slices sampled through maximum curvature volume at 200 m (a), 400 m (b), 600 m (c) and 800 m (d) in the hanging wall parallel to Fault J and projected as fault surface attribute. The green lines represent the location of the footwall unit quantitatively analyzed in Figure 6.24. Note the random pattern of curvature in all the slices. Vertical scale is in milliseconds in two way travel time and horizontal scale is in meters. Vertical exaggeration is ~1.6.

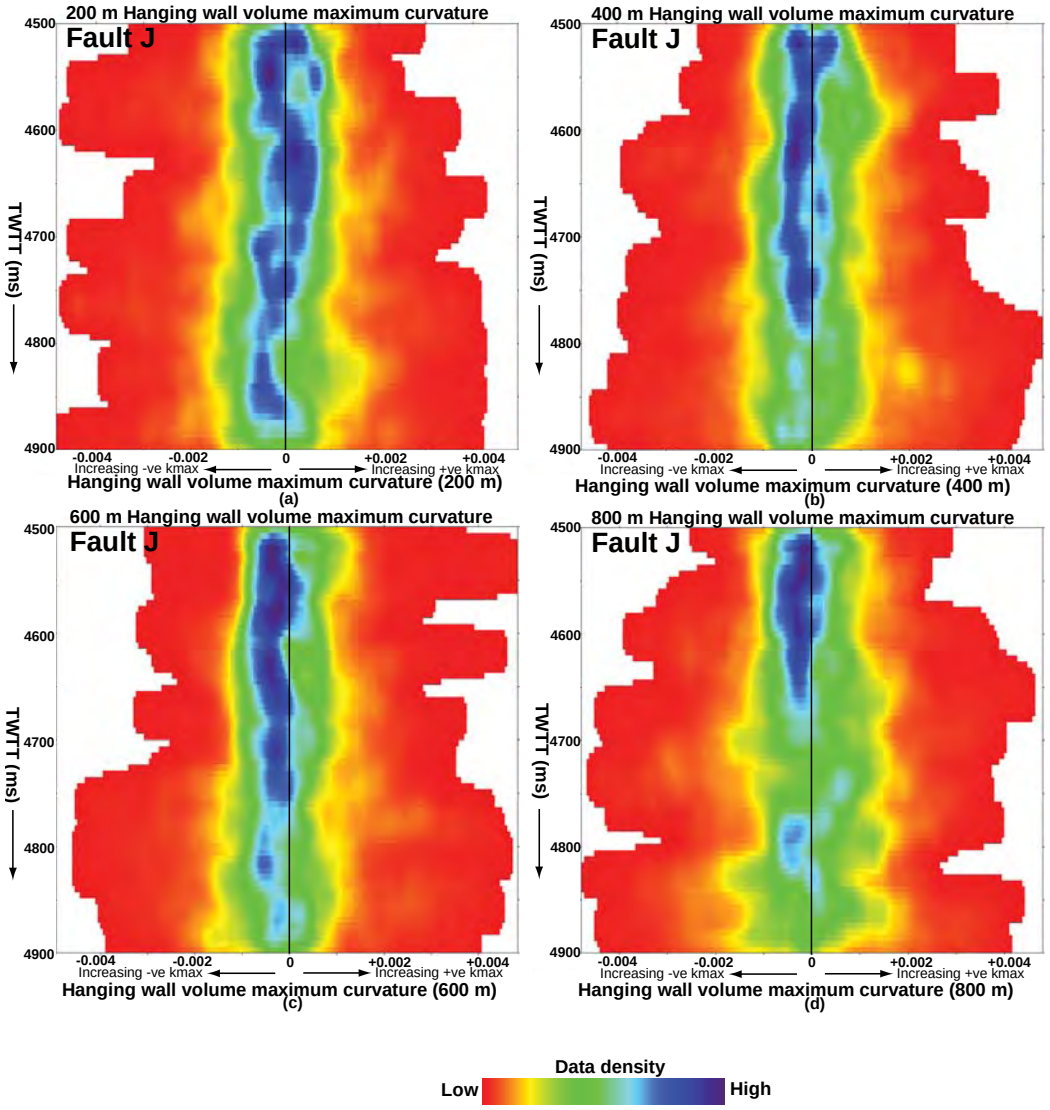

Figure 6.23: Density plots of volume maximum curvature sampled at 200 m (a), 400 m (b), 600 m (c) and 800 m (d) in the hanging wall of Fault J. The plots are quantitative estimates of volume maximum curvature extracted from the hanging wall units in Figure 6.21. The purple and red shades represent high and low density of curvature data respectively. Note the high density of low magnitudes of volume curvature in all the slices. Vertical scale is in milliseconds in two way time.

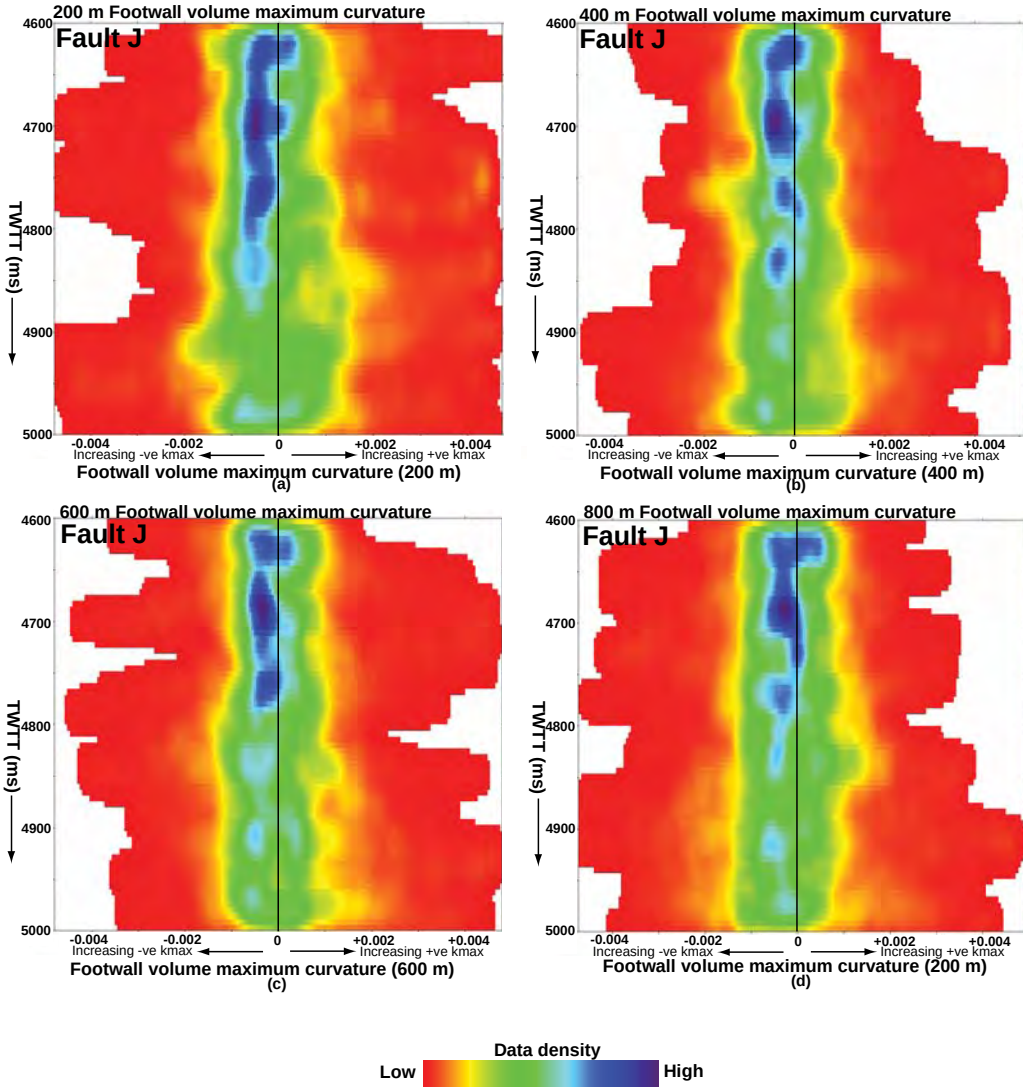

Figure 6.24: Density plots of volume maximum curvature sampled at 200 m (a), 400 m (b), 600 m (c) and 800 m (d) in the footwall of Fault J. The plots are quantitative estimates of volume maximum curvature extracted from the hanging wall units in Figure 6.22. The purple and red shades represent high and low density of curvature data respectively. Note the high density of low magnitude volume curvature in all the plots. Vertical scale is in milliseconds in two way time.

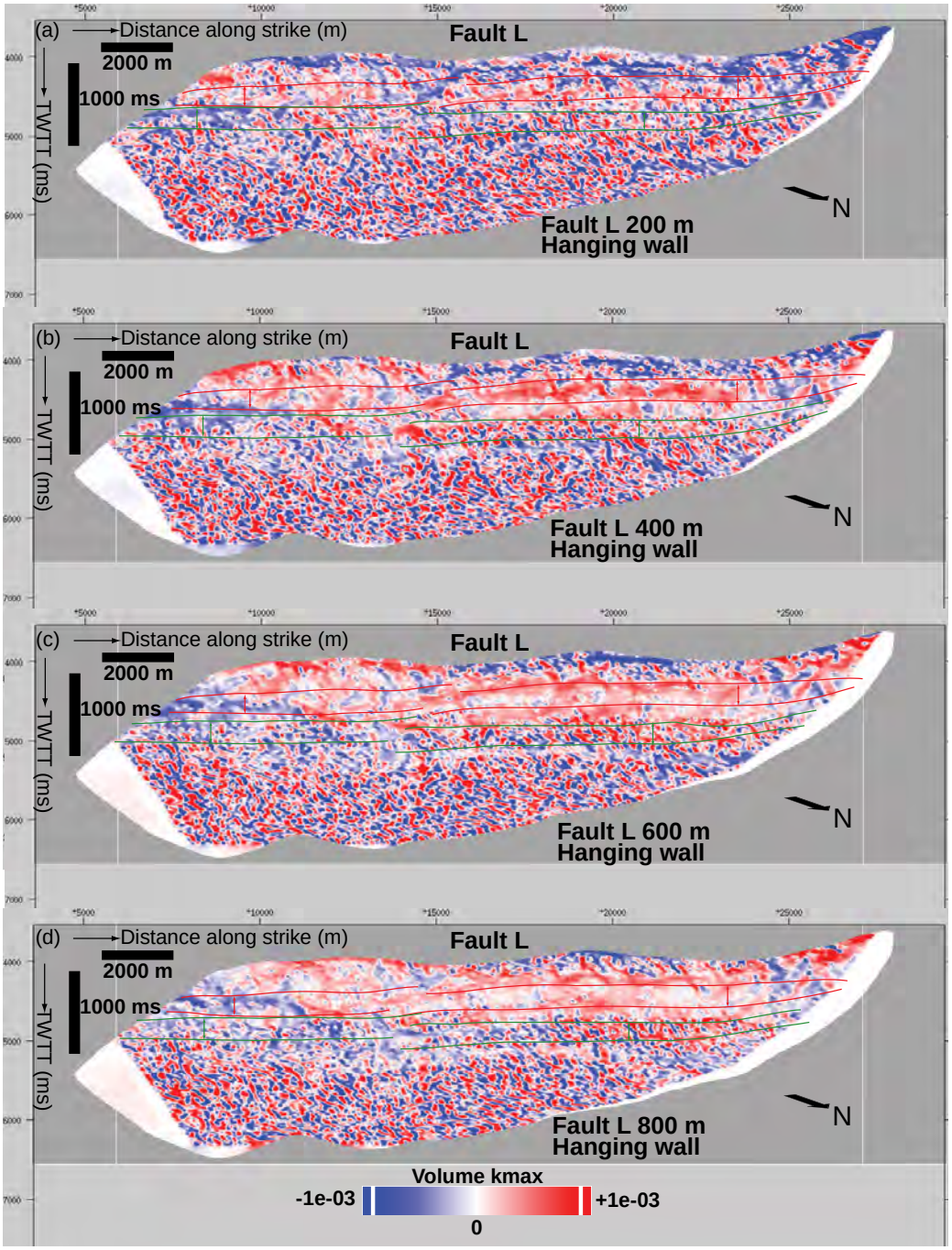

Figure 6.25: Strike views of maximum curvature slices sampled through maximum curvature volume at 200 m (a), 400 m (b), 600 m (c) and 800 m (d) in the hanging wall parallel to Fault L and projected as fault surface attribute. The red lines represent the hanging wall unit graphically analyzed in Figure 6.27, while the green lines represent projection of the footwall unit in the hanging wall. Note the coherent pattern of positive maximum curvature in the top halves of the slices and the random pattern of curvature in the bottom halves. Vertical scale is in milliseconds in two way travel time and horizontal scale is in meters. Vertical exaggeration is ~1.6.

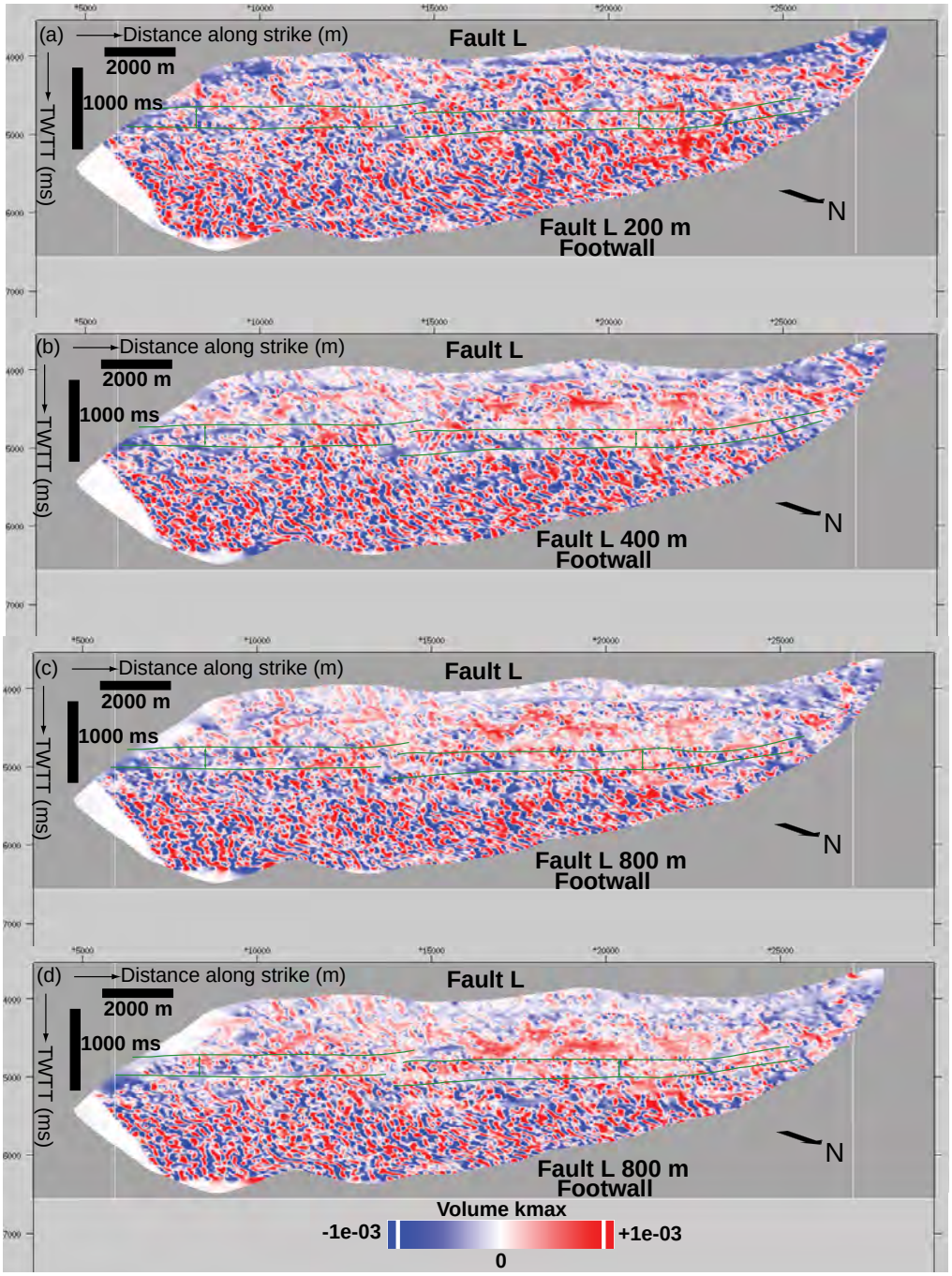

Figure 6.26: Strike views of maximum curvature slices sampled through maximum curvature volume at 200 m (a), 400 m (b), 600 m (c) and 800 m (d) in the hanging wall parallel to Fault L and projected as fault surface attribute. The green lines represent the location of the footwall unit graphically analyzed in Figure 6.28. Note the incoherent pattern of positive maximum curvature in the top halves of the slices and the random pattern of curvature in the bottom halves. Vertical scale is in milliseconds in two way travel time and horizontal scale is in meters. Vertical exaggeration is ~1.6.

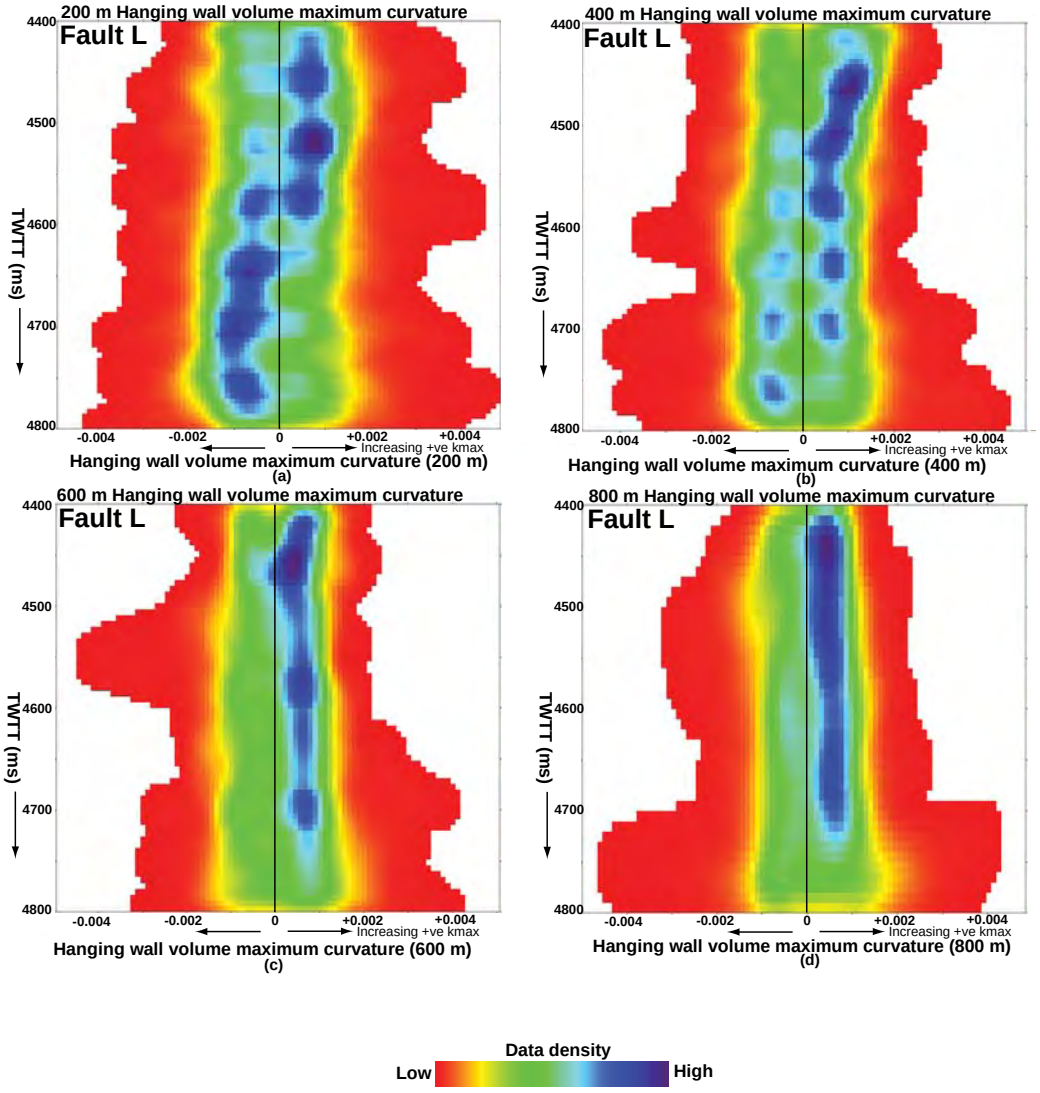

Figure 6.27: Density plots of volume maximum curvature sampled at 200 m (a), 400 m (b), 600 m (c) and 800 m (d) in the hanging wall of Fault L. The plots are quantitative estimates of volume maximum curvature extracted from the hanging wall units in Figure 6.25. The purple and red shades represent high and low density of curvature data respectively. Note the juxtaposition of high density positive and negative volume maximum curvature near the fault surface and the high density of positive volume maximum curvature towards 800 m. Vertical scale is in milliseconds in two-way-time.

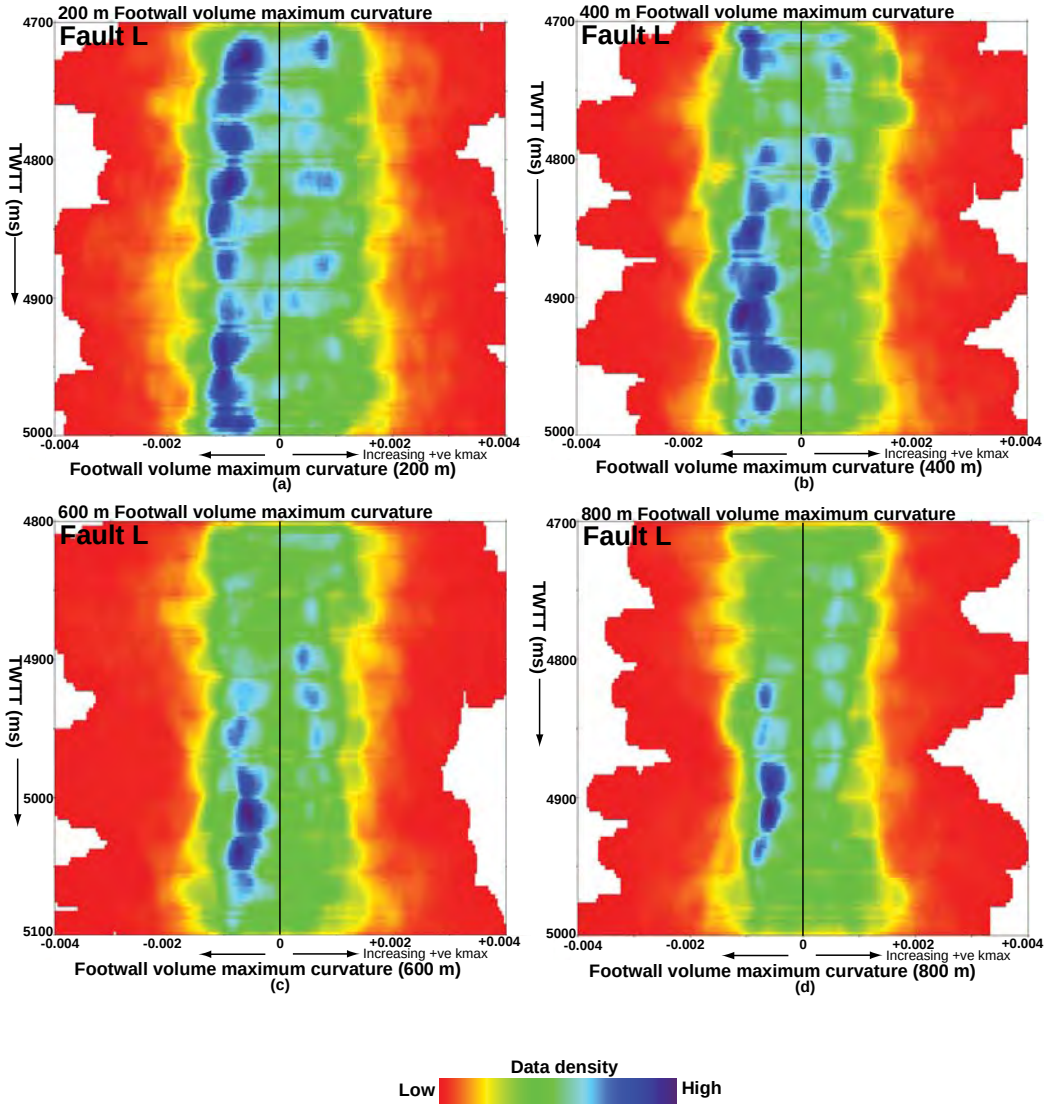

Figure 6.28: Density plots of volume maximum curvature sampled at 200 m (a), 400 m (b), 600 m (c) and 800 m (d) in the footwall of Fault L. The plots are quantitative estimates of volume maximum curvature extracted from the hanging wall units in Figure 6.26. The purple and red shades represent high and low density of curvature data respectively. Note the juxtaposition of positive and negative volume maximum curvature near the fault surface and the low density of volume curvature towards the background slices. Vertical scale is in milliseconds in two-way-time.

6.3.2.4 Volume similarity

The internal structure of the units adjacent to the four faults (Faults A, G, J & L) was also investigated using similarity attribute and the analysis applied to describe the qualitative structure adjacent to nine other faults (Faults B, C, H, I, K, M, N, O & P).

6.3.2.4.1 Qualitative assessment of volume similarity

In Fault A, similarity is low near the fault but becomes high as the distance away from the fault increases in the hanging wall. (Figure 6.29). Similarity in the footwall is higher than that observed in the hanging wall (Figure 6.30). Similarity across Fault B is uniformly high in the hanging wall in all the slices but lower in the footwall. (Figure 6.31). In Fault C, similarity is low near the fault but high away from the fault in both hanging wall and footwall. But near the fault, similarity is lower in the hanging wall than in the footwall (Figure 6.32).

In fault G, similarity is low near the fault but progressively becomes high as the distance away from the fault increases in the hanging wall (Figure 6.33). A similar pattern of similarity is observed in the footwall (Figure 6.34). Similarity in the hanging wall of Fault H is low in both the hanging wall and footwall irrespective of the distance away from the fault. Near the fault plane similarity in the hanging wall and footwall is about the same (Figure 6.35). In Fault I, similarity near the fault is low but high away from the fault in the hanging wall and footwall. Near the fault plane similarity in the hanging wall and footwall is about the same (Figure 6.36). The similarity pattern in the hanging wall of Fault J is similar to than seen in the hanging wall of Fault G (Figure 6.37), however, footwall similarity in Fault J is uniformly high in all the slices (Figure 6.38). But near the fault similarity is lower in the hanging wall

than in the footwall. Similarity in the hanging wall and footwall of Fault K is similar to that seen in Fault I (Figure 6.39). In Fault L, hanging wall similarity is lower close to the fault but becomes high towards the background (Figure 6.40). In the footwall similarity pattern is the same as in the hanging wall (Figure 6.41).

Similarity across Fault M is highly variable but appears to be lower near the fault in the hanging wall but high away from the fault and uniformly low in the footwall (Figure 6.42). Across Fault N, similarity is generally higher in the hanging wall but lower in the footwall near the fault. However, near the fault similarity is higher in the hanging wall than in the footwall (Figure 6.43). In Fault O, similarity is lower near the fault but higher away from the fault in the hanging wall and footwall. However, near the fault similarity is higher in the hanging wall than in the footwall (Figure 6.44). Across Fault P, similarity is uniformly low in the hanging wall and higher in the footwall (Figure 6.45).

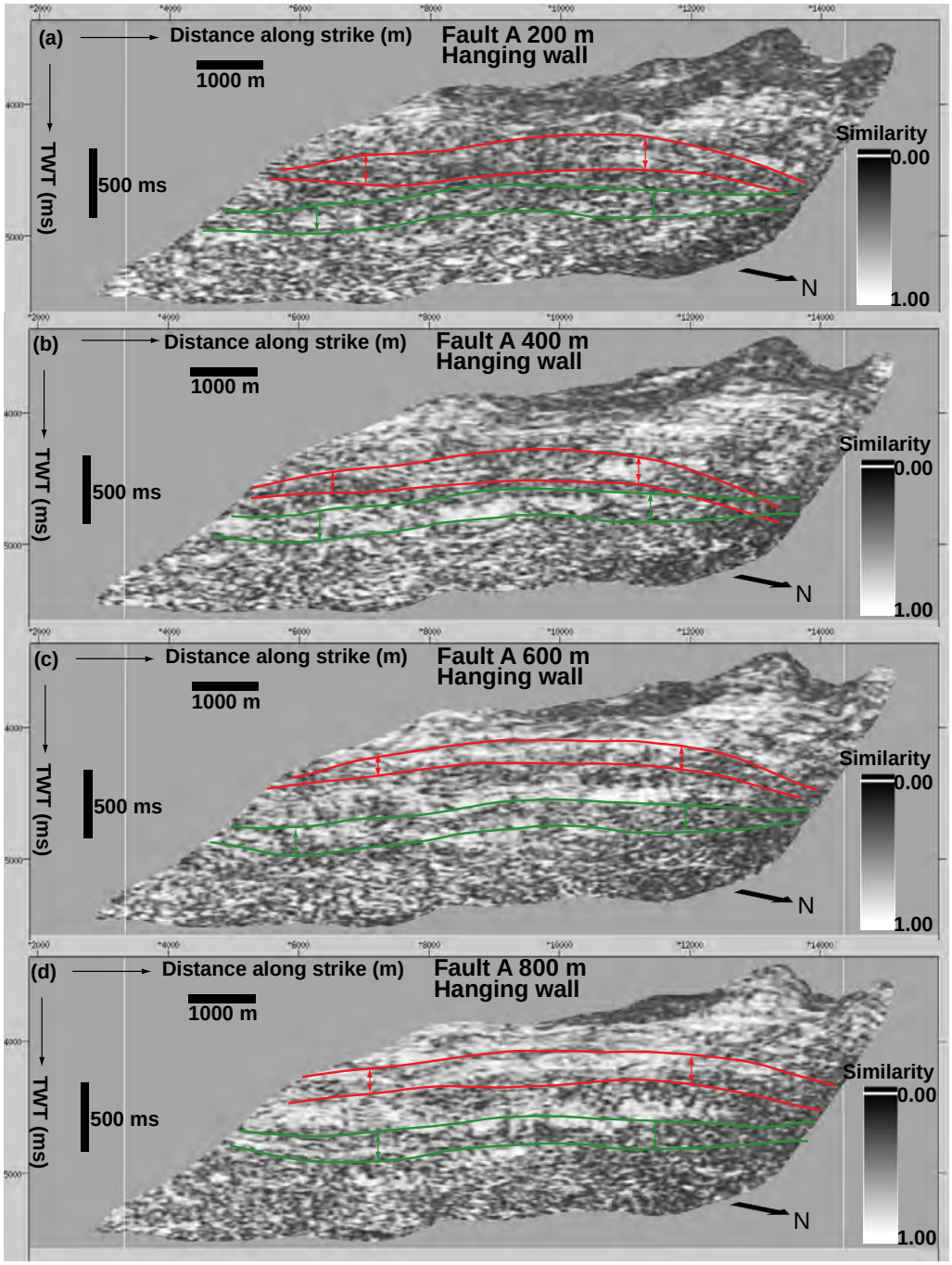

Figure 6.29: Strike views of volume similarity slices sampled at 200 m (a), 400 m (b), 600 m (c) and 800 m (d) in the hanging wall parallel to Fault A projected as fault surface attribute. The red lines represent the location of the hanging wall units graphically analyzed in Figure 6.46, while the green lines represent the projection of footwall units in the hanging wall. Note the high similarity of the slices as the distance from the fault increase to 800 m implying volume disruption as a result of discontinuities is higher next to the fault plane. Vertical scale is in milliseconds in two way travel time and horizontal scale is in meters. Vertical exaggeration is ~1.6.

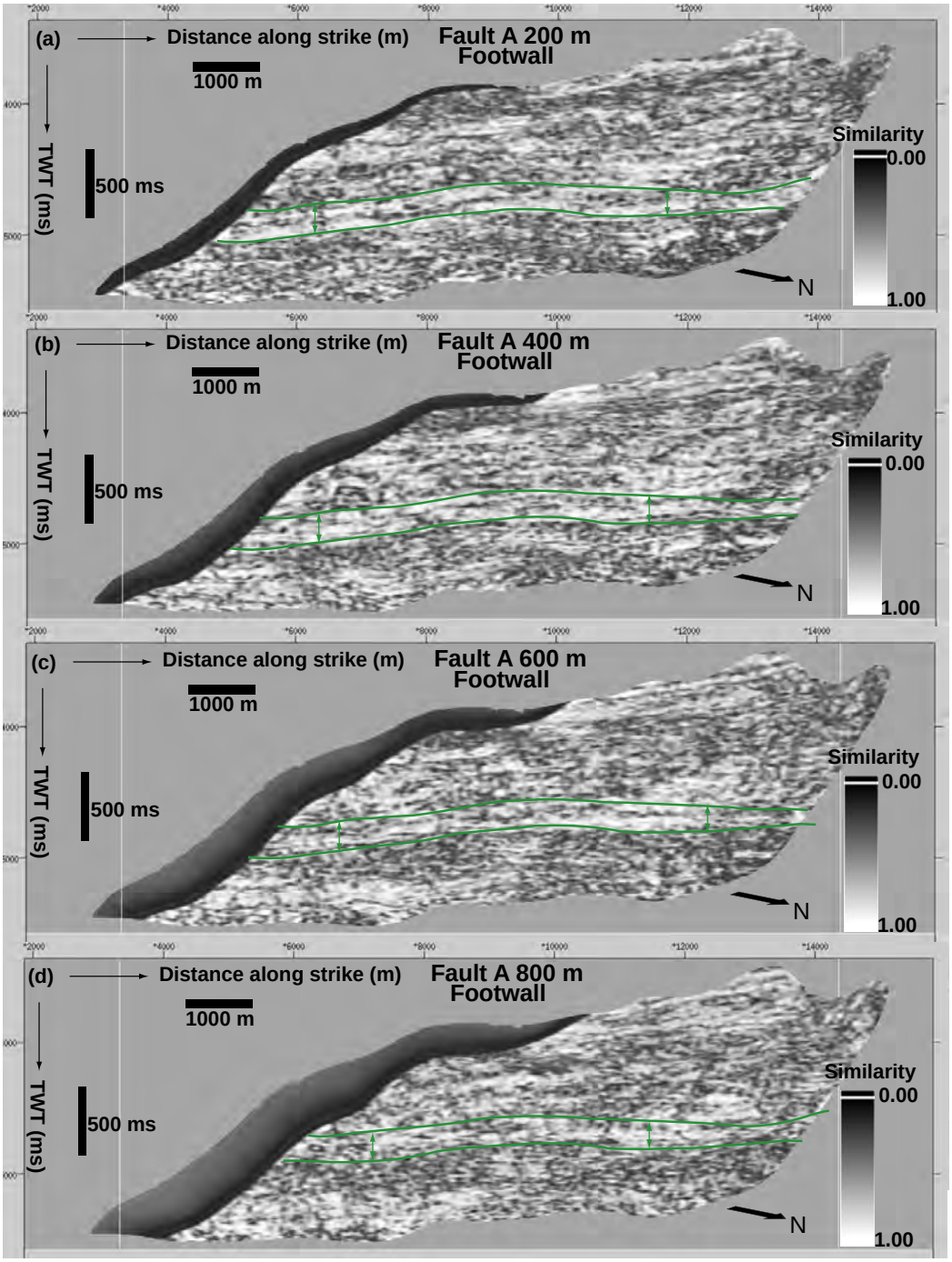

Figure 6.30: Strike views of volume similarity slices extracted at 200 m (a), 400 m (b), 600 m (c) and 800 m (d) in the foot wall parallel to Fault A projected as fault surface attribute. The green lines represent the location of the footwall unit graphically analyzed in Figure 6.47. Note the high similarity of all the slices in the footwall, implying that the footwall is generally less disrupted by discontinuities irrespective of the distance away from the fault plane. Vertical scale is in milliseconds in two way travel time and horizontal scale is in meters. Vertical exaggeration is ~1.6.

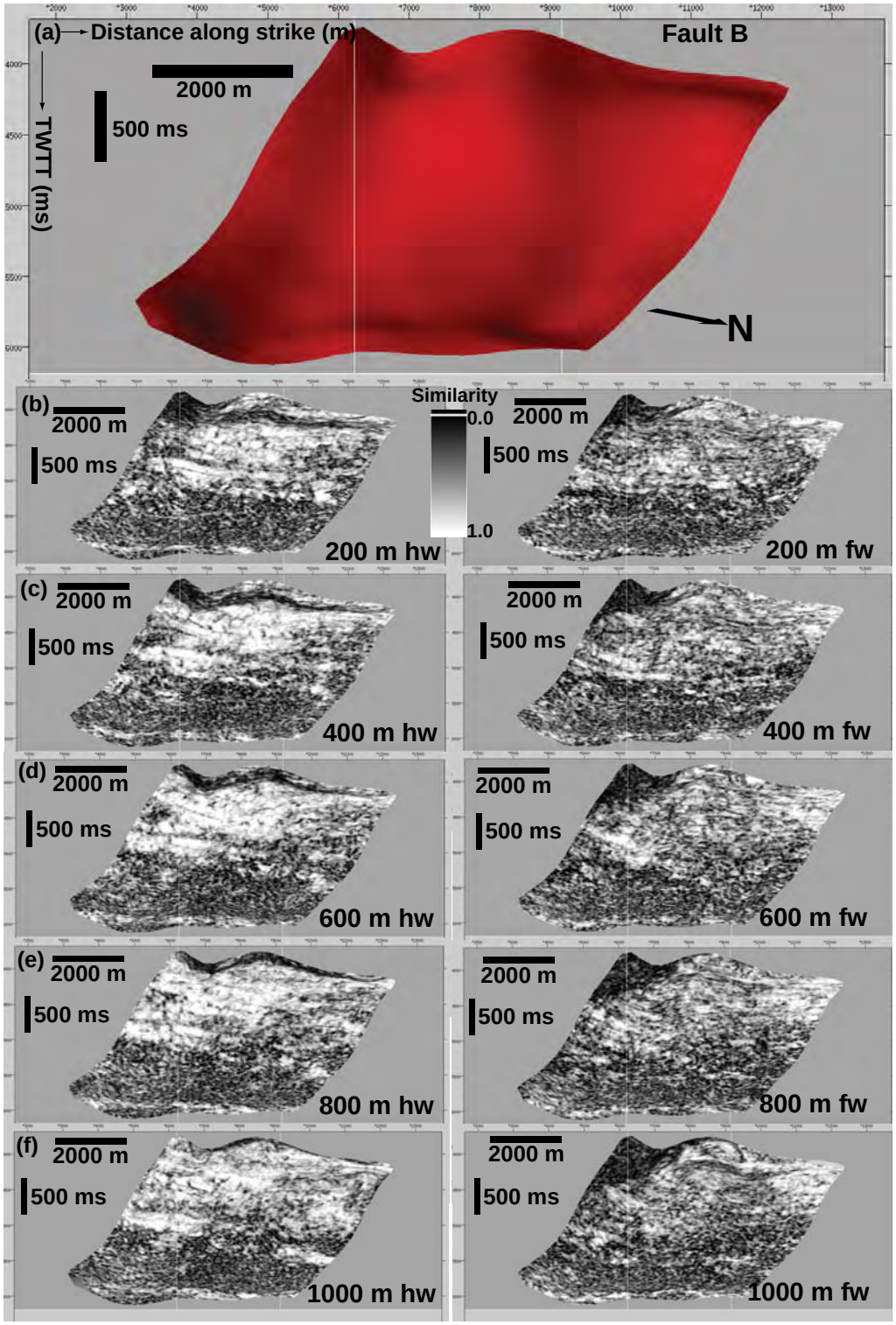

Figure 6.31: Strike views of the surface model of Fault B (a) and volume similarity slices sampled at 200 m (b), 400 m (c), 600 m (d), 800 m (e) and 1000 m (f) in the hanging wall (left) and footwall (right) parallel to the fault and projected as fault surface attribute. Note the high similarity of the hanging wall compared to the footwall. The implication is that the footwall is more disrupted than the hanging wall. Vertical scale is in milliseconds in two way travel time and horizontal scale is in meters. Vertical exaggeration is ~1.6.

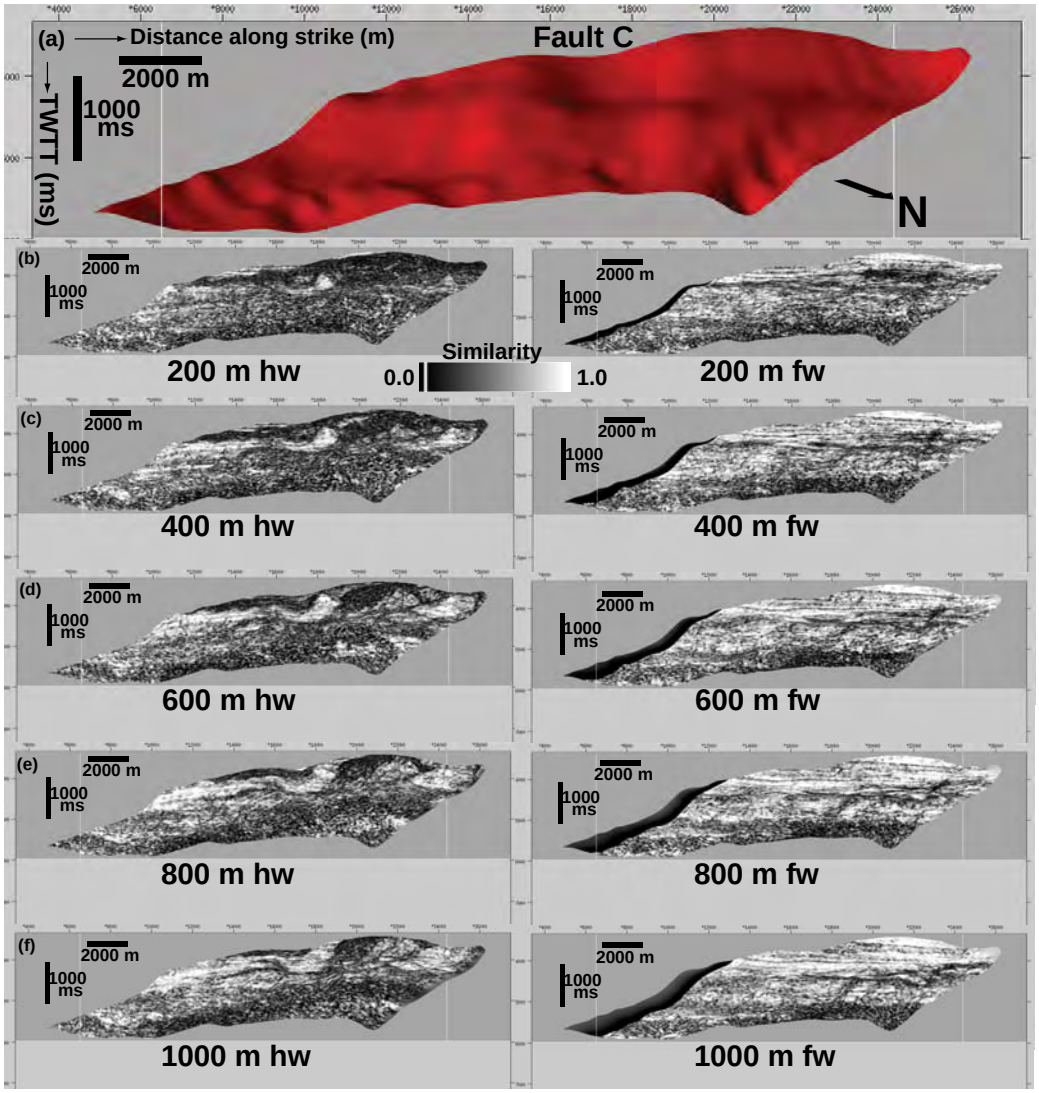

Figure 6.32: Strike views of the surface model of Fault C (a) and volume similarity slices sampled at 200 m (b), 400 m (c), 600 m (d), 800 m (e) and 1000 m (f) in the hanging wall (left) and footwall (right) parallel to the fault and projected as fault surface attribute. Note the low similarity of the hanging wall compared to the footwall. The implication is that the hanging wall is more disrupted than the footwall. Vertical scale is in milliseconds in two way travel time and horizontal scale is in meters. Vertical exaggeration is ~1.6.

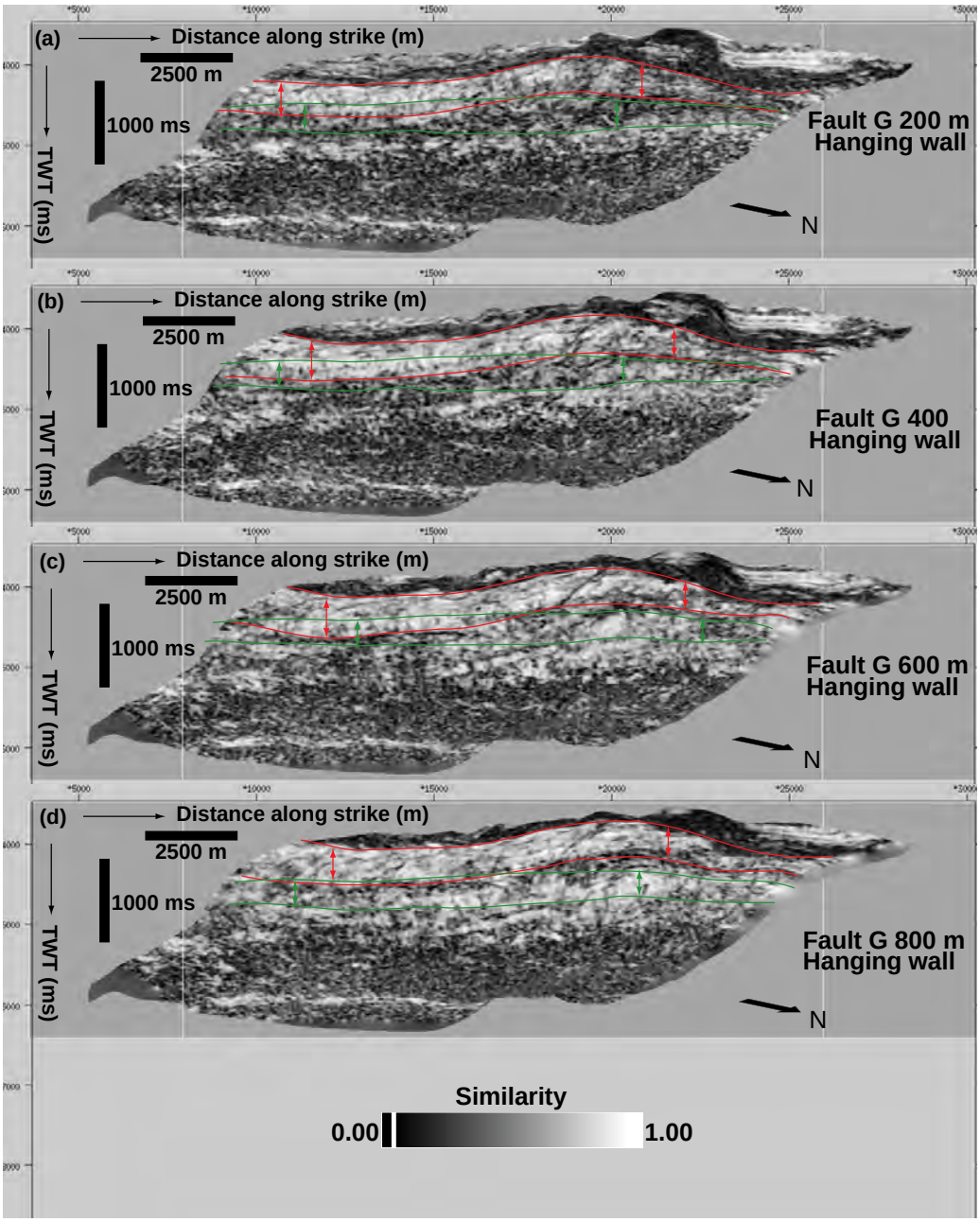

Figure 6.33: Strike views of volume similarity slices sampled at 200 m (a), 400 m (b), 600 m (c) and 800 m (d) in the hanging wall parallel to Fault G projected as fault surface attribute. The red lines represent the location of the hanging wall units graphically analyzed in Figure 6.48, while the green lines represent the projection of footwall units in the hanging wall. Note the low similarity near the fault and the high similarity away from the fault. Vertical scale is in milliseconds in two way travel time and horizontal scale is in meters. Vertical exaggeration is ~1.6.

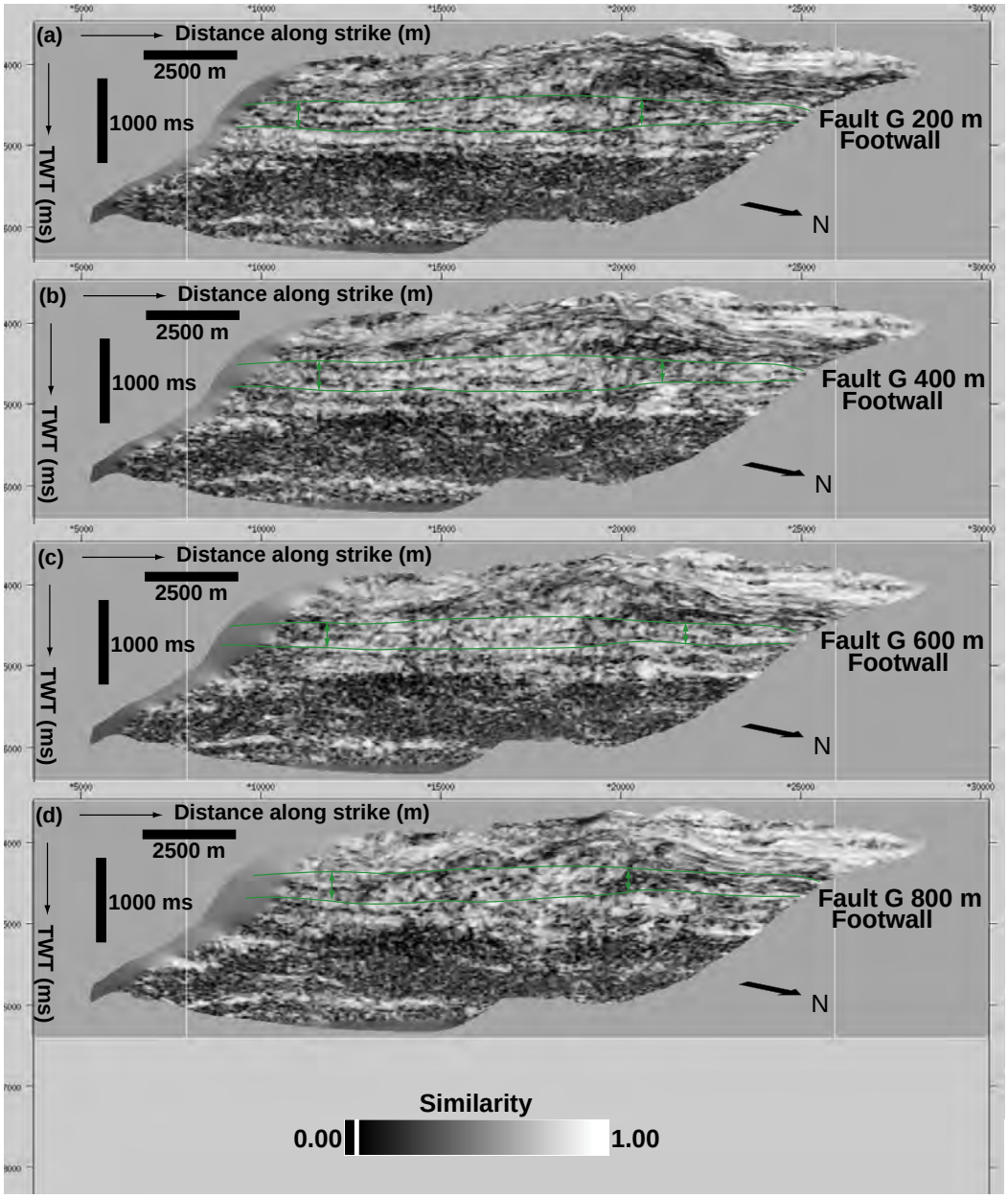

Figure 6.34: Strike views of volume similarity slices sampled at 200 m (a), 400 m (b), 600 m (c) and 800 m (d) in the footwall parallel to Fault G projected as fault surface attribute. The green lines represent the projection of footwall units graphically analyzed in Figure 6.49. Note the low similarity near the fault and the higher similarity away from the fault. Vertical scale is in milliseconds in two way travel time and horizontal scale is in meters. Vertical exaggeration is ~1.6.

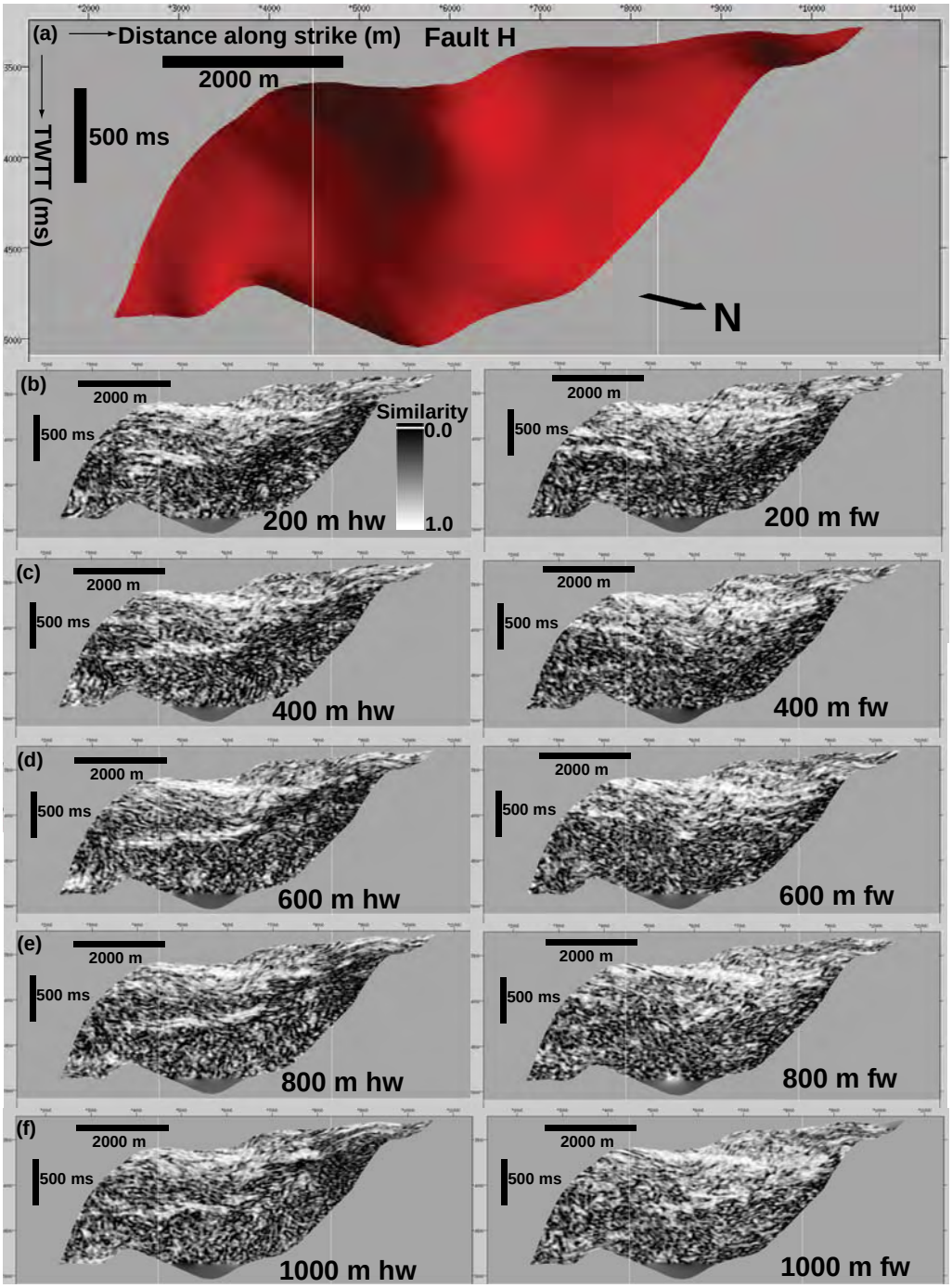

Figure 6.35: Strike views of the surface model of Fault H (a) and volume similarity slices sampled at 200 m (b), 400 m (c), 600 m (d), 800 m (e) and 1000 m (f) in the hanging wall (left) and footwall (right) parallel to the fault and projected as fault surface attribute. Note the fairly uniform pattern of high and low similarity in the upper and lower parts of all the slices in the hanging wall and footwall. Vertical scale is in milliseconds in two way travel time and horizontal scale is in meters. Vertical exaggeration is ~1.6.

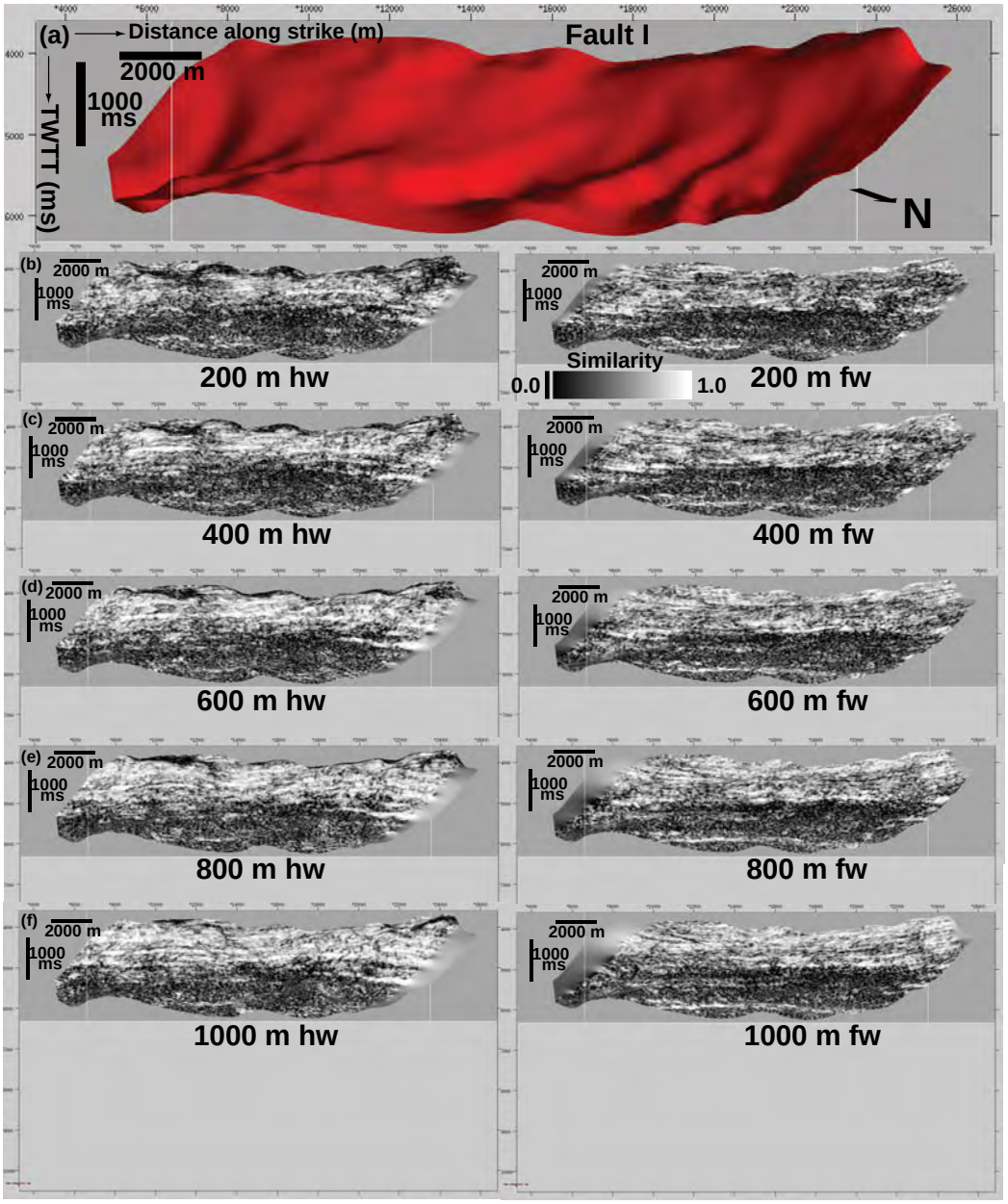

Figure 6.36: Strike views of the surface model of Fault I (a) and volume similarity slices sampled at 200 m (b), 400 m (c), 600 m (d), 800 m (e) and 1000 m (f) in the hanging wall (left) and footwall (right) parallel to the fault and projected as fault surface attribute. Note the fairly uniform pattern of high and low similarity in the upper and lower parts of all the slices. However, in both the hanging wall and footwall the slices near the fault are low in similarity compared to the background slices, implying disruptions near the fault. Vertical scale is in milliseconds in two way travel time and horizontal scale is in meters. Vertical exaggeration is ~1.6.

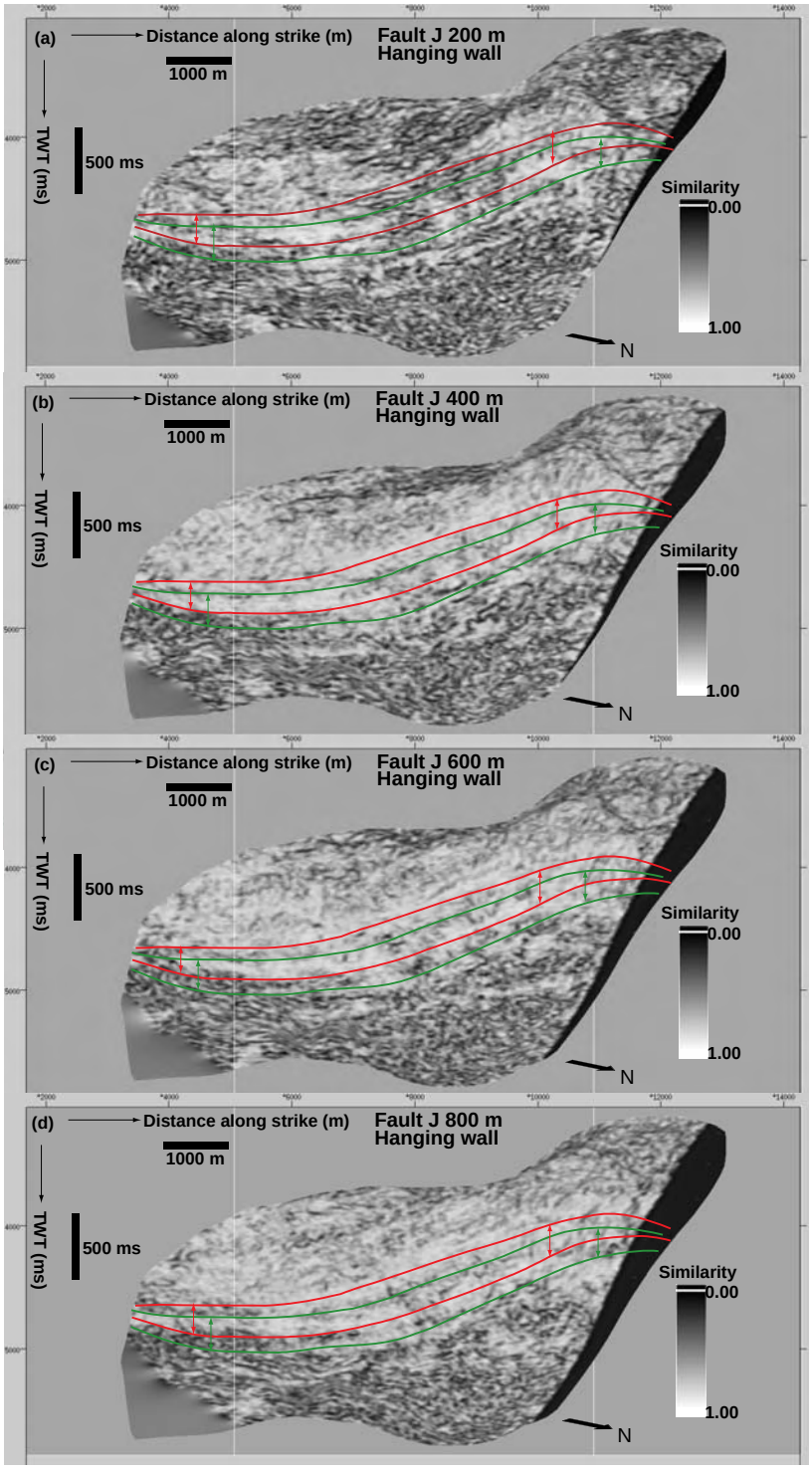

Figure 6.37: Strike views of volume similarity slices sampled at 200 m (a), 400 m (b), 600 m (c) and 800 m (d) in the hanging wall parallel to Fault J projected as fault surface attribute. The red lines represent the location of the hanging wall units graphically analyzed in Figure 6.50, while the green lines represent the projection of footwall units in the hanging wall. Note the low similarity near the fault and the high similarity away from the fault. Vertical scale is in milliseconds in two way travel time and horizontal scale is in meters. Vertical exaggeration is ~1.6.

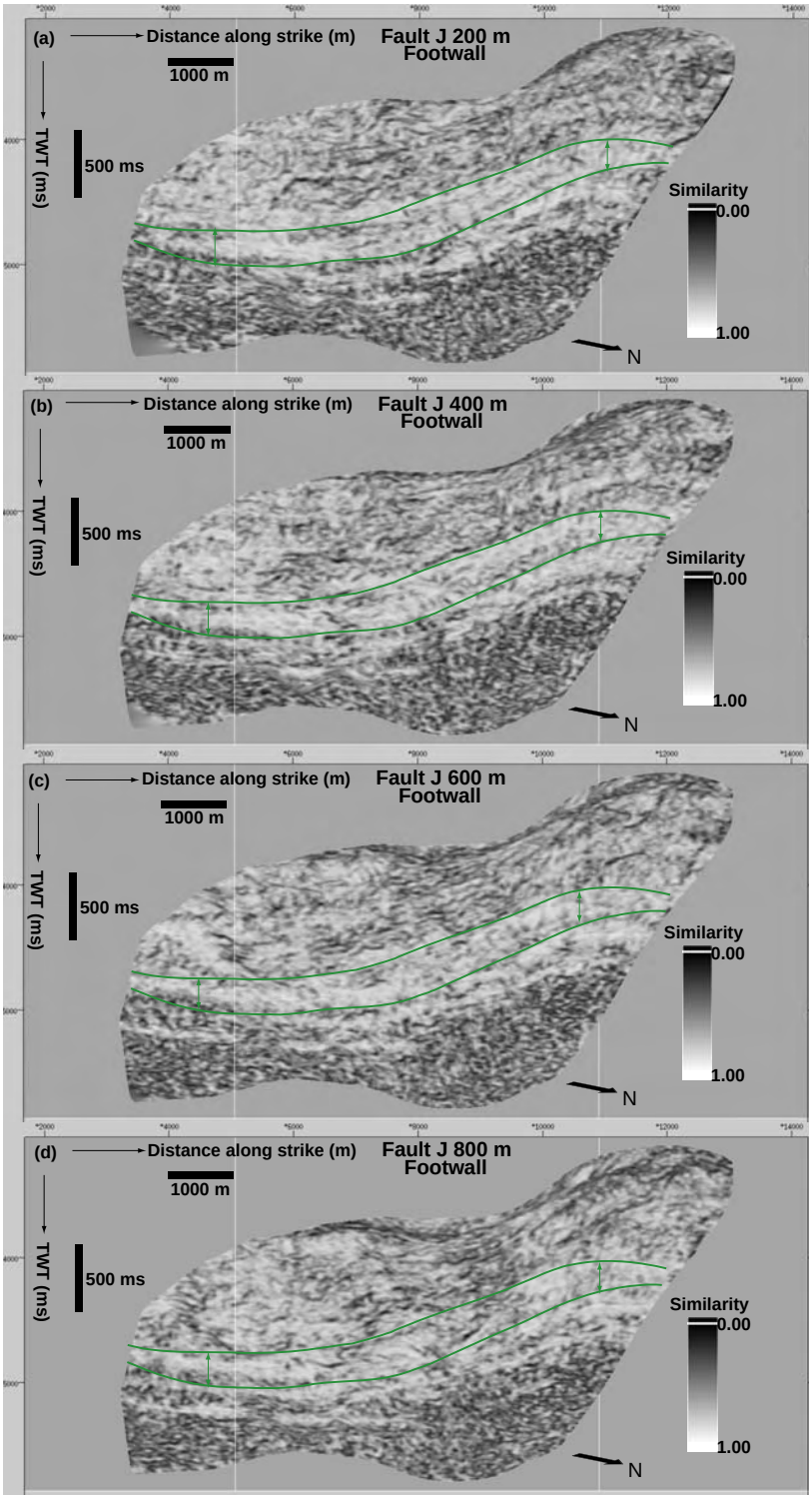

Figure 6.38: Strike views of volume similarity slices extracted at 200 m (a), 400 m (b), 600 m (c) and 800 m (d) in the foot wall parallel to Fault J projected as fault surface attribute. The green lines represent the location of the footwall unit graphically analyzed in Figure 6.51. Note the high similarity of all the slices in the footwall, implying that the footwall is generally less disrupted irrespective of the distance away from the fault plane. Vertical scale is in milliseconds in two way travel time and horizontal scale is in meters. Vertical exaggeration is ~1.6.

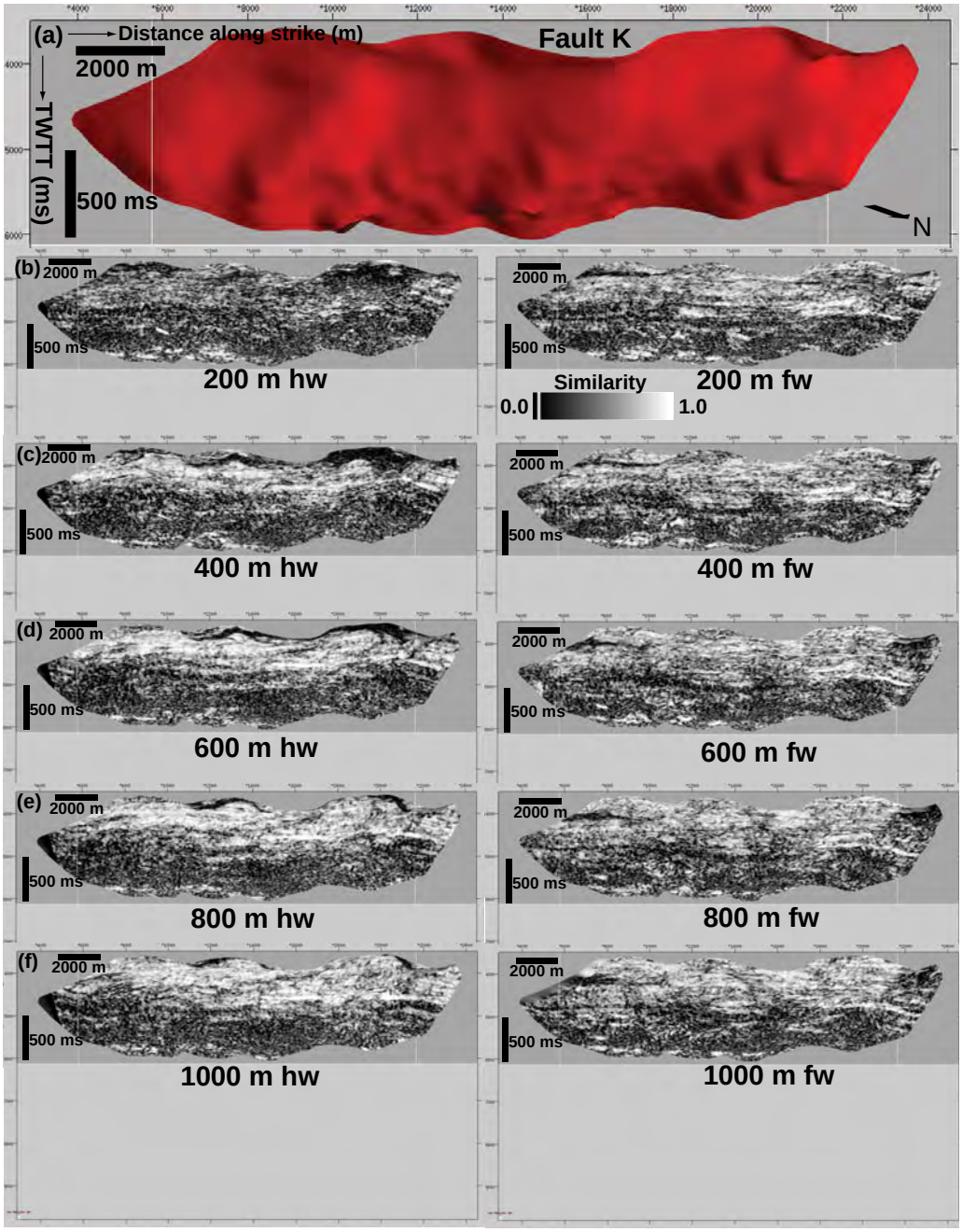

Figure 6.39: Strike views of the surface model of Fault K (a) and volume similarity slices sampled at 200 m (b), 400 m (c), 600 m (d), 800 m (e) and 1000 m (f) in the hanging wall (left) and footwall (right) parallel to the fault and projected as fault surface attribute. Note the low similarity of the slices near the fault surface. However, the hanging wall slice is lower in similarity compared to the footwall slice, implying more disruptions in the hanging wall than in the footwall near the fault Vertical scale is in milliseconds in two way travel time and horizontal scale is in meters. Vertical exaggeration is ~1.6.

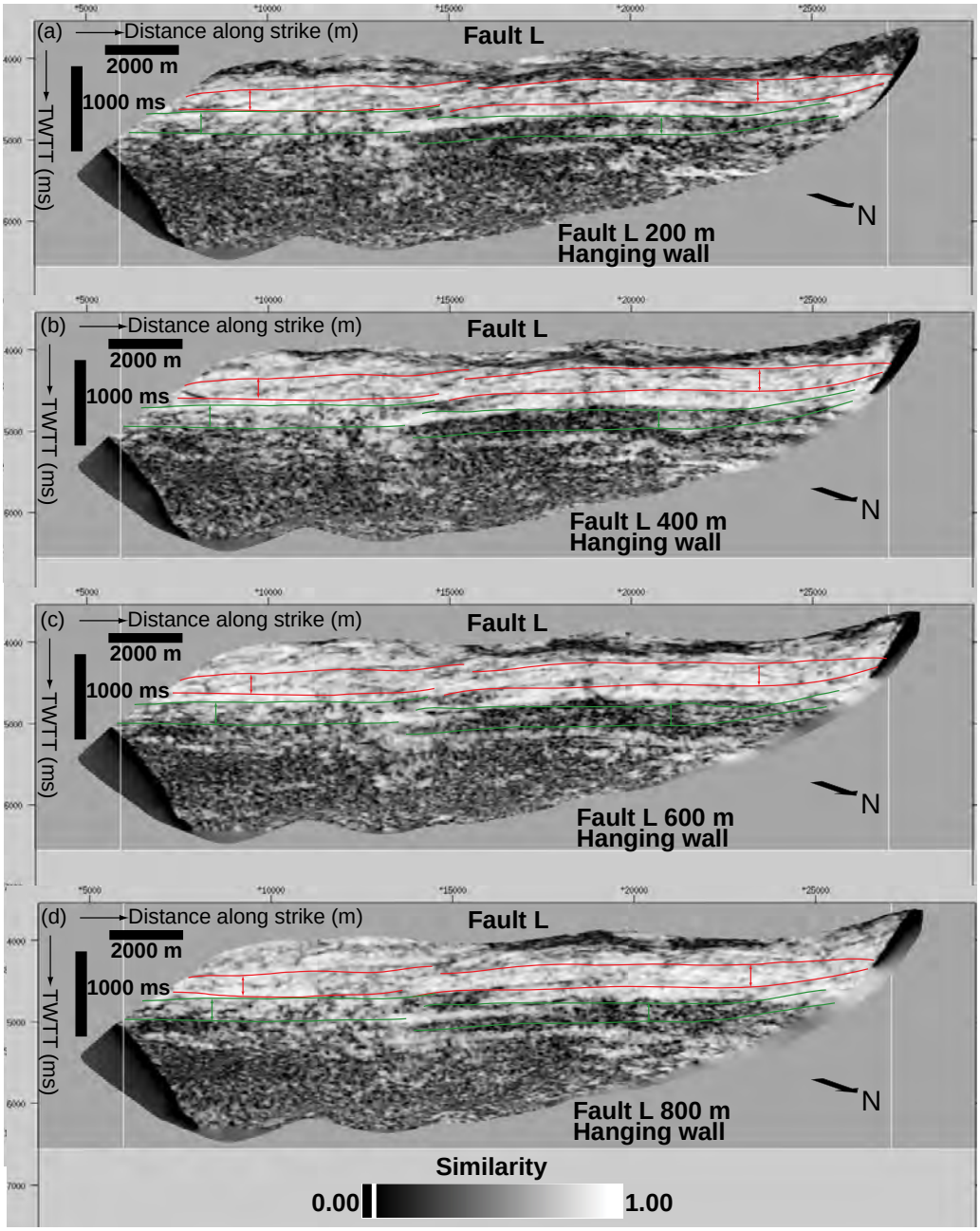

Figure 6.40: Strike views of volume similarity slices sampled at 200 m (a), 400 m (b), 600 m (c) and 800 m (d) in the hanging wall parallel to Fault L projected as fault surface attribute. The red lines represent the location of the hanging wall units graphically analyzed in Figure 6.52, while the green lines represent the projection of footwall units in the hanging wall. Note the high similarity of the slices as the distance from the fault increase to 800 m. Vertical scale is in milliseconds in two way travel time and horizontal scale is in meters. Vertical exaggeration is ~1.6.

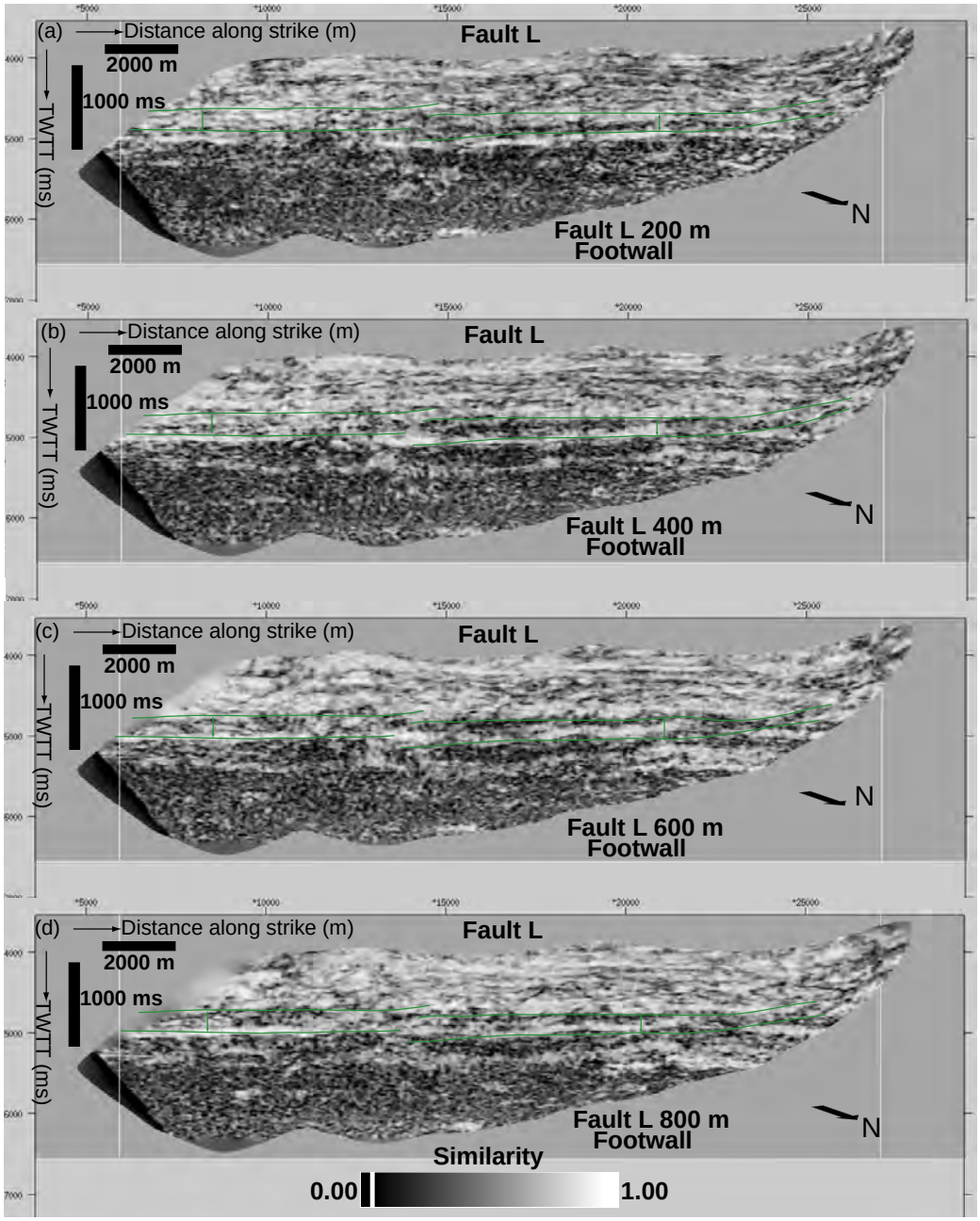

Figure 6.41: Strike views of volume similarity slices sampled at 200 m (a), 400 m (b), 600 m (c) and 800 m (d) in the footwall parallel to Fault L projected as fault surface attribute. The green lines represent the location of the footwall units graphically analyzed in Figure 6.53. Note the low similarity near the fault. Vertical scale is in milliseconds in two way travel time and horizontal scale is in meters. Vertical exaggeration is ~1.6.

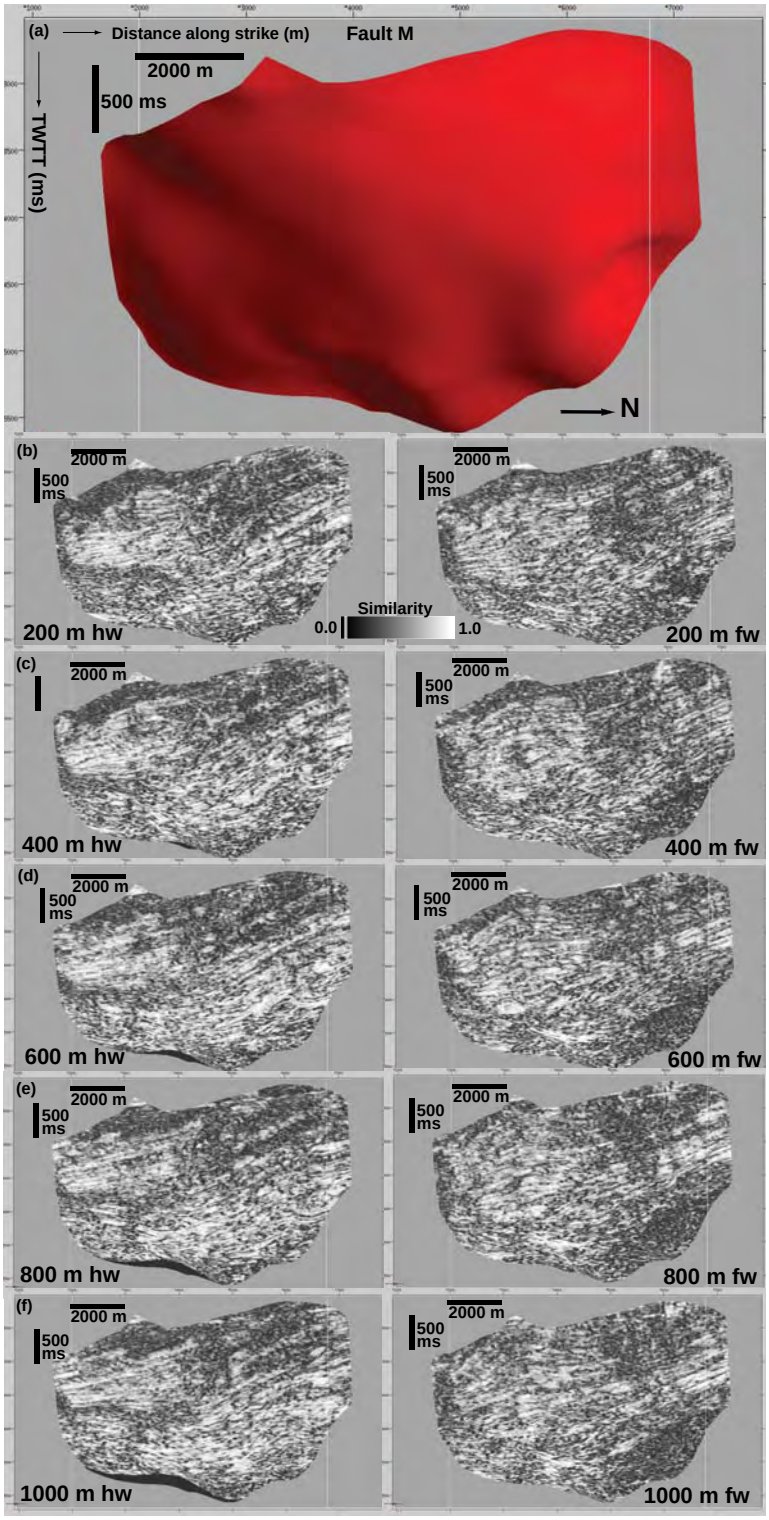

Figure 6.42: Strike views of the surface model of Fault M (a) and volume similarity slices sampled at 200 m (b), 400 m (c), 600 m (d), 800 m (e) and 1000 m (f) in the hanging wall (left) and footwall (right) parallel to the fault and projected as fault surface attribute. Note the fairly uniform pattern of high and low similarity in the all the slices. Vertical scale is in milliseconds in two way travel time and horizontal scale is in meters. Vertical exaggeration is ~1.6.

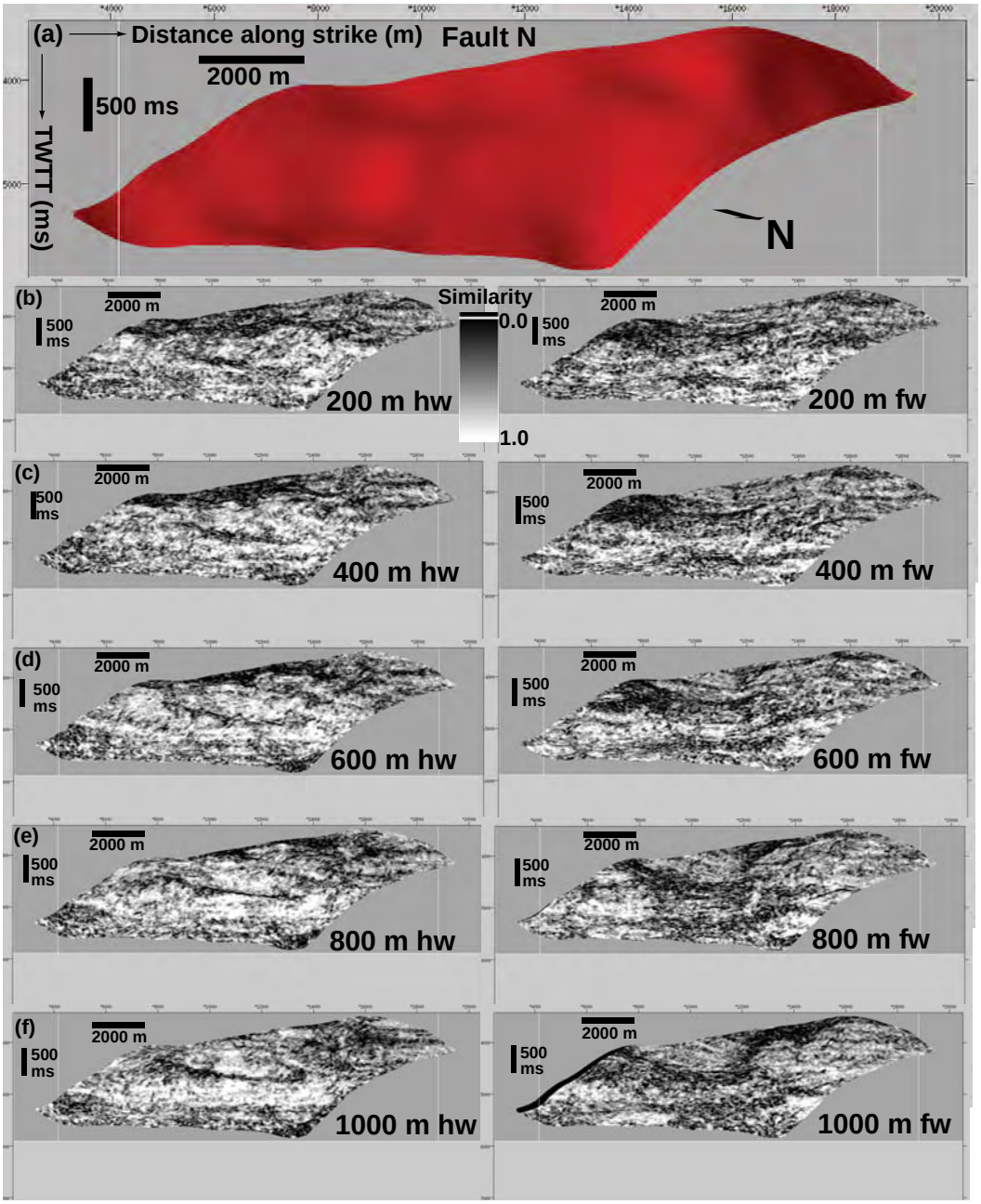

Figure 6.43: Strike views of the surface model of Fault N (a) and volume similarity slices sampled at 200 m (b), 400 m (c), 600 m (d), 800 m (e) and 1000 m (f) in the hanging wall (left) and footwall (right) parallel to the fault and projected as fault surface attribute. Note the low similarity of the footwall compared to the hanging wall, implying that the footwall is more disrupted than the hanging wall. Vertical scale is in milliseconds in two way travel time and horizontal scale is in meters. Vertical exaggeration is ~1.6.

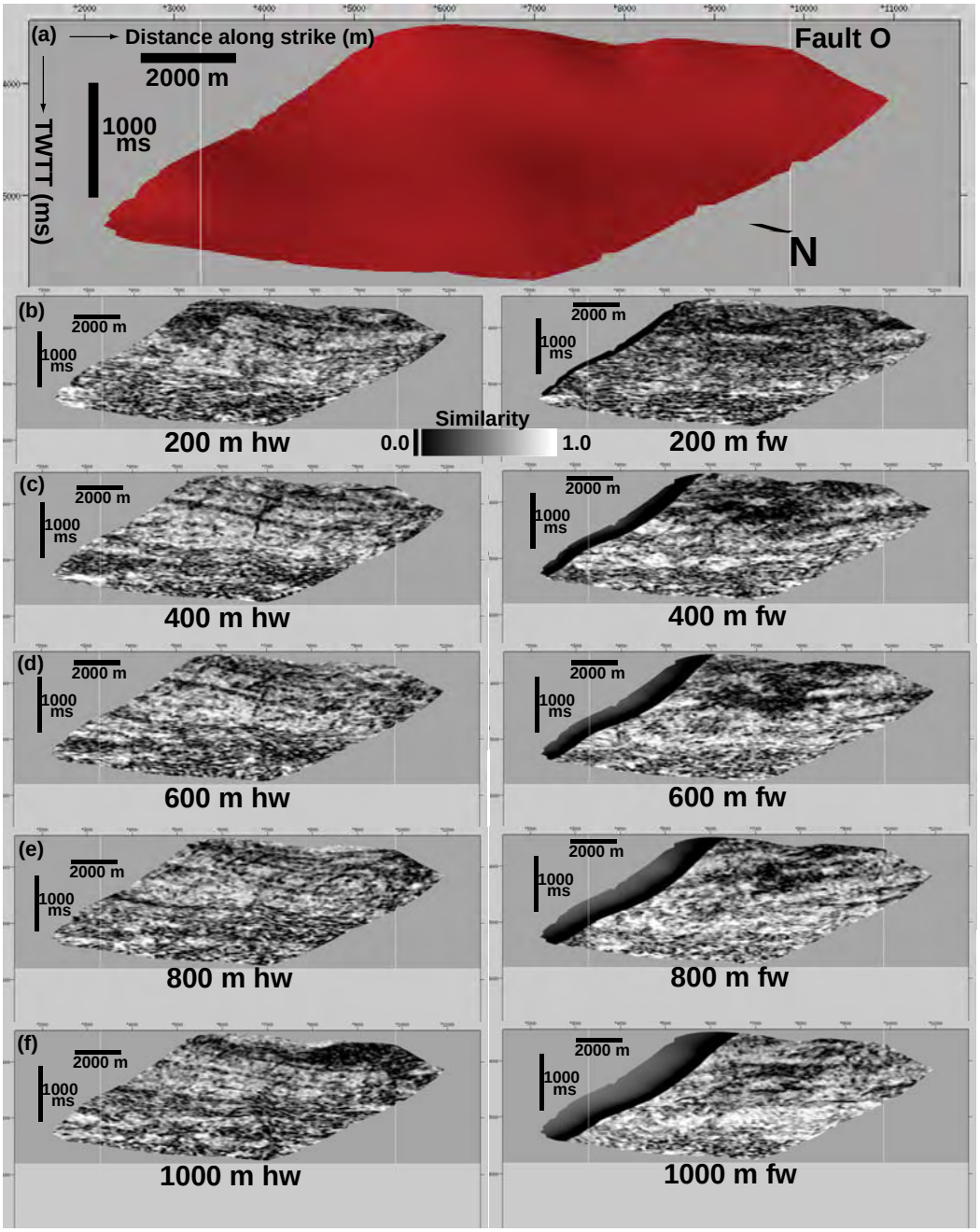

Figure 6.44: Strike views of the surface model of Fault O (a) and volume similarity slices sampled at 200 m (b), 400 m (c), 600 m (d), 800 m (e) and 1000 m (f) in the hanging wall (left) and footwall (right) parallel to the fault and projected as fault surface attribute. Note the low similarity of the footwall compared to the hanging wall, implying that the footwall is more disrupted than the hanging wall. Vertical scale is in milliseconds in two way travel time and horizontal scale is in meters. Vertical exaggeration is ~1.6.

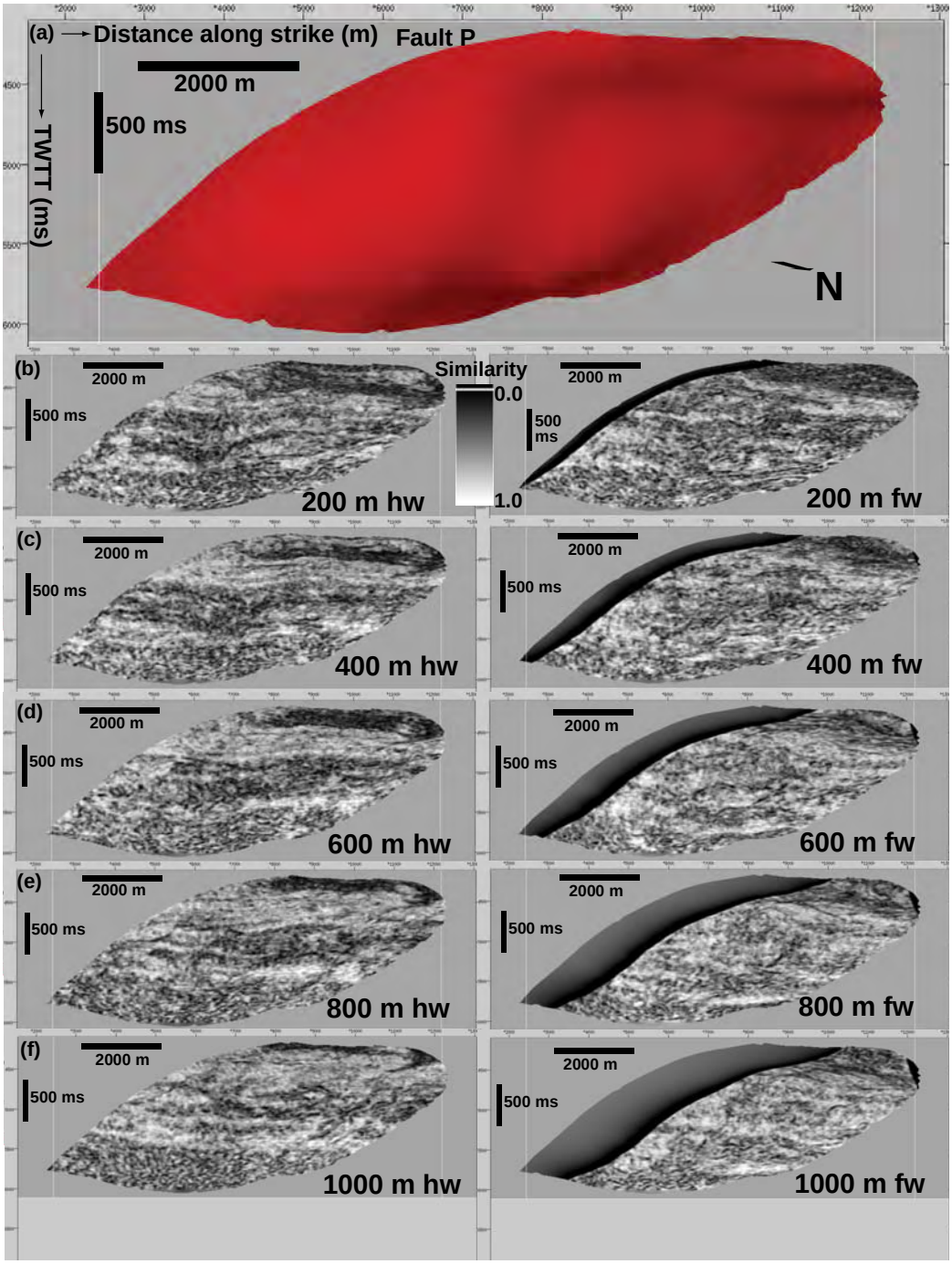

Figure 6.45: Strike views of the surface model of Fault P (a) and volume similarity slices sampled at 200 m (b), 400 m (c), 600 m (d), 800 m (e) and 1000 m (f) in the hanging wall (left) and footwall (right) parallel to the fault and projected as fault surface attribute. Note the fairly uniform pattern of similarity in all the slices. However, similarity near the faults is slightly lower in both the hanging wall and footwall. Vertical scale is in milliseconds in two way travel time and horizontal scale is in meters. Vertical exaggeration is ~1.6.

6.3.2.4.2 Quantitative assessment of volume similarity

In the hanging wall of Fault A, similarity close to the fault is low. Away from the fault plane, similarity increases right up to 800 m where it is highest (Figure 6.46). In the footwall, similarity is higher near the fault but becomes variable away from the fault (Figure 6.47). In Fault G, the pattern of similarity in the hanging wall is variable, but generally lower near the fault (Figure 6.48). In the footwall similarity is uniformly moderate to high in all the slices (Figure 6.49). Across Fault J, similarity is low in the hanging wall and footwall irrespective of the location of the slices (Figures 6.50 & 6.51). In Fault L, similarity in the hanging wall is high in all the slices (Figure 6.52). In the footwall similarity near the fault plane is variable, but generally high near the fault plane (Figure 6.53).

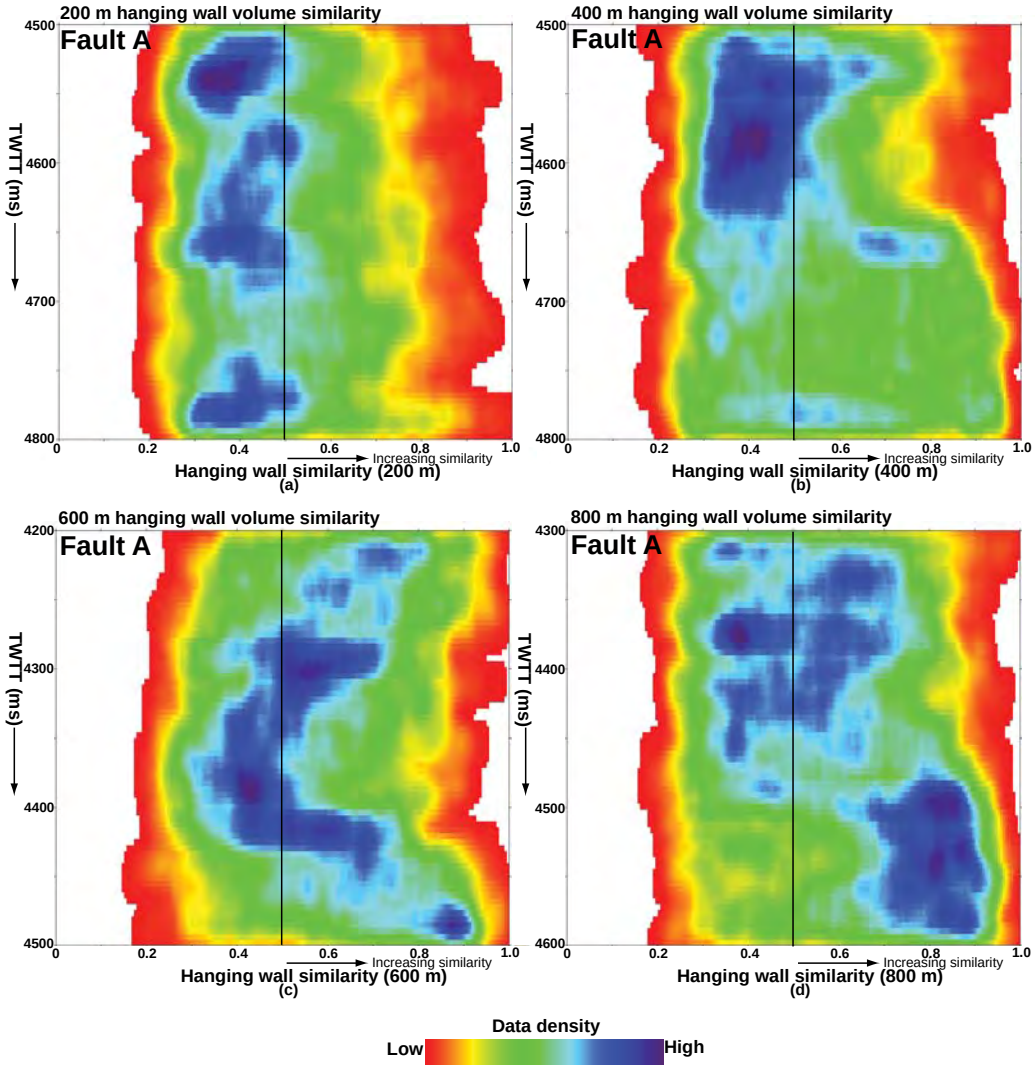

Figure 6.46: Density plots of volume similarity at (a) 200 m, (b) 400 m, (c) 600 m, and (d) 800 m in the hanging wall parallel to Fault A. The plots are quantitative estimates of volume similarity extracted from the hanging wall units in Figure 6.29.The purple and red shades represent high and low density of similarity data respectively. Note the low similarity in the plots near the fault. However, away from the fault the lower part of the units has high similarity. Vertical scale is in milliseconds in two way time.

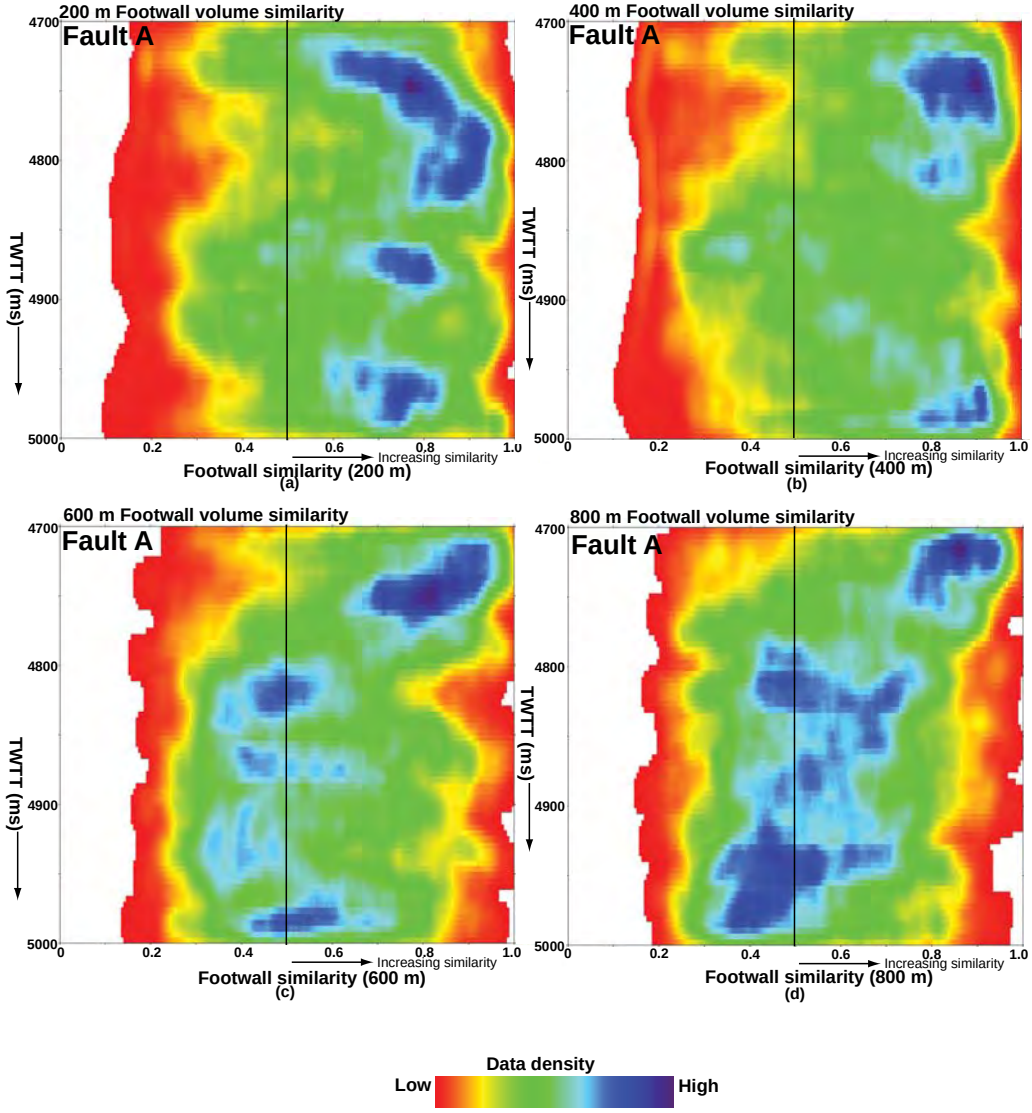

Figure 6.47: Density plots of volume similarity at (a) 200 m, (b) 400 m, (c) 600 m, and (d) 800 m in the footwall parallel to Fault A. The plots are quantitative estimates of volume similarity extracted from the footwall units in Figure 6.30. The purple and red shades represent high and low density of similarity data respectively. Note the high similarity near the fault but lower in the bottom halves of the slices away from the fault. Vertical scale is in milliseconds in two-way-time.

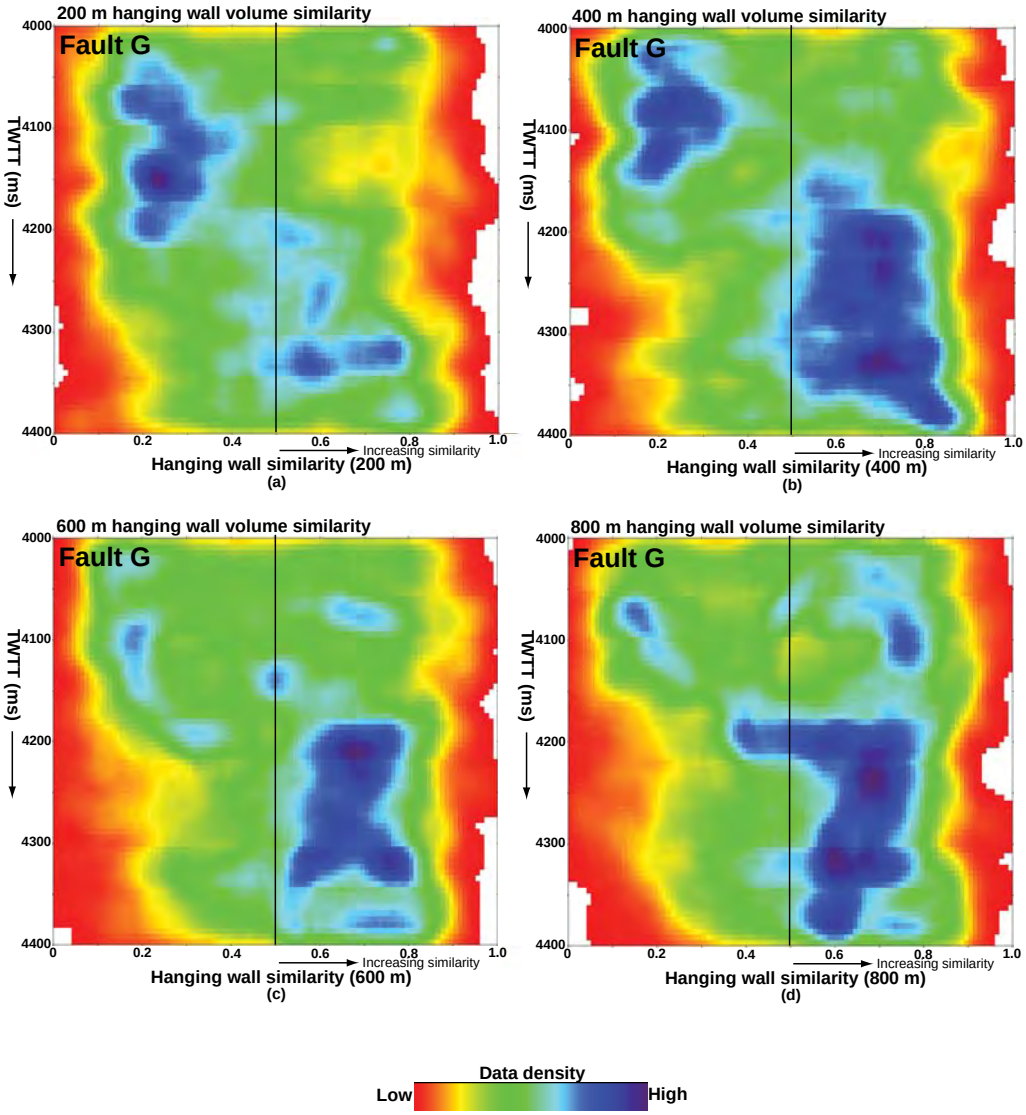

Figure 6.48: Density plots of volume similarity at (a) 200 m, (b) 400 m, (c) 600 m, and (d) 800 m in the hanging wall parallel to Fault G. The plots are quantitative estimates of volume similarity extracted from the hanging wall units in Figure 6.33.The purple and red shades represent high and low density of similarity data respectively. Note the variable pattern of similarity that generally increases as the distance away from the fault increases. However, near the fault plane the upper parts of the units are disrupted. Vertical scale is in milliseconds in two way time.

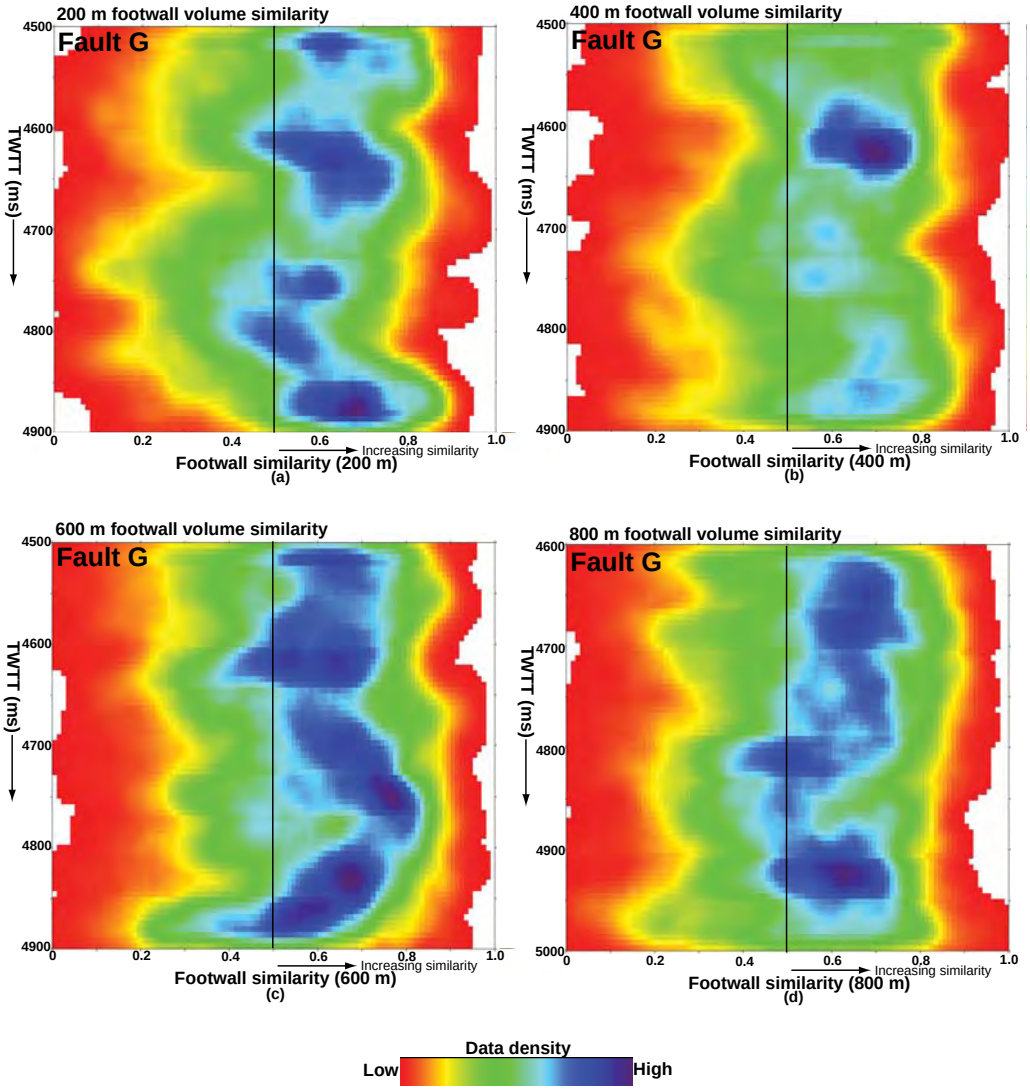

Figure 6.49: Density plots of volume similarity at (a) 200 m, (b) 400 m, (c) 600 m, and (d) 800 m in the footwall parallel to Fault G. The plots are quantitative estimates of volume similarity extracted from the footwall units in Figure 6.34. The purple and red shades represent high and low density of similarity data respectively. Note the highly variable pattern of similarity in all the slices. The implication is that parts of the footwall may be disrupted.

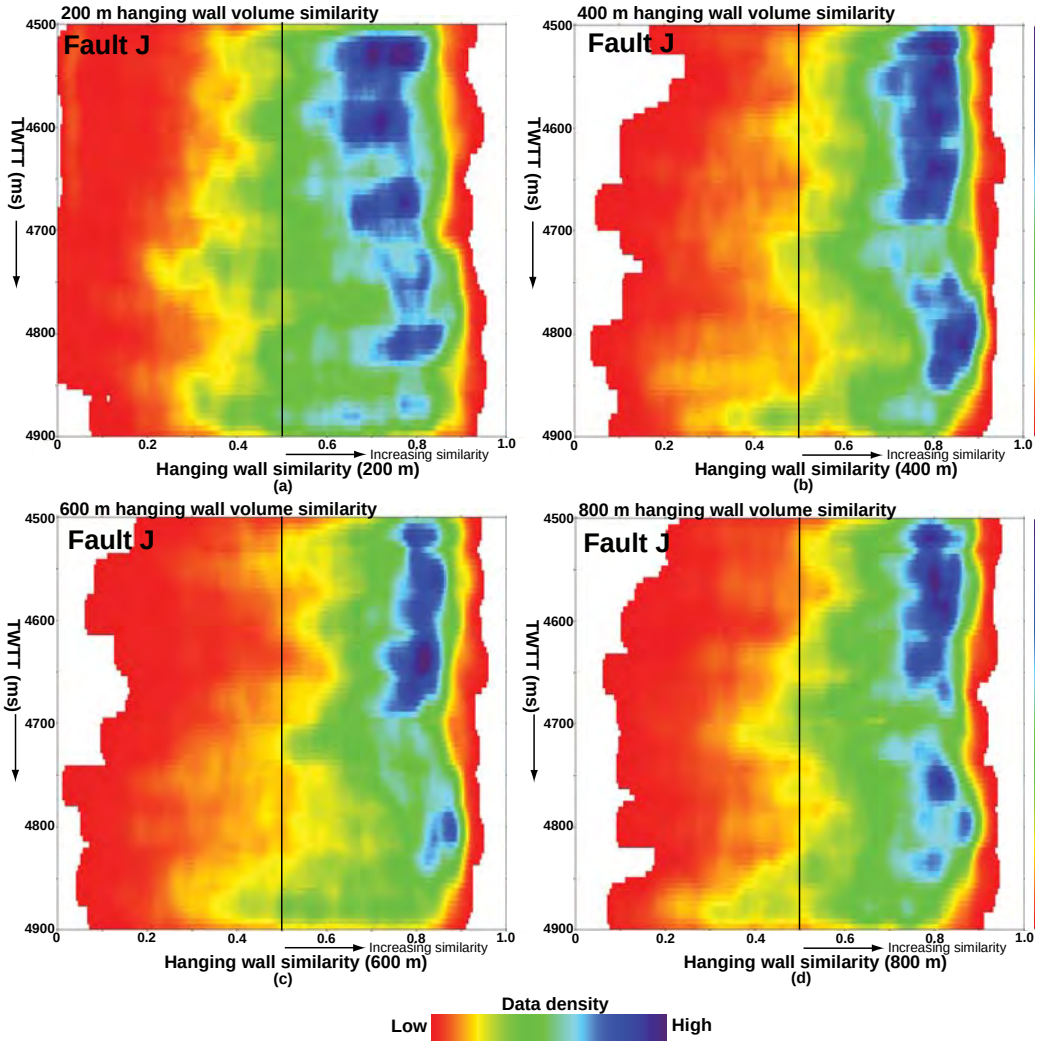

Figure 6.50: Density plots of volume similarity at (a) 200 m, (b) 400 m, (c) 600 m, and (d) 800 m in the hanging wall parallel to Fault J. The plots are quantitative estimates of volume similarity extracted from the hanging wall units in Figure 6.37.The purple and red shades represent high and low density of similarity data respectively. Note the high similarity in all the slices, implying that the units in the hanging wall are not significantly disrupted. Vertical scale is in milliseconds in two way time.

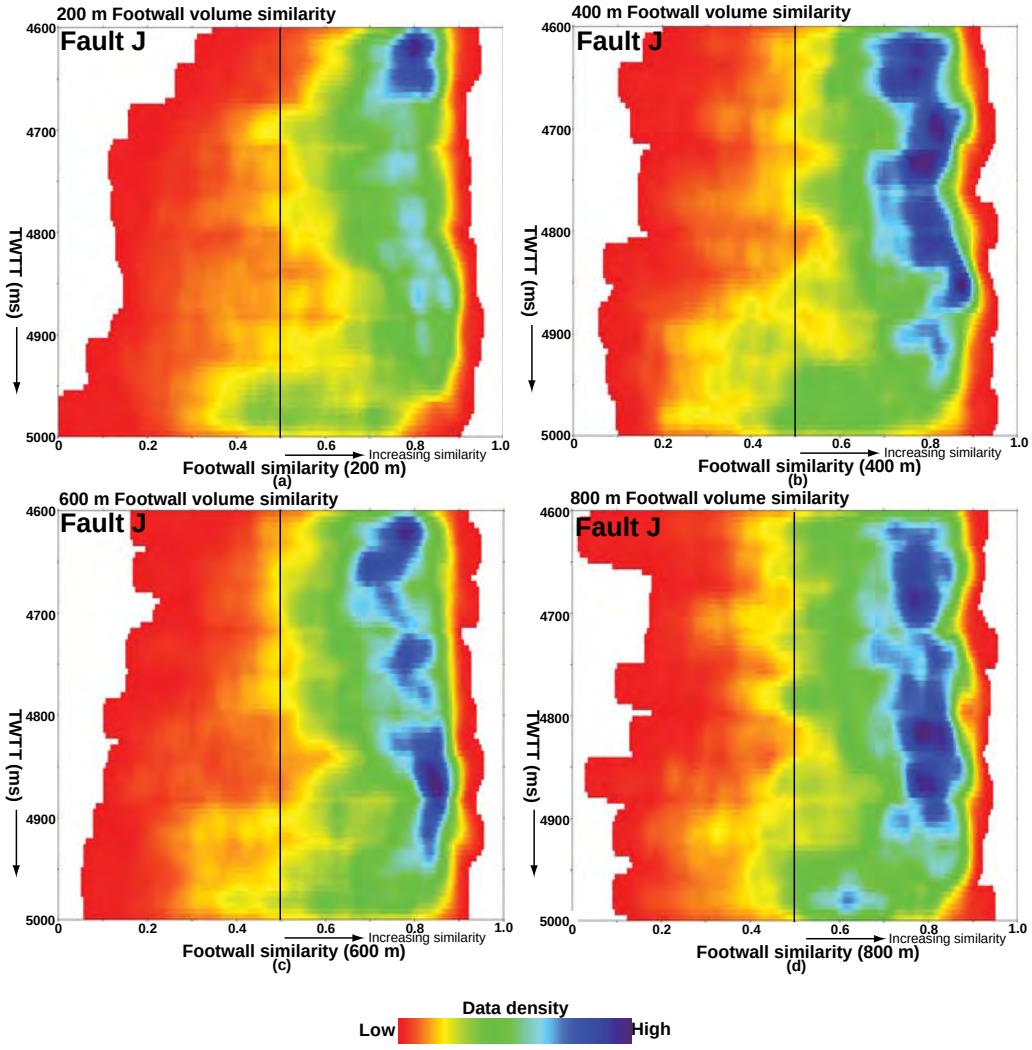

Figure 6.51: Density plots of volume similarity at (a) 200 m, (b) 400 m, (c) 600 m, and (d) 800 m in the footwall parallel to Fault J. The plots are quantitative estimates of volume similarity extracted from the footwall units in Figure 6.38.The purple and red shades represent high and low density of similarity data respectively. Note the high similarity in all the slices, implying that the units in the footwall are not significantly disrupted. Vertical scale is in milliseconds in two way time.

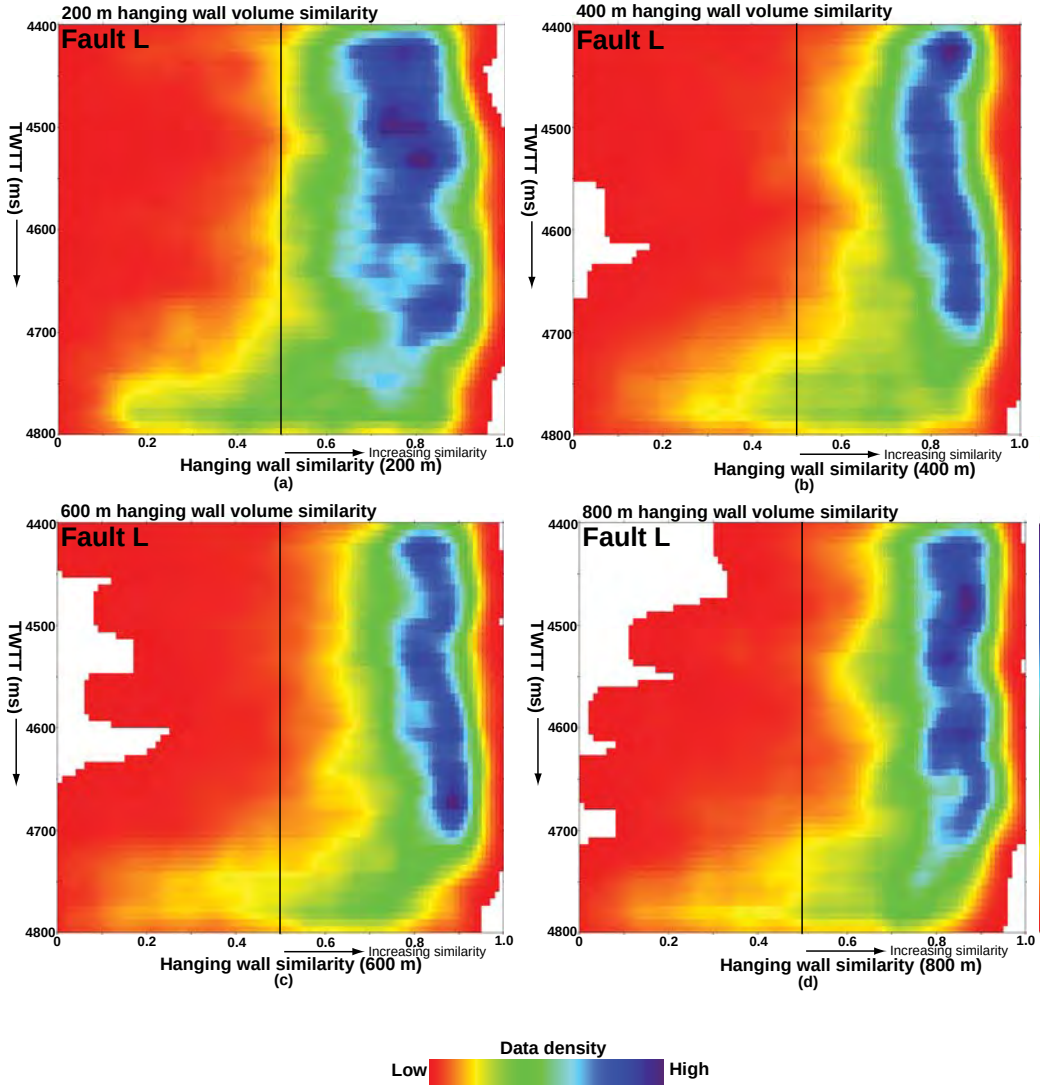

Figure 6.52: Density plots of volume similarity at (a) 200 m, (b) 400 m, (c) 600 m, and (d) 800 m in the hanging wall parallel to Fault L. The plots are quantitative estimates of volume similarity extracted from the hanging wall units in Figure 6.40.The purple and red shades represent high and low density of similarity data respectively. Note the high similarity in all the slices, implying that the units are not significantly disrupted. Vertical scale is in milliseconds in two way time.

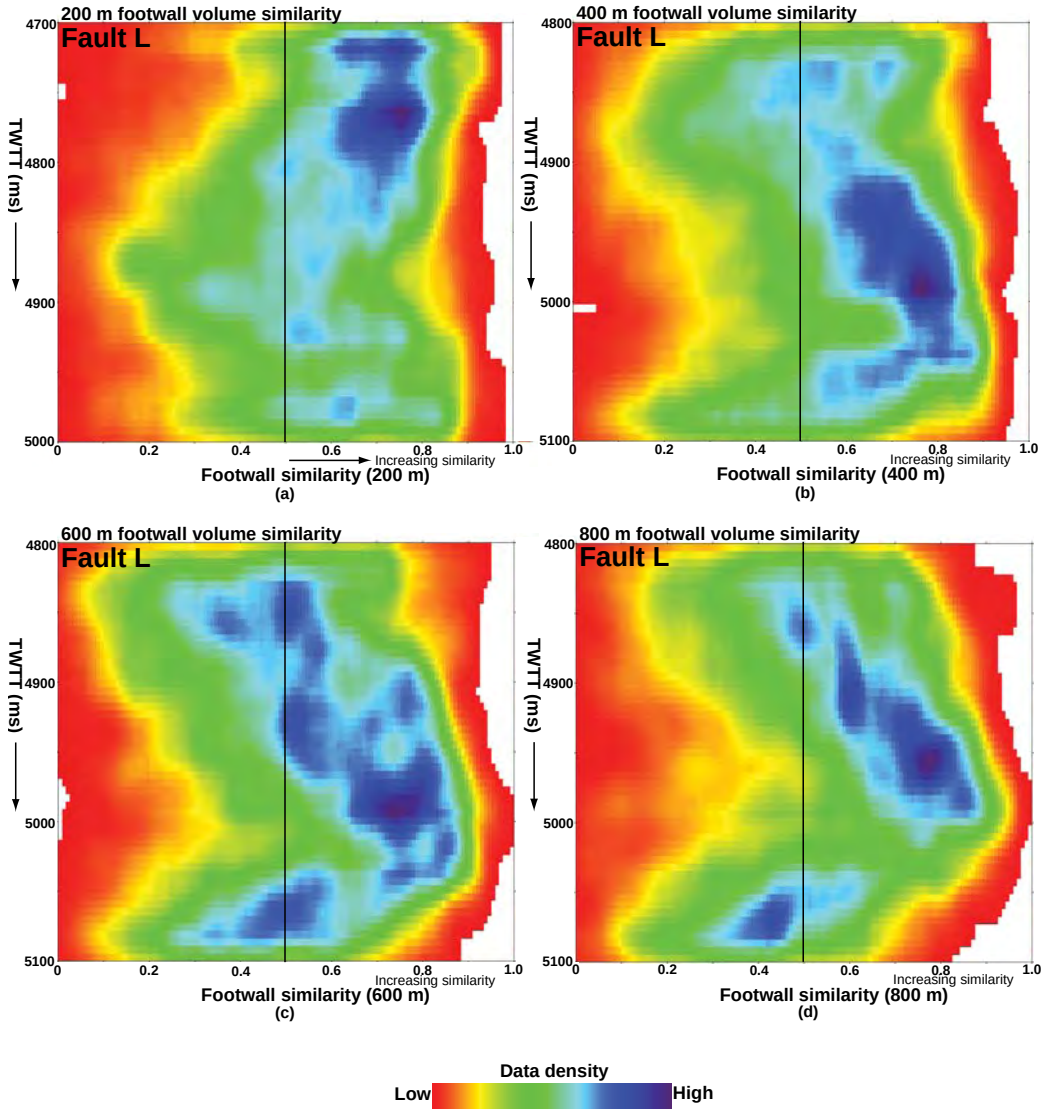

Figure 6.53: Density plots of volume similarity at (a) 200 m, (b) 400 m, (c) 600 m, and (d) 800 m in the footwall parallel to Fault L. The plots are quantitative estimates of volume similarity extracted from the hanging wall units in Figure 6.41.The purple and red shades represent high and low density of similarity data respectively. Note the highly variable pattern of similarity in all the slices. However, in the upper parts of the unit near the fault, similarity is higher but becomes low as the distance away from the fault increases especially in the upper and lower parts of the unit, implying that the units are not significantly disrupted near the fault in the footwall. Vertical scale is in milliseconds in two way time.

6.3.2.4.3 Interpretation

It appears volume disruption is high near the fault plane in the hanging wall of Fault A as shown by the widespread density of low similarity data in all the slices, but becomes higher as the distance away from the fault plane increases to 800 m. The middle and lower parts of the footwall away from the fault plane may be disrupted but not as intense as the hanging wall. The hanging wall of Fault C near the fault plane is disrupted as shown by the low similarity of the slices. However, disruptions appear to be less as the distance away from the fault increases. In the footwall near the fault, disruption is less compared to the hanging wall.

In Fault B, disruption near the fault surface in the hanging wall is not as intense as in the footwall; the footwall is thus more disrupted than the hanging wall. In Fault C, the hanging wall is more disrupted than the footwall near the fault plane, a similar pattern of disruption is seen near the fault across Fault G. In Faults H and I, disruptions in the hanging wall and footwall are about the same, while in Fault J, The high similarity is all the slices in the hanging wall and footwall implies that disruptions are less.

Across Fault K, the hanging wall is more disrupted than the footwall near the fault plane. In Fault L, disruptions are less near the fault in the hanging wall and footwall. However, away from the fault in the footwall, the variable similarity of the slices is probably an indication of disruption. In Fault M, the variable pattern of similarity near the fault in the hanging wall and footwall probably implies some disruptions, while across Fault N, the footwall is more disrupted than the hanging wall near the fault. A similar pattern of disruption is observed in Faults O and P. Table 6.1 is a summary of the pattern of disruptions observed in the hanging wall and footwall near all the faults based on the similarity pattern of the closest slices to the faults (200 m slices). The

next section assesses the spatial relationship between volume similarity and maximum curvature and how the two attributes can detect small-scale folding and discontinuities.

6.3.3 Quantitative links between volume similarity and maximum curvature

In the preceding sections, it has been seen how volume curvature can identify small-scale folding, whereas similarity picked out disruptions due to discontinuities in the volumes adjacent to the faults. By directly comparing volume curvature with similarity it is possible to distinguish between disruption due to discontinuities and folding of the units devoid of intense discontinuities.

Figures 6.54 and 6.55 show density crossplots of volume similarity and maximum curvature in the hanging wall and footwall of Fault A. Near the fault plane in the hanging wall, a strong correlation between juxtaposed high density positive and negative volume maximum curvature (bimodal) with moderate to low volume similarity is observed, i.e. absolute volume maximum curvature directly correlates with low similarity, implying disruption of the units (Figure 6.54a). As the distance from the fault increases to 800 m, volume curvature is predominantly unimodal (i.e. folded) and high in similarity, implying that while the reflectors are folded, reflectivity is largely continuous (Figure 6.54d). The progressive increase in positive volume maximum curvature coupled with the highly variable pattern of similarity away from the fault plane in the footwall of Fault A suggests folding of the units but not significantly disrupted.

In the footwall although volume curvature is high and bimodal, similarity is equally high implying that the units are folded but not intensely disrupted (Figure 6.55a). As

the distance away from the fault increases, volume curvature is largely unimodal and high in similarity (Figure 6.55c & 6.55d). The implication is that away from the fault in the footwall the units are folded but not disrupted. Therefore, the hanging wall is more disrupted than the footwall.

In Fault G, volume curvature in the hanging wall near the fault is predominantly negative and similarity is low, implying that the units are disrupted (Figure 6.56a). A similar pattern of curvature – similarity relationship is seen 400 m away from the fault (Figure 6.56b). At 400 m, curvature is bimodal with a high intensity of positive maximum curvature. The low similarity at this location implies that the units are also as disrupted as the slice closest to the fault. However, as the distance away from the fault increases volume curvature is unimodal and predominantly positive with high similarity implying that the units are folded but not as disrupted as close to the fault (Figure 6.56c & 6.56d).

In the footwall near the fault, a variable pattern of volume curvature – similarity is observed. Generally near the fault curvature is predominantly positive with a similarity pattern ranging from low to high implying that while the units are folded but not completely disrupted (Figure 6.57a) and this trend is replicated 400 m away from the fault (Figure 6.57b). However, at 800 m, the bimodal pattern of volume curvature with low similarity suggests disruptions away from the fault. The implication of these observations is that all the slices in the footwall exhibit an inconsistent pattern of disruption not well defined as in the hanging wall.

Graphical plots of volume maximum curvature adjacent to the four faults highlight ambiguities that may arise when volume curvature is used in isolation as proxy for small-scale deformation adjacent to faults. In previous work, it has been demonstrated

that the juxtaposition of high values of positive and negative maximum curvature in the vicinity of large faults in horizons mapped from seismic data is an indication of brittle deformation of the (e.g. Roberts, 2001; Klein *et al*. 2008; Nissen *et al*. 2007). Traditionally, high values of curvature are usually associated with strain in outcrop bedding surfaces and horizons mapped from seismic data (e.g. Lisle, 1994; Roberts, 2001). By convention, antiforms and domes have positive (convex up) curvature, while synforms and basins have negative (concave) curvatures irrespective of deformation (Roberts, 2001; Klein *et al*. 2008).

Seismic coherency accentuates parts of the amplitude volume where there are discontinuities in the amplitude field at the location of faults where reflector amplitudes are discontinuous (Bahorich & Farmer, 1995). In contrast, the intensity of volume curvature is high where reflectors are bent and not necessarily discontinuous (Klein *et al*. 2008). However, curvature may also be useful in identifying areas of highest strain since folded reflectors may eventually end up being disrupted at later stages of folding (Roberts, 2001; Klein *et al*. 2008; Lisle, 1994; Lisle & Martinez, 2005).

Keating & Fischer (2008) tested the underlying assumption that curvature is a direct proxy for strain in folded layers and proposed that curvature may not be a consistently reliable strain proxy especially in basement-involved fault-related folds. Although folding is a significant form of ductile deformation related to thin-skinned gravity tectonics in deepwater Niger Delta, results presented in this thesis corroborate findings by the authors.

Therefore, the direct correlation between high magnitudes of absolute volume maximum curvature (positive and negative) and low volume similarity observed in the volumes adjacent to Faults A and G are probably related to deformation. As the distance away from the fault increases, the high similarity and predominantly unimodal pattern of volume maximum curvature means that away from the faults folding related to the geometry of reflectors is the main pattern of volume structure.

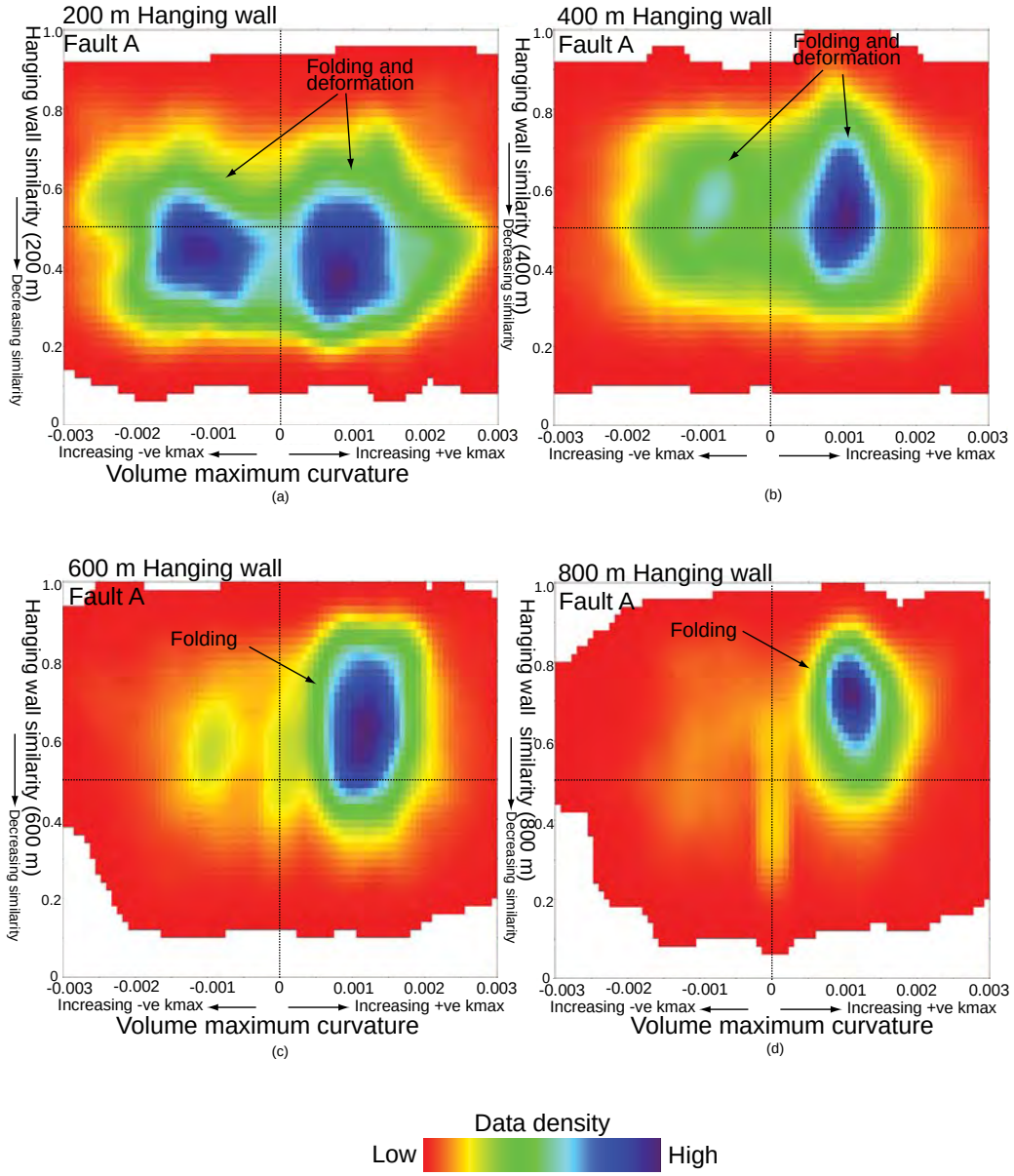

Figure 6.54: Density crossplots of volume maximum curvature and similarity at 200 m (a), 400 m (b), 600 m (c) and 800 m (d) in the hanging wall parallel to Fault A. The purple and red shades represent high and low density of seismic attribute data respectively. Note the strong correlation between high densities of absolute volume maximum curvature with low similarity in the 200 m plot implying volume disruption near the fault plane. Away from the fault plane, the plots show that the units are folded but not significantly disrupted.

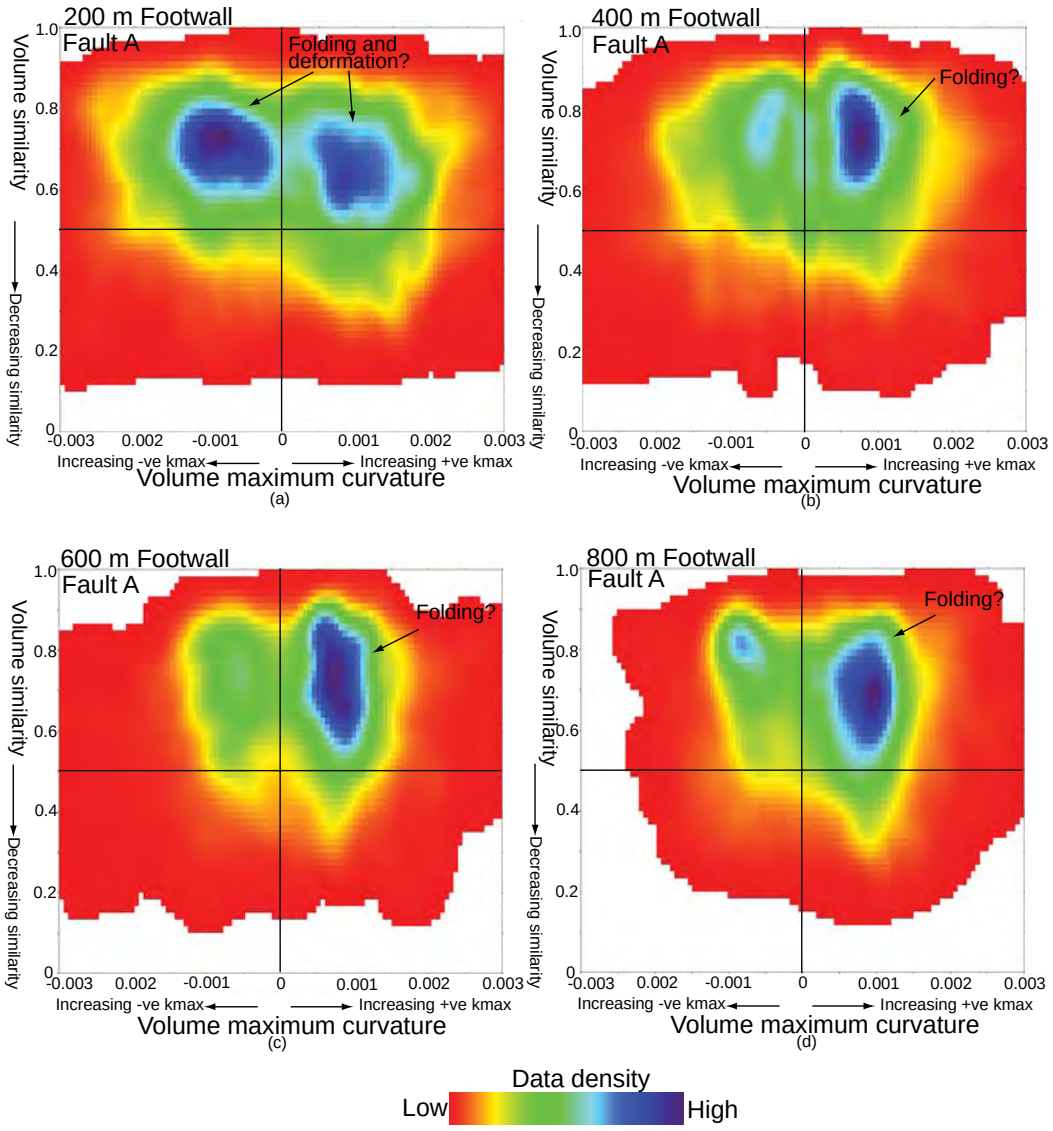

Figure 6.55: Density crossplots of volume seismic maximum curvature and similarity at 200 m (a), 400 m (b), 600 m (c) and 800 m (d) in the footwall parallel to Fault A. The purple and red shades represent high and low density of seismic attribute data respectively Note the correlation between high densities of absolute maximum curvature with fairly high similarity in the 200 m plot. This pattern of relationship implies less disruption in the footwall compared to the hanging wall close to the fault, the units are folded but not significantly disrupted as the distance away from the fault plane increases to 800 m.

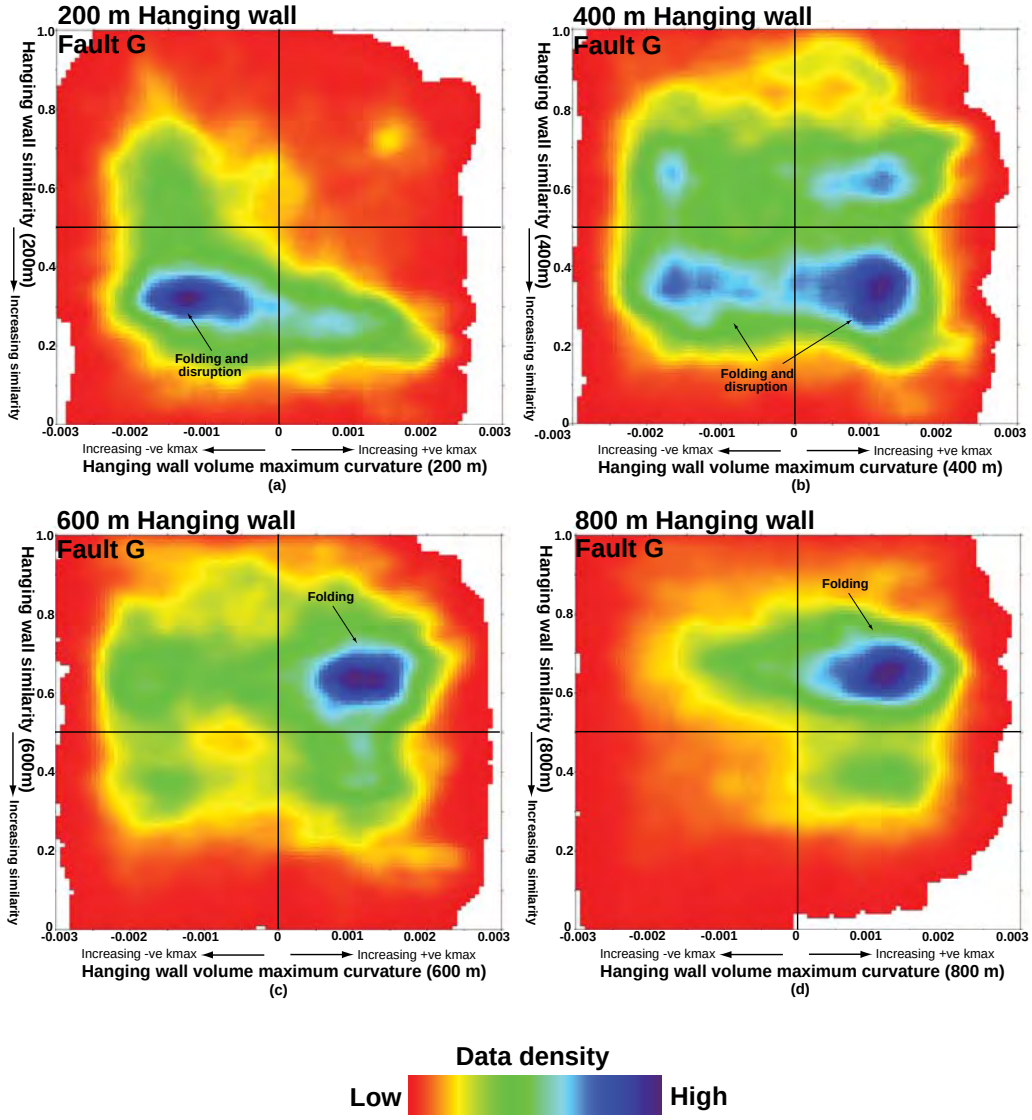

Figure 6.56: Density crossplots of volume maximum curvature and similarity at 200 m (a), 400 m (b), 600 m (c) and 800 m (d) in the hanging wall parallel to Fault G. The purple and red shades represent high and low density of seismic attribute data respectively. Note the strong correlation between high densities of negative and absolute volume maximum curvature with low similarity in the 100 m and 200 m plots implying disruption near the fault plane. Away from the fault plane, the plots show that the hanging wall is folded but not significantly disrupted.

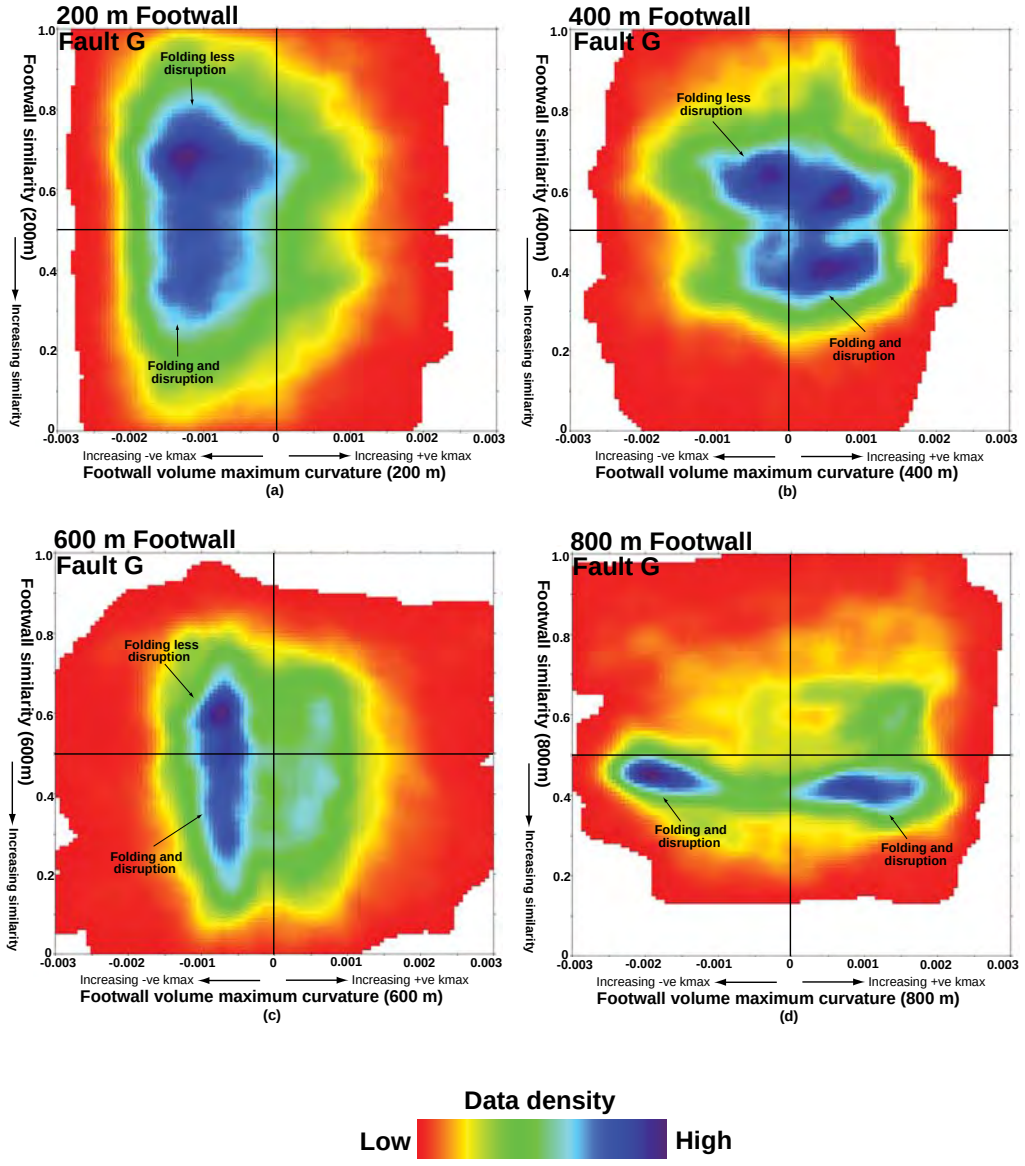

Figure 6.57: Density crossplots of volume maximum curvature and similarity at 200 m (a), 400 m (b), 600 m (c) and 800 m (d) in the footwall parallel to Fault G. The purple and red shades represent high and low density of seismic attribute data respectively. Note the variable pattern of volume curvature – similarity relationships. Parts of the units near the fault are folded and disrupted in all the plots. However, away from the fault most of the units are folded and disrupted.

6.3.4. Links between fault surface topography and volume structure

6.3.4.1 Introduction

The aim of this section is to investigate qualitative links between the pattern of fault surface curvature and the structure of the volumes adjacent to thrust faults selected from the database. Firstly, links between maximum curvature plots of four faults (Faults A, B, J & K) are compared with slices of maximum curvature data sampled 100 m adjacent to the faults in the hanging wall and footwall. Secondly, attribute plots of nine thrust fault planes selected from the database are used to investigate qualitative links between fault surface morphology (using curvature and gradient of fault surface topography) and the structure of the volumes in the vicinity of the faults using similarity attribute data sampled 100 m parallel and adjacent to the faults in the hanging wall and footwall.

The analysis presented in this section is meant to assess links between the overall pattern of volume structure adjacent to the faults and the pattern of fault surface attribute plots. In this analysis, no reflector units have been mapped adjacent to the faults. Finally, seismic attribute data from reflector units mapped across Faults A, G, J and L are plotted against fault surface attribute data to investigate quantitative links between fault geometry and volume structure.

6.3.4.2 Qualitative links between fault surface curvature and volume curvature

Figure 6.58 show maximum curvature plot of Fault A and volume maximum curvature sampled 100 m parallel to the fault in the hanging wall and footwall. The fault is strongly corrugated with antiforms and synforms exhibiting pronounced

patterns of positive and negative curvatures respectively oriented parallel to the fault transport direction at both high and low sampling resolutions.

In the hanging wall near the fault plane, volume curvature is random with a distinct pattern of positive and negative curvature similar to that seen in the curvature plot of the fault. In the footwall, volume curvature is similar to that in the hanging wall except that positive volume curvature is more coherent than in the hanging wall. Therefore, there is a good correlation between the pattern of fault surface curvature and the curvature of the volume in the vicinity of the fault as highlighted by the block arrows. In Fault G, the surface curvature pattern is not as pronounced as in Fault A. However, the plot is characterized by a pronounced zone of horizontal corrugation that is also seen in the volumes 100 m away from the fault in the hanging wall and footwall. In addition a pronounced zone of negative volume maximum curvature correlates with a zone of intense negative maximum curvature in the curvature plot of the fault seen at both high and low resolution (block arrows in Figure 6.59).

The curvature plot of Fault J is characterized by a discrete zone of pronounced negative maximum curvature and a couple of ridges exhibiting intense positive maximum curvature at both high and low curvature sampling resolution. Slices of volume maximum curvature adjacent to the faults show a good correlation with the regions highlighted by the block arrows in Figure 6.60. A similar relationship between fault surface curvature in parts of Fault K and volume structure adjacent to the faults is seen in Figure 6.61. Although these observations are qualitative, it highlights potential links between fault surface topography and small-scale disruptions in the volumes adjacent to the faults. In the next section, similarity attributes sampled adjacent to several faults are qualitatively compared with attribute plots of the faults.

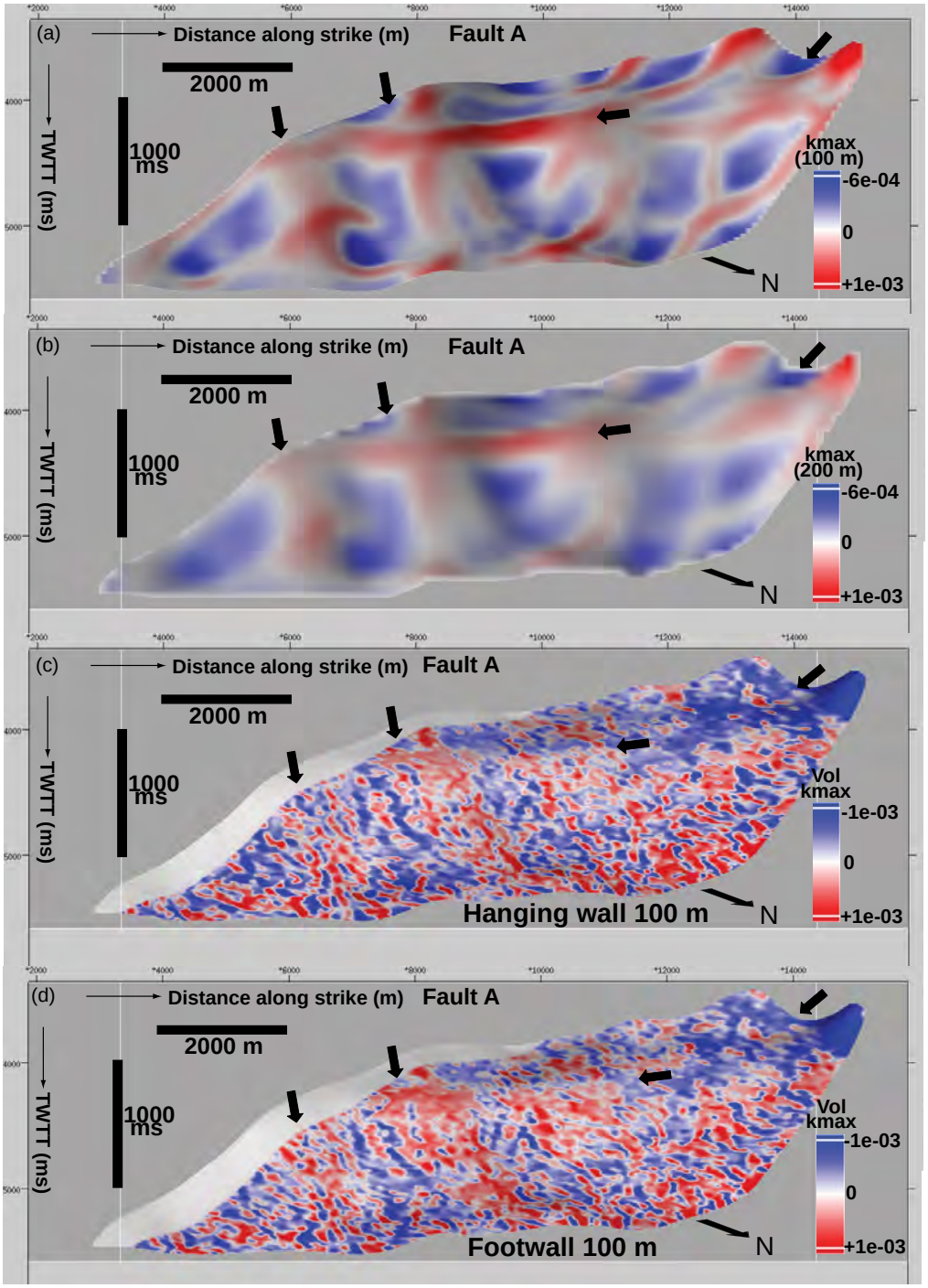

Figure 6.58: Surface maximum curvature plot of Fault A sampled at high resolution (a), surface maximum of Fault A sampled at low resolution (b), volume maximum curvature in the hanging wall at 100 m (c) and volume maximum curvature in the footwall at 100 m (d). Note the identical pattern of fault surface curvature and volume curvature highlighted by the block arrows Vertical scale is in milliseconds two way travel time and horizontal scale is in meters. Vertical exaggeration is ~1.6.

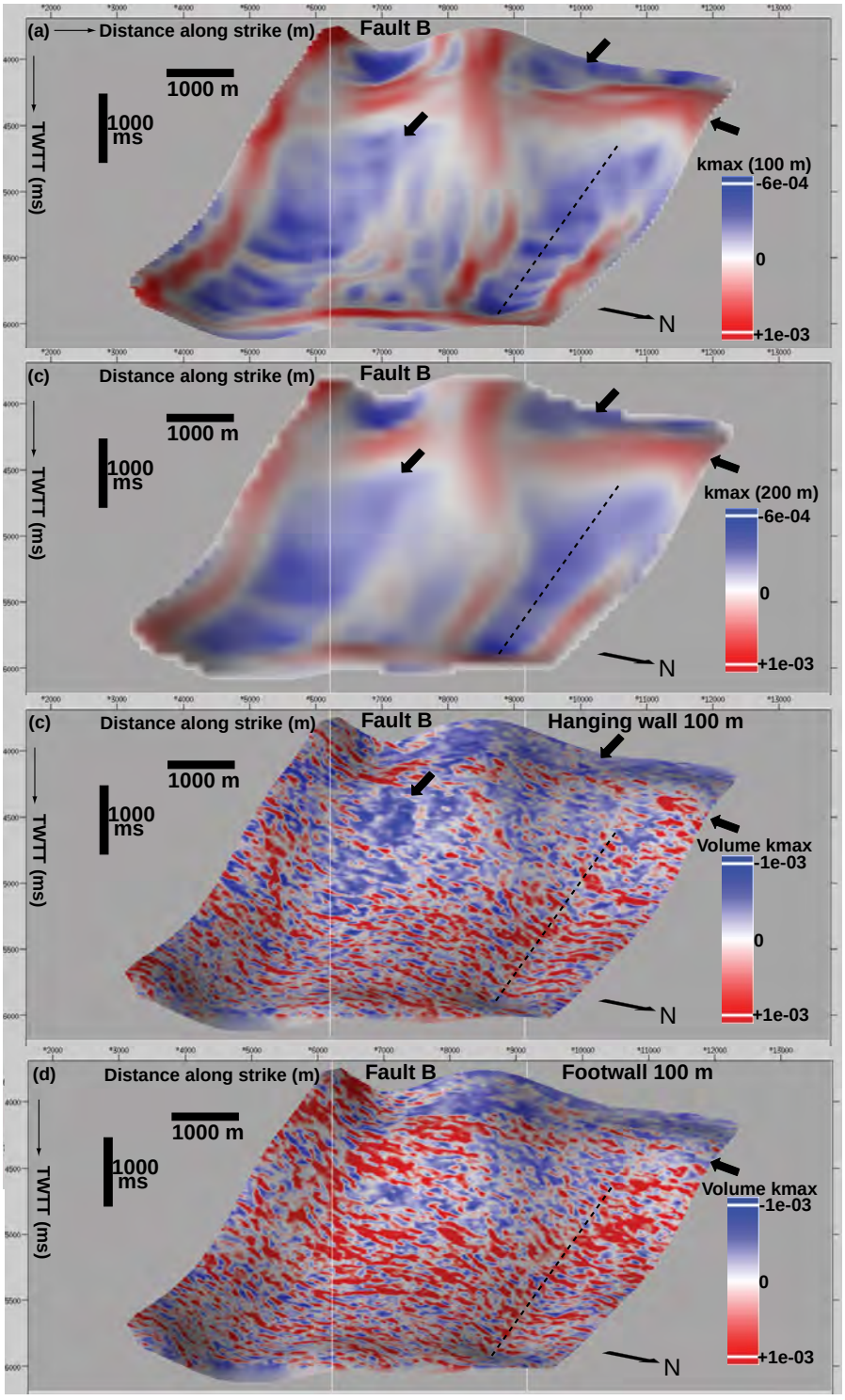

Figure 6.59: Surface maximum curvature plot of Fault B sampled at high resolution (a), surface maximum of Fault B sampled at low resolution (b), volume maximum curvature in the hanging wall at 100 m (c) and volume maximum curvature in the footwall at 100 m (d). Note the identical pattern of fault surface curvature and volume curvature highlighted by the block arrows. The dashed lines show regions where no correlation exists between fault and volume curvatures. Vertical scale is in milliseconds two way travel time and horizontal scale is in meters. Vertical exaggeration is ~1.6.

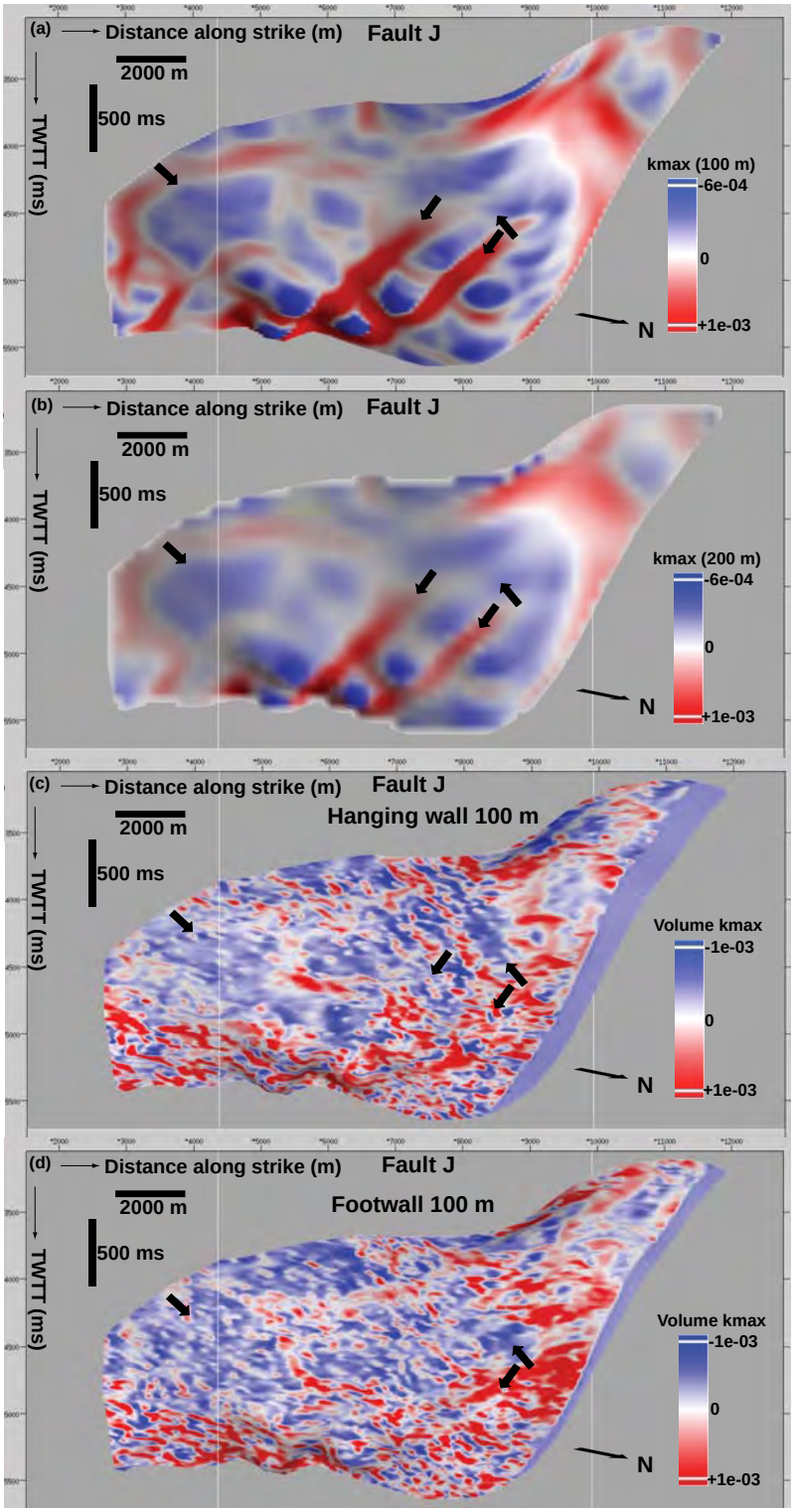

Figure 6.60: Surface maximum curvature plot of Fault J sampled at high resolution (a), surface maximum of Fault J sampled at low resolution (b), volume maximum curvature in the hanging wall at 100 m (c) and volume maximum curvature in the footwall at 100 m (d). Note the identical pattern of fault surface curvature and volume curvature highlighted by the block arrows Vertical scale is in milliseconds two way travel time and horizontal scale is in meters. Vertical exaggeration is ~1.6.

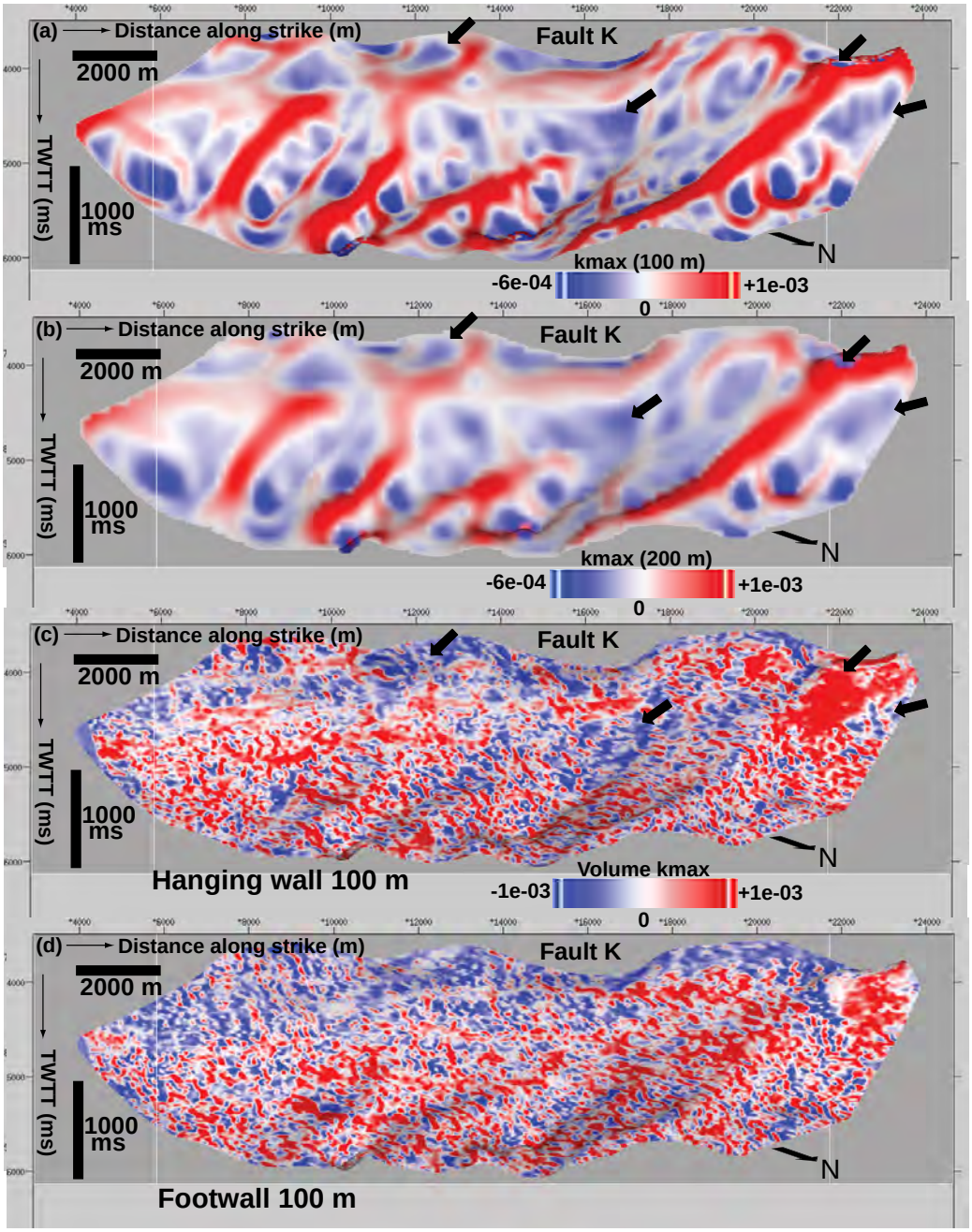

Figure 6.61: Surface maximum curvature plot of Fault K sampled at high resolution (a), surface maximum of Fault K sampled at low resolution (b), volume maximum curvature in the hanging wall at 100 m (c) and volume maximum curvature in the footwall at 100 m (d). Note the identical pattern of fault surface curvature and volume curvature highlighted by the block arrows in the hanging wall No links are observed between fault and volume curvatures in the footwall. Vertical scale is in milliseconds two way travel time and horizontal scale is in meters. Vertical exaggeration is ~1.6.

6.3.4.3 Qualitative links between fault surface morphology and volume similarity

6.3.4.3.1 Fault B

The curvature plot of Fault B sampled at high and low resolution shows two prominent regions of pronounced negative maximum curvature and a region of intense pattern of positive maximum curvature exhibited as a zone of pronounce horizontal corrugation seen in both the high and low resolution plots of fault surface maximum curvature (Figure 6.62a & 6.62b). These patterns of intense fault surface maximum curvature closely matches liner zones of low similarity in the hanging wall and footwall similarity slices (green arrows and the dashed lines in Figure 6.62c and 6.62d). The blue arrows highlight regions of low intensity of fault surface curvature matching zones of high similarity adjacent to the fault, implying that discrete zones of low similarity in the hanging wall and footwall may be due to the pronounced patterns of fault surface maximum curvature. The blue arrows highlights regions located at the transition between positive and negative maximum curvature exhibiting low curvature correlating with areas of high similarity in the hanging wall and footwall. However, the red circles highlight instances where although fault surface curvature is high, similarity is equally high in the hanging wall and footwall.

A similar relationship is observed when the Gaussian curvature plots of the fault sampled at high and low resolution is compared with similarity slices adjacent to the fault (Figure 6.63a & 6.63b). The green arrows show discrete zones of intense fault surface curvature that closely matches zones of low similarity in the hanging wall and footwall (Figure 6.63c & 6.63d). The dashed red lines highlight regions of change in curvature polarity closely matching linear zones of low similarity in the hanging wall

and footwall. The blue arrows highlights instances where low magnitudes of fault surface curvature located at the transition between negative and positive Gaussian curvature appears to be related to zones high in similarity in the hanging wall and footwall. The black arrows highlights regions at the bottom of the curvature plots exhibiting random pattern of curvature and low similarity. Similar links are also observed between intense and random pattern of gradient of fault surface topography and low similarity in the hanging wall and footwall (dashed lines and boxes in Figure 6.64a). The blue arrows highlight regions of fairly uniform surface gradient corresponding with zones of fairly high similarity in the hanging wall and footwall (Figure 6.64b & 6.64c).

6.3.4.3.2 Fault H

Figure 6.65a & 6.65b shows maximum curvature plots of Fault H sampled at high and low resolution respectively. The plots show regions of pronounced curvature in the centre of the fault. The green arrows highlights linear zones of low similarity at the hanging wall and footwall at the exact location of the zone of pronounced fault surface maximum curvature (Figure 6.65c & 6.65d). This observation implies that the discrete zone of low similarity may be due to the intense curvature of the fault at that point. The dashed circle shows highlights a zone of intense curvature that is related to an isolated circular region of low similarity in the hanging wall. The blue arrows and dashed lines highlight regions high in similarity in the hanging wall and footwall that closely matches zones of low intensity of fault surface curvature.

A similar relationship is observed when high and low resolution Gaussian curvature plots of the faults are compared when similarity slices sampled adjacent to the fault

(Figure 6.66). The green arrows highlight a discrete zone of low similarity at the centre of the hanging wall and footwall slices closely matching a zone of intense Gaussian curvature exhibiting curvature polarity reversal in the central parts of the fault (Figure 6.66c & 6.66d). This zone is also seen as discrete region of intense fault surface maximum curvature in Figure 6.65. The dashed red circle shows an isolated zone of low similarity in the hanging wall that closely matches a discrete zone of pronounced change in polarity of Gaussian curvature. The blue arrow and dashed line exemplifies instances where high similarity may be due to low magnitudes of fault surface Gaussian curvature. Similar links are also seen between pronounced change in the pattern of gradient of fault surface topography and discrete regions of low similarity at the centre of the hanging wall and footwall slices. The blue arrows highlight potential links between low intensity of fault surface gradient and high similarity in the hanging wall and footwall (Figure 6.67).

6.3.4.3.3 Fault J

The curvature plot of Fault J is characterized by a discrete zone of pronounced change in curvature from positive to negative corresponding with a sharp change in fault surface gradient at the top left of the plot (Figures 6.68a & 6.68b). The green arrows highlight close correlation between the patterns of maximum curvature and gradient of fault surface topography with discrete zones of low similarity in the hanging wall and footwall adjacent to the fault, implying that disruption in the hanging wall and footwall is related to curvature and gradient patterns on the fault surface.

6.3.4.3.4 Fault K

Maximum curvature plots of this fault sampled at high and low resolution shows that the fault is strongly corrugated with a highly variable pattern of gradient of fault surface topography (Figure 6.69a, 6.69b & 6.69d). The main structural feature of this fault is a corrugation exhibiting intense positive maximum curvature (dashed line in the curvature plots). The green arrow highlights a discrete zone of low similarity at the location of the corrugation and it appears the intensity of the corrugation and a sharp change in fault surface gradient at the same location may be responsible for the subtle pattern of low similarity in the hanging wall (dashed lines and green arrows in Figure 6.69d & 6.69e). The dashed rectangle also shows zones of intense pattern of fault surface curvature and rapid change in surface gradient that may be related to zones of low similarity in the central parts of the similarity slice in the hanging wall.

6.3.4.3.5 Fault M

Maximum curvature plots of the fault sampled at high and low resolution shows that the fault exhibits a pronounced pattern of negative maximum curvature in the central parts of the fault surrounded by regions of high positive maximum curvature (Figure 6.70a & 6.70b). The green arrows highlight regions where the intense pattern of curvature closely matches discrete zones of low similarity in the hanging wall and footwall (Figure 6.70c & 6.70d). The blue arrows highlight a fairly weak correlation between high similarity and low intensity of curvature. A similar relation between curvature and similarity is seen when the Gaussian curvature plot of the fault sampled at high and low resolution is compared with similarity slices adjacent to the fault (Figure 6.71). The green arrows show a good correlation between intense patterns of synclastic curvature with low similarity. The blue arrows show where high similarity

appears to be related to low magnitudes of curvature. However, the dashed circle highlights instances where although the intensity of Gaussian curvature is low similarity is high (Figure 6.71c & 6.71d).

6.3.4.3.6 Fault N

The main structural feature of the fault is a region of pronounced horizontal corrugation and a major source of intense positive maximum curvature seen in high and low resolution maximum curvature plots of the fault and probably related to a fault bend (green arrows in Figure 6.72a 7 6.72b). The green arrows highlights regions of low similarity in the top half of the hanging wall and footwall similarity slices that may be due to the pronounced pattern of horizontal corrugation. The dashed circles shows zones of low similarity in the hanging wall and footwall that closely matches a pronounced zone of negative maximum curvature. The blue arrows highlight instances where high similarity may be due to the low intensity of fault surface maximum curvature (Figure 6.72c & 6.72d).

A similar relationship is observed between high and low resolution Gaussian curvature plots of the fault and similarity slices sampled adjacent to the fault (Figure 6.73a & 6.73b). The green arrows highlight good correlation between low similarity in the upper parts of the similarity slices and a horizontal region of change in polarity of Gaussian curvature. This correlation is also seen in Figure 6.72. The dashed circles highlight regions where random pattern of intense Gaussian curvature closely matches discrete zones of low similarity in the hanging wall and footwall, while the blue arrows indicates regions of low intensity of Gaussian curvature with high similarity (Figure 6.73c & 6.73d).

6.3.4.3.7 Fault P

The structural feature of this fault is a pronounced pattern of horizontal corrugation in the upper parts of the fault and intense negative maximum curvature in the lower parts (Figure 6.74a 7 6.74b). The dashed line highlights an instance where intense pattern of curvature is not related to low similarity in the hanging wall and footwall. However, there appears to be a close correlation between the intense pattern of negative maximum curvature at high and low sampling resolution with zones of low similarity in the hanging wall and footwall (green arrows in Figure 6.74c & 6.74d)). The blue arrows highlight zones between the transitions between two patches of intense negative maximum curvature correspondingly high in similarity in the volumes adjacent to the fault.

The implication of these observations is that intense/pronounced pattern of fault surface curvature and change in polarity of Gaussian curvature may be related to low similarity and hence disruption in the volumes adjacent to the faults. However, instances where curvature – disruption relationships are inconsistent have also been seen. The next section investigates quantitative links between fault surface curvature and the structure of the volumes adjacent to Faults A, G, J and L using density plots of seismic attribute data extracted from reflector intervals mapped 50 m across the faults in the hanging wall and footwall.

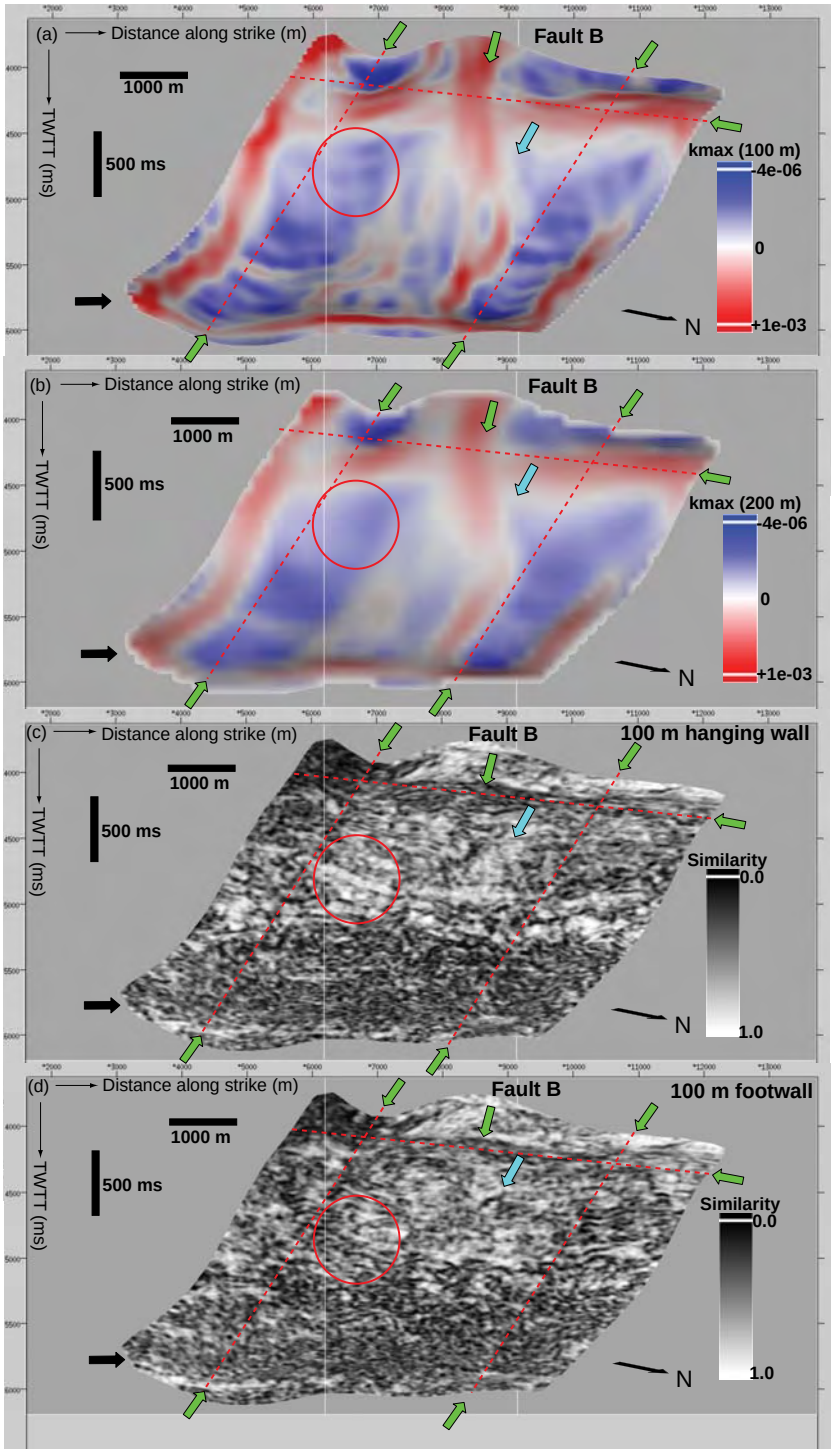

Figure 6.62: High resolution maximum curvature plot of Fault B (a), low resolution maximum curvature plot of Fault B (b), similarity slice sampled 100 m parallel to the fault in the hanging wall (c) and similarity slice sampled 100 m parallel to the fault in the footwall (d). The green arrows and red lines highlight links between intense fault surface curvature and low similarity adjacent to the fault, while the blue arrows highlight zones of low curvature and high similarity. The red circles show instances where no links between fault curvature and disruption adjacent to the fault is established. Vertical scale is in milliseconds in two way travel time and horizontal scale is in meters. Vertical exaggeration is ~1.6.

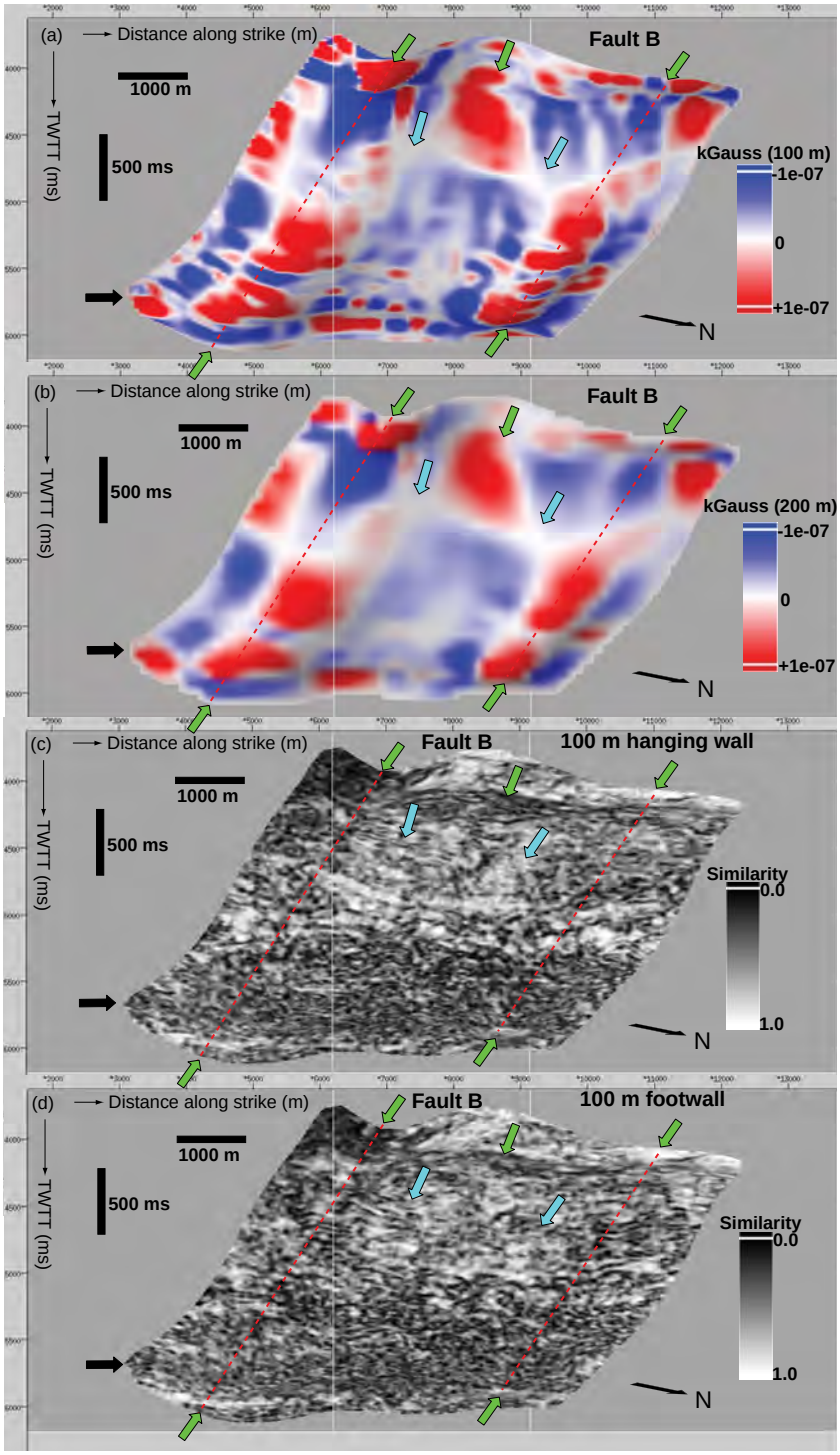

Figure 6.63: High resolution Gaussian curvature plot of Fault B (a), low resolution Gaussian curvature plot of Fault B (b), similarity slice sampled 100 m parallel to the fault in the hanging wall (c) and similarity slice sampled 100 m parallel to the fault in the footwall (d). The green arrows and red lines highlight links between intense fault surface curvature and low similarity adjacent to the fault, while the blue arrows highlight zones of low curvature and high similarity. Vertical scale is in milliseconds in two way travel time and horizontal scale is in meters. Vertical exaggeration is ~1.6.

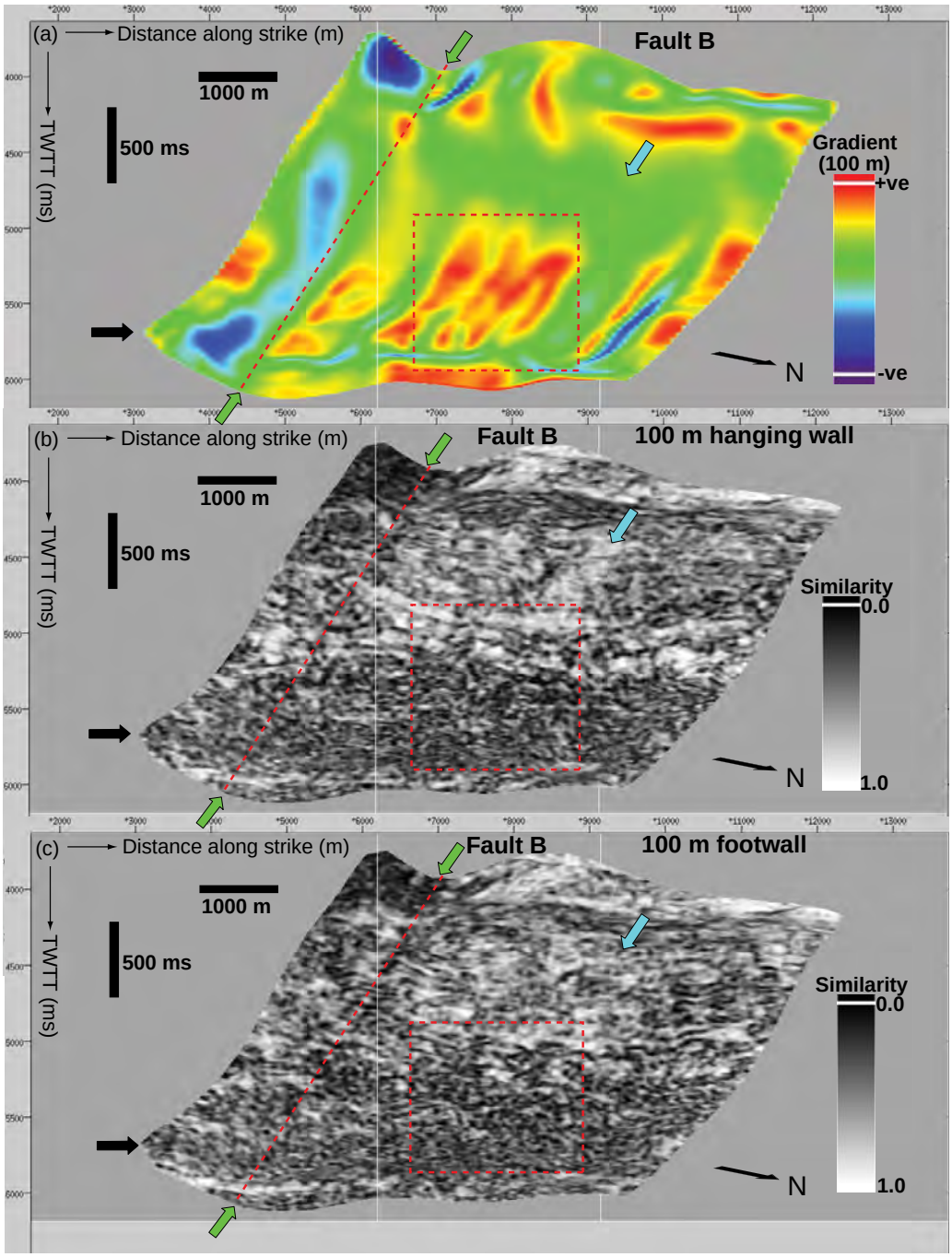

Figure 6.64: High resolution gradient of surface topographic plot of Fault B (a), similarity slice sampled 100 m parallel to the fault in the hanging wall (b) and similarity slice sampled 100 m parallel to the fault in the footwall (c). The green arrows, red lines and boxes highlight links between anomalies in fault surface gradient and low similarity adjacent to the fault, while the blue arrows highlight zones of low curvature and high similarity. Vertical scale is in milliseconds in two way travel time and horizontal scale is in meters. Vertical exaggeration is ~1.6.

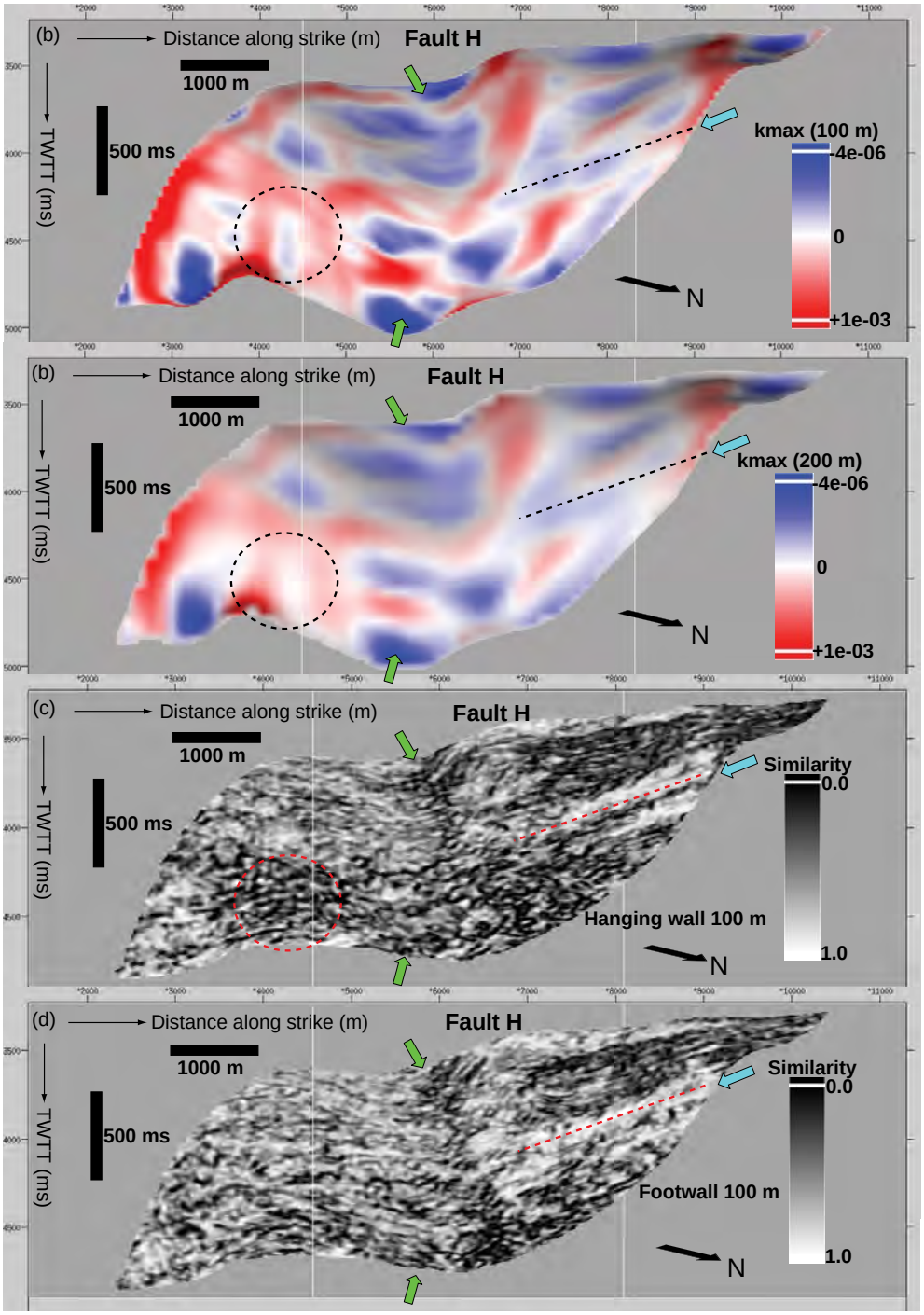

Figure 6.65: High resolution maximum curvature plot of Fault H (a), low resolution maximum curvature plot of Fault H (b), similarity slice sampled 100 m parallel to the fault in the hanging wall (c) and similarity slice sampled 100 m parallel to the fault in the footwall (d). The green arrows and red circles highlight links between high magnitudes of fault surface curvature and low similarity adjacent to the fault, while the blue arrows highlight zones of low curvature and high similarity. Vertical scale is in milliseconds in two way travel time and horizontal scale is in meters. Vertical exaggeration is ~1.6.

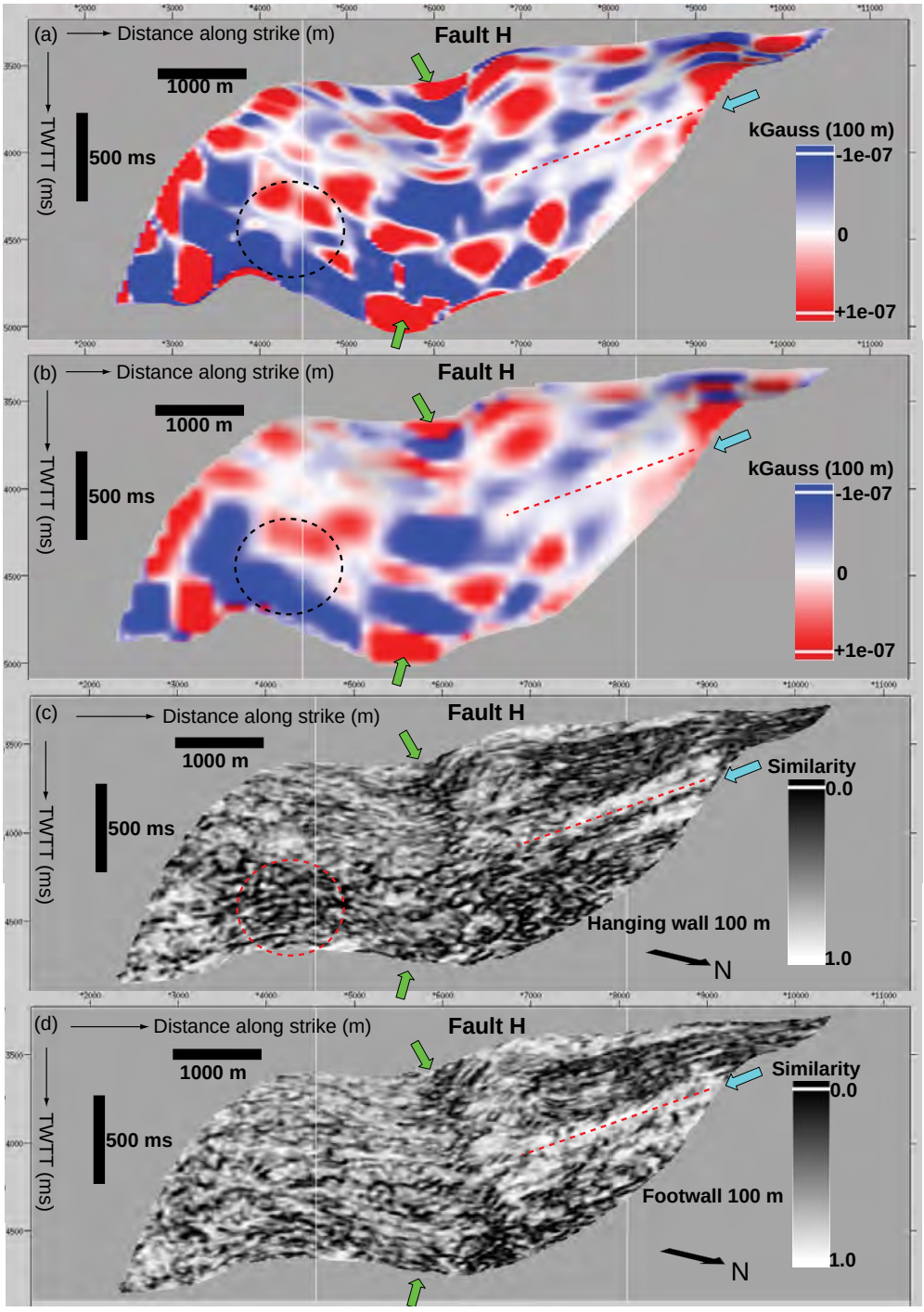

Figure 6.66: High resolution Gaussian curvature plot of Fault H (a), low resolution Gaussian curvature plot of Fault H (b), similarity slice sampled 100 m parallel to the fault in the hanging wall (c) and similarity slice sampled 100 m parallel to the fault in the footwall (d). The green arrows and red circles highlight links between intense fault surface curvature and low similarity adjacent to the fault, while the blue arrows highlight zones of low curvature and high similarity. Vertical scale is in milliseconds in two way travel time and horizontal scale is in meters. Vertical exaggeration is ~1.6.

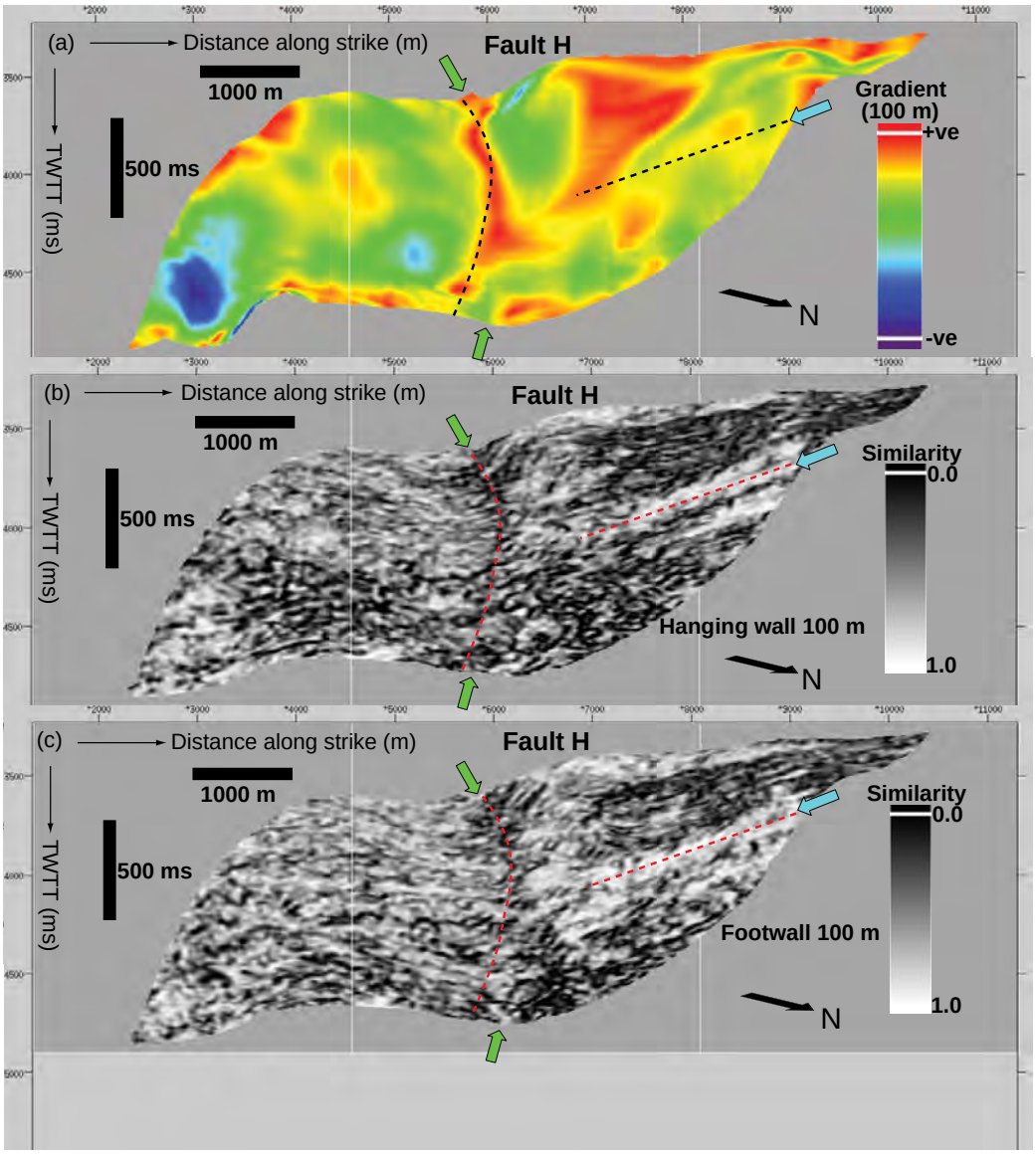

Figure 6.67: High resolution gradient of fault surface topography plot of Fault H (a), similarity slice sampled 100 m parallel to the fault in the hanging wall (b) and similarity slice sampled 100 m parallel to the fault in the footwall (c). The green arrows and red lines highlight links between anomalous fault surface gradient and low similarity adjacent to the fault, while the blue arrows highlight zones of low curvature and high similarity. Vertical scale is in milliseconds in two way travel time and horizontal scale is in meters. Vertical exaggeration is ~1.6.

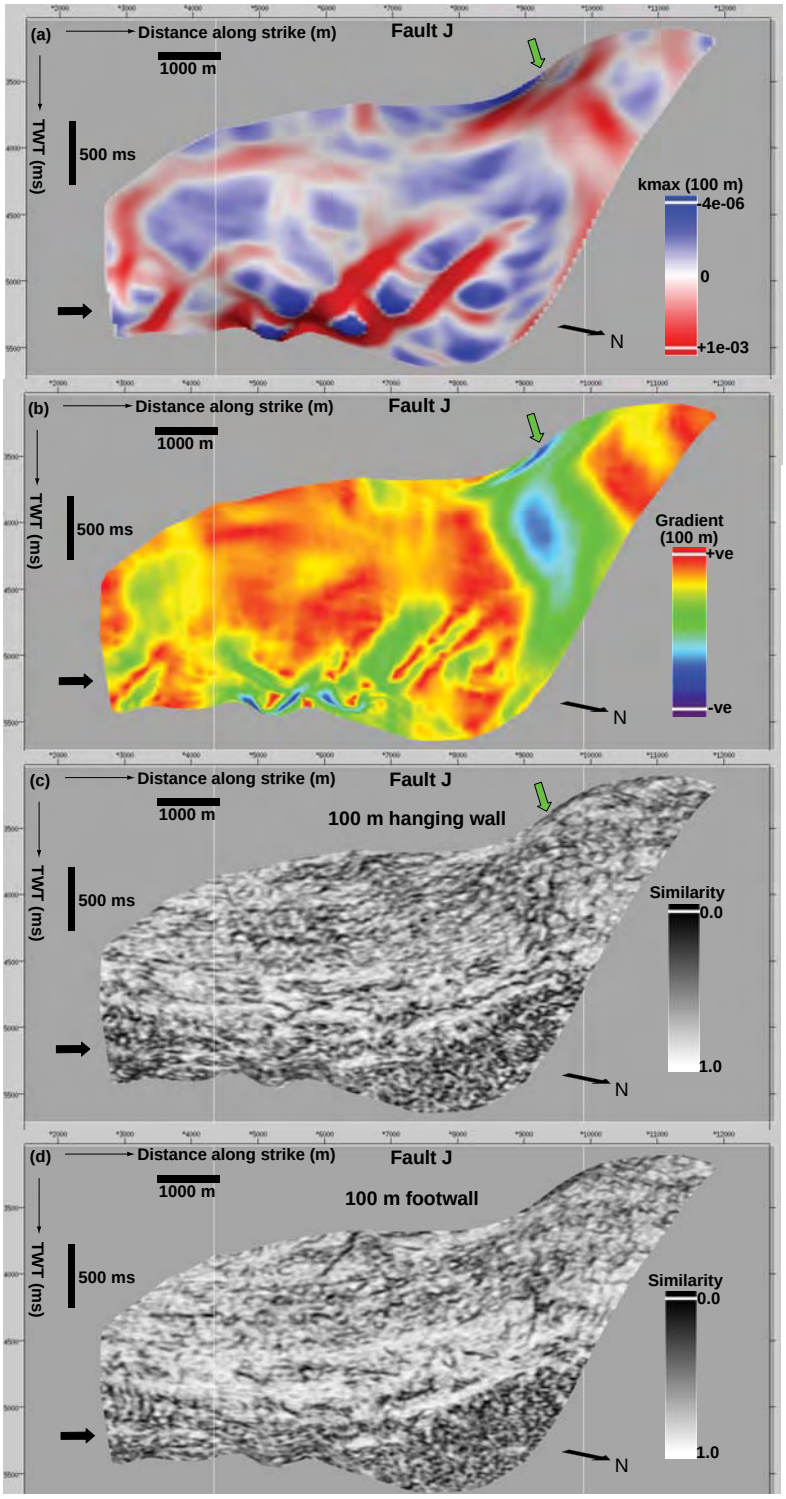

Figure 6.68: High resolution maximum curvature plot of Fault J (a), high resolution gradient of fault surface topography plot of Fault J (b), similarity slice sampled 100 m parallel to the fault in the hanging wall (c) and similarity slice sampled 100 m parallel to the fault in the footwall (d). The green arrows highlight links between intense fault surface curvature, anomalous surface gradient and low similarity adjacent to the fault. Vertical scale is in milliseconds in two way travel time and horizontal scale is in meters. Vertical exaggeration is ~1.6.

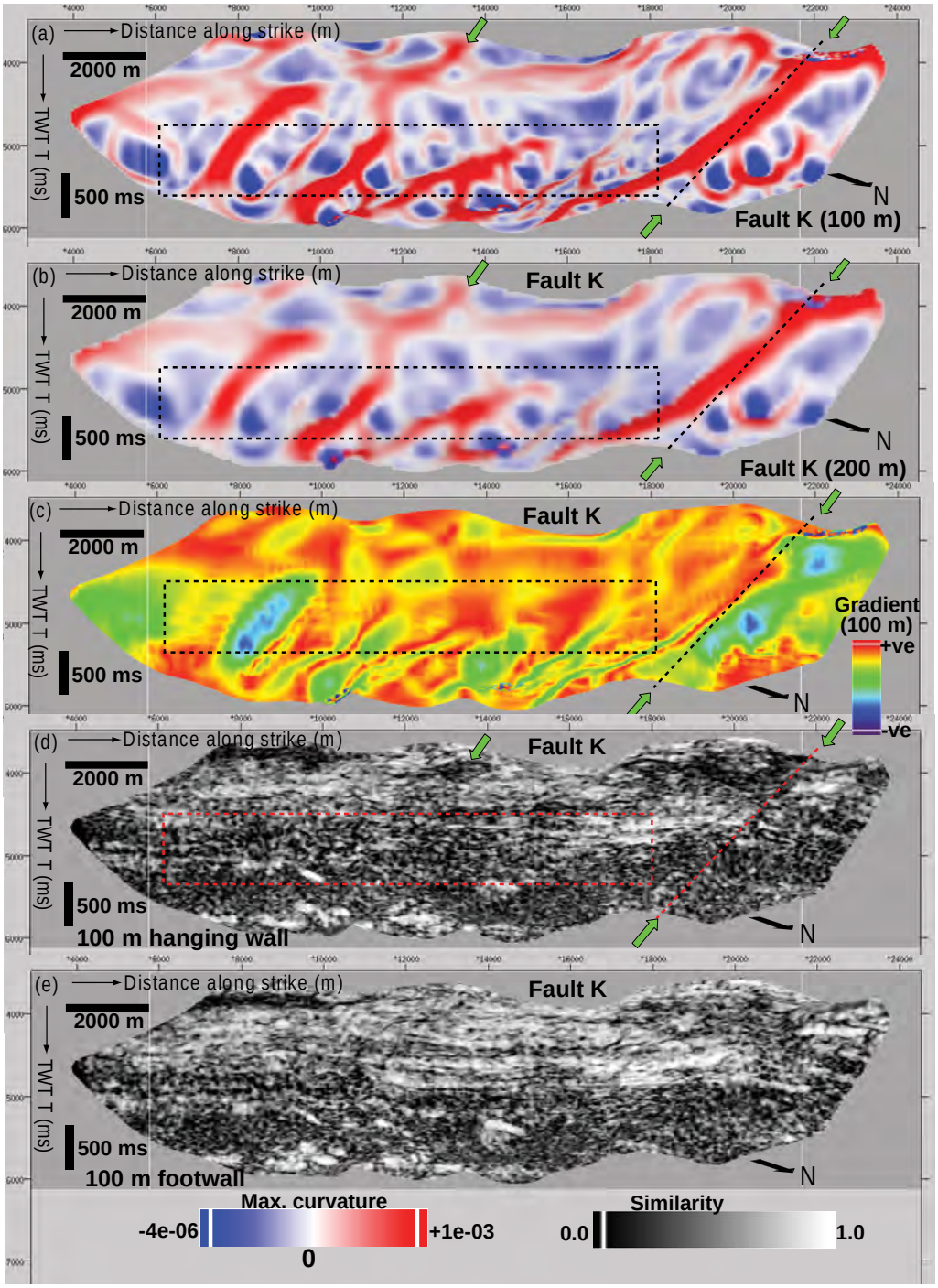

Figure 6.69: High resolution maximum curvature plot of Fault K (a), low resolution maximum curvature plot of Fault K (b), high resolution gradient of fault surface topography plot of Fault K (c), similarity slice sampled 100 m parallel to the fault in the hanging wall (d) and similarity slice sampled 100 m parallel to the fault in the footwall (e). The green arrows, red lines and boxes highlight links between intense fault surface curvature, anomalous fault surface gradient and low similarity in the hanging wall. Vertical scale is in milliseconds in two way travel time and horizontal scale is in meters. Vertical exaggeration is ~1.6.

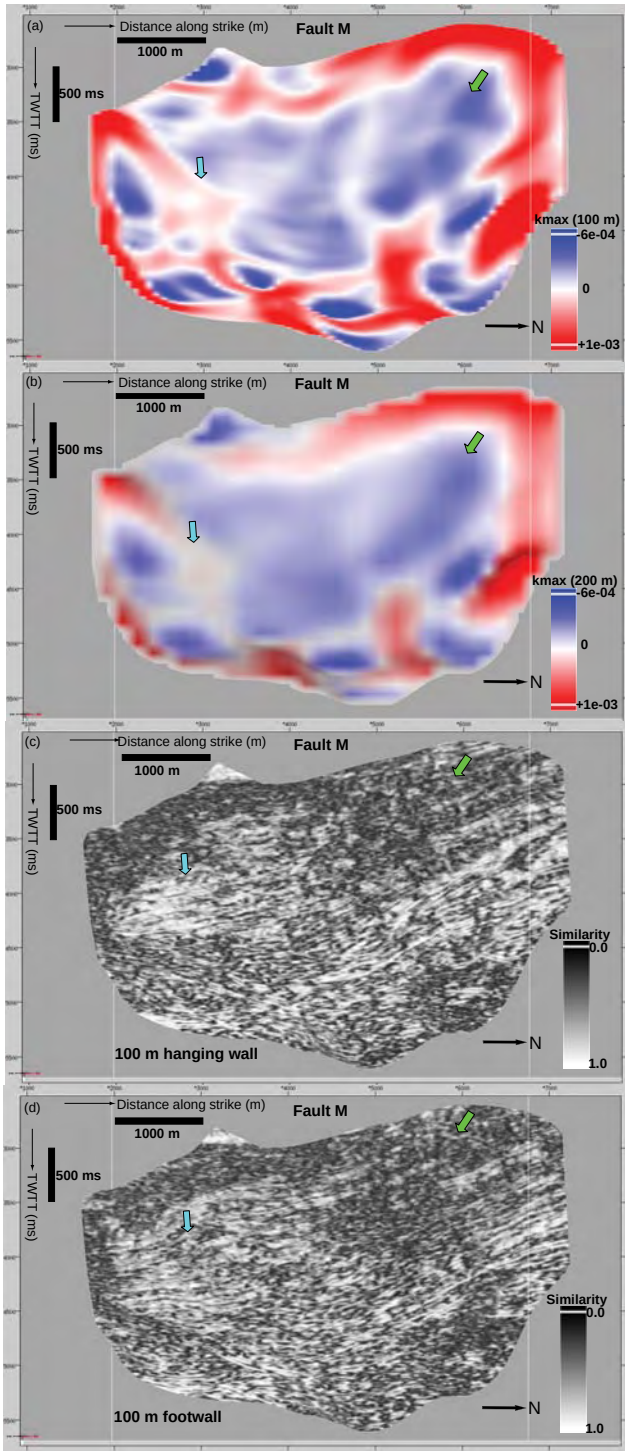

Figure 6.70: High resolution maximum curvature plot of Fault M (a), low resolution maximum curvature plot of Fault M (b), similarity slice sampled 100 m parallel to the fault in the hanging wall (c) and similarity slice sampled 100 m parallel to the fault in the footwall (d). The green arrows highlight links between discrete zones of intense fault surface curvature and low similarity in the hanging wall and footwall, while the blue arrows highlight zones of low curvature and high similarity. Vertical scale is in milliseconds in two way travel time and horizontal scale is in meters. Vertical exaggeration is ~1.6.

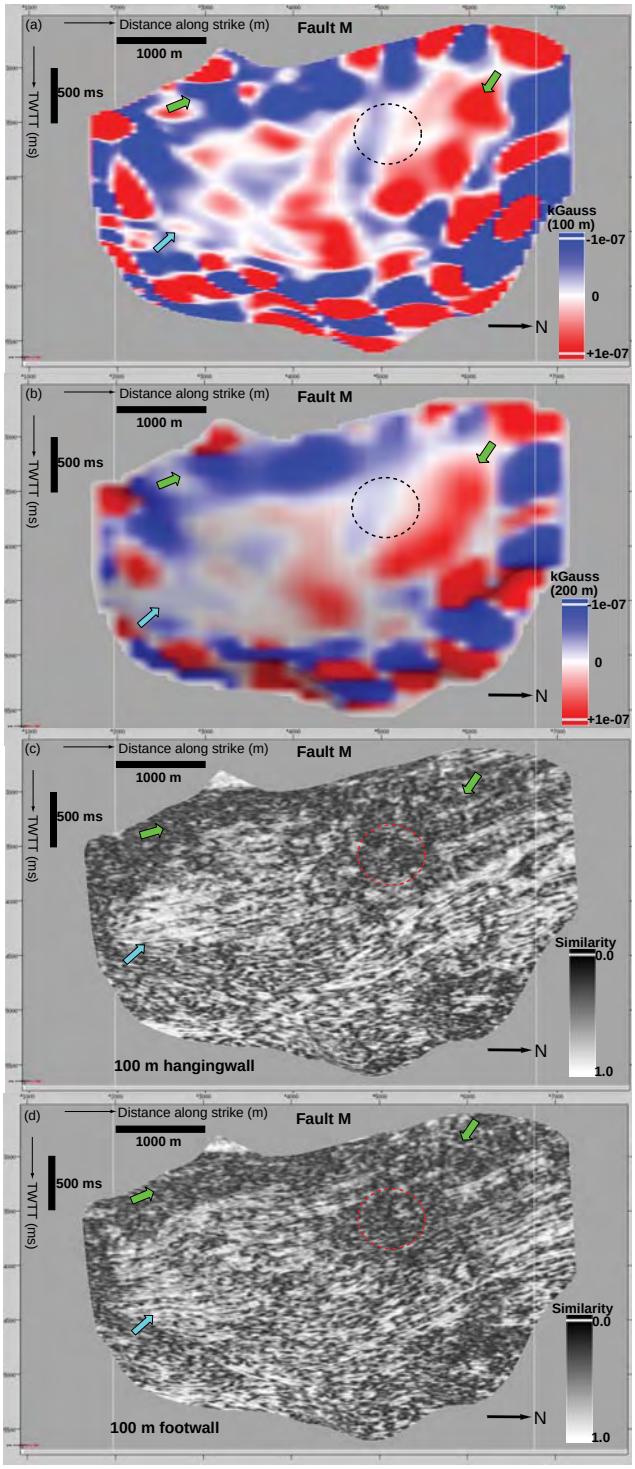

Figure 6.71: High resolution Gaussian curvature plot of Fault M (a), low resolution Gaussian curvature plot of Fault M (b), similarity slice sampled 100 m parallel to the fault in the hanging wall (c) and similarity slice sampled 100 m parallel to the fault in the footwall (d). The green arrows highlight links between intense fault surface curvature and low similarity in the hanging wall and footwall, while the blue arrows highlight zones of low curvature and high similarity. The circles show instances where no links between fault surface curvature and disruption adjacent to the fault is established. Vertical scale is in milliseconds in two way travel time and horizontal scale is in meters. Vertical exaggeration is ~1.6.

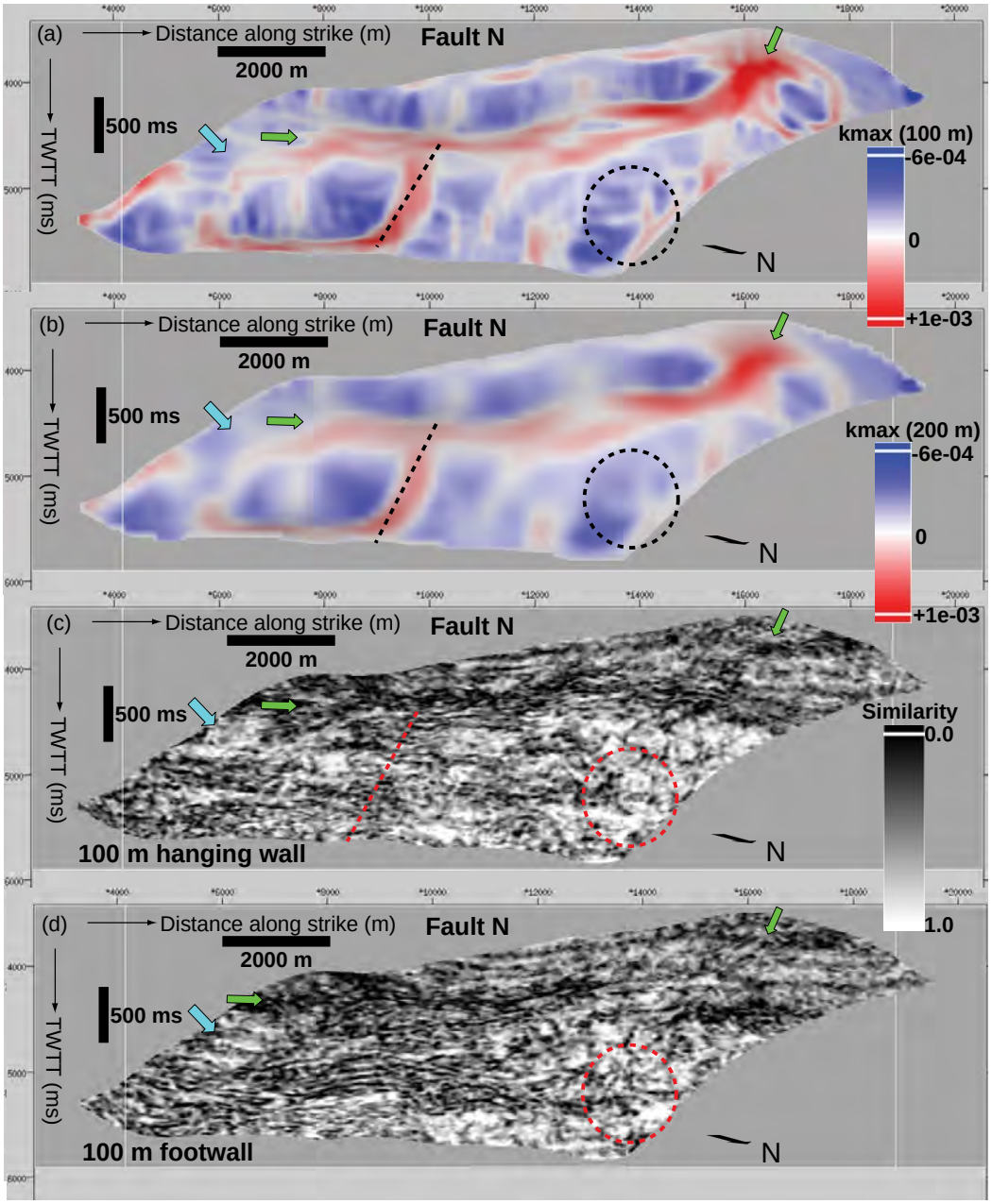

Figure 6.72: High resolution maximum curvature plot of Fault N (a), low resolution maximum curvature plot of Fault N (b), similarity slice sampled 100 m parallel to the fault in the hanging wall (c) and similarity slice sampled 100 m parallel to the fault in the footwall (d). The green arrows, red lines and circles highlight links between pronounced pattern of fault surface curvature and low similarity in the hanging wall and footwall, while the blue arrows highlight zones of low curvature and high similarity. Vertical scale is in milliseconds in two way travel time and horizontal scale is in meters. Vertical exaggeration is ~1.6.

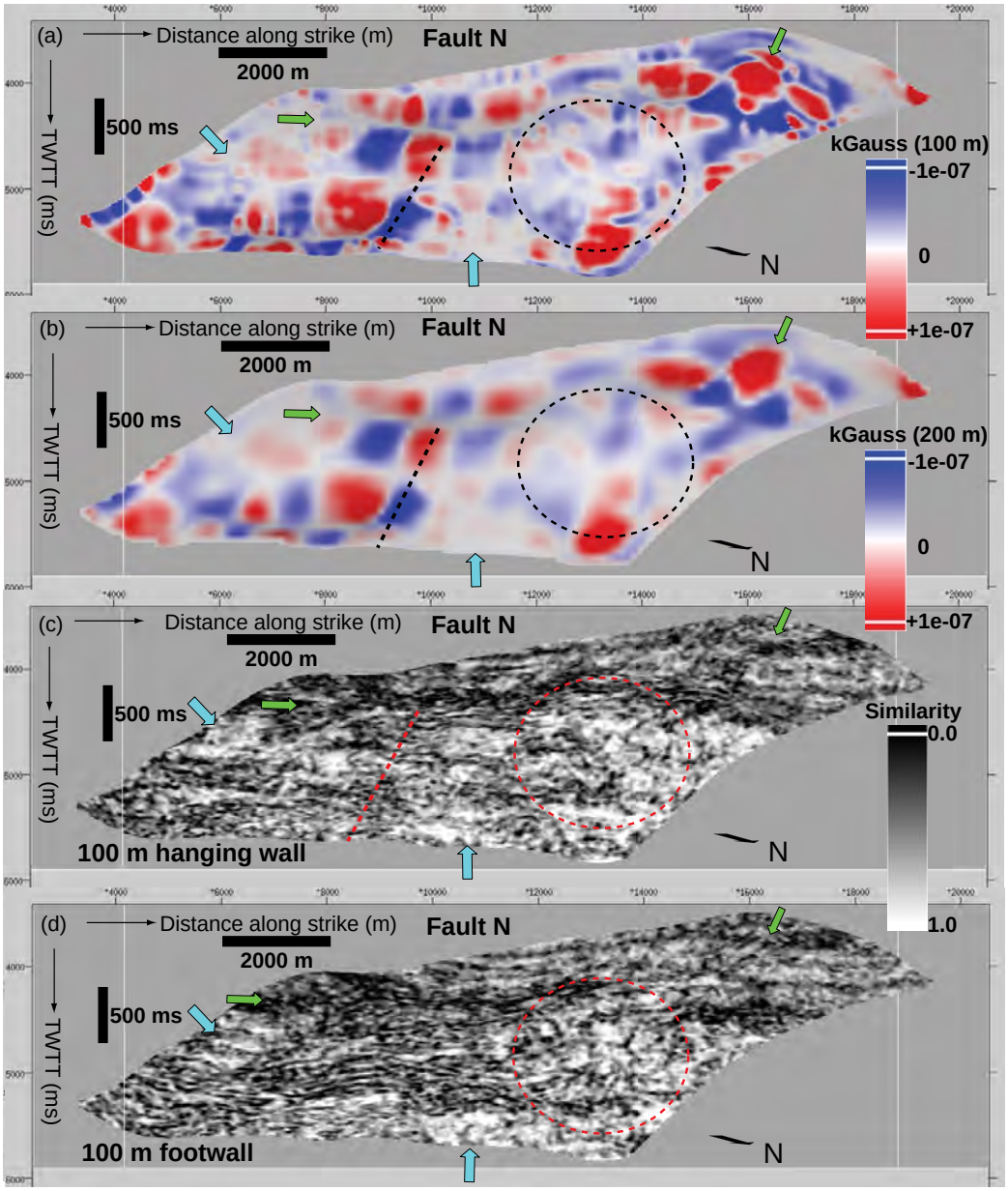

Figure 6.73: High resolution Gaussian curvature plot of Fault N (a), low resolution Gaussian curvature plot of Fault N (b), similarity slice sampled 100 m parallel to the fault in the hanging wall (c) and similarity slice sampled 100 m parallel to the fault in the footwall (d). The green arrows, red lines and circles highlight links between pronounced pattern of fault surface curvature and low similarity in the hanging wall and footwall adjacent to the fault, while the blue arrows highlight zones of low curvature and high similarity. Vertical scale is in milliseconds in two way travel time and horizontal scale is in meters. Vertical exaggeration is ~1.6.

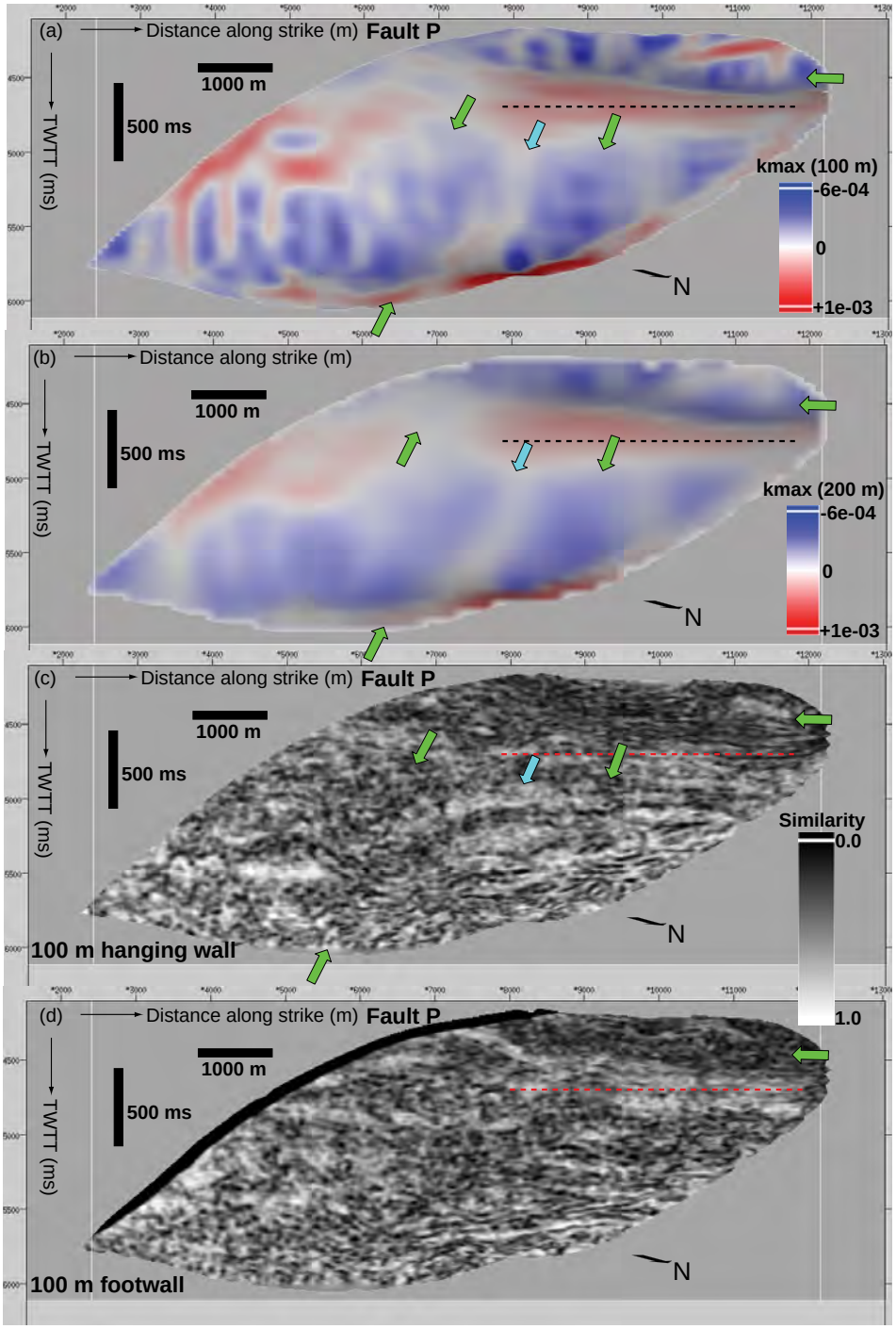

Figure 6.74: High resolution maximum curvature plot of Fault P (a), low resolution maximum curvature plot of Fault P (b), similarity slice sampled 100 m parallel to the fault in the hanging wall (c) and similarity slice sampled 100 m parallel to the fault in the footwall (d). The green arrows highlight links between pronounced pattern of fault surface curvature and low similarity in the hanging wall and footwall adjacent to the fault, while the blue arrows highlight zones of low curvature and high similarity. The red lines show instances where despite the intense pattern of fault surface curvature similarity is high. Vertical scale is in milliseconds in two way travel time and horizontal scale is in meters. Vertical exaggeration is ~1.6.

6.3.4.4 Quantitative links between fault surface curvature and volume structure

6.3.4.4.1 Fault A

Figures 6.75a and 6.75c show maximum curvature data extracted from the fault surface maximum curvature plot representing the region of the fault surface in the hanging wall and footwall being compared with similarity data extracted from adjacent reflector unit 50 m away from the fault in the hanging wall and footwall (Figure 6.75b and 6.75d). Generally fault surface curvature within the sampled interval is predominantly positive and up to 4e-04 in magnitude especially in the upper parts of the interval (between 4500 ms and 4650 ms two way travel time). However, curvature in the lower parts of the interval is low with high density of low magnitude curvature data plotting at or near the zero curvature axes. This implies that curvature is more intense in the upper parts of the fault.

The similarity of the reflector unit in the hanging wall is variable with values ranging between 3.0 and 5.0 (Figure 6.75b). However, the density of low similarity data is highest in the upper parts of the unit and closely matches the interval exhibiting the highest magnitude of curvature. In the lower parts of the plots low magnitudes of fault surface curvature correlates with a decreasing intensity of similarity (although similarity is low). This implies that in the upper parts of the plots, the low similarity of the hanging wall unit may be due to the high magnitudes of fault surface maximum curvature. In the footwall, similarity is much more variable than in the hanging wall (Figure 6.75d). However, the low magnitudes of fault surface curvature in the lower parts of the fault surface may be related to a less intense pattern of low similarity in the footwall (block white arrows).

Plots of fault surface Gaussian curvature and similarity adjacent to the faults shows that the upper parts of the unit in the hanging wall and central parts in the footwall may have been disrupted as a result of the pronounce pattern of fault curvature (black arrows in Figure 6.76). The low intensity of similarity in the lower parts of the units may be related to the low magnitudes of fault surface Gaussian curvature (white arrows in Figure 6.76).

6.3.4.4.2 Fault G

Figures 6.77a and 6.77c show maximum curvature data extracted from the fault surface maximum curvature plot representing the parts of the fault surface in the hanging wall and footwall being compared with the similarity of the units adjacent to the fault. In general, fault surface curvature is predominantly positive with moderate intensity of high magnitudes of curvature of up to 6e-04 between ~4200 ms and 4300 ms. However, the magnitudes of curvature appear to decrease towards the bottom parts of the fault with high density of curvatures less than 2e-04 in magnitude. Similarity in the hanging wall is high especially in the middle parts of the unit (~4200 ms to 4300 ms), but decreases towards the lower parts of the unit (Figure 6.77b). The high density of low similarity in the middle parts of the unit is probably due to the moderate magnitudes of fault surface curvature (block arrows).

In the footwall, no relationship is observed between the magnitudes of fault surface curvature and similarity (Figure 6.77d). These observations imply that the high magnitudes of fault surface curvature may be linked to disruptions in the central parts of the hanging wall unit. Plots of fault surface Gaussian curvature and similarity adjacent to the fault shows no direct links between the intensity of curvature and disruption in the hanging wall and footwall (Figure 6.78).

6.3.4.4.3 Fault J

Figures 6.79a and 6.79c show maximum curvature data extracted from the fault surface maximum curvature plot representing parts of the fault surface in the hanging wall and footwall being compared with similarity plots extracted from adjacent reflector unit 50 m away from the fault in the hanging wall and footwall (Figure 6.79b and 6.79d). Generally fault surface maximum curvature is both negative and positive but predominantly positive in the upper parts of the fault in the hanging wall (~4500 ms to 4700 ms). In these areas maximum curvature with magnitudes of between 0 and less than 4e-04 are observed. The similarity of the unit in the hanging wall is predominantly high with the highest density of data in the upper parts of the units (Figure 6.79b). These regions correspond with the interval exhibiting low magnitudes of fault surface curvature in Figure 6.79a.

In the footwall a similar pattern of similarity distribution similar to that in the hanging wall is observed (Figure 6.79d). It then implies that there is a correlation between low magnitudes of fault surface maximum curvature and high similarity in the upper parts of the units as shown by the large density of high similarity in the interval between ~4500 ms and 4700 ms in the hanging wall and ~4600 ms and 4700 ms in the footwall (block white arrows). Plots of fault surface Gaussian curvature and similarity adjacent to the fault shows weak links between low magnitudes of curvature and high similarity in the lower parts of the units in the hanging wall and footwall (white arrows in Figure 6.80).

6.3.4.4.4 Fault L

Figures 6.81a and 6.81c show maximum curvature data extracted from the fault surface maximum curvature plot representing parts of the fault surface in the hanging wall and footwall being compared with similarity plots extracted from the adjacent reflector unit 50 m away from the fault in the hanging wall and footwall (Figure 6.81b and 6.81d). Generally fault surface curvature is predominantly positive with magnitudes of less than 4e-04 observed as shown by the high density of low magnitude curvature data across the entire interval. Similarity in the hanging wall is highly variable but largely moderate to high in the hanging wall.

However, footwall similarity appears to be lower compared to the hanging wall. In reality no relationship is seen between the pattern of fault surface maximum curvature and disruptions in the volumes adjacent to the fault. Plots of fault surface Gaussian curvature and similarity adjacent to the fault shows no direct links between the intensity of curvature and disruptions in the hanging wall and footwall adjacent to the fault (Figure 6.82)

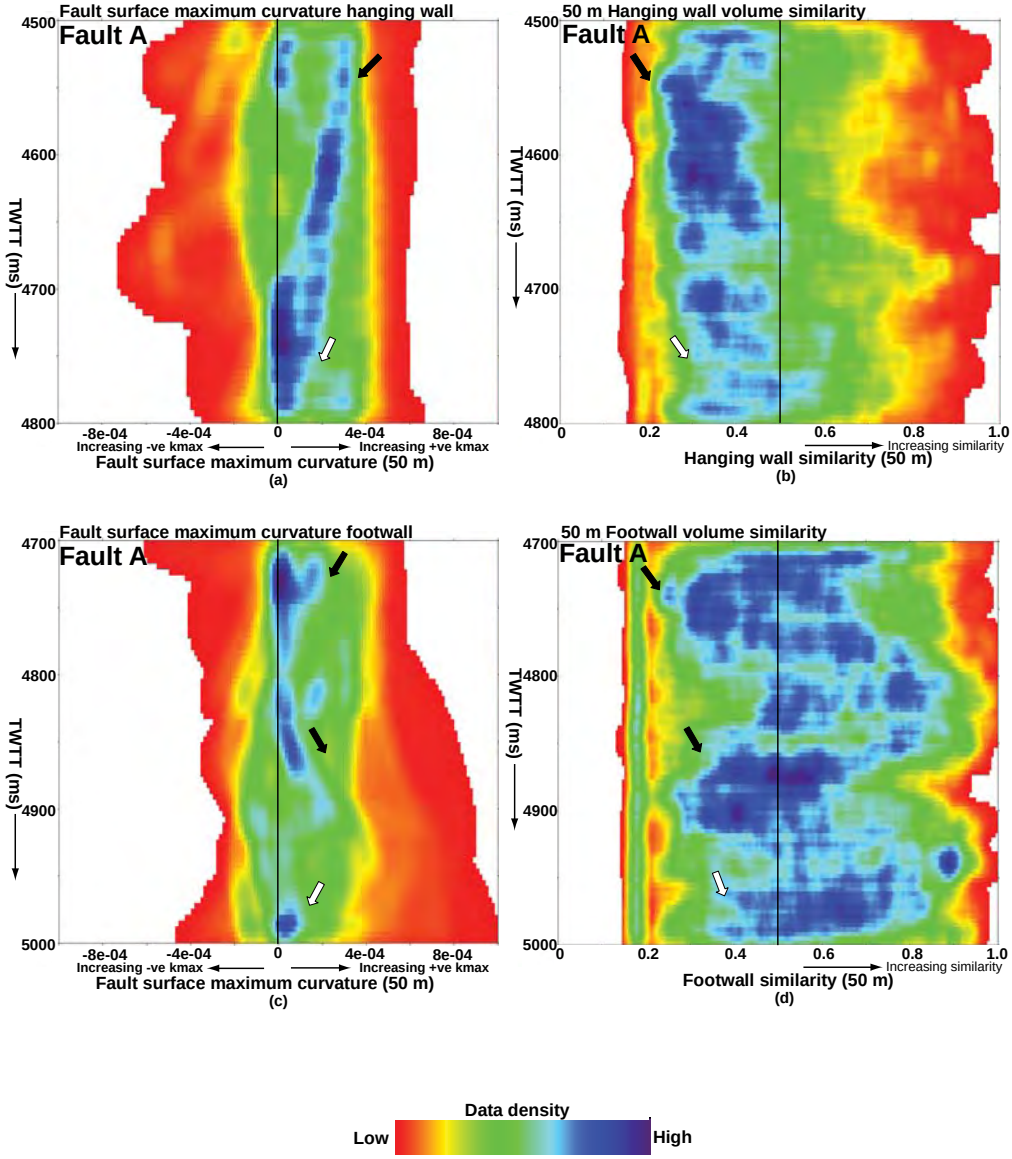

Figure 6.75: Density plots of Fault A surface maximum curvature in the hanging wall and footwall (a and c), similarity extracted from reflector unit mapped across the fault 50 m parallel to the fault in the hanging wall (b) and footwall (d). The purple and red shades represent high and low density of seismic attribute data respectively. Note the strong correlation between high densities of fault surface curvature and low similarity in the upper parts of hanging wall and footwall (block black arrows) implying that disruptions in the upper parts of the hanging wall and footwall are related to fault surface curvature. The white block arrows highlight a weak correlation between decreasing magnitude of fault surface curvature and low intensity of moderate to high similarity. Vertical scale is in milliseconds two way travel time.

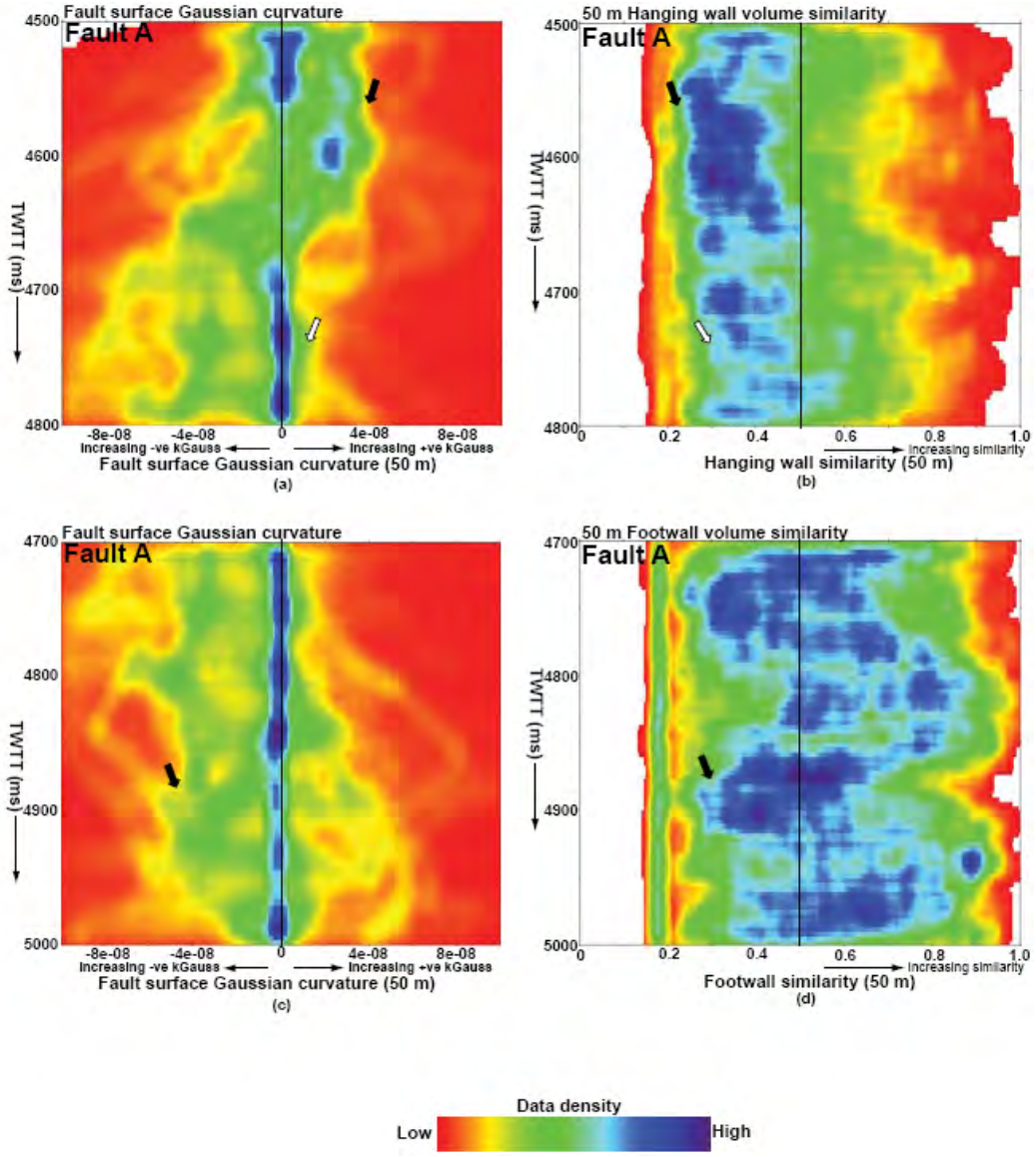

Figure 6.76: Density plots of Fault A surface Gaussian curvature in the hanging wall and footwall (a and c), similarity extracted from reflector unit mapped across the fault 50 m parallel to the fault in the hanging wall (b) and footwall (d). The purple and red shades represent high and low density of seismic attribute data respectively. Note the weak correlation between high magnitudes of fault surface curvature and disruption in the upper parts of the units in the hanging wall and central parts of the unit in the footwall (black arrows). The white arrows highlight weak links between low magnitudes of curvature and low density similarity in the lower parts of the unit in the hanging wall. Vertical scale is in milliseconds two way travel time.

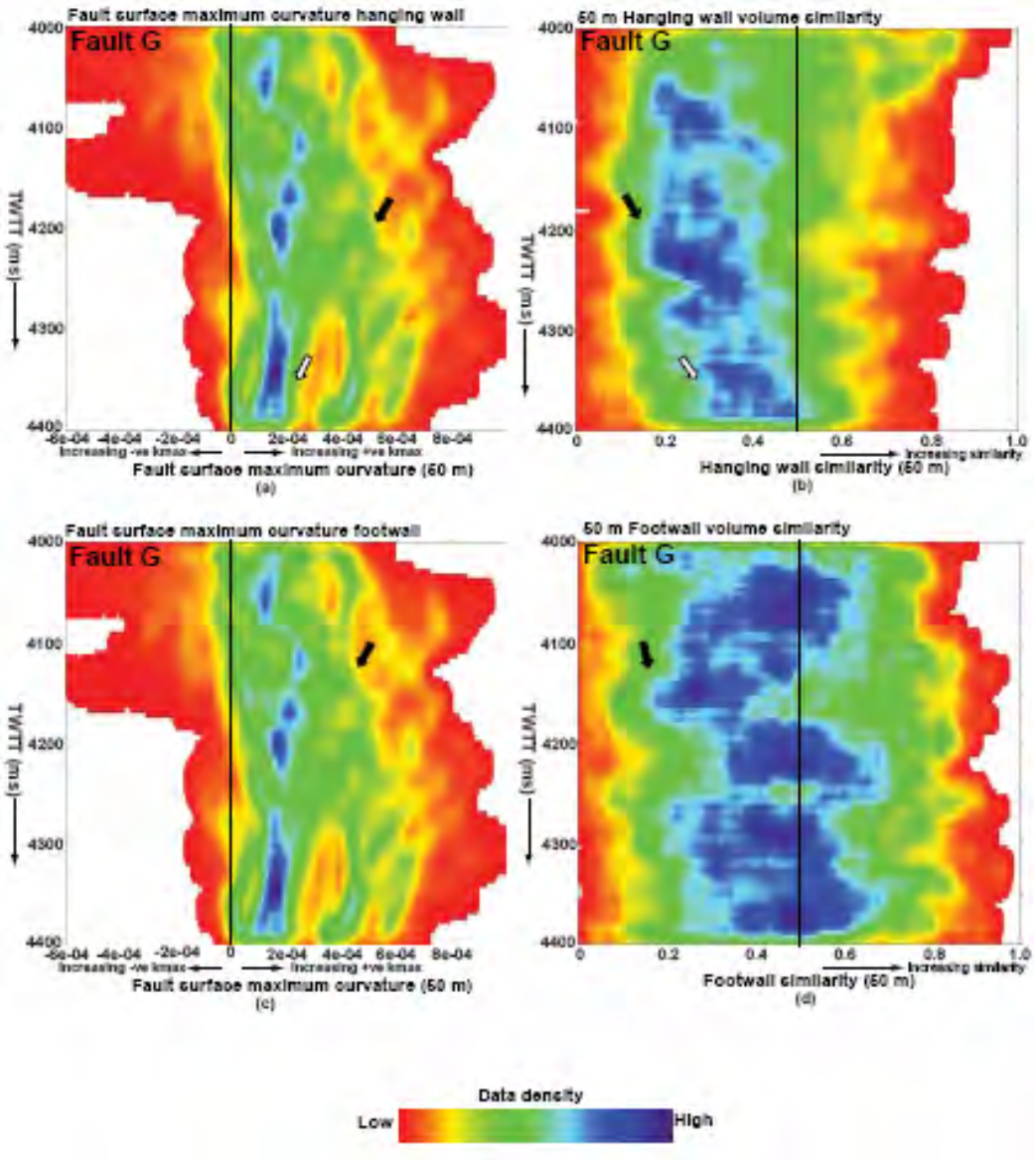

Figure 6.77: Density plots of Fault G surface maximum curvature in the hanging wall and footwall (a and c), similarity extracted from reflector unit mapped across the fault 50 m parallel to the fault in the hanging wall (b) and footwall (d). The purple and red shades represent high and low density of seismic attribute data respectively. Note the weak correlation between moderate densities of fault surface curvature and low similarity in the middle parts of hanging wall and central parts of footwall (block black arrows), implying disruptions in parts of the units are related to the intensity of fault curvature. The white block arrows highlight weak correlation between decreasing magnitude of fault surface curvature and low intensity of moderate to high similarity in the hanging wall. Vertical scale is in milliseconds two way travel time.

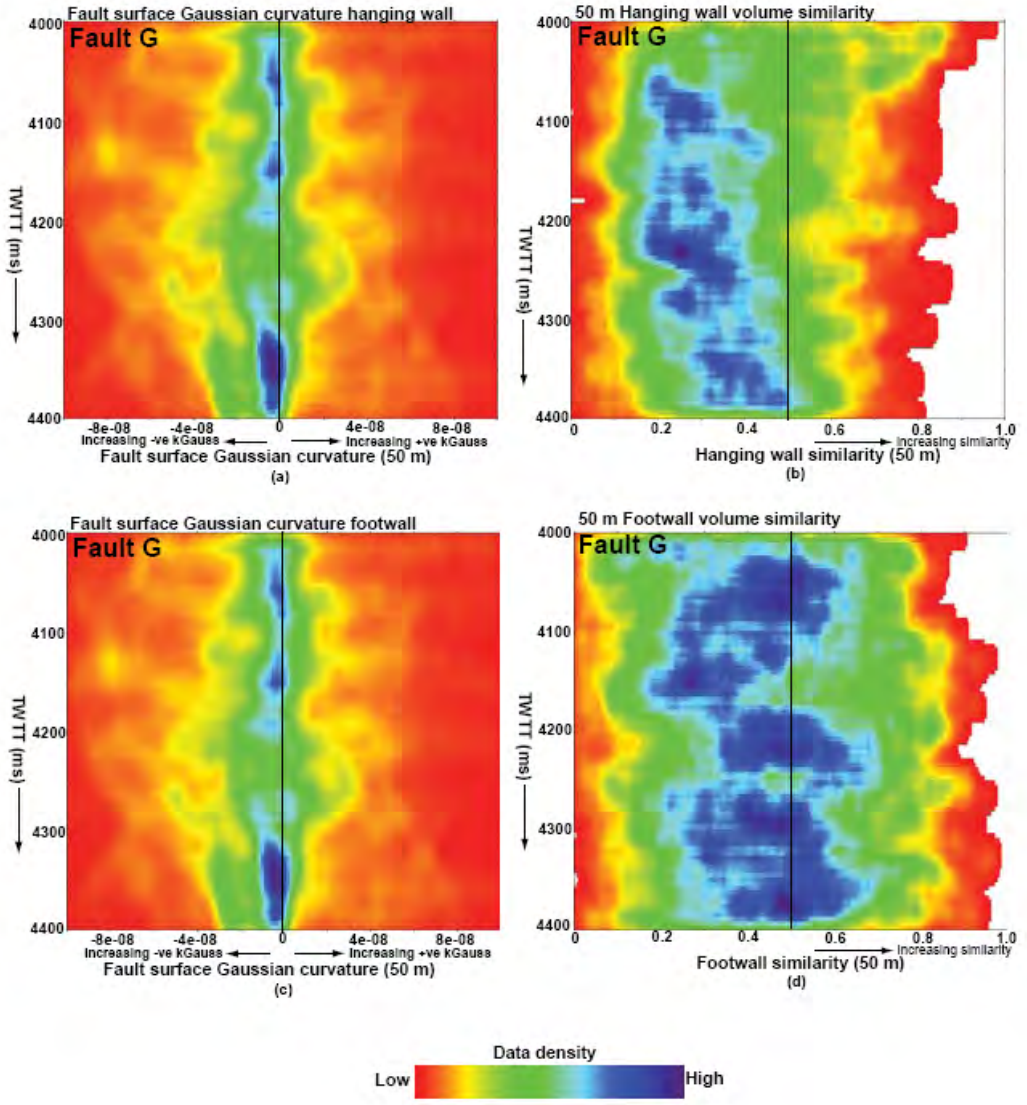

Figure 6.78: Density plots of Fault G surface Gaussian curvature in the hanging wall and footwall (a and c), similarity extracted from reflector unit mapped across the fault 50 m parallel to the fault in the hanging wall (b) and footwall (d). The purple and red shades represent high and low density of seismic attribute data respectively. No direct links are observed between the intensity of fault surface curvature and disruption in the hanging wall and footwall. Vertical scale is in milliseconds two way travel time.

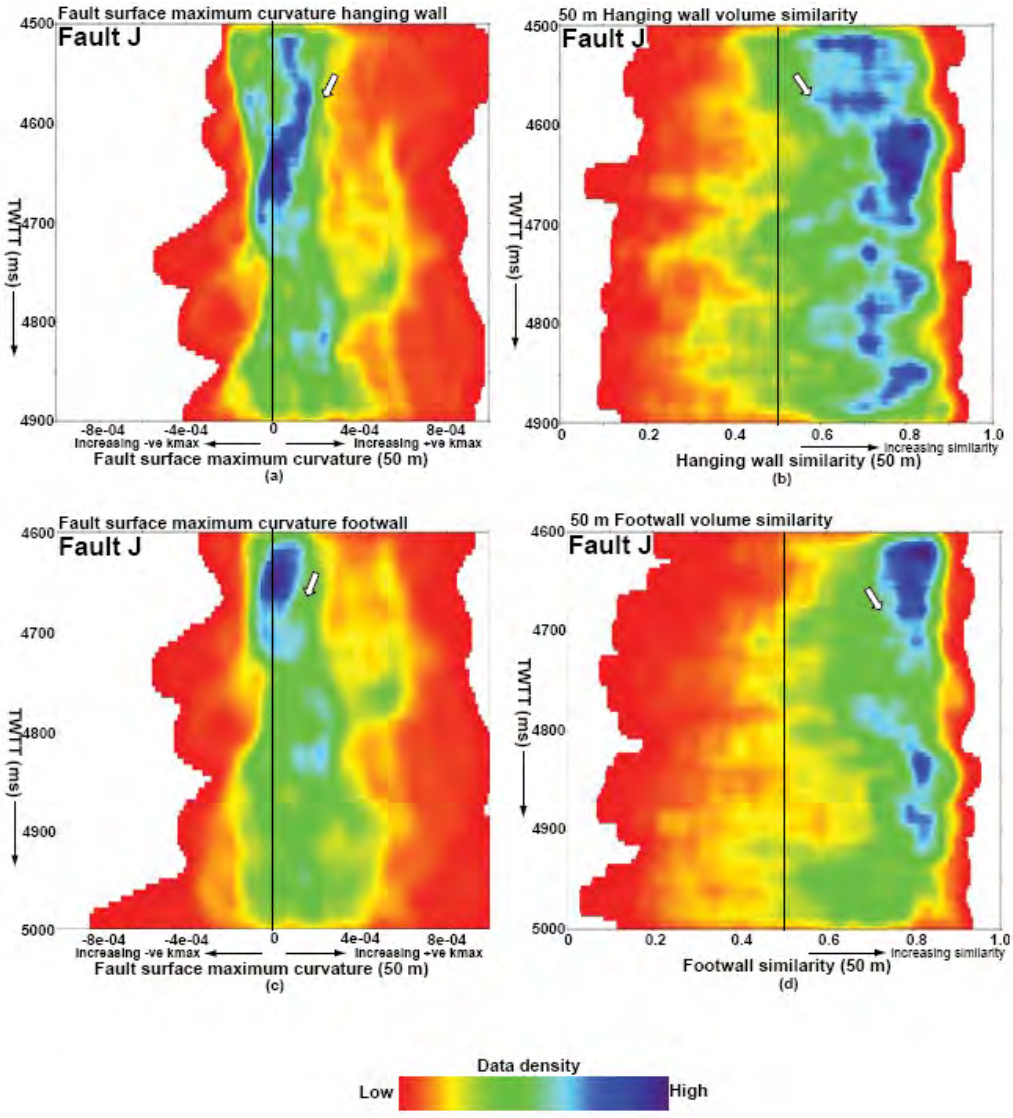

Figure 6.79: Density plots of Fault J surface maximum curvature in the hanging wall and footwall (a and c), similarity extracted from reflector unit mapped across the fault 50 m parallel to the fault in the hanging wall (b) and footwall (d). The purple and red shades represent high and low density of seismic attribute data respectively. The white block arrows highlight a weak correlation between decreasing magnitude of fault surface curvature and low intensity of moderate to high similarity in the upper parts of the plots. Vertical scale is in milliseconds two way travel time.

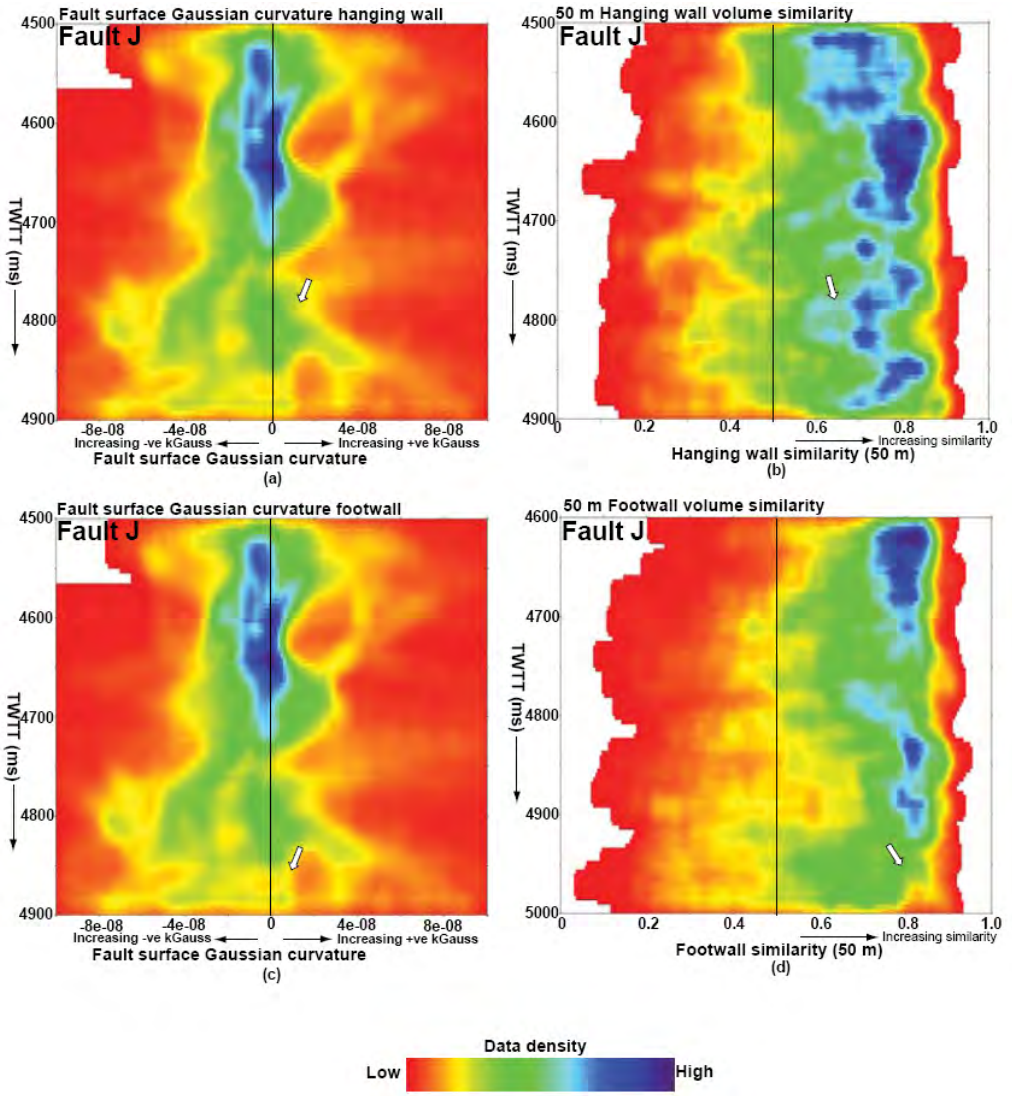

Figure 6.80: Density plots of Fault J surface Gaussian curvature in the hanging wall and footwall (a and c), similarity extracted from reflector unit mapped across the fault 50 m parallel to the fault in the hanging wall (b) and footwall (d). The purple and red shades represent high and low density of seismic attribute data respectively. The white block arrows highlight a weak correlation between decreasing magnitude of fault surface curvature and low density similarity in the lower parts of the plots. Vertical scale is in milliseconds two way travel time.

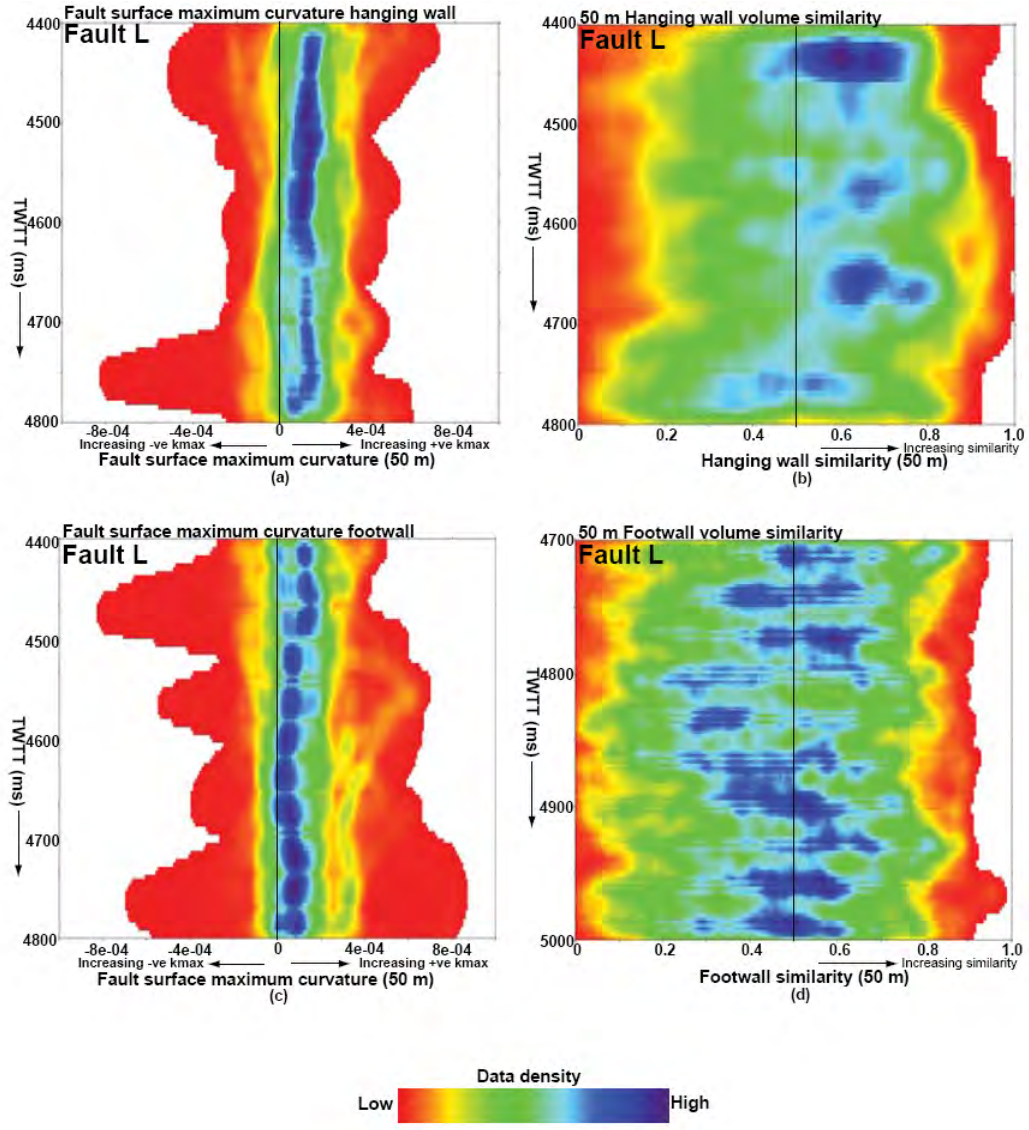

Figure 6.81: Density plots of Fault L surface maximum curvature in the hanging wall and footwall (a and c), similarity extracted from reflector unit mapped across the fault 50 m parallel to the fault in the hanging wall (b) and footwall (d). The purple and red shades represent high and low density of seismic attribute data respectively. Note the weak correlation between high density of low magnitude fault surface curvature and low density of low similarity in the footwall. In the hanging wall no links between fault surface curvature and disruptions are observed. Vertical scale is in milliseconds two way travel time.

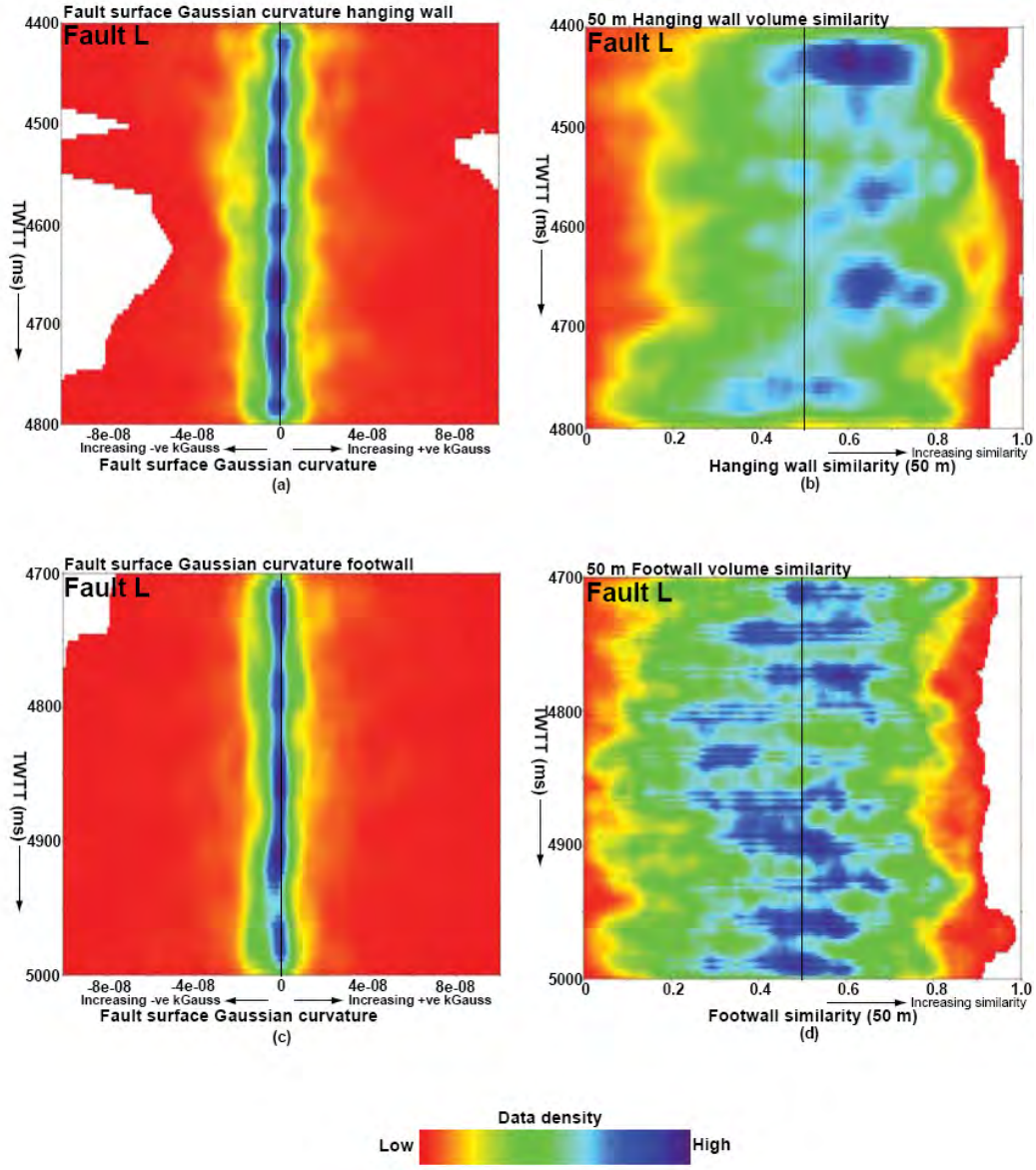

Figure 6.82: Density plots of Fault L surface Gaussian curvature in the hanging wall and footwall (a and c), similarity extracted from reflector unit mapped across the fault 50 m parallel to the fault in the hanging wall (b) and footwall (d). The purple and red shades represent high and low density of seismic attribute data respectively. No direct links are observed between magnitudes of fault surface curvature and disruption in the hanging wall and footwall. Vertical scale is in milliseconds two way travel time.

6.4 Discussion and conclusion

6.4.1 Internal structure of thrust faults

The principal methods of fault slicing and volume seismic attribute analysis have been described and examples of how the concept of sampling seismic attribute data parallel to interpreted fault surfaces has been used to investigate the internal structure adjacent to thirteen thrust faults using specially processed seismic attribute data (similarity and curvature). In addition, the methods have been used to illustrate how disruptions in fault zones can be mapped using more than one seismic attribute.

Relationships between multiple seismic attributes are important in understanding how disruptions detected at the same location using the attributes can be reliably interpreted. This is important in this thesis because seismic amplitude data and seismic attributes calculated from the data are used for the analysis and despite the usefulness of seismic attributes in identifying discontinuities, some anomalies observed in seismic attribute data may not entirely be related to the underlying geology but includes noise. The principal objective of investigating the seismic structure of the volumes in the vicinity of the faults is to explore links between fault surface morphology and the pattern of disruptions next to the faults.

The structure of the volumes adjacent to thrust faults was investigated from two perspectives. Firstly, the internal structure adjacent to nine thrust faults was investigated by visually analyzing the pattern of similarity observed in several fault slices sampled adjacent and parallel to the faults in the hanging wall and footwall. The pattern of disruption adjacent to the faults was then summarized in a table based on the similarity pattern of the slices closest to the faults. Secondly, the structure of

reflector units mapped and correlated across four faults in the hanging wall and footwall was investigated. The objective of this analysis is to constrain the investigation to reflector units whose seismic attribute characteristics can be related to deformation within specific Niger Delta stratigraphic units. The intervals were selected primarily because disruptions mapped within the units using seismic attribute analysis are assumed to be related to brittle deformation. The intensity of disruptions was interpreted based on the similarity pattern on a scale of 0 to 1. Similarity values closer to zero are interpreted as low and related to intense disruptions while values towards one are high and interpreted to represent low/no disruption. Values between 0 and 1 are interpreted as moderate disruption. In analyzing the maximum curvature data, it is assumed that the reflectors are likely to be folded/disruption based on the intensity of curvature.

6.4.1.1 Volume maximum curvature

Although the curvature of geological surfaces has previously been used as proxy for deformation, results from this thesis suggests that volume curvature is primarily a useful attribute in mapping reflector geometry. However, crossplots of curvature and similarity extracted from units mapped across two thrust faults show a direct correlation between high absolute magnitudes of volume maximum curvature and low similarity, implying that intense curvature seen in the volumes near some of the faults is related to disruptions. However, instances where high magnitudes of volume curvature with high similarity have been seen, implying intense folding of the reflectors devoid of significant disruptions. These observations highlight potential problems when using curvature as proxy for disruption in fault zones.

In previous work, it has been suggested that distinguishing deformation related to brittle and ductile processes can be difficult (Wynn & Stewart, 1998). This observation is particularly important in the Niger Delta with sedimentary sequences consisting of alternation of sands and clays, implying that deformation could both be brittle and ductile. Recent work suggests that curvature is not always reliable in predicting strain in outcrop and sub-surface structures. For example, Pearce *et al* (2011) investigated quantitative links between the curvature of folded beddings and fracture density and suggested insignificant correlation between curvature and fracture density and questioned the validity of using curvature as proxy for brittle deformation. In addition, Keating & Fischer (2008) alluded that the inconsistent relationship between curvature and strain may range from the fact that studied fractures may not have been formed during folding and that continued extension is accommodated by the reactivation of existing fractures instead of the formation of new ones.

In seismic data, seismic curvature is a measure of the shape of a reflector irrespective of deformation. However, since folded strata may end up being deformed, curvature may still be a useful tool in predicting the location of faults and discontinuities. This is probably a factor for the successful use of the attribute to predict fracture intensity in previous work (e.g. Murray, 1968; Masafero *et al*. 2003: Lisle, 1994; Sigismondi & Soldo, 2003; Samson & Mallet, 2003; Roberts, 2001: Antonellini & Aydin, 1995; Sterns, 1964; Sterns & Friedman, 1972; Ericsson *et al*. 1998; Cooke-Yarborough, 1994; Sullivan *et al.* 2006; Serrano *et al*. 2003; Narr, 1991).

Analysis of the volumes surrounding four faults using volume maximum curvature suggests a wide range of fault zone architecture. Qualitatively, two patterns of volume maximum curvature have been observed across the faults. Generally in the more

competent units, volume maximum curvature sampled adjacent to the faults has proved very effective in mapping the geometry of reflectors and in identifying folding related to disruption from folding devoid of intense disruption when the attribute is used in combination with similarity. However in the deeper parts of the wall rock volumes, the random/chaotic pattern of volume maximum curvature probably related to the seismic stratigraphy makes any meaningful interpretation possible.

Qualitative analysis of volume maximum curvature adjacent to two faults show intense bimodal pattern of curvature with low similarity, implying significant disruption in the hanging wall and footwall. However, as the distance away from the fault plane increases, volume curvature is predominantly unimodal and similarity becomes high implying that as the distance away from the faults increases, the wall rocks are largely folded but not disrupted. However, two instances where volume curvature is low and similarity is high near the faults have been observed, implying insignificant disruption next to the faults. In another example, an inconsistent pattern of volume maximum curvature and a highly variable pattern of similarity have been observed near the fault and as the distance away from the fault increases. The implication is that thrust zones can be complex with geometries that deviate from known models of thrusting.

6.4.1.2 Volume similarity

In general, the pattern of similarity across the thirteen faults analyzed shows a highly variable trend of disruption in the hanging wall and footwall based on the pattern of similarity observed in the slices sampled close to thirteen thrust faults (Table 6.1). In half of the faults analyzed similarity in the vicinity of the faults is low but becomes high as the distance away from the fault increases. In the other half similarity appears to be lower in the footwall than in the hanging wall.

Most models of thrust propagation assume that deformation around a thrust fault is concentrated in the hanging wall, while the footwall is considered rigid (e.g. Williams & Chapman, 1983; Suppe & Medwedeff, 1990). In addition classical models developed by Elliot (1976) proposed that thrust sheets undergo substantial internal deformation with significant layer-parallel shear and negligible shortening and thickening within the hanging wall of a ramp anticline during displacement over footwalls.

The implication of results presented in this thesis is that in half of the faults, the regions next to the faults are intensely deformed in the hanging wall, while in the other half the footwall is more deformed than the hanging wall. A similar complex pattern of thrusting was observed from field analysis of deformation along the Klimatia thrust zone in NW Greece and was interpreted to be due to multiple deformation events that post-date thrust initiation (Kostakioto *et al*. 2004). In Chapter Four, it was proposed that the existence of multiple detachment levels in Unit II that may be an indication of episodic pattern of compression in deepwater Niger Delta and may account for the highly variable pattern of volume structure observed in across the faults. Although, thrusting is usually associated with faulting and folding of the

hanging wall, these observations highlight the complex pattern of disruption in thrust zones that could impact on existing models of thrusting in deepwater Niger Delta fold and thrust belts. In addition the plots presented demonstrate that detailed analysis of the structure of fault zones can be facilitated using fault slicing and seismic attribute analysis.

	Pattern of disruption (based on the 200 m similarity slices)	
Fault	**Hanging wall**	**Footwall**
A	High	Low
B	Low	High
C	High	Low
G	High	Low
H	High	High
I	High	High
J	Low	Low
K	High	Low
L	Low	Low
M	Low	Low
N	Low	High
O	Low	High
P	Low	Low

Table 6.1: Summary of disruptions observed in the volumes adjacent to thirteen faults in the hanging wall and footwall based on the similarity pattern of the closest slices sampled adjacent to the faults (200 m). Note the variable pattern of disruption across the faults. In half of the faults the hanging wall is more disrupted than the footwall while in the other half the footwall is more disrupted than the hanging wall. In a few of the faults both the hanging wall and footwall near the faults are disrupted in about the same proportion.

6.4.2 Fault surface morphology and volume structure

The principal reason for calculating the structural attribute plots of thrust fault is to investigate potential links with the structure of the volumes adjacent to the faults. The key input for this investigation are seismic attribute data calculated in Chapter Three and structural attribute plots of the faults modelled in Chapter Five. The investigation was approached from two perspectives. Firstly, plots of fault surface curvature were visually compared with slices of volume maximum curvature sampled adjacent to the faults. Secondly, plots of fault surface curvature and gradient of fault surface

topography were qualitatively compared with slices of similarity sampled through similarity data parallel to the faults. Anomalous patterns of fault surface curvature and gradient were then interpreted relative to the pattern of volume similarity adjacent to the faults.

Qualitative comparison between fault surface curvature and volume maximum curvature across four faults shows a weak to strong links between the pattern of fault surface maximum curvature and volume maximum curvature. In one example, the pattern and orientation of fault surface corrugation was replicated in the volume adjacent to the fault. The implication of this observation is that since it is assumed that fault corrugations are oriented parallel to fault transport direction, the maximum curvature pattern in the wall rock can be used as an indirect seismic evidence of slip direction.

Qualitative analysis of structural attribute plots of nine faults and similarity slices sampled adjacent to the faults reveal a wide variety of results. Generally in most of the faults a weak to strong correlation between high magnitudes of fault surface curvature and disruptions in the volumes near the faults is observed. In nearly all the faults with pronounce pattern of horizontal corrugation exhibiting intense curvature related to fault bend, the volumes adjacent to the fault appears deformed in the hanging wall and footwall.

In two-dimensional models of the evolution of thrusted blocks, the hanging wall is assumed to deform to conform to the shape of the fault and parts of the hanging wall that move over planar segments of the fault plane are relatively less deformed (e.g. Suppe *et al.* 2004). However, with large amounts of displacement and irregular fault surface topography, the wall rocks will experience several phases of deformation with

discrete zones of disruption related to the translation of the wall rocks across the fault. However, instances where the links are inconsistent have also been documented. In the Niger Delta, models of fault-bend folding relate wall rock deformation to the translation of hanging wall over non-planar fault surfaces with curved ramp, resulting in the deformation of the hanging wall units. This observation may be applied to explain the intense disruptions observed in the hanging wall of some of the thrust faults with pronounce horizontal corrugations.

Quantitative, a weak to fairly strong correlation between high magnitudes of fault surface maximum curvature and disruptions in the volumes next to the faults have been established in some of the faults analyzed. Qualitative comparison between plots of fault surface gradient and similarity slices sampled adjacent to the some of the faults shows a weak to strong correlation between anomalous fault surface gradient and disruption in the volumes next to the faults.

Qualitative comparison between Gaussian curvature plots of the faults and volume similarity also indicates weak to strong correlation between high magnitudes of Gaussian curvature/change in polarity of Gaussian curvature with discrete zones of disruption in the volumes in the vicinity of some of the faults. The practical implication of these observations is that the translation of wall rocks across fault surfaces with finite Gaussian curvature (non-developable surfaces of Lisle, 1994) may have resulted in the disruption of the volumes in the vicinity of some of the faults due to the convergence and divergence of particle motion paths. The intensity of deformation will depend primarily on the magnitude and rate of change of Gaussian curvature in the fault transport direction. Irrespective of frictional effects and the dynamics of the faulting process, non-parallel (divergent and convergent) particle

flow paths are therefore an inherent consequence of translating wall rock volumes across a Gaussian-curved fault surface (Figure 6.83). Although in places, no links are observed between the pattern of fault surface Gaussian curvature and volume disruption next to the faults.

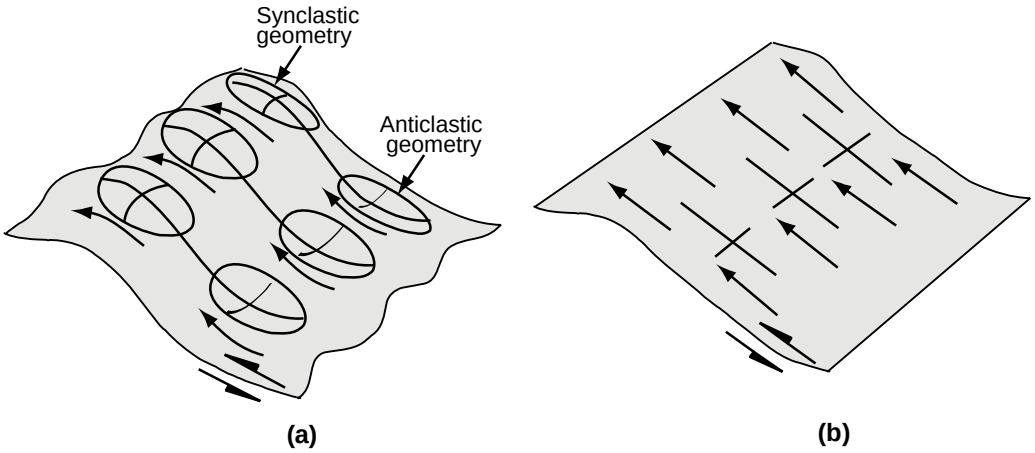

Figure 6.83: Schematic illustration of the potential effects of non-parallel (convergent and divergent) translation of wall rock volume across a curved surface. In Figure 6.83a, translation of wall rocks across non-developable anticlastic and synclastic surfaces causes the divergence and convergence of particle motion paths and consequently may result in deformation. However, in Figure 6.83b, wall rocks translated across developable surfaces (surfaces with zero Gaussian curvature), particle motion path is parallel to the fault surface and wall rocks may not be deformed.

CHAPTER SEVEN –CONCLUSIONS, LIMITATIONS AND FUTURE WORK

7.1 Conclusions

In this thesis, volumetric seismic attribute extraction and image enhancement techniques have been applied to a three-dimensional seismic data to investigate the structural and stratigraphic framework of parts of deepwater Niger referred to as the "Joint Development Zone". The seismic reflection data complemented with a dip-steered similarity attribute volume calculated on the seismic data was used to guide the detailed interpretation of cross sectional geometries of thrust faults. Three-dimensional structural attribute models of the faults were then plotted with the primary aim of investigating fault surface morphology. Finally the structure of the volumes adjacent to thirteen faults was investigated by analyzing the seismic attribute patterns of slices sampled through the data parallel to the faults and links with fault surface morphology assessed. Highlights of the key findings of this thesis are as follows:

- Faults in the study area possess scaling properties typical of thrust faults and can be classified into two groups based on the spacing between individual faults, the geometry of hanging wall folds and the location of the structures relative to an arcuate thrust front that separates the area into approximately two parts (proximal and distal). In the proximal parts of the study area (NE JDZ), faults are widely spaced with large structural closure of the hanging wall folds. In the distal parts of the study area (SE), the faults are closely spaced with low structural closure and appear to be complexly deformed. The large structural closure of hanging wall folds and the stacked amplitude anomalies and flat spots in the crestal part of the

folds indicates that the proximal part of the JDZ is prospective. These structures are prime trapping elements and focus of hydrocarbon exploration in other fold and thrust belts (e.g. Morgan, 2003; Briggs *et al*. 2006). In addition fault growth is by the gradational propagation of segments initially soft-linked through breached relays and connecting faults.

- The seabed horizon shows for the first time in unprecedented detail seafloor manifestation of gravity collapse and contractional deformation in the study area. The main structural features of the seabed are bathymetric ridges representing the hanging wall folds of thrust faults, large-scale deepwater channel systems and extensive pockmark craters probably caused by the upward migration of fluids from hydrocarbon charged sediments through discontinuities to the surface especially around the edges of a deepwater channel in the central parts of the study area.

- Structural attribute plots of sixteen faults shows that thrust faults in the study area exhibit corrugations, culminations and depressions oriented parallel to the direction of seaward gravitational collapse and compression of deltaic sediments in deepwater Niger Delta. The morphologies exhibited by the faults are consistent with slip surfaces previously observed in outcrop fault planes. The curvature plots presented in this thesis are the first to describe corrugations in three-dimensions as manifestations of the curvature of thrust fault planes in deepwater Niger Delta fold and thrust belt. Therefore, in this thesis additional data have been provided that can help bridge the scale gap between outcrop scale and seismic analysis of the surface geometries of thrust faults.

- Novel methods of investigating the structure of fault zones and links with fault surface morphology have been introduced in this thesis. Slices of seismic attribute data sampled parallel and adjacent to thirteen thrust faults suggests a highly variable pattern of disruption in thrust zones related to thrust initiation, folding and perhaps subsequent episodes of deformation. In addition, the pattern of fault surface maximum curvature is identical to that seen in the volumes sampled adjacent to the some of the faults. Although mapping the structure of fault zones and relating thrust zone geometry to fault surface morphology at the scale of seismic resolution is a significant challenge to this thesis, it is interpreted that disruptions in the immediate vicinity of some of the faults are most likely related to pronounced/random pattern of fault surface curvature, anomalous gradient of fault surface topography and change in pattern of Gaussian curvature in the fault transport direction

7.2 Limitations and future work

Although detailed description of workflow and data available for this thesis have been described, there are limitations that need to be taken into account when interpreting observations and results presented in this thesis and the overall contribution of the results and methods to structural geology in general and curvature – strain analysis in particular. It is anticipated that some of the limitations can be addressed when additional data becomes available.

The fact that this thesis is centred on a large seismic data and seismic attribute volumes in the time domain clearly represents a challenging task in mapping the depth dimensions of the faults. The ability to convert the seismic data from time to depth domain using stacking velocities obtained during seismic data acquisition would have

been invaluable to this thesis. Although faults may be geometrically distorted when converted from time to depth domain, curvature is a fractal property of fault surfaces that exists at all scales of observation (as demonstrated in Chapter Five) irrespective of the domain the faults are mapped from.

Although user-defined filters were used to extract seismic attribute data from reflector units mapped across four thrust faults and fault surface attribute data adjacent to the hanging wall and footwall units, it is possible that some of the extracted data may have come from outside the units of interest and the fault surface interval being sampled. Additionally attributes displayed at the edges of fault surfaces sometimes include zero or null values and could lead to under representation of fault surface attributes and potentially influence the density plots of volume seismic attributes used in investigating the quantitative structure of fault zones and links with fault surface topography.

The conclusions as well and the limitations of this thesis also bring forth some interesting avenues for future research that might improve the quality of the results. The most important avenue for future research obviously lies in confirming that the pattern of disruptions observed in the vicinity of the thrust faults analyzed are due to deformation and not noise related using well/core data sampled across fault zones. The absence of well data implies that all the observations and conclusions drawn from the seismic attribute analysis are entirely based on the assumption that seismic attribute anomalies are due to disruptions of the volumes adjacent to the faults related to the underlying geology.

REFERENCES

Abe, S., & Mair, K., 2010. 3-D DEM Modelling of fault roughness evolution. AGU, Vienna.

AL-Dossary, S., & Marfurt, K.J., 2006. 3-D volumetric multi-spectral estimates of reflector curvature and rotation. *Geophysics*, vol**. 17**, no.5, p41-45.

Antonellini, M., & Aydin, A., 1995. Effect of faulting on fluid flow in porous sandstone: geometry and spatial distribution. *AAPG Bulletin*, vol. **79**, p642-671.

Ajakaiye, D.E., & Bally, A.W., 2002a. Course manual and atlas of structural styles of reflection profiles from Niger Delta. *AAPG Continuing Education Course Note Ser*. vol. **41**. P1-107.

Ajakaiye, D.E., & Bally, A.W., 2002b. Some structural styles on reflection profiles from offshore Niger Delta. *Search and Discovery*, 10031, p1-6.

Avbovbo. A.A., 1978. Tertiary Lithostratigraphy of the Niger Delta. *AAPG Bulletin*, vol.**62**, p.295 – 300.

Bahorich, M.S., & Farmer, S.L., 1995. 3-D seismic coherency for faults and stratigraphic features. *The Leading Edge*, vol. **14**, p1053-1058.

Basford, H., & Paton, G., 2011. Investigation of fluid migration pathways using volumetric seismic damage zone analysis. Abstract *73rd EAGE Conference and Exhibition*, Vienna, Austria.

Berg, S.S., & Tore, S., 2005. Controls on damage zone asymmetry of a normal fault zone: outcrop analyses of a segment of the Moab fault, SE Utah. *Journal of Structural. Geology*, vol. **27**, p1803 - 1822.

Bergbauer, S., & Pollard, D.D., 2003. How to calculate normal curvatures of sampled geological surfaces. *Journal of Structural. Geology*, vol. **25**, p277 - 289.

Bergbauer, S., Mukerji, T., & Hennings, P., 2003. Improving curvature analyses of deformed horizons using scale-dependent filtering techniques. *AAPG Bulletin*, vol. **87**, p1255-1272.

Bergen, K.J., & Shaw, J.H., 2010. Displacement profiles and displacement-length scaling relationships of thrust faults constrained by seismic reflection data. *The Geological Society of America Bulletin*, vol. **122**, no. 7-8, p1209-1219.

Billotti, F., & Shaw, J.H., 2005. Deepwater Niger Delta fold and thrust belt modelled as a critical-taper wedge: the influence of elevated basal fluid pressure on structural styles. *AAPG Bulletin*, vol. **89**, no. 11, p1475-1491.

Blumentritt, C.H., Marfurt, K.J., &Ssullivan, E.C., 2005. Curvature computations illuminate fracture orientations, Lower-Mid Palaeozoic, Central Basin Platform, West Texas. *Geophysics* vol**. 71**, B159-B166.

Bouvier, J.D., Kaars-Sijpesteijn, C.H., Kluesner, D.F., Onyejekwe, C.C., Van der Pal, R.C., 1989. Three-dimensional seismic interpretation and fault sealing investigations, Nun River field, Nigeria. *AAPG Bulletin*, vol. **73**, no. 11, p1397-1414.

Briggs, S.E., Davies, R.J., Cartwright, J.A., & Morgan, R., 2006. Multiple detachment levels and their control on fold styles in the compressional domain of the deepwater west Niger Delta. *Basin Research*, vol. **18**, p435-450.

Briggs, S.E., Davies, R.J., & Cartwright, J.A., 2009. Crustal structure of the deepwater west Niger Delta passive margin from the interpretation of seismic reflection data. *Marine and Petroleum Geology*, vol. **26**, no. 6, p936-950.

Brouwer, F., 2007. Creating a good steering cube. *Opendtech* reference manual, p1-15.

Brown, A.R., Edwards, G.S., & Howard, R.E., 1987. Fault slicing – a new approach to the interpretation of fault detail. *Geophysics*, vol. **52**, no. 10, p1319-1327.

Brown, S.R., & Scholtz, C.H., 1985a. Broad bandwidth study of the topography of natural rock surfaces. *Journal of Geophysical research*. vol. **90** (B40), p12572-12582.

Brown, A.R., 2004. Interpretation of three-dimensional seismic data. *AAPG Memoir/ SEG Investigations in Geophysics*, no. 9.

Burke, K.C.B., 1972. Longshore drift, submarine canyons, and submarine fans. *AAPG Bulletin*, vol. **56**, p1975-1983.

Butler, W.H., 1987. Thrust sequences. Journal of the Geological Society, London, vol. **144**, p619-634.

Calladine, C.R., 1983. Theory of Shell Structures: Cambridge, Cambridge University Press, 763 p.

Candela, T., Renard, F., Bouchon, M., Brouste, A., Marsan, D., Schmittbuhl, J., & Voisin, C., 2009. Characterization of fault roughness at various scales: Implications of three-dimensional high resolution topography measurements. *Pure and Applied Geophysics*, DOI 10.1007/s00024-009-0521-2, p1-35.

Carena, S., & Suppe, J., 2002. Three-dimensional imaging of active structures using earthquake aftershocks: the Northridge thrust, California. *Journal of Structural Geology*, vol. **24**, p887-904.

Chester, F.M., & Chester, J.S., 2000. Stress and deformation along wavy frictional faults. *Journal of Geophysical Research*, vol. **105**, p23, 421-23, 430.

Chopra, S., & Marfurt, K.J., 2005. Seismic attributes – A historical perspective. *Geophysics*, vol. **70**, no. 5, p3SO-28SO.

Childs, C., Manzocchi, T., Walsh, J.J., Bonson, C.G., Nicol, A., & Schopfer, M.P.J., 2009. A geometric model of fault zone and fault rock thickness variations. *Journal of Structural Geology*, vol. **31**, p117-127.

Chopra, S., & Marfurt, K.J., 2006. Seismic attributes – a promising aid for geologic prediction. *CSEG* Recorder. p110-121.

Chopra, S., & Marfurt, K.J., 2007. Volumetric curvature attributes for fault/fracture characterization. *First Break* vol. **25,** p1-12.

Chopra, S., & Marfurt, K.J., 2009. Detecting stratigraphic features via cross-plotting of seismic discontinuity attributes and their volume visualization. *The Leading Edge*, vol. **28,** no. 12**,** p1422-1426.

Chopra, S., & Marfurt, K.J., 2007. Multi-spectral volumetric curvature adding value to 3D seismic data interpretation. CSPG/CSEG Convention, Calgary, Canada.

Chopra, S., & Marfurt, K.J., 2010. Integration of coherence and volumetric curvature images. *The Leading Edge*, vol. **29**, no. 9, p1092-1107.

Chopra, S., & Marfurt, K.J., 2011. Coherence and curvature attributes on preconditioned seismic data. *The Leading Edge*, vol. **30**, no. 4, p386-393.

Chopra, S., & Marfurt, K.J., 2011. Acquisition footprint removal for better fault and curvature attributes. Search and Discovery article no. 40719, p1-5.

Cobbold, P.R., Clark, B.J., & Loseth, H. 2009. Structural consequences of fluid overpressures and seepage forces in the outer thrust belt of the Niger Delta. *Petroleum Geoscience*, vol. **15**, no. 1, p3-15.

Connors, C.D., Denson, D.B., Kristiansen, G., & Angstadt, D.M., 1998. Compressive anticlines of the mid-outer slope, central Niger Delta. *AAPG Bulletin*, vol. **82**, p1903.

Cooke-Yarborough, P., 1994. Analysis of fractures yields improved gas production from Zeistein carbonates, Hewett Field, UKCS. *First Break*, **12**, p243-252.

Cooper, A., & Trayner, P., 1986. Thrust-surface geometry: implications for thrust-belt evolution and cross-sectional balancing techniques. *Journal of Structural Geology*, vol. **8**, p305-312.

Corredor, F., Shaw, J.H., & Bilotti, F., 2005. Structural styles in the deep-water fold and thrust belts of the Niger Delta. *AAPG Bulletin*, vol. **89**, p753-780.

Damuth, J.E., 1994. Neogene gravity tectonics and depositional processes on the deep Niger delta continental margin. *Marine and Petroleum Geology*, vol**.11**, no. 3, p320-346.

De Rooij, M., & Tingdahl, K, M., 2002. Meta-attributes; the key to multi-volume, multi-attribute interpretation. *The Leading Edge*, vol**. 21**, no. 10, p1050-1053.

Dee, S., Freeman, B., Yielding, G., Roberts, A., & Bretan, P., 2005. Best practices in structural geological analysis. *First Break*, vol. **23**, p49-54.

Dee, S.J., Yielding, G., Freeman, B., Healy, D., Kusznir, N.J., Grant, N., & Ellis, P., 2007. Elastic dislocation modelling for the prediction of small-scale fault and fracture characteristics. *In*: LONERGAN, L., JOLLY, R.J.H., RAWNSLEY, K., & SANDERSON, D.J. (eds.): Fractured reservoirs. *Geological Society*, London, vol. **270**, p139-155.

Doust, H., & Omatsola, E., 1990. Niger Delta divergent/passive margin basins, in J.D. Edwards and P.A. Santogrossi eds., *AAPG memoir* vol. **48**, p201 – 238.

Drozdweski, G., Douremann, O., Kunz, E., & Wrede, V., 1980. Beitraage zur tiefenteknic des Ruhrkarbons. Geolisches Landesmt Nordrhein-Westphalan, Krefeld.

Drozdweski, G., Eugel, H., Wolk, R., & Wrede, V., 1985. Beitraage zur tiefentektonik westdeutscher steinkholenlagerstaatten. Geolischen Landesmt Nordehein-Westphalen, Krefeld.

Dunham, E.M., Belanger, L., & Kozdon, J.E., 2011. Earthquake ruptures with strongly rate-weakening friction and of-fault plasticity, 2: Non-planar faults. *Bulletin of the Seismological Society of America*, in press.

Dutzer, J-F., Basford, H., & Purves, S., 2009. Investigating fault sealing potential through fault relative seismic volume analysis. *Petroleum Geology Conference*, London.

Ekweozor, C.M., & Doukoru, E.M., 1994. Northern delta depobelt portion of the Akata-Agbada petroleum system-from source to trap. *AAPG Memoir*, vol. **45**, p599-613.

EllioT, D., 1976. Energy balance and deformation mechanisms of thrust sheets. *Royal Society of London Philosophical Transactions*, Ser, A vol. **283**, p289-312.

Emery, K.O., Uchupi, E., Phillips, J., Brown, C., & Mascle, J., 1975. Continental margins off western Africa: Angola to Sierra Leone. *AAPG Bulletin*, vol. **59**, p2209-2265.

Erickson, S.G., Strayer, L.M., & Suppe, J., 2001. Initiation and reactivation of faults during movement over a thrust-ramp: numerical mechanical models. *Journal of Structural Geology*, vol. **23**, p11-23.

Ericsson, J.B., & McKean, H. C., & Hooper, R.J., 1998. Facies and curvature controlled 3D fracture models in Cretaceous carbonate reservoir, Arabian Gulf. *In*: JONES, G., FISCHER, Q., & KNIPE, R.J. (eds) Faulting, fault sealing and fluid flow in hydrocarbon reservoirs. *Geological Society*, London, Special Publications, vol. **147**, p299-312.

Evamy, B.D., Haronboure, J., Kamerling, P., Knaap, W.A., Mollay, F.A., & ROWLANDS, P.H., 1979. Hydrocarbon Habitat of Tertiary Niger Delta. *AAPG Bulletin*, vol.**62**, p277 – 298.

Faulkner, D.R., Lewis, A.C., Rutter, E.H., 2003. On the internal structure and mechanics of large strike-slip fault zones: field observations of the Carboniferous fault in southeastern Spain. *Tectonophysics*, vol. **367**, p235-251.

Ferrill, D.A., Stamatakos, J.A., & Simms, D., 1999. Normal fault corrugation: implications for growth and seismicity of active normal faults: *Journal of Structural. Geol*ogy, vol. **21**, p. 1027-1038.

Fisher, M.P., & Wilkerson, M.S., 2000. Predicting the orientation of joints from fold shapes: results of pseudo-three-dimensional modelling and curvature analysis. *Geology* vol. **28**, p15-18.

Fisk, J.C., & Marfurt, K.J., 2010. Correlating heterogeneous production to seismic curvature attributes in an Australian coalbed methane field. *SEG* Annual meeting Denver, Colorado, p2323-2328.

Fossen, H., 2010. Structural Geology. Cambridge University Press, Cambridge, UK. p151-188.

Fox, F.G., 1959. Structure and accumulation of hydrocarbon in southern foothills, Alberta, Canada. *AAPG Bulletin*, vol. **43**, p992-1025.

Gauss, C. F., 1827. Disquitiones Generales circa Superficies Curvas" (in Latin). *Comm. Soc. Gott.* **6**. ("General Discussions about Curved Surfaces").

Gay, A., Lopez, M., Cochonat, P., Sultan, N., Cauquil, E., & Brigaud, F., 2003. Sinuous pockmark belt as an indicator of a shallow buried turbiditic channel on the lower slope of the Congo basin, West African margin, Geological Society of London Special Publication, vol. **216,** p173-189.

Gillespie, P.A., 1991. Structural analysis of faults and folds with examples from the south Wales coalfield and Ruhr coalfield. Unpublished PhD thesis, University of Wales.

Gillespie, P.A., Howard, C., Walsh, J.J., & Watterson, J., 1993. Measurement and characterization of spatial distributions of fractures. *Tectonophysics* **226**, p113-141.

Ghosh, K., & MitrA, S., 2009. Structural controls of fracture orientations, intensity, and connectivity, Teton anticline, Sawtooth Range, Montana. *AAPG Bulletin*, vol. **93**, p995-1014.

Gross, M.R., Bahat, D., & Berker, A., 1997. Relationships between faulting and jointing based on fracture-spacing ratios and fault slip profiles; a new method to estimate strain in layered rocks. *Geological Society of America*, vol. **25**, no. 10, p887-890.

Gross, M.R., 1995. Fracture partitioning: Failure mode as a function of lithology in the Monterey Formation of coastal California. *Geological Society of America Bulletin*. vol. **107**, p779-792.

Gudmundsson, A., & Geyer, A., 2006. Effects of damage-zone thickness on fault displacement. TSK 11, Gottingen, p1-2.

Haberman, S.A., Rolon, M.A., Cavero, J., Sancho, V., Mendez, M., BENEDETTO, L., GOYA, F., VERDUR, H., BELLOSI, E., & CRANDALL, R., 2009. Detailed structural interpretation using 3D seismic curvature analysis, Neuquen and San Jose Basins, Argentina. *AAPG* Annual Convention, Denver, Colorado.

Haussegger, S., Kurz, W., Rabitsch, R., Kiechl, E., & Brosch, F., 2009. Analysis of the internal structure of a carbonate damage zone: Implications for the mechanism of fault breccia formation and fluid flow. *Journal of Structural Geology*, p1-14.

Hakami, A., Marfurt, K., & AL-Dossary, S., 2004. Curvature attributes and seismic interpretation: Case study from Forth Worth Basin, Texas, U.S. 7th Annual International Meeting, *SEG*, Expanded Abstracts, p544-547.

Hart, B.S., Pearson, R.A., & Rawling, G.C., 2002. 3D seismic horizon-based approaches to fracture-swarm sweet spot definition in tight-gas reservoirs. *The Leading Edge*, vol. **21**, p28-35.

Helmore, S., Plumley, A., & Humberstone, I., 2004. 3D seismic volume curvature attributes aid structural and stratigraphic interpretation, *PETEX* conference, London.

Hennings, P.H., Olson, J.E., & Thompson, L.B., 2010. Combining outcrop data and three-dimensional structural models to characterize fractured reservoirs: an example from Wyoming. *AAPG Bulletin*, vol. **84**, p830-849.

Hennings, A.T., Martin, R., & Paton, G., 2010. Data conditioning and seismic attribute analysis in the Eagle Ford Shale Play: Examples from Sinor Ranch, Live Oak County, Texas. *SEG Annual Meeting*, Denver, p1297-1301.

Higgins, S., Davies, R.J., & Clarke, B., 2009. Antithetic fault linkages in deep water fold and thrust belt. *Journal of Structural Geology*, vol. **29**, p1900-1914.

Hovland, M., Clenell, B., Gallager, J.W., & Lekvam, K., 1997. Gas hydrate and free gas volumes in marine sediments: Example from the Niger Delta front. *Marine and Petroleum Geology*, vol. **14**, no. 3, p245-255.

Iacopini, D., & Butler, R.W.H., 2011. Imaging deformation in submarine thrust belts using seismic attributes. *Earth & Planetary Science Letters*, vol. **302**, p414-422.

Imber, J., Childs, C., Nell P.A.R., Walsh, J.J., Hodgetts, D., & Flint, S., 2003. Hanging wall fault kinematics and footwall collapse in listric growth fault systems. *Journal of Structural Geology*, vol. **25**. p197-208.

Jackson, J., & McKenzie, D., 1999. A hectare of fresh striations on the Arkitsa Fault, central Greece. *Journal of Structural Geology*, vol. **21**, no. 1, p1-6.

Jackson, J.A., Norris, R., & Youngman, J., 1996. The structural evolution of active fault and fold systems in Central Otago, New Zealand: evidence revealed by drainage patterns. *Journal of Structural Geology*, vol. **18** (2/3), p217-234.

Jev, B.I., Kaars-Sijpesteijn, C.H., Peters, M.P.A.M, Watts, N.L., & Wilkie, J.T., 1993. Akaso field, Nigeria: Use of integrated 3-D seismic, fault slicing, clay smearing and RFT pressure data on fault trapping and dynamic leakage. *AAPG Bulletin*, vol. **77**, p1389-1404.

John, B.E., 1987. Geometry and evolution of a mid-crustal extensional fault system: Chemehuevi Mountains, southeastern California. From Coward, M.P., Dewey, J.F., & Hancock, P.L., (eds), 1987, Continental Extensional Tectonics, *Geological Society Special Publication*, no. 28, p313-335.

Jones, R.R., Kokkalas, S., McCaffrey, K.J.W., Imber, J., Clegg, P., Healy, D., WRIGHT, T.D., & TURNER, J.P., 2006. Quantification of fault-plane curvature and surface heterogeneity using terrestrial laser-scanning. Geophysical Research Abstracts, *EGU*, vol. **8**, 09326.

Jones, R.R., Kokkalas, S., P., Healy, D., 2006. Curvature of fault planes and heterogeneity of slip patches. American Geophysical Union Abstract, *AGU*, T11C-0453.

Jones, R.R., Kokkalas, S., & McCaffrey, K.J.W, 2009. Quantitative analysis and visualization of nonplanar fault surfaces using terrestrial laser scanning (LIDAR) – The Arkitsa fault, central Greece, as a case study. *Geosphere*, vol**. 5**, no. 6, p465-482.

Kaven, J.O., & Pollard, D.D., 2010. Three-dimensional geometry of a fault slip surface: implications for the mechanics of non-planar faults. *Journal of Geophysical Research*, submitted.

Keating, D.P., & Fischer, M.P., 2008. An experimental evaluation of the curvature-strain relation in fault-related folds. *AAPG Bulletin*, vol. **92**, no. 7, p869-884.

Kim, Y., Peacock, D.C.P., & Danserson, P.J., 2004. Fault damage zone. *Journal of Structural Geology*, vol. **26**, p503517.

Kim, Y., & Sanderson, D.J., 2005. The relationship between displacement and length of faults: a review. *Earth-Sciences Reviews*, vol. **68**, p317-334.

Klein, P., Richard, L., & James, H., 2008. 3D curvature attributes: a new approach for seismic interpretation. *First Break*, vol. **26**, p105-111.

Knox, G.J., & Omatsola, E.M., 1989. Development of the Cenozoic Niger Delta in terms of the "Escalator Regression" model and impact on hydrocarbon distribution. *In*: van der Linden, W.J.M., Cloetingh, S.A.P.L., Kaasschieter, J.P.K., & van der Gun, J.A.M. (eds) *Proceedings* KNGMG *symposiums coastal lowlands, geology and geotechnology*. Kluwer Academic Publishers, Amsterdam, p181-202.

Kokkalas, S., Jones, R.R., McCaffrey, K.J.W., & Clegg, P., 2007. Quantitative fault analysis at Arkitsa, Central Greece, using Terrestrial laser-scanning ("LiDAR"). *Bulletin of the Geological Society of Greece*, vol. **XXXVII**, p1-14.

Kostakioti, A., Xypolias, P., Kokkalas, S., & Doutsos, T., 2004. Quantitative analysis of deformation along the fault damage zone of the Klimatia thrust (NW Greece, Ionian Zone). *Bulletin of the Geological Society of Greece*, vol. **XXXVI**, p1643-1651.

Krueger, S.W., & Grant, N.T., 2006. Evolution of fault-related folds in the contractional toe of the deepwater Niger Delta, Paper presented at the *AAPG Annual Convention* Houston, Texas, 2006.

Kulke, H., 1995. Regional petroleum geology of the world, part II, Africa, America, Australia, and Antactica. Berlin, Gebruder Borntraeger, p143-172.

Lee, J., & Bruhn, R.L., 1996, Structural anisotropy of normal fault surfaces. *Journal of Structural Geology*, vol. **18**, no. 8, p1043-1059.

Lee, S., Wolberg, G., & Shin, S.Y., 1997. Scattered data interpolation with multilevel b-splines. *IEEE transactions on visualization and computer graphics*, no. 3, vol. **2**, p228-244.

Lisle, R.J., 1994. Detection of zones of abnormal strains in structures using Gaussian curvature analysis. *AAPG Bulletin*, vol. **78**, p1811-1819.

Lisle, R.J., & Robinson, J.M., 1995. The Mohr circle for curvature and its application to fold description: *Journal of Structural Geology*, vol. **17**, p739-750.

Lisle, R.J., & Martinez, F., 2005. Structural analysis of seismically mapped horizons using the developable surface model, *AAPG Bulletin*, vol. **89**, p839-848.

Lohr, T., 2007. Seismic and sub-seismic deformation on different scales in the NW German basin. PhD thesis, Freie Universitat Berlin.

Lohr, T., Krawczyk, C.M., Oncken, O., & Tanner, D.C., 2008. Evolution of a fault surface from 3D attribute analysis and displacement measurements. *Journal of Structural Geology*, vol. **30**, no. 6, p690-700.

Luo, Y., Higgs, W.G., & Kowalik, W.S., 1996. Edge detection and stratigraphic analysis using 3D seismic data. 66th Annual International Meeting, *Society of Exploration Geophysicists*, Expanded Abstracts, p324-327.

Mai, H., Marfurt, K.J., & Chavez-Perez, S., 2009. Coherence and volumetric curvatures and their spatial relationships to faults and folds, an example from Chicontepec basin, Mexico. 78th Annual International Meeting of the SEG, Expanded Abstract.

Mai, T.M., 2010. Seismic attribute analysis and its application on data from Canada, Mexico, USA and Vietnam. Unpublished PhD thesis, University of Oklahoma, USA.

Maloney, D., Davies, R., Imber, J., Higgins, S., & King, S., 2010. New insights into deformation mechanisms in the gravitationally driven Niger Delta deep-water fold and thrust belt. *AAPG Bulletin*, vol. **94**, no. 9, p1401-1424.

Marchal, D., Guiraud, M., & Rives, T., 2003. Geometric and morphologic evolution of normal fault planes and traces from 2D and 3D data. *Journal of Structural Geology*, vol. **25**, p135-158.

Marfurt, K.J., Kirlin, R.L., Farmer, S.L., & Bahorich, M.S., 1998. 3D seismic attributes using a semblance based algorithm. *Geophysics*, vol. **62**, p1150-1165.

Marfurt, K.J., Sudhaker, V., Gersztenkorn, A., Crawford, K.D., & Nissen, S.E., 1999. Coherency calculations in the presence of structural dip. *Geophysics*, vol. **64**, p104-111.

Marfurt, K.J., 2006. Seismic attribute mapping of structure and stratigraphy, SEG/EAGE DISC course.

Martel, S.J., Pollard, D.D., & Seagal, P., 1988. Development of simple fault zone in granitic rock, Mount Abbot quadrangle, Sierra Nevada, California. *Geological Society of America Bulletin*, vol. **100**, p1451-1465.

Martel, S.J., 1999. Mechanical controls on fault geometry. *Journal of Structural Geology*, vol. **21**, p585-596.

Mascle, J., 1976. Submarine Niger Delta structural framework. *Journal of Nigeria Min. Geol. Metal. Soc*. vol. **13**, p12-28.

Masafero, L.J., Bulnes, M., Poblet, J., & Casson, N., 2003. Kinematic evolution and fracture of the Valle Morado structure inferred from 3-D seismic data, Salta province, northwest Argentina. *AAPG Bulletin*, vol. **87**, p1083-1104.

McClay, K.R., & Ellis, P.G., 1987. Geometries of extensional fault systems developed in model experiments. *Geology*, vol. **15**, p341-344.

Morgan, R., 2003. Prospectivity in utltradeep water: the case for petroleum generation and migration within the outer parts of the Niger Delta apron. In: ARTHUR, T.J., McGREGOR, D.S., & CAMERON, N.R. (eds) *Petroleum Geology of Africa: new themes and developing technologies. Geological Society*, London, Special Publications, vol. **207**, p151-164.

Morley, C.K., 2003. Mobile shale related deformation in larged deltas developed on passive and active margins. *Geological Society* London, Special Publications, vol. **216**, p335-357.

Murray, G.H., 1968. Quantitative fracture study – Spanish Pool, Mckenzie County, North Dakota. *AAPG Bulletin*, vol. **52**, p57-65.

Mynatt, I., Bergbauer, S., & Pollard, D.D., 2007. Using differential geometry to describe 3-D folds. *Journal of Structural Geology*, vol. **29**, p1256-1266.

Narr, W., 1991. Fracture density in the deep subsurface: Techniques with applications to Point Arguello oil field. *AAPG Bulletin*, **75**, p1300-1323.

National Oceanic And Atmospheric Administration (http://maps.ngdc.noaa.gov/viewers/bathymetry)

Neetham, T., Yielding, G., & Freeman, B., 1996. Analysis of fault geometry and displacement patterns. *In*: Buchanan, P.G., & Nieuwland, D.A. (eds), Modern Developments in Structural Interpretation, Validation and Modelling, *Geological Society of London*, Special Publications, vol. **99**, p189-199.

Nissen, S.E., 2002. Seismic attributes for the explorationist. Kansas Geological Survey Open-file Report. 2002-49.

Nissen, S.E., Carr, T.R., Marfurt, K.J., & Sullivan, E.C., 2007. Using 3D seismic volumetric curvature attributes to identify fracture trends in a depleted Mississippian carbonate reservoir: Implications for assessing candidates for CO_2 sequestration. *In*: Grobe, M., Pashin, J., & Dodge, R. (eds). Carbon Dioxide sequestration in geological media-state of the art. Special publication, *AAPG*.

Nyquist, H., 1928. Thermal agitation of electrical charges in conductors.

Osborne, M.J., & Swarbrick, R.E., 1998. Mechanism for generating overpressure in sedimentary basins: a re-evaluation. *AAPG Bulletin*, **81**, p1023-1041.

Peacock, D.C.P., Knipe, R.J., & Sanderson, D.J., 2000. Glossary of normal faults. *Journal of Structural Geology*, vol. **22**, p291-305.

Pearce, M.A., Jones, R.R., Smith, S.A.F., McCaffrey, J.W., & Clegg, P., 2006. Numerical analysis of fold curvature using data acquired by high-precision GPS. *Journal of Structural Geology*, **28**, p1640-1646.

Pearce, M.A., Jones, R.R., Smith, S.A.F., & McCaffrey, K.J.W., 2011. Quantification of fold curvature and fracturing using terrestrial laser scanning. *AAPG Bulletin*, vol. **95**, no. 5, p1640-1646.

Prapasanobon, N., & Pigott, J.D., 2008. 3D seismic imaging of fault plane geomorphology: Examples from offshore Myanmar, Gulf of Thailand and onshore Maracaibo Basin, Venezuela. Extended abstract, *Proceedings of the International symposia on geoscience resources and environments of Asian terranes* (GREAT 2008).

Purves, S., Admasu, F., Basford, H., Dutzer, J.F., Papouin, M., & Henderson, J. 2010. Determining fault seal indicators from 3D seismic.

Renard, F., Voisin, C., Marsan, D., & Schmittbuhl, J., 2006. High resolution 3D laser scanner measurements of a strike-slip fault quantify its morphological anisotropy at all scales. *Geophysical Research Letters*, vol. **33**, L04305.

Pete, F.G., & Sahota, T.S., 1985. Surface curvature as a measure of image texture: IEEE Transactions on pattern analysis and machine intelligence. vol. **PAMI-7**, p734-738.

Reijers, T.J.A., Peters, S.W., & Nwajide, C.S., 1997. The Niger Delta basin. *In*: SELLEY, R.C., (ed), African basins, Sedimentary basins of the world 3. *Elsevier*, p151-172

Resor, P.G., & Meer, V.E., 2009. Slip heterogeneity on a corrugated fault. *Earth & Planetary Science Letters*, vol. **288**, p483-491.

Rijks, E.J.H., & Jauffred J.C.E.M., 1991. Attribute extraction: An important application in any detailed 3-D interpretation study: *The Leading Edge*, **10**, p11-19.

Power, W.L., Tullis, T.E., Brown, S.R., Boitnott, G.N., & Scholtz, C.H., 1987. Roughness of natural fault surfaces. *Geophysical Research Letters*, vol. **14**, no. 1, p29-32.

Rowan, M.G., 1997. Three-dimensional geometry and evolution of a segmented detachment fold, Mississippi fan foldbelt, Gulf of Mexico. *Journal of Structural Geology*, vol. **19** (3/4), p463-480.

Rowan, M.G., Peel, F.J., & Vendiville, B.C., 2004. Gravity-driven fold belts on passive margins. In*:* McClay, K.R., ed., Thrust tectonics and hydrocarbon systems. *AAPG Memoir*, vol. **82**, p157-182.

Roberts, A., 2001. Curvature attributes and their application to 3D interpreted horizons. *First Break*, vol. **19**, p85-99.

Sagy A., Brodsky, E.E., & Axen, G.J., 2007. Evolution of fault-surface roughness with slip. *Geology*, vol. **38,** no. 3, p283-286.

Sagy, A., & Brodsky, E.E., 2009. Geometric and rheological asperities in an exposed fault zone. *Journal of Geophysical Research*, vol. **114**, p1-15.

Samson, P., & Mallet, J.L., 1997. Curvature analysis of triangulated surfaces in structural geology. *Mathematical Geology*, vol. **29**, p391-412.

Smith, W.H.F., & Sandwell, D.T., 1997. Global sea floor topography from satellite altimetry and ship depth soundings. *Science*, vol. **277**, p1956-1962.

Scholz, C.N., 1990. The mechanics of Earthquake and Faulting. 2nd ed., p471, Cambridge University Press, Cambridge, UK.

Scultz, R.A., Okubo, C.H., & Wilkins, S.J., 2006. Displacement-length scaling relations for faults on terrestrial planets. *Journal of Structural Geology*, vol. **18**, p2182-2193.

Schultz-Ela, D.D, & Yeh, J., 1992. Predicting fracture permeability from bed curvature. *Proceedings – Symposium on Rock Mechanics*, Santa Fe, New Mexico.

Serrano, I., Lacazette, A., Blumentritt, C., Sullivan, E.C., Marfurt, K.J., & Murphy, M., 2003. Unravelling structural development and fracture distribution at Dollarhide Field, West Texas with new seismic attribute images (abs). *Geological Society of America* abstract with programs, vol. **35**, no. 6, p177.

Sheriff, R.E., & Geldert, L.P., 1995. Exploration seismology. Cambridge University Press. p477-475.

Sheriff, R.E., 2006. Encyclopedic Dictionary of Applied Geophysics. *Society for Exploration Geophysicists*, Tulsa, Oklahoma.

Shipton, Z.K., & Cowie, P.A., 2001. Damage zone and slip-surface evolution over μm to km scales in high porosity Navajo sandstone, Utah. Journal of Structural Geology, vol. **23**, p1825-1844.

Short, K.C., & Staeuble, A.J., 1967. Outline of geology of Niger Delta. *AAPG Bulletin*, vol. **51**, p761 – 779.

Sigismondi, M.E., & Soldo, J.C., 2003. Curvature attributes and seismic interpretation: Case studies from Argentina Basin. *The Leading Edge*, vol. **22**, no. 11, p1122-1126.

Smith, W.H.F., & Sandwell, D.T., 1997, Global seafloor topography from satellite altimetry and ship depth soundings: *Science*, v. **277**, p1957-1962.

Sterns, D.W., 1964. Macro fracture patterns on Teton anticline, northwest Montana. *AGU Transactions*, vol. **45**, p107-108.

Sterns, D.W., & Friedman, M., 1972. Reservoirs in fractured rocks. *In*: KING, R.E. (ed) Stratigraphic oil and gas fields – Classification, exploration methods and case histories. *AAPG Tulsa Memoirs*, vol. **16**, p82-106.

Stewart, S.A., & Podolski, R., 1998. Curvature analysis of gridded geological surfaces. *In*: Coward, M.P., DALTABAN, T.S., & JOHNSON, H. (eds) Structural Geology in Reservoir Characterization. *Geological Society*, London, Special Publications, vol. **127**, p133-147.

Stewart, S.A., & Wynn, T.J., 2000. Mapping spatial variation in rock properties in relation to scale-dependent structure using spectral curvature. *Geology*, vol. **28**, p691-694.

Streit, J.E., & Hillis, R.R., 2004. Estimating fault stability and sustainable fluid pressures for underground storage of CO2 in porous rock. *Energy* **29**, p1145-1456.

Sullivan, E.C., Marfurt, K.J., Lacazette, A., & Ammerman, M., 2006. Application of new seismic attributes to collapsed chimneys in the Fort Worth Basin. *Geophysics*, vol. **71**, pB111-119.

Sultan, N., Marsset, B., Ker, S., Marsset, T., Voisset, M., Vermant, A.M., Bayon, G., Cauquil, E., Adamy, J., Colliat, L., & Drapeau, D., 2010. Hydrate dissolution as a potential mechanism for pockmarks formation in the Niger Delta. *Journal of Geophysical Research*, vol. **115**, B08108, P1-33.

Suppe, J., Connors, C.D., & Zhang, Y., 2004. Shear fault-bend folding. In*:* McCLAY, K.R., (ed), Thrust tectonics and hydrocarbon systems. *AAPG Memoir*, vol. **82**, p303-323.

Suppe, J., 1984. Seismic interpretation of compressively reactivated normal fault near Hsinchu, western Taiwan. *Petroleum Geology of Taiwan*, no. 20, p85-96.

Suppe, J., & Medwedeff, D.A., 1990. Geometry and kinematics of fault-propagation folding: *Eclogae Geologicae Helvetiae*, vol. **83** (Laubscher vol.), p409-454.

Taner, M.T., Schuelke, J.S., O'doherty, R., & Baysal, E., 1994. Seismic attributes revisited. 64th Annual International Meeting, *SEG*, Expanded Abstracts, p1104-1106.

Thibaut, M., Gratier, J.P., Leger, M., & Morvan, J.M., 1996. An inverse method for determining three-dimensional fault geometry with thread criterion: application to strike-slip and thrust faults (Western Alps and California). *Journal of Structural Geology*, vol. **18**, p1127-1138.

Thomas, A., Mallet, L.J., & De Beaucourt. F., 1974. An analytic method for localizing structural discontinuities in rock mass. *Proceedings of the Congress of the International Society for Rock Mechanics.*

Tingdahl, K., 2003. Improving seismic chimney detection using directional attributes. *Developments in Petroleum Science*, vol. **51**, p157-173.

Tingdahl, K., & de Groot, P., 2003. Post-stack dip and azimuth processing. *Journal of Seismic Exploration*, vol. **12**, p113-126.

Tingdahl, K.M., & de Rooij, M., 2005. Semi-automatic detection of faults in 3-D seismic data. *Geophysical prospecting*, vol**. 53**, p533-542.

Thomas, A., Mallet, L.J., & De Beaucourt. F., 1974. An analytic method for localizing structural discontinuities in rock mass. *Proceedings of the Congress of the International Society for Rock Mechanics.*

Traptester Course Manual, 2010.

Twiss R., & Moores E., 1992. Introduction to faults, normal faults, strike-slip faults. Structural Geology, W.H. Freemans and Company, New York, pp. 51- 119.

Van der PAL, R.C., 1988. Fault slicing: a use of three-dimensional seismic data for fault analysis, practical aspects. Research report, Shell Research Rijswijk and Delft University of Technology, Faculty of Mining and Petroleum Engineering, Section of Applied Geophysics, p1-28.

van Gent, H., Back, S., Urai, J.L., & Kukla, P., 2010. Small-scale faulting in the Upper Cretaceous of the Groningen block (The Netherlands): 3D seismic interpretation, fault plane analysis and regional paleostress. *Journal of Structural Geology*, vol. **32**, p537-553.

Wagner, L., Lohr, T., Tanner, D.C., Krawczkyk, M., & Oncken, O., 2006. Structural investigation and strain analysis of a polyphase flower structure in the Lower Saxony Basin, Germany. *TSK* 11 Gottingen.

Walsh, J.J., & Watterson, J., 1991. Geometric and kinematic coherence and scale effects on normal fault systems. In: Yielding, G., & Freeman, B. (eds). The geometry of Normal faults. *The geological Society*, London Special Publications, vol. **56**, p193-203.

Weber, K.J., & Daukoru, E.M., 1975. Petroleum Geology of the Niger delta: *9th World Petroleum Congress Proceedings*, vol. **2**, p209-221.

White, N.J., Jackson, J.A., & McKenzie, D.P., 1986. The relationship between the geometry of normal faults and that of sedimentary layers in their hanging walls. *Journal of Structural Geology*, vol. **8**, p.897-909.

Whiteman, A., 1982. Nigeria: Its Petroleum Geology, Resources and Potential. London, Graham and Trotman.

Williams, G., & Vann, I., 1987. The geometry of listric normal faults and deformation in their hanging walls. *Journal of Structural Geology*, vol. **9**, p789-795.

Williams, G., & Chapman, T., 1983. Strains developed in the hanging walls of thrusts due to their slip/propagation rate: dislocation model. *Journal of Structural Geology*, vol. **5**, p563-571.

Wood, G.H., Trexler, J.P., & Kehn, T.M., 1969. Geology of the west0central part of the Southern Anthracite field and adjoining areas, Pennsylvania. *Geology Survey*, Professional paper.

Woodcock, N.H., Omma, J.E., & Dickson, J.A., 2006. Chaotic breccias along the Dent fault, NW England: Implosions or collapse of a fault void. *Journal of the Geological Society*, London, vol. **163**, p431-432.

Woodcock, N.H., Dickson, J.A.D., Tarasewicz, J.P.T., 2007. Transient permeability and reseal hardening in fault zones: evidence from dilation breccias textures. In: Geological Society of London Special Publications, vol. **270** p43–53.

Wright, T.D., & Turner, J.P., 2006. Characterization of 3D fault curvature. *European Geophysical Union conference abstracts*: Vienna.

Wright, T.D., 2008. Characterization of fault curvature: Implications for wall rock deformation and the enhancement of automated fault interpretation software. Unpublished PhD thesis, University of Birmingham, UK.

Wu, S., & Bally, A.W., 2000. Slope tectonics – comparison and contrasts of structural styles of salt and shale tectonics of the northern Gulf of Mexico with shale tectonics of offshore Nigeria in Gulf of Guinea. *In*: Mohriak, W., & Talwani, M. (eds). Atlantic rifts and continental margins, *American Geophysical Union*, p151 – 172.

Wynn, T.J., & Stewart, S.A., 2003. The role of spectral curvature mapping in characterizing subsurface strain distributions. *From*: AMEEN, M. (ed) *Fracture and* In-situ Stress Characterization of Hydrocarbon Reservoirs. *Geological Society*, London, Special Publications, vol**. 209**, p127-143.

Yamada, Y., & McClay, K., 2003a. Application of geometric models of inverted listric fault systems in sandbox experiments. Paper 1: 2-D hanging wall deformation and section restoration. *Journal of Structural Geology*, vol. **25**, p1551-1560.

Yamada, Y., & McClay, K., 2003b. Application of geometric models of inverted listric fault systems in sandbox experiments. Paper 2: Insights for possible along strike migration of material during 3-D hanging wall deformation. *Journal of Structural Geology*, vol. **25**, p1331-1336.

Yielding, G., Freeman, B., & Neetham, D.T., 1997. Qualitative Fault Seal Prediction. *AAPG Bulletin*, vol. **81**, no. 6, p897-917.